

# Development and applications of opposed migration aerosol classifiers (OMACs)

Thesis by  
Wilton Mui

In Partial Fulfillment of the Requirements for the  
degree of  
Doctor of Philosophy



CALIFORNIA INSTITUTE OF TECHNOLOGY  
Pasadena, California

2017  
(Defended January 4, 2017)

© 2017

Wilton Mui

ORCID: 0000-0003-3065-1296

All rights reserved



## ACKNOWLEDGEMENTS

I would firstly like to thank my advisor, Professor Richard C. Flagan. He has challenged me greatly and I have become a stronger person for it. Richard is a man of exceptional scientific integrity. He has been a patient and moderating force of perfection over expediency.

I would secondly like to thank the other members of my thesis committee: Professor John H. Seinfeld, Professor Jesse L. Beauchamp, and Professor Mitchio Okumura. I appreciate the opportunities for collaboration with their research groups, as well as for their guidance and advocacy through my thesis progress.

I would thirdly like to thank my colleagues at Caltech. I thank the members of the Flagan and Seinfeld groups for their emotional and scientific support, especially Kelvin Bates, Amanda Grantz, Andrew Metcalf, Paula Popescu, Katherine Schilling, Rebecca Schwantes, Lindsay Yee, Xerxes López-Yglesias, and Xuan Zhang.

Many thanks are extended to my early research mentor, Andrew Downard. His patience in teaching me the necessary laboratory and instrument design skills (while he was preoccupied with his own thesis defense preparation) was his greatest gift to me.

Daniel Thomas was one of my early collaborators, and I appreciate all his effort and patience with me while we were demonstrating the usefulness of my instrument outside of the aerosol field.

Jill Craven and Matt Coggon were my colleagues during the 2013 aircraft field campaign in Monterey, and my experience with them in stressful situations brought us closer together. I will fondly remember Jill for the positivity and support she always thrust upon others.

Johannes Leppä was a postdoctoral scholar during the latter half of my journey, and I thank him not only for his academic collaboration, but also for his providing a daily dose of social relief from research.

To my younger labmate, Huajun Mai, I thank him for the immense help he provided with his mathematical talent that made some of this thesis possible. I wish him nothing but happiness and success, whatever form that may take.

I would also like to thank the folks at Aerosol Dynamics Inc., Susanne Hering, Nathan Kreisberg, Gregory Lewis, Steve Spielman, and Arantazu Eiguren-

Fernandez, for their hospitality and support during our collaborations in Berkeley.

Immense gratitude is extended to my friend from day one at Caltech – Jennifer Walker. Not only has she been a great source of motivation for me to finish, but she has been a great cat-sitter for the various field campaigns of my Ph.D.

I would fourthly like to thank my boyfriend, Juan Bosco Berumen. In addition to being my casual therapist, he has also been a great caretaker of my cat during absences related to this thesis. I am not sure if I would have finished, if not for him repeatedly telling me "I believe in you."

I would fifthly like to thank my family. I thank my paternal grandmother, Yau Suet Ching Mui. She continually motivated me to make something great of myself, until the day she left this earth. From you, I learned ambition.

I thank my father, Wing Chai Mui, for having the strength and wit to support two sons as a single father on the wages of a restaurant server. From you, I learned duty and sacrifice.

I thank my first sister, Kitty Mui, for being the "tough" surrogate mother. From you, I learned resilience. I thank my second sister, Betty Mui, for being the "nurturing" surrogate mother. From you, I learned kindness. I thank my little brother, Norton Mui, for being my sidekick all those times during our childhood when we were on our own. From you, I learned responsibility.

I would lastly like to thank my cat, Amélie. She has been the one constant emotional support throughout this entire Ph.D. journey. I hope she accepts my apologies for the prolonged absences during my various field campaigns.

I dedicate this thesis to my grandmother. This work represents the current greatest scientific accomplishment of any of your descendants. It not only memorializes my work, but also your journey that made mine possible. I additionally dedicate this thesis to my cat. I hope that you have so far had a satisfactory life under my care.

## ABSTRACT

Particle electrical mobility classification has made important contributions in atmospheric and climate science, public health and welfare policy, and nanotechnology. The measurement of the particle size distribution is integral to characterization of the sub-micrometer aerosol particle population. The differential mobility analyzer (DMA) has been the primary instrument for such measurements. Aerosol particles are transmitted through the DMA on the condition that their migration *time* across an electrode separation distance is approximately equal to the advective transport *time* from the inlet to the outlet; these two travel *times* are induced by an electric field between the electrodes and an orthogonal particle-free carrier gas flow. However, scientific interest has increasingly shifted toward both the nanometer-scale particle size distribution and the miniaturization of instruments. The classical DMA suffers from severe resolution degradation and diffusional losses of nanometer-scale particles, as well as being ill-suited for lightweight, low-power applications. It is relatively recently that miniaturization of DMAs for portable applications has appeared in the scientific literature. Additionally, an abundance of efforts on DMA design have yielded instruments that can probe the nanometer-scale particle size regime, though their use is restricted to the laboratory as they require powerful pumps and operate at near-turbulent flow conditions.

The opposed migration aerosol classifier (OMAC) is a novel concept for particle electrical mobility classification introduced about a decade ago. In contrast to the DMA, the OMAC transmits particles on the condition that their migration *velocity* in an electric field is approximately equal to the advective transport *velocity* by a particle-free flow; the migration *velocity* is induced by an electric field between two porous electrodes, through which a particle-free cross-flow moves in an anti-parallel direction to the electric field. Because of this flow field arrangement, the length scale over which diffusion must act to affect resolution is the entire electrode separation distance in the OMAC, whereas in the DMA it is smaller by about a factor of the sample-to-carrier gas flow rate ratio. As a result, resolution degradation due to diffusion occurs at a lower operating voltage in the OMAC compared to the DMA. Not only does this suggest a larger dynamic range for the OMAC, but also the capability to classify nanometer-scale particles with greater resolution and lower operating voltages and flow rates.

Motivated by the theoretical advantages of an OMAC compared to a DMA, this

thesis details the design and characterization of OMAC classifiers to verify the performance of realized OMACs. The capabilities of prototype radial geometry OMACs were first investigated. They demonstrated sub-20 nm particle diameter classification at high resolution using modest flow rates, making them amenable to non-laboratory applications. Additionally, the delayed resolution degradation of OMACs was validated by the maintenance of resolution at operating voltages below those at which a DMA would have experienced severely degraded resolution.

Various applications were then carried out to validate the use of OMACs in both nanometer-scale and sub-micrometer particle size regimes. The first OMAC application was in the field of biomolecule analysis, in which the radial OMAC was operated as an ion mobility spectrometer coupled to a mass spectrometer to resolve conformations of sub-2 nm biomolecules. The resolving power of the radial OMAC was high enough to differentiate peptide stereoisomers and populations of thermally-induced biomolecule conformations.

In the aerosol measurement field, aerosol particle size distributions are typically obtained by passing the sample through an ionization source to impart charges on the sample particles, before mobility separation and detection. The detected signal must be inverted, using detector efficiencies, classifier transfer functions, and charge distributions, to obtain the true particle size distribution. While detector efficiencies and classifier transfer functions are typically well-quantified for the specific instruments used in the measurement, the charge distribution is almost never calculated for the specific measurement conditions. This is due both to the computational expense of, as well as the present impracticability of obtaining all the information needed for carrying out such calculations. Aerosol scientists typically use one parameterization of the charge distribution, regardless of the measurement conditions. Thus, the charge distribution represents the greatest source of bias in particle size distribution measurements. Having demonstrated high resolution of sub-2 nm ions, the radial OMAC was then used to obtain mobility distributions of gas ions formed in a bipolar aerosol charger. These ion mobility distributions were then used to quantify the particle size distribution bias due to the use of the common charge distribution parameterization.

In atmospheric nucleation field, the radial OMAC was deployed as part of an airborne particle detection payload over a large cattle feedlot. Again, the radial OMAC demonstrated the ability to obtain nanometer-scale particle size distributions, that, when paired with a concurrently-deployed DMA, allowed for the measurement of

ambient particle size distributions over the entire sub-micrometer size range. A spatially-dense set of such particle size distributions allowed for the calculation of particle growth rates from a clear nucleation event from cattle feedlot emissions.

Finally, OMACs were evaluated for their performance at low-flow rate operation to obtain sub-micron particle size distribution for deployment as portable exposure monitors, distributed network area monitors, and unmanned aerial vehicle instrumentation. The radial OMAC showed high fidelity to a reference instrument in reported ambient particle size distributions for nearly 48 hours of unattended operation. A planar geometry OMAC prototype was designed and characterized as well, indicating design and construction issues that caused deviations from ideal behavior. The planer OMAC qualitatively agreed with a reference instrument in reported ambient particle size distributions for about 12 hours of unattended operation. Both radial and planar OMACs were more compact, lower in weight, and less demanding in power consumption than a classical DMA, showing high potential for further miniaturized instrumentation development.

## PUBLISHED CONTENT AND CONTRIBUTIONS

Hodas, N. et al. (2015). “Influence of particle-phase state on the hygroscopic behavior of mixed organic-inorganic aerosols”. In: *Atmos. Chem. Phys.* 15.9, pp. 5027–5045. DOI: 10.5194/acp-15-5027-2015.

W.M. assisted with carrying out experiments.

Leppä, J. et al. (2017). “Charge distribution uncertainty in differential mobility analysis of aerosol”. In: *Aerosol Sci. Technol.* In review.

W.M. designed the experiments concerning lab ion mobility distribution, conducted the measurements and associated calibrations, assisted with data inversion, and wrote the text concerning the lab ion mobility distribution measurement.

Mui, W., H. Mai, et al. (2017). “Design, simulation, and characterization of a radial opposed migration ion and aerosol classifier (ROMIAC)”. In: *Aerosol Sci. Technol.* In review.

W.M. designed the instrument, modeled the instrument performance, designed the experiments, carried out the experiments, performed the analysis, created the figures and tables, and wrote the paper.

Mui, W., D. A. Thomas, et al. (2013). “Ion mobility-mass spectrometry with a radial opposed migration ion and aerosol classifier (ROMIAC)”. In: *Anal. Chem.* 85, pp. 6319–6326. DOI: 10.1021/ac400580u.

W.M. designed the instrument, modeled the instrument performance, designed the experiments, carried out the experiments, performed the analysis, created the figures and tables, and wrote the paper.

Prather, K. A. et al. (2013). “Bringing the ocean into the laboratory to probe the chemical complexity of sea spray aerosol”. In: *Proc. Natl. Acad. Sci. USA* 110.19, pp. 7550–5. DOI: 10.1073/pnas.1300262110.

W.M. collected and analyzed the hygroscopicity data, created the hygroscopicity figure, and wrote the text concerning aerosol hygroscopicity.

Wennberg, P. O. et al. (2012). “On the sources of methane to the Los Angeles atmosphere”. In: *Environ. Sci. Technol.* 46.17, pp. 9282–9. DOI: 10.1021/es301138y.

W.M. analyzed the data and created the figures and tables.

# TABLE OF CONTENTS

|  |        |
|--|--------|
| Acknowledgements . . . . .   | iii    |
| Abstract . . . . .   | v      |
| Published Content and Contributions . . . . .  | viii   |
| Table of Contents . . . . .  | ix     |
| List of Illustrations . . . . .  | xi     |
| List of Tables . . . . .   | xxviii |
| Chapter I: Preface . . . . .   | 1      |
| Chapter II: Design, simulation, and characterization of a radial opposed migration ion and aerosol classifier (ROMIAC) . . . . . | 5      |
| 2.1 Abstract . . . . .   | 5      |
| 2.2 Introduction . . . . .   | 6      |
| 2.3 Instrument design . . . . .  | 12     |
| 2.4 Simulation methods . . . . .   | 16     |
| 2.5 Experimental methods . . . . .   | 24     |
| 2.6 Results and discussion . . . . .   | 29     |
| 2.7 Conclusions . . . . .  | 39     |
| 2.8 Nomenclature . . . . .   | 41     |
| 2.9 Acknowledgments . . . . .  | 46     |
| Chapter III: Ion mobility–mass spectrometry with a radial opposed migration ion and aerosol classifier (ROMIAC) . . . . .        | 50     |
| 3.1 Abstract . . . . .   | 50     |
| 3.2 Introduction . . . . .   | 51     |
| 3.3 Materials and Methods . . . . .  | 52     |
| 3.4 Results and Discussion . . . . .   | 55     |
| 3.5 Conclusions . . . . .  | 65     |
| 3.6 Acknowledgments . . . . .  | 66     |
| Chapter IV: Charge distribution uncertainty in differential mobility analysis of aerosols . . . . .                              | 71     |
| 4.1 Abstract . . . . .   | 71     |
| 4.2 Introduction . . . . .   | 72     |
| 4.3 Methods . . . . .  | 75     |
| 4.4 Results . . . . .  | 84     |
| 4.5 Discussion and conclusions . . . . .   | 100    |
| Chapter V: Observations of new particle growth from a large cattle feedlot . . . . .   | 111    |
| 5.1 Introduction . . . . .   | 111    |
| 5.2 Methods . . . . .  | 112    |
| 5.3 Results and discussion . . . . .   | 120    |
| 5.4 Conclusions . . . . .  | 134    |
| 5.5 Acknowledgments . . . . .  | 136    |

|  |     |
|--|-----|
| Chapter VI: Development and operation of opposed migration aerosol classifiers (OMAC) with a Moderated Aerosol Growth with Internal water            |     |
| Cycling detector (MAGIC) for environmental monitoring . . . . .  | 141 |
| 6.1 Introduction . . . . .   | 141 |
| 6.2 Methods . . . . .  | 147 |
| 6.3 Results and Discussion . . . . .   | 158 |
| 6.4 Conclusions . . . . .  | 167 |
| 6.5 Acknowledgments . . . . .  | 172 |
| Appendix A: Supplementary Information for Design, simulation, and characterization of a radial opposed migration ion and aerosol classifier (ROMIAC) | 178 |
| A.1 Preliminary electrode mesh comparisons . . . . .   | 178 |
| A.2 Detailed results . . . . .   | 179 |
| Appendix B: Supplementary Information for Ion mobility–mass spectrometry with a radial opposed migration ion and aerosol classifier (ROMIAC) . . .   | 185 |
| B.1 Introduction to FRIPS . . . . .  | 185 |
| B.2 Materials and Methods . . . . .  | 186 |
| B.3 Calculations . . . . .   | 189 |
| B.4 Results . . . . .  | 192 |
| Appendix C: Supplementary Information for Charge distribution uncertainty in differential mobility analysis of aerosols . . . . .                    | 209 |
| Appendix D: US Patent 9,095,793 B2: Radial opposed migration aerosol classifier with grounded aerosol entrance and exit . . . . .                    | 229 |
| Appendix E: US Patent 9,138,663 B2: Opposed migration aerosol classifier gas and heat exchanger . . . . .  | 260 |
| Appendix F: Technical drawings of the radial opposed migration ion and aerosol classifier (ROMIAC) . . . . .   | 282 |
| Appendix G: Technical drawings of the planar opposed migration aerosol classifier (POMAC) . . . . .  | 303 |
| Appendix H: On the sources of methane to the Los Angeles atmosphere . . .  | 317 |
| Appendix I: Bringing the ocean into the laboratory to probe the chemical complexity of sea spray aerosol . . . . .                                   | 326 |
| Appendix J: Influence of particle-phase state on the hygroscopic behavior of mixed organic-inorganic aerosols . . . . .                              | 342 |



## LIST OF ILLUSTRATIONS

| <i>Number</i>  | <i>Page</i> |
|--|-------------|
| 2.1 (a) Simplified diagram of balanced drag, $\mathbf{F}_D$ , and electric, $\mathbf{F}_E$ , forces acting on a particle of mobility $Z^*$ in the ROMIAC classification region, resulting in a particle streamline that is parallel to the sample flow direction. (b) Simplified diagram of aerosol and cross-flow fluid velocities ( $u_a$ and $u_{cf}$ , respectively) and electrical migration velocity, $v_{mig}$ , acting on a particle of mobility $Z^*$ . Low $\mathcal{R}_{nd}$ operation results in fluid streamlines that significantly deviate from vertical. Particles of mobility $Z^*$ will thus experience a high advective velocity (relative to the cross-flow velocity) from sample inlet to outlet, increasing the transmission of all particles, and resulting in lower resolution. (c) High $\mathcal{R}_{nd}$ operation results in nearly vertical fluid streamlines, discriminating more heavily against the transmission of particles that are not of mobility $Z^*$ . . . . . | 14          |
| 2.2 Schematic of ROMIAC aerosol introduction, classification region, and classified aerosol outlet. Particles are introduced via a tangential inlet tube to be azimuthally distributed through a thin knife-edge gap into the classification region, where particles follow characteristic trajectories based on the degree of balance of drag and electric forces experienced. Particles of mobility $Z^*$ will be advected toward the center and extracted through the outlet. Key dimensions that define the classification region are indicated. The origin of the coordinate system is designated to be the center of the incoming cross-flow electrode. . . . .  | 15          |
| 2.3 (a) Cutaway view and (b) photograph of ROMIAC with key features numbered. Overall exterior dimensions are 10.5 cm in height and 11.4 cm in diameter. 1) aerosol inlet tube; 2) tangential inlet to distribution racetrack; 3) distribution knife-edge; 4) dielectric spacer; 5) classified aerosol outlet tube; 6) incoming cross-flow port; 7) high voltage porous electrode; 8) electrically grounded porous electrode; 9) outgoing cross-flow port. . . . .   | 17          |

- 2.4 Example COMSOL Multiphysics™ solutions for the case of  $Q_a/Q_{cf}/\mathcal{R}_{nd}/D_Z = 2 \text{ lpm} / 20 \text{ lpm} / 10 / 10 \text{ nm}$ . Aerosol inlet and outlet tube extremities are cropped out of view. Color scales are restricted in range to distinguish areas of interest. Physical features of interest that may not be obvious are labeled. (a) Section view showing vertical component of fluid flow velocity,  $u_z$ . Lines show fluid flow velocity streamlines that originate from the cross-flow inlet, and are truncated at the converging region near the aerosol outlet for clarity. Note that the vertical velocity increases approaching the centered aerosol outlet. Dashed lines  $z_1$  and  $z_2$  mark sections corresponding to those in subfigure b. (b) Overhead view showing non-vertical component of fluid flow velocity,  $\sqrt{u_x^2 + u_y^2}$ . Dashed circles  $z_1$  and  $z_2$  correspond to the cut planes in subfigure a. The white ring between  $z_1$  and  $z_2$  indicates the absence of data, not zero velocity. Note that the non-vertical velocity increases approaching the centered aerosol outlet. (c) Section view showing the normalized electric potential solution. Lines show electric field streamlines that originate from the high voltage electrode surface. (d) Section view showing the particle concentration solution at a voltage corresponding to  $Z^*$ . . . . . 21
- 2.5 Experimental setup diagrams for tandem-ROMIAC measurements. (a) Electrosprayed TAAX molecular standards calibration. (b) Atomized NaCl calibration. . . . . 26
- 2.6 Example measurements (points) and transfer function fits (lines) with listed operating conditions and fitting parameters. Top row: COMSOL Multiphysics™ simulation examples for (a) small  $D_Z$  at low  $\mathcal{R}_{nd,nom}$  operation and (b) large  $D_Z$  at high  $\mathcal{R}_{nd,nom}$  operation. Middle row: tandem-ROMIAC TAAX measurement examples for (c) small  $D_Z$  at low  $\mathcal{R}_{nd,nom}$  operation and (d) small  $D_Z$  at high  $\mathcal{R}_{nd,nom}$  operation. Bottom row: tandem-ROMIAC NaCl measurement examples for (e) large  $D_Z$  at low  $\mathcal{R}_{nd,nom}$  operation and (f) large  $D_Z$  at high  $\mathcal{R}_{nd,nom}$  operation. . . . . 30

- 2.7 Simulation results used to estimate  $f_{Z,bias}$ . (a)  $f_{u,z}$  (from COMSOL Multiphysics<sup>TM</sup>-driven kinematic particle trajectories) against  $\beta_{nom}$ . Best-fit line is  $f_{u,z} = 1.01 + 0.11\beta_{nom}$ . (b)  $f_{Z,bias}$  against estimated  $f_{u,z}$  colored by  $Pe_{mig}$ . (c) 1-to-1 comparison of simulation  $f_{Z,bias}$  against those estimated from an empirical function of  $f_{u,z}$  and  $Pe_{mig}$ . For convenience,  $Pe_{mig}$  values are listed in Table 2.1. . . . . 32
- 2.8 COMSOL Multiphysics<sup>TM</sup> simulation correction factor relationships, comparison of simulation values to empirical functions, and comparison of experimental values to empirical functions. Error bars in experimental results represent 2 standard deviations of multiple measurements. Top row: (a) simulation  $f_\beta$  against  $f_{u,z}$  colored by  $Pe_{mig}$ . (b) 1-to-1 comparison of simulation  $f_\beta$  against empirical model of  $f_{u,z}$  and  $Pe_{mig}$ . (c) 1-to-1 comparison of experiment-fitted  $f_\beta$  against empirical model of  $f_{u,z}$  and  $Pe_{mig}$ . Middle row: (d) simulation  $\tilde{\sigma}_{distor}^2$  against  $\beta_{eff}$ . (e) 1-to-1 comparison of simulation  $\tilde{\sigma}_{distor}^2$  against empirical model of  $\beta_{eff}$ . (f) 1-to-1 comparison of experiment-fitted  $\tilde{\sigma}_{distor}^2$  against empirical model of  $\beta_{eff}$ . Bottom row: (g) simulation  $\eta_{trans}$  against  $Pe_{mig}\beta_{eff}$  colored by  $\beta_{eff}$ . (h) 1-to-1 comparison of simulation  $\eta_{trans}$  against empirical model of  $Pe_{mig}$  and  $\beta_{eff}$ . (i) 1-to-1 comparison of experiment-fitted  $\eta_{trans}$  against empirical model of  $Pe_{mig}$  and  $\beta_{eff}$ . For convenience,  $Pe_{mig}$  and  $Pe_{mig}\beta$  values are listed in Table 2.1. . . . 34
- 2.9 (a) Theoretical (lines) and observed simulation and experimental (markers) resolution obtained with the ROMIAC against  $V$  and  $Pe_{mig}$ . Curves and markers for only three values of  $\mathcal{R}_{nd,nom}$  are displayed for clarity ( $\mathcal{R}_{nd,nom} = 5.3, 10, \text{ and } 20.2$ ). (b) Theoretical (lines) and observed simulation and experimental (markers) effective relative resolution obtained with the ROMIAC against  $V$  and  $Pe_{mig}$ . Markers for all operating conditions are shown, but curves for only three values of  $\mathcal{R}_{nd,nom}$  are displayed for clarity ( $\mathcal{R}_{nd,nom} = 5.3, 10, \text{ and } 20.2$ ). Error bars in experimental results represent 1 standard deviation of multiple measurements. For convenience,  $Pe_{mig}$  values are listed in Table 2.1. . . . . 37

- 3.1 a) ROMIAC–LTQ–MS atmospheric interface. The outer dimensions of the ROMIAC are 11.4 cm diameter and 10.6 cm length. b) Cross–sectional view of functional region of ROMIAC. Diagram is cylindrically symmetrical about indicated axis of revolution. Dotted lines are idealized ion trajectories through the ROMIAC. Sample ions enter via a tangential inlet, are drawn into the classification region, and experience opposing drag and electric forces that allow the target ion to exit through the outlet, while non–target ions impact either the upper or lower planes. . . . . 53
- 3.2 Tetra–alkyl ammonium halide (TAAX) anion–coordinated singly–charged multimer  $K_{0,i}$  as a function of  $k$  for  $[\text{TAA}_k\text{X}_{k-1}]^+$ . In  $\text{N}_2$  at atmospheric pressure and  $T_{\text{ESI}} = T_x = 298$  K. Error bars denote 1 standard deviation of triplicates. C3 species are iodinated while all other TAAX species are brominated. Detailed signal, Gaussian fit, and resolution values are found in Table B.5. Values for monomer reduced mobilities and errors from Viidanoja et al. 2005. . . . . 56
- 3.3 Experimental ion classifications of BK (top panel), AT1 (middle panel), and AT2 (bottom panel) ions, showing mass–resolved, normalized signal as a function of  $\phi$ . Error bars on the circular markers indicate 1 standard deviation of the normalized signal at that  $\phi$  for that one scan. Each resolvable Gaussian peak is labeled with a unique identifier number. The thick fitted line (gray for  $T_{\text{ESI}} = 298$  K and red for  $T_{\text{ESI}} = 400$  K) is the Gaussian–fitted function to the signal. Inset plots show the normalized proportion of each resolvable peak contribution to the total signal (gray for  $T_{\text{ESI}} = 298$  K and red for  $T_{\text{ESI}} = 400$  K). Error bars on rectangles indicate 1 standard deviation of the normalized proportion of each peak of the three scans for that species. a)  $\text{BK}^{+1}$  at  $T_{\text{ESI}} = 298$  K. b)  $\text{BK}^{+1}$  at  $T_{\text{ESI}} = 400$  K. c)  $\text{BK}^{+2}$  at  $T_{\text{ESI}} = 298$  K. d)  $\text{BK}^{+2}$  at  $T_{\text{ESI}} = 400$  K. e)  $\text{AT1}^{+1}$  at  $T_{\text{ESI}} = 298$  K. f)  $\text{AT1}^{+1}$  at  $T_{\text{ESI}} = 400$  K. g)  $\text{AT1}^{+2}$  at  $T_{\text{ESI}} = 298$  K. h)  $\text{AT1}^{+2}$  at  $T_{\text{ESI}} = 400$  K. i)  $\text{AT1}^{+3}$  at  $T_{\text{ESI}} = 298$  K. j)  $\text{AT1}^{+3}$  at  $T_{\text{ESI}} = 400$  K. k)  $\text{AT2}^{+1}$  at  $T_{\text{ESI}} = 298$  K. l)  $\text{AT2}^{+1}$  at  $T_{\text{ESI}} = 400$  K. m)  $\text{AT2}^{+2}$  at  $T_{\text{ESI}} = 298$  K. n)  $\text{AT2}^{+2}$  at  $T_{\text{ESI}} = 400$  K. . . . . 58

- 3.4 Mobility calibration  $\Omega_i$  of numbered peaks from Fig. 3.3. In  $N_2$  at atmospheric pressure with  $T_x = 298$  K. Black markers indicate  $T_{ESI} = 298$  K and red markers indicate  $T_{ESI} = 400$  K. Error bars denote 1 standard deviation of triplicates. Dashed boxes enclose dominant conformation at each  $T_{ESI}$ . Inset plot shows mobility calibration  $\Omega_i$  for UB peaks from Fig. B.5, in which only one dominant species for each charge state was identified. Detailed signal, Gaussian fit, and resolution values are found in Tables B.9 and B.10. . . . . 62
- 3.5 Free radical dissociation processes resulting from FRIPS reagent attachment to model peptides. The FRIPS methodology employed here is shown schematically in a). The TEMPO-based FRIPS reagent is coupled to the N-terminus of the peptide, and subsequent collisional activation leads to loss of the TEMPO moiety, generating an acetyl radical. This acetyl radical then abstracts a H atom from diverse sites along the peptide, leading to dissociation of the backbone or neutral loss of amino acid side chains. Unique product ions are proposed to occur at threonine residues via the mechanisms shown in b) and c), resulting in b)  $[a_6 + H]^+$  and  $z_7 - H$  ion generation and c)  $c_6$  ion generation. Backbone dissociation at histidine residues likely occurs via the mechanism illustrated in d), leading to  $a_6$  and  $a_8$  ion generation. (Sun et al. 2009) . . . . . 63
- 3.6 Experimental CID unique product ion classifications and separations of model peptide isomers, showing mass-resolved, normalized fragment signals as a function of  $\phi$ . In  $N_2$  at atmospheric pressure and  $T_{ESI} = T_x = 298$  K. Error bars on the circular markers indicate 1 standard deviation of the normalized signal at that  $\phi$  for that one scan. The thick gray line is the Gaussian-fitted function to the signal, and the dot marker shows the centroid of the fit, with horizontal error bars indicating the 95% confidence interval of the centroid. a) Non-TEMPO-tagged AARAAATAA CID fragments. b) Non-TEMPO-tagged AATAAARAA CID fragments. c) TEMPO-tagged AARAAATAA CID fragments. b) TEMPO-tagged AATAAARAA CID fragments. e) Non-TEMPO-tagged AARAAHAMA CID fragment. f) Non-TEMPO-tagged AARAAMAHA CID fragment. g) TEMPO-tagged AARAAHAMA CID fragment. h) TEMPO-tagged AARAAMAHA CID fragment. . . . . 64

- 4.1 Processes involved in a typical size distribution measurement (left), and in the present simulation approach (middle); schematic illustrations of these steps (right). Note that particles with the same size but different charge state fall into different mobility sections in the signal grid, since  $Z_p(q) = qZ_p(q = 1)$  (two topmost panels on the right). Furthermore, negative and positive particles provide separate signals, with neutral particles not detected. . . . . 82
- 4.2 Top row: Time evolution of the particle size distribution in Hyytiälä (left), Mukteshwar (middle) and New Delhi (right) simulations. The color denotes the particle size distribution,  $dN/d \log d_p$ , in  $\text{cm}^{-3}$ . Bottom left: Time evolution of the particle size distribution inferred from the signal of the Hyytiälä simulation. Bottom middle: The ratio,  $R(d_p, t)$ , of the inverted (lower left panel) and simulated (upper left panel) distributions. The subscript “sim” and “inv” refer to the simulated and inverted distributions, respectively. Bottom right: The time averaged ratio of the inverted and simulated distributions,  $R^{*-}$ , and its running average,  $R_{\text{ave}}^{*-}$ , according to Eqs. (4.9) and (4.10), respectively. The data in the lower panels is shown for Hyytiälä simulation with  $f_{\text{cha}} \neq f_{\text{inv}}$  and when negative particles were counted; the results for positive polarity were very similar. . . . . 85
- 4.3 Left panel: The bias observed in the inferred particle size distribution when  $f_{\text{cha}}$  was calculated using input values based on our measurements (Scenario 1 in Table 4.1) and  $f_{\text{inv}}$  was according to FHFV charge distribution. The line style denotes the simulation, and signal polarity is labeled. Right panel: The same as the left panel, except that the SR distribution, instead of the measured distribution, was used when calculating  $f_{\text{cha}}$ . . . . . 90
- 4.4 The bias observed in the inferred particle size distribution when  $f_{\text{cha}}$  was calculated using the measured ion mobility distribution and  $f_{\text{inv}}$  was calculated using the SR distribution, with other inputs being the same. The line style denotes the simulation, and signal polarity is labeled. . . . . 91

- 4.5 Upper panels: The bias observed in the inferred particle size distribution when  $f_{\text{cha}}$  corresponded to  $T$  and  $p$  representing conditions in laboratory ( $T = 298.15$  K &  $p = 96757$  Pa; “Lab.”), at 3 km altitude ( $T = 269$  K &  $p = 70120$  Pa; “3 km”), or at 10 km altitude ( $T = 223$  K &  $p = 26500$  Pa; “10 km”), and  $f_{\text{inv}}$  corresponded to  $T$  and  $p$  in laboratory. The line style denotes the conditions, with markers denoting different simulations, shown only in the “10 km” case. Results corresponding to negative (positive) particle measurements are shown on the left (right). The lines depicting the “10 km” cases are practically coincident for  $d_p < 20$  nm and  $d_p > 500$  nm. Lower panels: The same as the upper panels, except that the SR distribution, instead of the measured distribution, was used when calculating  $f_{\text{cha}}$ . . . . . 93
- 4.6 Left panel: The bias observed in the inferred particle size distribution when the ion masses ranged from 130 to 1000 Da ( $\rho_i = 800$  kg m<sup>-3</sup>), from 220 to 1800 Da ( $\rho_i = 1500$  kg m<sup>-3</sup>), or from 300 to 2700 Da ( $\rho_i = 2200$  kg m<sup>-3</sup>) when calculating  $f_{\text{cha}}$ , but were from 220 to 1800 Da when calculating  $f_{\text{inv}}$ , as indicated in the legend. Right panel: The same as the left panel, except that the SR distribution, instead of the measured distribution, was used when calculating  $f_{\text{cha}}$ . The corresponding ion masses are given in the legend. . . . . 94
- 4.7 Left panel: The bias observed in the inferred particle size distribution when particles were assumed to be conductive,  $\chi_p = \infty$ , or dielectric with  $\chi_p = 6$  or  $\chi_p = 2.6$  when calculating  $f_{\text{cha}}$ , but they were assumed to be conductive when calculating  $f_{\text{inv}}$ , as indicated in the legend. Right panel: The same as the left panel, except that the SR distribution, instead of the measured distribution, was used when calculating  $f_{\text{cha}}$ . . . . . 95
- 4.8 Left panel: The bias observed in the inferred particle size distribution when  $n_{i,T}^+/n_{i,T}^-$  was 1.0, 1.1, or 1.2 when calculating  $f_{\text{cha}}$ , but  $n_{i,T}^+/n_{i,T}^- = 1.0$  was used when calculating  $f_{\text{inv}}$ . The line style denotes the  $n_{i,T}^+/n_{i,T}^-$  when calculating  $f_{\text{cha}}$ , and the marker and line color denote the signal polarity. Right panel: The same as the left panel, except that the SR distribution, instead of the measured distribution, was used when calculating  $f_{\text{cha}}$ . . . . . 97

- 5.1 a) Geographic context of this study in the state of California. Harris Ranch is located in the San Joaquin Valley, bounded by the Diablo Range to the west and the Sierra Nevada Range to the east. Stars mark the location of Harris Ranch, CIRPAS near Monterey, as well as nearby major urban center San Francisco. Map data: Google, SIO, NOAA, US Navy, NGA, GEBCO, LDEO-Columbia, and NSF. b) Photograph over Harris Ranch, showing the extent of the beef cattle feed lot, which is a triangle approximately  $3.25 \text{ km}^2$  in area. . . 113
- 5.2 48-hour HYSPLIT back trajectories of air masses arriving at Harris Ranch at the approximate mid-time of the plume sampling period, using 40-km resolution EDAS meteorological data at thirty evenly-spaced levels between 30 and 1000 m AGL. a) RF18 horizontal extent of trajectories. Only the trajectory of every other altitude level is plotted for clarity. b) RF18 vertical extent of trajectories above mean sea level (AMSL). c) RF21 horizontal extent of trajectories. Only the trajectory of every other altitude level is plotted for clarity. d) RF21 vertical extent of trajectories AMSL. Circle markers show major urban areas San Francisco (SF) and Los Angeles (LA) for geographic context, while the triangle marker indicates Harris Ranch. 115
- 5.3 Overview of flight paths for research flights in this study. Paths are colored by LT, which is described by the colorbar. The location of CIRPAS is represented with a filled circle. a) RF18. b) RF21. The triangle marker indicates the location of Harris Ranch. . . . . 116
- 5.4 a) RF18 time series of altitude and pressure. The light blue area represents the time span of detailed plume analysis. The tags P1 and P2 indicate vertical profiles used for convective boundary layer height analysis. b) Vertical profile of potential temperature. c) Vertical profile of relative humidity. d) Vertical profile of  $N_3$  concentrations. The dashed lines in the bottom three subfigures indicate the CBL thickness corresponding to P1 and P2. The light gray region in subfigure (a) represents the CBL thickness interpolated between those determined from the vertical profiles. . . . . 121



|      |   |     |
|------|---|-----|
| 5.5  | a) RF18 time series of particle number size distribution. White areas indicate missing data from the DMA. b) Total particle number concentration measured with cabin CPCs and integrated particle number size distribution. c) Non-refractory mass fraction of species in aerosol phase measured by the AMS. Inorganic species are plotted against the right-side axis. . . . .   | 123 |
| 5.6  | a) RF21 time series of altitude and pressure. The light blue area represents the time span of detailed plume analysis. The tags P1–P4 indicate vertical profiles used for convective boundary layer height analysis. b) Vertical profile of potential temperature. c) Vertical profile of relative humidity. d) Vertical profile of $N_3$ concentrations. The dashed lines in the bottom three subfigures indicate the CBL thickness corresponding to P1, P2, and P4. The light gray region in subfigure (a) represents the CBL thickness interpolated between those determined from the vertical profiles. . . . . | 124 |
| 5.7  | a) RF21 time series of particle number size distribution. White areas indicate missing data from the DMA. b) Total particle number concentration measured with cabin CPCs and integrated particle number size distribution. c) Non-refractory mass fraction of species in aerosol phase measured by the AMS. Inorganic species are plotted against the right-side axis. . . . .   | 126 |
| 5.8  | Spatial distribution of total particle concentration measurements below the CBL thickness from cabin CPCs. The triangle marker indicates the location of Harris Ranch. a) RF18 $N_3$ concentrations. b) RF18 $N_{10}$ concentrations. c) RF18 $N_{3-10}$ concentrations. d) RF21 $N_3$ concentrations. e) RF21 $N_{10}$ concentrations. f) RF21 $N_{3-10}$ concentrations. . . . .  | 127 |
| 5.9  | Spatial distribution of particle phase non-refractory species mass fractions. The triangle marker indicates the location of Harris Ranch. a) RF18 $f_{\text{Org}}$ . b) RF18 $f_{\text{SO}_4}$ . c) RF18 $f_{\text{NO}_3}$ . d) RF18 $f_{\text{NH}_4}$ . e) RF21 $f_{\text{Org}}$ . f) RF21 $f_{\text{SO}_4}$ . g) RF21 $f_{\text{NO}_3}$ . h) RF21 $f_{\text{NH}_4}$ . . . . .   | 129 |
| 5.10 | Averaged in-plume AMS organic spectra against the averaged background AMS organic spectra for a) RF18 and b) RF21. The dashed gray line is a one-to-one reference line. . . . .   | 130 |

- 5.11 Arrow maps of wind direction and speed over Harris Ranch as measured by the Twin Otter for a) RF18 and b) RF21. Arrow lengths qualitatively describe wind speed. The triangle marker indicates the location of Harris Ranch. The black line indicates the trajectory of an air parcel passing directly over Harris Ranch, derived from interpolation of nearby wind directions and speeds. . . . . 131
- 5.12 Particle concentrations and composition recorded along a micrometeorology-driven trajectory over Harris Ranch. a) RF18 total particle number concentrations. b) RF18 total particle volume and surface area concentrations. c) RF18 non-refractory species particle mass fractions. d) RF21 total particle number concentrations. e) RF21 total particle volume and surface area concentrations. f) RF21 non-refractory species particle mass fractions. . . . . 133
- 5.13 Growth time representation of the particle number size distribution for a) RF18 and b) RF21. The dashed line demarcates the boundary between nucleation mode and background mode particles for the purposes of growth rate analysis. The solid black line indicates the diameter used for growth rate calculations in the mode-fitting method while the solid gray line indicates the diameter used for growth rate calculation in the count mean diameter method; the two methods give very similar results, making the two methods appear to be superimposed on each other. c) Summary table of the total growth rates ( $GR_{tot}$ ), self-coagulation growth rates ( $GR_{S-C}$ ), and condensation growth rates ( $GR_{cond}$ ) determined for both flights using both the mode-fit and count-mean-diameter (CMD) growth rate determination methods. . . . . 135
- 6.1 Distribution of aerosol sample fluid velocity entering the POMAC classification region along the width of the classification region (distance increases from aerosol inlet tubing) in an early design iteration for  $W = 27$  cm and  $Q_a = 0.6$  lpm. The two candidate stock shim thicknesses resulted in flow velocity distributions with less than 7% relative standard deviation. . . . . 148

- 6.2 Example two-dimensional COMSOL Multiphysics<sup>TM</sup> simulations in which the cross-flow velocity was permitted to randomly vary along the POMAC classification region length by up to a) 0% (homogeneous flow), b) 50%, and c) 100%. The incoming aerosol distribution gap is the thin channel on the left side of the figures, while the classification region and the classified aerosol outlet is to the right of the distribution gap. The figures are magnified such that much of the remaining classification region and the aerosol outlet are omitted for clarity. d) the resultant transmission of  $D_p = 100$  nm particles through the above POMAC simulations, showing insignificant effects on particle transmission for the explored degrees of electrode material inhomogeneity. . . . . 150
- 6.3 a) Simplified diagram illustrating ideal particle trajectories in the POMAC. The filled black triangles create a narrow flow resistance gap that allows for a relatively uniform velocity distribution of the aerosol sample across the classifier width prior to entering the classification region. Particles with a migration velocity equal in magnitude to the cross-flow velocity transit across the length of the classifier to the narrow flow resistance gap on the opposite end and exit the POMAC. b) Solidworks<sup>TM</sup> section drawing of the POMAC along the length of the classification region. c) Three-dimensional Solidworks<sup>TM</sup> rendering of the assembled POMAC, in a vertical orientation for most convenient interfacing with a CPC. . . . . 151
- 6.4 a) Photograph of the ROMIAC-MAGIC combined instrument for classification and detection of particles from  $10 < D_p < 200$  nm at  $Q_a/Q_{cf}/R_{nd} = 0.2$  lpm/0.45 lpm/2.25. b) A concept sketch of a future ROMIAC-MAGIC prototype that would improve the interface between the two instruments to reduce losses as well as the mass and dimensions of the ROMIAC. . . . . 152
- 6.5 Photograph of the POMAC-MAGIC combined instrument for classification and detection of particles from  $10 < D_p < 1000$  nm at  $Q_a/Q_{cf}/R_{nd} = 0.4$  lpm/0.6 lpm/1.5. . . . . 153
- 6.6 Experimental setup for a) transfer function calibrations of OMACs and b) SMPS vs. OMAC comparison ambient measurements. . . . . 157

- 6.7 a) ROMIAC calibration data (markers) and transfer function model fits (lines) for  $12 < D_p < 150$  nm. Empirical model fits for correction factors b)  $f_Z$ , c)  $f_\beta$ , and d)  $\tilde{\sigma}_{\text{distor}}^2$  as functions of  $Pe_{\text{mig}}$ . Dashed lines are a one-to-one line. e) Best-fit  $\eta_{\text{trans,OMAC}}$  values (markers) and unity line. f) Relative resolution achieved in ROMIAC calibration measurements, with theoretical relative resolution limits for the OMAC and DMA shown in solid and dashed lines, respectively. . . . 160
- 6.8 a) POMAC calibration data (markers) and transfer function model fits (lines) for  $20 < D_p < 500$  nm. Empirical model fits for correction factors b)  $f_Z$ , c)  $f_\beta$ , and d)  $\tilde{\sigma}_{\text{distor}}^2$  as functions of  $Pe_{\text{mig}}$ . Dashed lines are a one-to-one line. e) Best-fit  $\eta_{\text{trans,OMAC}}$  values (markers) and detection efficiency model (line). f) Relative resolution achieved in POMAC calibration measurements, with theoretical relative resolution limits for the OMAC and DMA shown in solid and dashed lines, respectively. . . . . 162
- 6.9 Detection efficiency of the MAGIC CPC for the aerosol flow rates of the ROMIAC ( $Q_a = 0.2$  lpm) and the POMAC ( $Q_a = 0.4$  lpm) used in this study. The dashed lines represent fits to a modified three-parameter model by Mertes, Schröder, and Wiedensohler (1995) for describing CPC efficiency. . . . . 163
- 6.10 Particle number size distributions for the 47-hour measurement outside the Aerosol Dynamics Inc. laboratory in Berkeley, CA reported by the a) ROMIAC-MAGIC system and b) SMPS. . . . . 164
- 6.11 Comparison metrics for the ROMIAC-MAGIC and SMPS 47-hour ambient sampling period calculated from the distributions in Fig. 6.10. a) Time series of geometric mean diameter. b) Time series of total particle number concentration. c) Time series of total particle volume concentration. d) Time series of total particle surface area concentration. e) One-to-one comparison of geometric mean diameter. f) One-to-one comparison of total particle number concentration. g) One-to-one comparison of total particle volume concentration. h) One-to-one comparison of total particle surface area concentration. The notation  $\Delta_{\text{avg}}$  denotes the mean percent difference of the ROMIAC-MAGIC value from the SMPS value. . . . . 166

|      |  |     |
|------|--|-----|
| 6.12 | Total surface area and number of particles per hour delivered to the pulmonary/alveolar regions of the lung for the particle size distributions of Fig. 6.10a. . . . .   | 167 |
| 6.13 | Particle number size distributions for the 13.5-hour measurement outside the Aerosol Dynamics Inc. laboratory in Berkeley, CA reported by the a) POMAC-MAGIC system and b) SMPS. . . . .   | 168 |
| 6.14 | Comparison metrics for the POMAC-MAGIC and SMPS 13.5-hour ambient sampling period calculated from the distributions in Fig. 6.13. Data collected after 2015-Dec-12 22:30 was omitted for comparison purposes since the MAGIC wick appeared to have dried out. a) Time series of geometric mean diameter. b) Time series of total particle number concentration. c) Time series of total particle volume concentration. d) Time series of total particle surface area concentration. e) One-to-one comparison of geometric mean diameter. f) One-to-one comparison of total particle number concentration. g) One-to-one comparison of total particle volume concentration. h) One-to-one comparison of total particle surface area concentration. The notation $\Delta_{\text{avg}}$ denotes the mean percent difference of the POMAC-MAGIC value from the SMPS value. . . . . | 169 |
| A.1  | Transmission efficiency measurements of TDDAB monomer through ROMIAC1 using 200-mesh and 325-mesh. Error bars represent 2 standard deviations of triplicate measurements. . . . .  | 179 |
| A.2  | 500-mesh upper electrode with (a) no hole cut out for the aerosol outlet tubing and (b) with hole cut out for aerosol outlet tubing. . . .   | 180 |
| A.3  | Transmission efficiency measurements of TDDAB monomer through ROMIAC1 using 500-mesh electrodes without and with a hole cut in the upper electrode for the aerosol outlet tubing. Error bars represent 2 standard deviations of triplicate measurements. . . . .   | 180 |
| B.1  | Schematic of FRIPS methodology; the TEMPO precursor is coupled to the N-terminus of the peptide, and subsequent collisional activation leads to loss of the TEMPO moiety, generating an acetyl radical. CID of this radical then leads to hydrogen atom abstraction and followed by dissociation of the amino acid side chain or backbone. . . . .   | 185 |

- B.2 Diagram of ESI–ROMIAC–LTQ–MS setup used to measure TAAX ion and peptide mobilities and cross sections. Flows were controlled both manually (with regulators and critical orifices) and automatically (with P–I–D input to solenoid valves) via a custom LabView program that responded to measured gas flows through the laminar flow elements. The program also varied the voltage across the ROMIAC electrodes. . . . . 188
- B.3 ROMIAC instrument calibration with TAAX salts. Vertical error bars represent 1 standard deviation of  $K_i$  values from Viidanoja et al. 2005. Horizontal error bars represent 1 standard deviation of  $\phi_i^*$  for a TAAX ion. Fit is linear with  $R^2 > 0.999$ . Slope is  $-0.0105 \pm (4.89 \times 10^{-5})$ . Intercept is  $-0.0195 \pm 0.00430$ . . . . . 193
- B.4 ROMIAC mobility calibration with peptides. Vertical error bars represent 3% error in  $\Omega_i$  values from Bush et al. 2010. Horizontal error bars represent 1 standard deviation of  $\phi_i^*$  for a peptide ion. Fit is linear with  $R^2 > 0.996$ . Slope is  $-244.779 \pm (5.573)$ . Intercept is  $-9.145 \pm 22.171$ . . . . . 197
- B.5 A single experimental classification of UB, showing mass–resolved, normalized signal as a function of  $\phi$ . Error bars on the circular markers indicate 1 standard deviation of the normalized signal at that  $\phi$  for that one scan. Each resolvable Gaussian peak is labeled with a unique identifier number. The thick gray line is the Gaussian–fitted function to the signal. a)  $UB^{+5}$  at  $T_{ESI} = 298$  K. b)  $UB^{+6}$  at  $T_{ESI} = 298$  K. c)  $UB^{+7}$  at  $T_{ESI} = 298$  K. d)  $UB^{+8}$  at  $T_{ESI} = 298$  K. . . . . 203
- B.6 Measured cross sections values in this study against those from other studies. Black markers indicate  $T_{ESI} = 298$  K and red markers indicate  $T_{ESI} = 400$  K. Horizontal error bars denote 1 standard deviation of triplicates. Vertical error bars indicate that study’s estimated error, if provided. Ref. A: Wu, Klasmeier, and Hill 1999. Ref. B: Baykut, Halem, and Raether 2009. Ref. C: Bush et al. 2010. . . . . 204
- B.7 CID spectra of the peptide isomers a) AARAAATAA and b) AATAAARAA. Corresponding FRIPS spectra are shown in c) and d). Labeled peaks are product ions specific to each isomer used for identification during separation by the ROMIAC; other peaks common to both isomers are not labeled for clarity. Product ions in the FRIPS spectrum are referenced to the acetyl radical generated by loss of the TEMPO moiety. 206

- B.8 Same as Fig. B.7, but for a) AARAAHAMA and b) AARAAMAHA. Corresponding FRIPS spectra are shown in c) and d). . . . . 206
- C.1 Left panel: The measured mobility distribution of the ions produced by  $^{85}\text{Kr}$  aerosol charger using particle free laboratory air as the sample. Right panel: The mobility distribution of the ions produced by  $^{241}\text{Am}$  aerosol charger using clean and dry laboratory air as the sample (G. Steiner and Reischl 2012). It should be noted that, unlike the mobility values, the diameter values do not match those reported by Steiner and Reischl due to different relation between mobility and size used in this study. . . . . 218
- C.2 The effective flux coefficients,  $\beta_{\text{eff},k}^{\pm}$ , of negative (left panels) and positive (right panels) ions to particles with  $k$  charges in  $T$  and  $p$  corresponding to the measured ion distribution (upper panels) and to the SR distribution (lower panels) at conditions at laboratory ( $T = 298.15$  K;  $p = 96757$  Pa; “Lab.”) and at 10 km altitude ( $T = 223$  K;  $p = 26500$  Pa; “10 km”). . . . . 219
- C.3 The ratio of effective flux coefficients of the SR distribution,  $\beta_{\text{eff}}$ , to those of the measured distribution,  $\beta_{\text{eff,base}}$ . The particle and ion charge states are denoted by  $k$  and  $i$ , respectively, with the fluxes of negative (positive) ions shown on the left (right). The particle charge states relative to the ion polarity are denoted with line style and color as indicated in the legend. The ion fluxes to particles with one similar or two opposite charges, and with two similar or three opposite charges are depicted only for particles with  $d_p > 10$  nm and  $d_p > 30$  nm, since doubly- and triply-charged particles, respectively, are extremely rare below these thresholds. . . . . 220
- C.4 The charge distributions in  $T$  and  $p$  corresponding to conditions at laboratory ( $T = 298.15$  K;  $p = 96757$  Pa; “Lab.”) and at 10 km altitude ( $T = 223$  K;  $p = 26500$  Pa; “10 km”), and the charge distribution according to Wiedensohler (1988; “Wied.”), as indicated by line style. Fractional populations of negative (positive) particles are shown on the left (right) with  $k$  denoting the particle charge state. Data is shown for the measured (upper panels) and SR (lower panels) distributions. . 221

- C.5 The ratio of effective flux coefficients at 10 km altitude,  $\beta_{\text{eff}}$ , to those at laboratory,  $\beta_{\text{eff,base}}$ . The particle and ion charge states are denoted by  $k$  and  $i$ , respectively, with the fluxes of negative (positive) ions shown on the left (right). The particle charge states relative to the ion polarity are denoted with line style and color as indicated in the legend. Data in upper and lower panels correspond to the measured and SR distributions, respectively. The ion fluxes to particles with one similar or two opposite charges, and with two similar or three opposite charges are depicted only for particles with  $d_p > 10$  nm and  $d_p > 30$  nm, since doubly- and triply-charged particles, respectively, are extremely rare below these thresholds. . . . . 222
- C.6 The same as Figure C.5, except that  $\beta_{\text{eff}}$  and  $\beta_{\text{eff,base}}$  are the effective flux coefficients of ions with masses in the range from 130 to 1000 Da and from 220 to 1800 Da, respectively, for the measured distribution (upper panels). For SR distribution (lower panels),  $\beta_{\text{eff}}$  and  $\beta_{\text{eff,base}}$  are the effective flux coefficients of ions with masses in the range from 43 to 460 Da and from 55 to 840 Da, respectively. . . . . 223
- C.7 The same as Figure C.5, except that  $\beta_{\text{eff}}$  and  $\beta_{\text{eff,base}}$  are the effective flux coefficients of ions with masses in the range from 300 to 2700 Da and from 220 to 1800 Da, respectively, for the measured distribution (upper panels). For SR distribution (lower panels),  $\beta_{\text{eff}}$  and  $\beta_{\text{eff,base}}$  are the effective flux coefficients of ions with masses in the range from 62 to 1200 Da and from 55 to 840 Da, respectively. . . . . 223
- C.8 The same as Figure C.5, except that  $\beta_{\text{eff}}$  and  $\beta_{\text{eff,base}}$  are the effective flux coefficients of ions to polystyrene ( $\chi_p = 2.6$ ) and conductive ( $\chi_p = \infty$ ) particles, respectively. The data for NaCl particles ( $\chi_p = 6$ ) were qualitatively the same as the data shown here for polystyrene particles, except that the ratios of  $\beta_{\text{eff}}$  and  $\beta_{\text{eff,base}}$  were closer to unity. 224
- C.9 Left panel: The bias observed in the inferred size distribution when the measured ion mobility distribution,  $Z_i$ , was used when calculating  $f_{\text{cha}}$ , but either the whole distribution,  $Z_i$ , mean mobility,  $Z_{i,\text{ave}}$ , or median mobility,  $Z_{i,\text{med}}$ , was used when calculating  $f_{\text{inv}}$ , as indicated in the legend. The line color denotes the signal polarity. Right panel: The same as the left panel, except that the SR distribution was used. . 224



- C.10 The bias observed in the inferred particle size distribution when the relative permittivity of ions,  $\chi_i$ , was assumed to be  $\infty$  (conductive), 6 (dielectric), or 1.00059 (air) when calculating  $f_{\text{cha}}$ , but  $\chi_i = 6$  was assumed when calculating  $f_{\text{inv}}$ , as indicated in the legend. Only data for positive polarity when using the measured distribution is shown, as values for the negative polarity would not differ from the baseline case, and the biases observed when using the SR distribution were practically the same. . . . . 225
- C.11 The bias observed in the inferred size distribution when up to 30 charges were considered when calculating the signal, but the number of charges considered in the inversion,  $q_{\text{max}}$ , was 15, 6 or 3. The line color denotes the signal polarity, with a noticeable difference between the polarities observed only when  $q_{\text{max}} = 3$ . The bias observed when using the measured and SR distributions are depicted on the left and right, respectively. . . . . 226

## LIST OF TABLES

| <i>Number</i>  | <i>Page</i> |
|--|-------------|
| 2.1 Nominal flow conditions and particle diameters for simulations and experiments in this study. $Pe_{mig}$ and $Pe_{mig}\beta$ values are calculated for convenience in using Figs. 2.7–2.9. . . . .   | 25          |
| 2.2 Geometry parameters, fitting factors, and typical flow conditions for various DMAs. . . . .  | 40          |
| 3.1 Dominant conformation bradykinin (BK), angiotensin I (AT1), angiotensin II (AT2), and bovine ubiquitin (UB) $\Omega_i$ values. <sup>a</sup> . . . . .  | 60          |
| 4.1 Simulation Scenarios used when calculating the charge distributions. For Scenarios 1–7 and 12–13, the flux coefficients were calculated for 35 values of ion mobility, $Z_i$ , that covered the range 0.5–2.5 $cm^2V^{-1}s^{-1}$ . For Scenarios 8 and 9 the ranges were 0.65–3.1 $cm^2V^{-1}s^{-1}$ and 1.7–7.0 $cm^2V^{-1}s^{-1}$ , respectively. For Scenarios 10 and 11, only the mean and median, respectively, of negative and positive ion mobilities were used. For each scenario, the calculations were performed using the measured ion mobility distribution and the SR distribution, with the ion mass and mobility values corresponding to the latter given in parenthesis. . . . . | 80          |

|     |  |     |
|-----|--|-----|
| 4.2 | Biases observed in the particle size distributions inferred from measurements in which the charge distribution used in the pseudo-instrument differed from that in the inversion analysis, i.e., $f_{\text{cha}} \neq f_{\text{inv}}$ . The ranges of biases are given separately for negative and positive particles, $R_{\text{ave}}^{*, -}$ and $R_{\text{ave}}^{*, +}$ , respectively, and for particles smaller than or larger than 10 nm in diameter. The values in parenthesis were obtained using the SR distribution instead of the measured distribution. A value of $R_{\text{ave}}^{*, \pm}$ that differs from unity reveals underestimation or overestimation of the particle concentration. The first row provides the baseline-case, i.e., $f_{\text{cha}} = f_{\text{inv}}$ (according to Scenario 1). In the second row, $f_{\text{cha}}$ was that from Scenario 1, but FHFV charge distribution was employed in the inversion. In the third row, $f_{\text{cha}}$ was calculated using the measured distribution, while $f_{\text{inv}}$ was calculated using SR distribution, with both being according to Scenario 1. In other rows, the parameter that was changed when calculating $f_{\text{cha}}$ and $f_{\text{inv}}$ is given in the first column, with the values used when calculating $f_{\text{cha}}$ and $f_{\text{inv}}$ given in the second and third column, respectively; the other inputs were the same. . . . . | 88  |
| 4.3 | The biases, $n_{\text{inv}}/n_{\text{sim}}$ , observed in the total particle concentrations that result from using different charge distributions in the pseudo-instrument than in the inversion analysis, i.e., $f_{\text{cha}} \neq f_{\text{inv}}$ . The biases are given as a range from minimum to maximum bias during the simulation followed by the bias observed at the instance of the highest particle concentration. The values in parenthesis were obtained using the SR distribution in place of the measured ion mobility distribution presented in this study. The biases are given separately for particle size ranges of 2–1000 nm and 10–800 nm, and also for particle size distributions based on counting negative and positive particles. . . . .   | 98  |
| 5.1 | List of aerosol particle instrumentation on the Twin Otter aircraft used in this study, along with the particle property measured and particle size range covered. . . . .   | 118 |
| A.1 | Detailed simulation results. . . . .   | 182 |
| A.2 | ROMIAC1 detailed experimental results. . . . .   | 183 |
| A.3 | ROMIAC2 detailed experimental results. . . . .   | 184 |
| B.1 | LTQ–MS settings. . . . .   | 189 |
| B.2 | $m/z$ ranges used for mass-resolving ions. <sup>a</sup> . . . . .  | 190 |

|      |   |     |
|------|---|-----|
| B.3  | Instrument calibration tetra-alkyl ammonium halide (TAAX) anion-coordinated singly-charged multimer $\Omega_i$ and $K_{0,i}$ . <sup>a</sup> . . . . .   | 194 |
| B.4  | TAAX instrument calibration detailed results. <sup>a</sup> . . . . .  | 195 |
| B.5  | TAAX salt ions detailed results. . . . .  | 196 |
| B.6  | Peptide mobility calibration detailed results. <sup>a</sup> . . . . .   | 198 |
| B.7  | Mobility calibration bradykinin (BK), angiotensin I (AT1), angiotension II (AT2), and bovine ubiquitin (UB) $\Omega_i$ at $T_{\text{ESI}} = 298$ K, and comparison to literature values. <sup>a</sup> . . . . . | 199 |
| B.8  | Mobility calibration bradykinin (BK), angiotensin I (AT1), and angiotension II (AT2) $\Omega_i$ at $T_{\text{ESI}} = 400$ K, and comparison to literature values. <sup>a</sup> . . . . .                        | 200 |
| B.9  | Peptides: detailed results at $T_{\text{ESI}} = 298$ K. . . . .   | 201 |
| B.10 | Peptides: detailed results at $T_{\text{ESI}} = 400$ K. . . . .   | 202 |
| B.11 | Model peptides: detailed results at $T_{\text{ESI}} = 298$ K. . . . .   | 205 |

## Chapter 1

### PREFACE

Nearly a century has passed since the development of the first differential mobility analyzer (DMA) by Henry Erikson (1921). His instrument passed air between polonium to ionize gas molecules, which were then subjected to an electric field to deposit on a strip connected to an electrometer for detection. By changing the distance of the strip from the sample inlet, scientists had, for the first time, the ability to probe the mobility distribution of gas ions.

The many innovations over the next several decades by G. W. Hewitt (1957), Kenneth Whitby (1966), William Clark, E. O. Knutson (1975), Benjamin Liu (1974; 1975), and David Pui led to the TSI Model 3071 DMA, perhaps the most successful commercial instrument for electrical sub-micron aerosol measurement. It has been the *de facto* instrument for research-grade aerosol mobility measurement for the past three decades.

Many variations of the DMA have been developed since then, particularly with the objective of minimizing diffusional losses such that classifying aerosol particles less than  $\sim 20$  nm in diameter can be achieved with greater transmission and resolution. Many approaches have centered around the minimization of residence time within the DMA, implemented through instrument miniaturization, aspect ratio reduction, or operation at high gas flow rates (but short of inducing turbulence).

The history of DMAs has been thoroughly and entertainingly described by Richard Flagan (1998). In 2004, he introduced the idea of an opposed migration aerosol classifier (OMAC; Flagan 2004) to the aerosol science community. It is fundamentally different from the DMA in the orientation of gas flow relative to the electric field in a classification region. This results in the benefit that particles must diffuse over a greater length scale to adversely affect resolution compared to a DMA. This inherent advantage of an OMAC affords it a greater dynamic range and makes it an attractive candidate to pursue a goal of small aerosol particle classification.

In my time here at the institute, I have created OMAC prototypes that have successfully classified sub-20 nm particles. Unlike predecessor OMACs before my time, they are radial in geometry and have proven quite useful for the classification of ions.

These "ROMIACs" have been exhaustively characterized, as described in Chapter 2, in hopes that this will save future users from an effort as tedious as calibration.

The following next few chapters describe the various applications of these ROMIACs so far. I caution the reader to follow the nomenclature established in each chapter, rather than assume that nomenclature spans the entire thesis. The nomenclature is generally consistent, though there are hazards in Chapter 3, regarding biomolecules, and Chapter 4, regarding ion charge distribution. Notably,  $\Omega$  is used in Chapter 3 and its supplementary section to refer to collisional cross section, as is the convention in the spectrometry community, while elsewhere,  $\Omega$  refers to a classifier transfer function, as is the convention in the aerosol science community. In the supplementary information for Chapter 4,  $\beta$  refers to ion-to-particle attachment coefficients, as established by the seminal work of Hoppel and Frick (1986). However,  $\beta$  in the rest of the thesis refers to the operating flow rate ratio of an aerosol particle classifier, following the convention of the aerosol instrumentation community, at least after Mark Stolzenburg's landmark thesis in which he derived the diffusional transfer function for a DMA (1988).

Chapter 3 describes the first ever application of a ROMIAC, through a collaboration with J. L. Beauchamp in the separation of biomolecules. Though this application may seem tangential to an aerosol scientist, the study showed that the ROMIAC can achieve very high resolution by differentiating between sub-2 nm stereoisomers.

In an experiment proposed by my colleague Johannes Leppä, the ROMIAC was used to obtain the steady-state ion mobility distribution from the air passed through a bipolar aerosol charger. These measurements were part of a collection of scenarios in Chapter 4 used to quantify the bias that results in inverting raw aerosol size distribution data with the oft-assumed (by aerosol scientists) Fuchs/Hoppel-Frick/Wiedensohler steady-state charge distribution.

In the summer of 2013, I had the rewarding experience of taking part in an aircraft field campaign in Monterey, California. The ROMIAC complemented the DMA's 30–800 nm particle size distribution with the sub-20 nm particle size distribution. The ROMIAC did not see much for many flights, as there are few small particles when flying through clouds or over the ocean. However, the data it returned when flying over Harris Ranch, a large cattle feedlot in Coalinga, California, was quite spectacular in its clarity of depicting a plume of freshly formed particles from the feedlot emissions. The analysis of these feedlot plumes is described in Chapter 5.

In the last two years of my doctoral studies, I have had the pleasure of collaborating with Susanne Hering of Aerosol Dynamics Inc. in Berkeley, California in the development of miniaturized OMACs, described in Chapter 6. My first visit to her lab was in January 2014, when we used the ROMIAC at low flow rates to extend the measurement range up to 200 nm diameter particles. After great results, we worked together a second time in December 2015 with a prototype planar OMAC in an attempt to extend the measurement range up to 1000 nm particles. Though the performance of this new planar OMAC fell short of expectations, there were many valuable lessons learned that will undoubtedly be useful to the next OMAC developer.

## References

- Erikson, H. A. (1921). “The change of mobility of the positive ions in air with age”. In: *Am. Phys. Soc.* 18.2, pp. 100–101.
- Flagan, R. C. (1998). “History of electrical aerosol measurements”. In: *Aerosol Sci. Technol.* 28.4, pp. 301–380. DOI: 10.1080/02786829808965530.
- (2004). “Opposed migration aerosol classifier (OMAC)”. In: *Aerosol Sci. Technol.* 38.9, pp. 890–899. DOI: 10.1080/027868290505242.
- Hewitt, G. W. (1957). “The charging of small particles for electrostatic precipitation”. In: *Trans. Am. Inst. of Electr. Eng., Part I: Commun. and Electron.* 76.3, pp. 300–306.
- Hoppel, W. A. and G. M. Frick (1986). “Ion-aerosol attachment coefficients and the steady-state charge distribution on aerosols in a bipolar ion environment”. In: *Aerosol Sci. Technol.* 5.1, pp. 1–21. DOI: 10.1080/02786828608959073.
- Knutson, E. O. and K. T. Whitby (1975). “Aerosol classification by electrical mobility: apparatus, theory, and applications”. In: *J. Aerosol Sci.* 6, pp. 443–451. DOI: 10.1016/0021-8502(75)90060-9.
- Liu, B. Y. H. and D. Y. H. Pui (1975). “On the performance of the electrical aerosol analyzer”. In: *J. Aerosol Sci.* 6.3, pp. 249–264.
- Liu, B. Y. H., K. T. Whitby, and D. Y. H. Pui (1974). “A portable electrical analyzer for size distribution measurement of submicron aerosols”. In: *JAPCA* 24.11, pp. 1067–1072. DOI: 10.1080/00022470.1974.10470016.
- Stolzenburg, M. R. (1988). “An ultrafine aerosol size distribution measuring system”. Ph.D. Thesis. University of Minnesota.
- Whitby, K. T. and W. E. Clark (1966). “Electric aerosol particle counting and size distribution measuring system for the 0.015 to 1  $\mu\text{m}$  size range”. In: *Tellus A* 18.2-3, pp. 573–586. DOI: 10.3402/tellusa.v18i2-3.9340.



## *Chapter 2*

# DESIGN, SIMULATION, AND CHARACTERIZATION OF A RADIAL OPPOSED MIGRATION ION AND AEROSOL CLASSIFIER (ROMIAC)

By Wilton Mui, Huajun Mai, Andrew J. Downard, John H. Seinfeld, and Richard C. Flagan

This chapter is was submitted to, and is currently under review by, *Aerosol Science and Technology* as:

Mui, W. et al. (2017). “Design, simulation, and characterization of a radial opposed migration ion and aerosol classifier (ROMIAC)”. In: *Aerosol Sci. Technol.* In review.

### **2.1 Abstract**

We present the design, simulation, and characterization of the radial opposed migration ion and aerosol classifier (ROMIAC), a compact differential electrical mobility classifier. We evaluate the performance of the ROMIAC using a combination of finite element modeling and experimental validation of two nearly-identical instruments using tetra-alkyl ammonium halide mass standards and sodium chloride particles. Mobility and efficiency calibrations were performed over a wide range of particle diameters and flow rates to characterize ROMIAC performance under the range of anticipated operating conditions. The ROMIAC performs as designed, though performance deviates from that predicted using simplistic models of the instrument. The underlying causes of this non-ideal behavior are found through finite element simulations that predict the performance of the ROMIAC with greater accuracy than the simplistic models. It is concluded that analytical performance models based on idealized geometries, flows, and fields should not be relied on to make accurate *a priori* predictions about instrumental behavior if the actual geometry or fields deviate from the ideal assumptions. However, if such deviations are accurately captured, finite element simulations have the potential to predict instrumental performance. The present prototype of the ROMIAC maintains its resolution over three orders of magnitude in particle mobility, obtaining sub-20 nm particle size distributions in a compact package with relatively low flow rate operation requirements.

## 2.2 Introduction

### Differential mobility analyzer

The differential mobility analyzer (DMA) has long been the primary instrument used to measure size distributions of aerosol particles smaller than  $1\ \mu\text{m}$  in diameter. This instrument separates charged particles according to their electrical mobilities,  $Z$ , in an electric field that is transverse to a particle-free sheath flow (Knutson and Whitby 1975). Particles within a narrow range of mobilities migrate across a channel between two electrodes in the time required to transit the length from the entrance port to a downstream sample extraction port in the counter-electrode, where they exit in a classified sample flow; others deposit on the walls of the DMA or are discharged in an exhaust flow.

In the ideal, non-diffusive limit, the range of particle mobilities in the classified sample flow is determined by the relative aerosol and sheath flow rates (Knutson and Whitby 1975). The most common DMA is that of Knutson and Whitby, which probes particles ranging from 10–1000 nm in mobility-equivalent diameter,  $D_Z$ , though the range that can be scanned with reasonable size resolution is narrower unless the flow rates are varied. Earlier DMAs had probed molecular ions, e.g., see Erikson (1921) and Flagan (1998). The Knutson-Whitby DMA (KWDMA) is usually operated with sheath and exhaust flow rates ( $Q_{\text{sh}}$  and  $Q_{\text{ex}}$ , respectively) 10 times those of the aerosol and classified sample flows ( $Q_a$  and  $Q_c$ ). The operating conditions of the DMA are generally described in terms of the flow rate ratio  $\beta = (Q_a + Q_c)/(Q_{\text{sh}} + Q_{\text{ex}})$ , which is the primary factor determining the resolving power of the instrument, and  $\delta = (Q_c - Q_a)/(Q_c + Q_a)$ , a measure of the flow imbalance. DMAs are typically operated with balanced flows, i.e.,  $Q_a = Q_c$  and  $\delta = 0$ .

The performance of a DMA is conveniently described in terms of the transfer function, which is defined as the probability that a particle of mobility  $Z$  will be transmitted through the classifier when the voltage and flow rates are tuned to transmit particles of characteristic mobility  $Z^*$ , which corresponds to particles that enter the classifier at the centroid of the incoming aerosol sample flow, and exit at the outgoing classified aerosol flow. In their landmark paper, Knutson and Whitby (1975) employed fluid and particle stream functions to derive the so-called transfer function for particles that do not diffuse as they transit the DMA. The fluid stream function,  $\psi$ , is defined such that

$$ru_r = \frac{\partial \psi}{\partial z}, \quad \text{and} \quad ru_z = -\frac{\partial \psi}{\partial r}, \quad (2.1)$$

where  $r$  is the classifier radial coordinate,  $z$  is the classifier axial coordinate, and  $u_r$  and  $u_z$  are the radial and axial fluid velocities, respectively; the stream function automatically satisfies the mass continuity for the gas. Particles of electrical mobility  $Z$  also migrate at velocity  $\vec{v}$  under the action of the applied electric field, i.e.,  $\vec{v} = Z\vec{E}$ . This migration can be described in terms of the electric flux function,  $\phi$ , which is defined such that

$$rE_r = \frac{\partial \phi}{\partial z}, \quad \text{and} \quad rE_z = -\frac{\partial \phi}{\partial r}. \quad (2.2)$$

For a steady electric field, a pseudo-steady-state can be assumed for the particle motion, so these contributions to the particle motion can be described in terms of a particle stream function, which is defined as

$$\Gamma = \psi + Z\phi. \quad (2.3)$$

When particles are sufficiently large that diffusion can be neglected, particles follow trajectories along which  $\Gamma = \text{constant}$ , though both  $\psi$  and  $\phi$  change along the migration trajectory, so

$$\Gamma_{\text{out}} - \Gamma_{\text{in}} = \Delta\Gamma = 0 = \Delta\psi + Z\Delta\phi. \quad (2.4)$$

Thus, Knutson and Whitby (1975) noted that the migration of particles across a range of stream functions,  $\Delta\psi$ , requires that it also migrate across a range of electric flux functions,  $\Delta\phi = -\Delta\psi/Z$ . Assuming the flow in a cylindrical DMA to be parallel to the electrodes, the volumetric flow rate,  $Q$ , between the outer electrode,  $R_2$ , and a radial position,  $r$ , is  $Q(r) = \int_{R_2}^r 2\pi r u_z(r) dr = 2\pi\psi(r)$ . They further defined the characteristic trajectory within a DMA as that for which a non-diffusive particle will be transmitted from the radial position at which 50% of the cumulative incoming aerosol flow enters to the corresponding 50% radius for the cumulative classified aerosol outlet flow. The mobility of the particle that follows this 50%-50% trajectory is denoted as  $Z^*$ . The range of stream function values crossed is defined by the specified inlet and outlet flow fractions, i.e.,  $\psi_{\text{in}}^* = Q_a/4\pi$ , and  $\psi_{\text{out}}^* = (Q_{sh} + Q_{ex} + Q_a)/4\pi$ ; thus,

$$\Delta\psi^* = \frac{Q_{sh} + Q_{ex}}{4\pi}. \quad (2.5)$$

The change in electric flux function that a particle traverses,  $\Delta\phi^*$ , depends upon the spatial variation of the electric field. In the special case of a long, cylindrical DMA column for which the aspect ratio  $\alpha = L/(R_2 - R_1) \gg 1$ , where  $L$  is the axial length of the electrode, the gas velocity can reasonably be assumed to be parallel to the electrode surfaces and the electric field can be assumed to be perpendicular to them, i.e.,  $E_r = -\frac{V}{r \ln \frac{R_2}{R_1}}$  and  $E_z = 0$ , where  $V$  is the voltage applied to the central electrode, and  $R_1$  and  $R_2$  are the radii of the inner electrode and the outer electrode, respectively. Then,

$$\Delta\phi^*|_{\alpha \gg 1} = -\frac{VL}{\ln \frac{R_2}{R_1}}, \quad (2.6)$$

and, since  $Z^* = -\frac{\Delta\psi^*}{\Delta\phi^*}$ , we find

$$Z_{CDMA, \alpha \gg 1}^* = \frac{(Q_{sh} + Q_{ex})}{4\pi VL} \ln \frac{R_2}{R_1}. \quad (2.7)$$

In this special case, the transmission characteristics of such a classifier can be determined to a high degree of accuracy from first principles with simple analytic expressions. The DMA can then be considered to provide a primary particle *mobility* standard, at least for large, non-diffusive particles. Stolzenburg (1988; see also Flagan 1999) showed that particles that are transmitted at high voltage satisfy this large particle condition. Moreover, for spherical particles, the DMA becomes a primary particle *size* standard since the electrical mobility is a well-known function of particle diameter.

Rather than focusing on the absolute sizing accuracy, most recent DMA characterization studies have focused on the resolution of the instrument,  $\mathcal{R}$ , which is defined as the ratio of the mobility of the particles that are transmitted with the highest efficiency,  $Z_{\text{peak}}$ , to the range of mobilities that are transmitted with at least half of that efficiency, i.e.,  $\mathcal{R} = Z_{\text{peak}}/\Delta Z_{50\%}$ . At high classification voltage in long-column cylindrical DMA,  $Z_{\text{peak}} \approx Z^*$ . When classifying large particles (at high voltage), the resolution approaches the asymptotic limit for ideal, non-diffusive (kinematic) classification determined using the triangular transfer function of Knutson and Whitby

(1975) for balanced flows,  $\delta = 0$  (trapezoidal if  $\delta \neq 0$ ). In this limit, the non-diffusive (large particle) resolution for a DMA operated with balanced incoming sample and classified aerosol flows, i.e., when  $\delta = 0$ , is

$$\mathcal{R}_{\text{nd}} = \beta^{-1}, \quad (2.8)$$

and the peak transmission efficiency for a DMA operated at constant voltage occurs for particles of mobility  $Z^*$ .

### **Advancing nanometer particle classification**

Over the past two and a half decades, a number of innovations have extended the classification capabilities of the DMA to smaller particles, beginning with the Vienna short-column DMA that enabled measurements of particles as small as 3.5 nm (Winklmayr et al. 1991). Other designs have been developed to probe the sub-10 nm range. These include adaptations of the Knutson and Whitby DMA to produce the nanoDMA (Chen et al. 1998), and the radial DMA (RDMA; Zhang, Akutsu, et al. 1995). Development has continued, enabling classification of particles as small as 1 nm (Rosell-Llompart et al. 1996; Labowsky and Mora 2006; Brunelli, Flagan, and Giapis 2009).

The ability to classify particles in the low-nanometer regime enabled measurements of gas ions and stimulated efforts to develop instruments that attain much higher resolution than traditional DMAs for applications in molecular separations. de la Mora and coworkers (Rosser and Mora 2005; Martínez-Lozano and Mora 2006; Martínez-Lozano, Labowsky, and Mora 2006) have demonstrated DMAs that attain  $\mathcal{R} \sim 100$  at voltages near the electrostatic breakdown (arcing) limit, albeit over a very limited range of mobilities. To achieve this resolution, these DMAs operate at Reynolds numbers well beyond that typically associated with the onset of turbulence. Although the exceptionally high flow rates required for these supercritical, laminar-flow, high-resolution DMAs (100 to 1000 liters per minute (lpm) or more) limit their applicability, these instruments have enabled a number of important studies, especially when used as a front-end to a mass spectrometer (Hogan and Mora 2010; Rus et al. 2010; Hogan and Mora 2011; Oberreit, Rawat, et al. 2015).

A key feature of DMAs that extend the sizing range to the low nanometer regime is the use of a low aspect ratio classifier, i.e.,  $\alpha = \frac{\text{length of classification region}}{\text{migration distance between electrodes}} \sim 1$  (Rosell-Llompart et al. 1996). While some such instruments have maintained gas flow that is nearly parallel to the electrodes, and thus perpendicular to the electric

field between the electrodes, others have not, leading to flow and electric fields that vary with both  $r$  and  $z$ . The value of  $\Delta\psi^*$  in such instruments is still that specified by the Knutson and Whitby definition of the characteristic particle streamline, but the presence of both radial and axial components to the electric field may preclude simple, analytical expressions for  $\Delta\phi^*$ . Instead,  $\Delta\phi^*$  may be determined numerically or by calibration with suitable mobility standards. Deviations from the value of  $Z_{\text{ideal}}^*$  suggested by idealized, i.e., high aspect ratio, models have been reported by introducing an empirical mobility correction factor,  $f_Z$ , thereby accounting for both the low aspect ratio perturbations to particle trajectories and fields and the effects of imperfections in the instrument, i.e.,

$$Z^* = f_Z Z_{\text{ideal}}^* = \frac{f_Z \Delta\psi^*}{\Delta\phi^*}. \quad (2.9)$$

Since  $\Delta\psi^*$  is specified by the definition of the characteristic trajectory, Eq. (2.9),  $Z^*$  gives an estimate of  $\Delta\phi^*$ , provided the calibration is performed using mobility standards that are large enough that they require voltages well beyond the diffusional broadening threshold (Flagan 1999). The transfer function for DMA classification of diffusive particles is well described by the semi-analytical model of Stolzenburg (1988), even for DMAs that deviate from the idealized, parallel-flow and perpendicular-field instrument.

While particles in the low-nanometer regime can be classified with DMAs, transmission efficiencies are often quite low at the smallest particle sizes because of high diffusional losses. A recent intercomparison of several nanoparticle DMAs found transmission efficiencies of 1.16 nm particles that ranged from nondetectable to as high as 17% (Jiang et al. 2011). Diffusional losses in DMAs are accentuated by adverse potential gradients in the transition between the grounded exterior plumbing and the high voltage electrode. Depending on the DMA design, this adverse gradient may occur at either the entrance or exit of the DMA, but it is present in *nearly* all DMA designs. However, by careful design of those regions of the DMA, the effect of the adverse potential gradient can be reduced (Kousaka et al. 1986; Zhang and Flagan 1996; Franchin et al. 2016). While the adverse gradient is integral to the design of all commonly used DMAs, Labowsky and Mora (2006) described a novel instrument in which particles are introduced and extracted from the grounded side of the classifier; that classifier can, however, only be used with an electrometer or other charged particle detector because neutral particles will be included in the classified-sample outlet flow. Tammet demonstrated a highly modified DMA in

which the field is created by applying a potential between a pair of screens that are inclined with respect to the sheath flow (Hannes Tammet 2003; H. Tammet 2011). This symmetric inclined grid mobility analyzer classifies ions and particles of both polarities (hence “symmetric”) in the 0.4–7.5 nm range with  $\mathcal{R}$  of 2–3.

Yet another approach to classifying particles is the transient drift-tube ion-mobility spectrometer of Oberreit, McMurry, and Hogan (2014). In this device, a bolus of particles is introduced into a drift tube with no electric field applied, thereby avoiding losses associated with exposure of the particle sample to an adverse electric field. At the start of the transient separation, an electric field is applied that induces those particles located past a critical point to migrate toward the opposite end of the drift tube, where a large counterflow enters around the perimeter, and a smaller analyte flow exits at the center. The particle’s mobility is inferred from its time-of-flight down the drift tube. This method relies on the availability of fast-response particle detectors that have recently become available.

Flagan (2004) proposed and modeled an alternate differential mobility classifier that has some features of that of Tammet (2003; 2011); like the DMA, this opposed migration aerosol classifier (OMAC) can continuously extract particles within a narrow range of mobilities for detection or use in other experiments. In this device, migration between two permeable electrodes that define the classification channel is opposed by a cross-flow ( $Q_{cf}$ ) of particle-free gas through those electrodes. Particles, the electrical migration of which is balanced by the cross-flow, are advected between the porous electrodes by a smaller sample flow. The performance of the OMAC is similar to that of the DMA, except that the voltage at which diffusion *begins* to degrade resolution is much lower, and scales as  $V \propto \mathcal{R}_{nd}$  (Downard, Dama, and Flagan 2011) rather than as  $V \propto \mathcal{R}_{nd}^2$  as in the DMA (Flagan 1999). Because the length scale over which diffusion must act to affect resolution is the entire channel width,  $b$ , in the OMAC, but only  $\sim \beta b$  in the DMA, the dynamic range of the OMAC can, in theory, be made much larger than that of *any* DMA of comparable resolving power and dimensions.

This paper describes the design, simulation, and experimental characterization of a radial form of this new instrument. This Radial, Opposed-Migration, Ion and Aerosol Classifier (ROMIAC) enables measurement of ions and particles well into the low-nanometer regime, with resolution that has enabled mobility separation of peptide stereoisomers (Mui et al. 2013). Here, we describe the use of 3-dimensional finite element simulations in modeling the performance of an instrument capable of

probing a wide range ( $\sim 600\times$ ) of mobilities (1 to 20 nm in diameter) at select fixed flow rates, and with  $\mathcal{R}$  as high as  $\sim 20$ . We also report on the experimental validation of two nearly-identical prototypes of the ROMIAC. Finally, we demonstrate that computational modeling is required to explain behavior that idealized models do not capture. We note that the development of the ROMIAC involved several iterations of design and simulation to attain the performance of the final design that we report below.

## 2.3 Instrument design

### Desired features

Flagan (2004) described the OMAC concept in terms of a simple, rectilinear classification channel similar to that used in the first DMA (Erikson 1921; Flagan 1998). Most DMAs have, however, employed a cylindrical, axisymmetric geometry that eliminates the edge effects of the side walls in a rectilinear design. While a cylindrical OMAC could be built, producing cylindrical electrodes that are uniformly porous over their entire areas would be a technical challenge.

The RDMA (Zhang, Akutsu, et al. 1995) attains the simplicity of planar electrodes, while eliminating the edge effects. Early unpublished prototypes of rectilinear OMACs yielded lower than predicted resolution, possibly the result of edge effects. In this study we have, therefore, undertaken the design and development of a radial-flow OMAC. This instrument ultimately has important applications for molecular separations as well as for aerosols; it was first applied to molecular ion classification, including the separation of peptide stereoisomers (Mui et al. 2013). As such, it has been labeled the radial opposed migration ion and aerosol classifier (ROMIAC).

Introducing the aerosol through the ground electrode, and extracting the particles through the same ground electrode eliminates the adverse potential gradient drawback common to DMAs, and, thereby, potentially enhances particle transmission relative to designs with an adverse potential gradient. A consequence of this design is that both the flow and electric field in the classification region deviate from the ideal ones considered in the initial conceptual models (Flagan 2004; Downard, Dama, and Flagan 2011). The classified-aerosol outlet port is located at the center of the grounded screen electrode. Although the classified aerosol could exit through an open port through that electrode, that would distort the electric field. Instead, the classified aerosol outlet port in the present design rests directly on the grounded electrode screen, thereby maintaining a uniform electric field throughout



the classification region at the potential expense of losses from diffusive deposition.

Uniform distribution of aerosol flow across the width (in the case of a rectilinear classifier) or around the introduction radius (in the case of cylindrical or radial classifiers) is essential if high resolution is to be attained. Aerosols are usually introduced into and extracted from classifiers via small (e.g., 6 mm, or 1/4 inch) tubing. The relatively high velocity flow in the sample introduction port must transition into a uniform flow around the perimeter of a radial flow instrument, or across the width of a rectilinear one. For radial classifiers, reasonably uniform distribution of incoming aerosol can be achieved by introducing the aerosol tangentially into a circular “race-track” around the outer radius of the classifier, as in the cylindrical Vienna DMA (Winklmayr et al. 1991) and the radial DMAs (Zhang, Akutsu, et al. 1995; Brunelli, Flagan, and Giapis 2009), provided adequate pressure drop is maintained between the racetrack and the classification region.

### **Idealized design model**

Transmission of a particle through any mobility classifier is governed by the balance of opposed drag and electric forces,  $\mathbf{F}_D$  and  $\mathbf{F}_E$ , respectively (Fig. 2.1a). Unlike a DMA in which the particles must migrate across a sheath flow that enters parallel to the aerosol flow, the cross-flow in the ROMIAC is introduced orthogonally to the electrodes and aerosol flow, so the fluid streamlines are inclined relative to the electric field lines (Fig. 2.1b-c). The axial component of the fluid velocity (which is, nominally, the cross-flow velocity,  $u_{cf}$ ) must balance the electrical migration velocity,  $v_{mig}$ , for a particle to remain within the classification channel; the smaller, radial component of the fluid velocity (which is, nominally, the aerosol flow velocity,  $u_a$ ) transports particles from the sample inlet to the outlet.

In a ROMIAC configured such that aerosol enters the region between two parallel disc-shaped electrodes at the outer radius and classified aerosol is extracted from an outlet at the center of one of the electrodes, the relationship between the migration and cross-flow velocity for an idealized instrument in which the aerosol flow is initially uniformly distributed across the classification channel is

$$v_{mig} = EZ^* = \frac{Q_{cf}}{\pi (R_{elec}^2 - R_o^2)}, \quad (2.10)$$

where  $E = \nabla V \approx V/b$  is the electric field strength,  $b$  is the electrode separation distance, and  $R_{elec}$  and  $R_o$  are the electrode and outlet radii of the classifier, re-

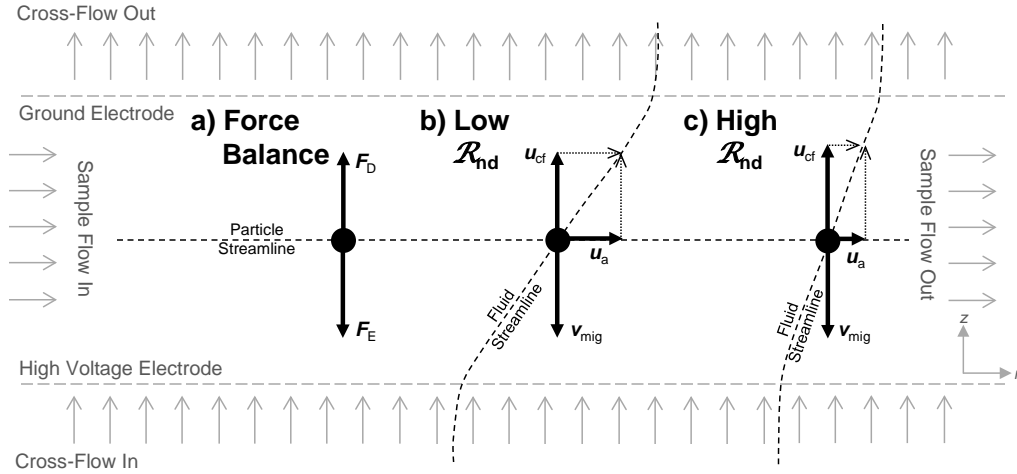


Figure 2.1: (a) Simplified diagram of balanced drag,  $F_D$ , and electric,  $F_E$ , forces acting on a particle of mobility  $Z^*$  in the ROMIAC classification region, resulting in a particle streamline that is parallel to the sample flow direction. (b) Simplified diagram of aerosol and cross-flow fluid velocities ( $u_a$  and  $u_{cf}$ , respectively) and electrical migration velocity,  $v_{mig}$ , acting on a particle of mobility  $Z^*$ . Low  $\mathcal{R}_{nd}$  operation results in fluid streamlines that significantly deviate from vertical. Particles of mobility  $Z^*$  will thus experience a high advective velocity (relative to the cross-flow velocity) from sample inlet to outlet, increasing the transmission of all particles, and resulting in lower resolution. (c) High  $\mathcal{R}_{nd}$  operation results in nearly vertical fluid streamlines, discriminating more heavily against the transmission of particles that are not of mobility  $Z^*$ .

spectively. The ROMIAC deviates from this simplistic model in that the aerosol enters through the grounded electrode, as illustrated in Fig. 2.2, which identifies key dimensions of the ROMIAC and illustrates characteristic trajectories of particles of different mobilities.

### Design criteria and prototype specifications

The initial objective in the design of the ROMIAC was to enable particle size distribution measurements with constant resolution from 1 to 20 nm in diameter. The instrument flow rates were chosen to be compatible with existing condensation particle counters or electrometers that would be used to detect the classified particles. Hence, the aerosol and classified sample flow rates were initially constrained to be  $Q_a = Q_c \approx 1$  lpm. Additionally, the ROMIAC was designed to classify sub-20 nm aerosol using pumps that were of modest weight and power consumption for airborne measurements, thus constraining  $Q_{cf} < 50$  lpm. To enable measurements over a wide range of mobilities with minimal variation in  $\mathcal{R}$ , an electrode spacing of

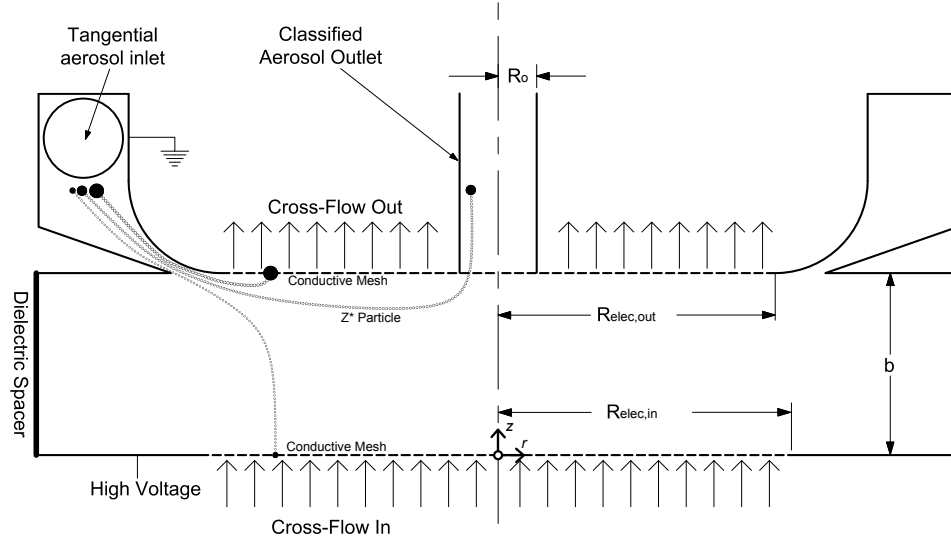


Figure 2.2: Schematic of ROMIAC aerosol introduction, classification region, and classified aerosol outlet. Particles are introduced via a tangential inlet tube to be azimuthally distributed through a thin knife-edge gap into the classification region, where particles follow characteristic trajectories based on the degree of balance of drag and electric forces experienced. Particles of mobility  $Z^*$  will be advected toward the center and extracted through the outlet. Key dimensions that define the classification region are indicated. The origin of the coordinate system is designated to be the center of the incoming cross-flow electrode.

$b = 10$  mm was selected for the nominal design, allowing for a maximum voltage of  $\sim 10$  kV (since particle diffusion effects are minimized at high voltages), though the prototype was designed with the flexibility to allow measurements to be made with electrode spacings as small as 1 mm for operation at lower peak voltages.

The foregoing specifications formed the basis for the prototype design of the ROMIAC. The aerosol flows from a tube with inner radius  $R_o = 2.4$  mm, i.e., standard 1/4 inch stainless steel tubing, into an electrically grounded, tangential racetrack; the aerosol then passes through a narrow, azimuthal knife-edge gap to enter the classification region. In order to achieve the pressure drop required to ensure uniform flow through the entire annular aerosol entrance slot, the gap between the knife edge and the rounded edge of the ground electrode needs to be small. In the prototype ROMIAC, this gap can be adjusted by the insertion of precision shims, each of thickness  $\Delta b_{\text{shim}} = 0.381$  mm, for the instrument reported here. The inter-electrode gap,  $b_{\text{nom}}$ , was defined by a 10 mm thick Delrin spacer. The cross-flow enters the ROMIAC through a conductive stainless steel mesh of radius  $R_{\text{elec,in}} = 16.1$  mm and

exits through the same material of radius  $R_{\text{elec,out}} = 15.2$  mm. Mechanical design considerations constrain the outlet electrode mesh to have a slightly smaller radius than the entrance slot, and, therefore, the inlet electrode mesh (Fig. 2.2). The classified sample outlet port is located at the center of the outlet grounded electrode, with inner radius  $R_o = 2.4$  mm. Figure 2.3 shows the realized design of the ROMIAC, which has overall exterior dimensions of 10.5 cm in height and 11.4 cm in diameter. The two prototypes used in this study are deemed “nearly-identical” because they share identical dimensions and components, with the exception of the electrode meshes. The mesh used in one ROMIAC (“ROMIAC1”) was 325-mesh (30% open area) while the mesh used in the other ROMIAC (“ROMIAC2”) was 200-mesh (34% open area). Preliminary measurements were conducted in which ROMIAC1 had either 325-mesh or 200-mesh electrodes, with little difference in transmission efficiency observed; these measurements were also conducted with ROMIAC1 with 500-mesh (25% open area) electrodes, both without and with a hole cut in the outlet electrode (so that particles would not pass through a screen to exit through the outlet port), which also showed little difference in transmission efficiency (Appendix A). The residence time for particles in the ROMIAC is estimated at  $\sim 0.7$  s based on an assumed  $Q_a = 1$  lpm and the volumes of the tubing and classification region; measurements associated with, but not reported, in Mui et al. (2013) suggested that a coupled ROMIAC-mass spectrometer showed response times of  $\lesssim 0.5$  s for a step increase in signal.

## 2.4 Simulation methods

### Three-dimensional finite element analysis

Preliminary simulations entailed solving the flow and electrical fields within the ROMIAC as a 2-dimensional, axisymmetric model in COMSOL Multiphysics™. The fluid and electrostatic maps were then imported and interpolated within Matlab™ to provide fluid flow and electric field values at any arbitrary point in  $r$ - $z$  space to drive particle dynamics equations and simulate Monte Carlo diffusive particle trajectories within the classification region. Brownian diffusion of particles was simulated with pseudorandom fluctuations in the  $r$ - and  $z$ -directions. Though computationally inexpensive, the 2-dimensional models did not capture the effect of the tangential inlet and distribution racetrack on particle transmission. Particles had to be introduced in the region near the converging entrance upstream of the knife edge gap to enter the classification region, due to the inaccurate representation of the inlet region in 2-dimensional space.

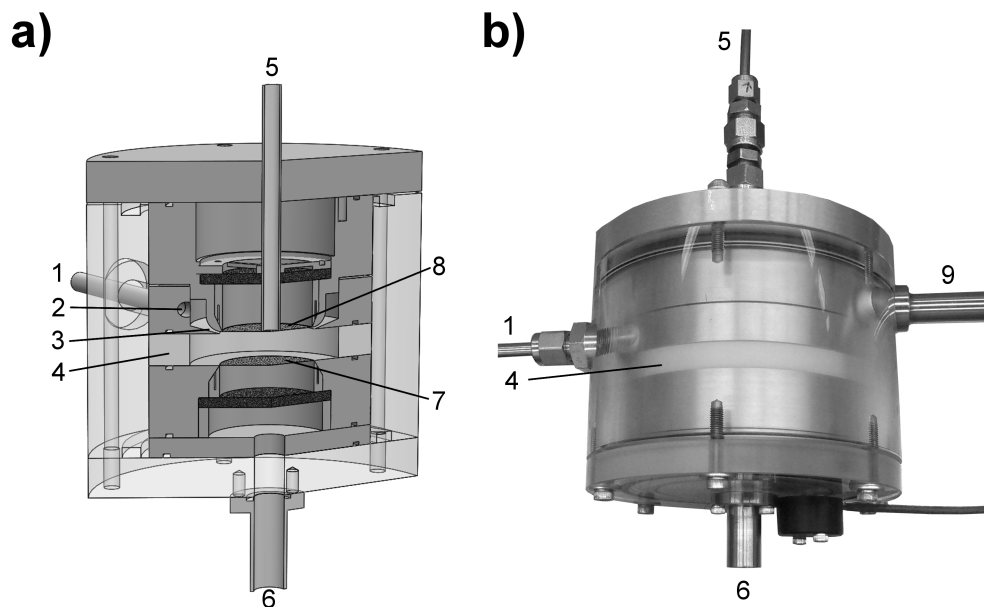


Figure 2.3: (a) Cutaway view and (b) photograph of ROMIAC with key features numbered. Overall exterior dimensions are 10.5 cm in height and 11.4 cm in diameter. 1) aerosol inlet tube; 2) tangential inlet to distribution racetrack; 3) distribution knife-edge; 4) dielectric spacer; 5) classified aerosol outlet tube; 6) incoming cross-flow port; 7) high voltage porous electrode; 8) electrically grounded porous electrode; 9) outgoing cross-flow port.

Preliminary 3-dimensional models in COMSOL Multiphysics™ were explored using the charged-particle tracing feature of the software. However, the need to account for Brownian diffusion rendered early models too computationally expensive and impractical. An improved 3-dimensional model in COMSOL Multiphysics™ was developed in which the particles were modeled as “large ions” by solving the convective diffusion equation, thereby capturing the effect of Brownian diffusion with only slightly more computational expense than earlier 2-dimensional models. Only the 3-dimensional convective diffusion equation model will be discussed for the remainder of this study.

The model geometry was created to reflect the interior volumes in which the ions or particles are classified. These volumes include the full length of inlet tubing, the tangential introduction, the distribution racetrack, the distribution knife-edge gap, the classification region, and the full length of outlet tubing. The geometry included the effects of design compromises that were required to facilitate fabrication and assembly of the instrument. These compromises resulted in the electrode mesh not being perfectly aligned with the intended electrode plane, causing the electrode

separation distance to be greater than the sum of  $b_{\text{nom}} = 10$  mm and  $\Delta b_{\text{shim}} = 0.381$  mm. The additional distance due to imperfect alignment of the electrode plane and the mesh was estimated from a fully assembled 3-dimensional model of the ROMIAC in Solidworks™ (Fig. 2.3a) as  $\Delta b_{\text{mesh}} = 0.94$  mm, leading to a total electrode gap separation distance of  $b_{\text{total}} = b_{\text{nom}} + \Delta b_{\text{shim}} + \Delta b_{\text{mesh}} = 11.32$  mm.

The flow in the ROMIAC was modeled in the COMSOL Multiphysics™ fluid-flow module, assuming laminar, single-phase flow of a compressible fluid (air at 298 K) by solving the Navier-Stokes equations. Walls were assigned a no-slip boundary condition. The incoming aerosol boundary was located at the beginning of the inlet tube, with an assumed, atmospheric-pressure boundary condition. The classified aerosol outlet boundary was likewise located at the end of the outlet tube, with an assumed normal outflow velocity boundary condition of  $Q_a/(\pi R_o^2)$ . The porous electrodes served as the boundaries for the cross-flows, assuming a normal inflow and outflow velocity condition of  $Q_{\text{cf}}/(\pi R_{\text{elec,in}}^2)$  and  $Q_{\text{cf}}/[\pi(R_{\text{elec,out}}^2 - R_o^2)]$ , respectively.

The electrostatics module was used to solve the Poisson equation for the electric fields. The Delrin electrode spacer ( $b_{\text{nom}} = 10$  mm), which is the only dielectric component in the classification region, was assigned a zero charge boundary condition. All boundaries above the Delrin spacer were assigned a ground boundary condition ( $V = 0$ ), while all boundaries below the Delrin spacer were assigned an electric potential boundary condition.

Particle concentrations in most atmospheric aerosol studies are low enough to qualify as a dilute species. The chemical species transport module was used to solve for the transport of dilute species by diffusion using Fick's law, convection using the fluid-flow solution, and migration using the electric-field solution. All boundaries, except for the aerosol inlet and outlet, were assigned a zero concentration boundary condition, which assumes that all particles will be lost upon contact with a wall. The aerosol inlet boundary was assigned a particle number concentration condition of  $12 \times 10^3 \text{ cm}^{-3}$ ; equivalently, a molar concentration condition of  $2 \times 10^{-14} \text{ mol} \cdot \text{m}^{-3}$  was supplied to COMSOL Multiphysics™. Compared to the electric field, space charge effects are negligible at this concentration. Positive, singly-charged particles were simulated as “large ions” via their particle diffusivities,  $\mathcal{D} = ZkT/e$ , where  $k$  is the Boltzmann constant,  $T$  is the temperature, and  $e$  is the elementary charge.

For a given set of flow rates, the fluid flow field and a unity-scaled electric field were solved once. For a given  $D_Z$ , a parametric voltage sweep followed, solving

for the steady-state particle concentration solution at each voltage. The average concentrations at the ROMIAC inlet and outlet boundaries,  $\bar{c}_{\text{in}}$  and  $\bar{c}_{\text{out}}$  respectively, were calculated as the ratio of the velocity-weighted particle number flux to the fluid volumetric flux:

$$\bar{c} = \frac{\int_0^{R_0} [2\pi r |u_z(r)| c(r)] dr}{Q_a}, \quad (2.11)$$

where  $c$  is the particle number concentration, the  $r$  coordinate is local to the inlet or outlet, and the  $z$  coordinate is oriented to the inlet or outlet tube axis.

### Simulation data inversion

Downard, Dama, and Flagan (2011) derived a transfer function for a rectilinear OMAC by solving the convective-diffusive equation in Cartesian coordinates. Though this transfer function has the advantage of accounting for particle losses, it is difficult to use for data-fitting due to convergence issues. For a given  $\mathcal{R}_{\text{nd}}$  operating condition, this transfer function converges below voltages less than those usually probed experimentally, e.g., at  $\mathcal{R}_{\text{nd}} = 10$ , this transfer function converges for voltages  $\lesssim 20$  V, but the vast majority of applied voltages would be above 20 V.

Following the flux coordinate method of Stolzenburg (1988) with a shear-flow approximation to the OMAC velocity profile in a rectilinear OMAC (Flagan 2004), Mai and Flagan (2017) demonstrated that the transfer function that Stolzenburg derived for the DMA is a reasonable approximation for the OMAC. The derivation and details of this transfer function are outside the scope of this study and will be the subject of a future publication. Hence, we apply the Stolzenburg transfer function to the OMAC for the present purposes. The probability that a particle of dimensionless mobility  $\tilde{Z} = Z/Z^*$  is transmitted through the OMAC is fitted to the functional form:

$$\Omega(\tilde{Z}, \beta, \delta, \tilde{\sigma}) = \frac{\tilde{\sigma}}{\sqrt{2}\beta(1-\delta)} \left[ \mathcal{E}\left(\frac{\tilde{Z} - (1+\beta)}{\sqrt{2}\tilde{\sigma}}\right) + \mathcal{E}\left(\frac{\tilde{Z} - (1-\beta)}{\sqrt{2}\tilde{\sigma}}\right) - \mathcal{E}\left(\frac{\tilde{Z} - (1+\delta\beta)}{\sqrt{2}\tilde{\sigma}}\right) - \mathcal{E}\left(\frac{\tilde{Z} - (1-\delta\beta)}{\sqrt{2}\tilde{\sigma}}\right) \right], \quad (2.12)$$

where  $\tilde{\sigma}^2 = G\tilde{Z}/(\mathcal{R}_{\text{nd}}\text{Pe}_{\text{mig}})$  is the dimensionless measure of diffusional broadening,  $\text{Pe}_{\text{mig}} = eVf/kT$  is the migration Péclet number (ratio of transport by electrophoretic

migration to that by diffusion),  $f$  is a factor that accounts for nonuniformities in the electric field (unity in the case of radial classifiers), and  $\mathcal{E}(y) = y \operatorname{erf}(y) + \pi^{-1/2} e^{-y^2}$ . For simple shear flow, Mai and Flagan (2017) found the geometry factor for the rectilinear OMAC to be:

$$G = \begin{cases} \frac{8}{3}, & \xi = 0 \\ \frac{4 \left\{ \frac{4}{15} \left[ (1-|\xi|^{5/2}) - (1-|\xi|)^{5/2} \right] + \frac{1}{3} \left( \frac{\xi}{\alpha} \right)^2 \left[ (1-|\xi|^{3/2}) - (1-|\xi|)^{3/2} \right] \right\}}{|\xi|(1-|\xi|)}, & 0 < |\xi| < 1 \\ 2 \left[ \frac{4}{3} + \left( \frac{1}{\alpha} \right)^2 \right], & |\xi| \geq 1, \end{cases} \quad (2.13)$$

where  $\xi = \beta^{-1}(\tilde{Z} - 1) = \mathcal{R}_{\text{nd}}(\tilde{Z} - 1)$  and  $\alpha = L/b$  is the aspect ratio, where  $L$  is the electrode length. In the case of the ROMIAC, we use  $L = R_{\text{elec}} - R_o$  to estimate  $G$ .

Equation (2.12) captures the performance of the OMAC, but the specific parameter values must be empirically determined to make the description quantitative. To this end, we introduce correction factors as has been done for the DMA (Stolzenburg 1988). Figure 2.4 shows an example of a COMSOL Multiphysics™ solution for the fluid flow, electric, and particle concentration fields. As seen in Fig. 2.4, the fluid cross-flow velocity increases near the outlet radius, relative to the cross-flow velocity near the aerosol inlet radius. The magnitude of this effect varies with the flows through the instrument, so, for every pair of  $Q_a$  and  $Q_{\text{cf}}$ , there is a cross-flow velocity correction factor,  $f_{u,z} = \bar{u}_{z,\text{eff}}/\bar{u}_z$ , where  $\bar{u}_z = Q_{\text{cf}}/[\pi(R_{\text{elec,out}}^2 - R_o^2 + R_{\text{elec,in}}^2)/2]$  and  $\bar{u}_{z,\text{eff}}$  is the effective mean cross-flow velocity experienced by a particle of mobility  $Z^*$  following a typical (non-diffusive) trajectory through the ROMIAC classification region. To obtain an estimate of  $\bar{u}_{z,\text{eff}}$  from the COMSOL simulations, particles were initiated at the 50% point of the incoming aerosol flow velocity distribution across the knife-edge gap and allowed to change position in  $r$ - $z$  space based on local flow and electric field conditions over constant 0.1 ms time steps. The applied voltage was such that the particle would be transmitted at the greatest efficiency, and the calculations were repeated until the particle reached the outgoing aerosol flow streamline corresponding to the 50% point of the outgoing aerosol flow velocity distribution across the aerosol outlet. The effective average vertical velocities reported are the azimuthally-averaged local  $u_z$  values stored for each particle location at every time step.

Furthermore, fabrication tolerances and the way the aerosol enters the classification



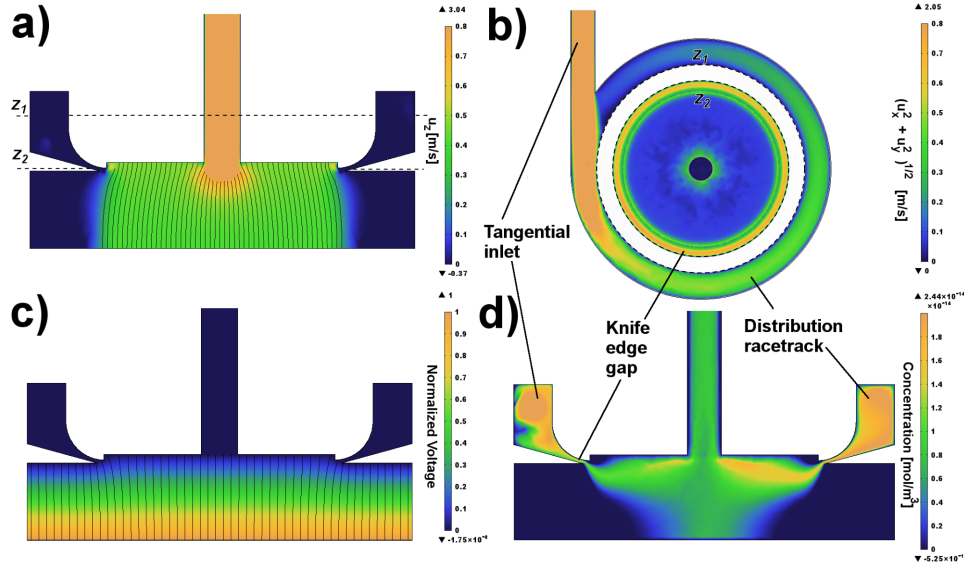


Figure 2.4: Example COMSOL Multiphysics™ solutions for the case of  $Q_a/Q_{cf}/\mathcal{R}_{nd}/D_Z = 2 \text{ lpm} / 20 \text{ lpm} / 10 / 10 \text{ nm}$ . Aerosol inlet and outlet tube extremities are cropped out of view. Color scales are restricted in range to distinguish areas of interest. Physical features of interest that may not be obvious are labeled. (a) Section view showing vertical component of fluid flow velocity,  $u_z$ . Lines show fluid flow velocity streamlines that originate from the cross-flow inlet, and are truncated at the converging region near the aerosol outlet for clarity. Note that the vertical velocity increases approaching the centered aerosol outlet. Dashed lines  $z_1$  and  $z_2$  mark sections corresponding to those in subfigure b. (b) Overhead view showing non-vertical component of fluid flow velocity,  $\sqrt{u_x^2 + u_y^2}$ . Dashed circles  $z_1$  and  $z_2$  correspond to the cut planes in subfigure a. The white ring between  $z_1$  and  $z_2$  indicates the absence of data, not zero velocity. Note that the non-vertical velocity increases approaching the centered aerosol outlet. (c) Section view showing the normalized electric potential solution. Lines show electric field streamlines that originate from the high voltage electrode surface. (d) Section view showing the particle concentration solution at a voltage corresponding to  $Z^*$ .

region cause  $Z^*$  to deviate from that predicted from the  $V$  value used in the idealized, simplistic model in Eq. (2.10). Thus, we introduce a mobility correction factor  $f_Z = Z_{\text{eff}}^*/Z^*$  to relate the effective peak particle mobility transmitted,  $Z_{\text{eff}}^*$ , to the classifier geometry and operating conditions, i.e.,

$$Z_{\text{eff}}^* = f_Z Z^* = f_Z \left( \frac{Q_{\text{cf}}}{\pi (R_{\text{elec}}^2 - R_0^2)} \right) \left( \frac{b}{V} \right). \quad (2.14)$$

The mobility correction factor for the present ROMIAC has three contributions:

(1) Reduced electric field strength from electric field distortions near the screen electrodes and/or possible modifications to the value of  $\Delta b_{\text{mesh}}$  in the assembled ROMIAC. These deviations from the simplistic model cause the observed  $Z^*$  to be higher than predicted by Eq. (2.10). The effects of reduced field strength on transmitted mobility are described by a mobility correction factor,  $f_{Z,E}$ . In the case of the COMSOL Multiphysics<sup>TM</sup> simulations, we assign a known value for  $\Delta b_{\text{mesh}}$  obtained from the Solidworks<sup>TM</sup> assembly, and the electric field is prescribed as though the permeable electrodes are solid, so  $f_{Z,E} = 1$ .

(2) The aerosol is introduced and extracted near the grounded electrode plane (between  $z = b_{\text{nom}}$  and  $z = b_{\text{nom}} + \Delta b_{\text{shim}}$ ) rather than initially filling the space between the two electrodes (at  $z = b_{\text{total}}/2$ ), as might be assumed in deriving a simplistic model of the OMAC. Consequently, when the applied voltage is that calculated from Eq. (2.10), the particles of mobility  $Z^*$  are advecting close to the grounded, cross-flow outlet electrode, enhancing diffusive particle losses. Therefore, the peak signal at the ROMIAC aerosol outlet will occur when the applied voltage is raised above the voltage suggested by the simplistic model, so as to move trajectories away from the cross-flow outlet electrode, and reduce losses.

(3) The effect of the central aerosol outlet on the vertical velocity that was described above.

We shall refer to the mobility correction factor due to reduced electric field strength (contribution 1) as  $f_{Z,E}$  and the aerosol introduction and extraction bias (grouping contributions 2 and 3 together) as  $f_{Z,\text{bias}}$ . Acknowledging all mobility correction contributions, we state that  $f_Z = f_{Z,E} \times f_{Z,\text{bias}}$ .

The aerosol outlet flow direction being parallel to, and in the same direction as the cross-flow also implies that  $Q_c$  makes an additional contribution to  $Q_{\text{cf}}$  for resolving

power purposes, at least for a portion of a particle's trajectory. The previous definition of non-diffusive resolution for the ROMIAC is a *nominal* value,  $\mathcal{R}_{\text{nd,nom}} = [\beta(1 + |\delta|)]^{-1}$ , from which we anticipate deviations. As such, the ROMIAC data may, under some circumstances, show an apparent relative resolution  $\mathcal{R}/\mathcal{R}_{\text{nd,nom}} > 1$  due to the aforementioned flow bias. We introduce a flow-rate-ratio correction factor for the ROMIAC, defined as  $f_\beta = \beta_{\text{eff}}/\beta$ , due to flow distortions in a small aspect ratio instrument.  $\beta_{\text{eff}}$  is the effective flow-rate ratio required to fit the data to Eq. (2.12). Correspondingly,  $\mathcal{R}_{\text{nd,eff}} = [\beta_{\text{eff}}(1 + |\delta|)]^{-1}$  is the effective non-diffusive resolution limit for the ROMIAC.

DMA's do not generally attain the resolving power of an ideal instrument due to imperfections in the fabrication, flows, and electric fields; a correction factor for  $\tilde{\sigma}$  has long been used to fit DMA data to transfer functions. Similarly, we define  $f_{\tilde{\sigma}} = \tilde{\sigma}_{\text{eff}}/\tilde{\sigma}$ , where  $\tilde{\sigma}_{\text{eff}}$  is the effective diffusional broadening parameter that results in the best fit of the transfer function to the data. Incorporating the correction factors into Eq. (2.12) yields the effective ROMIAC transfer function

$$\begin{aligned} \Omega_{\text{eff}}(\tilde{Z}_{\text{eff}}(f_Z), \beta, \delta, \tilde{\sigma}, f_\beta, f_{\tilde{\sigma}}) = & \frac{\tilde{\sigma} f_{\tilde{\sigma}}}{\sqrt{2}\beta f_\beta(1 - \delta)} \\ & \left[ \mathcal{E}\left(\frac{\tilde{Z}_{\text{eff}} - (1 + \beta f_\beta)}{\sqrt{2}\tilde{\sigma} f_{\tilde{\sigma}}}\right) \right. \\ & + \mathcal{E}\left(\frac{\tilde{Z}_{\text{eff}} - (1 - \beta f_\beta)}{\sqrt{2}\tilde{\sigma} f_{\tilde{\sigma}}}\right) \\ & - \mathcal{E}\left(\frac{\tilde{Z}_{\text{eff}} - (1 + \delta\beta f_\beta)}{\sqrt{2}\tilde{\sigma} f_{\tilde{\sigma}}}\right) \\ & \left. - \mathcal{E}\left(\frac{\tilde{Z}_{\text{eff}} - (1 - \delta\beta f_\beta)}{\sqrt{2}\tilde{\sigma} f_{\tilde{\sigma}}}\right) \right], \quad (2.15) \end{aligned}$$

where  $\tilde{Z}_{\text{eff}} = Z/Z_{\text{eff}}^* = Z/(f_Z Z^*)$  is the effective dimensionless mobility, and  $\tilde{\sigma}$  is still calculated using  $\mathcal{R}_{\text{nd}}$ , as defined above, rather than  $\mathcal{R}_{\text{nd,eff}}$ .

The transfer function  $\Omega_{\text{eff}}$  does not account for particle losses either in the classification region, or in the entrance and exit passages of the instrument. In the DMA, losses in the classification region are minor since particles are far from the walls for most of their transit; in the ROMIAC, particles are exposed to the classification channel's porous electrodes throughout their transit. We empirically characterize

the combined effects of all of these loss mechanisms in the instrument efficiency, which is defined as the fraction of particles of mobility  $Z^*$  transmitted through the classifier, given its transfer function, i.e.,

$$\frac{\bar{c}_{\text{out}}}{\bar{c}_{\text{in}}} = \frac{\int [n_s(Z)\eta_{\text{charge}}(Z)\Omega_{\text{eff}}(\tilde{Z}_{\text{eff}}(f_Z), \beta, \delta, \tilde{\sigma}, f_\beta, f_{\tilde{\sigma}}) \eta_{\text{trans}}(Z)\eta_{\text{det}}(Z)] dZ}{\int [n_s(Z)\eta_{\text{charge}}(Z)\eta_{\text{det}}(Z)] dZ}, \quad (2.16)$$

where  $n_s(Z)$  is the source aerosol size distribution,  $\eta_{\text{charge}}(Z)$  is the charging probability (unity in the simulations),  $\eta_{\text{trans}}(Z)$  is the classifier transmission efficiency, and  $\eta_{\text{det}}(Z)$  is the detector counting efficiency (unity in the simulations).

Inversion of the simulation data is fairly straightforward, as the source distribution is set as a single diameter in COMSOL Multiphysics™ and is, therefore, truly a Dirac delta function. Thus, the classifier transmission efficiency and transfer function are constant over the width of the source distribution and charging probability functions, and Eq. (2.16) can be simplified to

$$\frac{\bar{c}_{\text{out}}}{\bar{c}_{\text{in}}} = \Omega_{\text{eff}}(\tilde{Z}_{\text{eff}}(f_Z), \beta, \delta, \tilde{\sigma}, f_\beta, f_{\tilde{\sigma}}) \eta_{\text{trans}}(Z). \quad (2.17)$$

Simulations were conducted over a wide range of flow rates for particle diameters ranging from 1 to 20 nm. Table 2.1 lists the flow rates and particle diameters for which simulations were conducted. For each simulation, the results were fitted to Eq. (2.17) by finding values of  $f_{Z,\text{bias}}$  (since  $f_{Z,E}$  is unity for the simulations),  $f_\beta$ ,  $f_{\tilde{\sigma}}$ , and  $\eta_{\text{trans}}$  using the Matlab™ nonlinear least-squares solver (“lsqcurvefit” function) with multiple local minima optimization.

## 2.5 Experimental methods

### Tandem-ROMIAC calibrations

Two nearly-identical ROMIAC classifiers were constructed, ROMIAC1 and ROMIAC2. Tandem-ROMIAC measurements were performed with ROMIAC1 serving as the source classifier and ROMIAC2 serving as the test classifier (and vice versa, to compare the two nearly-identical classifiers). Experiments were conducted using the same set of flow rates and particle diameters, so that the simulated and experimental performance could be compared. Each transmission measurement was repeated at least 3 times.

Table 2.1: Nominal flow conditions and particle diameters for simulations and experiments in this study.  $Pe_{mig}$  and  $Pe_{mig}\beta$  values are calculated for convenience in using Figs. 2.7–2.9.

| $Q_a$ (lpm) | $Q_{cf}$ (lpm) | $\mathcal{R}_{nd}$ | $\beta$ | $D_z$ (nm)                    |                               |                               |                              |                               |
|-------------|----------------|--------------------|---------|-------------------------------|-------------------------------|-------------------------------|------------------------------|-------------------------------|
|             |                |                    |         | $Pe_{mig}$                    | $Pe_{mig}\beta$               |                               |                              |                               |
| 2           | 13.3           | 6.7                | 0.15    | $\frac{1.16^{SE}}{750 110}$   | $\frac{1.47^{SE}}{1.2e3 180}$ | $\frac{1.70^{SE}}{1.6e3 240}$ | $\frac{5^{SE}}{1.4e4 1.2e3}$ | $\frac{10^{SE}}{5.5e4 8.2e3}$ |
| 2.5         | 13.3           | 5.3                | 0.19    | $\frac{1.16^{SE}}{750 140}$   | $\frac{1.47^{SE}}{1.2e3 230}$ | $\frac{1.70^{SE}}{1.6e3 310}$ | $\frac{5^{SE}}{1.4e4 2.6e3}$ | $\frac{20^{SE}}{2.1e5 3.2e4}$ |
| 3           | 13.3           | 4.4                | 0.23    | $\frac{1.16^{SE}}{750 170}$   | $\frac{1.47^{SE}}{1.2e3 280}$ | $\frac{1.70^{SE}}{1.6e3 370}$ | $\frac{5^{SE}}{1.4e4 3.2e3}$ | $\frac{20^{SE}}{2.1e5 4e4}$   |
| 2           | 16.6           | 8.3                | 0.12    | $\frac{1.16^{SE}}{940 110}$   | $\frac{1.47^{SE}}{1.5e3 180}$ | $\frac{1.70^{SE}}{2e3 240}$   | $\frac{5^{SE}}{1.7e4 2.1e3}$ | $\frac{10^{SE}}{5.5e4 1.3e4}$ |
| 2.5         | 16.6           | 6.6                | 0.15    | $\frac{1.16^{SE}}{940 140}$   | $\frac{1.47^{SE}}{1.5e3 230}$ | $\frac{1.70^{SE}}{2e3 300}$   | $\frac{5^{SE}}{1.7e4 2.6e3}$ | $\frac{18^{SE}}{2.2e5 2.6e4}$ |
| 3           | 16.6           | 5.5                | 0.18    | $\frac{1.16^{SE}}{940 170}$   | $\frac{1.47^{SE}}{1.5e3 270}$ | $\frac{1.70^{SE}}{2e3 360}$   | $\frac{5^{SE}}{1.7e4 3.1e3}$ | $\frac{18^{SE}}{2.2e5 3.2e4}$ |
| 2           | 20             | 10                 | 0.10    | $\frac{1.16^{SE}}{1.1e3 110}$ | $\frac{1.47^{SE}}{1.8e3 180}$ | $\frac{1.70^{SE}}{2.4e3 240}$ | $\frac{5^{SE}}{2.1e4 2.1e3}$ | $\frac{10^{SE}}{6.8e4 1.2e4}$ |
| 2.5         | 20             | 8                  | 0.13    | $\frac{1.16^{SE}}{1.1e3 150}$ | $\frac{1.47^{SE}}{1.8e3 240}$ | $\frac{1.70^{SE}}{2.4e3 320}$ | $\frac{5^{SE}}{2.1e4 2.7e3}$ | $\frac{15^{SE}}{1.8e5 1.8e4}$ |
| 3           | 20             | 6.7                | 0.15    | $\frac{1.16^{SE}}{1.1e3 170}$ | $\frac{1.47^{SE}}{1.8e3 270}$ | $\frac{1.70^{SE}}{2.4e3 360}$ | $\frac{5^{SE}}{2.1e4 3.1e3}$ | $\frac{15^{SE}}{1.8e5 2.4e4}$ |
| 2.1         | 13.9           | 6.6                | 0.15    | $\frac{1.16^{SE}}{790 120}$   | $\frac{1.47^{SE}}{1.3e3 190}$ | $\frac{1.70^{SE}}{1.7e3 250}$ | $\frac{5^{SE}}{1.4e4 2.2e3}$ | $\frac{15^{SE}}{1.8e5 2.7e4}$ |
| 2.25        | 20             | 8.9                | 0.11    | $\frac{1.16^{SE}}{1.1e3 120}$ | $\frac{1.47^{SE}}{1.8e3 200}$ | $\frac{1.70^{SE}}{2.4e3 270}$ | $\frac{5^{SE}}{2.1e4 2.3e3}$ | $\frac{20^{SE}}{2.2e5 3.3e4}$ |
| 2           | 30             | 15                 | 0.07    | $\frac{1.16^S}{1.7e3 120}$    | $\frac{1.47^{SE}}{2.7e3 190}$ | $\frac{1.70^{SE}}{3.6e3 260}$ | $\frac{5^{SE}}{3.1e4 2.2e3}$ | $\frac{15^{SE}}{1.8e5 2e4}$   |
| 1.7         | 34.3           | 20.2               | 0.05    | $\frac{1.16^S}{1.9e3 100}$    | $\frac{1.47^{SE}}{3.1e3 160}$ | $\frac{1.70^{SE}}{4.1e3 210}$ | $\frac{5^S}{3.6e4 1.8e3}$    | $\frac{12^S}{1.8e5 1.2e4}$    |
|             |                |                    |         |                               |                               |                               |                              | $\frac{12^S}{2e5 1e4}$        |

<sup>S</sup>COMSOL Multiphysics™ simulation conducted for this  $D_z$

<sup>E</sup>Tandem-ROMIAC experiment conducted for this  $D_z$ . (Electrosprayed molecular standards for  $D_z < 2$  nm and atomized NaCl for  $D_z \geq 5$  nm)

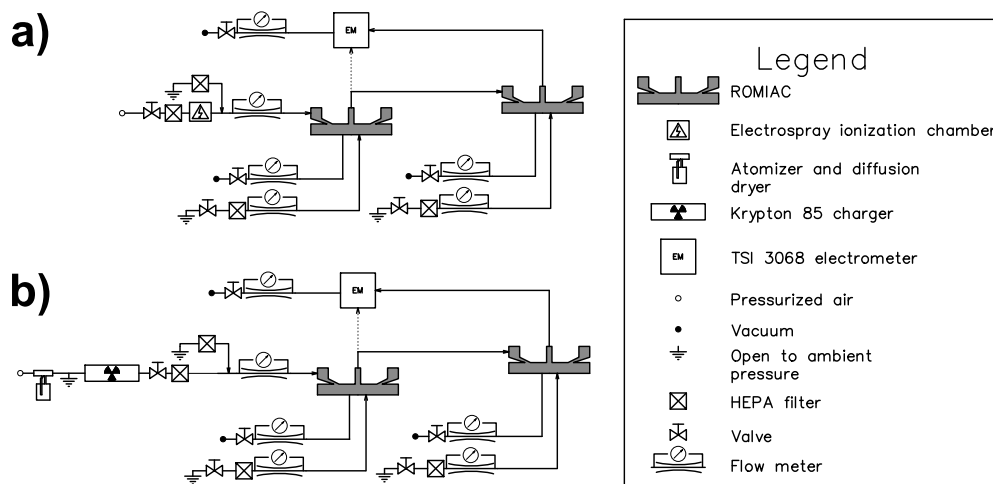


Figure 2.5: Experimental setup diagrams for tandem-ROMIAC measurements. (a) Electro sprayed TAAX molecular standards calibration. (b) Atomized NaCl calibration.

The first type of tandem-ROMIAC experiment probes the performance for sub-2 nm particles, using the experimental system shown in Fig. 2.5a. Molecular standards were generated by electrospray ionization of tetra-alkyl ammonium halide (TAAX) solutions without use of an aerosol neutralizer. This study used 25  $\mu\text{M}$  to 1 mM solutions of tetra-propyl ammonium iodide (TPAI), tetra-heptyl ammonium bromide (THAB), or tetra-dodecyl ammonium bromide (TDDAB) in methanol. The electrosprayed ions were classified by the source ROMIAC operated at a constant voltage with  $Q_a/Q_{cf}/R_{nd} = 2.1 \text{ lpm} / 13.9 \text{ lpm} / 6.6$ , and then initially sent to a TSI 3068 electrometer to obtain a steady-state reference concentration. The classified aerosol flow was then directed to the test ROMIAC, which was stepped through voltages, before being detected by the electrometer to obtain a mobility distribution. The classified aerosol was then again sent directly to the electrometer to obtain a confirmatory steady-state reference concentration. Only the monomers of TPAI, THAB, and TDDAB were used as the molecular standards, since the classifier could unambiguously and completely differentiate these ions from other species without requiring the use of a mass spectrometer. The mobility diameters of the TPAI, THAB, and TDDAB monomers are 1.16, 1.47, and 1.7 nm, respectively (Ude and Mora 2005).

The second type of tandem-ROMIAC experiment probes the performance of particles from 5 to 20 nm, using the experimental system depicted in Fig. 2.5b. A

0.2% by weight NaCl solution was atomized to produce an aerosol that was then sent through a Nafion dryer and a  $^{85}\text{Kr}$  neutralizer. The source and test classifiers were operated at the same flow rates so the same transfer function *form* could be applied to both instruments during data inversion. As in the TAAX-ion experiments, the aerosol was initially transmitted through the source classifier at a fixed voltage directly to the electrometer to obtain a steady-state reference concentration; it was then directed through the test classifier, stepping through voltages to obtain a mobility distribution; the classified aerosol concentration was monitored using the electrometer. At the end of each measurement, the source aerosol reference concentration measurement was repeated. Because the distribution coming from the source aerosol is not truly monodisperse, the mobility distribution of the aerosol coming from the atomizer must be obtained for proper data inversion. After each tandem atomized NaCl measurement, the source classifier was also stepped through voltages and transmitted aerosol directly to the electrometer to obtain the atomizer output mobility distribution.

For both types of experiments, the ROMIAC cross-flows were operated as an open loop, with the incoming cross-flow coming from HEPA-filtered ambient air and the outgoing cross-flow produced by a vacuum pump. Laboratory ambient air temperature and relative humidity were about 24 °C and 15%, respectively. Pressurized clean, dry air was used as the carrier gas for the electrospray ionization chamber and atomizer. Aerosol flow rates were measured by monitoring the flow rate through laminar flow elements using differential pressure transducers (Dwyer 607-4), while cross-flow rates were measured using thermal mass flow meters (TSI 201130 and 40241). Tubing lengths connecting the source and test classifiers to the electrometer were matched so that equivalent diffusive losses would occur when measuring the signal from either ROMIAC. Electrosprayed TAAX experiments used EMCO High Voltage CA12N power supplies, while atomized NaCl experiments used Bertan 602C-100N power supplies, to provide the ROMIAC applied voltages. Custom LabView™ software was used for data acquisition and applied voltage control. A summary of all the experiments, along with nominal flow rates and particle diameter range, is presented in Table 2.1.

### **Experimental data inversion**

The electrosprayed TAAX calibrations were performed such that the aerosol from the source classifier was a completely resolved TPAI, THAB, or TDDAB monomer, thus making the aerosol truly monodisperse from the perspective of the test clas-

sifier. This simplifies the inversion to the case of the simulation data, since the classifier transmission efficiency and transfer function (as well as charging probability) are constant over the width of the source distribution. The electrometer is assumed to have unity detection efficiency. A distinction in the case of inverting the electrosprayed TAAX data is that  $\Delta b_{\text{mesh}}$  is not known, and therefore,  $f_{Z,E}$  cannot be assumed to be unity. We assume that the simulation values of  $f_{Z,\text{bias}}$  hold true for the experimental measurements for the same flow rates and particle diameters. Thus the results were fitted to Eq. (2.17) by finding values of  $f_{Z,E} = (b_{\text{nom}} + \Delta b_{\text{shim}} + \Delta b_{\text{mesh}})/b_{\text{nom}}$ ,  $f_{\beta}$ ,  $f_{\tilde{\sigma}}$ , and  $\eta_{\text{trans}}$  (and assuming  $f_{Z,\text{bias}}$  from the simulations) in the same manner as the simulation data.

Inversion of the atomized NaCl data is more complex since the aerosol from the source classifier is not monodisperse. Tandem ROMIAC experiments using two, nearly-identical classifiers were operated at the same flow rates, under the assumption that their transfer function *forms* are the same. For these data, we follow the approach used by Stolzenburg (1988) (see also Zhang and Flagan 1996; Hagwood, Sivathanu, and Mulholland 1999) for inversion of tandem classifier data. Briefly, the particle concentration from the atomizer measured by the source (first) classifier stepping through voltages  $V_1$  is

$$\bar{c}_{\text{out}1}(V_1) = \int [n_{\text{eff}}(Z)\Omega_{\text{eff}1}(\tilde{Z}_{\text{eff}1}(f_{Z1}), \beta, \delta, \tilde{\sigma}, f_{\beta1}, f_{\tilde{\sigma}1})] dZ, \quad (2.18)$$

where  $n_{\text{eff}}(Z) = n_s(Z)\eta_{\text{charge}}(Z)\eta_{\text{trans}1}(Z)\eta_{\text{det}}(Z)$  is the effective source distribution. Because the particle size range being probed is limited to the low nanometer regime, and the charge distribution is the same for both classifiers, we did not have to contend with multiply-charged particles or the charge distribution for these calibration measurements. Quantification of the individual components of  $n_{\text{eff}}(Z)$  is unnecessary. The particle-size-independent  $f_{Z,E1}$  correction factor for the source classifier come from the results of the electrosprayed TAAX experiments, while  $f_{Z,\text{bias}1}$ ,  $f_{\beta1}$ , and  $f_{\tilde{\sigma}1}$  are from the simulations for the same flow rates and particle diameters, since the relationships for these factors derived from the sub-2 nm TAAX experiments should not be extrapolated for the  $D_Z = 5$  to 20 nm size range. The  $n_{\text{eff}}(Z)$  is assumed to be well-represented by a log normal distribution with three parameters found by fitting to the measured atomizer distribution. With a functional approximation of  $n_{\text{eff}}(Z)$ , the particle concentration from the test (second) classifier, stepping through voltages  $V_2$ , of the aerosol coming from the source classifier at fixed  $V_1$  can be used to solve for  $f_{Z2}$ ,  $f_{\beta2}$ ,  $f_{\tilde{\sigma}2}$ , and  $\eta_{\text{trans},2}$ :



$$\begin{aligned}
\frac{\bar{c}_{\text{out}2}(V_1, V_2)}{\bar{c}_{\text{in}2}(V_1)} &= \frac{\bar{c}_{\text{out}2}(V_1, V_2)}{\bar{c}_{\text{out}1}(V_1)} \\
&= \frac{\int [n_{\text{eff}}(Z)\Omega_{\text{eff}1}(\tilde{Z}_{\text{eff}1}(f_{Z1}), \beta, \delta, \tilde{\sigma}, f_{\beta1}, f_{\tilde{\sigma}1}) \Omega_{\text{eff}2}(\tilde{Z}_{\text{eff}2}(f_{Z2}), \beta, \delta, \tilde{\sigma}, f_{\beta2}, f_{\tilde{\sigma}2})\eta_{\text{trans}2}(Z)] dZ}{\int [n_{\text{eff}}(Z)\Omega_{\text{eff}1}(\tilde{Z}_{\text{eff}1}(f_{Z1}), \beta, \delta, \tilde{\sigma}, f_{\beta1}, f_{\tilde{\sigma}1})] dZ}, \quad (2.19)
\end{aligned}$$

where  $f_{Z,E2}$  for the test classifier can be calculated by dividing the best-fit  $f_{Z2}$  by the simulation-estimated  $f_{Z,\text{bias}2}$  for the same flow rates and particle diameters.

## 2.6 Results and discussion

The simulations and experiments combine to produce data from which the fraction of particles of a given size or mobility that are transmitted through the instrument can be deduced by the aforementioned methods. Figure 2.6 shows representative plots of this fraction,  $c_{\text{out}}/c_{\text{in}}$ . Figures 2.6a-b show the results obtained from simulations for relatively low operating resolution classification of small particles, i.e.,  $\mathcal{R}_{\text{nd,nom}} = 4.4$  and  $D_Z = 1.47$  nm, and moderate operating resolution classification of larger particles,  $\mathcal{R}_{\text{nd,nom}} = 15$  and  $D_Z = 12$  nm, respectively. The fit to the Stolzenburg transfer function in Eq. (2.15) is also shown, and the fit parameters are given. Figures 2.6c-d each compare measured transmission fractions for the two ROMIACs for THAB ions ( $D_Z = 1.47$  nm) at the same two flow rate conditions that were simulated. Figures 2.6e-f show tandem-ROMIAC data for large (10–12 nm) NaCl particles. In each case, the quality of the fit of the simulation or experimental data was high, suggesting that this representation of the transfer function is suitable for use in inverting the ROMIAC data (or OMAC in general), once the empirical correction factors are known. As noted in the simulation data inversion section, these correction factors address specific physical issues that cause the actual instrument to deviate from the simplistic model used to describe the instruments. Therefore, we discuss each of the mechanisms that requires correction in turn, and provide the quantitative descriptions of the correction factors in the discussion that follows.

### Cross flow velocity nonuniformity

In the simplified, conceptual model of the OMAC or ROMIAC, the areas of the two porous electrodes are assumed to be identical, and the cross-flow velocity is assumed to be uniform throughout the classification region. Locating both the aerosol inlet and outlet ports in the grounded electrode enabled classification without forcing the

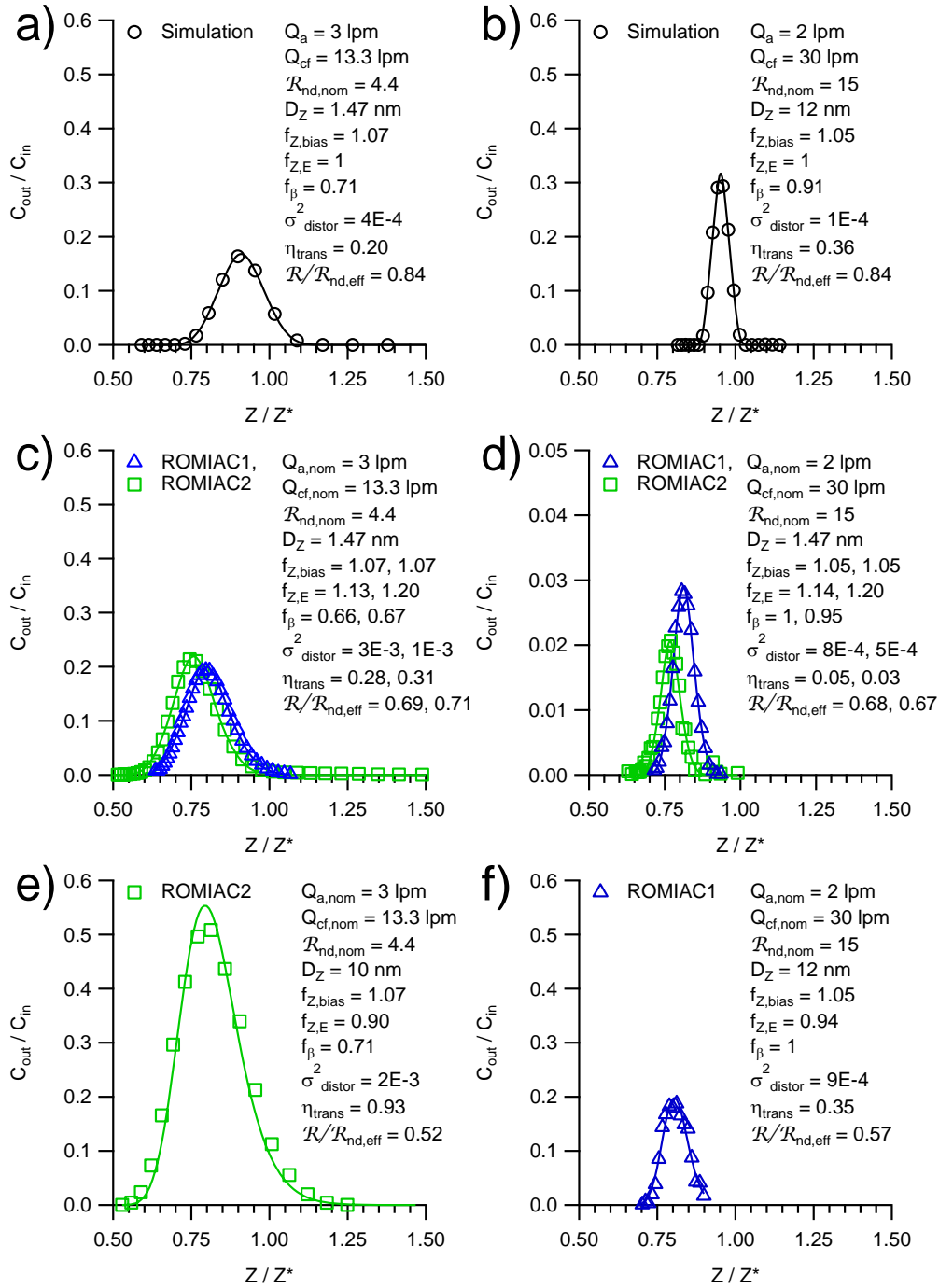


Figure 2.6: Example measurements (points) and transfer function fits (lines) with listed operating conditions and fitting parameters. Top row: COMSOL Multi-physics™ simulation examples for (a) small  $D_Z$  at low  $\mathcal{R}_{nd,nom}$  operation and (b) large  $D_Z$  at high  $\mathcal{R}_{nd,nom}$  operation. Middle row: tandem-ROMIAC TAAX measurement examples for (c) small  $D_Z$  at low  $\mathcal{R}_{nd,nom}$  operation and (d) small  $D_Z$  at high  $\mathcal{R}_{nd,nom}$  operation. Bottom row: tandem-ROMIAC NaCl measurement examples for (e) large  $D_Z$  at low  $\mathcal{R}_{nd,nom}$  operation and (f) large  $D_Z$  at high  $\mathcal{R}_{nd,nom}$  operation.

particles to pass through an adverse potential gradient, but makes it impossible to achieve the uniformity of the idealized instrument.

Since the ROMIAC geometry precludes direct measurement of the gas velocity within the classification region, we employ the simulations to assess the impact and magnitude of this flow distortion. As seen in Fig. 2.4a, the cross-flow velocity varies only slowly with radial and axial position within the classification region. The cross-flow velocity converges and accelerates as it approaches the grounded top electrode.

An estimate of  $f_{u,z}$  was obtained by using COMSOL Multiphysics™ flow field solutions to derive Matlab™-calculated non-diffusive particle trajectory simulations, recording the azimuthally-averaged vertical velocity acting on the particles at each time step as they are transmitted through the ROMIAC. Figure 2.7a shows the dependence of  $f_{u,z}$  on the nominal flow rate ratio  $\beta_{\text{nom}}$  (averaged for all  $D_Z$  for a given operating  $\beta$  listed in Table 2.1) from the COMSOL Multiphysics™-Matlab™ kinematic trajectory simulations. The linear relationship ( $r^2 = 0.85$ ) is

$$f_{u,z} = 1.01 + 0.11\beta_{\text{nom}}. \quad (2.20)$$

The error in estimating  $\bar{u}_z$  acting on particles during classification is related to flow distortions in the ROMIAC with increasing  $\beta_{\text{nom}}$ . Additionally, having a cross-flow outlet electrode of lesser area than the cross-flow inlet electrode would result in generally higher vertical velocities near the outlet electrode. Since the particles are introduced and extracted near the outlet electrode in this ROMIAC, the particles generally experience higher vertical velocities than presumed in calculating  $\bar{u}_z$  based upon simplistic geometry models.

Figure 2.7b shows the linear dependence of  $f_{Z,\text{bias}}$  on  $f_{u,z}$  and an additional dependence on the particle migration Péclet number, as indicated by the color banding. Acknowledging these dependencies, an empirical function of these two parameters to predict the mobility correction factor due to inlet/outlet bias is

$$f_{Z,\text{bias}} = 1.13f_{u,z} + \frac{0.03}{\log_{10}(\text{Pe}_{\text{mig}})} - 0.11 \quad (2.21)$$

with  $r^2 = 0.98$ . The one-to-one comparison of the simulation  $f_{Z,\text{bias}}$  values to those predicted by Eq. (2.21) is shown in Fig. 2.7c.

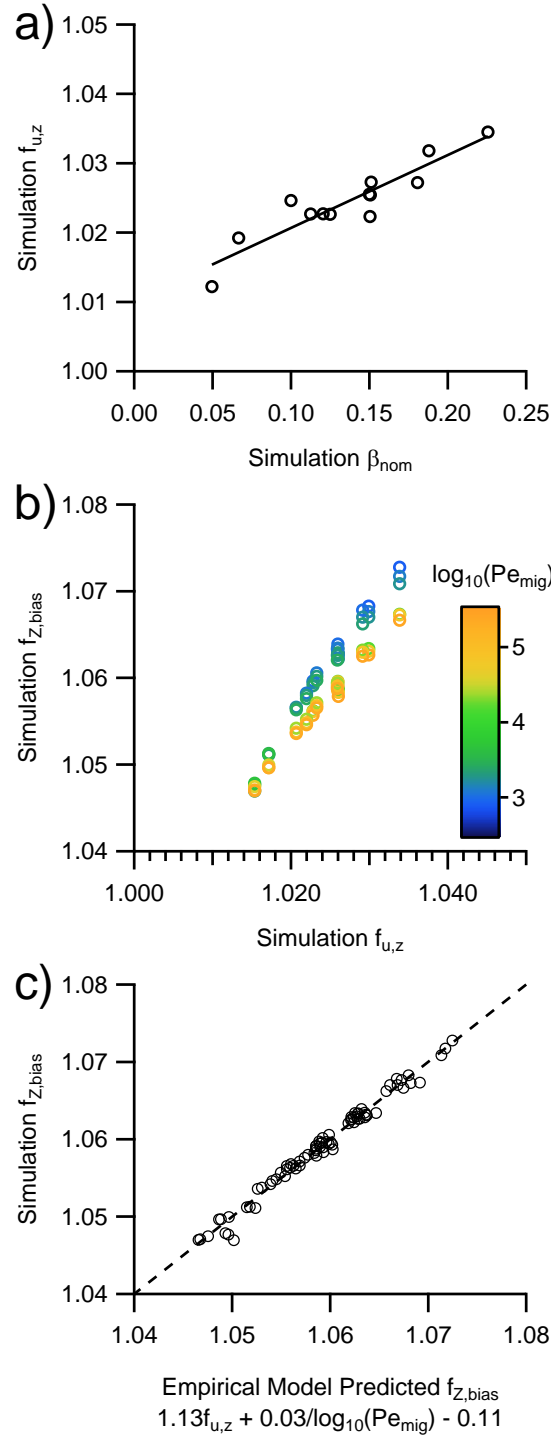


Figure 2.7: Simulation results used to estimate  $f_{Z,bias}$ . (a)  $f_{u,z}$  (from COMSOL Multiphysics™-driven kinematic particle trajectories) against  $\beta_{nom}$ . Best-fit line is  $f_{u,z} = 1.01 + 0.11\beta_{nom}$ . (b)  $f_{Z,bias}$  against estimated  $f_{u,z}$  colored by  $Pe_{mig}$ . (c) 1-to-1 comparison of simulation  $f_{Z,bias}$  against those estimated from an empirical function of  $f_{u,z}$  and  $Pe_{mig}$ . For convenience,  $Pe_{mig}$  values are listed in Table 2.1.

### Electric field strength reduction

Equation (2.21) was used to estimate the  $f_{Z,\text{bias}}$  component of  $f_Z$  in fitting the tandem-ROMIAC TAAX experiments to Eq. (2.17). Therefore, the remaining discrepancy between the nominal and a greater effective mobility is due to an additional electric field strength reduction beyond that resulting from an interelectrode spacing of  $b_{\text{nom}} = 10$  mm, quantified as  $f_{Z,E}$ . For ROMIAC1 and ROMIAC2, their average mobility correction factors (with relative standard deviation) due to the electric field strength reduction were  $f_{Z,E,\text{ROMIAC1}} = 1.04(\pm 8.0\%)$  and  $f_{Z,E,\text{ROMIAC2}} = 1.04(\pm 11.1\%)$ , respectively. Though it is possible that the value of  $\Delta b_{\text{mesh}}$  is greater than that estimated from the Solidworks™ assembled model, an additional explanation for the observed reduction in electric field strength is that the electric field may be distorted near the screen electrodes.

### Flow rate ratio

The observed resolution of the ROMIAC is somewhat higher than predicted from the simple ratio of flow rates, i.e.,  $\mathcal{R} > \beta^{-1}$ . As discussed above, the outgoing aerosol flow,  $Q_c$ , which exits through the same plane as the outgoing  $Q_{cf}$ , increases  $\bar{u}_z$  (for a portion of the particle's trajectory) against which a particle must migrate in order to successfully reach the aerosol outlet. As a result,  $f_\beta$  should vary inversely with the vertical velocity  $f_{u,z}$ . Figures 2.6a-d indeed show that the fitted  $f_\beta$  values are higher for the cases where the operating resolutions are higher and the particles would not experience as much vertical velocity enhancement (Fig. 2.7a). However, Fig. 2.6c,e and d,f also suggest that another factor, such as particle size, can influence  $f_\beta$ .

Figure 2.8a shows the inverse dependence of simulation  $f_\beta$  values on  $f_{u,z}$  and  $\text{Pe}_{\text{mig}}$ . Acknowledging these dependencies, an empirical function of these two parameters to predict the simulation flow rate ratio correction factor is

$$f_\beta = \frac{18.4}{f_{u,z}} + \frac{0.6}{\log_{10}(\text{Pe}_{\text{mig}})} - 17.3 \quad (2.22)$$

with  $r^2 = 0.84$ . The one-to-one comparison of the simulation  $f_\beta$  values to those predicted by Eq. (2.22) is shown in Fig. 2.8b. The comparison of the empirical function to experimental  $f_\beta$  values is shown in Fig. 2.8c, demonstrating that the empirical model is able to predict many of the experimental values.

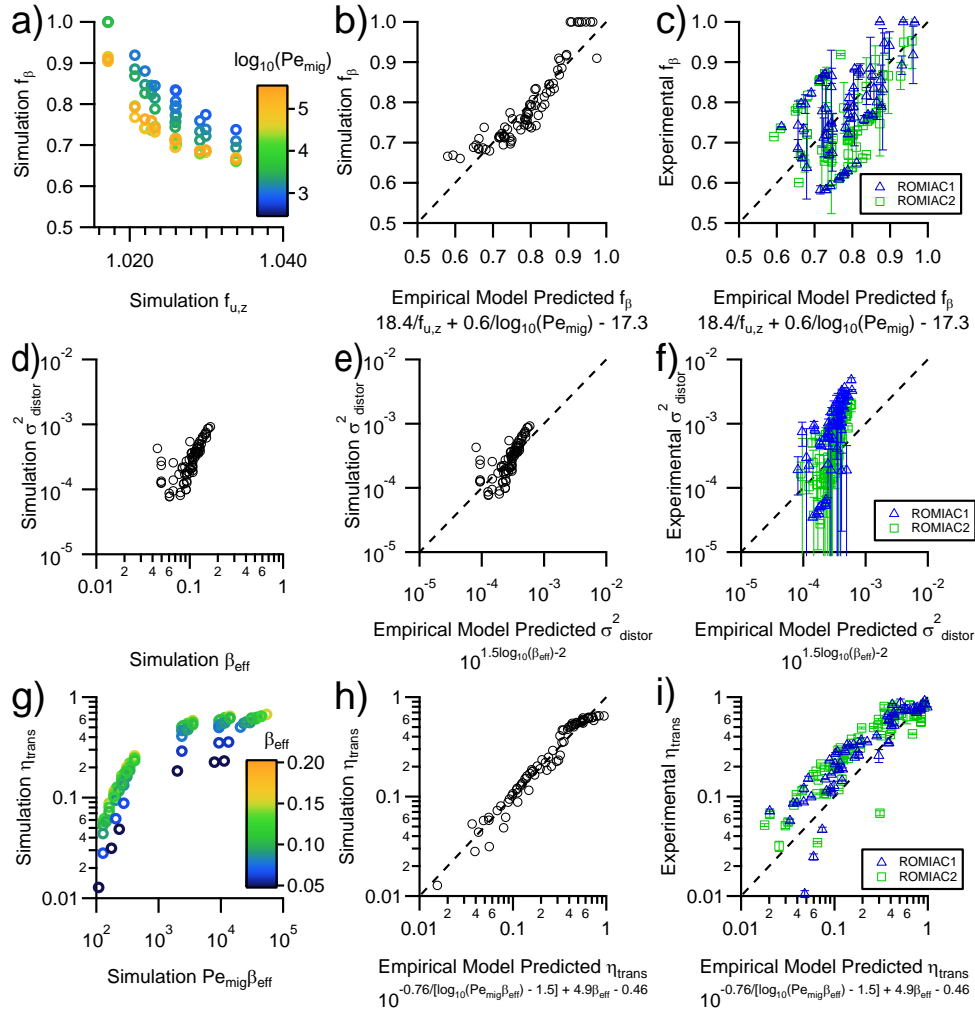


Figure 2.8: COMSOL Multiphysics™ simulation correction factor relationships, comparison of simulation values to empirical functions, and comparison of experimental values to empirical functions. Error bars in experimental results represent 2 standard deviations of multiple measurements. Top row: (a) simulation  $f_\beta$  against  $f_{u,z}$  colored by  $Pe_{mig}$ . (b) 1-to-1 comparison of simulation  $f_\beta$  against empirical model of  $f_{u,z}$  and  $Pe_{mig}$ . (c) 1-to-1 comparison of experiment-fitted  $f_\beta$  against empirical model of  $f_{u,z}$  and  $Pe_{mig}$ . Middle row: (d) simulation  $\tilde{\sigma}_{distor}^2$  against  $\beta_{eff}$ . (e) 1-to-1 comparison of simulation  $\tilde{\sigma}_{distor}^2$  against empirical model of  $\beta_{eff}$ . (f) 1-to-1 comparison of experiment-fitted  $\tilde{\sigma}_{distor}^2$  against empirical model of  $\beta_{eff}$ . Bottom row: (g) simulation  $\eta_{trans}$  against  $Pe_{mig}\beta_{eff}$  colored by  $\beta_{eff}$ . (h) 1-to-1 comparison of simulation  $\eta_{trans}$  against empirical model of  $Pe_{mig}$  and  $\beta_{eff}$ . (i) 1-to-1 comparison of experiment-fitted  $\eta_{trans}$  against empirical model of  $Pe_{mig}$  and  $\beta_{eff}$ . For convenience,  $Pe_{mig}$  and  $Pe_{mig}\beta$  values are listed in Table 2.1.

### Diffusional broadening parameter

The parameter  $\tilde{\sigma}$  accounts for the role that Brownian diffusion of particles plays in degrading the classification efficiency. Other factors that cause particles to deviate from their ideal trajectories through a classifier can lead to similar degradation that is empirically described through the value of  $f_{\tilde{\sigma}}$ . Examination of the flow in the aerosol introduction plenum (Fig. 2.4b) reveals that the tangential velocity around this racetrack decreases dramatically from the tangential inlet. While the pressure drop through the knife-edge inlet is designed to be large enough to ensure uniform flow through that slot, some azimuthal variation in the flow rate must exist due to the pressure drop in the flow around the racetrack. Thus, particle losses may vary within this region, though this would only affect the transmission efficiency and not the resolution since this region precedes the classification region and can be regarded as extra tubing through which particles travel. Other factors may lead to particles along different trajectories experiencing different gas velocities or electric fields.  $f_{\tilde{\sigma}}$  represents the apparent diffusivity enhancement of particles across classifier output mobility channels as a result of flow distortions owing to the real-instrument geometry.

This particle-size-independent dispersion contribution is modeled as an empirically-determined additive term,  $\tilde{\sigma}_{\text{distor}}^2$  (Stolzenburg 1988; Flagan 1999; Jiang et al. 2011), such that  $\tilde{\sigma}_{\text{eff}}^2 = \tilde{\sigma}^2 + \tilde{\sigma}_{\text{distor}}^2 = (f_{\tilde{\sigma}}\tilde{\sigma})^2$ . Solving for  $\tilde{\sigma}_{\text{distor}}^2$  yields

$$\tilde{\sigma}_{\text{distor}}^2 = \tilde{\sigma}^2 \left( f_{\tilde{\sigma}}^2 - 1 \right). \quad (2.23)$$

Figure 2.8d shows the empirically-derived dependence of  $\tilde{\sigma}_{\text{distor}}^2$  on  $\beta_{\text{eff}}$ :

$$\tilde{\sigma}_{\text{distor}}^2 = 10^{1.5 \log_{10}(\beta_{\text{eff}}) - 2} \quad (2.24)$$

with  $r^2 = 0.53$ . The one-to-one comparison of the simulation  $\tilde{\sigma}_{\text{distor}}^2$  values to those predicted by Eq. (2.24) is shown in Fig. 2.8e; experimental  $\tilde{\sigma}_{\text{distor}}^2$  values show an even stronger dependence on  $\beta_{\text{eff}}$  (Fig. 2.8f) than the simulation suggests.

### Efficiency

Figure 2.8g shows the relationship between  $\eta_{\text{trans}}$  and  $\text{Pe}_{\text{mig}}\beta_{\text{eff}}$ , with an apparent additional dependence on  $\beta_{\text{eff}}$ . An empirical function to predict  $\eta_{\text{trans}}$  from  $\text{Pe}_{\text{mig}}$  and  $\beta_{\text{eff}}$  is

$$\eta_{\text{trans}} = 10^{-0.76[\log_{10}(\text{Pe}_{\text{mig}}\beta_{\text{eff}})-1.5]+4.9\beta_{\text{eff}}-0.46}, \quad \text{Pe}_{\text{mig}}\beta_{\text{eff}} \geq 10^{1.5} \quad (2.25)$$

with  $r^2 = 0.96$ , shown in Fig. 2.8h. An asymptotic analysis of the transfer function for an idealized, rectilinear OMAC (Downard, Dama, and Flagan 2011) supports the observed dependence of  $\eta_{\text{trans}}$  on  $\beta$ . The experimental  $\eta_{\text{trans}}$  values are compared with those predicted by Eq. (2.25) in Fig. 2.8i. Both classifiers tended to exhibit  $\eta_{\text{trans}}$  higher by a factor of 2 than either the simulations, or that predicted by Eq. (2.25).

Two possible causes for this deviation are numerical diffusion in the simulations, or overestimation of the losses to the walls (the porous electrode surfaces could allow some particles to escape capture). Similar 3-dimensional COMSOL Multiphysics™ models conducted for a high aspect ratio (length/electrode spacing ratio = 44) DMA showed deviations of  $\leq 5\%$  of the peak from the semi-analytical DMA transfer function of Stolzenburg (1988); this suggests that numerical diffusion plays a relatively minor role in the discrepancy between the ROMIAC simulation and experimental  $\eta_{\text{trans}}$  values, and that much of the deviation is due to the zero particle concentration boundary condition applied to the walls in the model that is overestimating particle losses. Nonetheless, the experimental results still appear to reflect the  $\text{Pe}_{\text{mig}}\beta_{\text{eff}}$  dependence from the simulation-derived empirical function.

## Resolution

Figure 2.9a shows the resolutions achieved by the ROMIAC (only  $\mathcal{R}_{\text{nd,nom}} = 5.3$ , 10, and 20.2 are shown for clarity). For a given flow-rate-ratio and voltage in the diffusion-dominated regime, DMA-type classifiers suffer from greater degradation of resolution than OMAC-type classifiers. The simulation and experimental data show that in the diffusion-dominated regime, the ROMIAC generally achieves resolutions associated with the theoretical OMAC curves. The maximum observed resolution in Fig. 2.9a was  $\mathcal{R} \approx 18$  for TDDAB monomer classified by ROMIAC2.

The relative resolution  $\mathcal{R}/\mathcal{R}_{\text{nd}}$  provided by a classifier cannot exceed unity, even in the non-diffusive regime. In the case of the ROMIAC, relative resolution can appear to exceed unity if  $\mathcal{R}_{\text{nd,nom}}$  is used as the upper limit. Because  $Q_c$  contributes to the cross-flow for a portion of a particle's trajectory through the ROMIAC, the effective non-diffusive resolution  $\mathcal{R}_{\text{nd,eff}}$  is used to estimate the relative resolution, as it accounts for the resolution enhancement from the aerosol outlet position and flow direction.



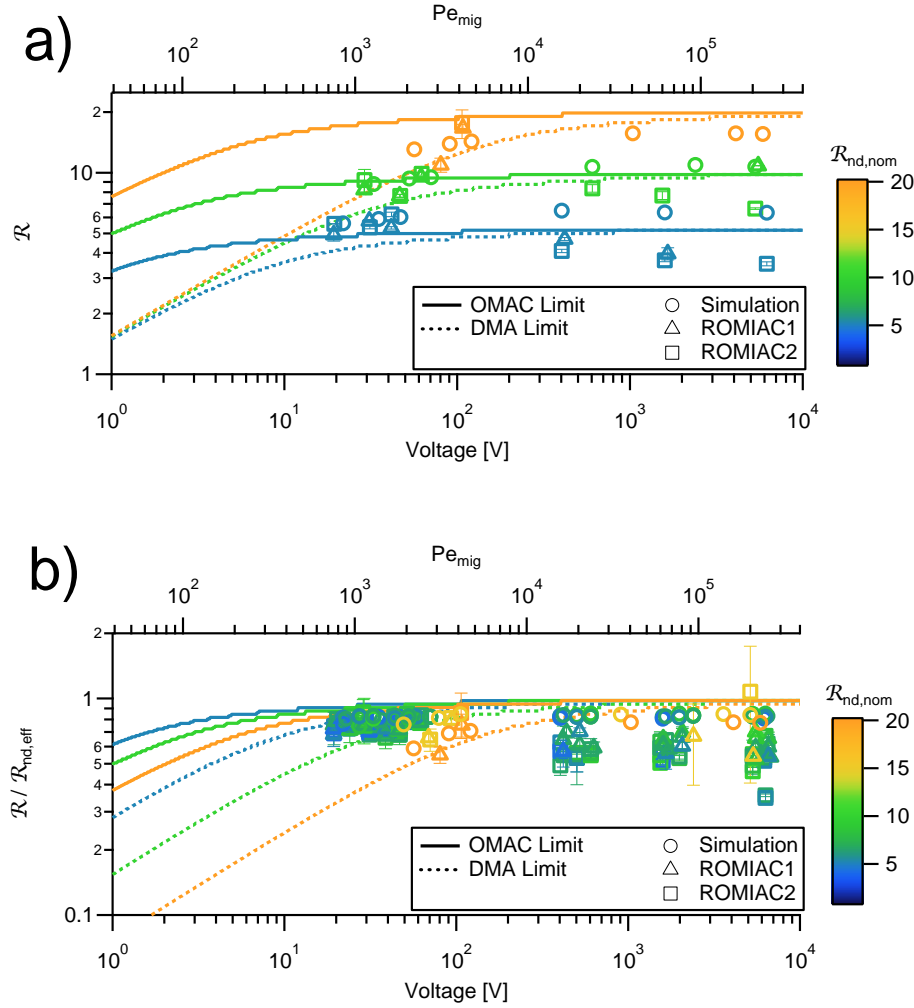


Figure 2.9: (a) Theoretical (lines) and observed simulation and experimental (markers) resolution obtained with the ROMIAC against  $V$  and  $Pe_{mig}$ . Curves and markers for only three values of  $R_{nd,nom}$  are displayed for clarity ( $R_{nd,nom} = 5.3, 10$ , and  $20.2$ ). (b) Theoretical (lines) and observed simulation and experimental (markers) effective relative resolution obtained with the ROMIAC against  $V$  and  $Pe_{mig}$ . Markers for all operating conditions are shown, but curves for only three values of  $R_{nd,nom}$  are displayed for clarity ( $R_{nd,nom} = 5.3, 10$ , and  $20.2$ ). Error bars in experimental results represent 1 standard deviation of multiple measurements. For convenience,  $Pe_{mig}$  values are listed in Table 2.1.

Figure 2.9b shows the effective relative resolution of the simulations and experiments for the ROMIAC against voltage and  $Pe_{\text{mig}}$ . The simulations achieve the highest  $\mathcal{R}/\mathcal{R}_{\text{nd,eff}}$  values, reaching  $\sim 0.83$  in the non-diffusive regime, though  $\mathcal{R}/\mathcal{R}_{\text{nd,eff}}$  starts decreasing at  $Pe_{\text{mig}} < 5 \times 10^3$ . The experimental effective relative resolutions are comparable to the simulations at  $Pe_{\text{mig}} < 5 \times 10^3$ , but are lower than the simulation values for greater  $Pe_{\text{mig}}$  values, at  $\sim 0.65$  in the non-diffusive regime. Like the diffusional broadening enhancement, degraded relative resolution can potentially be attributed to flow disturbances owing to non-ideal geometry and azimuthal flow asymmetry, just as such nonidealities degrades resolution in some DMAs. The results indicate that  $\mathcal{R}/\mathcal{R}_{\text{nd,eff}}$  show little variation over about three orders of magnitude of  $V$  or  $Pe_{\text{mig}}$  for  $4 < \mathcal{R}_{\text{nd,nom}} \leq 20$ .  $\mathcal{R}/\mathcal{R}_{\text{nd,eff}}$  did not deteriorate even as the voltage was reduced to that required to classify  $\sim 1$  nm particles. This uniform relative resolution over a wide range of mobilities was possible since diffusion becomes important in an OMAC at roughly an order of magnitude lower  $V$  than in a DMA, as shown by the dashed and dotted lines in Fig. 2.9.

### Comparison to other classifier studies

Table 2.2 lists the flow rates, resolutions, and particle diameters used in other cylindrical and radial classifier studies. The key dimensions of the ROMIAC are generally smaller than those of early radial DMAs such as the Spectrometre de Mobilité Electrique Circulaire (SMEC; H Fissan et al. 1998) or that of Zhang, Akutsu, et al. (1995) that probed larger particles, but larger than those of the nano-RDMA (Brunelli, Flagan, and Giapis 2009) that measures only particles in the lower portion of the ROMIAC measurement range. The  $f_Z$  factors of the ROMIAC are separated into contributions, while Zhang and Flagan (1996) present  $f_Z$  for the RDMA as a function of  $Pe_{\text{mig}}$  and the nano-RDMA presents an overall  $f_Z$  value. Values of  $f_{Z,E}$  for the ROMIAC are comparable to that for the nano-RDMA  $f_Z$  value.

The effective length,  $L_{\text{eff}}$ , is a parameter that has been used in numerous studies of other instruments (e.g., Cheng (2001) and Jiang et al. (2011)) to represent inlet and outlet losses in terms of the equivalent length of straight tubing that would result in the same diffusive losses as the classifier. While this metric does not describe the actual instrument, it captures some of the flow-rate and particle size dependence of the particle losses within the instrument. The ROMIAC  $\eta_{\text{trans}}$  values did not, however, fit the Gormley-Kennedy diffusion model form as proposed for DMAs by Cheng (2001), as the ROMIAC  $\eta_{\text{trans}}$  values describe the total efficiency of the

classifier (inlet, classification region, and outlet) and depend on  $\beta_{\text{eff}}$  in addition to  $Q_a$ . It is possible to fit the ROMIAC  $\eta_{\text{trans}}$  values to a Gormley-Kennedy diffusion model if it is assumed that the model represents the *extrinsic* transmission of particles (outside the classification region) while using a separate linear function of  $\beta_{\text{eff}}$  to model the *intrinsic* classification region transmission of particles. However, the resulting  $L_{\text{eff}}$  value cannot be compared directly to those calculated for DMAs owing to the additional losses in the ROMIAC. In contrast to the DMA classification region, where particle trajectories at peak efficiency are far from walls, the trajectories in an OMAC are close to walls and, therefore, have non-negligible losses inside the classification region; these losses are not properly accounted for by the Stolzenburg derivation of the transfer function used for data inversion in this study. Nonetheless, the ROMIAC has demonstrated  $\eta_{\text{trans}}$  up to 0.49 for sub-2 nm particles.

The flow rates and resolutions used in this study fall within the range of those typically used in many other classifiers. The present ROMIAC was designed for a non-diffusive resolution comparable to that commonly used in DMAs. The ROMIAC attains apparent  $\mathcal{R}/\mathcal{R}_{\text{nd,nom}}$  values well above unity, though, after correcting for  $\beta_{\text{eff}}$ ,  $\mathcal{R}/\mathcal{R}_{\text{nd,eff}}$  values range from 0.35–1.07. The particle diameter ranges in this study are on the lower end of those commonly probed with DMAs, as the ROMIAC was designed with the purpose of sub-20 nm classification.

## 2.7 Conclusions

This study demonstrates the ability of the ROMIAC to classify particles ranging from 1.16–20 nm in diameter over a wide range of classifier operating resolutions, while using cross-flow rates less than 40 lpm in a compact package. Additionally, experimental results validate empirical relationship dependencies derived from finite element simulations when geometry, flows, and electric field details are accurately captured. The relative resolution of the ROMIAC has little variation over a mobility span of three orders of magnitude, whereas that of a DMA varies by a factor of 2–3 at a flow ratio of 10, thus validating the broader dynamic range of OMAC-type instruments.

Analytical models of particle classifiers, such as those of Knutson and Whitby (1975), Stolzenburg (1988) and Flagan (2004) are applicable for instruments whose design and operation satisfy the assumptions on which those predictions are based, but geometric and experimental factors, i.e., small aspect ratios and field nonidealities, can lead to deviations in instrument behavior from such models, as seen both

Table 2.2: Geometry parameters, fitting factors, and typical flow conditions for various DMAs.

| Cylindrical Classifier | Inner Radius (cm) | Outer Radius (cm) | Channel Length (cm) | $f$   | $f_z$             | $L_{\text{eff}}$ (m) | $Q_a$ (lpm) | $Q_{\text{sh}}$ (lpm) | $\mathcal{R}_{\text{nd,nom}}$ | $\mathcal{R}/\mathcal{R}_{\text{nd,nom}}$ | $D_z$ range (nm)     | Source(s)   |
|------------------------|-------------------|-------------------|---------------------|-------|-------------------|----------------------|-------------|-----------------------|-------------------------------|---|----------------------|---|
| TSL-Long               | 0.937             | 1.958             | 44.44               | 0.707 |                   | 7.1                  | 1–3         | 5–20                  | 4–20                          | 0.5–1                                     | 8–1000               | H. Fissan et al. (1996)<br>Birmili et al. (1997)<br>Flagan (1999)                                     |
| TSL-Short              | 0.937             | 1.958             | 11.11               | 0.707 |                   |                      | 1           | 10                    | 10                            | 0.6–0.8                                   | 5–50                 | H. Fissan et al. (1996)<br>Flagan (1999)  |
| TSL-Nano               | 0.937             | 1.905             | 4.987               | 0.716 |                   | 1.4, 2.24            | 1–1.5       | 7.5–30                | 10–30                         | 0.3–1                                     | 1.16–50              | Chen et al. (1998)<br>Jiang et al. (2011)   |
| Grimm nanoDMA          | 1.3               | 2                 | 1.3                 | 0.81  |                   | 3.87                 | 2           | 21.9                  | 11                            | 0.5–0.6                                   | 1.16–1.70            | Jiang et al. (2011)   |
| Vienna-Long            | 2.9               | 3.7               | 60                  | 0.867 |                   | 4.6                  | 1–3         | 10–12                 | 4–10                          | 0.6–0.8                                   | 10–1000              | Winklmayr et al. (1991)<br>Birmili et al. (1997)  |
| Vienna-Short           | 2.5               | 3.3               | 11                  | 0.837 |                   | 4.6                  | 2–5         | 20–28                 | 5.6–10                        | 0.4–0.9                                   | 1–150                | Winklmayr et al. (1991)<br>Birmili et al. (1997)<br>Karlsson and Martinsson (2003)                    |
| Karlsruhe-Vienna       | 2.29              | 3.3               | 2.5                 | 0.838 |                   | 11.53                | 6           | 61.4                  | 10                            | 0.5–0.7                                   | 1.16–1.70            | Jiang et al. (2011)   |
| Rosell-Llompert        | 2.5               | 3.3               | 1.6                 | 0.867 |                   |                      | 1.45–3.6    | 10.78–202.2           | 7.4–56                        | 0.17–0.31                                 | 1.12–1.90            | Rosell-Llompert et al. (1996)<br>Flagan (1999)  |
| Radial Classifier      | Inner Radius (cm) | Outer Radius (cm) | Gap Thickness (cm)  | $f$   | $f_z$             | $L_{\text{eff}}$ (m) | $Q_a$ (lpm) | $Q_{\text{sh}}$ (lpm) | $\mathcal{R}_{\text{nd,nom}}$ | $\mathcal{R}/\mathcal{R}_{\text{nd,nom}}$ | $D_z$ range (nm)     | Source(s)   |
| SMEC                   | ~0.5              | 6.5               | 0.4                 | 1.0   |                   | 16                   | 1           | 10                    | 10                            | 0.4–1                                     | 6–50                 | H. Fissan et al. (1996)   |
| Caltech RDMA           | 0.24              | 5.04              | 1.0                 | 1.0   | 0.989–1.07        | 0.083–1.99           | 0.3–2       | 3–20                  | 10                            | 0.2–0.79                                  | 1.16–200             | Zhang, Akutsu, et al. 1995<br>Zhang and Flagan (1996)<br>Birmili et al. (1997)<br>Jiang et al. (2011) |
| Caltech nano-RDMA      | 0.24              | 0.75              | 1.0                 | 1.0   | 1.15              | 0.87                 | 0.6–1.5     | 6–15                  | 10–17                         | 0.3–0.6                                   | 1.16–1.8             | Brunelli, Flagan, and Giapis (2009)<br>Jiang et al. (2011)  |
| ROMIAC                 | 0.24              | 1.61 <sup>a</sup> | 1.0 <sup>a</sup>    | 1.0   | 1.04 <sup>b</sup> |                      | 1.7–3       | 13.3–34.3             | 4.4–20                        | 0.4–1.4 <sup>c</sup>                      | 1.16–20 <sup>a</sup> | Mui et al. (2013)<br>This study   |

<sup>a</sup>Nominal value.<sup>b</sup>Mean values for ROMIAC1 and ROMIAC2, respectively. Value reported is  $f_{z,E}$ .<sup>c</sup> $\mathcal{R}/\mathcal{R}_{\text{nd,eff}}$  values range from 0.35 – 1.07.

in this study and others (Rosell-Llompart et al. 1996; Zhang and Flagan 1996; Chen et al. 1998; Karlsson and Martinsson 2003; Brunelli, Flagan, and Giapis 2009; Jiang et al. 2011; Liu and Chen 2016). Owing to such deviations, one should be cautious about *a priori* predictions of performance, unless rigorous numerical models of the flows and fields within the instrument are available.

Finite element simulations enabled the design of an OMAC-type classifier that attains specified performance levels; similar fidelity is anticipated for other instruments, as has been previously demonstrated in the design of cylindrical and radial DMAs (Chen et al. 1998; Brunelli, Flagan, and Giapis 2009). The ROMIAC prototype described in this study attained resolutions up to  $\sim 20$ ; the first description of the OMAC (Flagan 2004) suggested that the attainable resolution can be much greater, and the use of computational simulation tools would be the recommended approach for development of a high-resolution OMAC. These simulations can also reduce the dependence on experimental calibrations, provided sufficient computational resources are available to minimize the effects of numerical diffusion.

The ROMIAC presented here offers moderately high resolution particle sizing through the low nanometer/ gas ion regime at modest flow rates, making it a viable instrument for the study of new particle formation, atmospheric particle growth rates, and ultrafine particle inhalation exposure. To characterize the instrument over the range of particle sizes and operating conditions explored, a number of corrections to the highly idealized model first proposed for the OMAC as a result of the substantial deviations of the design from the assumptions behind the simplistic model. Nonetheless, the instrument performs as designed; empirical corrections based on calibration studies are consistent with those obtained from the results of the design simulations; DMAs that probe this same size range have required similar corrections owing to the distortions of the flows and fields in many low aspect ratio instruments. While the present instrument has been designed to probe particles in the low nanometer regime, the instrument can readily be adapted to probing particles throughout the range covered by the many different DMA designs to enable application to studies of particles in the cloud condensation nuclei and light scattering domains.

## 2.8 Nomenclature

$b$  electrode separation distance

$b_{\text{nom}}$  nominal electrode separation distance

$\Delta b_{\text{mesh}}$  additional electrode separation distance due to mesh offset from electrode plane

$\Delta b_{\text{shim}}$  additional electrode separation distance due to shim

$b_{\text{total}}$  total electrode separation distance

$c$  particle concentration

$\bar{c}$  velocity-weighted average particle concentration

$c_{\text{in}}$  particle concentration at aerosol inlet

$\bar{c}_{\text{in}}$  average particle concentration at aerosol inlet

$\bar{c}_{\text{in}2}$  average particle concentration at aerosol inlet of test (second) classifier in tandem experiments

$c_{\text{out}}$  particle concentration at aerosol outlet

$\bar{c}_{\text{out}}$  average particle concentration at aerosol outlet

$\bar{c}_{\text{out}1}$  average particle concentration at aerosol outlet of source (first) classifier in tandem experiments

$\bar{c}_{\text{out}2}$  average particle concentration at aerosol outlet of test (second) classifier in tandem experiments

$\mathcal{D}$  particle diffusivity

$D_Z$  particle electrical mobility diameter

$e$  elementary charge

$E$  electric field strength

$\vec{E}$  electric field vector

$E_r$  electric field strength along radial coordinate

$E_z$  electric field strength along axial coordinate

$f$  electric field nonuniformity correction factor (unity for flat electrode classifiers)

$f_{u,z}$  axial cross-flow velocity correction factor

$f_Z$  total mobility correction factor

$f_{Z1}$  total mobility correction factor for source (first) classifier in tandem experiments

$f_{Z2}$  total mobility correction factor for test (second) classifier in tandem experiments

$f_{Z,bias}$  mobility correction factor due to biases from aerosol introduction and cross-flow velocity

$f_{Z,bias1}$  mobility correction factor due to biases from aerosol introduction and cross-flow velocity for source (first) classifier in tandem experiments

$f_{Z,bias2}$  mobility correction factor due to biases from aerosol introduction and cross-flow velocity for test (second) classifier in tandem experiments

$f_{Z,E}$  mobility correction factor due to error in estimation of electric field strength

$f_{Z,E1}$  mobility correction factor due to error in estimation of electric field strength for source (first) classifier in tandem experiments

$f_{Z,E2}$  mobility correction factor due to error in estimation of electric field strength for test (second) classifier in tandem experiments

$f_{Z,E,ROMIAC1}$  mobility correction factor due to error in estimation of electric field strength for ROMIAC1

$f_{Z,E,ROMIAC2}$  mobility correction factor due to error in estimation of electric field strength for ROMIAC2

$f_{\beta}$  flow rate ratio correction factor

$f_{\beta1}$  flow rate ratio correction factor for source (first) classifier in tandem experiments

$f_{\beta2}$  flow rate ratio correction factor for test (second) classifier in tandem experiments

$f_{\tilde{\sigma}}$  dimensionless diffusion parameter correction factor

$f_{\tilde{\sigma}1}$  dimensionless diffusion parameter correction factor for source (first) classifier in tandem experiments

$f_{\tilde{\sigma}2}$  dimensionless diffusion parameter correction factor for test (second) classifier in tandem experiments

$\mathbf{F}_D$  drag force

$\mathbf{F}_E$  electric force

$G$  geometry factor

$k$  Boltzmann constant

$L$  axial DMA electrode length or rectilinear OMAC electrode length

|                               |   |
|-------------------------------|---|
| $L_{\text{eff}}$              | effective classifier length   |
| $n_{\text{eff}}$              | effective source distribution   |
| $n_s$                         | source mobility distribution  |
| $\text{Pe}_{\text{mig}}$      | migration Péclet number   |
| $Q$                           | volumetric flow rate  |
| $Q_a$                         | volumetric incoming aerosol flow rate                                       |
| $Q_c$                         | volumetric outgoing classified aerosol flow rate                            |
| $Q_{\text{cf}}$               | volumetric OMAC cross-flow rate   |
| $Q_{\text{ex}}$               | volumetric DMA excess flow rate   |
| $Q_{\text{sh}}$               | volumetric DMA sheath flow rate   |
| $r$                           | radial coordinate   |
| $\mathcal{R}$                 | resolution  |
| $\mathcal{R}_{\text{nd}}$     | non-diffusive resolution  |
| $\mathcal{R}_{\text{nd,eff}}$ | effective non-diffusive resolution  |
| $\mathcal{R}_{\text{nd,nom}}$ | nominal non-diffusive resolution  |
| $R_1$                         | central electrode radius of a cylindrical DMA                               |
| $R_2$                         | outer electrode radius of a cylindrical DMA                                 |
| $R_{\text{elec}}$             | radius of ROMIAC electrode  |
| $R_{\text{elec,in}}$          | radius of incoming cross-flow ROMIAC electrode (lower electrode in figures) |
| $R_{\text{elec,out}}$         | radius of outgoing cross-flow ROMIAC electrode (upper electrode in figures) |
| $R_o$                         | radius of aerosol outlet  |
| $T$                           | temperature   |
| $u_a$                         | aerosol fluid velocity  |
| $u_{\text{cf}}$               | cross-flow fluid velocity   |
| $u_r$                         | radial fluid velocity   |
| $u_z$                         | axial fluid velocity  |



$\bar{u}_z$  nominal average axial fluid velocity

$\bar{u}_{z,\text{eff}}$  azimuthally-averaged effective axial fluid velocity

$\vec{v}$  particle velocity vector

$v_{\text{mig}}$  particle electrical migration velocity

$V$  applied voltage

$V_1$  voltage applied to source (first) classifier in tandem experiments

$V_2$  voltage applied to test (second) classifier in tandem experiments

$z$  axial coordinate

$Z$  particle electrical mobility

$\Delta Z_{50\%}$  range of electrical mobilities transmitted with at least 50% of the efficiency of  $Z^*$

$Z^*$  particle electrical mobility following characteristic trajectory

$Z_{\text{eff}}^*$  effective particle electrical mobility at peak efficiency

$Z_{\text{ideal}}^*$  particle electrical mobility suggested by idealized classifier behavior models

$\tilde{Z}$  dimensionless particle electrical mobility

$\tilde{Z}_{\text{eff}}$  effective dimensionless particle electrical mobility (incorporating  $f_Z$ )

$\tilde{Z}_{\text{eff}1}$  effective dimensionless particle electrical mobility of source (first) classifier in tandem experiments

$\tilde{Z}_{\text{eff}2}$  effective dimensionless particle electrical mobility of test (second) classifier in tandem experiments

$Z_{\text{peak}}$  particle electrical mobility at peak efficiency

$\alpha$  aspect ratio; classification channel length to width ratio

$\beta$  aerosol flow rate to cross-flow (or sheath flow) rate ratio

$\beta_{\text{eff}}$  effective aerosol flow rate to cross-flow (or sheath flow) rate ratio

$\beta_{\text{nom}}$  nominal aerosol flow rate to cross-flow (or sheath flow) rate ratio

$\delta$  aerosol flow rate imbalance ratio

$\Gamma$  particle stream function

$\tilde{\sigma}$  dimensionless diffusion parameter

$\tilde{\sigma}_{\text{eff}}$  effective dimensionless diffusion parameter

$\tilde{\sigma}_{\text{distor}}^2$  particle-size-independent dispersion contribution due to flow distortions

$\eta_{\text{charge}}$  charging probability

$\eta_{\text{det}}$  detector counting efficiency

$\eta_{\text{trans}}$  classifier transmission efficiency

$\eta_{\text{trans1}}$  classifier transmission efficiency of source (first) classifier in tandem experiments

$\eta_{\text{trans2}}$  classifier transmission efficiency of test (second) classifier in tandem experiments

$\phi$  electric flux function

$\Delta\phi$  electric flux difference

$\Delta\phi^*$  electric flux difference for a particle of mobility  $Z^*$

$\psi$  fluid stream function

$\Delta\psi^*$  fluid streamline difference for a particle of mobility  $Z^*$

$\Omega$  transfer function

$\Omega_{\text{eff}}$  effective transfer function

$\Omega_{\text{eff1}}$  effective transfer function of source (first) classifier in tandem experiments

$\Omega_{\text{eff2}}$  effective transfer function of test (second) classifier in tandem experiments

$\xi$  centered and scaled  $\tilde{Z}$

## 2.9 Acknowledgments

We thank Daniel Thomas, Amanda Grantz, Ranganathan Gopalakrishnan, Paula Popescu, Johannes Leppä, and Natasha Hodas for helpful discussions. Andrew Metcalf and Xerxes López-Yglesias are acknowledged for their assistance with the particle trajectory simulations and LabView controls. This research was supported by National Science Foundation Grant No. CBET-1236909 and a National Science Foundation Graduate Research Fellowship under Grant No. DGE-1144469. (W.M.), and the Jacobs Institute for Molecular Engineering for Medicine (R.C.F. and A.J.D.).

## References

- Birmili, W. et al. (1997). "Determination of differential mobility analyzer transfer functions using identical instruments in series". In: *Aerosol Sci. Technol.* 27.2, pp. 215–223. DOI: 10.1080/02786829708965468.
- Brunelli, N. A., R. C. Flagan, and K. P. Giapis (2009). "Radial differential mobility analyzer for one nanometer particle classification". In: *Aerosol Sci. Technol.* 43.1, pp. 53–59. DOI: 10.1080/02786820802464302.
- Chen, D.-R. et al. (1998). "Design and evaluation of a nanometer aerosol differential mobility analyzer (Nano-DMA)". In: *J. Aerosol Sci.* 29.5-6, pp. 497–509. DOI: 10.1016/S0021-8502(97)10018-0.
- Cheng, Y.-S. (2001). "Condensation detection and diffusion size separation techniques". In: *Aerosol Measurement: Principles, Techniques, and Applications*. Ed. by P. A. Baron and K. Willeke. 2nd. New York: John Wiley & Sons, Inc. Chap. 19, pp. 569–601.
- Downard, A. J., J. F. Dama, and R. C. Flagan (2011). "An asymptotic analysis of differential electrical mobility classifiers". In: *Aerosol Sci. Technol.* 45.6, pp. 717–729. DOI: 10.1080/02786826.2011.558136.
- Erikson, H. A. (1921). "The change of mobility of the positive ions in air with age". In: *Am. Phys. Soc.* 18.2, pp. 100–101.
- Fissan, H. et al. (1996). "Experimental comparison of four differential mobility analyzers for nanometer aerosol measurements". In: *Aerosol Sci. Technol.* 24.1, pp. 1–13.
- Fissan, H et al. (1998). "Analytical and empirical transfer functions of a simplified spectrometre de mobilite electrique circulaire (SMEC) for nano particles". In: *J. Aerosol Sci.* 29.3, pp. 289–293.
- Flagan, R. C. (1998). "History of electrical aerosol measurements". In: *Aerosol Sci. Technol.* 28.4, pp. 301–380. DOI: 10.1080/02786829808965530.
- (1999). "On differential mobility analyzer resolution". In: *Aerosol Sci. Technol.* 30.6, pp. 556–570. DOI: 10.1080/027868299304417.
- (2004). "Opposed migration aerosol classifier (OMAC)". In: *Aerosol Sci. Technol.* 38.9, pp. 890–899. DOI: 10.1080/027868290505242.
- Franchin, A. et al. (2016). "A new high transmission inlet for the Caltech nano-RDMA for size distribution measurements of sub-3 nm ions at ambient concentrations". In: *Atmos. Meas. Tech.* 9.6, pp. 2709–2720. DOI: 10.5194/amtd-8-5847-2015.
- Hagwood, C., Y. Sivathanu, and G. Mulholland (1999). "The DMA transfer function with Brownian motion a trajectory/Monte-Carlo approach". In: *Aerosol Sci. Technol.* 30.1, pp. 40–61. DOI: 10.1080/027868299304877.

- Hogan, C. J. and J. F. de la Mora (2010). “Ion-pair evaporation from ionic liquid clusters”. In: *J. Am. Soc. Mass Spectrom.* 21, pp. 1382–6. DOI: 10.1016/j.jasms.2010.03.044.
- (2011). “Ion mobility measurements of nondenatured 12–150 kDa proteins and protein multimers by tandem differential mobility analysis-mass spectrometry (DMA-MS)”. In: *J. Am. Soc. Mass Spectrom.* 22.1, pp. 158–72. DOI: 10.1007/s13361-010-0014-7.
- Jiang, J. et al. (2011). “Transfer functions and penetrations of five differential mobility analyzers for sub-2 nm particle classification”. In: *Aerosol Sci. Technol.* 45.4, pp. 480–492. DOI: 10.1080/02786826.2010.546819.
- Karlsson, M. N. A. and B. G. Martinsson (2003). “Methods to measure and predict the transfer function size dependence of individual DMAs”. In: *J. Aerosol Sci.* 34.5, pp. 603–625. DOI: 10.1016/S0021-8502(03)00020-X.
- Knutson, E. O. and K. T. Whitby (1975). “Aerosol classification by electrical mobility: apparatus, theory, and applications”. In: *J. Aerosol Sci.* 6, pp. 443–451. DOI: 10.1016/0021-8502(75)90060-9.
- Kousaka, Y. et al. (1986). “Effect of Brownian diffusion on electrical classification of ultrafine aerosol particles in differential mobility analyzer”. In: *J. Chem. Eng. Jpn.* 19.5, pp. 401–407.
- Labowsky, M. and J. F. de la Mora (2006). “Novel ion mobility analyzers and filters”. In: *J. Aerosol Sci.* 37.3, pp. 340–362. DOI: 10.1016/j.jaerosci.2005.07.001.
- Liu, Q. and D.-R. Chen (2016). “Experimental evaluation of miniature plate DMAs (mini-plate DMAs) for future ultrafine particle (UFP) sensor network”. In: *Aerosol Sci. Technol.* 50.3, pp. 297–307.
- Mai, H. and R. C. Flagan (2017). “Opposed migration aerosol classifier transfer function”. In: *Aerosol Sci. Technol.* In prep.
- Martínez-Lozano, P., M. Labowsky, and J. F. de la Mora (2006). “Experimental tests of a nano-DMA with no voltage change between aerosol inlet and outlet slits”. In: *J. Aerosol Sci.* 37.11, pp. 1629–1642. DOI: 10.1016/j.jaerosci.2006.02.001.
- Martínez-Lozano, P. and J. F. de la Mora (2006). “Resolution improvements of a nano-DMA operating transonically”. In: *J. Aerosol Sci.* 37.4, pp. 500–512. DOI: 10.1016/j.jaerosci.2005.05.009.
- Mui, W. et al. (2013). “Ion mobility-mass spectrometry with a radial opposed migration ion and aerosol classifier (ROMIAC)”. In: *Anal. Chem.* 85, pp. 6319–6326. DOI: 10.1021/ac400580u.

- Oberreit, D. R., P. H. McMurry, and C. J. Hogan (2014). "Mobility analysis of 2 nm to 11 nm aerosol particles with an aspirating drift tube ion mobility spectrometer". In: *Aerosol Sci. Technol.* 48.1, pp. 108–118. DOI: 10.1080/02786826.2013.861893.
- Oberreit, D. R., V. K. Rawat, et al. (2015). "Analysis of heterogeneous water vapor uptake by metal iodide cluster ions via differential mobility analysis-mass spectrometry". In: *J. Chem. Phys.* 143.104204, pp. 1–11. DOI: 10.1063/1.4930278.
- Rosell-Llompart, J. et al. (1996). "Sizing nanoparticles and ions with a short differential mobility analyzer". In: *J. Aerosol Sci.* 27.5, pp. 695–719.
- Rosser, S. and J. F. de la Mora (2005). "Vienna-type DMA of high resolution and high flow rate". In: *Aerosol Sci. Technol.* 39.12, pp. 1191–1200. DOI: 10.1080/02786820500444820.
- Rus, J. et al. (2010). "IMS-MS studies based on coupling a differential mobility analyzer (DMA) to commercial API-MS systems". In: *Int. J. Mass Spectrom.* 298.1-3, pp. 30–40. DOI: 10.1016/j.ijms.2010.05.008.
- Stolzenburg, M. R. (1988). "An ultrafine aerosol size distribution measuring system". Ph.D. Thesis. University of Minnesota.
- Tammet, H. (2011). "Symmetric inclined grid mobility analyzer for the measurement of charged clusters and fine nanoparticles in atmospheric air". In: *Aerosol Sci. Technol.* 45.4, pp. 468–479. DOI: 10.1080/02786826.2010.546818.
- Tammet, Hannes (2003). "Method of inclined velocities in the air ion mobility analysis". In: *Proceedings of the 12th International Conference on Atmospheric Electricity*. Vol. 1, pp. 399–402.
- Ude, S. and J. F. de la Mora (2005). "Molecular monodisperse mobility and mass standards from electrosprays of tetra-alkyl ammonium halides." In: *J. Aerosol Sci.* 36.10, pp. 1224–1237. DOI: 10.1016/j.jaerosci.2005.02.009.
- Winklmayr, W. et al. (1991). "A new electromobility spectrometer for the measurement of aerosol size distributions in the size range from 1 to 1000 nm". In: *J. Aerosol Sci.* 22.3, pp. 289–296. DOI: 10.1016/S0021-8502(05)80007-2.
- Zhang, S.-H., Y. Akutsu, et al. (1995). "Radial differential mobility analyzer". In: *Aerosol Sci. Technol.* 23.3, pp. 357–372.
- Zhang, S.-H. and R. C. Flagan (1996). "Resolution of the radial differential mobility analyzer for ultrafine particles". In: *J. Aerosol Sci.* 27.8, pp. 1179–1200.

*Chapter 3***ION MOBILITY–MASS SPECTROMETRY WITH A RADIAL  
OPPOSED MIGRATION ION AND AEROSOL CLASSIFIER  
(ROMIAC)**

By Wilton Mui, Daniel A. Thomas, Andrew J. Downard, Jesse L. Beauchamp, John H. Seinfeld, and Richard C. Flagan

This chapter was originally published in *Analytical Chemistry* as:

Mui, W. et al. (2013). “Ion mobility-mass spectrometry with a radial opposed migration ion and aerosol classifier (ROMIAC)”. In: *Anal. Chem.* 85, pp. 6319–6326. DOI: 10.1021/ac400580u.

**3.1 Abstract**

The first application of a novel differential mobility analyzer, the radial opposed migration ion and aerosol classifier (ROMIAC), is demonstrated. The ROMIAC uses antiparallel forces from an electric field and a cross-flow gas to both scan ion mobilities and continuously transmit target mobility ions with 100% duty cycle. In the ROMIAC, diffusive losses are minimized, and resolution of ions, with collisional cross-sections of 200–2000 Å<sup>2</sup> is achieved near the non-dispersive resolution of ~ 20. Higher resolution is theoretically possible with greater cross-flow rates. The ROMIAC was coupled to a linear trap quadrupole mass spectrometer and used to classify electrosprayed C2–C12 tetra-alkyl ammonium ions, bradykinin, angiotensin I, angiotensin II, bovine ubiquitin, and two pairs of model peptide isomers. Instrument and mobility calibrations of the ROMIAC show that it exhibits linear responses to changes in electrode potential, making the ROMIAC suitable for mobility and cross-section measurements. The high resolution of the ROMIAC facilitates separation of isobaric isomeric peptides. Monitoring distinct dissociation pathways associated with peptide isomers fully resolves overlapping peaks in the ion mobility data. The ability of the ROMIAC to operate at atmospheric pressure and serve as a front-end analyzer to continuously transmit ions with a particular mobility facilitates extensive studies of target molecules using a variety of mass spectrometric methods.

### 3.2 Introduction

Ion mobility spectrometry (IMS) methods, including drift cells (Wittmer et al. 1994; Guevremont et al. 1997; Wu, Siems, et al. 1998; Bush et al. 2010), traveling wave ion mobility cells (Giles et al. 2004), high-field asymmetric waveform devices (FAIMS; Purves, Barnett, and Guevremont 2000; Purves, Barnett, Ells, et al. 2000; Shvartsburg, Creese, et al. 2010), and differential mobility analyzers (DMA; Kaufman 1998; Ude and Mora 2005; Mora, Ude, and Thomson 2006; Labowsky and Mora 2006; Hogan and Mora 2011; Jiang et al. 2011), have all been employed to separate ions. An advantage of the FAIMS and DMA methods is that they provide 100% duty cycle transmission of ions, but FAIMS spectra are less readily interpretable to collisional cross sections. On the other hand, DMA techniques often present challenges in providing resolutions above 10 and require very large pump flow rates.

The DMA spatially separates ions by their electrical mobility in an electric field that is transverse to the analyte ion flow (Knutson and Whitby 1975). Sampling efficiencies for DMAs are generally low for ions (mobilities  $> 0.019 \frac{\text{cm}^2}{\text{V}\cdot\text{s}}$ ) due to diffusional losses and those induced by distorted electric fields in the transition from electrically-grounded regions to an entrance or exit at high potential. Recent advances in DMA design have enabled separation of ions with mobilities as large as  $1.85 \frac{\text{cm}^2}{\text{V}\cdot\text{s}}$  (Rosser and Mora 2005; Brunelli, Flagan, and Giapis 2009), allowing studies of molecular cluster structures (Gamero-Castaño and Mora 2000; Hogan and Mora 2010), biomolecule characterization (Hogan, Ruotolo, et al. 2011; Hogan and Mora 2011), and peptide and protein classification (Kaufman et al. 1996; Bacher et al. 2001; Kaddis et al. 2007); however, losses from distorted electric fields remained significant. More recently several DMAs with equipotential sample inlet and outlet have been successfully demonstrated to overcome this problem (Martínez-Lozano, Labowsky, and Mora 2006; Labowsky and Mora 2006; Tammet 2011).

The opposed migration aerosol classifier (OMAC) also features equipotential sample inlet and outlet (Flagan 2004). The theory underlying the OMAC shows it can operate at lower voltages than the DMA without suffering diffusional degradation of resolving power, resulting in higher resolution and dynamic range. These advantages arise from flowing sample ions through a channel formed by two permeable electrodes. A clean gas cross-flow enters and exits the classification channel through the porous electrodes, antiparallel to the electric field. This departure from the traditional DMA geometry increases the distance through which ions must diffuse to degrade resolution, resulting in an increase of both maximum attainable

mobility and range of mobilities that can be probed at a fixed flow rate (Flagan 2004; Downard, Dama, and Flagan 2011). The radial geometry presented further decreases diffusional losses and enhances resolution by elimination of electric field deformities from proximate dielectric walls. We refer to the instrument as a radial opposed migration ion and aerosol classifier (ROMIAC).

We describe the ROMIAC application in ion mobility–mass spectrometry (IM–MS), demonstrating the mobility analyzer capabilities of the ROMIAC with tetra–alkyl ammonium halide (TAAX) salts, peptides, and model peptide isomers tagged with a free radical initiated peptide sequencing (FRIPS) reagent (Hodyss, Cox, and Beauchamp 2005) to enhance separation by monitoring dissociation pathways specific for each isomer. Resolutions observed are  $\sim 20$ , the maximum achievable given the flow rates used; higher resolutions are possible with greater cross–flow rates. Nonetheless, relatively high resolutions are achieved in an instrument that is inexpensive, has low pumping and voltage requirements, and can couple with any mass spectrometer having an atmospheric pressure interface.

### 3.3 Materials and Methods

#### Front–End Classifier

Figure 3.1 shows a photograph of the ROMIAC and the atmospheric interface to a linear trap quadrupole mass spectrometer (LTQ–MS), as well as a simplified diagram of the ROMIAC with idealized particle trajectories through the instrument.

The electrophoretic migration velocity of an ion is  $\mathbf{v}_{\text{mig}} = K_i \mathbf{E}$ , where  $K_i$  is the ion mobility and  $\mathbf{E} = -\nabla\phi \approx -\phi/b$  is the electric field produced when a potential  $\phi$  is applied to the high voltage electrode across a gap of distance  $b$ , with  $b = 10$  mm in the present experiments. Given a volumetric flow rate of the cross–flow gas,  $Q_x$ , the nominal mobility of the ions transmitted is  $K_i \approx |(4Q_x b)/(\pi d^2 \phi)|$  where  $d$  is the diameter of the classification region (3.22 cm). The experimental resolution, which is calculated as the ratio of the target mobility,  $K_i^*$ , to the range of mobilities transmitted with half the maximum efficiency,  $\Delta K_{i,\text{FWHM}}$ , can be related to the voltage at peak efficiency,  $\phi_i^*$ , and voltage range at half–maximum,  $\Delta\phi_{\text{FWHM}}$ , i.e.,

$$\mathcal{R} = \frac{K_i^*}{\Delta K_{i,\text{FWHM}}} = \frac{\phi_i^*}{\Delta\phi_{\text{FWHM}}}. \quad (3.1)$$

The non–dispersive resolution of the ROMIAC is identical to that of the DMA in the same limit (Knutson and Whitby 1975), i.e.,  $\mathcal{R}_{\text{nd}} = Q_x/Q_s$ , where  $Q_s$  is the



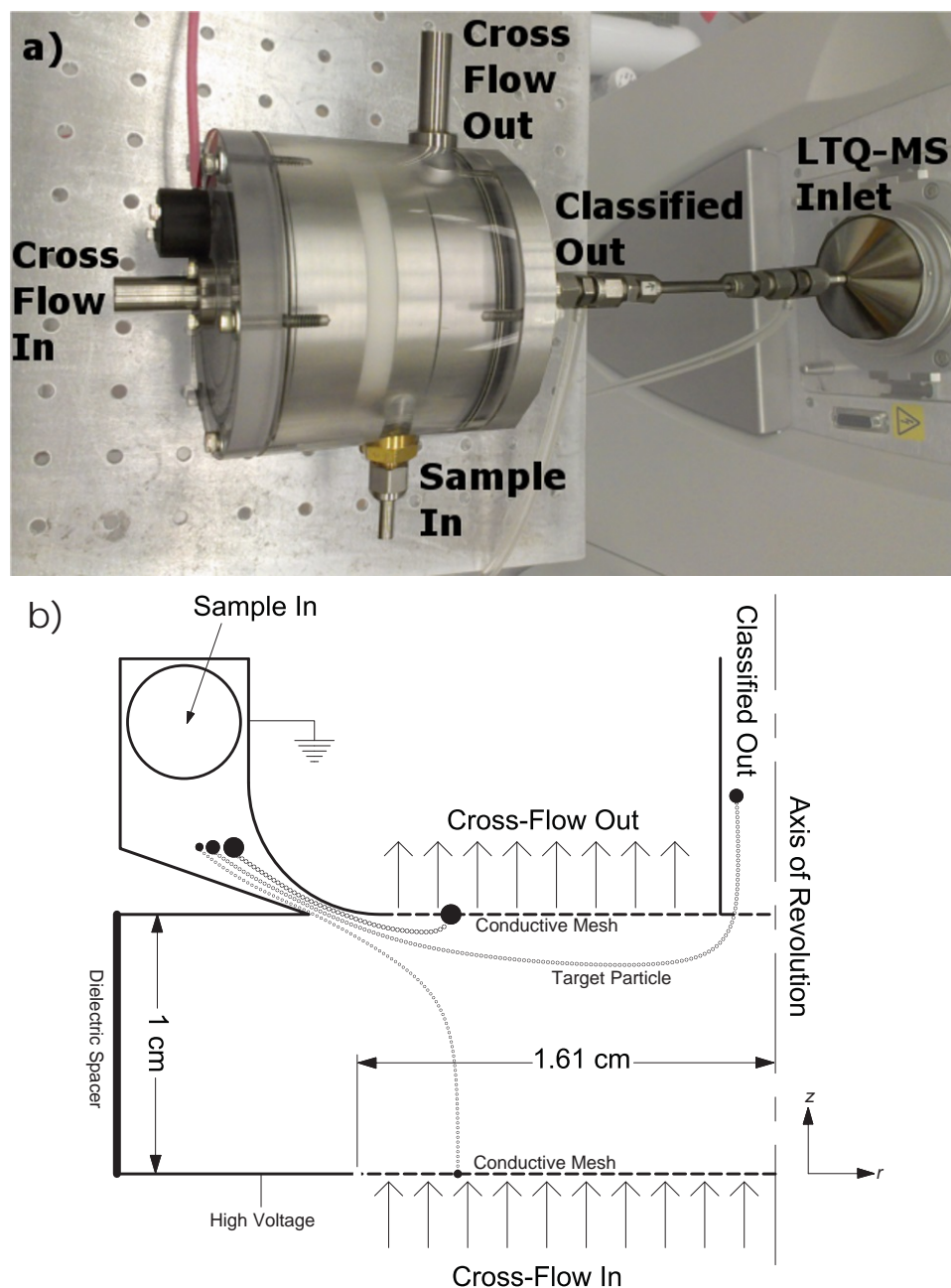


Figure 3.1: a) ROMIAC-LTQ-MS atmospheric interface. The outer dimensions of the ROMIAC are 11.4 cm diameter and 10.6 cm length. b) Cross-sectional view of functional region of ROMIAC. Diagram is cylindrically symmetrical about indicated axis of revolution. Dotted lines are idealized ion trajectories through the ROMIAC. Sample ions enter via a tangential inlet, are drawn into the classification region, and experience opposing drag and electric forces that allow the target ion to exit through the outlet, while non-target ions impact either the upper or lower planes.

volumetric flow rate of the sample, assuming that the incoming and outgoing cross-flows are balanced, as are the incoming ion sample flow and outgoing classified ion flow,  $Q_c$ . The resolution may be degraded due to diffusion, and the range of electric potentials over which ions of a given mobility are transmitted will broaden.

### Sample Preparation

C2–C8 and C12 (designating the carbon chain length of the alkyl groups) TAAX salts (Sigma–Aldrich) were dissolved in solutions of 50% methanol and 50% water (v/v). TAAX salts were of the brominated form, except for the iodinated C3 TAAX. TAAX solution concentrations were 50  $\mu$ M, except for the 25  $\mu$ M C7 solution. Bradykinin (BK), angiotensin I (AT1), angiotensin II (AT2), and bovine ubiquitin (UB) were obtained from Sigma–Aldrich and dissolved in 49% methanol, 49% water, and 2% acetic acid (v/v) to make 50  $\mu$ M solutions. Model peptides AARAAATAA, AATAAARAA, AARAAHAMA, and AARAAMAHA, were obtained from Biomer Technologies and used without further purification. Solutions of the underivatized form of these peptides were made from a 1 mg/mL stock solution in water, which was then diluted in 49% methanol, 49% water, and 2% acetic acid (v/v) for a 50  $\mu$ M solution. The (2,2,6,6–tetramethylpiperidin–1–yl)oxyl (TEMPO)–based FRIPS reagent was synthesized as described in Appendix B (Lee et al. 2009). Model peptides were derivatized by reacting the peptides with a FRIPS reagent solution and acetonitrile in a triethylammonium bicarbonate buffer (pH 8.5) for 2 hr (details in Appendix B). The final derivatized model peptide sample solution was 49% methanol, 49% water, and 2% acetic acid (v/v).

### Experimental Setup

The experimental setup consists of an electrospray ion source (ESI), the ROMIAC, and a Finnigan LTQ–MS (Thermo Electron Corp.); a detailed schematic is shown in Fig. B.2.  $N_2$  gas enters the ESI chamber perpendicular to the spray needle and conveys ions to the ROMIAC. The ESI gas temperature,  $T_{ESI}$ , is heated for some experiments via heating tape wrapped around the gas inlet tubes to the ESI chamber. All TAAX, UB, and model peptide measurements were performed at  $T_{ESI} = 298$  K, while BK, AT1, and AT2 measurements were done at both  $T_{ESI} = 298$  K and 400 K.

The cross-flow gas through the ROMIAC is also  $N_2$  that is regulated with a proportioning solenoid valve and is exhausted through a vacuum pump with the flow rate kept constant by a critical orifice at the inlet to the vacuum pump. All experiments were run at  $Q_x = 34.3$  lpm and  $Q_s = 1.70$  lpm, resulting in  $\mathcal{R}_{nd} = 20.2$ , and the

cross-flow gas temperature,  $T_x$ , was 298 K. Analytes were at atmospheric pressure the entire journey from the ESI spray needle to the LTQ-MS inlet, the duration of which is estimated to be on the order of tens to hundreds of milliseconds.

A proportional-integral-differential (PID) algorithm written in LabView provided feedback control of the sample and classified flow based on signals from the differential pressure transducers that monitor the pressure drops across laminar flow elements. Ion mobility spectra were obtained by stepping through a range of voltages and monitoring the LTQ-MS signal. Greater detail of the experimental setup is in Appendix B.

The LTQ-MS scanned from  $m/z$  50–2000 and averaged over three microscans of 10 ms maximum duration. For model peptide collision induced dissociation (CID) experiments, the singly-protonated parent ion was isolated with a width of 3  $m/z$  (window of  $m/z$  in the trap during isolation prior to collisional activation). Detailed experimental and LTQ-MS settings are in Table B.1. Table B.2 lists the ranges of  $m/z$  used to mass-resolve all TAAX and peptide species. TAAX, BK, AT1, AT2, and UB experiments were repeated three times, while model peptide experiments were performed once due to limited sample availability.

### Calibration Procedure

In consideration of the study by Fernandez-Maestre et al. (Fernández-Maestre et al. 2010), both an instrument calibration (IC) and mobility calibration (MC) were performed. In short, the IC uses standards whose mobilities are minimally affected by either clustering of carrier gas contaminants, such as water and ESI solvents, or by complex size and shape factors (Wytenbach, Bleiholder, and Bowers 2013) to determine the linearity of the ROMIAC-selected ion mobility in response to the voltage, while the MC uses standards that are sensitive to such contaminants or shape drag factors similar to those of the target analytes, in order to infer collisional cross sections,  $\Omega_i$ , of other biomolecules. Further calibration details and results are found in Appendix B.

## 3.4 Results and Discussion

### Tetra-Alkyl Ammonium Ion Mobilities

TAAX anion-coordinated singly-charged multimer species were classified and detected, with their estimated reduced mobility,  $K_{0,i}$ , in Fig. 3.2, and  $\Omega_i$  values in Table B.5. Generally,  $\Omega_i$  increased and  $K_{0,i}$  decreased as multimer length increased. Most observed resolutions were near  $\mathcal{R}_{nd} = 20.2$ , with lower values of  $R \sim 10$  occurring

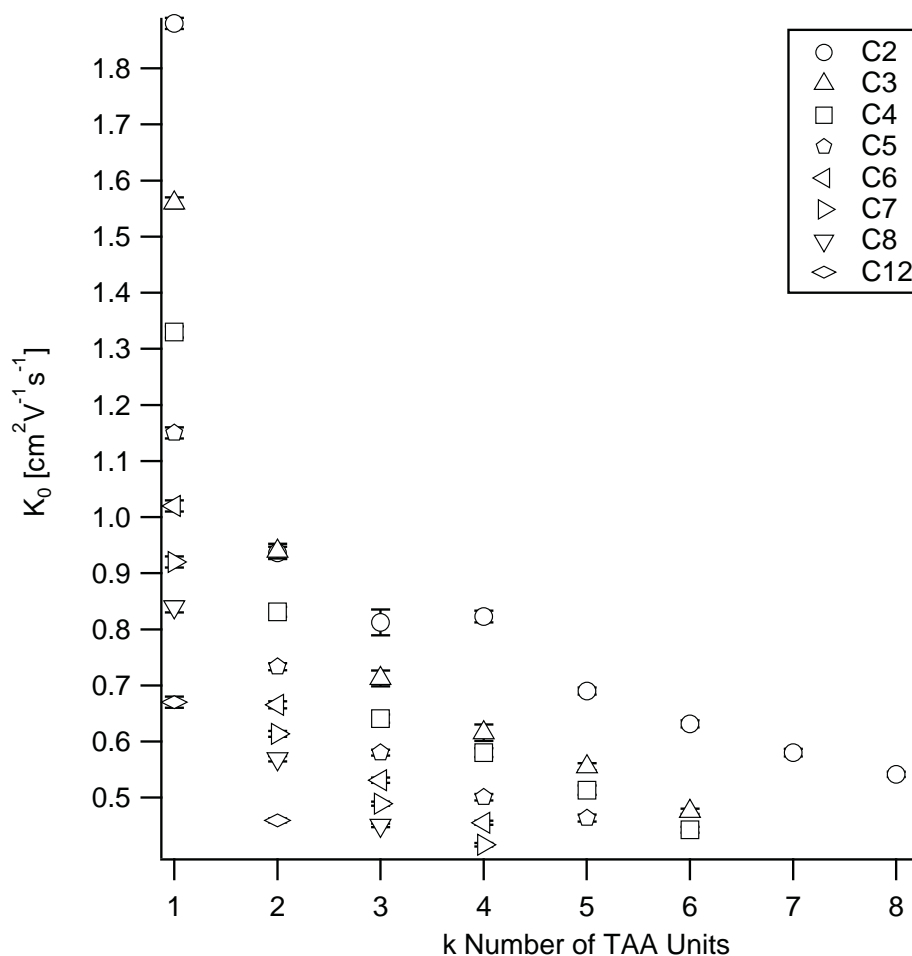


Figure 3.2: Tetra-alkyl ammonium halide (TAAX) anion-coordinated singly-charged multimer  $K_{0,i}$  as a function of  $k$  for  $[\text{TAA}_k\text{X}_{k-1}]^+$ . In  $\text{N}_2$  at atmospheric pressure and  $T_{\text{ESI}} = T_x = 298$  K. Error bars denote 1 standard deviation of triplicates. C3 species are iodinated while all other TAAX species are brominated. Detailed signal, Gaussian fit, and resolution values are found in Table B.5. Values for monomer reduced mobilities and errors from Viidanoja et al. 2005.

for C2 trimer, C3 trimer and tetramer, C4 tetramer and pentamer, and C5 pentamer (Table B.5), likely due to poor signal intensity. Due to the extremely linear IC with TAAX monomer standards ( $R^2 > 0.999$ ; see Appendix B), the  $K_{0,i}$  values for these TAAX multimers can be used as additional calibration standards in concert with those of Viidanoja et al. 2005.

### Peptide and Protein Mobility Spectra and Conformations

Mass-resolved mobility spectra of BK, AT1, and AT2 are shown in Fig. 3.3, while those of UB are in Fig. B.5. Generally,  $R \sim 20$  for singly-charged species

with relatively large  $\Omega_i$ , and  $\sim 5$ –15 for multiply-charged, smaller species (Tables B.9 and B.10); these lower resolutions may result from the presence of multiple conformations within the peak envelope or from changes in conformation within the classification region (Wytenbach, Helden, and Bowers 1996; Counterman et al. 1998; Shvartsburg et al. 2006a; Shvartsburg et al. 2006b; Pierson, Chen, et al. 2011; Wytenbach and Bowers 2011). The dominant conformation for each charge state of BK, AT1, and AT2 appears at the same respective voltage at both  $T_{\text{ESI}}$  values, indicating the electrospray temperature does not significantly affect  $\Omega_i$ , as the ESI gas is rapidly replaced by the ambient temperature cross-flow gas in the classification region. Generally, for singly-charged states, increasing  $T_{\text{ESI}}$  to 400 K leads to a more diverse conformation set with larger  $\Omega_i$ .  $\text{BK}^{+3}$  was present when the LTQ sampled directly from the ESI source, but not when sampling from the ROMIAC, which was likely due to deprotonation of  $\text{BK}^{+3}$  by ESI solvent molecules and/or greater mobility and thus losses of  $\text{BK}^{+3}$  to local electric fields while transiting the ROMIAC and associated tubing.

Conformations smaller than the dominant conformation (transmitted at lower voltages) were observed for singly-charged BK, AT1, and AT2 (peaks 1, 2, 4, 14, and 28 in Fig. 3.3). Two explanations for these signals are: 1) a higher charge state ion entered the ROMIAC and was transmitted through at a lower voltage than the singly-charged state, deprotonated at some point between the ROMIAC inlet and the LTQ-MS inlet, and was, therefore, detected as the singly-charged state by the LTQ-MS, and/or 2) the ESI also produced populations of peptide aggregates with a single charge per monomer unit, which were transmitted through at a lower voltage than the singly-charged monomer state. There is support for both possibilities, with Hogan and Mora 2011 observing charge loss from declustering proteins, and Counterman et al. 1998 observing multiply-charged multimers appearing in mass spectra at higher mobilities than the singly-charged monomer ion, especially for BK.

Larger conformations (transmitted at higher voltages than the parent conformation) were also observed (peaks 6–8, 10, 12, 16, 17, 19, 21–23, 27, 30, 31, 33, and 35), shown in Fig. 3.3, especially at higher  $T_{\text{ESI}}$ . These are unfolded conformations caused by either greater Coulombic repulsion (in the case of multiply-charged BK, AT1, and AT2) or thermally-induced unfolding (in the case of  $T_{\text{ESI}} = 400$  K). The peaks corresponding to  $\text{BK}^{2+}$  and  $\text{AT2}^{2+}$  did not shift significantly as the  $T_{\text{ESI}}$  was increased from 298 K to 400 K (Fig. 3.3c–d and Fig. 3.3m–n), suggesting that, for

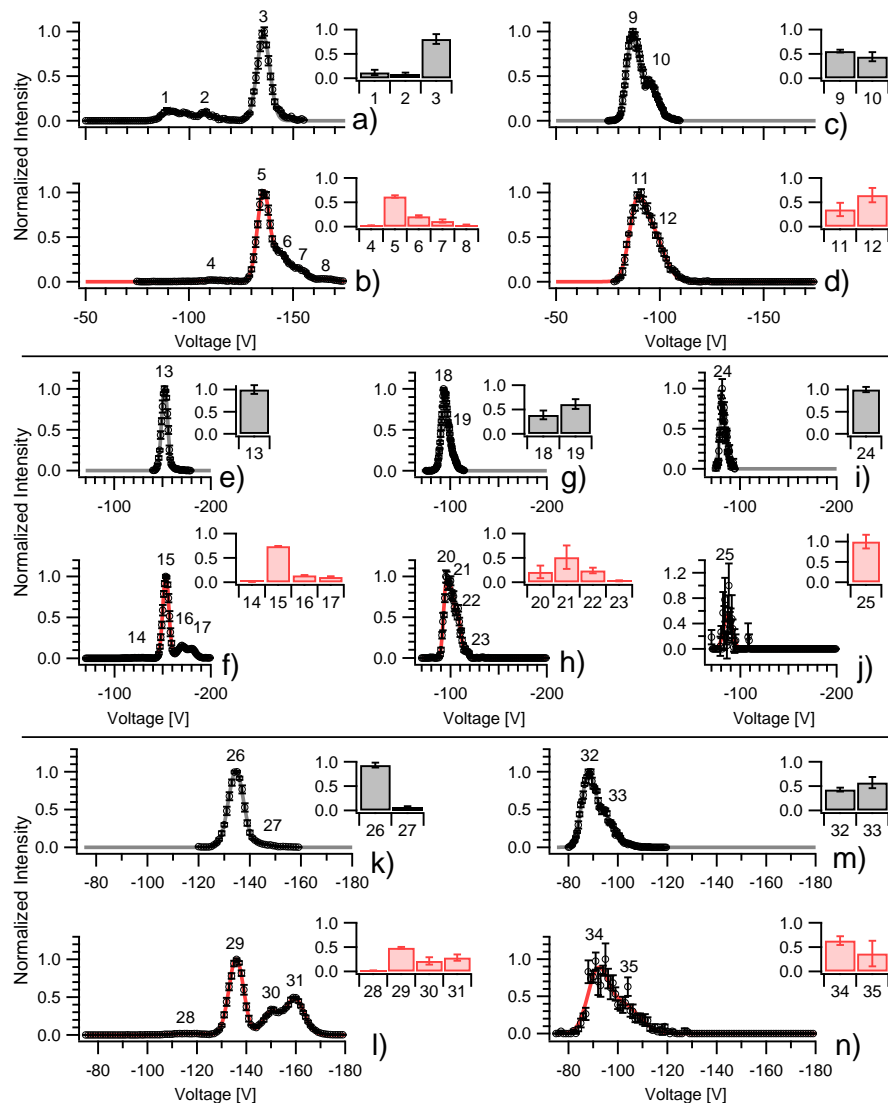


Figure 3.3: Experimental ion classifications of BK (top panel), AT1 (middle panel), and AT2 (bottom panel) ions, showing mass-resolved, normalized signal as a function of  $\phi$ . Error bars on the circular markers indicate 1 standard deviation of the normalized signal at that  $\phi$  for that one scan. Each resolvable Gaussian peak is labeled with a unique identifier number. The thick fitted line (gray for  $T_{\text{ESI}} = 298$  K and red for  $T_{\text{ESI}} = 400$  K) is the Gaussian-fitted function to the signal. Inset plots show the normalized proportion of each resolvable peak contribution to the total signal (gray for  $T_{\text{ESI}} = 298$  K and red for  $T_{\text{ESI}} = 400$  K). Error bars on rectangles indicate 1 standard deviation of the normalized proportion of each peak of the three scans for that species. a)  $\text{BK}^{+1}$  at  $T_{\text{ESI}} = 298$  K. b)  $\text{BK}^{+1}$  at  $T_{\text{ESI}} = 400$  K. c)  $\text{BK}^{+2}$  at  $T_{\text{ESI}} = 298$  K. d)  $\text{BK}^{+2}$  at  $T_{\text{ESI}} = 400$  K. e)  $\text{AT1}^{+1}$  at  $T_{\text{ESI}} = 298$  K. f)  $\text{AT1}^{+1}$  at  $T_{\text{ESI}} = 400$  K. g)  $\text{AT1}^{+2}$  at  $T_{\text{ESI}} = 298$  K. h)  $\text{AT1}^{+2}$  at  $T_{\text{ESI}} = 400$  K. i)  $\text{AT1}^{+3}$  at  $T_{\text{ESI}} = 298$  K. j)  $\text{AT1}^{+3}$  at  $T_{\text{ESI}} = 400$  K. k)  $\text{AT2}^{+1}$  at  $T_{\text{ESI}} = 298$  K. l)  $\text{AT2}^{+1}$  at  $T_{\text{ESI}} = 400$  K. m)  $\text{AT2}^{+2}$  at  $T_{\text{ESI}} = 298$  K. n)  $\text{AT2}^{+2}$  at  $T_{\text{ESI}} = 400$  K.

these ions, the larger conformations form due to Coulombic repulsion rather than thermal unfolding. Comparing AT1<sup>2+</sup> at the two ESI temperatures (Fig. 3.3g–h), it appears that peaks 18, 19 represent the same conformations as peaks 20, 21 (suggesting that peaks 19 and 21 exist due to Coulombic repulsion), but that peaks 22 and 23 are unfolded states. It is debatable whether such less folded structures reflect solution states or arise from ESI-induced changes, but conformations unique to elevated  $T_{\text{ESI}}$  are likely due to thermally-induced unfolding. Similarly, the singly-charged states of BK, AT1, and AT2 all showed larger conformations at  $T_{\text{ESI}} = 400$  K, leaving thermally-induced unfolding as the best explanation. Note that Wytenbach, Helden, and Bowers 1996 observed one  $\Omega_i$  value for BK that is independent of temperature; that state may be the most compact, lowest energy state BK conformation, since it was generated via MALDI, and thus there would be sufficient internal energy for rearrangement to a stable gas-phase structure following ionization. In contrast, we observed larger unfolded BK<sup>+1</sup> conformations at  $T_{\text{ESI}} = 400$  K (Fig. 3.3b), and since our method imparts little energy to the molecules during ionization or classification, the conformations observed could represent metastable states generated during ESI (Pierson, Valentine, and Clemmer 2010; Papadopoulos et al. 2012; Silveira et al. 2013) at elevated temperatures and then cooled by collisions with room temperature N<sub>2</sub> during classification. UB scans (only conducted at  $T_{\text{ESI}} = 298$  K; Fig. B.5) showed only one conformation for each charge state (+5 to +8) with most  $R \sim 10$ –20, though it is possible that the +5 charge state signal is composed of multiple conformations since its resolution was only  $\sim 9$  (Table B.9) (Shvartsburg et al. 2006b; Shvartsburg et al. 2006a; Wytenbach and Bowers 2011).

### Peptide and Protein Cross-Sections

In keeping convention with IMS community literature and as suggested by Wytenbach and coworkers, we decided not to scale  $\Omega_i$  values from the Mason–Schamp equation by a shape factor that can vary from unity to  $\sim 1.5$  (Wytenbach, Bleiholder, and Bowers 2013).

Table 3.1 details  $\Omega_i$  values estimated in this study (Wu, Klasmeier, and Hill 1999; Baykut, Halem, and Raether 2009; Bush et al. 2010); we report values from both instrument and MC, but only compare MC  $\Omega_i$  values with those in IMS studies also conducted in N<sub>2</sub> carrier gas. The estimated MC  $\Omega_i$  of calibrant peptide ions in this study agree with other literature  $\Omega_i$  values within  $\sim 5\%$  for  $T_{\text{ESI}} = 298$  K and  $\sim 10\%$  for  $T_{\text{ESI}} = 400$  K. Dominant ion MC  $\Omega_i$  values agree with literature to within  $\sim 10\%$  regardless of the  $T_{\text{ESI}}$  used in our experiments, and there is closer agreement with

Table 3.1: Dominant conformation bradykinin (BK), angiotensin I (AT1), angiotensin II (AT2), and bovine ubiquitin (UB)  $\Omega_i$  values.<sup>a</sup>

| Peptide             | Peak No. | <sup>b</sup> $\Omega_i$ [ $\text{\AA}^2$ ] | <sup>c</sup> $\Omega_i$ [ $\text{\AA}^2$ ] | <sup>d</sup> $\% \Delta$ | <sup>e</sup> $\% \Delta$ | <sup>f</sup> $\% \Delta$ |
|---------------------|----------|--|--|--------------------------|--------------------------|--------------------------|
| *BK <sup>+1</sup>   | 3        | 316±3.8                                    | 261±29.5                                   | -10.6%                   |                          |                          |
| #&BK <sup>+1</sup>  | 5        | 315±2.9                                    | 260±27.9                                   | -10.9%                   |                          |                          |
| *&BK <sup>+2</sup>  | 9        | 398±4.8                                    | 334±30.8                                   | 4.8%                     |                          | -2.8%                    |
| #&BK <sup>+2</sup>  | 11       | 409±5.78                                   | 343±28.6                                   | 7.6%                     |                          | -0.2%                    |
| *AT1 <sup>+1</sup>  | 13       | 352±3.8                                    | 292±30.0                                   |                          |                          |                          |
| #AT1 <sup>+1</sup>  | 15       | 355±3.0                                    | 294±28.8                                   |                          |                          |                          |
| *AT1 <sup>+2</sup>  | 18       | 434±8.9                                    | 365±34.8                                   |                          | -5.0%                    |                          |
| #AT1 <sup>+2</sup>  | 20       | 439±4.3                                    | 369±30.5                                   |                          | -4.0%                    |                          |
| *&AT1 <sup>+3</sup> | 24       | 568±9.9                                    | 482±37.0                                   |                          | 1.9%                     | 1.7%                     |
| #AT1 <sup>+3</sup>  | 25       | 602±8.5                                    | 510±31.7                                   |                          | 7.9%                     | 7.7%                     |
| *AT2 <sup>+1</sup>  | 26       | 312±2.7                                    | 258±28.5                                   | -9.8%                    |                          |                          |
| #&AT2 <sup>+1</sup> | 29       | 315±2.8                                    | 260±28.0                                   | -8.9%                    |                          |                          |
| *&AT2 <sup>+2</sup> | 32       | 405±5.0                                    | 340±31.1                                   | 7.0%                     | -4.1%                    | 1.6%                     |
| #&AT2 <sup>+2</sup> | 34       | 430±14.9                                   | 362±21.4                                   | 13.7%                    | 1.9%                     | 7.9%                     |
| *UB <sup>+5</sup>   | 36       | 1636±16.3                                  | 1390±57.3                                  |                          |                          |                          |
| *UB <sup>+6</sup>   | 37       | 1895±22.0                                  | 1613±65.3                                  |                          |                          |                          |
| *&UB <sup>+7</sup>  | 38       | 2149±25.3                                  | 1831±71.2                                  |                          |                          | -4.1%                    |
| *&UB <sup>+8</sup>  | 39       | 2409±231.6                                 | 2055±79.8                                  |                          |                          | 3.2%                     |

<sup>a</sup>In N<sub>2</sub> at atmospheric pressure and  $T_x = 298$  K. Values are the average of three scans. Peak numbers correspond to those labeled in Fig. 3.3 and Fig. B.5.

<sup>b</sup>Cross section estimated from instrument calibration (using TAAX ions; Fig. B.3).

<sup>c</sup>Cross section estimated from mobility calibration (using peptides and proteins; Fig. B.4).

<sup>d,e,f</sup>Percent difference between this study's mobility calibration  $\Omega_i$  value and that published in (d) Wu, Klasmeier, and Hill 1999, (e) Baykut, Halem, and Raether 2009, and (f) Bush et al. 2010

\* $T_{\text{ESI}} = 298$  K.

# $T_{\text{ESI}} = 400$  K.

&Peak was used for mobility calibration.



Baykut, Halem, and Raether 2009 and Bush et al. 2010 than with Wu, Klasmeier, and Hill 1999. Considering errors, nearly all dominant ion MC  $\Omega_i$  values are in agreement with those previously published. A graphical comparison of all  $\Omega_i$  values from this study to those available from the sources in Table 3.1 is shown in Fig. B.6. The largest disagreements are generally from conformations smaller than the dominant ion (peaks 1, 2, 4, and 28); as discussed earlier, these peaks may result from charge loss or ESI production of multiply-charged multimers. Note that if the IC is used instead of the MC to estimate peptide  $\Omega_i$ , the peptides generally appear to be much larger (up to ~40%) than previously published  $\Omega_i$ , but the methods previously utilized do not allow for direct comparison to the  $\Omega_i$  values obtained here. Hill and coworkers utilized a much higher buffer gas temperature (520 K) (Wu, Klasmeier, and Hill 1999), Baykut et al. used a modified ion funnel (Baykut, Halem, and Raether 2009), and Bush and coworkers employed an RF-confining drift cell (Bush et al. 2010). Given the strong dependence on temperature of  $\Omega_i$  in N<sub>2</sub> (Wytttenbach, Bleiholder, and Bowers 2013), it is possible that these values are reasonable for room-temperature measurements in the absence of field-induced heating of the classified ions. Figure 3.4 summarizes the MC  $\Omega_i$  for each peak numbered in Figs. 3.3 and B.5. For a given peptide at a given  $T_{\text{ESI}}$ , the MC  $\Omega_i$  increases as charge state increases.

### Model Peptide Isomer Separation

Two sets of peptide isomers, AARAAATAA/AATAAARAA and AARAAHAMA/AARAAMAHA, were separated by the ROMIAC followed by CID within the ion trap, both with and without attachment of the FRIPS reagent. Shown in Figs. B.7–B.8 are the mass spectra observed for unique product ions (UPI) for each isomeric peptide. UPI in untagged peptides (three each for AARAAATAA and AATAAARAA, one each for AARAAHAMA and AARAAMAHA) were generated via charge-driven dissociation (Paizs and Suhai 2005) of the peptide backbone (Fig. B.7a–b and B.8a–b), whereas addition of the FRIPS reagent resulted in free radical chemistry that was highly selective for specific amino acids in the peptide sequence (Fig. B.7c–d and B.8c–d; two UPI each for AARAAATAA and AATAAARAA, one UPI each for AARAAHAMA and AARAAMAHA). This chemistry resulted from the generation of an acetyl radical at the N-terminus of the peptide via loss of the TEMPO moiety upon CID, followed by H atom abstraction and dissociation, as illustrated in Fig. 3.5a (details in Appendix B). The UPI utilized to differentiate the model peptide isomers are formed according to the processes shown in Fig. 3.5b–d.

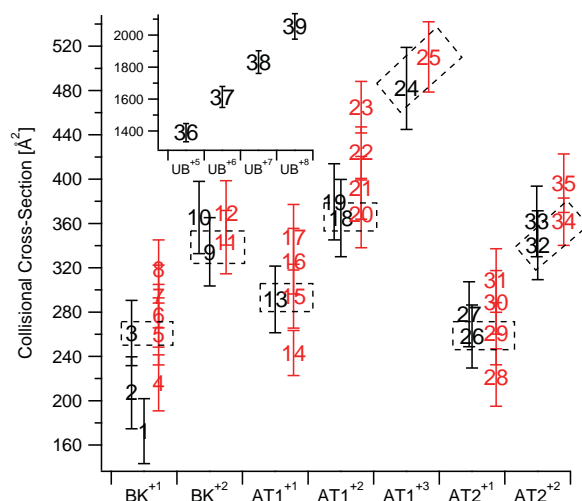


Figure 3.4: Mobility calibration  $\Omega_i$  of numbered peaks from Fig. 3.3. In  $N_2$  at atmospheric pressure with  $T_x = 298$  K. Black markers indicate  $T_{ESI} = 298$  K and red markers indicate  $T_{ESI} = 400$  K. Error bars denote 1 standard deviation of triplicates. Dashed boxes enclose dominant conformation at each  $T_{ESI}$ . Inset plot shows mobility calibration  $\Omega_i$  for UB peaks from Fig. B.5, in which only one dominant species for each charge state was identified. Detailed signal, Gaussian fit, and resolution values are found in Tables B.9 and B.10.

For threonine-containing peptides, observed  $[a_6 + H]^+$  and  $z_7 - H$  ions are generated via H atom abstraction from the  $C_\beta$  of the threonine side chain, followed by  $N - C_\alpha$  bond cleavage and subsequent loss of isocyanic acid from the N-terminal product ion (Fig. 3.5a). The  $z_7 - H$  ion may further decompose to give the  $y_6$  ion. The  $c_6$  ion is formed by a similar process in which H atom transfer to the N-terminal carbonyl oxygen occurs in concert with  $N - C_\alpha$  bond cleavage (Fig. 3.5b). For isomeric peptides containing histidine, UPI are formed by abstraction of H from the  $C_\beta$  of histidine followed by cleavage of the  $C_\alpha - C$  bond (Fig. 3.5c) (Sun et al. 2009).

For untagged AARAAATAA and AATAAARAA, the signals from the three UPI for each isomer (Fig. B.7 a–b) peak signal appear at the same voltage (considering errors), precluding resolution of the isomers (Fig. 3.6a–b). However, the addition of the FRIPS reagent separates the two UPI (Fig. B.7c–d) for each isomer by  $\sim 7$  V, or  $\sim 14 \text{ \AA}^2$  (Fig. 3.6c–d and Table B.11). A similar but less dramatic separation enhancement occurred for the AARAAHAMA and AARAAMAHA isomers; UPI from the untagged peptides (Fig. B.8a–b) were separated by  $\sim 1$  V (Fig. 3.6e–f), but FRIPS reagent addition increased separation of these product ions (Fig. B.8c–d) by  $\sim 3$  V, or  $\sim 4 \text{ \AA}^2$  (Fig. 3.6g–h and Table B.11). The difference in sep-

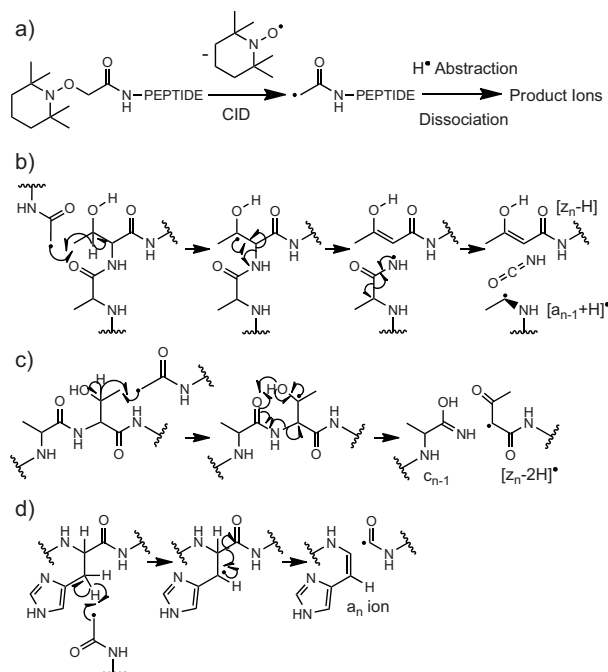


Figure 3.5: Free radical dissociation processes resulting from FRIPS reagent attachment to model peptides. The FRIPS methodology employed here is shown schematically in a). The TEMPO-based FRIPS reagent is coupled to the N-terminus of the peptide, and subsequent collisional activation leads to loss of the TEMPO moiety, generating an acetyl radical. This acetyl radical then abstracts a H atom from diverse sites along the peptide, leading to dissociation of the backbone or neutral loss of amino acid side chains. Unique product ions are proposed to occur at threonine residues via the mechanisms shown in b) and c), resulting in b) [a<sub>6</sub> + H]<sup>•</sup> and z<sub>7</sub> - H ion generation and c) c<sub>6</sub> ion generation. Backbone dissociation at histidine residues likely occurs via the mechanism illustrated in d), leading to a<sub>6</sub> and a<sub>8</sub> ion generation. (Sun et al. 2009)

aration enhancement between the two pairs of model peptides with FRIPS reagent addition is not surprising, since the protonation site is not relocated in the AARAA-HAMA/AARAAMAHA case. It is evident in both cases, however, that the addition of the tag to the N-terminus improves separation. The reason for this improvement is not entirely clear, but is likely due to disruption of interactions between the altered N-terminus and other sites on the peptide backbone. In addition, the radical-driven dissociation of the TEMPO-tagged peptides generates a more distinct spectrum than CID, although the overall sequence information is diminished.

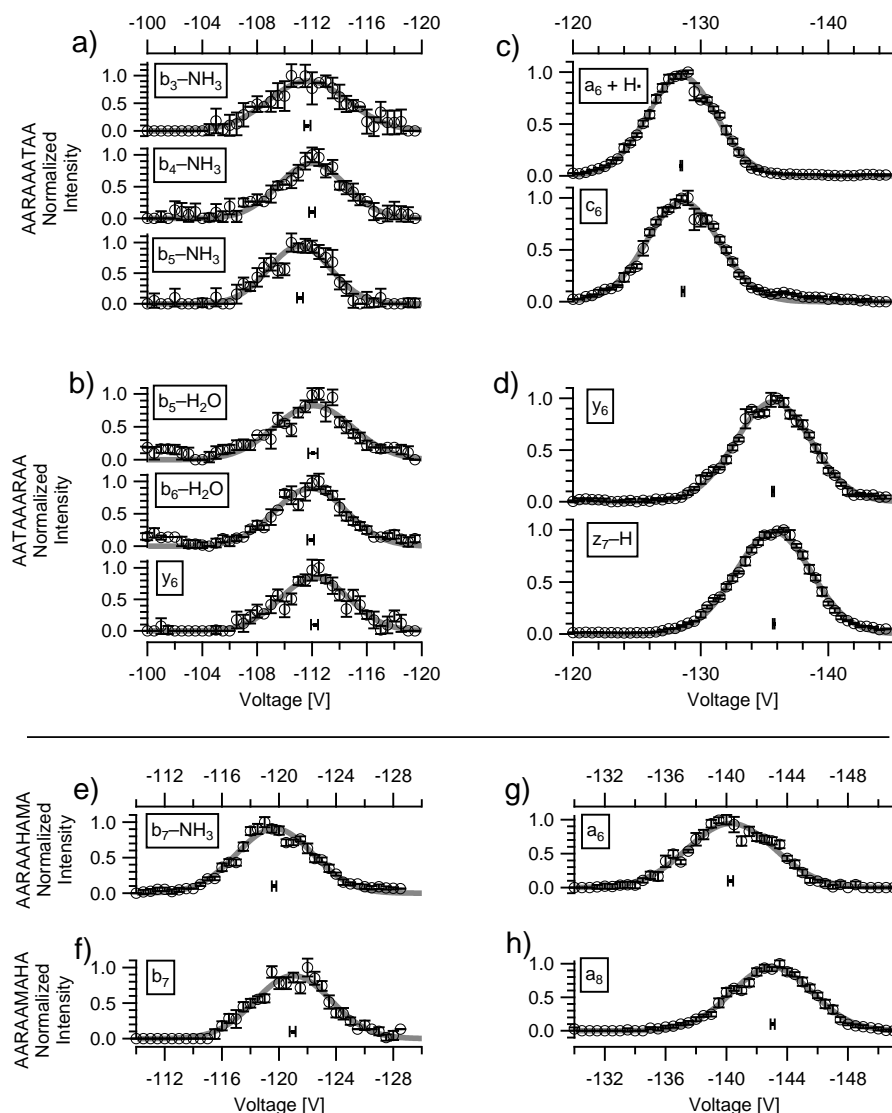


Figure 3.6: Experimental CID unique product ion classifications and separations of model peptide isomers, showing mass-resolved, normalized fragment signals as a function of  $\phi$ . In  $\text{N}_2$  at atmospheric pressure and  $T_{\text{ESI}} = T_x = 298$  K. Error bars on the circular markers indicate 1 standard deviation of the normalized signal at that  $\phi$  for that one scan. The thick gray line is the Gaussian-fitted function to the signal, and the dot marker shows the centroid of the fit, with horizontal error bars indicating the 95% confidence interval of the centroid. a) Non-TEMPO-tagged AARAAATAA CID fragments. b) Non-TEMPO-tagged AATAAARAA CID fragments. c) TEMPO-tagged AARAAATAA CID fragments. b) TEMPO-tagged AATAAARAA CID fragments. e) Non-TEMPO-tagged AARAAHAMA CID fragment. f) Non-TEMPO-tagged AARAAMAHA CID fragment. g) TEMPO-tagged AARAAHAMA CID fragment. h) TEMPO-tagged AARAAMAHA CID fragment.

### 3.5 Conclusions

IM–MS with a ROMIAC was used to classify TAAX (C2–C12) and peptide (BK, AT1, AT2, and UB) ions with  $\Omega_i$  from 200–2000 Å<sup>2</sup>, achieving high resolutions close to  $\mathcal{R}_{nd}$  ( $\sim 20$ ). Greater resolution is possible, but limited in the current study by flow rate measurement capabilities.  $K_{0,i}$  of additional TAAX multimers were estimated and can also be used for IC standards. Estimation of  $\Omega_i$  of peptides is shown to agree with previously published values, considering errors. Model peptide isomer separation was successfully conducted with untagged AARAAHAMA/AARAAMAHA using ROMIAC–IMS; separation was demonstrably enhanced with TEMPO–tagging, consequentially allowing the separation of AARAAATAA/AATAAARAA isomers.

The ROMIAC is desirable for further IMS applications, as it suffers fewer diffusional losses of ions than the conventional DMA and achieves greater resolutions. Additionally, although FAIMS is the only other IMS method that provides continuous transmission of ions, separations based on mobility are more easily interpreted with ROMIAC–IMS than with FAIMS, which separates ions based on differences in high and low field mobilities and not molecular size. The ROMIAC is a compact, inexpensive instrument with low pump demands that can be interfaced to any mass spectrometer with an atmospheric pressure inlet. Improvements to the ROMIAC–MS interface, e.g. sealing and tubing length reduction between the ROMIAC and the LTQ–MS, should greatly enhance ion transfer efficiency and hence sensitivity. ROMIAC–IMS affords a new approach to high throughput multi–dimensional chemical analysis. Other IMS applications of the ROMIAC include its use as a prefilter to reject abundant ion components and enhance the MS capability for detection of low abundance ions. For example, it could be used for real–time investigations of low abundance human serum proteins, especially those known to be markers for disease, by eliminating abundant uninteresting proteins and thereby improving the dynamic range of MS to detect the desired proteins. Of even greater ambition would be the potential use of heated electrospray ionization to identify biomolecules based on unique conformation mobility array "fingerprints" as an inexpensive alternative to mass spectrometry. The ROMIAC can be employed in other fields requiring sub–10 nm particle classification, such as nanoparticle–coating application or identification and study of atmospheric seed particle nucleation processes.

### **3.6 Acknowledgments**

Andrew Metcalf, Xerxes Lopez–Yglesias, and Kate Upton are acknowledged for technical assistance with the LabView program and MS support. Financial support comes from a NSF Graduate Research Fellowship (W.M.); the Beckman Institute at Caltech (J.L.B. and D.A.T.); the Jacobs Institute for Molecular Engineering for Medicine (R.C.F. and A.J.D.). This work was supported by the National Science Foundation under Grant No. CBET-1236909.

## References

- Bacher, G. et al. (2001). "Charge-reduced nano electrospray ionization combined with differential mobility analysis of peptides, proteins, glycoproteins, noncovalent protein complexes and viruses." In: *J. Mass Spectrom.* 36.9, pp. 1038–52. DOI: 10.1002/jms.208.
- Baykut, G., O. von Halem, and O. Raether (2009). "Applying a dynamic method to the measurement of ion mobility". In: *J. Am. Soc. Mass Spectrom.* 20.11, pp. 2070–81. DOI: 10.1016/j.jasms.2009.07.013.
- Brunelli, N. A., R. C. Flagan, and K. P. Giapis (2009). "Radial differential mobility analyzer for one nanometer particle classification". In: *Aerosol Sci. Technol.* 43.1, pp. 53–59. DOI: 10.1080/02786820802464302.
- Bush, M. F. et al. (2010). "Collision cross sections of proteins and their complexes: a calibration framework and database for gas-phase structural biology." In: *Anal. Chem.* 82.22, pp. 9557–65. DOI: 10.1021/ac1022953.
- Counterman, A. E. et al. (1998). "High-order structure and dissociation of gaseous peptide aggregates that are hidden in mass spectra". In: *J. Am. Soc. Mass Spectrom.* 9.8, pp. 743–59. DOI: 10.1016/S1044-0305(98)00052-X.
- Downard, A. J., J. F. Dama, and R. C. Flagan (2011). "An asymptotic analysis of differential electrical mobility classifiers". In: *Aerosol Sci. Technol.* 45.6, pp. 717–729. DOI: 10.1080/02786826.2011.558136.
- Fernández-Maestre, R. et al. (2010). "Chemical standards in ion mobility spectrometry". In: *Analyst* 135.6, pp. 1433–42. DOI: 10.1039/b915202d.
- Flagan, R. C. (2004). "Opposed migration aerosol classifier (OMAC)". In: *Aerosol Sci. Technol.* 38.9, pp. 890–899. DOI: 10.1080/027868290505242.
- Gamero-Castaño, M. and J. F. de la Mora (2000). "Mechanisms of electrospray ionization of singly and multiply charged salt clusters." In: *Anal. Chim. Acta.* 406, pp. 67–91. DOI: 10.1016/S0003-2670(99)00596-6.
- Giles, K. et al. (2004). "Applications of a travelling wave-based radio-frequency-only stacked ring ion guide." In: *Rapid Comm. Mass Sp.* 18.20, pp. 2401–14. DOI: 10.1002/rcm.1641.
- Guevremont, R. et al. (1997). "Combined ion mobility/time-of-flight mass spectrometry study of electrospray-generated ions". In: *Anal. Chem.* 69.19, pp. 3959–65. DOI: 10.1021/ac970359e.
- Hodyss, R., H. A. Cox, and J. L. Beauchamp (2005). "Bioconjugates for tunable peptide fragmentation: free radical initiated peptide sequencing (FRIPS)." In: *J. Am. Chem. Soc.* 127.36, pp. 12436–7. DOI: 10.1021/ja052042z.
- Hogan, C. J. and J. F. de la Mora (2010). "Ion-pair evaporation from ionic liquid clusters". In: *J. Am. Soc. Mass Spectrom.* 21, pp. 1382–6. DOI: 10.1016/j.jasms.2010.03.044.

- Hogan, C. J. and J. F. de la Mora (2011). "Ion mobility measurements of nondenatured 12-150 kDa proteins and protein multimers by tandem differential mobility analysis-mass spectrometry (DMA-MS)". In: *J. Am. Soc. Mass Spectrom.* 22.1, pp. 158–72. DOI: 10.1007/s13361-010-0014-7.
- Hogan, C. J., B. T. Ruotolo, et al. (2011). "Tandem differential mobility analysis-mass spectrometry reveals partial gas-phase collapse of the GroEL complex." In: *J. Phys. Chem. B* 115, pp. 3614–21. DOI: 10.1021/jp109172k.
- Jiang, J. et al. (2011). "Transfer functions and penetrations of five differential mobility analyzers for sub-2 nm particle classification". In: *Aerosol Sci. Technol.* 45.4, pp. 480–492. DOI: 10.1080/02786826.2010.546819.
- Kaddis, C. S. et al. (2007). "Sizing large proteins and protein complexes by electrospray ionization mass spectrometry and ion mobility." In: *J. Am. Soc. Mass Spectrom.* 18.7, pp. 1206–16. DOI: 10.1016/j.jasms.2007.02.015.
- Kaufman, S. L. (1998). "Analysis of biomolecules using electrospray and nanoparticle methods: the gas-phase electrophoretic mobility molecular analyzer (GEMMA)". In: *J. Aerosol Sci.* 29.5, pp. 537–552. DOI: 10.1016/S0021-8502(97)00462-X.
- Kaufman, S. L. et al. (1996). "Macromolecule analysis based on electrophoretic mobility in air: globular proteins." In: *Anal. Chem.* 68.11, pp. 1895–904. DOI: 10.1021/ac951128f.
- Knutson, E. O. and K. T. Whitby (1975). "Aerosol classification by electrical mobility: apparatus, theory, and applications". In: *J. Aerosol Sci.* 6, pp. 443–451. DOI: 10.1016/0021-8502(75)90060-9.
- Labowsky, M. and J. F. de la Mora (2006). "Novel ion mobility analyzers and filters". In: *J. Aerosol Sci.* 37.3, pp. 340–362. DOI: 10.1016/j.jaerosci.2005.07.001.
- Lee, M. et al. (2009). "Gas-phase peptide sequencing by TEMPO-mediated radical generation." In: *Analyst* 134.8, pp. 1706–12. DOI: 10.1039/b904115j.
- Martínez-Lozano, P., M. Labowsky, and J. F. de la Mora (2006). "Experimental tests of a nano-DMA with no voltage change between aerosol inlet and outlet slits". In: *J. Aerosol Sci.* 37.11, pp. 1629–1642. DOI: 10.1016/j.jaerosci.2006.02.001.
- Mora, J. F. de la, S. Ude, and B. A. Thomson (2006). "The potential of differential mobility analysis coupled to MS for the study of very large singly and multiply charged proteins and protein complexes in the gas phase". In: *Biotechnol. J.* 1.9, pp. 988–97. DOI: 10.1002/biot.200600070.
- Paizs, B. and S. Suhai (2005). "Fragmentation pathways of protonated peptides". In: *Mass Spectrom. Rev.* 24.4, pp. 508–48. DOI: 10.1002/mas.20024.
- Papadopoulos, G. et al. (2012). "Conformational distribution of bradykinin [bk + 2 H]<sup>2+</sup> revealed by cold ion spectroscopy coupled with FAIMS". In: *J. Am. Soc. Mass Spectrom.* 23.7, pp. 1173–81. DOI: 10.1007/s13361-012-0384-0.



- Pierson, N. A., L. Chen, et al. (2011). "Number of solution states of bradykinin from ion mobility and mass spectrometry measurements". In: *J. Am. Chem. Soc.* 133.35, pp. 13810–13813. DOI: 10.1021/ja203895j.
- Pierson, N. A., S. J. Valentine, and D. E. Clemmer (2010). "Evidence for a quasi-equilibrium distribution of states for bradykinin  $[M + 3H]^{3+}$  ions in the gas phase". In: *J. Phys. Chem. B* 114, pp. 7777–7783. DOI: 10.1021/jp102478k.
- Purves, R. W., D. A. Barnett, B. Ells, et al. (2000). "Investigation of bovine ubiquitin conformers separated by high-field asymmetric waveform ion mobility spectrometry: cross section measurements using energy-loss experiments with a triple quadrupole mass spectrometer". In: *J. Am. Soc. Mass Spectrom.* 11.8, pp. 738–45. DOI: 10.1016/S1044-0305(00)00136-7.
- Purves, R. W., D. A. Barnett, and R. Guevremont (2000). "Separation of protein conformers using electrospray-high field asymmetric waveform ion mobility spectrometry-mass spectrometry". In: *Int. J. Mass Spectrom.* 197.1-3, pp. 163–177. DOI: 10.1016/S1387-3806(99)00240-7.
- Rosser, S. and J. F. de la Mora (2005). "Vienna-type DMA of high resolution and high flow rate". In: *Aerosol Sci. Technol.* 39.12, pp. 1191–1200. DOI: 10.1080/02786820500444820.
- Shvartsburg, A. A., A. J. Creese, et al. (2010). "Separation of peptide isomers with variant modified sites by high-resolution differential ion mobility spectrometry." In: *Anal. Chem.* 82.19, pp. 8327–34. DOI: 10.1021/ac101878a.
- Shvartsburg, A. A. et al. (2006a). "Characterizing the structures and folding of free proteins using 2-D gas-phase separations: observation of multiple unfolded conformers". In: *Anal. Chem.* 78.10, pp. 3304–3315. DOI: 10.1021/ac060283z.
- (2006b). "High-resolution field asymmetric waveform ion mobility spectrometry using new planar geometry analyzers". In: *Anal. Chem.* 78.11, pp. 3706–14. DOI: 10.1021/ac052020v.
- Silveira, J. A. et al. (2013). "Cryogenic ion mobility-mass spectrometry captures hydrated ions produced during electrospray ionization". In: *J. Phys. Chem. A* 117.5, pp. 953–61. DOI: 10.1021/jp311278a.
- Sun, Q. et al. (2009). "Side chain chemistry mediates backbone fragmentation in hydrogen deficient peptide radicals". In: *J. Proteome Res.* 8, pp. 958–966. DOI: 10.1021/pr800592t.
- Tammet, H. (2011). "Symmetric inclined grid mobility analyzer for the measurement of charged clusters and fine nanoparticles in atmospheric air". In: *Aerosol Sci. Technol.* 45.4, pp. 468–479. DOI: 10.1080/02786826.2010.546818.
- Ude, S. and J. F. de la Mora (2005). "Molecular monodisperse mobility and mass standards from electrosprays of tetra-alkyl ammonium halides." In: *J. Aerosol Sci.* 36.10, pp. 1224–1237. DOI: 10.1016/j.jaerosci.2005.02.009.

- Viidanoja, J. et al. (2005). "Tetraalkylammonium halides as chemical standards for positive electrospray ionization with ion mobility spectrometry/mass spectrometry". In: *Rapid Comm. Mass Sp.* 19.21, pp. 3051–5. DOI: 10.1002/rcm.2172.
- Wittmer, D. et al. (1994). "Electrospray ionization ion mobility spectrometry". In: *Anal. Chem.* 66, pp. 2348–2355. DOI: 10.1021/ac00086a021.
- Wu, C., J. Klasmeier, and H. H. Hill (1999). "Atmospheric pressure ion mobility spectrometry of protonated and sodiated peptides". In: *Rapid Comm. Mass Sp.* 13.12, pp. 1138–42. DOI: 10.1002/(SICI)1097-0231(19990630)13:12<1138::AID-RCM625>3.0.CO;2-8.
- Wu, C., W. F. Siems, et al. (1998). "Electrospray ionization high-resolution ion mobility spectrometry-mass spectrometry". In: *Anal. Chem.* 70.23, pp. 4929–4938. DOI: 10.1021/ac980414z.
- Wytenbach, T., C. Bleiholder, and M. T. Bowers (2013). "Factors contributing to the collision cross section of polyatomic ions in the kilodalton to gigadalton range: application to ion mobility measurements". In: *Anal. Chem.* Article ASAP. DOI: 10.1021/ac3029008.
- Wytenbach, T. and M. T. Bowers (2011). "Structural stability from solution to the gas phase: native solution structure of ubiquitin survives analysis in a solvent-free ion mobility-mass spectrometry environment". In: *J. Phys. Chem. B* 115.42, pp. 12266–75. DOI: 10.1021/jp206867a.
- Wytenbach, T., G. von Helden, and M. T. Bowers (1996). "Gas-phase conformation of biological molecules: Bradykinin". In: *J. Am. Chem. Soc.* 118.35, pp. 8355–8364. DOI: 10.1021/ja9535928.

## *Chapter 4*

# CHARGE DISTRIBUTION UNCERTAINTY IN DIFFERENTIAL MOBILITY ANALYSIS OF AEROSOLS

By Johannes Leppä, Wilton Mui, Amanda M. Grantz, and Richard C. Flagan

This chapter is was submitted to, and is currently under review by, *Aerosol Science and Technology* as:

Leppä, J. et al. (2017). “Charge distribution uncertainty in differential mobility analysis of aerosol”. In: *Aerosol Sci. Technol.* In review.

### 4.1 Abstract

The inference of particle size distributions from differential mobility analyzer (DMA) data requires knowledge of the charge distribution on the particles being measured. The charge distribution produced by a bipolar aerosol charger depends on the properties of the ions produced in the charger, and on the kinetics of charge transfer from molecular ions or ion clusters to the particles. A single parameterization of a theoretically predicted charge distribution is employed in most DMA analyses regardless of the atmospheric conditions being probed. Deviations of the actual charge distribution from that assumed in the data analysis will bias the estimated particle size distribution. We examine these potential biases by modeling measurements and data inversion using charge distributions calculated for a range of atmospheric conditions. Moreover, simulations were performed using the ion-to-particle flux coefficients predicted for a range of properties of both the particles and ions. To probe the biases over the full range of particle sizes, the measurements were simulated through an atmospheric new particle formation event. The differences between the actual charge distribution and that according to the commonly used parameterization resulted in biases as large as a factor of 5 for nucleation-mode particles, and up to 80 % for larger particles. Incorrect estimates of the relative permittivity of the particles or not accounting for the temperature and pressure effects for measurements at 10 km altitude produced biases in excess of 50 %; three-fold biases were predicted to result from erroneous estimates of the ion mobility distribution. We further report on the effects of the relative permittivity of the ions, the relative concentrations of

negative and positive ions, and truncation of the number of charge states considered in the inversion.

## 4.2 Introduction

The differential mobility analyzer, (DMA; Knutson and Whitby 1975), is the primary instrument used to measure size distributions of submicron aerosol particles. It separates particles from a small aerosol flow according to the velocities with which they migrate across a larger, clean, particle-free sheath flow under the influence of an electric field. The migration velocity of a particle depends on its electrical mobility, and only particles carrying an electric charge are transmitted and counted. Over the 1 nm to 1  $\mu\text{m}$  size domain now covered by DMAs, only a small fraction of particles acquire charge; the probability that a particle carries a single or multiple charges varies widely. That probability must be known to infer the particle size distribution from the numbers of charged particles that are transmitted through the mobility classifier. To ensure a stable and known charge distribution, most DMA measurements of particle size distributions are made using a so-called bipolar diffusion charger in which the aerosol is exposed to an ion cloud produced by radioactive decay, soft x-rays, or other methods. This device is also called an aerosol *neutralizer* because the mean charge state acquired is approximately neutral. The ions then undergo charge-transfer reactions with the aerosol particles, some of which increase the number of charges, while others neutralize previously attached charges. Ideally, a steady-state charge distribution is established, providing a well-defined charge state that can be used in concert with well-established models of the performance of the DMA (e.g., M. R. Stolzenburg 1988; S.-H. Zhang and Flagan 1996; Flagan 1999; Hagwood, Sivathanu, and Mulholland 1999) to infer the particle size distribution from counts of the small fraction of the particles that are charged.

Most studies of the charge distribution derive from the pioneering work of Fuchs (1963) who developed a heuristic model to describe the flux of gas ions to the surfaces of neutral and charged particles ranging from ones small compared to the mean-free-path,  $\lambda_i$ , of the ions (free molecular regime) to ones much larger than  $\lambda_i$  (continuum regime). In this way, he derived attachment coefficients throughout the transition regime. Those attachment coefficients can be used to predict the charge distribution under different scenarios. The most common scenario explored is the steady-state bipolar charge distribution produced by exposure of the aerosol to an ion cloud generated by energetic particles from radioactive decay. This pioneering science laid the groundwork for the use of mobility-based methods for particle size

distribution measurements. By bringing the aerosol particles to a known charge distribution, number concentrations obtained as a function of electrical mobility in DMA analysis can be inverted to deduce the particle size distribution. New sources of gas ions have been developed to replace the radioisotope sources of the traditional neutralizer, thereby reducing regulatory barriers to transporting instruments and using them in a number of environments. The alternative methods for ion production include soft x-ray sources (Shimada et al. 2002; Jiang, Hogan, et al. 2007; Yun et al. 2009), dual-corona discharge (Qi and Kulkarni 2013), surface-discharge microplasma (Kwon et al. 2006), and carbon fiber ionizer (Han et al. 2009). Shimada et al. (2002) demonstrated attainment of a steady-state bipolar charge distribution by the combination of direct charging by soft x-rays and diffusion charging, establishing the viability of the soft x-ray source for aerosol neutralization.

Fuchs (1963) used his attachment coefficients to derive the steady-state bipolar charge distribution that results when, as in the neutralizer, the aerosol is exposed to a large excess of gas ions. At small sizes, most particles in this steady-state distribution carry at most one elementary unit of charge,  $e$ , but the probability that a particle will carry multiple charges increases rapidly with increasing size above threshold of about 20 nm. Hoppel and Frick (1986) corrected some subtle errors in the original model and undertook extensive computer simulations to predict the steady-state bipolar charge distribution under atmospheric conditions. Recognizing the need for an accessible model for use in inferring particle size distributions from DMA measurements, Wiedensohler (1988) fitted the results of the Hoppel and Frick (HF) simulations to a readily evaluated empirical expression, establishing the bipolar charge distribution that has been used in the interpretation of particle size distributions in most DMA-based measurements made to date. The Fuchs/Hoppel-Frick/Wiedensohler (FHFw) charge distribution has thus played such a central role in enabling DMA measurements to provide a comprehensive view of the dynamics of small aerosol particles that it is incorporated into the ISO 15900 standard.

Though the theory of bipolar aerosol charging is well established and extensively used, questions about the accuracy of the predicted charge distribution remain. Soon after calculating the steady-state bipolar charge distribution, Hoppel and Frick (1990) observed that small electric fields within, or downstream of the aerosol neutralizer can dramatically bias the charge distribution. More recently, the ion-to-particle flux coefficients have received renewed attention with Ouyang, Gopalakrishnan, and Hogan (2012) probing the influence of attractive singular contact potentials

on the collision process, Gopalakrishnan, Thajudeen, et al. (2013) deriving equations to account for non-spherical geometries of the particles, and López-Yglesias and Flagan revising the FHFV model (2013). Further, a method to estimate the charge distribution without the need to calculate the flux coefficients was developed (Gopalakrishnan, Meredith, et al. 2013) and found to be in good agreement with the FHFV model at room temperature and atmospheric pressure (Gopalakrishnan, P. H. McMurtry, and Hogan 2015). Finally, recent studies suggest that achieving the steady-state bipolar charge distribution in the charger, which is a critical assumption in most mobility-based particle size distribution measurements, could depend on the concentrations of measured particles (de La Verpilliere, Swanson, and Boies 2015; Tigges, Jain, and Schmid 2015) and on the aerosol flowrate through the charger (He and Dhaniyala 2014), adding to the uncertainty.

In a recent reexamination of the FHFV model, López-Yglesias and Flagan (López-Yglesias and Flagan 2013a; López-Yglesias and Flagan 2013b) identified some errors, as well as some numerical approximations that arose due to the computing resources available at the time of HF simulations. The effects were minor through the mid-range of sizes where most measurements have traditionally been made, but for particles in the low nanometer regime ( $< 20$  nm diameter), and for particles larger than a few hundred nanometers, the errors can become significant. That study refined the general Fuchs/HF model of the charging kinetics, and examined the effects of the refinements, albeit with some simplifying assumptions. Notably, the positive and negative gas ions were assumed to have the same mobilities as those used in the original HF simulations to facilitate direct comparison of the two versions of the model. Results from that study suggest that biases could result when the bipolar charge distribution predicted for sea level charging of conductive particles is applied to different kinds of aerosols, or to measurements at different altitudes. That study did not, however, provide sufficient calculations to draw any quantitative conclusions about the uncertainties in the particle size distribution that may result from the combined effects of imperfect knowledge of ion and particle properties, and model limitations.

The present study employs the refined FHFV model of aerosol particle charging to explore how both ion and particle properties, and atmospheric conditions may influence the interpretation of DMA data, and to quantify potential biases in the measured particle size distribution caused by differences between the charge distribution acquired in the charger and that assumed for data analysis by inversion. More specif-

ically, we will separately study parameters that define the steady-state bipolar charge distribution and assess the potential bias in the particle size distribution caused by each of these parameters. The probed parameters include relative permittivity of the particles, mobility distribution, mass and relative permittivity of the charger ions, and the relative concentrations of positive and negative ions. As measurements are conducted at a range of altitudes, including airborne measurements (e.g., Clarke et al. 1998; Mirme et al. 2010; Coggon et al. 2014) and measurements at high altitude field stations such as Jungfraujoch, Switzerland (3580 m asl; Weingartner, Nyeki, and Baltensperger 1999), we also explore the bias that results from failing to account for the pressure and temperature variation with altitude. Finally, we will quantify the bias due to insufficient number of particle charge states considered in the inversion. While we discuss DMA-based particle size distribution measurements, the conclusions are not specific to the DMA, and apply to measurements made with other mobility classifiers.

### 4.3 Methods

Unless otherwise noted, we use the following notation throughout this article: diameter refers to mobility equivalent diameter, flux coefficient refers to ion-to-particle flux coefficient, charge distribution refers to steady-state bipolar charge distribution, concentration refers to number concentration, and particle size distribution refers to distribution of particle number concentration with respect to particle size.

The following procedure was used to quantify the magnitude of bias in the measured particle size distribution due to differences between the charge distribution acquired in the charger,  $f_{\text{cha}}$ , and that assumed for data analysis by inversion,  $f_{\text{inv}}$ : (1) We used known particle size distributions from aerosol dynamics simulations as a synthetic sample aerosol. These particle size distributions will be referred to as simulated distributions. (2) The simulated distributions were converted into “signals” emulating the working principle of a DMA, including an assumption on  $f_{\text{cha}}$ . This pseudo-instrument approach acknowledges that high resolution DMA measurements are now possible over the entire size range, albeit not with a single instrument. (3) Particle size distributions were inferred from the synthetic signals using the same inversion algorithm that has been applied to the raw signals from an actual instrument. The inversion algorithm included an assumption on  $f_{\text{inv}}$ , and these particle size distributions are referred to as inverted distributions. (4) The simulated and inverted distributions were compared to each other, with any differences between the two distributions originating from the difference between

$f_{\text{cha}}$  and  $f_{\text{inv}}$ , provided that the inversion characterizes other features of the pseudo-instrument correctly. This procedure represents measurement conditions in which the instrument is characterized perfectly, except for the charge distribution acquired in the charger, which allowed us to quantify the bias in the particle size distribution caused by  $f_{\text{cha}} \neq f_{\text{inv}}$ . Some features of the pseudo-instrument were simpler than corresponding features of an actual instrument, which does not affect the conclusions of this study as long as the inversion algorithm characterizes those features correctly. A similar procedure could be used to study other features of the inversion algorithm, but the focus of this study is on the charge distribution acquired in the aerosol charger.

In the remainder of this section, we will present the steps of the analysis in more detail. We will also present the assumptions made when calculating the ion-to-particle flux coefficients, which were needed for calculating the charge distributions.

### Calculation of the charge distributions

The charge distribution,  $f$ , of an aerosol is defined as the collection of fractional populations,  $f_k$ , of all charge states considered, i.e.,

$$f = \{f_{-y}, f_{-y+1}, \dots, f_{-2}, f_{-1}, f_0, f_1, f_2, \dots, f_{y-1}, f_y\}, \quad (4.1)$$

where  $y = k_{\text{max}}$ , which is the maximum number of charges a particle is assumed to acquire.  $f_k(d_p)$ , denotes the fraction of particles with a diameter,  $d_p$ , that have the charge state  $k$ , i.e.,  $f_k(d_p) = n_k(d_p)/n_T(d_p)$ , where  $n_k$  and  $n_T$  are the concentration of particles having charge state  $k$  and the total particle concentration, respectively.

The charge distribution in bipolar steady-state can be estimated using a Brownian dynamics method (Gopalakrishnan, Meredith, et al. 2013) or deduced from the ion-to-particle flux coefficients by solving a system of population balance equations (e.g., Hussin et al. 1983; Hoppel and Frick 1986), with the latter method used in this study. To that end, we calculated the flux coefficients using the refined FHFV model as described by López-Yglesias and Flagan (2013a) with two notable differences: Firstly, while the initial work with this model assumed that all ions of one polarity have the same mobility,  $Z_i$ , in this study we follow the approach by Lee et al. (2005) to describe the ions using a discrete mobility distribution,  $n_i^\pm(Z_i)$ ; both ambient (e.g., Ehn, Junninen, Petäjä, et al. 2010) and laboratory (e.g., Gerhard Steiner et al. 2014; Maißer et al. 2015) measurements have revealed that a range of ions are generally present, which has previously been accounted for in studies where the Brownian



dynamics method was used to estimate the charge distribution (Gopalakrishnan, Meredith, et al. 2013; Maißer et al. 2015; Gopalakrishnan, P. H. McMurry, and Hogan 2015). Secondly, we account for the polarization of air molecules in the relation between ion mass and mobility.

To describe the charger ions, we used the ion mobility distribution of the ions produced from HEPA-filtered laboratory air passing through a TSI 3077 bipolar  $^{85}\text{Kr}$  aerosol charger, which was measured using a Radial Opposed Migration Ion and Aerosol Classifier (ROMIAC; Mui, Thomas, et al. 2013; Mui, Mai, et al. 2017), and a TSI 3068 electrometer. For comparison, we also used an ion mobility distribution based on that measured by G. Steiner and Reischl (2012). These distributions will be described as the measured and the SR distributions, respectively; a more detailed description of these distributions can be found in the online supplemental information (Appendix C).

The flux coefficients were calculated for particle diameters ranging from 1 nm to 10  $\mu\text{m}$ , using 90 size sections uniformly spaced on a logarithmic scale; flux coefficients were calculated for particle charge states up to  $\pm 30$  charges. The following input parameters were varied when calculating the flux coefficients: temperature ( $T$ ) and pressure ( $p$ ), relative permittivity of the particles ( $\chi_p$ ), ion mobility ( $Z_i$ ), relative permittivity of the ions ( $\chi_i$ ), and ion mass ( $m_i$ ).

The flux coefficients were calculated for 35, logarithmically-spaced values of the ion mobility in the range  $0.5\text{--}2.5 \text{ cm}^2\text{V}^{-1}\text{s}^{-1}$ . The range was chosen such that it covers the values observed in both the measured distribution and SR distribution. The corresponding ion masses were calculated using the Stokes-Millikan law in the form

$$Z_i = \sqrt{1 + \frac{m_g}{m_i} \frac{q_i}{3\pi\mu}} \frac{1 + \text{Kn} (1.257 + 0.4 \exp(-1.1/\text{Kn}))}{d_{i,\text{mass}} + d_g} L, \quad (4.2)$$

where  $m_g$  is the mass of a carrier gas molecule,  $q_i$  is the charge of the ion (one elementary charge),  $\mu$  is the viscosity of the carrier gas,  $d_{i,\text{mass}} = (6m_i/\pi\rho_i)^{1/3}$  is the mass diameter of the ion and Kn is the Knudsen number defined as  $2\lambda/(d_{i,\text{mass}} + d_g)$ , where  $\lambda$  is the mean free path of the carrier gas. The effective diameter of a gas molecule,  $d_g$ , was assumed to be 0.3 nm (Ku and Mora 2009), while the density of the ion,  $\rho_i$ , was used as a free parameter. The empirical coefficients, 1.257, 0.4 and 1.1, in the slip correction factor were according to Davies (1945). The first term on the right hand side of Eq. (4.2) accounts for the finite mass of the ion, as suggested

by Tammet (1995). The polarization correction factor,  $L$ , is given as (Larriba and Hogan 2013):

$$L_{\varphi \leq 1} \approx \left( 1 + \varphi \left( \frac{1}{3.1} + \frac{1}{\xi} \left( \frac{1}{16} + \frac{4}{33} \varphi \right) \right) \right); \quad \text{if } \varphi \leq 1 \quad (4.3a)$$

$$L_{\varphi \geq 1} \approx \left( 1 + \varphi \left( \frac{1}{4} - \frac{2.3}{1000} \varphi + \frac{1}{\xi} \left( \frac{9}{56} - \frac{6.8}{1000} \varphi \right) \right) \right); \quad \text{if } \varphi \geq 1, \quad (4.3b)$$

where  $\xi$  is the momentum scattering coefficient,  $\varphi = U_{\text{pol}} ((d_{\text{i, mass}} + d_{\text{g}}) / 2) / k_{\text{B}} T$  with  $k_{\text{B}}$  being the Boltzman constant, and the polarization energy at distance  $r$  is given by

$$U_{\text{pol}}(r) = -\frac{aq_{\text{i}}^2 e^2}{8\pi\chi_0\chi_{\text{g}}r^4}, \quad (4.4)$$

where  $a$  is the polarizability of gas molecules ( $\sim 1.7 \text{ \AA}^3$  in air),  $\chi_0$  is the vacuum permittivity and  $\chi_{\text{g}}$  is the relative permittivity of air. The empirical coefficients in Eq. (4.2) correspond to  $\xi = 1.36$ , which does not hold exactly for all types of ions (Ouyang, Larriba-Andaluz, et al. 2013; Larriba-Andaluz et al. 2015). While a recent study by Maißer et al. (2015) suggests that a single mobility-mass relationship may not be applied to all ions, Eqs. (4.2–4.4) have been shown to be in good agreement with experimental results Larriba and Hogan 2013; Ouyang, Larriba-Andaluz, et al. 2013). To remove the small discontinuity at  $\varphi = 1$  in Eqs. (4.3a) and (4.3b), we defined  $L$  as

$$L = \frac{L_{\varphi \leq 1}}{1 + \exp((\varphi - 1) 10)} + \frac{L_{\varphi > 1}}{1 + \exp((1 - \varphi) 10)}, \quad (4.5)$$

which results to better performance of iterative algorithms at  $\varphi \approx 1$ , but has negligible effect on the actual values of  $L$ .

We chose  $T = 298 \text{ K}$  and  $p = 96757 \text{ Pa}$  to represent laboratory conditions in Pasadena, CA, where the ion mobilities were measured. When other values of  $T$  and  $p$  were used when calculating the flux coefficient, the ion mobility in those conditions was calculated according to Eq. (4.2) assuming that the ion mass stays constant.

The input parameters used in the calculations are summarized in Table 4.1. The values of  $T$  and  $p$  correspond to conditions in our laboratory (Scenarios 1–7 and 10–13), conditions at 3 km altitude (Scenario 8) and conditions at 10 km altitude

(Scenario 9). The altitudes of 3 and 10 km were chosen to approximately correspond to the maximum flight altitude of an unpressurized aircraft and a common flight altitude of a commercial passenger jet, respectively. Lacking data to guide a simulation under those conditions, we employ the same aerosol scenarios as in the laboratory conditions. The particle was assumed to be conductive ( $\chi_p = \infty$ ), polystyrene ( $\chi_p = 2.6$ ), a commonly used material for instrument calibration, or NaCl ( $\chi_p = 6$ ), the main component of sea-salt aerosol. The chosen values of the relative permittivity of the ion correspond to conductive material ( $\chi_i = \infty$ ), air at room temperature ( $\chi_i = 1.00059$ ) or NaCl ( $\chi_i = 6$ ). The values of  $\rho_i$  were chosen to cover a wide range of reasonable values, including the bulk densities of major chemical compounds in ions as identified by Ehn, Junninen, Petäjä, et al. (2010).

We also probed the influence of using effective ion properties for Scenario 1, as in Hoppel and Frick (1986), by using  $f$  calculated using only the mean,  $Z_{i,ave}$ , or median,  $Z_{i,med}$ , mobility of the ion mobility distribution, and setting the ratio of total concentration of positive and negative ions,  $n_{i,T}^+/n_{i,T}^-$ , to 1.1 or 1.2, instead of 1 which was used otherwise.  $n_{i,T}^+/n_{i,T}^- = 1$  is often assumed for bipolar chargers based on the assumption that the processes governing the ion concentrations are the ion production by energetic particles, and removal due to ion-ion recombination, both of which affect the negative and positive concentrations in exactly the same way. Differences of ion mobilities can, however, introduce a polarity bias as particles are lost to surfaces of the charger or downstream plumbing. The values of 1.1 and 1.2 were arbitrarily chosen, but are of reasonable magnitude based on previous studies (Hoppel and Frick 1990; Tigges, Jain, and Schmid 2015). In the case of varying the value of  $n_{i,T}^+/n_{i,T}^-$ , the shapes of the mobility distributions of negative and positive ions were kept constant. It should be noted that the value of  $n_{i,T}^+/n_{i,T}^-$  affects the charge distribution, but not the flux coefficients.

### **Aerosol dynamic simulations**

Recent observations of nucleation events in a wide range of atmospheric conditions have created much interest in measurements of ultrafine aerosol particles that could not be quantified at the time the FHFV charge distribution model was developed (e.g., Kulmala, Vehkamäki, et al. 2004; Kulmala and Kerminen 2008), and stimulated many advances in aerosol instrumentation, including two-stage condensation particle counters (Iida, M. Stolzenburg, and P. McMurry 2009) and mobility analyzers suitable for sub-10 nm particle measurements (e.g., Rosser and Mora 2005; Brunelli, Flagan, and Giapis 2009; Mui, Thomas, et al. 2013; Mui, Mai, et al. 2017).

Table 4.1: Simulation Scenarios used when calculating the charge distributions. For Scenarios 1–7 and 12–13, the flux coefficients were calculated for 35 values of ion mobility,  $Z_i$ , that covered the range  $0.5\text{--}2.5\text{ cm}^2\text{V}^{-1}\text{s}^{-1}$ . For Scenarios 8 and 9 the ranges were  $0.65\text{--}3.1\text{ cm}^2\text{V}^{-1}\text{s}^{-1}$  and  $1.7\text{--}7.0\text{ cm}^2\text{V}^{-1}\text{s}^{-1}$ , respectively. For Scenarios 10 and 11, only the mean and median, respectively, of negative and positive ion mobilities were used. For each scenario, the calculations were performed using the measured ion mobility distribution and the SR distribution, with the ion mass and mobility values corresponding to the latter given in parenthesis.

| Scenario | $T$ (K) | $p$ (Pa) | $\chi_p$ | $\chi_i$ | $m_i$ (Da)                           | $\rho_i$ (kg m <sup>-3</sup> ) | $Z_i$ (cm <sup>2</sup> V <sup>-1</sup> s <sup>-1</sup> ) | $n_{iT}^+/n_{iT}^-$ |
|----------|---------|----------|----------|----------|--------------------------------------|--------------------------------|--|---------------------|
| 1        | 298.15  | 96757    | $\infty$ | 6        | 220 – 1800<br>(55 – 840)             | 1500                           | 0.6 – 1.6<br>(0.9 – 2.5)                                 | 1                   |
| 2        | 298.15  | 96757    | $\infty$ | 6        | 130 – 1000<br>(43 – 460)             | 800                            | 0.6 – 1.6<br>(0.9 – 2.5)                                 | 1                   |
| 3        | 298.15  | 96757    | $\infty$ | 6        | 300 – 2700<br>(62 – 1200)            | 2200                           | 0.6 – 1.6<br>(0.9 – 2.5)                                 | 1                   |
| 4        | 298.15  | 96757    | 2.6      | 6        | 220 – 1800<br>(55 – 840)             | 1500                           | 0.6 – 1.6<br>(0.9 – 2.5)                                 | 1                   |
| 5        | 298.15  | 96757    | 6        | 6        | 220 – 1800<br>(55 – 840)             | 1500                           | 0.6 – 1.6<br>(0.9 – 2.5)                                 | 1                   |
| 6        | 298.15  | 96757    | $\infty$ | $\infty$ | 220 – 1800<br>(55 – 840)             | 1500                           | 0.6 – 1.6<br>(0.9 – 2.5)                                 | 1                   |
| 7        | 298.15  | 96757    | $\infty$ | 1.00059  | 220 – 1800<br>(55 – 840)             | 1500                           | 0.6 – 1.6<br>(0.9 – 2.5)                                 | 1                   |
| 8        | 269     | 70120    | $\infty$ | 6        | 220 – 1800<br>(55 – 840)             | 1500                           | 0.8 – 2.0<br>(1.2 – 3.1)                                 | 1                   |
| 9        | 223     | 26500    | $\infty$ | 6        | 220 – 1800<br>(55 – 840)             | 1500                           | 1.9 – 4.7<br>(2.8 – 7.0)                                 | 1                   |
| 10       | 298.15  | 96757    | $\infty$ | 6        | $m_i^-/m_i^+$<br>250/530<br>(95/190) | 1500                           | $Z_{i,ave}^-/Z_{i,ave}^+$<br>1.53/1.12<br>(2.14/1.66)    | 1                   |
| 11       | 298.15  | 96757    | $\infty$ | 6        | $m_i^-/m_i^+$<br>230/460<br>(90/190) | 1500                           | $Z_{i,ave}^-/Z_{i,ave}^+$<br>1.56/1.20<br>(2.19/1.66)    | 1                   |
| 12       | 298.15  | 96757    | $\infty$ | 6        | 220 – 1800<br>(55 – 840)             | 1500                           | 0.6 – 1.6<br>(0.9 – 2.5)                                 | 1.1                 |
| 13       | 298.15  | 96757    | $\infty$ | 6        | 220 – 1800<br>(55 – 840)             | 1500                           | 0.6 – 1.6<br>(0.9 – 2.5)                                 | 1.2                 |

Thus, atmospheric nucleation events in clean and polluted environments were selected for this study of potential biases in mobility-based particle size distribution measurements.

Since knowledge of the charge distribution is incomplete, we probed potential biases using the aerosol evolution simulations during a new particle formation event, thereby eliminating measurement biases from the baseline data. The new particle formation events were simulated using the Ion-UHMA model (University of Helsinki Multicomponent Aerosol Model for neutral and charged particles; Leppä et al. 2009) and covered a particle diameter range from 1.6 nm to 1.0  $\mu\text{m}$  using 240 logarithmically spaced size sections. The parameters used as input in the model were the formation rate of 1.6 nm particles, concentrations of condensing vapors, initial particle size distribution and the increase in the height of the boundary layer, which was modeled by diluting particle concentrations as if being mixed with particle free air. The values for these parameters were arbitrarily chosen to produce new particle formation events with characteristics similar to those observed in the field measurements at Hyytiälä, Finland, (e.g., Mäkelä et al. 1997), at Mukteshwar, India, (Neitola et al. 2011; Hyvärinen et al. 2011) and New Delhi, India (Makkonen et al. 2012). These locations were chosen to represent clean background conditions (Hyytiälä), polluted background conditions (Mukteshwar) and polluted urban conditions (New Delhi).

### **Conversion of simulated data into a synthetic signal: pseudo-instrument**

The new particle formation event simulations provided the time evolution of the particle size distribution. Using models of instrument performance, called transfer functions, these particle size distributions were translated into a signal emulating actual instruments. This conversion is referred to as pseudo-instrument (Figure 4.1). We first calculated the particle mobilities,  $Z_p$ , corresponding to the particle diameters in the simulation grid according to Eq. (4.2) assuming singly-charged particles with a density of  $1500 \text{ kg m}^{-3}$ . We then made a grid of 100 diameters,  $d_s$ , covering size range from 1.0 nm to 1.0  $\mu\text{m}$  using logarithmic steps, to represent the channels of the pseudo-instrument, and calculated the mobilities,  $Z_s$ , corresponding to those channels. The signal,  $S_m$ , for a channel  $m$  was then calculated according to

$$S_m^\pm = \sum_{l=1}^w \sum_{j=1}^{k_{\max}} f_{\pm j}(Z_{p,l}) n_T(Z_{p,l}) \Omega_m(jZ_{p,l}), \quad (4.6)$$

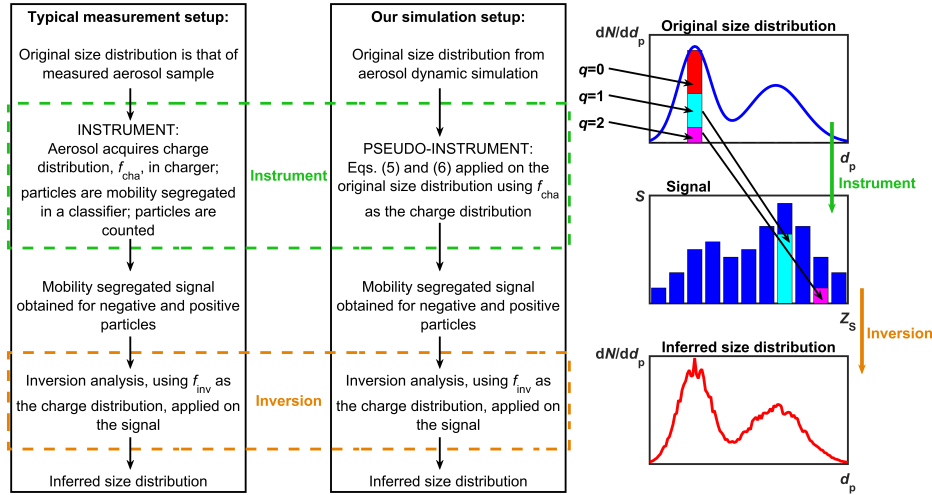


Figure 4.1: Processes involved in a typical size distribution measurement (left), and in the present simulation approach (middle); schematic illustrations of these steps (right). Note that particles with the same size but different charge state fall into different mobility sections in the signal grid, since  $Z_p(q) = qZ_p(q=1)$  (two topmost panels on the right). Furthermore, negative and positive particles provide separate signals, with neutral particles not detected.

where  $Z_{p,l}$  is the electrical mobility of a singly-charged particle corresponding to section  $l$  in the mobility grid of the simulation,  $f_{\pm j}(Z_{p,l})$  is the fraction of negative or positive particles with mobility  $Z_{p,l}$  and charge state  $j$ ,  $n_T(Z_{p,l})$  is the concentration of particles with mobility  $Z_{p,l}$ , and  $w$  is the number of sections in the mobility grid. The transfer function of the pseudo-instrument,  $\Omega_m$ , describing the probability that a particle with electrical mobility  $jZ_{p,l}$  is detected in channel  $m$  (corresponding to electrical mobility  $Z_{S,m}$ ), was defined as

$$\Omega_m(jZ_{p,l}) = \begin{cases} \log \frac{jZ_{p,l}}{Z_{S,m-1}} / \log \frac{Z_{S,m}}{Z_{S,m-1}}; & \text{if } Z_{S,m-1} < jZ_{p,l} \leq Z_{S,m} \\ 1 - \log \frac{jZ_{p,l}}{Z_{S,m}} / \log \frac{Z_{S,m+1}}{Z_{S,m}}; & \text{if } Z_{S,m} < jZ_{p,l} \leq Z_{S,m+1} \\ 0; & \text{otherwise} \end{cases} \quad (4.7)$$

In other words, for the simplicity of the presentation, the transfer function was assumed to be a triangle on a logarithmic mobility axis, i.e., the transfer function of a channel with nominal mobility of  $Z_{S,m}$  has the maximum value of 1 at the mobility  $jZ_{p,l} = Z_{S,m}$  and the value decreases as a function of  $\log(jZ_{p,l})$  on both sides of the

maximum reaching 0 at  $jZ_{p,l} = Z_{S,m-1}$  and at  $jZ_{p,l} = Z_{S,m+1}$ . Consecutive channels overlap in a way that the sum of the transfer functions is unity over the mobility range, i.e., all particles are sampled with identical efficiency.  $\Omega_m$  is very similar to the ideal transfer function presented by Knutson and Whitby (1975), except for the function being triangular on a logarithmic mobility axis instead of linear one. The exact shape of the chosen transfer function does not affect the conclusions of this study, however, provided that the transfer function is reasonably similar to those used to characterize actual instruments and, especially, that the same transfer function is used both in the pseudo-instrument and in the inversion algorithm. The detection efficiency of the pseudo-instrument was assumed to be unity and wall losses were assumed to be negligible. Neither of these approximations are valid for actual instruments over the entire particle diameter range considered in this study, but if the detection efficiency and wall losses are known and used correctly in the inversion, they will not introduce additional biases. Exploring those biases is not in the scope of this study, which examines only the biases associated with the charge distribution. It should be noted that when using Eqs. (4.6) and (4.7), the signal consists of concentrations as a function of electrical mobility with the multiply-charged particles contributing to the signal corresponding to a higher mobility than that of the singly-charged particles of the same size (see “Instrument” on Figure 4.1).

The charge distributions used in Eq. (4.6) for the different simulation Scenarios are those listed in Table 4.1, representing the charge distributions acquired in the charger,  $f_{\text{cha}}$ . With the procedure described above, the pseudo-instrument emulates an instrumentation setup employing a bipolar aerosol charger followed by an idealized classifier, such as DMA, and a detector, such as CPC; complexities of diffusional broadening of DMA transfer functions, losses, and sigmoidal counting efficiency curves for the detector are not relevant to our present purpose, and are not considered.

The signals were calculated from the data of Hyytiälä simulation (see Sect. 4.3) using the charge distributions corresponding to all Scenarios listed in Table 4.1. Additionally, the signals were calculated using the data from the Mukteshwar and New Delhi simulation with charge distribution corresponding to either Scenario 1 or 9. Motivation for our choice of charge distributions is provided in Sect. 4.4. Regardless of the charge distribution and simulation data used, the signals were calculated for both negative and positive polarities.

### **Inferring the particle size distributions from the synthetic signals**

Particle size distributions were calculated from the synthetic signals described in Sect. 4.3 using an inversion algorithm (“Inversion” in Figure 4.1). The inversion algorithm uses an interior-point gradient method for solving totally nonnegative least squares problems (Merritt and Y. Zhang 2005). In the inversion, the detection efficiency of the detector and the transfer function of the classifier were assumed to be the same as in the pseudo-instrument described in Sect.4.3.

We examine the effects of different assumptions regarding the charge distribution, by employing distributions,  $f_{\text{inv}}$ , that were derived based upon different sets of ion and particle parameters than those used to obtain the “true” charge distribution in the pseudo-instrument,  $f_{\text{cha}}$ . Because the pseudo-instrument is otherwise perfectly characterized in the inversion algorithm, the differences between the simulated and the corresponding inverted distributions can be attributed to the difference in the charge distributions,  $f_{\text{cha}}$  and  $f_{\text{inv}}$ . The present simulations therefore reveal the uncertainty imposed by imperfect knowledge of the actual charge distribution.

For practical reasons, the maximum number of particle charges considered in the inversion,  $q_{\text{max}}$ , needs to be limited. In order to study a possible bias in the inferred particle size distribution caused by too small of a value of  $q_{\text{max}}$ , we used values of 3, 6 and 9 in the inversion, even though the value used when calculating the signal was 30. These limited values of  $q_{\text{max}}$  were only applied to inversion using the charge distribution corresponding to Scenario 1;  $q_{\text{max}} = 15$  was used in the inversion otherwise.

The uncertainties in the DMA-based particle size distribution measurements are not expected to result from the numerical inaccuracies in the inversion algorithm per se (Wiedensohler et al. 2012). If the assumptions the inversion algorithm is based on do not characterize the instrument properly, however, biases will arise.

## **4.4 Results**

### **Aerosol dynamic simulations, signal and inversion analysis**

The time evolution of the particle size distributions in the Hyytiälä, Mukteshwar and New Delhi simulations is shown in Figure 4.2. Each of these three simulations captures a new particle formation event with the nucleation mode particles growing into Aitken regime. The total particle concentrations and the relative concentrations in different size ranges differed significantly among these scenarios. While the simulated particle diameter range was 1.6–1000 nm, the results are shown for 2–1000



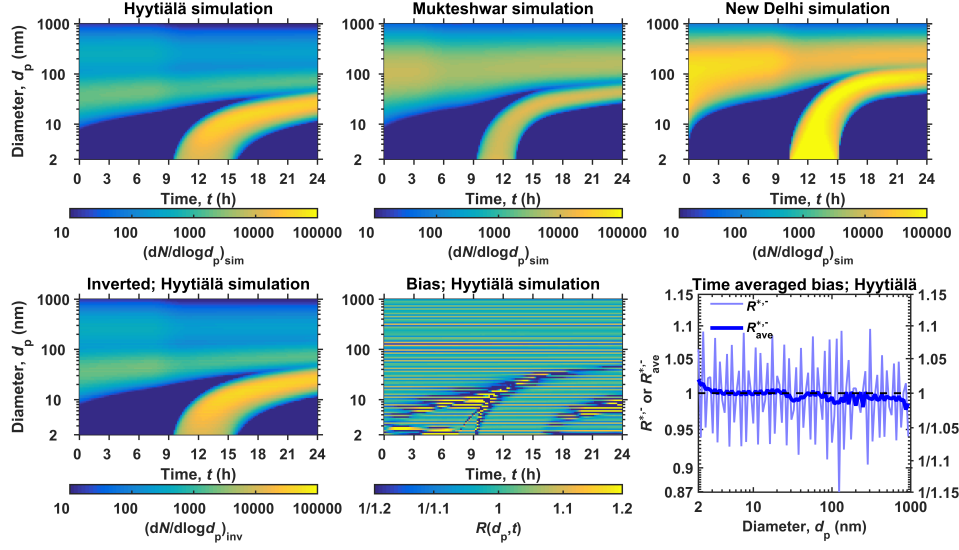


Figure 4.2: Top row: Time evolution of the particle size distribution in Hyytiälä (left), Mukteshwar (middle) and New Delhi (right) simulations. The color denotes the particle size distribution,  $dN/d\log d_p$ , in  $\text{cm}^{-3}$ . Bottom left: Time evolution of the particle size distribution inferred from the signal of the Hyytiälä simulation. Bottom middle: The ratio,  $R(d_p, t)$ , of the inverted (lower left panel) and simulated (upper left panel) distributions. The subscript “sim” and “inv” refer to the simulated and inverted distributions, respectively. Bottom right: The time averaged ratio of the inverted and simulated distributions,  $R^{*-}$ , and its running average,  $R_{\text{ave}}^{*-}$ , according to Eqs. (4.9) and (4.10), respectively. The data in the lower panels is shown for Hyytiälä simulation with  $f_{\text{cha}} \neq f_{\text{inv}}$  and when negative particles were counted; the results for positive polarity were very similar.

nm; signals from particles smaller than 2 nm in diameter represent a convolution of charger ions and aerosol particles (see supplemental information, Appendix C).

To assess the reliability of our theoretical approach (Figure 4.1), we used the same charge distribution both when computing the synthetic signal with the pseudo-instrument and when inferring the size distribution with the inversion analysis, i.e.,  $f_{\text{cha}} = f_{\text{inv}}$ . In this case, there was no bias caused by the difference in the charge distributions used in different phases of the analysis; any difference between the simulated and inverted distributions resulted from numerical inaccuracies. Both the simulated distribution and corresponding inverted distribution for the Hyytiälä simulation are given in Figure 4.2. The ratio of the two,  $R(d_p, t)$ , is also shown. The ratio of the inverted and simulated distribution,  $R(d_p, t)$ , as a function of time,  $t$ , and diameter is

$$R(d_p, t) = \frac{(dN/d \log d_p)_{\text{inv}}(d_p, t)}{(dN/d \log d_p)_{\text{sim}}(d_p, t)} = \frac{n_{\text{inv}}(d_p, t)}{n_{\text{sim}}(d_p, t)}, \quad (4.8)$$

where  $(dN/d \log d_p)_{\text{sim}} = n_{\text{sim}}$  and  $(dN/d \log d_p)_{\text{inv}} = n_{\text{inv}}$  refer to simulated and inverted distributions, respectively. The value of  $R(d_p, t)$  for any particular particle size varied little with time over the periods during which the concentration of particles in that size was significant. This feature allowed us to remove the time dependence in  $R(d_p, t)$  by calculating the time-averaged ratios of inverted to simulated distribution,  $R^*(d_p)$ , using the simulated distribution as the weighing factor, and summing over  $v$  particle size distributions in the time series, i.e.,

$$R^*(d_p) = \frac{\sum_{m=1}^v R(d_p, t_m) n_{\text{sim}}(d_p, t_m)}{\sum_{m=1}^v n_{\text{sim}}(d_p, t_m)}. \quad (4.9)$$

When  $f_{\text{cha}} = f_{\text{inv}}$ , the value of  $R^*(d_p)$  fluctuated on both sides of unity with the vast majority of values being within 10 % of unity (Figure 4.2). This fluctuation was a numerical issue caused by switching from one grid to another along the analysis (Figure 4.1): the particles in diameter grid corresponding to simulation are converted to a signal with a mobility grid, and the signal is then converted to a particle size distribution corresponding to another diameter grid. To better visualize the results, we calculated the running five-point average of the  $R^*(d_p)$ ,  $R_{\text{ave}}^*(d_p)$ , as

$$R_{\text{ave}}^*(d_{p,l}) = \begin{cases} \sum_{m=1}^{l+2} R^*(d_{p,m}) / (l+2); & \text{if } l \leq 2 \\ \sum_{m=l-2}^{l+2} R^*(d_{p,m}) / 5; & \text{if } 3 \leq l \leq u-2 \\ \sum_{m=l-2}^u R^*(d_{p,m}) / (u-l+3); & \text{if } l \geq u-1, \end{cases} \quad (4.10)$$

where  $u$  is the number of diameters,  $d_{p,l}$ , in the diameter grid of the inverted distribution. For the smoothed data with  $f_{\text{cha}} = f_{\text{inv}}$ ,  $R_{\text{ave}}^*(d_p)$  deviated from unity by less than 2 %, except at the very ends of the diameter range. Thus, any larger deviation of  $R_{\text{ave}}^*(d_p)$  was likely caused by the difference between  $f_{\text{cha}}$  and  $f_{\text{inv}}$ .

### **Bias in the inferred particle size distribution due to $f_{\text{cha}} \neq f_{\text{inv}}$**

As was seen when  $f_{\text{cha}} = f_{\text{inv}}$ ,  $R(d_p, t)$  did not show any systematic variation with time even when  $f_{\text{cha}} \neq f_{\text{inv}}$  (data not shown), so we employ  $R_{\text{ave}}^*(d_p)$  to explore the biases resulting from employing erroneous charge distribution models in the

data inversion, i.e., when the charge distribution used in the inversion differs from the actual charge distribution on the aerosol that enters the instrument (i.e., the “true” distribution; see Figure 4.1). We begin with a case that represents a typical situation in measurements: the charger generates a certain  $f_{\text{cha}}$  on the sampled aerosol, but values found in the literature are used for  $f_{\text{inv}}$ . Common data analysis procedures have applied the FHFV charge distribution to measurements made at a range of temperatures and altitudes, implicitly assuming that the charge distribution determined for sea level ambient conditions is applicable to disparate environmental conditions. To examine the biases that may result from this mismatch, we examine the differences in particle size distribution estimations that result when  $f_{\text{inv}}$  is determined under different environmental conditions than  $f_{\text{cha}}$ . For charge distribution estimations, both  $f_{\text{cha}}$  and  $f_{\text{inv}}$  were calculated using either the measured or SR ion mobility distributions. The environmental conditions examined, and the resulting values of  $R_{\text{ave}}^*$  are given in Table 4.2 for different particle diameter ranges. The results shown focus on the observed biases in the inferred particle size distribution, but the differences in the flux coefficients resulting to those biases are provided in the supplementary information (Appendix C).

### **Bias in the inferred particle size distribution due to using literature values for $f_{\text{inv}}$**

Let us assume that the conditions of Scenario 1 represent the conditions in the charger, in which case the  $f_{\text{cha}}$  is the charge distribution calculated for those conditions. For typical measurements, however, the  $f_{\text{inv}}$  is estimated using a parameterization that was derived by Wiedensohler (1988) from the theoretical results of Hoppel and Frick (1986). These two charge distributions differ significantly (see supplemental information, Appendix C). Before we examine the effects on full particle size distribution measurements, consider a monodisperse aerosol for which particles acquire no more than one charge. In this case, the charge distributions acquired in the charger and used in the inversion are,  $f_{\text{cha}} = \{f_{-1,\text{cha}}, f_{0,\text{cha}}, f_{1,\text{cha}}\}$  and  $f_{\text{inv}} = \{f_{-1,\text{inv}}, f_{0,\text{inv}}, f_{1,\text{inv}}\}$ , respectively, and we can write Eq. (4.6) as

$$S^{\pm} = \sum_{l=1}^w \sum_{j=1}^{k_{\text{max}}} f_{\pm j, \text{cha}}(Z_{p,l}) n_{\text{sim}}(Z_{p,l}) \Omega(jZ_{p,l}) = n_{\text{sim}} f_{\pm 1, \text{cha}}, \quad (4.11)$$

where  $S^{\pm}$  is the signal when negative or positive particles were counted,  $k_{\text{max}} = 1$ ,  $n_{\text{sim}}$  is the number concentration in the simulation, and we assume that there

Table 4.2: Biases observed in the particle size distributions inferred from measurements in which the charge distribution used in the pseudo-instrument differed from that in the inversion analysis, i.e.,  $f_{\text{cha}} \neq f_{\text{inv}}$ . The ranges of biases are given separately for negative and positive particles,  $R_{\text{ave}}^{*-}$  and  $R_{\text{ave}}^{*+}$ , respectively, and for particles smaller than or larger than 10 nm in diameter. The values in parenthesis were obtained using the SR distribution instead of the measured distribution. A value of  $R_{\text{ave}}^{*,\pm}$  that differs from unity reveals underestimation or overestimation of the particle concentration. The first row provides the baseline-case, i.e.,  $f_{\text{cha}} = f_{\text{inv}}$  (according to Scenario 1). In the second row,  $f_{\text{cha}}$  was that from Scenario 1, but FHFV charge distribution was employed in the inversion. In the third row,  $f_{\text{cha}}$  was calculated using the measured distribution, while  $f_{\text{inv}}$  was calculated using SR distribution, with both being according to Scenario 1. In other rows, the parameter that was changed when calculating  $f_{\text{cha}}$  and  $f_{\text{inv}}$  is given in the first column, with the values used when calculating  $f_{\text{cha}}$  and  $f_{\text{inv}}$  given in the second and third column, respectively; the other inputs were the same.

| Parameter               | $f_{\text{cha}}$                | $f_{\text{inv}}$               | $R_{\text{ave}}^{*-}$<br>$d_p < 10 \text{ nm}$ | $R_{\text{ave}}^{*-}$<br>$d_p > 10 \text{ nm}$ | $R_{\text{ave}}^{*+}$<br>$d_p < 10 \text{ nm}$ | $R_{\text{ave}}^{*+}$<br>$d_p > 10 \text{ nm}$ |
|-------------------------|---------------------------------|--------------------------------|--|--|--|--|
| -                       | Scenario 1                      | Scenario 1                     | 1.00 – 1.02<br>(1.00 – 1.02)                   | 0.98 – 1.01<br>(0.98 – 1.01)                   | 1.00 – 1.02<br>(1.00 – 1.02)                   | 0.98 – 1.01<br>(0.98 – 1.01)                   |
| -                       | Scenario 1                      | Wiedensohler<br>(1988)         | 0.26 – 0.63<br>(0.48 – 0.96)                   | 0.63 – 1.19<br>(0.94 – 1.16)                   | 0.19 – 0.55<br>(0.59 – 0.82)                   | 0.55 – 1.11<br>(0.78 – 0.90)                   |
| -                       | Measured<br>distribution        | SR<br>distribution             | 0.54 – 0.65                                    | 0.65 – 1.04                                    | 0.33 – 0.67                                    | 0.67 – 1.25                                    |
| $T \ \& \ p$            | 269 K &<br>70120 Pa             | 298.15 K &<br>96757 Pa         | 0.79 – 0.81<br>(0.87 – 0.96)                   | 0.76 – 1.09<br>(0.85 – 1.07)                   | 0.83 – 0.93<br>(0.91 – 1.04)                   | 0.82 – 1.13<br>(0.90 – 1.08)                   |
| $T \ \& \ p$            | 223 K &<br>26500 Pa             | 298.15 K &<br>96757 Pa         | 0.60 – 0.68<br>(0.90 – 1.89)                   | 0.54 – 1.32<br>(0.77 – 1.24)                   | 0.81 – 2.03<br>(1.05 – 2.00)                   | 0.58 – 1.54<br>(0.70 – 1.24)                   |
| $m_i \ (\rho_i)$        | 130 – 1000 Da<br>(43 – 460 Da)  | 220 – 1800 Da<br>(55 – 840 Da) | 1.30 – 1.38<br>(1.18 – 1.40)                   | 0.97 – 1.30<br>(0.96 – 1.18)                   | 1.22 – 1.58<br>(1.16 – 1.24)                   | 0.91 – 1.22<br>(0.95 – 1.16)                   |
| $m_i \ (\rho_i)$        | 300 – 2100 Da<br>(62 – 1200 Da) | 220 – 1800 Da<br>(55 – 840 Da) | 0.83 – 0.85<br>(0.83 – 0.89)                   | 0.84 – 1.00<br>(0.89 – 1.00)                   | 0.77 – 0.90<br>(0.84 – 0.89)                   | 0.90 – 1.22<br>(0.89 – 1.03)                   |
| $\chi_p$                | 2.6                             | $\infty$                       | 0.65 – 0.74<br>(0.67 – 0.74)                   | 0.74 – 1.08<br>(0.74 – 1.06)                   | 0.67 – 0.69<br>(0.70 – 0.77)                   | 0.67 – 1.05<br>(0.77 – 0.97)                   |
| $\chi_p$                | 6                               | $\infty$                       | 0.83 – 0.87<br>(0.84 – 0.87)                   | 0.87 – 1.03<br>(0.87 – 1.03)                   | 0.83 – 0.84<br>(0.86 – 0.88)                   | 0.81 – 1.04<br>(0.88 – 0.99)                   |
| $n_{i,T}^+ / n_{i,T}^-$ | 1.1                             | 1.0                            | 0.91 – 0.93<br>(0.91 – 0.93)                   | 0.76 – 1.07<br>(0.78 – 1.03)                   | 1.10 – 1.12<br>(1.10 – 1.13)                   | 1.09 – 1.30<br>(1.10 – 1.24)                   |
| $n_{i,T}^+ / n_{i,T}^-$ | 1.2                             | 1.0                            | 0.83 – 0.85<br>(0.83 – 0.85)                   | 0.59 – 1.08<br>(0.63 – 1.00)                   | 1.20 – 1.22<br>(1.20 – 1.23)                   | 1.19 – 1.56<br>(1.20 – 1.45)                   |

exists a channel with nominal mobility equaling the mobility of the monodisperse distribution, i.e.,  $\Omega = 1$ . With those assumptions, the number concentration after the inversion becomes

$$n_{\text{inv}}^{\pm} = \frac{S^{\pm}}{f_{\pm 1, \text{inv}}}. \quad (4.12)$$

Using Eqs. (4.11) and (4.12), we can write the ratio of concentrations in the simulation and after the inversion as

$$R^{\pm} = \frac{n_{\text{inv}}^{\pm}}{n_{\text{sim}}^{\pm}} = \frac{f_{\pm 1, \text{cha}}}{f_{\pm 1, \text{inv}}}, \quad (4.13)$$

from which we see that if the fractional population used in the inversion,  $f_{\pm 1, \text{inv}}$ , is higher than the one acquired in the charger,  $f_{\pm 1, \text{cha}}$ , then the particle size distribution is underestimated and vice versa. In the case of a polydisperse aerosol, especially one that includes large, multiply-charged particles, the situation is more complicated, but the same logic still holds.

As expected based on Eq. (4.13), and noting that  $f_{\text{cha}}$  was considerably lower than literature estimates (supplemental information, Appendix C), the concentrations of particles smaller than 15 nm were significantly underestimated when the measured ion mobility distribution was used (Figure 4.3). Depending on whether negative or positive particles were counted, the concentrations of the smallest particles could be underestimated by a factor of 5, though the bias factor decreases with increasing particle size, reaching a level of  $\sim 1.5$  at  $d_p = 15$  nm. For particles with  $d_p > 15$  nm, the biases for both polarities vary between underestimation by a factor of 1.5 for the largest positively-charged particles and overestimation by a factor of 1.2 for negatively-charged particles. The magnitude of the bias did not vary significantly among the aerosol scenarios for Hyttiälä, Mukteshwar or New Delhi.

The biases observed when SR distribution was used for  $f_{\text{cha}}$  were similar to those when the measured distribution was used, with the following differences: the concentration of the smallest particles was underestimated by a factor of 2 and the bias for particles with  $d_p > 15$  nm was at most 30 %. Further, if negative (positive) particles were counted, the concentration was overestimated (underestimated) for the range of  $15 \text{ nm} < d_p < 700 \text{ nm}$ .

It should be noted that the bias in the particle size distribution resulting from the Wiedensohler parameterization reflects the difference between the parameterization

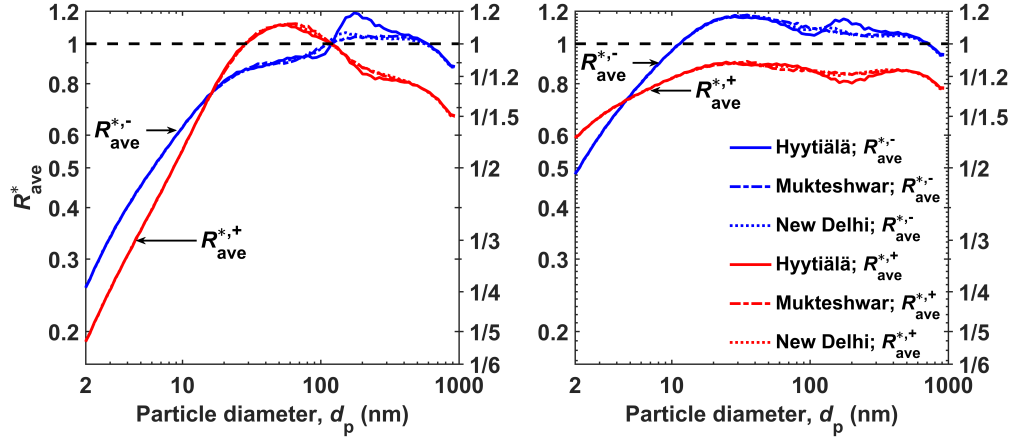


Figure 4.3: Left panel: The bias observed in the inferred particle size distribution when  $f_{\text{cha}}$  was calculated using input values based on our measurements (Scenario 1 in Table 4.1) and  $f_{\text{inv}}$  was according to FHFV charge distribution. The line style denotes the simulation, and signal polarity is labeled. Right panel: The same as the left panel, except that the SR distribution, instead of the measured distribution, was used when calculating  $f_{\text{cha}}$ .

and the charge distribution that corresponds to the measured and SR distributions in the ambient conditions of our measurements. As temperature, pressure, and properties of ions and particles change in different measurement environments, the  $f_{\text{cha}}$  also changes, as does the bias.

### Bias in the inferred particle size distribution due to ion mobility distribution

The mean mobilities of charger ions found in the literature vary from  $0.97 \text{ cm}^2 \text{V}^{-1} \text{s}^{-1}$  (Lee et al. 2005) to  $2.09 \text{ cm}^2 \text{V}^{-1} \text{s}^{-1}$  (G. Steiner and Reischl 2012) with the mobilities of the positive ions being systematically lower than those of the negative ones observed for the same measurement setup (see, e.g., Tigges, Jain, and Schmid 2015, for a review of literature values). Compared to the literature values, the mean mobilities of the measured distribution in this study,  $Z_{i,\text{ave}}^+ = 1.12 \text{ cm}^2 \text{V}^{-1} \text{s}^{-1}$  and  $Z_{i,\text{ave}}^- = 1.53 \text{ cm}^2 \text{V}^{-1} \text{s}^{-1}$ , are closer to the low mobilities, while the mean mobilities of SR distribution,  $Z_{i,\text{ave}}^+ = 1.66 \text{ cm}^2 \text{V}^{-1} \text{s}^{-1}$  and  $Z_{i,\text{ave}}^- = 2.14 \text{ cm}^2 \text{V}^{-1} \text{s}^{-1}$ , are found at the other extreme. When the measured distribution was used for  $f_{\text{cha}}$  and the SR distribution for  $f_{\text{inv}}$ , the concentrations of 2 nm particles were underestimated by a factor of 3 when the positive particles were counted (Figure 4.4). The bias was observed to decrease with increasing particle size, and a bias of less than 25 % was observed for sizes  $> 15 \text{ nm}$ , with overestimation observed in the size range of  $21 \text{ nm} < d_p < 230 \text{ nm}$ . If negative particles were counted, the concentrations of 2 nm

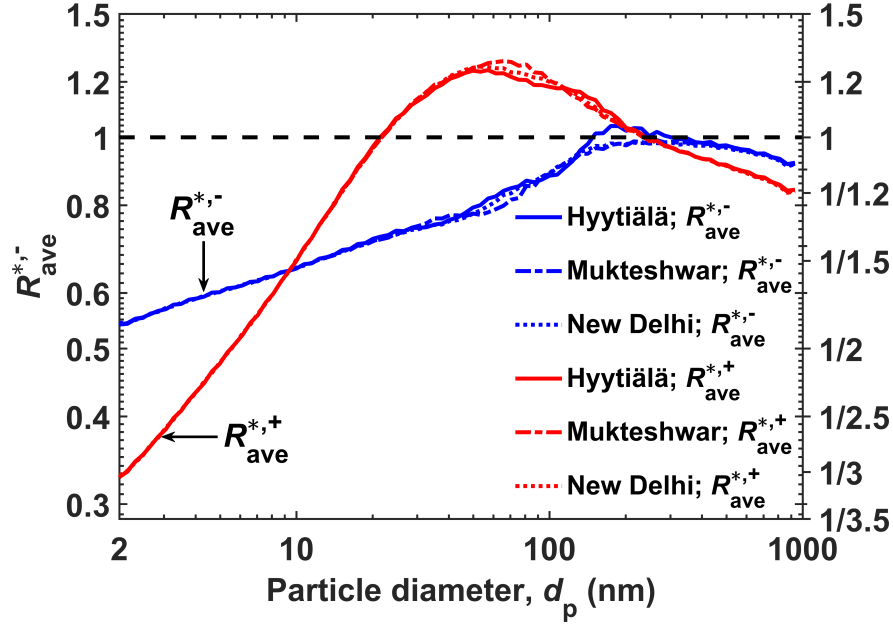


Figure 4.4: The bias observed in the inferred particle size distribution when  $f_{\text{cha}}$  was calculated using the measured ion mobility distribution and  $f_{\text{inv}}$  was calculated using the SR distribution, with other inputs being the same. The line style denotes the simulation, and signal polarity is labeled.

particles were underestimated by a factor of 1.9 with the bias again decreasing with increasing particle size, and a bias < 10 % was observed for particles > 110 nm in diameter. The magnitude of the bias did not vary significantly among the aerosol scenarios, i.e., Hyytiälä, Mukteshwar or New Delhi.

In Sects. 4.4–4.4, either the measured or SR distribution was used when calculating both the  $f_{\text{cha}}$  and the  $f_{\text{inv}}$ , with the results presented separately for both distributions.

### **Bias in the inferred particle size distribution due to temperature and pressure effects**

Most size distribution measurements are conducted at the ground level, but airborne measurements are increasingly used in climate change research (Clarke et al. 1998; Mirme et al. 2010; Coggon et al. 2014), as are measurements at alpine sites that allow long-term probing of the free troposphere (Weingartner, Nyeki, and Baltensperger 1999). While  $T$  and  $p$  are typically measured in conjunction with particle size distribution measurements, they are typically not, however, taken into account when estimating  $f_{\text{inv}}$ . To examine the biases that may result when the ion distribution obtained at one altitude are used to interpret mobility distribution

obtained at a different altitude, we calculated the signal using the charge distribution corresponding to conditions at 3 and 10 km altitude, but used the charge distribution corresponding to  $T$  and  $p$  at laboratory conditions in the inversion, as has been done in most studies involving measurements at higher altitudes to date. Lacking data to guide a simulation under these conditions, we employ the same aerosol scenarios. At 3 km altitude, when the measured distribution was used and negative (positive) particles were counted, the observed particle size distribution bias factor was as large as 1.32 (1.22), with underestimation being more frequent when  $d_p < 300$  nm (170 nm) and overestimation more frequent in sizes  $> 300$  nm (170 nm) (Figure 4.5). When the SR distribution was used, the biases were qualitatively similar, but the magnitudes were slightly smaller, with the maximum bias factor being 1.17 (1.11) when negative (positive) particles were counted. At 10 km altitude, the bias was even larger than at 3 km altitude. The highest overestimation was about 2 fold at  $d_p = 2.0$  nm for both the measured and SR distribution when positive particles were counted. When negative particles were counted, the concentration at  $d_p = 2.0$  nm was overestimated by a factor of 1.89 for the SR distribution, but underestimated by a factor of 1.46 for the measured distribution. This was the only occasion in which the observed bias due to the parameter(s) being probed,  $T$  and  $p$  in this case, was considerable, but qualitatively different for the measured and SR distributions. Except for the  $d_p < 30$  nm when negative particles were counted, the biases with the measured and SR distributions were qualitatively similar, though the biases were in general somewhat smaller in the case of SR distribution.

The bias in the particle size distributions of both the Mukteshwar and New Delhi simulations were similar to those for Hyytiälä (Figure 4.5). For  $d_p < 30$  nm, the biases differed little between the simulation scenarios, as expected from Eq. (4.13) because the vast majority of the particles in that size range carried at most one charge. Moreover, the biases for  $d_p > 570$  nm differed little because multiply-charged larger particles did not contribute significantly to the signal for those sizes, which was, at least partly, due to lack of  $> 1 \mu\text{m}$  particles considered in the simulation scenarios. Over the  $30 \text{ nm} < d_p < 570 \text{ nm}$  size range, the biases were qualitatively similar and within a factor of 1.3 from each other, except in the case of the measured distribution and negative particles being counted, when the bias in the Hyytiälä simulation was by a factor of  $\sim 1.5$  smaller than that of the other two simulations. This was the largest difference in the biases between the three simulation scenarios observed in this study. We will therefore focus our discussion in the remainder of this section on the Hyytiälä simulation.



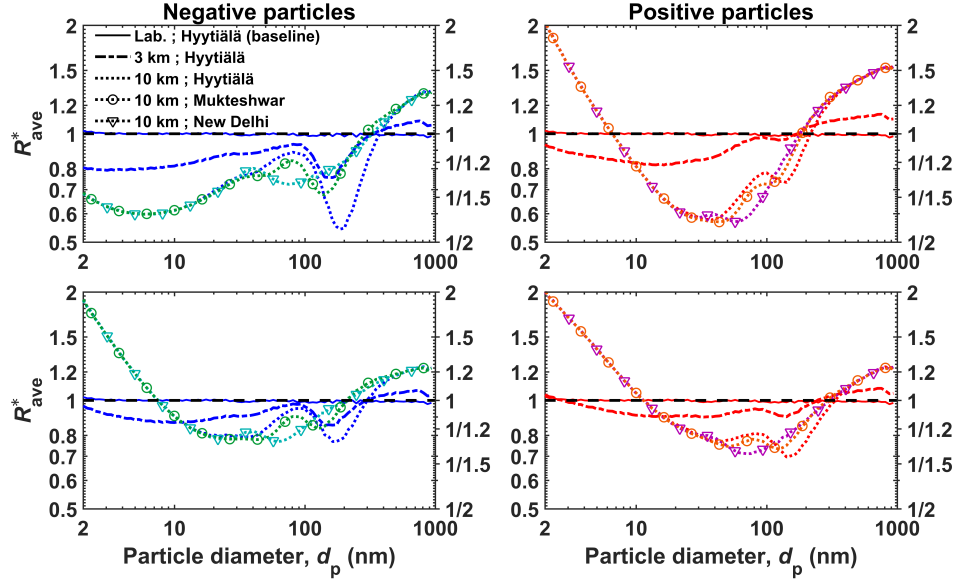


Figure 4.5: Upper panels: The bias observed in the inferred particle size distribution when  $f_{\text{cha}}$  corresponded to  $T$  and  $p$  representing conditions in laboratory ( $T = 298.15$  K &  $p = 96757$  Pa; “Lab.”), at 3 km altitude ( $T = 269$  K &  $p = 70120$  Pa; “3 km”), or at 10 km altitude ( $T = 223$  K &  $p = 26500$  Pa; “10 km”), and  $f_{\text{inv}}$  corresponded to  $T$  and  $p$  in laboratory. The line style denotes the conditions, with markers denoting different simulations, shown only in the “10 km” case. Results corresponding to negative (positive) particle measurements are shown on the left (right). The lines depicting the “10 km” cases are practically coincident for  $d_p < 20$  nm and  $d_p > 500$  nm. Lower panels: The same as the upper panels, except that the SR distribution, instead of the measured distribution, was used when calculating  $f_{\text{cha}}$ .

### Bias in the inferred particle size distribution due to material properties of charger ions and measured particles

Since the masses of the charger ions were not measured, we estimated them according to Eq. (4.2) by making an assumption on the effective density of the ions,  $\rho_i$ . The real value of  $\rho_i$  probably varied between ion species, but a single value was used for the whole ion distribution for the sake of simplicity. This approximation does not affect the conclusions of this study. Based on the values reported in literature (e.g., Ehn, Junninen, Schobesberger, et al. 2011), we used  $\rho_i = 1500$  kg m<sup>-3</sup> when calculating  $f_{\text{inv}}$ . The resulting ion masses ranged from 220 Da to 1800 Da, corresponding to mobility range of the measured ions, 0.6–1.6 cm<sup>2</sup>V<sup>-1</sup>s<sup>-1</sup>, or from 55 Da to 840 Da, corresponding to mobility range of the SR distribution, 0.9–2.5 cm<sup>2</sup>V<sup>-1</sup>s<sup>-1</sup>. When the ion masses used to calculate  $f_{\text{cha}}$  differed significantly from this value, a considerable bias in the inferred particle size distribution was observed (Figure 4.6).

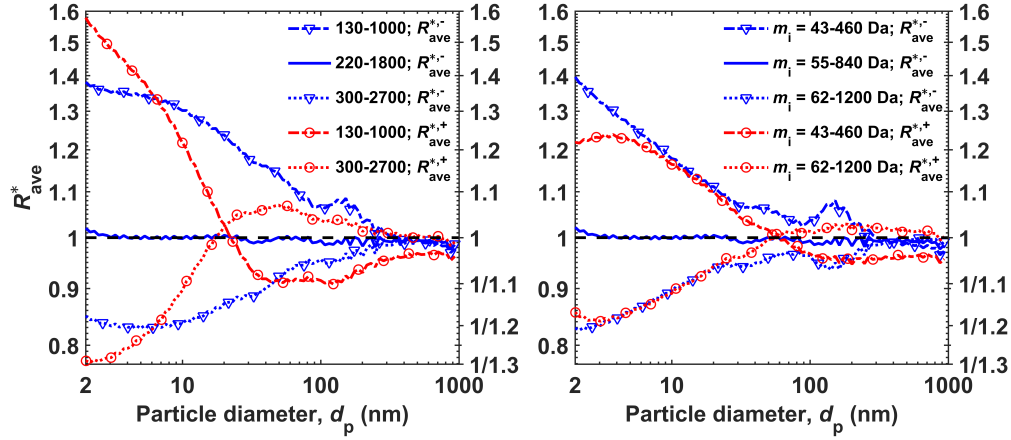


Figure 4.6: Left panel: The bias observed in the inferred particle size distribution when the ion masses ranged from 130 to 1000 Da ( $\rho_i = 800 \text{ kg m}^{-3}$ ), from 220 to 1800 Da ( $\rho_i = 1500 \text{ kg m}^{-3}$ ), or from 300 to 2700 Da ( $\rho_i = 2200 \text{ kg m}^{-3}$ ) when calculating  $f_{cha}$ , but were from 220 to 1800 Da when calculating  $f_{inv}$ , as indicated in the legend. Right panel: The same as the left panel, except that the SR distribution, instead of the measured distribution, was used when calculating  $f_{cha}$ . The corresponding ion masses are given in the legend.

If the ion masses were smaller (larger) when calculating  $f_{cha}$  than when calculating  $f_{inv}$ , the  $n_{inv}$  was overestimated (underestimated), i.e.,  $R_{ave}^*(d_p) > 1$  ( $R_{ave}^*(d_p) < 1$ ). The bias was the largest for the smallest sizes because a low ion mass increases the charging probability. The biases were slightly smaller on average for the SR distribution than for the measured distribution.

In most particle size distribution measurements, the chemical composition of the measured particles, and, therefore, their relative permittivities,  $\chi_p$ , are unknown. Notable exceptions occur in the use of a known aerosol for calibration purposes, and, of course, when the chemical composition is measured in conjunction with the particle size distribution. The Hoppel and Frick (1986) simulations on which most DMA data inversions to date have been based were based on conductive particles. Assuming particles to be conductive when calculating  $f_{inv}$  leads to underestimation of the particle concentrations, especially for sizes  $< 200$  nm in diameter, when the permittivity used when calculating  $f_{cha}$  was considerably lower (Figure 4.7). Regardless of whether negative or positive particles were counted and whether the measured or SR distribution was used, when  $f_{cha}$  was calculated for  $\chi_p = 2.6$ , corresponding to the common material of calibration aerosol particles, polystyrene, and conductive particles,  $\chi_p = \infty$ , were assumed when calculating  $f_{inv}$ , particle concentration estimates were 40–50 % low at nanometer sizes. Assuming NaCl

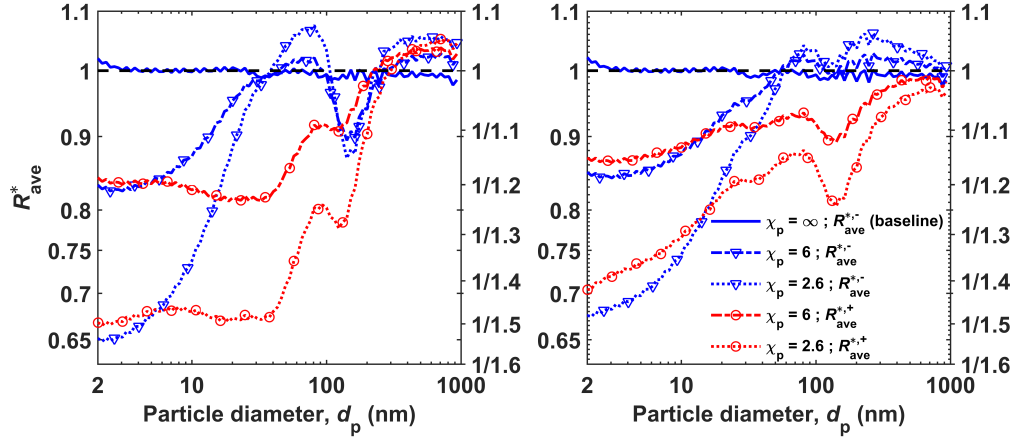


Figure 4.7: Left panel: The bias observed in the inferred particle size distribution when particles were assumed to be conductive,  $\chi_p = \infty$ , or dielectric with  $\chi_p = 6$  or  $\chi_p = 2.6$  when calculating  $f_{\text{cha}}$ , but they were assumed to be conductive when calculating  $f_{\text{inv}}$ , as indicated in the legend. Right panel: The same as the left panel, except that the SR distribution, instead of the measured distribution, was used when calculating  $f_{\text{cha}}$ .

particles,  $\chi_p = 6$ , instead of polystyrene when calculating  $f_{\text{cha}}$  decreased the bias to about 20 %. Thus, conductive particles represent a reasonable approximation, even for compounds with relatively small relative permittivity.

Minor biases, typically < 5 %, in the particle size distribution were observed due to incorrect assumption on the relative permittivity of the ions or describing the whole ion mobility distribution using only the mean or median mobility when calculating the charge distribution in the inversion, or due to truncation of the number of charge states considered in the inversion. Biases were found to be smaller when the mean mobility was used instead of the median, and considering at least 6 charge states was sufficient to remove any considerable bias. It should be noted that a higher number of charge states could be needed in other situations, especially if particles larger than 1000 nm in diameter were included (López-Yglesias and Flagan 2013b). More details about this part of the study can be found in the supplementary information (Appendix C).

### Bias in the inferred particle size distribution due to relative concentrations of positive and negative ions

It is often assumed that the loss of ions in a bipolar charger is dominated by the ion-ion recombination, which results in symmetric concentrations of negative and

positive ions. While we did not observe any considerable difference in the negative and positive ion concentrations, the higher mobility of negative ions could result in a smaller concentration of negative than positive ions due to losses occurring between the charger and the electrometer. Furthermore, the aerosol charge distribution could change between the charger and the classifying unit due to attachment of the charger ions in the stream following the charger (Hoppel and Frick 1990; Tigges, Jain, and Schmid 2015). Differences in the negative and positive ion concentrations would be expected if ion loss by attachment to particles was substantial. In that case, however, a greater concern would be whether the charge distribution reaches steady-state or not (de La Verpilliere, Swanson, and Boies 2015; Tigges, Jain, and Schmid 2015), but that is beyond the scope of this study.

To explore the role of uncertainties in the charger ion imbalance on the inferred particle size distributions, we examined scenarios in which  $n_{i,T}^+/n_{i,T}^- = 1.0, 1.1$  and  $1.2$  when calculating  $f_{\text{cha}}$ , but applied the common assumption of  $n_{i,T}^+/n_{i,T}^- = 1.0$  when calculating  $f_{\text{inv}}$ . Underestimating the value of  $n_{i,T}^+/n_{i,T}^-$  when calculating  $f_{\text{inv}}$  resulted in underestimating the particle concentrations, i.e.,  $R^* < 1$  when probing negative particle signal, and  $R^* > 1$  for positive particles (Figure 4.8). This can be demonstrated for singly-charged particles, by writing the fractional population as (Hussin et al. 1983; Gagné et al. 2012)

$$f_{\pm 1}(d_p) \approx \frac{\beta_0^\pm(d_p, Z_i^\pm) n_{i,T}^\pm}{\beta_{\pm 1}^\mp(d_p, Z_i^\mp) n_{i,T}^\mp}, \quad (4.14)$$

where  $\beta_q^\pm$  is the flux coefficient of positive or negative ion with a particle with  $q$  number of charges. For singly-charged, monodisperse particles, by denoting the value of  $n_{i,T}^+/n_{i,T}^-$  when calculating  $f_{\pm 1, \text{cha}}$  and  $f_{\pm 1, \text{inv}}$  as  $r_{\text{cha}}$  and  $r_{\text{inv}}$ , respectively, Eqs. (4.13) and (4.14) yield

$$R^\pm = \frac{\left( \frac{\beta_0^\pm(d_p, Z_i^\pm) n_{i,T}^\pm}{\beta_{\pm 1}^\mp(d_p, Z_i^\mp) n_{i,T}^\mp} \right)_{\text{cha}}}{\left( \frac{\beta_0^\pm(d_p, Z_i^\pm) n_{i,T}^\pm}{\beta_{\pm 1}^\mp(d_p, Z_i^\mp) n_{i,T}^\mp} \right)_{\text{inv}}} = \frac{\left( \frac{n_{i,T}^\pm}{n_{i,T}^\mp} \right)_{\text{cha}}}{\left( \frac{n_{i,T}^\pm}{n_{i,T}^\mp} \right)_{\text{inv}}} = \left( \frac{r_{\text{cha}}}{r_{\text{inv}}} \right)^{\pm 1}. \quad (4.15)$$

Equation (4.15) accurately represented the bias in the particle size distribution due to different ion concentrations for  $d_p < 25$  nm, i.e., when the majority of particles were singly-charged (Figure 4.8). For sizes  $> 25$  nm, multiply-charged particles

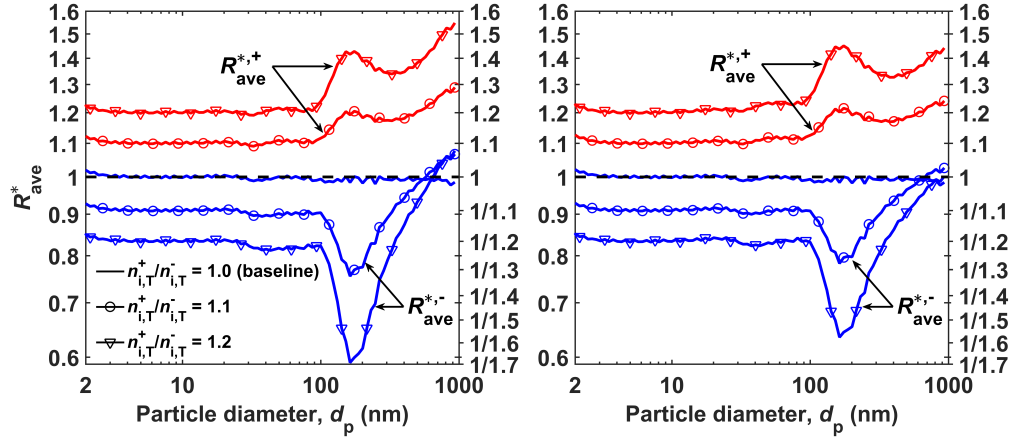


Figure 4.8: Left panel: The bias observed in the inferred particle size distribution when  $n_{i,T}^+/n_{i,T}^-$  was 1.0, 1.1, or 1.2 when calculating  $f_{\text{cha}}$ , but  $n_{i,T}^+/n_{i,T}^- = 1.0$  was used when calculating  $f_{\text{inv}}$ . The line style denotes the  $n_{i,T}^+/n_{i,T}^-$  when calculating  $f_{\text{cha}}$ , and the marker and line color denote the signal polarity. Right panel: The same as the left panel, except that the SR distribution, instead of the measured distribution, was used when calculating  $f_{\text{cha}}$ .

affected the bias, especially when  $d_p > 100$  nm. The observed bias was not sensitive to whether the measured distribution or the SR distribution was used.

### Bias in the total particle concentration

In Sect. 4.4, the bias in the particle size distribution due to various parameters affecting the aerosol charge distribution was presented. This section covers how those biases translate to bias in the total particle concentration. Unlike the biases in the particle size distribution, the biases in the total particle concentrations were time dependent. In all three simulation scenarios, i.e., Hyytiälä, Mukteshwar and New Delhi, the most important process changing the particle size distribution was the new particle formation and growth event (Figure 4.2). Consequently, in some cases, a considerable time variation was observed in the total particle concentration bias (Table 4.3). When time variation in the particle concentration bias was observed, one of the extreme (high or low) was typically seen during the new particle formation event. For that reason, the values given in Table 4.3 denote both the range of bias and the value of bias during the moment of highest particle concentration, which occurred during the new particle formation in all three simulation scenarios.

The observed biases in the total particle concentration exceeded 50 % in the following three cases: 1) the  $f_{\text{cha}}$  was calculated for the laboratory conditions, but  $f_{\text{inv}}$  was according to Wiedensohler (1988); 2) the measured distribution was used for  $f_{\text{cha}}$ ,

Table 4.3: The biases,  $n_{\text{inv}}/n_{\text{sim}}$ , observed in the total particle concentrations that result from using different charge distributions in the pseudo-instrument than in the inversion analysis, i.e.,  $f_{\text{cha}} \neq f_{\text{inv}}$ . The biases are given as a range from minimum to maximum bias during the simulation followed by the bias observed at the instance of the highest particle concentration. The values in parenthesis were obtained using the SR distribution in place of the measured ion mobility distribution presented in this study. The biases are given separately for particle size ranges of 2–1000 nm and 10–800 nm, and also for particle size distributions based on counting negative and positive particles.

| Parameter             | $f_{\text{cha}}$                | $f_{\text{inv}}$               | Simulation | $n_{\text{inv}}/n_{\text{sim}}$ ; negative<br>2 nm < $d_p$ < 1000 nm | $n_{\text{inv}}/n_{\text{sim}}$ ; positive<br>2 nm < $d_p$ < 1000 nm | $n_{\text{inv}}/n_{\text{sim}}$ ; negative<br>10 nm < $d_p$ < 800 nm | $n_{\text{inv}}/n_{\text{sim}}$ ; positive<br>10 nm < $d_p$ < 800 nm |
|-----------------------|---------------------------------|--------------------------------|------------|--|--|--|--|
| -                     | Scenario 1                      | Wiedensohler<br>(1988)         | Hyytiälä   | 0.42 – 0.94; 0.55<br>(0.68 – 1.15; 0.86)                             | 0.35 – 1.03; 0.47<br>(0.70 – 0.89; 0.78)                             | 0.72 – 0.95; 0.77<br>(1.03 – 1.15; 1.09)                             | 0.69 – 1.03; 0.78<br>(0.85 – 0.89; 0.87)                             |
| -                     | Scenario 1                      | Wiedensohler<br>(1988)         | Mukteshwar | 0.61 – 0.99; 0.63<br>(0.83 – 1.12; 0.87)                             | 0.54 – 1.00; 0.57<br>(0.76 – 0.87; 0.78)                             | 0.87 – 0.99; 0.88<br>(1.07 – 1.12; 1.09)                             | 0.84 – 1.00; 0.87<br>(0.85 – 0.87; 0.87)                             |
| -                     | Scenario 1                      | Wiedensohler<br>(1988)         | New Delhi  | 0.42 – 1.03; 0.49<br>(0.66 – 1.13; 0.77)                             | 0.33 – 1.05; 0.42<br>(0.68 – 0.88; 0.73)                             | 0.80 – 1.03; 0.94<br>(1.05 – 1.14; 1.10)                             | 0.76 – 1.05; 1.00<br>(0.84 – 0.89; 0.87)                             |
| -                     | Present study                   | SR                             | Hyytiälä   | 0.60 – 0.84; 0.63  | 0.48 – 1.17; 0.59  | 0.69 – 0.85; 0.70  | 0.80 – 1.17; 0.89  |
| -                     | Present study                   | SR                             | Mukteshwar | 0.70 – 0.91; 0.70  | 0.68 – 1.15; 0.70  | 0.80 – 0.91; 0.81  | 0.98 – 1.15; 1.00  |
| -                     | Present study                   | SR                             | New Delhi  | 0.60 – 0.95; 0.62  | 0.46 – 1.19; 0.54  | 0.74 – 0.95; 0.85  | 0.88 – 1.19; 1.14  |
| $T$ & $p$             | 269 K &<br>70120 Pa             | 298.15 K &<br>96757 Pa         | Hyytiälä   | 0.80 – 0.90; 0.81<br>(0.88 – 0.94; 0.88)                             | 0.83 – 0.93; 0.85<br>(0.91 – 0.98; 0.93)                             | 0.84 – 0.90; 0.85<br>(0.88 – 0.94; 0.89)                             | 0.83 – 0.94; 0.83<br>(0.91 – 0.94; 0.91)                             |
| $T$ & $p$             | 223 K &<br>26500 Pa             | 298.15 K &<br>96757 Pa         | Hyytiälä   | 0.62 – 0.81; 0.62<br>(0.81 – 1.42; 1.07)                             | 0.62 – 1.14; 1.01<br>(0.81 – 1.56; 1.23)                             | 0.65 – 0.81; 0.67<br>(0.81 – 0.87; 0.82)                             | 0.62 – 0.74; 0.67<br>(0.81 – 0.95; 0.90)                             |
| $T$ & $p$             | 223 K &<br>26500 Pa             | 298.15 K &<br>96757 Pa         | Mukteshwar | 0.67 – 0.81; 0.67<br>(0.86 – 1.21; 1.12)                             | 0.76 – 1.20; 1.08<br>(0.81 – 1.28; 1.21)                             | 0.73 – 0.81; 0.73<br>(0.86 – 0.92; 0.87)                             | 0.76 – 0.86; 0.77<br>(0.81 – 0.87; 0.86)                             |
| $T$ & $p$             | 223 K &<br>26500 Pa             | 298.15 K &<br>96757 Pa         | New Delhi  | 0.63 – 0.83; 0.64<br>(0.84 – 1.46; 1.27)                             | 0.68 – 1.51; 1.25<br>(0.80 – 1.59; 1.41)                             | 0.68 – 0.83; 0.80<br>(0.83 – 0.93; 0.88)                             | 0.67 – 0.95; 0.75<br>(0.80 – 0.91; 0.81)                             |
| $m_i$ ( $\rho_i$ )    | 130 – 1000 Da<br>(43 – 460 Da)  | 220 – 1800 Da<br>(55 – 840 Da) | Hyytiälä   | 1.12 – 1.34; 1.32<br>(1.05 – 1.29; 1.22)                             | 0.93 – 1.41; 1.29<br>(1.00 – 1.21; 1.19)                             | 1.11 – 1.26; 1.25<br>(1.05 – 1.14; 1.12)                             | 0.92 – 1.13; 1.07<br>(1.00 – 1.13; 1.11)                             |
| $m_i$ ( $\rho_i$ )    | 300 – 2100 Da<br>(62 – 1200 Da) | 220 – 1800 Da<br>(55 – 840 Da) | Hyytiälä   | 0.84 – 0.93; 0.84<br>(0.85 – 0.96; 0.88)                             | 0.81 – 1.05; 0.86<br>(0.86 – 1.00; 0.88)                             | 0.86 – 0.94; 0.86<br>(0.92 – 0.96; 0.93)                             | 0.95 – 1.05; 0.99<br>(0.92 – 1.00; 0.93)                             |
| $\chi_p$              | 2.6                             | $\infty$                       | Hyytiälä   | 0.69 – 1.02; 0.72<br>(0.71 – 0.98; 0.73)                             | 0.68 – 0.76; 0.68<br>(0.74 – 0.86; 0.75)                             | 0.80 – 1.02; 0.84<br>(0.80 – 0.99; 0.82)                             | 0.68 – 0.77; 0.68<br>(0.79 – 0.87; 0.81)                             |
| $\chi_p$              | 6                               | $\infty$                       | Hyytiälä   | 0.84 – 1.00; 0.86<br>(0.86 – 0.99; 0.87)                             | 0.82 – 0.88; 0.83<br>(0.87 – 0.93; 0.88)                             | 0.91 – 1.00; 0.93<br>(0.90 – 1.00; 0.92)                             | 0.82 – 0.89; 0.82<br>(0.90 – 0.93; 0.90)                             |
| $n_{i,T}^+/n_{i,T}^-$ | 1.1                             | 1.0                            | Hyytiälä   | 0.89 – 0.91; 0.91<br>(0.90 – 0.91; 0.91)                             | 1.10 – 1.12; 1.10<br>(1.10 – 1.13; 1.10)                             | 0.89 – 0.91; 0.91<br>(0.89 – 0.91; 0.91)                             | 1.10 – 1.12; 1.10<br>(1.10 – 1.13; 1.11)                             |
| $n_{i,T}^+/n_{i,T}^-$ | 1.2                             | 1.0                            | Hyytiälä   | 0.80 – 0.83; 0.83<br>(0.82 – 0.84; 0.83)                             | 1.20 – 1.25; 1.20<br>(1.20 – 1.26; 1.20)                             | 0.80 – 0.83; 0.83<br>(0.81 – 0.84; 0.84)                             | 1.20 – 1.25; 1.20<br>(1.21 – 1.26; 1.21)                             |

but the SR distribution was used for  $f_{\text{inv}}$ ; 3) the  $f_{\text{cha}}$  was calculated for conditions at 10 km altitude, but  $f_{\text{inv}}$  was calculated for laboratory conditions (Table 4.3). The highest bias, underestimation by a factor of  $\sim 3$ , was observed for the first case listed above, but only if the measured distribution was used and only for the Hyytiälä and New Delhi simulations; the total particle concentration was less affected by the new particle formation in the Mukteshwar simulation. In the first case listed above, if the SR distribution was used instead of the measured one, the highest observed bias was underestimation by a factor of 1.5, again only for the Hyytiälä and New Delhi simulations. Further, biases above a factor of 1.2 were observed if, when calculating  $f_{\text{inv}}$ , the ion masses were overestimated, the  $n_{\text{i,T}}^+/n_{\text{i,T}}^- = 1.2$  was not accounted for, or polystyrene particles were assumed to be conductive.

### **Charge distribution uncertainty as an explanation to bias observed in the DMA-based measurements of total particle concentrations**

Recently, Wiedensohler (1988) conducted multiple DMA intercomparison workshops with one of the aims being to determine the present uncertainties of particle mobility spectrometers, such as Scanning Mobility Particle Sizer (SMPS) and Differential Mobility Particle Sizer (DMPS). In that study, the FHFV charge distribution (Wiedensohler 1988) was applied when inverting the signal from each instrument. As the instruments were sampling the same aerosol, it is reasonable to assume that the ion species in the charger of each of the instruments were similar, unless the ion production was influenced by the prior use of the instrument (G. Steiner and Reischl 2012; Maißer et al. 2015). Differences in the charge distributions acquired in the instruments could still arise from the different charger types (Jiang, Kim, et al. 2014; He and Dhaniyala 2014). Such differences could either lead to different ratios of negative to positive ion concentrations, or cause the aerosol to reach different non-steady-state bipolar charge distributions. The latter is not addressed in this study. The former effect would lead to consistent biases between instruments for  $d_p < 25$  nm (Figure 4.8); instead, the observed biases exhibited a strong diameter dependence. In short, the differences between the particle size distributions obtained with different instruments were probably not caused by variation in the steady-state bipolar charge distribution, but the failure to achieve steady-state remains a possibility.

As shown in Sect. 4.4, biases in the inferred particle size distributions result in corresponding biases in the total particle concentrations, depending on the particle size distribution itself. In the study by Wiedensohler et al. (2012), the total particle concentrations obtained by integrating the particle size distributions over the diam-

eter range from 10 nm to 800 nm were observed to be smaller than those measured using a reference condensation particle counter (CPC). For short periods of time, underestimation in excess of 20 % was observed when comparing the reference particle mobility spectrometer against the reference CPC; it was argued that this could be due to presence of considerable number of particles with  $d_p \sim 10$  nm, only a fraction of which was counted by the particle mobility spectrometer. The results presented above suggest that these biases might, instead, result from differences between the assumed FHFV charge distribution and that acquired in the charger. The present results suggest that the bias was not likely to be caused by non-unity ratio of positive to negative ions; it is also unlikely that the  $T$  and  $p$  in those measurement conditions would have played a major role.

The FHFV charge distribution was derived for the charging of conductive particles by negative and positive ions with mobilities (masses) of  $1.60 \text{ cm}^2\text{V}^{-1}\text{s}^{-1}$  (130 Da) and  $1.35 \text{ cm}^2\text{V}^{-1}\text{s}^{-1}$  (148 Da), respectively. If the actual charger ions had been less mobile, considerably more massive, or if the measured particles were composed of a material with very low relative permittivity, underestimations of the observed magnitude would be expected (Table 4.3). The simplifying assumptions made by Hoppel and Frick (1986) when calculating the flux coefficients could also contribute to the underestimation (López-Yglesias and Flagan 2013a). Thus, while the presence of particles near the lower detection threshold of the instruments could produce the observed difference between the particle concentrations obtained by integrating the particle size distribution and the CPC measurements, errors in the charge distribution assumed in the inversion are more likely at the root of this discrepancy than is the sensitivity of the DMA.

#### 4.5 Discussion and conclusions

Because recent reexamination of the theory of aerosol particle charging revealed differences between the actual charging probability and that assumed in most DMA-based particle size distribution analysis, we examined the effect that such differences may have on how well particle size distributions determined from mobility-based measurements reproduce actual particle size distributions. To make the simulations relevant to ambient measurements, an experimentally measured ion mobility distribution emanating from a bipolar aerosol charger was applied to aerosols from common scenarios that span a wide range of sizes encountered in atmospheric measurements, namely atmospheric nucleation events. However, ion properties have been shown to depend upon the charger used and, perhaps, even on the history of



the experimental system due to trace species that may volatilize from walls of the apparatus. The influence of ion and particle properties on the particle size distribution inferred from DMA data was examined. We further examined the influence of temperature and pressure on the resulting charge distribution, and on the interpretation of DMA data. An idealized instrument was employed to span the size range of the aerosol particles to prevent bias in the inferred particle size distribution resulting from sources other than the charge distribution. Not surprisingly, when the charge distribution on the sampled aerosol particles differs from that assumed in the data inversion, biases result. We have quantified such biases for a range of scenarios.

The mean mobility of the measured charger ions was at the low end of values reported in the literature. When the charge distribution assumed in the inversion was based on an ion mobility distribution measured by G. Steiner and Reischl (2012), which had a considerably higher mean mobility, the concentration of 2 nm particles was underestimated by up to a factor of 3. This bias decreased rapidly with increasing particle size, but over- and underestimation in the range of 1.2 to 1.5 was still observed over the range of  $10 \text{ nm} < d_p < 100 \text{ nm}$ .

Most DMA-based particle size distribution measurements to date have been interpreted using the charge distribution derived by Hoppel and Frick (1986) using simulations based upon the theory of Fuchs (1963), and reduced to a practical form in the parameterization by Wiedensohler (1988). The nature of the gas ions responsible for particle charging was not known at the time of those pioneering works, so it is not surprising that biases occur, as measurements extend to particle sizes and measurement environments that could not be probed with instruments available at the time. Over the mid-range of particle sizes probed in most previous measurements,  $20 \text{ nm} < d_p < 1000 \text{ nm}$ , the FHFV charge distribution introduces relatively little bias in the measured particle size distribution. However, at the large and small particle extremes, the biases can become substantial; when FHFV charge distribution was assumed in the inversion, the concentrations of particles below 10 nm were underestimated by a factor of 1.6 to 5, when the charger ions were characterized by the mobility distribution presented in this study, or by a factor of up to 2, when the charger ion mobilities were according to G. Steiner and Reischl (2012). This bias decreased rapidly with increasing size. Above 10 nm, the bias was less than 30 % for most particle sizes, with underestimating (overestimating) the concentrations for negative (positive) charge measurements.

When particle size distribution measurements are performed at mountain-top sites,

or at higher altitudes in airborne measurements, pressure and temperature effects lead to large deviations. Particle concentrations estimated from simulated measurements at 10 km altitude, were overestimated by a factor as large as 2 in the nucleation mode aerosol, i.e., particles smaller than a few nanometers in size. Again, the biases depend strongly on diameter, underestimating the concentrations for some sizes, and overestimating for others; at 100 nm, the inferred particle concentrations were 54 to 77 % of the sampled particle concentration, depending on the ion mobility distribution. As expected, the bias was smaller at lower altitude (3 km), and generally resulted in underestimation. A bias as large as 27 % was observed for  $d_p < 100$  nm.

Material properties also influence the data interpretation. The original Hoppel-Frick (1986) charge distributions were calculated for conductive particles. For particles with a very low relative permittivity (dielectric particles), predicted concentrations could be underestimated if the charge distribution used in the inversion was assumed to be that for conductive particles. For polystyrene particles,  $\chi_p = 2.6$ , concentration estimates were as much as 54 % low for  $d_p < 10$  nm, with the bias decreasing with increasing particle size. For NaCl particles,  $\chi_p = 6$ , the bias was reduced to half of that found for polystyrene particles. The ion relative permittivity, however, had negligible effect.

Though we measured the ion mobility distribution, the charge distribution calculations required an estimate of the mass of ions (for convenience, represented in terms of an effective bulk density of the ions). By estimating  $\rho_i = 1500 \text{ kg m}^{-3}$ , an over (under) estimation of up to a factor of 1.6 (1.3) was observed in the particle size distribution, if the actual  $\rho_i$  had been  $800 \text{ kg m}^{-3}$  ( $2200 \text{ kg m}^{-3}$ ). The bias decreased with increasing particle size with negligible bias observed when  $d_p > 300$  nm.

The concentrations of negative and positive ions in the charger are often assumed to be the same, but a charge imbalance could result from differences in the loss rates of negative and positive ions due to ion-aerosol attachment (de La Verpilliere, Swanson, and Boies 2015; Tigges, Jain, and Schmid 2015) or as the aerosol passes through the transition between the charger and the detector (Hoppel and Frick 1990). Assuming charge balance ( $n_{i,T}^+/n_{i,T}^- = 1$ ) in the inversion instead of a reasonable imbalance of  $n_{i,T}^+/n_{i,T}^- = 1.1$  or  $1.2$  in the charger led to approximately 10 or 20 %, respectively, under- or overestimation of the concentration of sub 20 nm particles, depending on signal polarity. For the small particles that acquired at most one charge, the bias in the inferred particle size distribution varied linearly with the magnitude of the error in the charge imbalance ratio. For larger particles that may acquire multiple charges,

the bias varied strongly with diameter, reaching levels up to 70 %. It should be noted that the process resulting in charge imbalance could also result to the aerosol not reaching a steady-state charge distribution, which could be an even more concerning issue (de La Verpilliere, Swanson, and Boies 2015; Tigges, Jain, and Schmid 2015), but beyond the scope of this study.

The simulations used to estimate the charge distribution in this study were computationally intensive. We have explored a broad range of the parameter space that may be encountered in mobility-based particle size distribution measurements, but, clearly, much more needs to be done for other measurement scenarios not examined here. To lessen the computational burden, we examined the effects of simplifying such simulations by using a single value of ion mobility, instead of whole mobility distribution. Using the mean ion mobility was found to result in a smaller bias than using the median ion mobility, with the maximum bias factors being 1.06 and 1.18, respectively.

Simulations were performed in which the maximum number of charges considered in the inversion was as low as 3; this simplified the inversion analysis considerably, but increased the bias in particle size distribution estimates for larger particles. Our simulations reveal that consideration of 6 charges eliminated the bias for submicron particles; more charges would be needed if supermicron particles were considered.

Three new particle formation event scenarios were examined in this study. The observed biases in the inferred particle size distributions were insensitive to the shape of the actual particle size distribution under consideration: in the most pronounced example within these simulations, the difference in the bias factors corresponding to these three scenarios only approached 30 % for particles with  $d_p > 300$  nm, though a value as high as 50 % observed over a very narrow size range. In general the differences were much smaller than these extremes.

While the biases in the particle size distributions stayed constant in time, a considerable time variation was observed in the bias in the total particle concentration, especially during the new particle formation event. The largest bias, an underestimation by a factor of 3, was observed when the charge distribution acquired in the charger was according to our measurements, but the FHFV charge distribution was assumed in the inversion. Biases above a factor of 1.5 also occurred if the ion mobility distribution assumed in the inversion was substantially different from the one acquired in the charger, or the conditions at 10 km altitude were not taken into account.

In a previous study, the particle concentration obtained by integrating the particle size distribution sometimes underestimated the total particle concentration when compared to a CPC measurement (Wiedensohler et al. 2012). The biases due to the charge distribution assumed in the inversion explained these underestimations. For the 10 to 800 nm particle size range, discrepancies up to 20 % between total particle concentrations based on particle mobility spectrometer and CPC measurements could be attributed to uncertainty in the ion mass, relative permittivity of the particles, or concentration ratio of negative and positive ions. Considerably higher discrepancies could be explained by not properly accounting for the ion mobilities or  $T$  and  $p$  effects when calculating the charge distribution assumed in the inversion.

The weak link in differential mobility analysis of particle size distributions is the charge distribution, not the size/mobility resolution of the DMA. As convenient as it may be, there is not likely to be a one-size-fits-all charge distribution. Combined with recent studies that show strong variation in the charge distribution from one charger to another (Jiang, Kim, et al. 2014; Kallinger and Szymanski 2015), the present study makes it clear that better understanding of the charge distribution is required to make mobility-based particle size distribution measurements truly quantitative. Using a different charge distribution in the inversion than that present on the aerosol particles introduces biases in the inferred particle size distribution. Moreover, measurements made in different environments may encounter different charge distributions. G. Steiner and Reischl (2012) showed that the molecules that form ions in different chargers differ from one charger to another; they attributed this difference to contaminants accumulated during prior use of the device. Thus, even measurement history may be a factor. Measurements made at high altitude are particularly problematic.

While the biases can be substantial, the present results make it possible to constrain their magnitudes over the entire range for which DMAs are used to characterize atmospheric and other aerosols. By our current estimates, the most extreme variation arises when the FHFV parameterization (Wiedensohler 1988) is applied to particles as small as 1 nm, where deviations may approach an order of magnitude.

We have based these estimates on our current best estimate of the ion-to-particle flux coefficients, taking into account ion and particle properties as well as atmospheric conditions. Further work is required to fully characterize both the ions and the aerosol properties over the range of conditions at which these techniques are applied. Regardless of what is the true charge distribution, using the wrong one

in inverting the data can lead to substantial biases. While we have only examined bipolar charge distributions, the same sources of uncertainty apply to techniques using unipolar charge distributions. Because of the fundamental importance of the charge distribution to mobility-based analysis of aerosols, a future paper will provide parameterizations of attachment coefficients and steady-state bipolar charge distributions as a function of ion and particle properties, as well as atmospheric parameters, especially temperature and pressure. Further work and, likely, new experimental methods or instruments will be needed to fully constrain this source of uncertainty in measurements of fine and ultrafine aerosol particles.

## References

- Brunelli, N. A., R. C. Flagan, and K. P. Giapis (2009). “Radial differential mobility analyzer for one nanometer particle classification”. In: *Aerosol Sci. Technol.* 43.1, pp. 53–59. DOI: 10.1080/02786820802464302.
- Clarke, A. D. et al. (1998). “Particle production in the remote marine atmosphere: Cloud outflow and subsidence during ACE 1”. In: *J. Geophys. Res.-Atmos.* 103.D13, pp. 16397–16409.
- Coggon, M. M. et al. (2014). “Observations of continental biogenic impacts on marine aerosol and clouds off the coast of California”. In: *J. Geophys. Res.-Atmos.* 119.11, pp. 6724–6748. ISSN: 21698996. DOI: 10.1002/2013JD021228.
- Davies, C. N. (1945). “Definitive equations for the fluid resistance of spheres”. In: *P. Phys. Soc.* 57.4, pp. 259–270. ISSN: 0959-5309. DOI: 10.1088/0959-5309/57/4/301.
- de La Verpilliere, J. L., J. J. Swanson, and A. M. Boies (2015). “Unsteady bipolar diffusion charging in aerosol neutralisers: A non-dimensional approach to predict charge distribution equilibrium behaviour”. In: *J. Aerosol Sci.* 86, pp. 55–68. DOI: 10.1016/j.jaerosci.2015.03.006.
- Ehn, M., H. Junninen, T. Petäjä, et al. (2010). “Composition and temporal behavior of ambient ions in the boreal forest”. In: *Atmos. Chem. Phys.* 10.17, pp. 8513–8530. ISSN: 16807316. DOI: 10.5194/acp-10-8513-2010.
- Ehn, M., H. Junninen, S. Schobesberger, et al. (2011). “An instrumental comparison of mobility and mass measurements of atmospheric small ions”. In: *Aerosol Sci. Technol.* 45.4, pp. 522–532. DOI: 10.1080/02786826.2010.547890.
- Flagan, R. C. (1999). “On differential mobility analyzer resolution”. In: *Aerosol Sci. Technol.* 30.6, pp. 556–570. DOI: 10.1080/027868299304417.
- Fuchs, N. A. (1963). “On the stationary charge distribution on aerosol particles in a bipolar ionic environment”. In: *Geofisica pura e applicata* 56.1, pp. 185–193.
- Gagné, S. et al. (2012). “Aerosol charging state at an urban site: New analytical approach and implications for ion-induced nucleation”. In: *Atmos. Chem. Phys.* 12.10, pp. 4647–4666. ISSN: 16807324. DOI: 10.5194/acp-12-4647-2012.
- Gopalakrishnan, R., P. H. McMurry, and C. J. Hogan (2015). “The bipolar diffusion charging of nanoparticles: A review and development of approaches for non-spherical particles”. In: *Aerosol Sci. Technol.* 49.12, pp. 1181–1194. DOI: 10.1080/02786826.2015.1109053.
- Gopalakrishnan, R., M. J. Meredith, et al. (2013). “Brownian dynamics determination of the bipolar steady state charge distribution on spheres and non-spheres in the transition regime”. In: *J. Aerosol Sci.* 63, pp. 126–145. DOI: 10.1016/j.jaerosci.2013.04.007.

- Gopalakrishnan, R., T. Thajudeen, et al. (2013). “The unipolar diffusion charging of arbitrary shaped aerosol particles”. In: *J. Aerosol Sci.* 64, pp. 60–80. DOI: 10.1016/j.jaerosci.2013.06.002.
- Hagwood, C., Y. Sivathanu, and G. Mulholland (1999). “The DMA transfer function with Brownian motion a trajectory/Monte-Carlo approach”. In: *Aerosol Sci. Technol.* 30.1, pp. 40–61. DOI: 10.1080/027868299304877.
- Han, B. et al. (2009). “A novel bipolar charger for submicron aerosol particles using carbon fiber ionizers”. In: *J. Aerosol Sci.* 40.4, pp. 285–294. ISSN: 00218502. DOI: 10.1016/j.jaerosci.2008.11.005.
- He, M. and S. Dhaniyala (2014). “Experimental characterization of flowrate-dependent bipolar diffusion charging efficiencies of sub-50nm particles”. In: *J. Aerosol Sci.* 76, pp. 175–187. DOI: 10.1016/j.jaerosci.2014.06.009.
- Hoppel, W. A. and G. M. Frick (1986). “Ion-aerosol attachment coefficients and the steady-state charge distribution on aerosols in a bipolar ion environment”. In: *Aerosol Sci. Technol.* 5.1, pp. 1–21. DOI: 10.1080/02786828608959073.
- (1990). “The nonequilibrium character of the aerosol charge distributions produced by neutralizers”. In: *Aerosol Sci. Technol.* 12.3, pp. 471–496. ISSN: 0278-6826. DOI: 10.1080/02786829008959363.
- Hussin, A. et al. (1983). “Bipolar diffusion charging of aerosol particles-I: experimental results within the diameter range 4-30 nm”. In: *J. Aerosol Sci.* 14.5, pp. 671–677. DOI: 10.1016/0021-8502(83)90071-X.
- Hyvärinen, A.-P. et al. (2011). “Effect of the summer monsoon on aerosols at two measurement stations in Northern India-Part 2: Physical and optical properties”. In: *Atmos. Chem. Phys.* 11.16, pp. 8283–8294. ISSN: 16807316. DOI: 10.5194/acp-11-8283-2011.
- Iida, K., M.R. Stolzenburg, and P.H. McMurry (2009). “Effect of working fluid on sub-2 nm particle detection with a laminar flow ultrafine condensation particle counter”. In: *Aerosol Sci. Technol.* 43.1, pp. 81–96. DOI: 10.1080/02786820802488194.
- Jiang, J., C. J. Hogan, et al. (2007). “Aerosol charging and capture in the nanoparticle size range (6-15 nm) by direct photoionization and diffusion mechanisms”. In: *J. Appl. Phys.* 102.3, p. 034904. ISSN: 00218979. DOI: 10.1063/1.2768061.
- Jiang, J., C. Kim, et al. (2014). “Aerosol charge fractions cownstream of six bipolar chargers: effects of ion source, source activity, and flowrate”. In: *Aerosol Sci. Technol.* 48.12, pp. 1207–1216. ISSN: 0278-6826. DOI: 10.1080/02786826.2014.976333.
- Kallinger, P. and W. W. Szymanski (2015). “Experimental determination of the steady-state charging probabilities and particle size conservation in non-radioactive and radioactive bipolar aerosol chargers in the size range of 5–40 nm”. In: *J. Nanopart. Res.* 17.4, pp. 1–12. DOI: 10.1007/s11051-015-2981-x.

- Knutson, E. O. and K. T. Whitby (1975). “Aerosol classification by electrical mobility: apparatus, theory, and applications”. In: *J. Aerosol Sci.* 6, pp. 443–451. DOI: 10.1016/0021-8502(75)90060-9.
- Ku, B. K. and J. F. de la Mora (2009). “Relation between electrical mobility, mass, and size for nanodrops 1–6.5 nm in diameter in air”. In: *Aerosol Sci. Technol.* 43.3, pp. 241–249. DOI: 10.1080/02786820802590510.
- Kulmala, M. and V.-M. Kerminen (2008). “On the formation and growth of atmospheric nanoparticles”. In: *Atmos. Res.* 90.2, pp. 132–150. DOI: 10.1016/j.atmosres.2008.01.005.
- Kulmala, M., H. Vehkamäki, et al. (2004). “Formation and growth rates of ultrafine atmospheric particles: a review of observations”. In: *J. Aerosol Sci.* 35.2, pp. 143–176. DOI: 10.1016/j.jaerosci.2003.10.003.
- Kwon, S. B. et al. (2006). “Charge neutralization of submicron aerosols using surface-discharge microplasma”. In: *J. Aerosol Sci.* 37.4, pp. 483–499. ISSN: 00218502. DOI: 10.1016/j.jaerosci.2005.05.007.
- Larriba, C. and C. J. Hogan (2013). “Ion mobilities in diatomic gases: Measurement versus prediction with non-specular scattering models”. In: *J. Phys. Chem. A* 117.19, pp. 3887–3901. ISSN: 10895639. DOI: 10.1021/jp312432z.
- Larriba-Andaluz, C. et al. (2015). “Gas molecule scattering & ion mobility measurements for organic macro-ions in He versus N<sub>2</sub> environments”. In: *Phys. Chem. Chem. Phys.* 17.22, pp. 15019–15029. ISSN: 1463-9084. DOI: 10.1039/c5cp01017a.
- Lee, H. M. et al. (2005). “Effects of mobility changes and distribution of bipolar ions on aerosol nanoparticle diffusion charging”. In: *J. Chem. Eng. Jpn.* 38.7, pp. 486–496. DOI: 10.1252/jcej.38.486.
- Leppä, J. et al. (2009). “Ion-UHMA: A model for simulating the dynamics of neutral and charged aerosol particles”. In: *Boreal Environ. Res.* 14, pp. 559–575. ISSN: 12396095.
- López-Yglesias, X. and R. C. Flagan (2013a). “Ion-aerosol attachment coefficients and the steady-state charge distribution on aerosols in a bipolar ion environment”. In: *Aerosol Sci. Technol.* 47.6, pp. 688–704. DOI: 10.1080/02786828608959073.
- (2013b). “Population balances of micron-sized aerosols in a bipolar ion environment”. In: *Aerosol Sci. Technol.* 47.6, pp. 681–687. DOI: 10.1080/02786826.2013.783684.
- Maißer, A. et al. (2015). “The mass-mobility distributions of ions produced by a Po-210 source in air”. In: *J. Aerosol Sci.* 90, pp. 36–50. DOI: 10.1016/j.jaerosci.2015.08.004.
- Mäkelä, J. M. et al. (1997). “Observations of ultrafine aerosol particle formation and growth in boreal forest”. In: *Geophys. Res. Lett.* 24.10, pp. 1219–1222. ISSN: 1433-044X. DOI: 10.1007/s00113-009-1567-4.



- Makkonen, R. et al. (2012). “Air pollution control and decreasing new particle formation lead to strong climate warming”. In: *Atmos. Chem. Phys.* 12.3, pp. 1515–1524. DOI: 10.5194/acp-12-1515-2012.
- Merritt, M. and Y. Zhang (2005). “Interior-point gradient method for large-scale totally nonnegative least squares problems”. In: *J. Optimiz. Theory App.* 126.1, pp. 191–202. ISSN: 00223239. DOI: 10.1007/s10957-005-2668-z.
- Mirme, S. et al. (2010). “Atmospheric sub-3 nm particles at high altitudes”. In: *Atmos. Chem. Phys.* 10, pp. 437–451. ISSN: 1680-7324. DOI: 10.5194/acp-10-437-2010.
- Mui, W., H. Mai, et al. (2017). “Design, simulation, and characterization of a radial opposed migration ion and aerosol classifier (ROMIAC)”. In: *Aerosol Sci. Technol.* In review.
- Mui, W., D. A. Thomas, et al. (2013). “Ion mobility-mass spectrometry with a radial opposed migration ion and aerosol classifier (ROMIAC)”. In: *Anal. Chem.* 85, pp. 6319–6326. DOI: 10.1021/ac400580u.
- Neitola, K. et al. (2011). “New particle formation infrequently observed in Himalayan foothills—why?” In: *Atmos. Chem. Phys.* 11.16, pp. 8447–8458. ISSN: 16807316. DOI: 10.5194/acp-11-8447-2011.
- Ouyang, H., R. Gopalakrishnan, and C. J. Hogan (2012). “Nanoparticle collisions in the gas phase in the presence of singular contact potentials”. In: *J. Chem. Phys.* 137.6, p. 064316. ISSN: 00219606. DOI: 10.1063/1.4742064.
- Ouyang, H., C. Larriba-Andaluz, et al. (2013). “The collision cross sections of iodide salt cluster ions in air via differential mobility analysis-mass spectrometry”. In: *J. Am. Soc. Mass Spectrom.* 24.12, pp. 1833–1847. ISSN: 10440305. DOI: 10.1007/s13361-013-0724-8.
- Qi, C. and P. Kulkarni (2013). “Miniature dual-corona ionizer for bipolar charging of aerosol”. In: *Aerosol Sci. Technol.* 47.1, pp. 81–92. ISSN: 0278-6826. DOI: 10.1080/02786826.2012.728301.
- Rosser, S. and J. F. de la Mora (2005). “Vienna-type DMA of high resolution and high flow rate”. In: *Aerosol Sci. Technol.* 39.12, pp. 1191–1200. DOI: 10.1080/02786820500444820.
- Shimada, M. et al. (2002). “Bipolar charging of aerosol nanoparticles by a soft X-ray photoionizer”. In: *J. Chem. Eng. Jpn.* 35.8, pp. 786–793.
- Steiner, G. and G. P. Reischl (2012). “The effect of carrier gas contaminants on the charging probability of aerosols under bipolar charging conditions”. In: *J. Aerosol Sci.* 54, pp. 21–31. DOI: 10.1016/j.jaerosci.2012.07.008.
- Steiner, Gerhard et al. (2014). “High-resolution mobility and mass spectrometry of negative ions produced in a 241Am aerosol charger”. In: *Aerosol Sci. Technol.* 48.3, pp. 261–270. DOI: 10.1080/02786826.2013.870327.

- Stolzenburg, M. R. (1988). “An ultrafine aerosol size distribution measuring system”. Ph.D. Thesis. University of Minnesota.
- Tammet, H. (1995). “Size and mobility of nanometer particles , clusters and ions”. In: *J. Aerosol Sci.* 26.1, pp. 459–475. doi: 10.1016/0021-8502(94)00121-E.
- Tigges, L., A. Jain, and H.-J. Schmid (2015). “On the bipolar charge distribution used for mobility particle sizing: Theoretical considerations”. In: *J. Aerosol Sci.* 88, pp. 119–134. doi: 10.1016/j.jaerosci.2015.05.010.
- Weingartner, E., S. Nyeki, and U. Baltensperger (1999). “Seasonal and diurnal variation of aerosol size distributions (  $10 < D < 750$  nm ) at a high-alpine site ( Jungfraujoch 3580 m asl )”. In: *J. Geophys. Res.* 104.D21, pp. 26809–26820. doi: 10.1029/1999jd900170.
- Wiedensohler, A. (1988). “An approximation of the bipolar charge distribution for particles in the submicron size range”. In: *J. Aerosol Sci.* 19.3, pp. 387–389.
- Wiedensohler, A. et al. (2012). “Mobility particle size spectrometers: harmonization of technical standards and data structure to facilitate high quality long-term observations of atmospheric particle number size distributions”. In: *Atmos. Meas. Tech.* 5, pp. 657–685. doi: 10.5194/amt-5-657-2012.
- Yun, K. M. et al. (2009). “Effect of X-ray energy and ionization time on the charging performance and nanoparticle formation of a soft X-ray photoionization charger”. In: *Adv. Powder Technol.* 20.6, pp. 529–536. doi: 10.1016/j.apt.2009.07.002.
- Zhang, S.-H. and R. C. Flagan (1996). “Resolution of the radial differential mobility analyzer for ultrafine particles”. In: *J. Aerosol Sci.* 27.8, pp. 1179–1200.

*Chapter 5***OBSERVATIONS OF NEW PARTICLE GROWTH FROM A  
LARGE CATTLE FEEDLOT**

By Wilton Mui, Johannes Leppä, Matthew M. Coggon, Jill S. Craven, Amanda M. Grantz, Huajun Mai, Hafliði H. Jonsson, John H. Seinfeld, and Richard C. Flagan

**5.1 Introduction**

Aerosol particles impact climate directly by absorbing and scattering solar radiation and indirectly by influencing planetary albedo as cloud condensation nuclei (Seinfeld and Pandis 2006). The atmospheric aerosol includes primary particles that are released directly into the atmosphere and secondary particles that form as a result of gas-to-particle conversion. Secondary aerosols include low volatility products of reaction that condense directly onto primary “seeds” and new particles that form directly from the gas phase in nucleation events.

New particle formation (NPF) is temporally and spatially variable in both occurrence and extent, adding considerably to the uncertainty of the radiative forcing of “aerosols” lumped as a whole (IPCC 2013). Furthermore, NPF sources, composition, and nucleation and growth rates are incompletely understood, making it difficult to account for new particles in general circulation models and climate prediction, though progress is being made (Dunne et al. 2016).

The first step in NPF is nucleation, whereby gas molecules form stable clusters (thought to be  $\sim 1\text{--}2$  nm in diameter,  $D_p$ ) by overcoming the surface free energy barrier to the growth of small particles (Seinfeld and Pandis 2006; Kulmala, Riipinen, et al. 2007). Nucleation accounts for 40–70% of aerosol in the global atmosphere (Spracklen, Carslaw, Kulmala, Kerminen, Mann, et al. 2006; Kulmala and Kerminen 2008; Spracklen, Carslaw, Kulmala, Kerminen, Sihto, et al. 2008; Merikanto et al. 2009; M. Wang and Penner 2009; Yu and Luo 2009; Yu, Luo, et al. 2010; Makkonen et al. 2012). Once the clusters pass this barrier, they may continue to grow to form the so-called nucleation mode ( $D_p < 10$  nm) of the atmospheric aerosol, or they can be lost by coagulation with larger particles in the background aerosol.

Sulfuric acid is generally thought to dominate atmospheric nucleation, due to its low

vapor pressure and hydrogen bonding with water molecules in the air (Seinfeld and Pandis 2006). However, binary sulfuric acid-water vapor nucleation does not occur at typical ambient concentrations of sulfuric acid. Ternary sulfuric acid-ammonia-water vapor nucleation occurs at vapor concentrations more representative of the ambient atmosphere, due to the lowering of the nucleation barrier resulting from the neutralization of sulfuric acid by ammonia (Qiu and Zhang 2013). In the past decade, increasing evidence has pointed to the additional importance of amines, the only other relatively ubiquitous group of basic trace gases besides ammonia, in nucleation. Though their atmospheric abundance is 2–3 orders of magnitude less than ammonia (Hutchinson, Mosier, and Andrew 1982; Schade and Crutzen 1995), their greater basicity and ability to lower the nucleation barrier even more than ammonia translates to their role in enhancing or even supplanting ammonia in the ternary sulfuric acid-ammonia-water vapor nucleation system (Kurten et al. 2008; Pratt, Hatch, and Prather 2009; Loukonen et al. 2010; Smith, Barsanti, et al. 2010; Erupe, Viggiano, and Lee 2011; Paasonen et al. 2012).

Animal husbandry operations are the largest source of atmospheric amines and a major source of ammonia (Ge, Wexler, and Clegg 2011; Sintermann et al. 2014), so it is reasonable to suspect that such operations may play an important role in NPF, and, ultimately, may contribute significantly to anthropogenic sources of aerosol. This study reports airborne observations of nucleation in plumes emanating from a major cattle feedlot. Micrometeorological wind measurements and high-spatial-resolution measurements of nucleation mode particle number size distributions allow estimation of the growth rate from the freshly-formed particles as a function of plume age.

## 5.2 Methods

### **Nucleation in California Environments field campaign**

The Nucleation in California Environments (NICE) campaign was conducted from July 8, 2013 to August 7, 2013 at the Center for Interdisciplinary Remotely-Piloted Aircraft Studies (CIRPAS; Bluth et al. 1996), based in Monterey, California (Fig. 5.1a). Research flights (RF) were conducted using the CIRPAS UV-18A Twin Otter aircraft and sampled aerosols in plumes from cargo ships, wildfires, urban areas, and agricultural activities.

In this study we focus on flights sampling Harris Ranch (36.305°N, 120.268 °W), a large animal feedlot operation located in the San Joaquin Valley, near Coalinga,

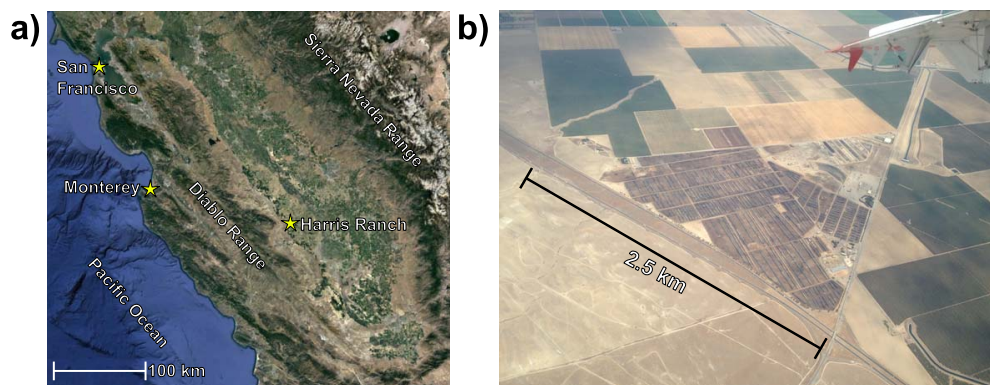


Figure 5.1: a) Geographic context of this study in the state of California. Harris Ranch is located in the San Joaquin Valley, bounded by the Diablo Range to the west and the Sierra Nevada Range to the east. Stars mark the location of Harris Ranch, CIRPAS near Monterey, as well as nearby major urban center San Francisco. Map data: Google, SIO, NOAA, US Navy, NGA, GEBCO, LDEO-Columbia, and NSF. b) Photograph over Harris Ranch, showing the extent of the beef cattle feed lot, which is a triangle approximately  $3.25 \text{ km}^2$  in area.

California. Harris Ranch, which is immediately bounded to the west by the Diablo Mountain range (Fig. 5.1a), contains up to 100,000 head of cattle (Sorooshian et al. 2008), in an area of approximately  $3.25 \text{ km}^2$  (Fig. 5.1b).

Two flights in the NICE campaign over Harris Ranch provided a consistent wind direction over the site throughout the flights, and exhibited unambiguous NPF events in the plume immediately downwind of Harris Ranch. The first flight was RF18, which occurred on July 31, 2013 from 7:56–12:27 local time (LT; Pacific Daylight Time; UTC-7:00); RF21 occurred on August 5, 2013 from 9:25–14:46 LT.

### Air mass origins

A single 48-hour back trajectory from Harris Ranch was calculated for each flight using NOAA's Hybrid Single-Particle Lagrangian Integrated Trajectory (HYSPLIT) model (Stein et al. 2015), and 40-km resolution Eta Data Assimilation System (EDAS) meteorological archive data. The HYSPLIT back trajectory for RF18 was started at 10:00 LT (approximately the mid-time of the plume sampling period) from 30–1000 m above ground level (AGL) with thirty evenly-spaced vertical levels. Figure 5.2a shows that a single southerly marine-originated air mass passed over the urban San Francisco Bay Area and reversed direction, going around the northern end of the Diablo Range into the San Joaquin Valley toward Harris Ranch. Figure 5.2b shows that there was no vertical mixing of the air mass before arriving at Harris

Ranch.

A similar back trajectory was calculated for RF21 starting at 12:00 LT. In contrast to RF18, the air arriving at Harris Ranch during RF21 appears to be a mixture of two or three distinct air masses. Figure 5.2c shows that 1) the air at the lowest altitudes over Harris Ranch during RF21 originated from a northerly marine-originated air mass that passed over Monterey and the Diablo Range, 2) the air at altitudes of 400–800 m AGL over Harris Ranch appears to be continental urban air that reversed direction and split in two before passing the San Francisco Bay and remote coastal regions south of Monterey, and 3) air above 800 m AGL over Harris Ranch originating from a separate northerly marine-originated air mass that passed over remote coastal regions south of Monterey.

### **Flight overviews**

Figure 5.3 shows the flight paths for the two flights. In each case, the Twin Otter departed Monterey and then ascended to 1000-1500 meters above mean sea level (AMSL) to traverse the Diablo Range, before a spiral down descent to as low as allowed by visual flight rules. This flight then focused on locating and mapping the particle plumes downwind from the source, before returning to Monterey. Over agricultural areas, visual flight rules allowed for the Twin Otter to be as low as approximately 200 meters AGL. In both flights, the Twin Otter primarily sampled the areas south and southwest of Harris Ranch due to the prevailing northeasterly winds and high particle counts in those areas.

Two vertical profiles were conducted over Harris Ranch during RF18, while four vertical profiles were conducted for RF21, to determine the height of the convective boundary layer (CBL) at different times during the sampling period. The CBL height was linearly interpolated in time between profile measurements. This height was used to exclude data points that were above the CBL from further analysis since there would potentially be vertical variation in particle population properties above the CBL. Additionally, the CBL height was used to correct for the effect of dilution from the increase in CBL height relative to the moment when the Twin Otter first descended on the site. Skies were clear with strong solar insolation during both flights. The ambient pressure observed when the aircraft was beneath the CBL was typically  $\sim 96000$  Pa, the ambient temperature was  $\sim 297$  K, and the ambient relative humidity ranged from 31–44% over Harris Ranch.

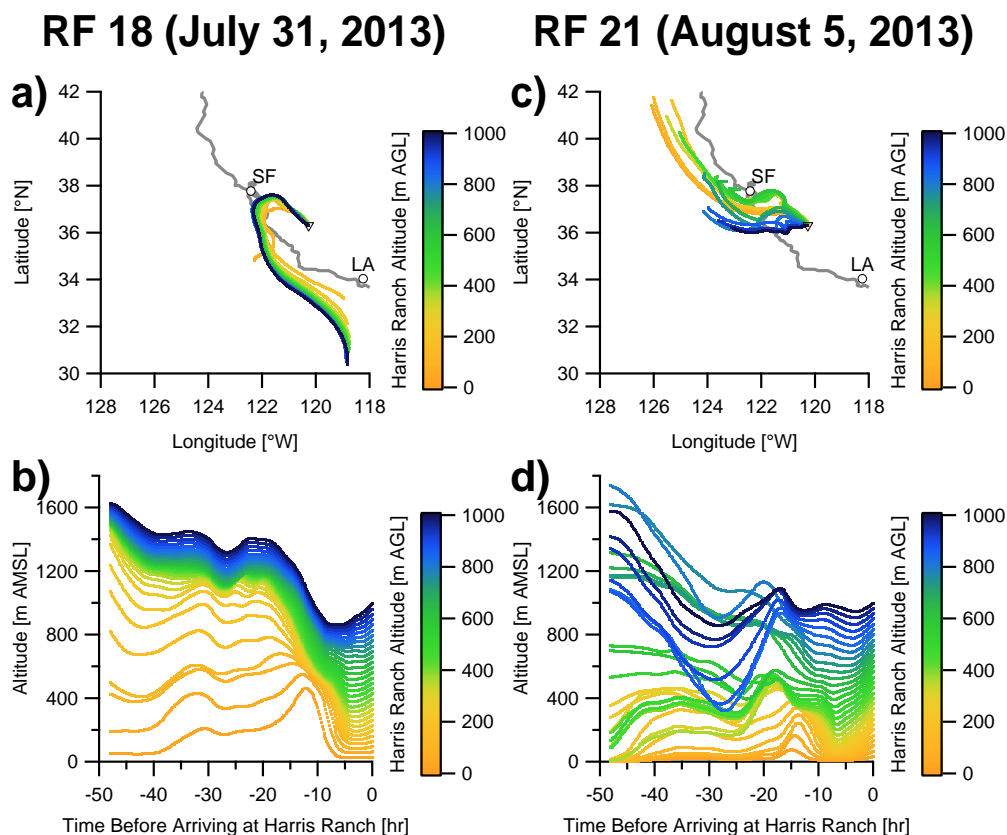


Figure 5.2: 48-hour HYSPLIT back trajectories of air masses arriving at Harris Ranch at the approximate mid-time of the plume sampling period, using 40-km resolution EDAS meteorological data at thirty evenly-spaced levels between 30 and 1000 m AGL. a) RF18 horizontal extent of trajectories. Only the trajectory of every other altitude level is plotted for clarity. b) RF18 vertical extent of trajectories above mean sea level (AMSL). c) RF21 horizontal extent of trajectories. Only the trajectory of every other altitude level is plotted for clarity. d) RF21 vertical extent of trajectories AMSL. Circle markers show major urban areas San Francisco (SF) and Los Angeles (LA) for geographic context, while the triangle marker indicates Harris Ranch.

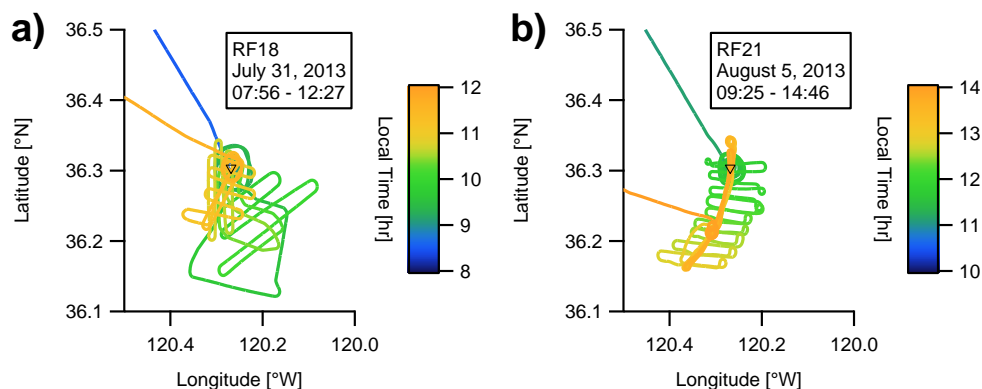


Figure 5.3: Overview of flight paths for research flights in this study. Paths are colored by LT, which is described by the colorbar. The location of CIRPAS is represented with a filled circle. a) RF18. b) RF21. The triangle marker indicates the location of Harris Ranch.

## Instrumentation

### Twin Otter

The Twin Otters's airspeed is  $\sim 55$  m/s. Various meteorological instruments (such as those for pressures, temperatures, relative humidity, position, wind speed and direction) are located in the Twin Otter radome, fuselage, and cabin, as described by Kalogiros and Q. Wang (2002). The Twin Otter has a sub-isokinetic community aerosol inlet with virtually 100% transmission efficiency for submicron aerosol particles (Hegg et al. 2005), that connects to a community sampling tube that spans the length of the aircraft. Cabin sampling instruments included a TSI 3025 ultrafine condensation particle counter (UCPC) and a TSI 3010 condensation particle counter (CPC) for measuring the total number concentration of particles larger than 3 and 10 nm in diameter, respectively. Both particle counters obtained number concentrations every second. These total number concentrations are labeled  $N_3$  and  $N_{10}$ , respectively. The difference  $N_{3-10}$  is the total number concentration of particles between 3 and 10 nm in diameter. The two cabin particle counters were located near the front of the aircraft, near the upstream end of the community aerosol inlet. The signals of instruments farther downstream the community aerosol inlet (i.e., those obtaining particle size distribution and composition information) were shifted in time to align their signal peaks with the particle concentration peaks reported by the cabin particle counters.



## Particle size distribution

Two particle mobility classifiers, each preceded by a  $^{210}\text{Po}$  aerosol neutralizer, were used to obtain the particle size distribution from 3 nm to 815 nm in mobility diameter,  $D_Z$ . The radial opposed migration ion and aerosol classifier (ROMIAC; Mui et al. 2017) was used to obtain  $3 < D_Z < 18$  nm particle size distributions. It was operated in voltage-stepping mode, with a cross-flow rate of 14 liters per minute and a sample flow rate of 2.9 liters per minute, for a non-dispersive resolution of 4.8. The classified sample from the ROMIAC was then sent to a TSI 3025 UCPC. The ROMIAC obtained size distributions every 45 seconds.

A differential mobility analyzer (DMA) was used to obtain particle size distributions from  $30 < D_Z < 815$  nm. The DMA was operated in voltage-scanning mode with a sheath flow rate of 2.5 liters per minute and a sample flow rate of 0.5 liters per minute, for a non-dispersive resolution of 5. The classified sample from the DMA was then sent to a TSI 3010 CPC. The DMA obtained size distributions every 110 seconds.

The ROMIAC data were inverted using the transfer function and empirical calibration functions from Mui et al. (2017). The DMA data was inverted using the scanning DMA transfer function described by Mai and Flagan (2017). The time delays due to the tubing lengths between the aerosol community inlet and the ROMIAC or DMA inlet were accounted for in the inversion. The ion-to-particle flux coefficients, and the corresponding charge distribution, used in the data inversions were calculated using the model by López-Yglesias and Flagan (2013). The mean temperature and pressure values observed during RF21, i.e.,  $T = 298.23$  K and  $p = 95539$  Pa, were used in the flux coefficient calculations. The relative permittivity of the particles was assumed to be 6, which was shown by Leppä, Mui, et al. (2017) to be a safe compromise between conductive and highly dielectric particles. The mobilities of negative and positive ions were assumed to be  $1.53 \text{ cm}^2 \text{V}^{-1} \text{s}^{-1}$  and  $1.12 \text{ cm}^2 \text{V}^{-1} \text{s}^{-1}$ , respectively, with the corresponding masses of negative and positive ions being 256 Da and 549 Da, respectively. The Stokes-Millikan equation, including corrections for both the finite mass of the particle and polarization of air, was used to relate ion mass to mobility. The ratio of concentrations of negative and positive ions was assumed to be unity. After inversion, the ROMIAC and DMA distributions were merged, and the distribution between  $18 < D_Z < 30$  nm was estimated through linear interpolation. The total particle number concentration,  $N_{\text{int}}$ , was determined by integrating the merged ROMIAC-DMA particle size distribution.

Table 5.1: List of aerosol particle instrumentation on the Twin Otter aircraft used in this study, along with the particle property measured and particle size range covered.

| <b>Instrument</b>         | <b>Measurement</b>                          | <b>Particle Size Range</b> |
|---------------------------|---|----------------------------|
| TSI 3010<br>CPC           | Total Number<br>Concentration               | >10 nm                     |
| TSI 3025<br>UCPC          | Total Number<br>Concentration               | >3 nm                      |
| ROMIAC +<br>TSI 3025 UCPC | Particle Number<br>Size Distribution        | 3 to 18 nm                 |
| DMA +<br>TSI 3010 CPC     | Particle Number<br>Size Distribution        | 30 to 815 nm               |
| AMS                       | Particle-Phase Bulk<br>Chemical Composition | 50 to 800 nm               |

### Particle composition

An Aerodyne compact Time of Flight Aerosol Mass Spectrometer (AMS; Drewnick et al. 2005; Sorooshian et al. 2008) measured the chemical composition of non-refractory components of aerosol particles from 50 to 800 nm in diameter; the species discussed in this study are sulfate ( $\text{SO}_4$ ), nitrate ( $\text{NO}_3$ ), ammonium ( $\text{NH}_4$ ), and organics (Org). The AMS was operated in a manner as to collect mass spectra ensemble-averaged over all particle sizes every  $\sim 8$  seconds. The AMS was not calibrated and thus absolute mass concentrations of nonrefractory species are not reported; instead, the aerosol mass fraction is discussed, i.e.,  $f_{\text{SO}_4}$ ,  $f_{\text{NO}_3}$ ,  $f_{\text{NH}_4}$ , and  $f_{\text{Org}}$ .

Table 5.1 summarizes the instrumentation, and particle size range covered, on the Twin Otter aircraft for this study.

### Trajectories

The Twin Otter wind speed and direction measurements were used to create a point cloud in latitude-longitude space. Starting at the coordinates of Harris Ranch, both forward and backward trajectory paths were calculated based on the average wind speed and direction values in a 500 m radius in 10 s time steps. Preliminary trajectories using time steps from 10–300 s indicated that trajectories converged when time steps were  $\lesssim 30$  s. At each time step, the 500 m radius-averaged  $N_3$ ,  $N_{10}$ ,  $N_{\text{int}}$ , AMS mass fractions and mass spectra, and merged ROMIAC-DMA particle number size distribution were calculated. The elapsed time in the forward and backward trajectories is termed the “growth time”,  $t_{\text{growth}}$ , with the implication that this represents the time during which newly-formed particles experience changes in

size and composition.

Trajectories were also used to determine the  $t_{\text{growth}}$  corresponding to the minimum  $N_{\text{int}}$  upwind of Harris Ranch and the maximum value of  $N_{\text{int}}$  downwind of Harris Ranch, in order to identify the AMS mass spectra that were measured at locations along the trajectory between this range of  $t_{\text{growth}}$ ; these AMS mass spectra are considered to be “in-plume”, but not yet affected by dilution that occurs farther downwind of Harris Ranch and reduces  $N_{\text{int}}$ . Background mass spectra were identified as those collected above 1000 m AMSL prior to descending on Harris Ranch, or those measured upwind of the source. These in-plume and background mass spectra were then compared to identify which species are enhanced in the plume.

### Growth Rate

After obtaining the time evolution of the particle number size distribution as a function of growth time, the size distributions were divided into two parts, namely the nucleation mode and the background population, which consists of particles larger than those assigned to the nucleation mode. The boundary between the nucleation and background populations was chosen by hand such that the observed mode emerging in the smallest sizes was tightly contained in the nucleation mode as those fine particles grew.

The observed particle growth rate of the newly-formed particle mode,  $dD_p/dt$ , was estimated by two methods: 1) by fitting a lognormal distribution to each nucleation mode of the size distribution to obtain the mode-fitted total growth rate,  $GR_{\text{tot,fit}}$  (Dal Maso et al. 2005), and 2) by calculating the count-mean diameter of the nucleation mode part to obtain the count-mean-diameter (CMD) total growth rate,  $GR_{\text{tot,CMD}}$  (Leppä, Anttila, et al. 2011). Both of these methods estimate the growth rate of the average diameter of the growing mode, including all the processes that change the shape of the growing mode; the resulting  $GR_{\text{tot,fit}}$  and  $GR_{\text{tot,CMD}}$  values were comparable, as will be shown below.

The total growth rate, described by  $GR_{\text{tot,fit}}$  and  $GR_{\text{tot,CMD}}$ , results from the contribution of several mechanisms. These mechanisms include coagulation within the nucleation mode, loss of nucleation mode particles by coagulation with background particles, and growth of new particles into the nucleation mode size range by gas-to-particle conversion. The effect of the new particle formation is opposite to that of coagulation scavenging, as the former introduces new particles into the smallest size range, while the latter depletes the smallest particles more effectively

than larger ones. The former mechanism decreases the mean diameter by adding particles to the lower end of the nucleation mode; the rapid depletion of the smallest particles by coagulation scavenging increases the mean diameter. Comparing these two processes, we can safely assume that the particle sources are greater than sinks *only when* the concentration of particles in the nucleation mode is *increasing*. To estimate a lower bound of growth rate due to condensation,  $GR_{\text{cond}}$ , we calculated  $GR_{\text{tot,fit}}$ ,  $GR_{\text{tot,CMD}}$  and the maximum growth rate due to self-coagulation,  $GR_{\text{S-C}}$ , using data from the period of increasing particle concentration in the nucleation mode. Particle charges were taken into account when calculating  $GR_{\text{S-C}}$  (Leppä, Anttila, et al. 2011). The values of  $GR_{\text{cond,fit}}$  and  $GR_{\text{cond,CMD}}$  were then calculated by subtracting  $GR_{\text{S-C}}$  from  $GR_{\text{tot,fit}}$  and  $GR_{\text{tot,CMD}}$ .

### 5.3 Results and discussion

#### Temporal analysis

##### RF18

Figure 5.4a shows the aircraft altitude and static pressure as a function of local time. The Twin Otter arrived at Harris Ranch at about 8:25 LT, descending from ~1000 m AMSL and maintaining an altitude of ~430 m AMSL for about 2 hr, then ascended to 540 m AMSL for about 1.5 hr before returning to Monterey. The plume analysis period was restricted to 8:30–11:30 LT. The AGL altitude during the analysis period varied from 130–440 m AGL due to sampling near the edges of the Diablo Mountain range.

A vertical profile was obtained at the beginning and end of the analysis period, shown in Fig. 5.4a. Figures 5.4b-d show the potential temperature, relative humidity, and  $N_3$  concentrations as a function of AGL altitude during RF18. The profiles indicate a well-mixed boundary layer 340 m thick at the start of the sampling time and growing to 540 m thick at the end.

Figure 5.5a shows the particle number size distribution for RF18. Initial transects of the particle plume near the feedlot appear as narrow-diameter-range bands of high concentrations for  $D_Z < 10$  nm. Later plume transects further downwind of the feedlot show broader-diameter-range bands of high particle concentrations for  $D_Z < 20$  nm, as well as a larger mode in the  $20 < D_Z < 30$  nm, suggesting particle growth occurring as the plume ages. Two persistent background modes were observed in RF18, one at  $35 < D_Z < 70$  nm and the other at  $150 < D_Z < 250$  nm.

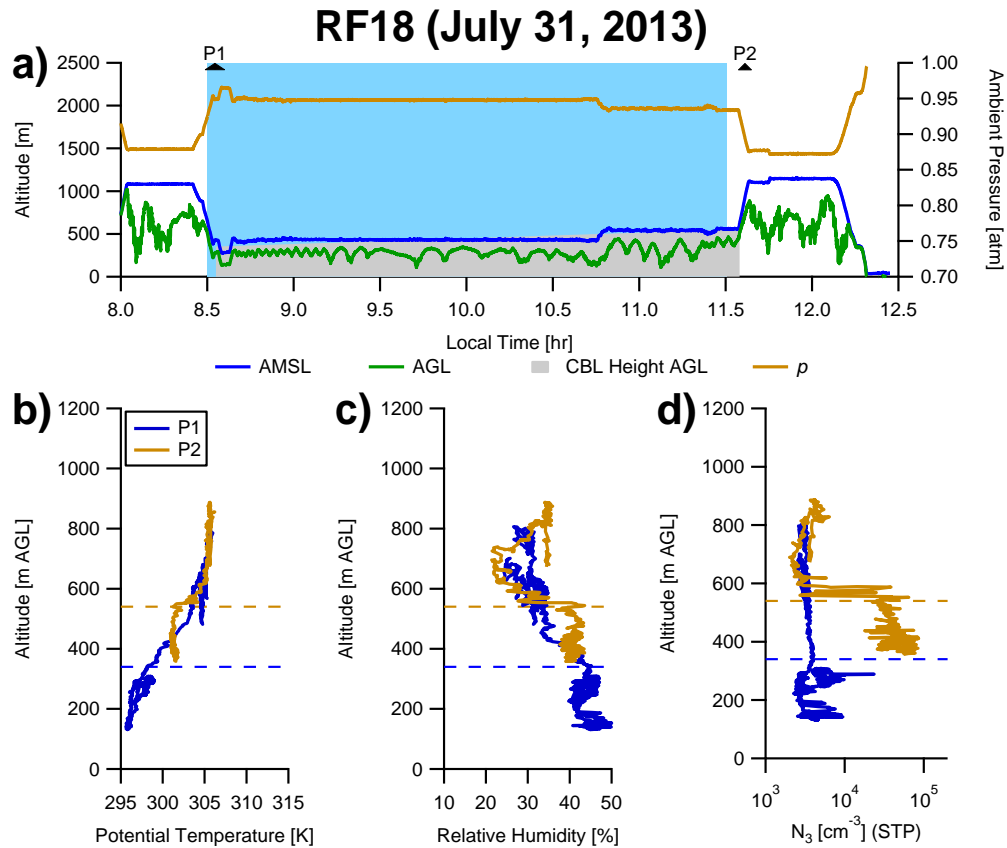


Figure 5.4: a) RF18 time series of altitude and pressure. The light blue area represents the time span of detailed plume analysis. The tags P1 and P2 indicate vertical profiles used for convective boundary layer height analysis. b) Vertical profile of potential temperature. c) Vertical profile of relative humidity. d) Vertical profile of  $N_3$  concentrations. The dashed lines in the bottom three subfigures indicate the CBL thickness corresponding to P1 and P2. The light gray region in subfigure (a) represents the CBL thickness interpolated between those determined from the vertical profiles.

The total particle number concentrations measured are shown in Fig. 5.5b. Just upwind of the cattle lot,  $N_{10}$  and  $N_3$  values were both  $\sim 3 \times 10^3 \text{ cm}^{-3}$ , but downwind concentrations of the two measures diverged, with  $N_{10}$  values  $\sim 2 \times 10^4 \text{ cm}^{-3}$  and  $N_3$  values saturating at  $1 \times 10^5 \text{ cm}^{-3}$ . It should be noted that the cabin TSI 3025 UCPC saturates at concentrations of  $1 \times 10^5 \text{ cm}^{-3}$ , and thus under reports particle concentrations above that level. The  $N_{\text{int}}$  concentration measurements do not suffer from such a limitation, showing total particle number concentrations as high as  $2 \times 10^5 \text{ cm}^{-3}$ . The cabin CPC difference values ( $N_{3-10}$ ) are a measure of nucleation mode particle concentrations. High nucleation mode particle concentrations occur immediately downwind of the cattle lot, exceeding  $N_{10}$  concentrations by about a factor of 4.

Figure 5.5c shows the measured non-refractory species mass fractions in the aerosol phase. While there is relatively little temporal variation in  $f_{\text{SO}_4}$  and  $f_{\text{NH}_4}$ , there is very clear  $f_{\text{NO}_3}$  enhancement (up to  $\sim 0.15 - 0.20$ ) and  $f_{\text{Org}}$  depletion coincident with periods of high particle concentrations inside the plume. Nonetheless, the aerosol mass fraction over the Harris Ranch area is dominated by  $f_{\text{Org}}$ , from  $\sim 0.65$  in-plume to  $\sim 0.80$  outside the plume.

## RF21

Time traces of aircraft altitude and pressure are shown in Fig. 5.6a. The aircraft transited the Diablo Range at  $\sim 1000 \text{ m AMSL}$  and descended on Harris Ranch at about 11:00 LT; it then maintained an altitude of  $\sim 450 \text{ m AMSL}$  for nearly the entire plume sampling period, with brief sampling period at  $\sim 780 \text{ m AMSL}$  for 0.5 hr before returning to Monterey. The altitude during the sampling period varied from 100–550 m AGL.

The plume analysis period for RF21 was later in the day than for RF18, from 11:00–14:00 LT, allowing the CBL to develop to greater thickness. Four vertical profiles were taken during the sampling period, though the CBL thickness was ambiguous from measurements for profile P3. Figures 5.6b-d show the development of the CBL thickness from 300 to 630 m, determined from changes in potential temperature, relative humidity, and  $N_3$  concentrations.

The particle number size distribution for RF21 is shown in Fig. 5.7a. As in RF18, narrow-diameter-range bands of high particle concentrations were observed early in the sampling period during transects near the feedlot; in transects farther downwind from the source, the size distributions in high-concentration observations

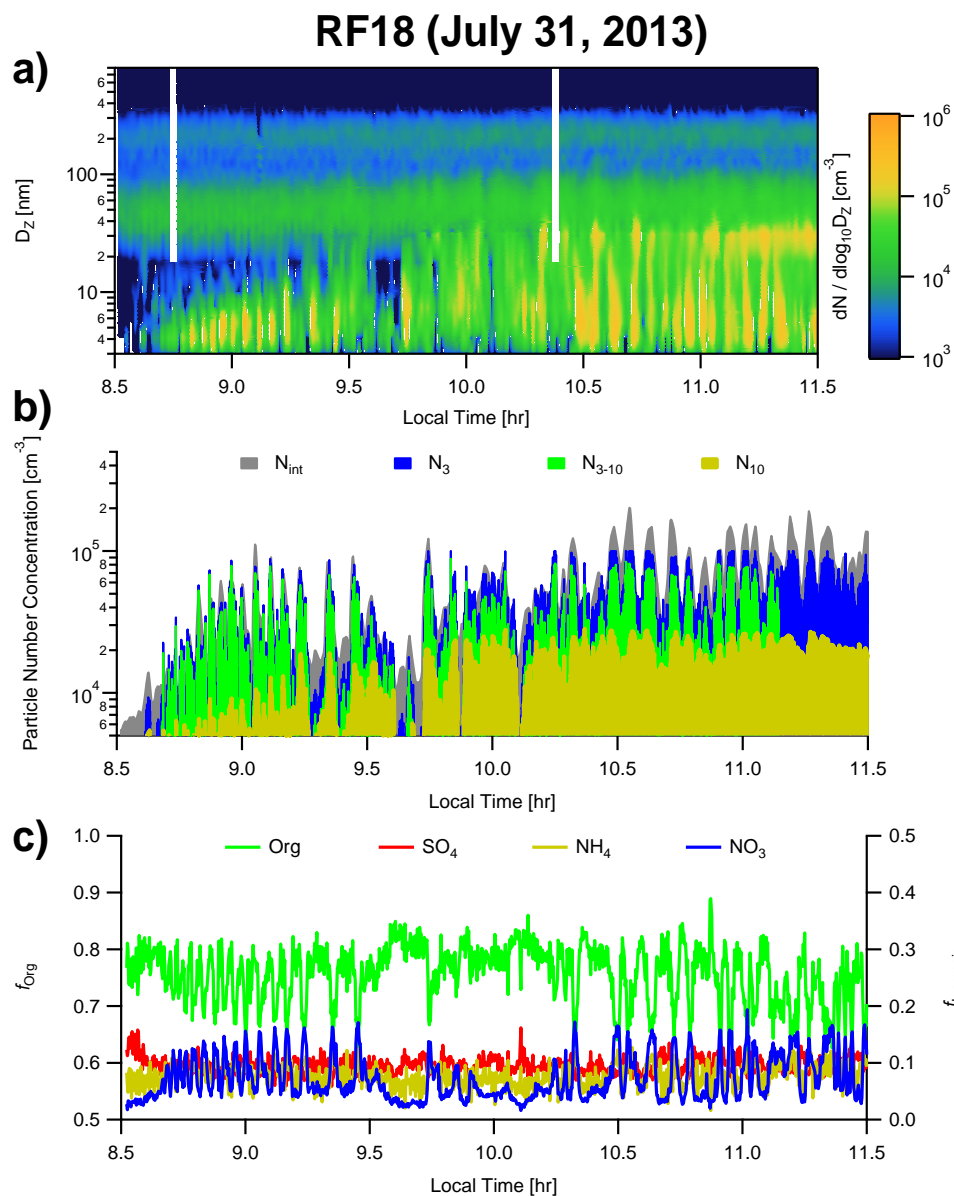


Figure 5.5: a) RF18 time series of particle number size distribution. White areas indicate missing data from the DMA. b) Total particle number concentration measured with cabin CPCs and integrated particle number size distribution. c) Non-refractory mass fraction of species in aerosol phase measured by the AMS. Inorganic species are plotted against the right-side axis.

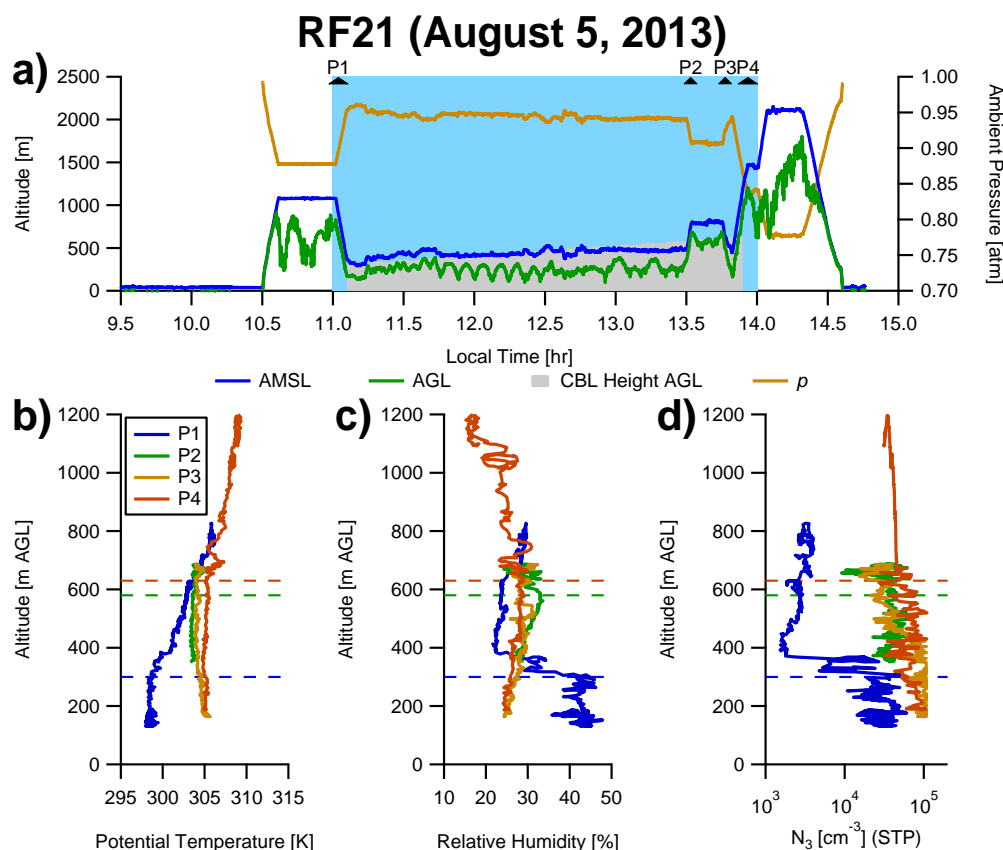


Figure 5.6: a) RF21 time series of altitude and pressure. The light blue area represents the time span of detailed plume analysis. The tags P1–P4 indicate vertical profiles used for convective boundary layer height analysis. b) Vertical profile of potential temperature. c) Vertical profile of relative humidity. d) Vertical profile of  $N_3$  concentrations. The dashed lines in the bottom three subfigures indicate the CBL thickness corresponding to P1, P2, and P4. The light gray region in subfigure (a) represents the CBL thickness interpolated between those determined from the vertical profiles.



broadened. Unlike RF18, a high-concentration background aerosol was observed with two modes, one at  $D_Z \approx 30$  nm, and another at  $D_Z \approx 150$  nm, throughout RF21. These background modes broadened as the flight progressed. The DMA stopped recording data at 12:40 LT for unknown reasons, resulting in missing size distribution information for the background modes late in the flight.

Figure 5.7b shows the total number concentrations measured during RF21. The  $N_{10}$  concentrations were relatively stable at  $\sim 2.5 \times 10^4 \text{ cm}^{-3}$  throughout the sampling period; nearly all the additional particles measured downwind of Harris Ranch were nucleation mode particles. Again, the TSI 3025 UCPC saturated at the very high particle concentrations; the integrated particle number size distributions indicated total particle concentrations of at least  $6 \times 10^5 \text{ cm}^{-3}$ .

The time series of non-refractory species mass fraction in Fig. 5.7c is similar to that from RF18.  $f_{\text{SO}_4}$  and  $f_{\text{NH}_4}$  do not display a clear correlation with in-plume measurements. Again,  $f_{\text{NO}_3}$  is enhanced in-plume ( $\sim 0.15$ ) while  $f_{\text{Org}}$  is depleted in-plume (down to 0.65) relative to outside the plume ( $\sim 0.82$ ).

## Spatial analysis

### Particle concentration

Figure 5.8a-c show the spatial distribution of  $N_3$ ,  $N_{10}$ , and  $N_{3-10}$  measurements, respectively, for RF18, after removing points that were acquired above the CBL thickness. The  $N_{10}$  measurements in Fig. 5.8b show a large region of high particle concentrations ( $\sim 2 \times 10^4 \text{ cm}^{-3}$ ) southwest of Harris Ranch, with additional spots of high concentrations east and southeast of the feedlot. However, Figs. 5.8a and 5.8c show that the NPF region is immediately southwest of Harris Ranch with  $N_{3-10}$  concentrations of  $\sim 1 \times 10^5 \text{ cm}^{-3}$ .

The spatial distributions of total particle concentrations for RF21, which were acquired later in the day than in RF18, show a much clearer plume of high-concentration  $N_3$  and  $N_{3-10}$  measurements ( $\sim 6 \times 10^5 \text{ cm}^{-3}$ ; Figs. 5.8d and 5.8f). The NPF plume in RF21 is more distinct than in RF18 owing to consistently-oriented winds, as will be discussed below.

### Particle composition

The spatial distributions of non-refractory species mass fraction measured by the AMS are shown in Fig. 5.9. As noted above,  $f_{\text{Org}}$  was depleted in regions with high

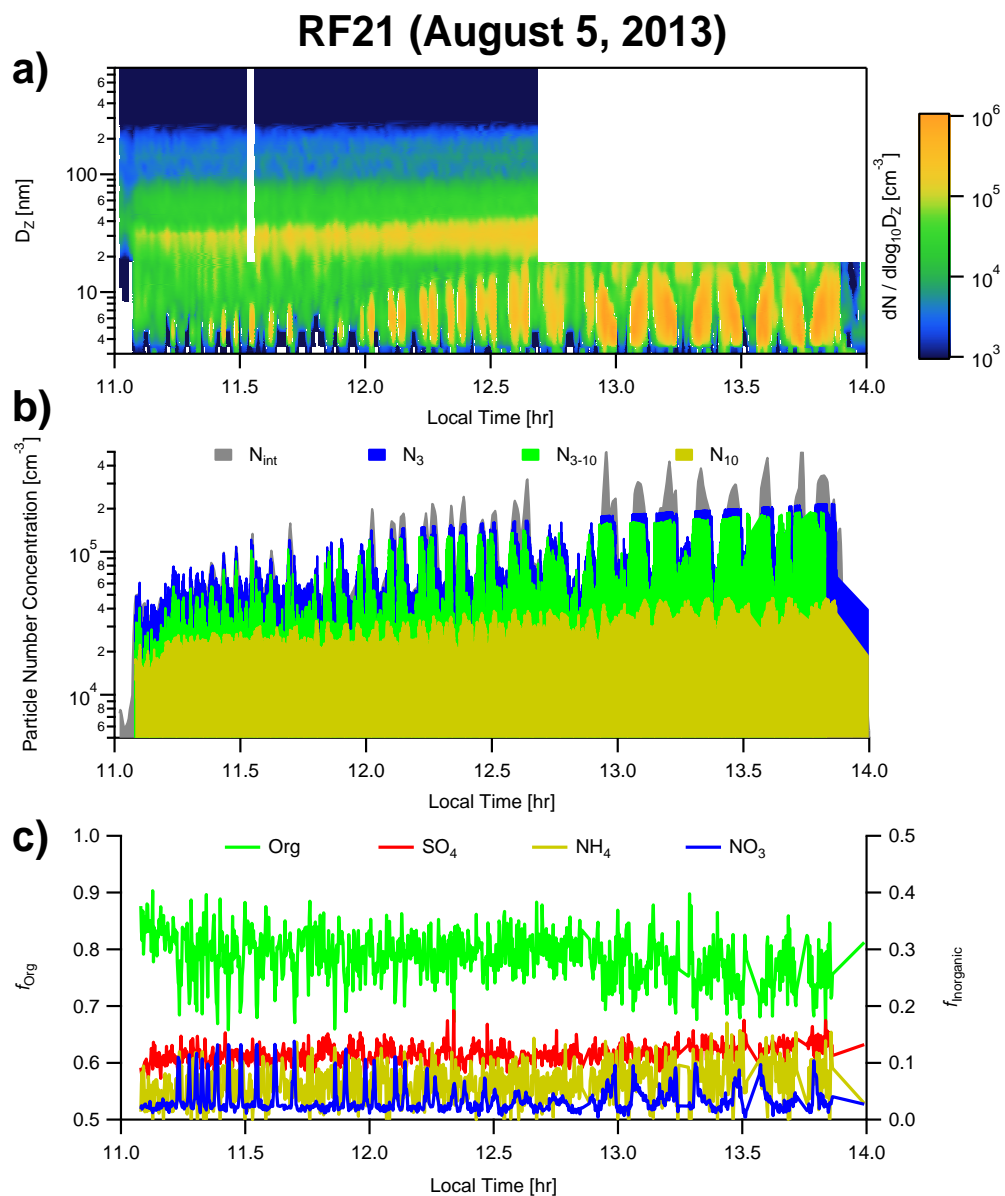


Figure 5.7: a) RF21 time series of particle number size distribution. White areas indicate missing data from the DMA. b) Total particle number concentration measured with cabin CPCs and integrated particle number size distribution. c) Non-refractory mass fraction of species in aerosol phase measured by the AMS. Inorganic species are plotted against the right-side axis.

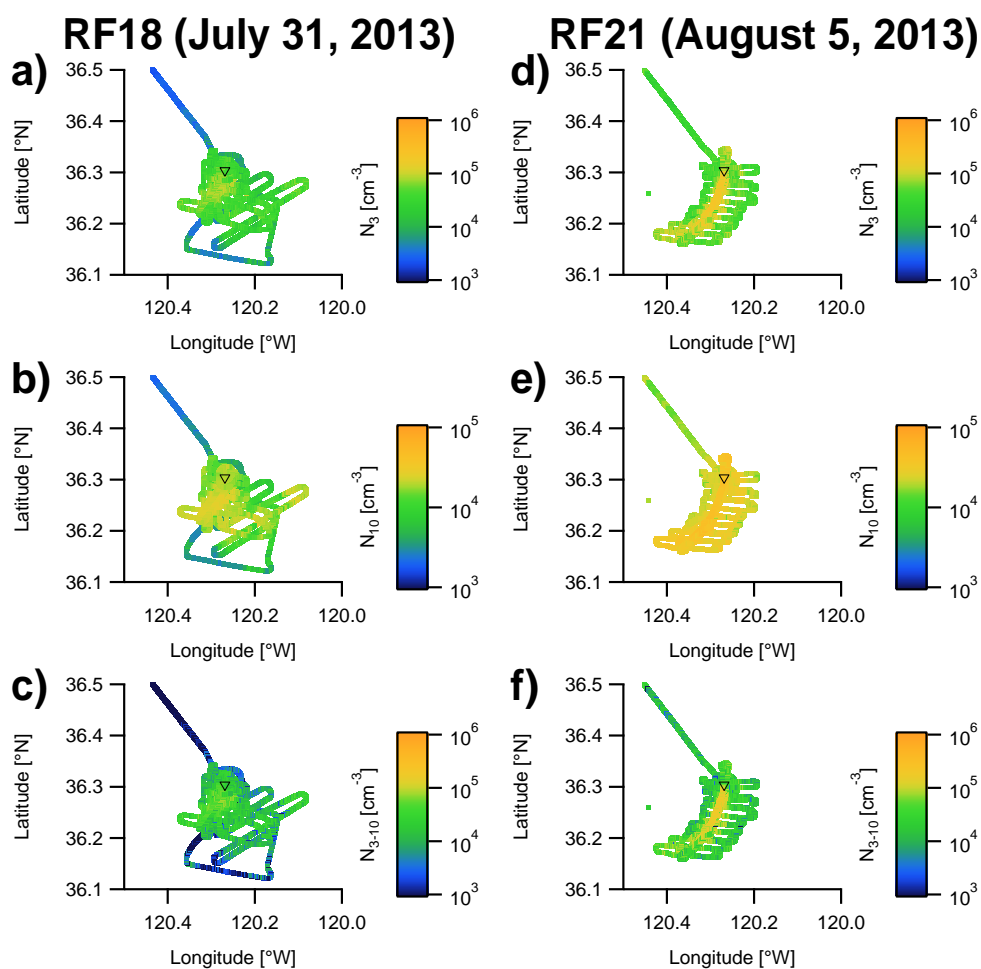


Figure 5.8: Spatial distribution of total particle concentration measurements below the CBL thickness from cabin CPCs. The triangle marker indicates the location of Harris Ranch. a) RF18  $N_3$  concentrations. b) RF18  $N_{10}$  concentrations. c) RF18  $N_{3-10}$  concentrations. d) RF21  $N_3$  concentrations. e) RF21  $N_{10}$  concentrations. f) RF21  $N_{3-10}$  concentrations.

concentrations of nucleation mode particles (Figs. 5.8c and 5.8f; Figs. 5.9a and 5.9e), while  $f_{\text{NO}_3}$  was enriched (Figs. 5.9c and 5.9g). While the temporal variation of  $f_{\text{NH}_4}$  is ambiguous from Figs. 5.5c and 5.7c, the spatial distribution of  $f_{\text{NH}_4}$  shown in Figs. 5.9d and 5.9h suggest in-plume enhancement of  $f_{\text{NH}_4}$  in the particle phase. The association of particle phase  $f_{\text{SO}_4}$  remains unclear in the spatial analysis, as  $f_{\text{SO}_4}$  appears to be relatively depleted in the plume in RF18 (Fig. 5.9b) while relatively enriched in the RF21 plume (Fig. 5.9f).

“Background” AMS organic species spectra were identified as those obtained at  $\sim 1000$  m AMSL or those upwind of Harris Ranch. “In-plume” AMS organic species spectra were identified as those downwind of Harris Ranch and along the plume centerline. Figure 5.10 compares average background and in-plume spectra for both flights. The averaged background and in-plume spectra were similar for both flights, with a noticeable enhancement of the signal at  $m/z = 30$ ; this is a marker for both the  $\text{NO}_3$  fragment and amine fragments. Though it is unclear how much amines contribute to the  $m/z = 30$  enhancement in these flights, past literature strongly supports the presence of amines in the downwind emissions from Harris Ranch (Sorooshian et al. 2008).

It is important to note that the AMS measurements capture the ensemble-averaged bulk composition of particles from 50–800 nm, but not those in the nucleation mode. Thus, the composition of nucleation mode particles might be unrelated to that of the larger background mode particles. However, at a minimum, the AMS measurements suggest that nitric acid and ammonia vapor might contribute to the formation and growth of nucleation mode particles. The relative depletion of organics in the plume measurements may suggest that species such as amines do not participate in new particle formation and growth, but it is also possible that amines could drive the initial formation of stable clusters with nitric acid vapors (despite the concentration of amines being typically 2–3 orders of magnitude less than ammonia); farther downwind, ammonia could become the dominant, condensing, basic species once the clusters have grown sufficiently large that the basicity of amines no longer has a competitive advantage over the abundance of ammonia. In other words, amines may be the initial activators in forming clusters with nitric acid, but ammonia dominates particle growth after cluster stability is achieved.

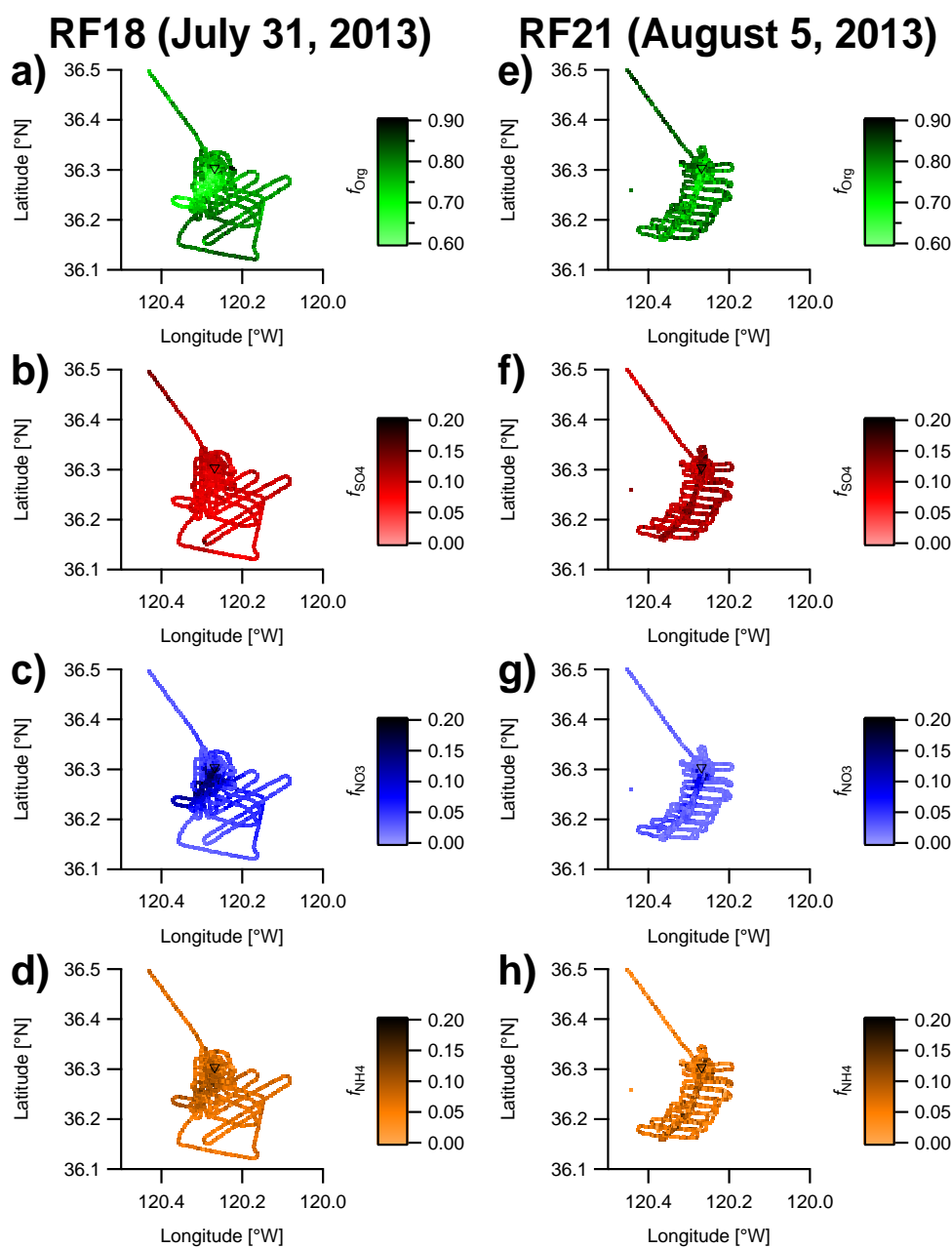


Figure 5.9: Spatial distribution of particle phase non-refractory species mass fractions. The triangle marker indicates the location of Harris Ranch. a) RF18  $f_{\text{Org}}$ . b) RF18  $f_{\text{SO}_4}$ . c) RF18  $f_{\text{NO}_3}$ . d) RF18  $f_{\text{NH}_4}$ . e) RF21  $f_{\text{Org}}$ . f) RF21  $f_{\text{SO}_4}$ . g) RF21  $f_{\text{NO}_3}$ . h) RF21  $f_{\text{NH}_4}$ .

RF18 (July 31, 2013)

RF21 (August 5, 2013)

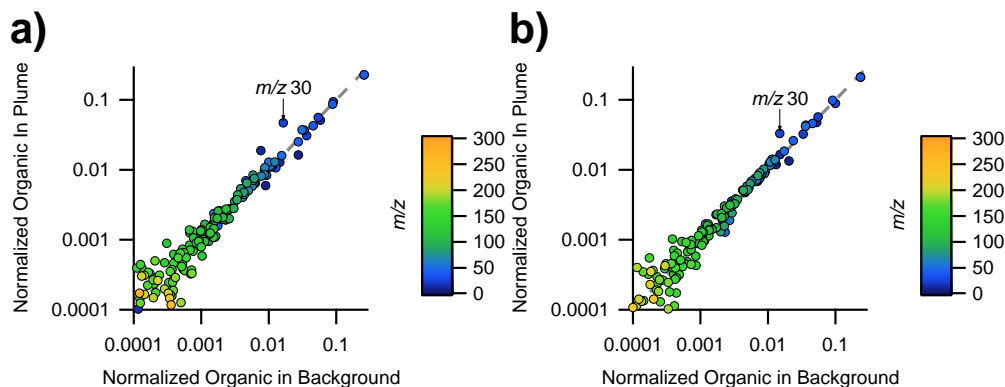


Figure 5.10: Averaged in-plume AMS organic spectra against the averaged background AMS organic spectra for a) RF18 and b) RF21. The dashed gray line is a one-to-one reference line.

### Growth time analysis

#### Micro-meteorological trajectories

Wind speed and direction measurements from the Twin Otter were used to model the likely trajectory of an air parcel passing directly over Harris Ranch. Figure 5.11 shows wind speed and direction quiver plots for both flights. Winds during RF21 were generally faster and more directionally-consistent, especially immediately downwind of the feedlot. The air parcel trajectory for RF18 likely originated from northeast of the feedlot, while that for RF21 originated from north of the feedlot. In both flights, the trajectory carried the air parcel southwest from Harris Ranch, which is consistent with the location of high  $N_{3-10}$  concentrations in Figs. 5.8c and 5.8f.

#### Growth time representation of particle concentrations and composition

The transit time downwind from Harris Ranch is the time available for particle formation and growth to occur, or so-called “growth time”. The portion of trajectories southwest of Harris Ranch represent air parcels associated with the new emissions, and have positive growth times, while the remaining portion of trajectories north of Harris Ranch represent air parcels that have yet to come into contact with Harris Ranch emissions, and have negative growth times.

The particle number concentrations recorded along the trajectories are shown in

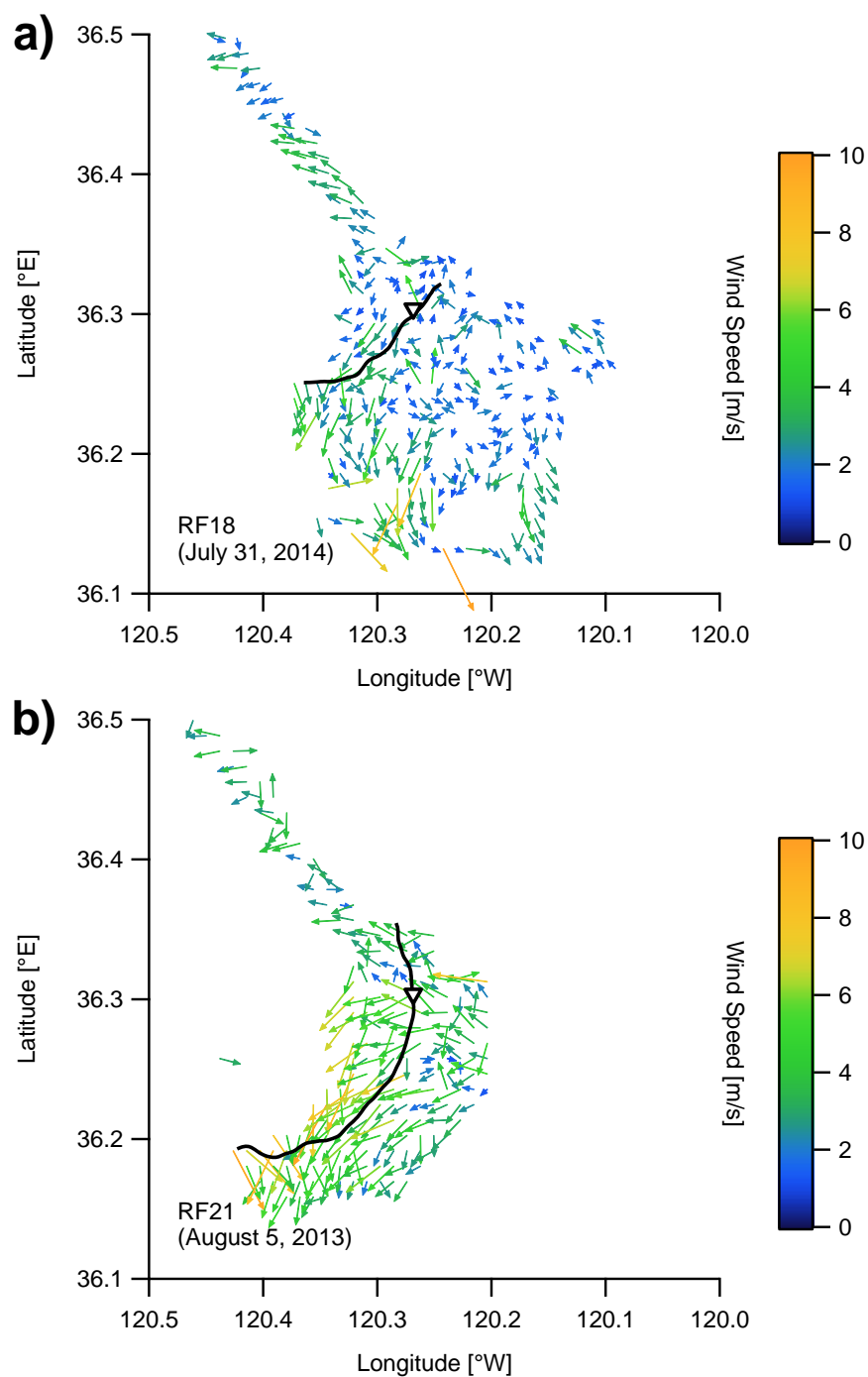


Figure 5.11: Arrow maps of wind direction and speed over Harris Ranch as measured by the Twin Otter for a) RF18 and b) RF21. Arrow lengths qualitatively describe wind speed. The triangle marker indicates the location of Harris Ranch. The black line indicates the trajectory of an air parcel passing directly over Harris Ranch, derived from interpolation of nearby wind directions and speeds.

Figs. 5.12a and 5.12c. A sudden increase in particle concentration suggests the influence of the feedlots emissions on the air parcel trajectory, which appears to occur at -0.25 hr in RF18 and at 0 hr in RF21. The negative growth time for the appearance of new particles in RF18 results from variable and slow winds that transported some particles upwind of Harris Ranch. In both flights,  $N_{10}$  shows only a  $\sim 20\%$  increase in concentration after passing over Harris Ranch, but  $N_3$ ,  $N_{3-10}$ , and  $N_{\text{int}}$  show 2- to 3-fold increases in concentration in RF18 and 3- to 10-fold increases in RF21. The difference in the magnitudes of the increases may be due to temporal variation in emissions from cattle feedlots between morning and afternoon, solar radiation and oxidation of organic species enhancing NPF and growth, or the more consistent winds in the latter flight.

The relative weakness of the NPF event in RF18 is evident in the relatively stable integrated particle volume concentration during this flight (Fig. 5.12b). In contrast, the particle volume and surface area concentration increases in RF21 (Fig. 5.12e) show that condensational growth and scavenging of nucleation mode particles by larger background particles were substantial, resulting in a total volume concentration increase of 50% and total surface area concentration increase of 66%.

The mass fractions recorded along the trajectories are shown in Figs. 5.12c and 5.12f. In both flights,  $f_{\text{Org}}$  decreased and  $f_{\text{NO}_3}$  increased immediately downwind of Harris Ranch, then relaxed toward pre-feedlot values farther downwind owing to dilution effects or changing favorability of vapor condensation due to plume aging. That condensation of nitric acid is so heavily favored over condensation of organic species immediately downwind of the feedlot suggests that high basicity species such as amines are responsible. The values of both  $f_{\text{SO}_4}$  and  $f_{\text{NH}_4}$  did not appear to vary much as a function of growth time.

### Particle growth rates

Figure 5.13 shows the growth time representation of the particle number size distribution along the trajectories shown in Figs. 5.11a-b. In each flight, NPF is evident in the nucleation mode. Background aerosol observed in both flights show a mode at  $D_Z \approx 30$  nm. A second mode in the background aerosol appears at  $D_Z \approx 200$  nm in RF18 and at  $D_Z \approx 150$  nm in RF21. RF18 has higher number concentrations in the larger background mode than does RF21, while RF21 has higher number concentrations in the nucleation and smaller background modes.

The total growth rate,  $\text{GR}_{\text{tot}}$ , calculated from the mode-fitting (solid black line in



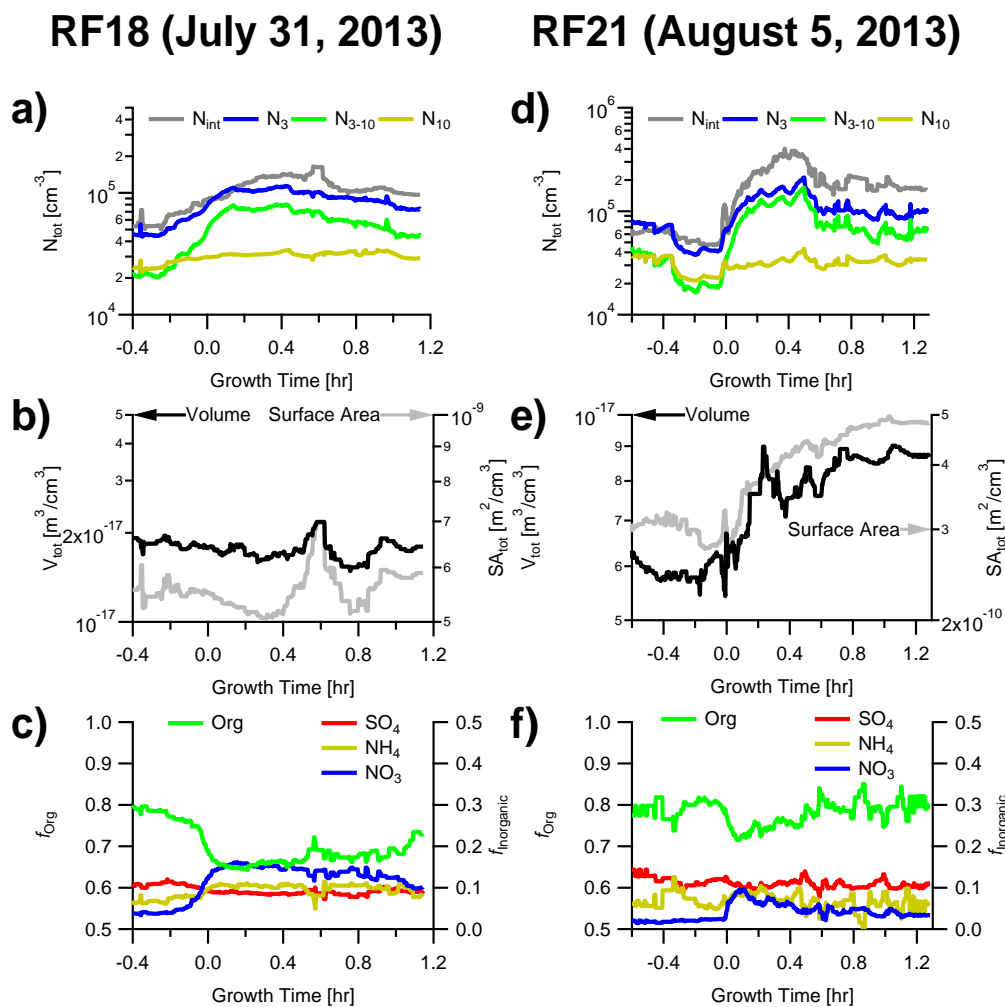


Figure 5.12: Particle concentrations and composition recorded along a micrometeorology-driven trajectory over Harris Ranch. a) RF18 total particle number concentrations. b) RF18 total particle volume and surface area concentrations. c) RF18 non-refractory species particle mass fractions. d) RF21 total particle number concentrations. e) RF21 total particle volume and surface area concentrations. f) RF21 non-refractory species particle mass fractions.

Figs. 5.13a-b) and from the CMD (solid gray line in Figs. 5.13a-b) methods give very similar values, as evident from the near superposition of both lines. For RF18,  $GR_{tot} = 3.7\text{--}3.8$  nm/hr. The maximum growth rate due to self-coagulation,  $GR_{S-C}$ , during the period of increasing nucleation mode particle concentration is 0.5 nm/hr. Thus, the lower bound on the condensational growth rate,  $GR_{cond}$ , in RF18 was 3.2–3.3 nm/hr. Similarly, in RF21 the total growth rate is 3.9–4.2 nm/hr. However, because of the higher nucleation mode particle concentrations, the maximum  $GR_{S-C}$  is 2 nm/hr, putting the lower bound on  $GR_{cond}$  in RF21 at 1.9–2.2 nm/hr. The  $GR_{tot}$  values and lower bounds on  $GR_{cond}$  are consistent with growth rates observed in the CBL in rural environments by others in a review by Kulmala, Vehkamäki, et al. (2004), though it is unclear whether the growth rates reported in many other studies are total or condensational growth rates.

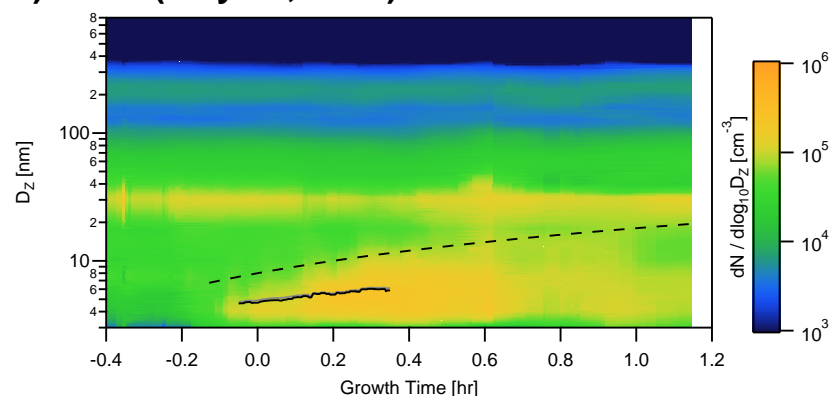
### Future work and limitations

Following the methods of other studies (Kulmala, Dal Maso, et al., 2001; Verheggen and Mozurkewich, 2002; Brock et al., 2011), it should be possible to determine a nucleation rate and condensable vapor concentration from the particle number size distributions alone. However, numerous assumptions would be required of the properties of the condensing vapors in this study, as there were no gas-phase measurements in this study that would lend support to such assumptions. Incorporating AMS calibration factors into the data analysis would allow for absolute mass concentrations from the background particle composition data, which could provide further support for assumptions made of condensing vapors. For future field studies, vapor measurements are necessary, as well as direct measurement of the composition of nucleation mode particles to allow for the most defensible conclusions on the condensing vapor species, such as via online thermal desorption chemical ionization mass spectrometry for sub-20 nm particles, as was done by Smith, Moore, et al. (2004).

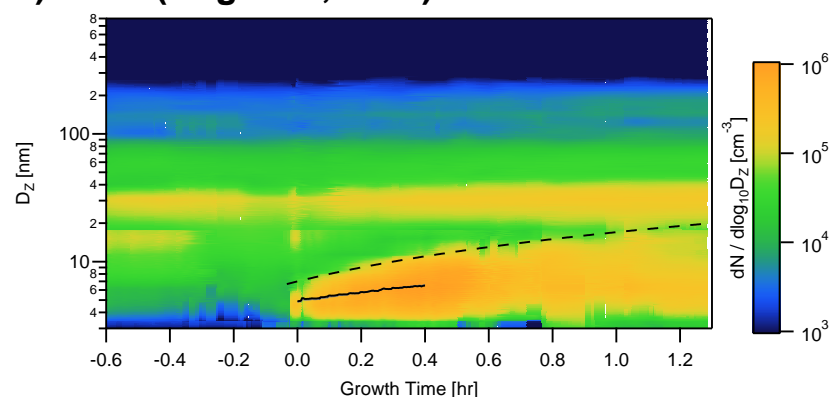
## 5.4 Conclusions

This study reports airborne-measured size distributions and concentrations of particles from 3 nm to 800 nm in diameter, as well as non-refractory species mass fraction of particles from 50 nm to 800 nm, immediately downwind of Harris Ranch, a large cattle feedlot in California. Two separate morning and afternoon flights revealed differences in NPF intensity and concentrations, but similarities in effects on composition on the background mode particles.

**a) RF18 (July 31, 2013)**



**b) RF21 (August 5, 2013)**



**c)**

|                            | RF18            |            | RF21            |            |
|----------------------------|-----------------|------------|-----------------|------------|
|                            | <i>Mode Fit</i> | <i>CMD</i> | <i>Mode Fit</i> | <i>CMD</i> |
| $GR_{tot}$                 | 3.8             | 3.7        | 3.9             | 4.2        |
| $GR_{S-C} (max)$           | 0.5             | 0.5        | 2               | 2          |
| $GR_{cond} (lower\ bound)$ | 3.3             | 3.2        | 1.9             | 2.2        |

(All growth rate values have units of nm/hr)

Figure 5.13: Growth time representation of the particle number size distribution for a) RF18 and b) RF21. The dashed line demarcates the boundary between nucleation mode and background mode particles for the purposes of growth rate analysis. The solid black line indicates the diameter used for growth rate calculations in the mode-fitting method while the solid gray line indicates the diameter used for growth rate calculation in the count mean diameter method; the two methods give very similar results, making the two methods appear to be superimposed on each other. c) Summary table of the total growth rates ( $GR_{tot}$ ), self-coagulation growth rates ( $GR_{S-C}$ ), and condensation growth rates ( $GR_{cond}$ ) determined for both flights using both the mode-fit and count-mean-diameter (CMD) growth rate determination methods.

Micrometeorology-driven trajectories of air parcels directly over Harris Ranch demonstrate that its emissions can result in an order of magnitude increase of total particle number concentration. Moreover, the composition of the background mode particles in the plume downwind from the feedlot suggests increased condensation of nitric acid vapor, which may be caused by the presence of a highly basic vapors in the plume, such as amines. Growth rate calculations on the trajectory-derived particle number size distribution indicate total growth rates of  $\sim 4$  nm/hr, with a lower bound of  $\sim 2 - 3$  nm/hr growth due to condensation.

## 5.5 Acknowledgments

We thank the crew members from Zivko Aeronautics: Brian Angiolillo, Greg Cooper, Marko Jaakkola, and Bryce Kujat; and from CIRPAS: Jesus Galvan, Nava Roy, and Roy K. Woods for their work in integrating instruments into the Twin Otter, piloting the aircraft, providing guidance on research flight itineraries, and troubleshooting and repairing instruments and related software. We also thank Lindsay Maudlin, Gouri Prabhakar, Armin Sorooshian, and Zhen Wang of the University of Arizona for their scientific collaboration and guidance during the NICE campaign. Additional thanks is extended to Kelvin Bates, Andrew Metcalf, Christina Williamson, and Xuan Zhang for helpful discussions regarding data analysis. This research was supported by National Science Foundation Grant No. CBET-1236909 and a National Science Foundation Graduate Research Fellowship under Grant No. DGE-1144469 (W.M.), by the Magnus Ehrnrooth Foundation, the Jane and Aatos Erkkö Foundation, and the Emil Aaltonen Foundation (J.L.).

## References

- Bluth, R. T. et al. (1996). "Center for Interdisciplinary Remotely-Piloted Aircraft Studies (CIRPAS)". In: *B. Am. Meteorol. Soc.* 77.11, pp. 2691–2699.
- Brock, C. A. et al. (2011). "Formation and growth of organic aerosols downwind of the Deepwater Horizon oil spill". In: *Geophys. Res. Lett.* 38.17, p. L17805. doi: 10.1029/2011GL048541.
- Dal Maso, M. et al. (2005). "Formation and growth of fresh atmospheric aerosols: Eight years of aerosol size distribution data from SMEAR II, Hyytiälä, Finland". In: *Boreal Environ. Res.* 10.5, pp. 323–336.
- Drewnick, F. et al. (2005). "A new time-of-flight aerosol mass spectrometer (TOF-AMS)—instrument description and first field deployment". In: *Aerosol Sci. Technol.* 39.7, pp. 637–658. doi: 10.1080/02786820500182040.
- Dunne, E. M. et al. (2016). "Global particle formation from CERN CLOUD measurements". In: *Science* 354.6316, pp. 1119–1124. doi: 10.1126/science.aaf2649.
- Erupe, M. E., A. A. Viggiano, and S.-H. Lee (2011). "The effect of trimethylamine on atmospheric nucleation involving H<sub>2</sub>SO<sub>4</sub>". In: *Atmos. Chem. Phys.* 11.10, pp. 4767–4775. doi: 10.5194/acp-11-4767-2011.
- Ge, X., A. S. Wexler, and S. L. Clegg (2011). "Atmospheric amines - Part I. A review". In: *Atmos. Env.* 45.3, pp. 524–546. doi: 10.1016/j.atmosenv.2010.10.012.
- Hegg, D. A. et al. (2005). "Determination of the transmission efficiency of an aircraft aerosol inlet". In: *Aerosol Sci. Technol.* 39.10, pp. 966–971. doi: 10.1080/02786820500377814.
- Hutchinson, G. L., A. R. Mosier, and C. E. Andrew (1982). "Ammonia and amine emissions from a large cattle feedlot". In: *J. Environ. Qual.* 11.2, pp. 188–293.
- IPCC (2013). *Climate change 2013: The physical science basis. Contribution of Working Group I to the Fifth Assessment report of the Intergovernmental Panel on Climate Change*. Ed. by T. F. Stocker et al. Cambridge, UK and New York, NY, USA: Cambridge University Press, p. 1535.
- Kalogiros, J. A. and Q. Wang (2002). "Calibration of a radome-differential GPS system on a twin otter research aircraft for turbulence measurements". In: *J. Atmos. Ocean Tech.* 19.2, pp. 159–171. doi: 10.1175/1520-0426(2002)019<0159:COARDG>2.0.CO;2.
- Kulmala, M., M. Dal Maso, et al. (2001). "On the formation, growth and composition of nucleation mode particles". In: *Tellus B* 53.4, pp. 479–490.
- Kulmala, M. and V.-M. Kerminen (2008). "On the formation and growth of atmospheric nanoparticles". In: *Atmos. Res.* 90.2, pp. 132–150. doi: 10.1016/j.atmosres.2008.01.005.

- Kulmala, M., I. Riipinen, et al. (2007). “Toward direct measurement of atmospheric nucleation”. In: *Science* 318.89, pp. 89–92. DOI: 10.1126/science.1144124.
- Kulmala, M., H. Vehkamäki, et al. (2004). “Formation and growth rates of ultrafine atmospheric particles: a review of observations”. In: *J. Aerosol Sci.* 35.2, pp. 143–176. DOI: 10.1016/j.jaerosci.2003.10.003.
- Kurten, T. et al. (2008). “Amines are likely to enhance neutral and ion-induced sulfuric acid-water nucleation in the atmosphere more effectively than ammonia”. In: *Atmos. Chem. Phys.* 8.14, pp. 4095–4103. DOI: 10.5194/acpd-8-7455-2008.
- Leppä, J., T. Anttila, et al. (2011). “Atmospheric new particle formation: Real and apparent growth of neutral and charged particles”. In: *Atmos. Chem. Phys.* 11.10, pp. 4939–4955. DOI: 10.5194/acp-11-4939-2011.
- Leppä, J., W. Mui, et al. (2017). “Charge distribution uncertainty in differential mobility analysis of aerosol”. In: *Aerosol Sci. Technol.* In review.
- López-Yglesias, X. and R. C. Flagan (2013). “Ion-aerosol attachment coefficients and the steady-state charge distribution on aerosols in a bipolar ion environment”. In: *Aerosol Sci. Technol.* 47.6, pp. 688–704. DOI: 10.1080/02786828608959073.
- Loukonen, V. et al. (2010). “Enhancing effect of dimethylamine in sulfuric acid nucleation in the presence of water – a computational study”. In: *Atmos. Chem. Phys.* 10.10, pp. 4961–4974. DOI: 10.5194/acp-10-4961-2010.
- Mai, H. and R. C. Flagan (2017). “Numerical simulation of a scanning DMA transfer function”. In: *Aerosol Sci. Technol.* In prep.
- Makkonen, R. et al. (2012). “Air pollution control and decreasing new particle formation lead to strong climate warming”. In: *Atmos. Chem. Phys.* 12.3, pp. 1515–1524. DOI: 10.5194/acp-12-1515-2012.
- Merikanto, J. et al. (2009). “Impact of nucleation on global CCN”. In: *Atmos. Chem. Phys.* 9.21, pp. 8601–8616. DOI: 10.5194/acpd-9-12999-2009.
- Mui, W. et al. (2017). “Design, simulation, and characterization of a radial opposed migration ion and aerosol classifier (ROMIAC)”. In: *Aerosol Sci. Technol.* In review.
- Paasonen, P. et al. (2012). “On the formation of sulphuric acid–amine clusters in varying atmospheric conditions and its influence on atmospheric new particle formation”. In: *Atmos. Chem. Phys.* 12.19, pp. 9113–9133. DOI: 10.5194/acp-12-9113-2012.
- Pratt, K. A., L. E. Hatch, and K. A. Prather (2009). “Seasonal volatility dependence of ambient particle phase amines”. In: *Environ. Sci. Technol.* 43.14, pp. 5276–5281. DOI: 10.1021/es803189n.
- Qiu, C. and R. Zhang (2013). “Multiphase chemistry of atmospheric amines”. In: *Phys. Chem. Chem. Phys.* 15.16, pp. 5738–5752. DOI: 10.1039/c3cp43446j.

- Schade, G. W. and P. J. Crutzen (1995). "Emission of aliphatic amines from animal husbandry and their reactions: Potential source of N<sub>2</sub>O and HCN". In: *J. Atmos. Chem.* 22.3, pp. 319–346. DOI: 10.1007/BF00696641.
- Seinfeld, J. H. and S. N. Pandis (2006). *Atmospheric Chemistry and Physics: From air pollution to climate change*. 2nd. New York: John Wiley & Sons.
- Sintermann, J. et al. (2014). "Trimethylamine emissions in animal husbandry". In: *Biogeosciences* 11.18, pp. 5073–5085. DOI: 10.5194/bg-11-5073-2014.
- Smith, J. N., K. C. Barsanti, et al. (2010). "Observations of aminium salts in atmospheric nanoparticles and possible climatic implications". In: *P. Natl. Acad. Sci. USA* 107.15, pp. 6634–6639. DOI: 10.1073/pnas.0912127107.
- Smith, J. N., K. F. Moore, et al. (2004). "Atmospheric measurements of sub-20 nm diameter particle chemical composition by thermal desorption chemical ionization mass spectrometry". In: *Aerosol Sci. Technol.* 38.2, pp. 100–110. DOI: 10.1080/02786820490249036.
- Sorooshian, A. et al. (2008). "Comprehensive airborne characterization of aerosol from a major bovine source". In: *Atmos. Chem. Phys.* 8.17, pp. 5489–5520. DOI: 10.5194/acpd-8-10415-2008.
- Spracklen, D. V., K. S. Carslaw, M. Kulmala, V.-M. Kerminen, G. W. Mann, et al. (2006). "The contribution of boundary layer nucleation events to total particle concentrations on regional and global scales". In: *Atmos. Chem. Phys.* 6.12, pp. 5631–5648. DOI: 10.5194/acpd-6-7323-2006.
- Spracklen, D. V., K. S. Carslaw, M. Kulmala, V.-M. Kerminen, S.-L. Sihto, et al. (2008). "Contribution of particle formation to global cloud condensation nuclei concentrations". In: *Geophys. Res. Lett.* 35.6, p. L06808. DOI: 10.1029/2007GL033038.
- Stein, A. F. et al. (2015). "NOAA's HYSPLIT atmospheric transport and dispersion modeling system". In: *B. Am. Meteorol. Soc.* 96.12, pp. 2059–2077. DOI: 10.1175/BAMS-D-14-00110.1.
- Verheggen, B. and M. Mozurkewich (2002). "Determination of nucleation and growth rates from observation of a SO<sub>2</sub> induced atmospheric nucleation event". In: *J. Geophys. Res.* 107.D11, p. 4123. DOI: 10.1029/2001JD000683.
- Wang, M. and J. E. Penner (2009). "Aerosol indirect forcing in a global model with particle nucleation". In: *Atmos. Chem. Phys.* 9.1, pp. 239–360. DOI: 10.5194/acpd-8-13943-2008.
- Yu, F. and G. Luo (2009). "Simulation of particle size distribution with a global aerosol model: contribution of nucleation to aerosol and CCN number concentrations". In: *Atmos. Chem. Phys.* 9.20, pp. 7691–7710. DOI: 10.5194/acpd-9-10597-2009.

- Yu, F., G. Luo, et al. (2010). “Spatial distributions of particle number concentrations in the global troposphere: Simulations, observations, and implications for nucleation mechanisms”. In: *J. Geophys. Res.* 115.D17, p. D17205. doi: 10.1029/2009JD013473.



*Chapter 6*

## DEVELOPMENT AND OPERATION OF OPPOSED MIGRATION AEROSOL CLASSIFIERS (OMAC) WITH A MODERATED AEROSOL GROWTH WITH INTERNAL WATER CYCLING DETECTOR (MAGIC) FOR ENVIRONMENTAL MONITORING

By Wilton Mui, Susanne V. Hering, Amanda M. Grantz, Steven R. Spielman, and  
Richard C. Flagan

### 6.1 Introduction

The environmental impacts of aerosol particles on human health (Wilson and Spengler 1996) and climate (IPCC 2013) of aerosol particles are well-established, the widespread measurement of which necessitates scientifically-sound yet economically-appropriate instrumentation. While there currently exist many compact and inexpensive products on the market for acquiring *total* particle number concentrations, there exist few similarly affordable and lightweight options for obtaining particle number *size distributions*. Without the particle number size distribution, quantification of aerosol particle environmental impacts is ambiguous.

#### Particle inhalation exposure monitoring

Aerosol particles of diameter  $D_p < 100$  nm are referred to as “ultrafine” particles (UFP), while those in the range of  $100 \text{ nm} < D_p < 2.5 \text{ }\mu\text{m}$  belong to the larger “accumulation” mode (Seinfeld and Pandis 2006). Particles in the accumulation mode have longer atmospheric lifetimes than UFP, and therefore human exposure to accumulation mode particles may generally be longer in duration. However, for a given mass of compositionally-identical particulate matter, inhalation of UFP produces a greater biological response than accumulation mode particles, due to greater diffusivities that allow for deposition in the inner-most regions of the respiratory tract and greater particle surface area contact with alveolar cells (G. Oberdörster, E. Oberdörster, and J. Oberdörster 2005; Maynard and Kuempel 2005; Carlson et al. 2008). Upon pulmonary deposition, UFP can cause oxidative stress on alveolar cells due to surface reactivity or transition metal production of hydroxyl radicals, triggering immune responses such as cytokine production and inflammation (Don-

aldson, X. Y. Li, and MacNee 1998). Additionally, the surface composition of certain UFP may grant them access to the bloodstream (Kreyling et al. 2011), mitochondria (N. Li, Sioutas, et al. 2003), and the brain (G. Oberdörster, Sharp, et al. 2004) via endocytic, pinocytic, or axonal transport mechanisms. The association of UFP exposure with respiratory and cardiovascular diseases, cancer, and mortality is well-established (Samet et al. 2000; Hoek et al. 2002; Peters et al. 2004; Delfino, Sioutas, and Malik 2005; G. Oberdörster, E. Oberdörster, and J. Oberdörster 2005; Bräuner et al. 2007; Holguin 2008; Salam, Islam, and Gilliland 2008; Shah et al. 2008; Patel and Miller 2009; N. Li, Harkema, et al. 2010; Stewart et al. 2010).

Regulatory air quality standards for the protection of human health are enforced as mass concentrations of particles, e.g. the US Environmental Protection Agency's National Ambient Air Quality Standards sets an annual mean limit of  $12 \mu\text{g}/\text{m}^3$  for particulate matter of diameter  $D_p < 2.5$  micrometers ( $\text{PM}_{2.5}$ ; USEPA 2015), while the Occupational Safety and Health Administration sets a limit for total titanium dioxide dust of  $15 \text{ mg}/\text{m}^3$ . While suspended particle mass concentration regulations are convenient and inexpensive to measure and enforce, they are inappropriate for quantification of ultrafine particle exposure. Due to the higher correlation of biological response to particle surface area exposure, rather than particle mass, the particle surface area would be a more appropriate metric (Fissan et al. 2007).

However, the inability to conveniently, and directly measure particle surface area hinders the regulatory adoption of this metric for inhalation exposure. Instruments of convenience, for which portability is a proxy, currently exist that indirectly quantify particle surface area, and generally rely on unipolar diffusion charging of particles followed by selective electrical current measurement with an electrometer, e.g. the Aerasense (Marra, Voetz, and Kiesling 2010), TSI nano surface area monitor (NSAM; Asbach et al. 2009), and the Naneos Partector (Fierz et al. 2014). Particle surface area can be estimated with these instruments for unimodal size distributions, but in the absence of true particle size distribution measurements, the accuracy of measurements for multimodal size distributions is dubious. On the other hand, the lightest instruments that can directly measure the UFP size distribution are not amenable to portable applications, weighing 5–10 kg, e.g. the Kanomax PAM or the TSI Nanoscan, and requiring 2–4 minutes per particle size distribution scan, which may not capture ephemeral high particle concentration exposure events that often occur in hazardous occupational exposure and consumer product nanoparticle exposure.

A related issue is the lack of inexpensive, miniature particle sizing and counting instrumentation suitable for effective community exposure assessment. Like the aforementioned frequently transient nature of occupational exposure times, such high temporal variation of exposure also occurs in the community. Vehicular emissions are an example of a temporally variable source, with particle nucleation and transformation timescales  $\lesssim 10$  s (Ketzel and Berkowicz 2004; Carpentieri, Kumar, and Robins 2011; Carpentieri and Kumar 2011). Joodatnia, Kumar, and Robins (2013) found that one-second averaged particle number concentrations can exceed the average concentration for an individual vehicle trip by up to a factor of 30, and that relative standard deviations of trip-averaged particle number concentrations generally exceed 100%.

In addition to the transient nature of ultrafine particle exposure, there is also high spatial variation in ultrafine particle concentrations and exposures. Y. Zhu, Hinds, Kim, and Sioutas (2002), Y. Zhu, Hinds, Kim, Shen, et al. (2002), Y. Zhu, Hinds, Shen, et al. (2004), and Y. Zhu, Kuhn, et al. (2006) found exponentially decreasing particle concentrations at downwind distances  $\sim 10$ – $100$  m from major Los Angeles highways, while other studies showed that people living within 90 m downwind of a highway were exposed to high concentrations and smaller particle sizes than people living farther (K. M. Zhang and Wexler 2004; K. M. Zhang, Wexler, Y. F. Zhu, et al. 2004; K. M. Zhang, Wexler, Niemeier, et al. 2005). Even in the South Coast Air Basin (SCAB) of the Greater Los Angeles area, which is governed by two air pollution agencies (the South Coast Air Quality Management District (SCAQMD) for stationary sources and the California Air Resources Board (CARB) for mobile sources), there are only 19 monitoring stations collecting  $\text{PM}_{2.5}$  data. These monitoring stations are spaced about 20 km apart; for the SCAQMD jurisdiction area of  $27,800 \text{ km}^2$ , there is about one  $\text{PM}_{2.5}$  monitoring station for every  $1500 \text{ km}^2$  of the air basin area, which is roughly the area contained within just the Los Angeles city limits. Thus there is a need for miniaturized, inexpensive particle number size distribution sensor systems for deployment in a telemetric distributed network area in order to quantify spatially and temporally heterogeneous community exposure to ultrafine particles.

### **Particle number size distribution monitoring for constraining aerosol radiative forcing**

Aerosol particles affect the climate directly through light scattering and absorption, and indirectly through their role as cloud condensation nuclei (CCN), the abundance

of which affects cloud lifetime and planetary albedo (Seinfeld and Pandis 2006). However, both the interaction of aerosol particles with light and with atmospheric water are partially size-dependent phenomena that are inadequately quantified. Even in the most recent Intergovernmental Panel on Climate Change Fifth Assessment Report, many of the radiative forcing mechanisms with low confidence levels in their magnitude remain to be aerosol-related (IPCC 2013).

Aerosol optical depth (AOD) is a function of scattering, absorption, and extinction coefficients, which in turn can, in principle, be calculated from the aerosol size distribution. Estimation of the global mean AOD relies heavily on satellite retrieval, which is not well constrained due to substantial discrepancies with ground-based measurements, and even amongst satellite measurements. Additionally, light-based particle detection methods are typically not suitable for detection of particles of diameter  $\lesssim 100$  nm, such as CCN particles. CCN are particles that, in conditions of typical atmospheric water vapor supersaturation levels of  $\lesssim 2\%$ , serve as catalytic surfaces for water molecules to condense onto and form cloud droplets. In some cases, the aerosol size distribution is the main determinant of CCN concentrations (Dusek et al. 2006; Ervens et al. 2007).

Many aerosol radiative forcing components can be further constrained with more frequent and widespread measurement of ambient particle number size distributions. Such measurements are especially lacking in remote regions, in which aerosol size distributions are obtained during expensive and infrequent intensive field campaigns. The miniaturization of instruments that employ particle mobility sizing methods, which are the only means to obtain sub-micron particle size distribution data suitable for atmospheric research, allows for deployment on unmanned aerial vehicles (UAV) and in telemetric distributed network monitoring areas. Both implementations of miniaturized particle mobility sizing instruments would offer a relatively inexpensive means to obtain aerosol distribution data with high spatial and temporal resolution, as well as the ability to more conveniently characterize the aerosol in remote regions.

### **Miniature differential mobility analyzers**

The classical differential mobility analyzer (DMA) transmits particles of a desired mobility on the condition that the electrical migration transit time across the gap between two electrodes is equal to the advective transit time across the length of the classifier (Knutson and Whitby 1975; M. R. Stolzenburg 1988). The electrical migration transit time is determined by the distance and electric field strength between

two parallel or concentric electrodes. The advective transit time is determined, in large part, by a particle-free sheath flow  $Q_{sh}$  and, in small part, by the sample flow  $Q_a$ . Long used for several decades in the classification of sub-micron aerosol particles, the DMA is usually actualized in a cylindrical geometry with physical dimensions  $\sim 0.5$  m and mass  $\sim 20$  kg, and operated with  $Q_{sh} \gtrsim 10$  lpm and  $Q_a \gtrsim 1$  lpm, requiring the use of powerful and heavy pumps to drive the sheath flow. Deployment of remote sensing instruments on common multi-rotor UAV is facilitated when payloads are generally less than 5 kg and power requirements are minimized (Colomina and Molina 2014).

Recent efforts in DMA miniaturization have yielded classifiers amenable to UAV deployment. Steer et al. (2014) developed a portable planar DMA with exterior dimensions of  $30 \text{ cm} \times 32.5 \text{ cm} \times 26 \text{ cm}$  and weighing 5.7 kg. They demonstrated classification of  $20 < D_p < 400$  nm, operating at conditions of  $Q_a/Q_{sh} = 0.2$  lpm / 1.8 lpm, and achieving a mean sizing accuracy of 4.2%. Liu and Chen (2016) made similar efforts in the evaluation of two prototype miniature planar DMAs with exterior dimensions of  $12.4 \text{ cm} \times 6.2 \text{ cm} \times 1.7 \text{ cm}$  and weighing an estimated 0.8 kg. These two prototypes were evaluated at various operating conditions of  $Q_a$  from 0.3–0.6 lpm and  $Q_{sh}$  from 1–6 lpm, to classify  $10 < D_p < 300$  nm particles with a  $\pm 2.5\%$  mobility accuracy. Interestingly, they make use of a sheath flow correction factor to better describe the mobility of classified particles from their miniature DMAs, similar to the flow-rate-ratio correction factor used in the characterization of the radial opposed migration ion and aerosol classifier (ROMIAC; Mui, Mai, et al. 2017)

### **Opposed migration aerosol classifier**

The opposed migration aerosol classifier (OMAC) is fundamentally different from the DMA in that the condition for particle transmission is simply the balance of the electrical migration velocity and an opposed cross-flow velocity occurring between two permeable electrodes that define the classification channel (Flagan 2004; Downard, Dama, and Flagan 2011; Mui, Thomas, et al. 2013; Mui, Mai, et al. 2017). Particles whose electrical migration is balanced by the cross-flow rate,  $Q_{cf}$ , are advected between the porous electrodes by a smaller sample flow,  $Q_a$ . This condition is expressed as

$$EZ^* = \frac{Q_{cf}}{A}, \quad (6.1)$$

where  $E \approx V/b$  is the electric field,  $V$  is the applied voltage,  $b$  is the electrode separation distance,  $Z^*$  is the target particle mobility, and  $A$  is the area of an electrode. The performance of the OMAC is similar to that of the DMA, except that the voltage,  $V_{\text{diff}}$ , at which diffusion begins to degrade the resolution below the non-diffusive limit,  $\mathcal{R}_{\text{nd}} = Q_{\text{cf}}/Q_{\text{a}} = \beta^{-1}$ , is much lower, and scales as  $V_{\text{diff}} \propto \mathcal{R}_{\text{nd}}$  as opposed to  $V_{\text{diff}} \propto 0.6\mathcal{R}_{\text{nd}}^2$  for the DMA (Downard, Dama, and Flagan 2011). Thus, the dynamic range of the OMAC is, in theory, much larger than that of *any* DMA.

### **Water condensation particle counter**

The Moderated Aerosol Growth with Internal water Cycling detector (MAGIC) is a condensation particle counter (CPC) that was developed by Aerosol Dynamics Inc. and described in detail by Hering and M. R. Stolzenburg (2005), Hering, M. R. Stolzenburg, et al. (2005), and Hering, Spielman, and Lewis (2014). The detector uses a laminar-flow, water-based condensation growth tube, which is lined with a continuous wet wick and has three temperature regions: 1) a low temperature aerosol conditioning section, 2) a high temperature section where particle growth is (non-intuitively) initiated because the mass diffusivity of water vapor is greater than the thermal diffusivity of air, and 3) a low temperature moderator section where supersaturation is maintained to allow particles to continue growing to a size readily detectable by the optics head.

The MAGIC detector has several features that make it amenable to applications such as portable/wearable personal exposure monitoring, unattended network monitoring, and UAV measurements in remote environments. First, the cool moderator section recovers water vapor from the initiator section (as well as atmospheric water vapor) via condensation and replenishes the supply of water in the wick to the initiator section via capillary action. This allows for extended continuous operation without refilling the working-fluid for as long as three weeks, depending on the ambient relative humidity. Second, the absence of a liquid reservoir allows for the detector to operate in any arbitrary orientation and when subjected to accelerative forces. Third, the use of non-toxic water as the working-fluid, rather than organics such as butanol or diethylene glycol used in nearly all other CPCs, minimizes the hazards posed to users of the detector.

## 6.2 Methods

### Instruments

#### Radial opposed migration aerosol and ion classifier (ROMIAC)

The ROMIAC is an OMAC-type classifier designed for nucleation-mode aerosol particle classification, using a radial geometry to reduce the exposure of high-diffusivity sample particles to undesirable edge effects in the classification region. The design, simulation, and characterization at various operating resolutions, ranging from about 5–20, to classify  $1 < D_p < 20$  nm particles was described by Mui, Mai, et al. (2017). The operating flow rates can be decreased from those used in the prior study such that larger particles of  $D_p \sim 100$  nm can be successfully classified at more modest resolutions. The ROMIAC was operated with  $Q_a/Q_{cf}/R_{nd} = 0.2$  lpm/0.45 lpm/2.25 to classify particles from  $10 < D_p < 200$  nm. The classification region of the ROMIAC has an average diameter of 3.13 cm and a height of 1.13 cm, while the exterior measures 11.5 cm in diameter and 10.5 cm in height (Mui, Mai, et al. 2017). The volume of the ROMIAC classification region is thus  $8.7 \text{ cm}^3$ , while the ROMIAC as a whole physically occupies a volume of  $1091 \text{ cm}^3$ , with a mass of 1.94 kg.

#### Planar opposed migration aerosol classifier (POMAC)

The POMAC was designed for sub-micron aerosol particle classification, using a planar geometry for improved interfacing with condensation particle counters (CPC). Three-dimensional finite element analysis models were conducted in COMSOL Multiphysics<sup>TM</sup> to solve the fluid flow fields, via the Navier-Stokes equations, within the POMAC, similar in manner to the simulations performed by Mui, Mai, et al. (2017) for the design of the ROMIAC. As in the case of the ROMIAC, the aerosol sample needs to be relatively uniformly distributed about the entrance to the classification region via flow resistance through a thin gap,  $b_{intro}$ , which for practical construction is defined by the thickness of stock metal shim. For an early iteration of the design, three-dimensional flow simulations were conducted with  $Q_a = 0.6$  lpm in a POMAC having a classification region width  $W = 27$  cm for  $b_{intro}$  created from 0.25 and 0.51 mm (0.01 inch and 0.02 inch, respectively) stock shim. Figure 6.1 shows the fluid velocity distributions along  $W$ . For both stock shim thicknesses, the relative standard deviation of the fluid velocity is less than 7%.

Further COMSOL Multiphysics<sup>TM</sup> simulations of the POMAC electric field were conducted by solving the Poisson equation. The transmission of particles was

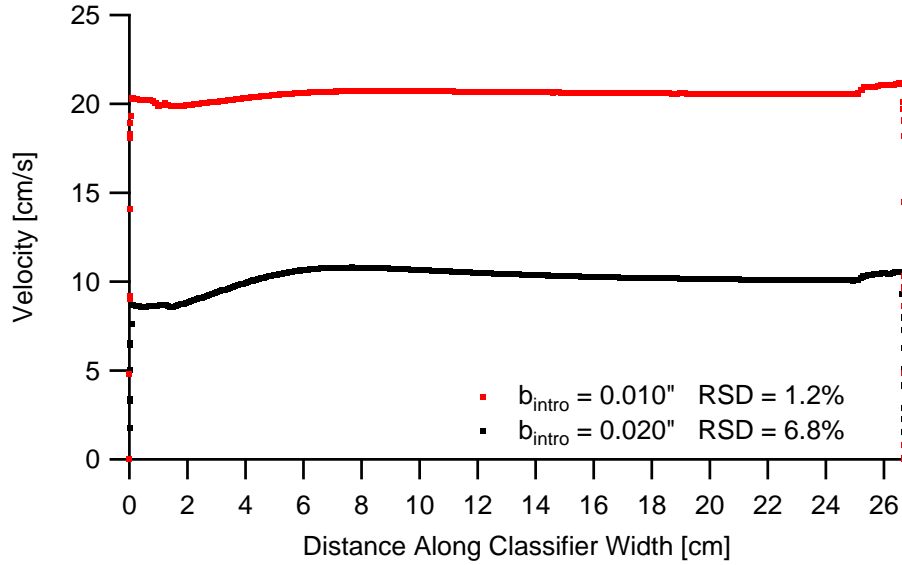


Figure 6.1: Distribution of aerosol sample fluid velocity entering the POMAC classification region along the width of the classification region (distance increases from aerosol inlet tubing) in an early design iteration for  $W = 27$  cm and  $Q_a = 0.6$  lpm. The two candidate stock shim thicknesses resulted in flow velocity distributions with less than 7% relative standard deviation.

simulated by varying the electrode voltage difference and treating the particles as “large ions” that diffuse following Fick’s law, are advected from the fluid flow solution, and are electrically migrated from the electric field solution. Due to the relative uniformity of the aerosol sample fluid velocity through  $b_{\text{intro}}$  in the three-dimensional fluid flow simulations, the electric field and particle transport models were conducted as two-dimensional simulations to minimize computational expense requirements.

Initial physical iterations of the POMAC used stainless steel woven wire mesh as the porous conductive electrode material, as was done for the ROMIAC. While the ROMIAC required the woven mesh to span distances of  $\sim 1$  cm, a POMAC for sub-micron particle classification would require the woven mesh to span distances an order of magnitude greater. Early data indicated that the woven mesh was possibly deflecting due to the combined effects of the force of the cross-flow impinging on the screens and an electric field of up to 1 kV/mm, resulting in a transient value for  $b$  and inconsistent mobility classification behavior. The use of sintered metal frits or metal filter paper was considered, but the homogeneity of the pores, and thus of the cross-flow velocity, was a concern. Additional simulations were conducted to investigate the impact of pore inhomogeneity on particle transmission. Figure 6.2a-



c shows example two-dimensional COMSOL Multiphysics<sup>TM</sup> simulations in which the inhomogeneity of the cross-flow velocity entering and exiting the classification region was permitted to randomly vary along the length of the classification region by up to 0% (homogeneous flow), 50%, and 100%, respectively. Figure 6.2d shows the resulting insignificant effect of such degrees of cross-flow inhomogeneity on the transmission of 100 nm particles. However, if the degree of inhomogeneity was taken to an extreme and particles encountered an extensive length of classification region with non-ideal cross-flow velocities, then particles would not be transmitted at the ideal voltage.

In the final design iteration of a prototype POMAC, aerosol enters the POMAC through a 3.18 mm (1/8 inch) stainless steel tubing into a rectilinear holding volume composed of electrically-grounded aluminum prisms. Stock steel shim separating the two prisms was used to create a thin  $b_{\text{intro}} = 0.51$  mm gap between the holding volume and the classification region, providing sufficient flow resistance to force the sample aerosol to enter the classification region at relatively uniform velocities along the width of the classification region. The classification region had dimensions of length  $L = 11.05$  cm,  $W = 11.05$  cm, and  $b = 1.02$  mm (for a classification region volume of  $12.5 \text{ cm}^3$ ), in order to nominally classify particles of  $10 < D_p < 1000$  nm when operated at  $Q_a/Q_{cf}/R_{nd} = 0.4 \text{ lpm}/0.6 \text{ lpm}/1.5$ . Porous Bekaert Bekipor<sup>®</sup> stainless steel filter paper was used, instead of stainless steel wire woven mesh, as the material for the POMAC electrodes due to their rigidity and ability to resist deflection across spans greater than  $\sim 1$  cm. If the voltage difference applied to the electrodes was such that a charged particle's migration velocity was counteracted by a cross-flow velocity of equal magnitude, the particle would transit the length of the classification region and encounter another identically-dimensioned flow resistance gap, holding volume, and stainless steel tubing leading to the POMAC aerosol outlet.

A simplified diagram of idealized aerosol particle trajectories in the POMAC classification region is shown in Fig. 6.3a, while Fig. 6.3b shows a Solidworks<sup>TM</sup> section drawing of the aerosol sample holding volumes, flow resistance gaps, and classification regions in the POMAC. A three-dimensional Solidworks<sup>TM</sup> rendering of the POMAC is shown in Fig. 6.3c. The exterior dimensions of the POMAC are 19.5 cm long, 16 cm wide, and 5 cm thick, occupying a physical volume of  $1560 \text{ cm}^3$  and weighing 2.20 kg.

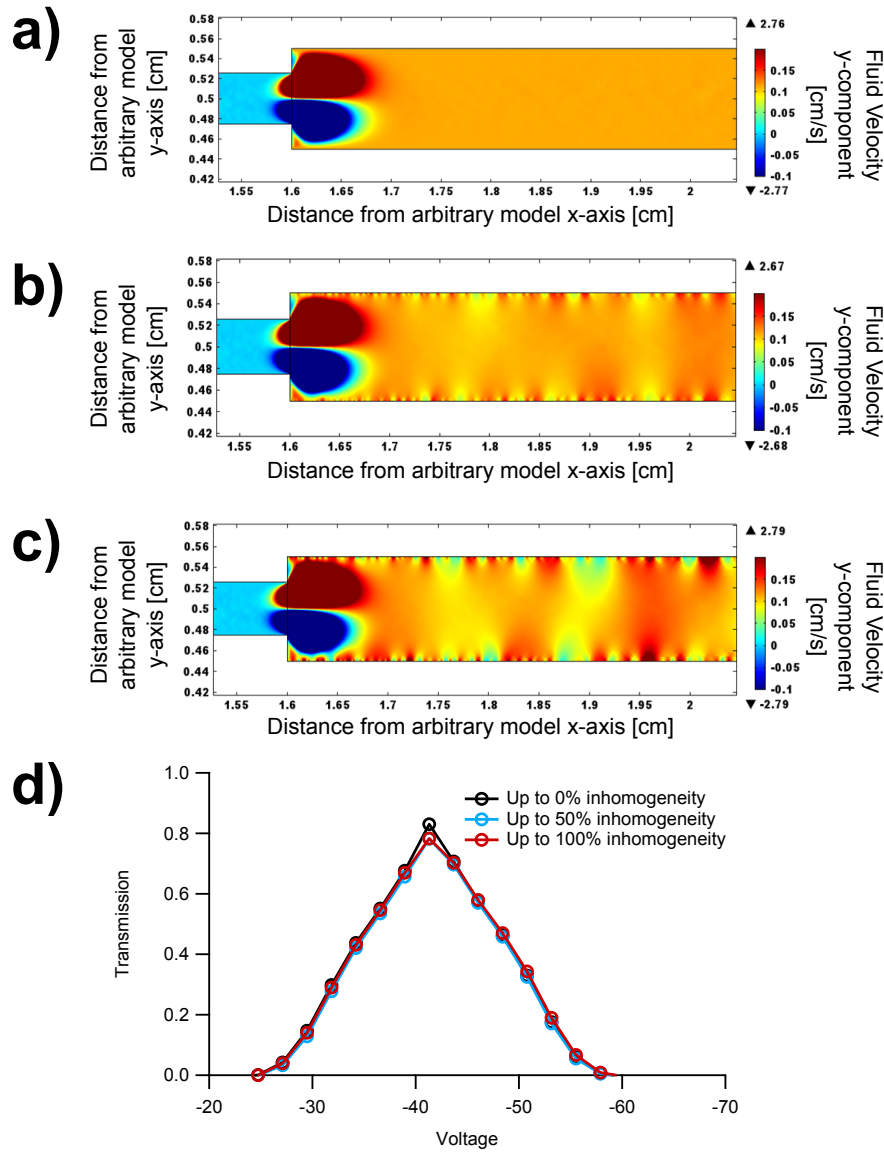


Figure 6.2: Example two-dimensional COMSOL Multiphysics™ simulations in which the cross-flow velocity was permitted to randomly vary along the POMAC classification region length by up to a) 0% (homogeneous flow), b) 50%, and c) 100%. The incoming aerosol distribution gap is the thin channel on the left side of the figures, while the classification region and the classified aerosol outlet is to the right of the distribution gap. The figures are magnified such that much of the remaining classification region and the aerosol outlet are omitted for clarity. d) the resultant transmission of  $D_p = 100$  nm particles through the above POMAC simulations, showing insignificant effects on particle transmission for the explored degrees of electrode material inhomogeneity.

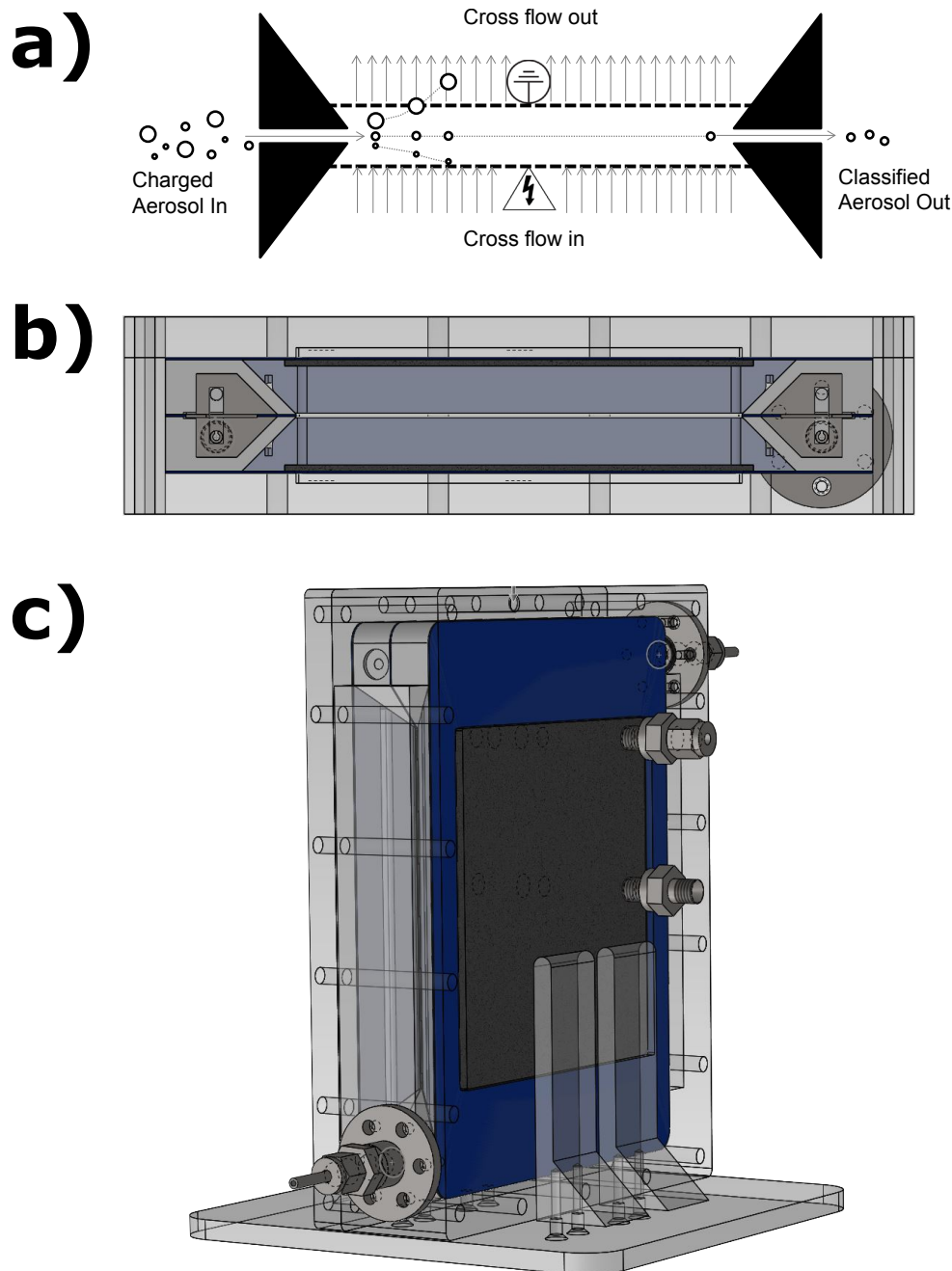


Figure 6.3: a) Simplified diagram illustrating ideal particle trajectories in the POMAC. The filled black triangles create a narrow flow resistance gap that allows for a relatively uniform velocity distribution of the aerosol sample across the classifier width prior to entering the classification region. Particles with a migration velocity equal in magnitude to the cross-flow velocity transit across the length of the classifier to the narrow flow resistance gap on the opposite end and exit the POMAC. b) Solidworks<sup>TM</sup> section drawing of the POMAC along the length of the classification region. c) Three-dimensional Solidworks<sup>TM</sup> rendering of the assembled POMAC, in a vertical orientation for most convenient interfacing with a CPC.

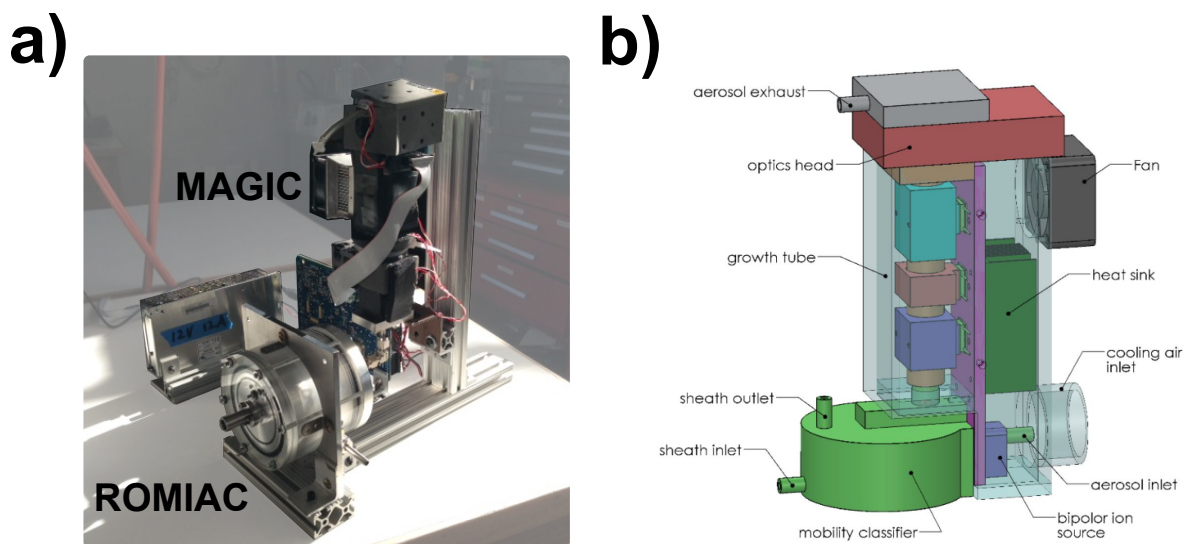


Figure 6.4: a) Photograph of the ROMIAC-MAGIC combined instrument for classification and detection of particles from  $10 < D_p < 200$  nm at  $Q_a/Q_{cf}/R_{nd} = 0.2$  lpm/0.45 lpm/2.25. b) A concept sketch of a future ROMIAC-MAGIC prototype that would improve the interface between the two instruments to reduce losses as well as the mass and dimensions of the ROMIAC.

## MAGIC

Calibration of MAGIC was performed using atomized NaCl aerosol classified by a high-flow DMA (HF-DMA; M. Stolzenburg, Kreisberg, and Hering 1998) and comparing the measured particle concentrations to those measured by a femtoampere aerosol electrometer developed at Fachhochschule Nordwestschweiz (University of Applied Sciences and Arts Northwestern Switzerland).

The ROMIAC and MAGIC detector were interfaced via a stainless steel 90° elbow connector as shown in Fig. 6.4a. A concept design for a future prototype ROMIAC-MAGIC is depicted in Fig. 6.4b, showing enhanced interfacing that reduces diffusive particle losses and the elimination of unnecessary material for a more compact ROMIAC. Similarly, the POMAC and MAGIC detector were interfaced with a 90° piece of conductive flexible tubing, as shown in Fig. 6.5. The similar dimensions and form factors of the POMAC and MAGIC suggest a convenient interfacing between the two instruments in future iterations. The MAGIC detector operates on a 12 V power supply and has exterior dimensions of 10 cm in width, 14 cm in depth, and 21 cm in height, with a weight of 0.7 kg.

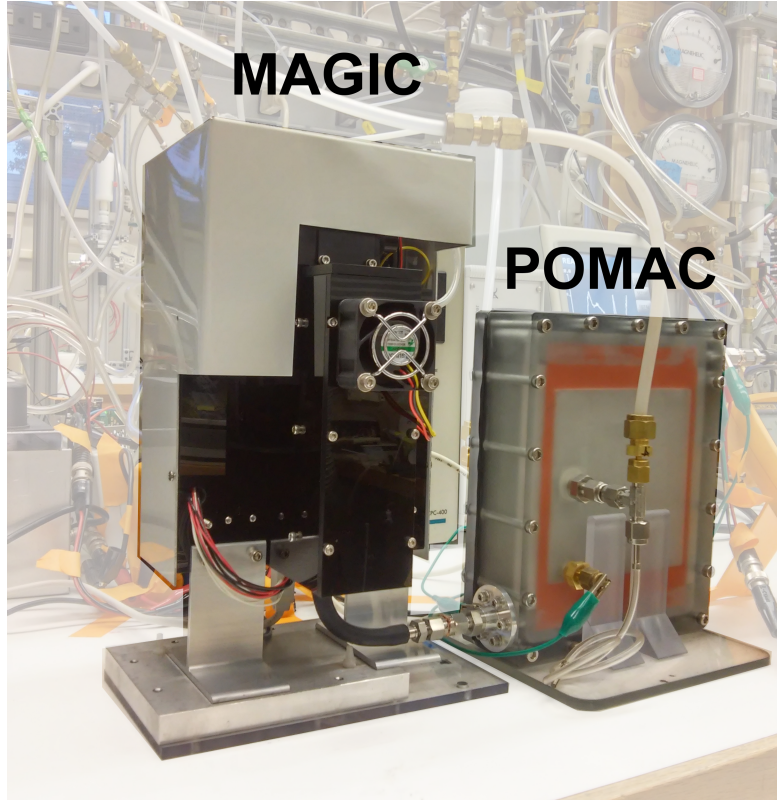


Figure 6.5: Photograph of the POMAC-MAGIC combined instrument for classification and detection of particles from  $10 < D_p < 1000$  nm at  $Q_a/Q_{cf}/R_{nd} = 0.4$  lpm/0.6 lpm/1.5.

### Sub-micron aerosol classifier calibrations

#### ROMIAC

A NaCl solution was atomized and particles transited through a TSI 3077  $^{85}\text{Kr}$  aerosol neutralizer prior to classification by a TSI 3081 DMA column operated at fixed voltages  $V_1$  (corresponding to an output aerosol of  $D_p = 12, 15, 20, 50$ , and  $100$  nm) and flow rates of  $Q_a/Q_{sh}/R_{nd} = 1$  lpm / 10 lpm / 10. The DMA operated in an open-loop sheath flow configuration using HEPA-filtered laboratory air. The classified aerosol from the DMA was then split into two flows, with one flow sent to a TSI 3010 CPC to obtain a reference particle number concentration. The other flow was sent to the ROMIAC, operating at flow rates of  $Q_a/Q_{cf}/R_{nd} = 0.2$  lpm / 0.45 lpm / 2.25 with increasing stepped voltages  $V_2$  to probe the transfer function of the ROMIAC. The ROMIAC operated in a closed-loop cross-flow configuration with a Gast 10D1125-101-1052 pump. The classified aerosol from the ROMIAC was then sent to another TSI 3010 CPC to obtain particle number concentrations at

each voltage step  $V_2$ . The voltage for the DMA and the ROMIAC was provided by two Bertan 602C-100N power supplies. This setup is illustrated in Fig. 6.6a.

### POMAC

An ammonium sulfate and ammonium nitrate mixture was atomized and particles transited through a TSI 3087 soft x-ray aerosol neutralizer prior to classification by a HF-DMA (M. Stolzenburg, Kreisberg, and Hering 1998) operated at fixed voltage  $V_1$  (corresponding to an output aerosol of  $D_p = 20, 30, 40, 60, 85, 120, 170, 240, 360$ , and  $500$  nm) and flow rates of  $Q_a/Q_{sh}/R_{nd} = 1.5$  lpm / 15 lpm / 10. The DMA operated in an open-loop sheath flow configuration using HEPA-filtered compressed air. The classified aerosol from the HF-DMA was then split into two flows, with one flow sent to a TSI 3787 CPC to obtain a reference particle number concentration. The other flow was sent to the POMAC, operating at flow rates of  $Q_a/Q_{sh}/R_{nd} = 0.4$  lpm / 0.6 lpm / 1.5 with increasing stepped voltages  $V_2$  to probe the transfer function of the POMAC. The POMAC operated in a closed-loop cross-flow configuration with a Gast 10D1125-101-1052 pump. The classified aerosol from the POMAC was then sent to the MAGIC CPC to obtain particle number concentrations at each voltage step  $V_2$ . The voltage for the HF-DMA was provided by a Bertan 205B-10R power supply and that for the POMAC was provided by an EMCO High Voltage CA12N power supply. This setup is illustrated in Fig. 6.6a.

### Calibration transfer function inversion

The raw calibration data expresses the ratio of the observed particle concentrations downstream of the test OMAC,  $c_{out,OMAC}(V_1, V_2)$ , to that of a reference CPC measuring the particle concentrations immediately downstream of the source aerosol DMA,  $c_{out,DMA}(V_1)$ , that is,

$$\frac{c_{out,OMAC}(V_1, V_2)}{c_{out,DMA}(V_1)} = \frac{\int [n_s(Z)\eta_{charge}(Z)\Omega_{DMA}(Z)\Omega_{OMAC}(Z)\eta_{trans,OMAC}(Z)\eta_{det,OMAC-CPC}(Z)] dZ}{\int [n_s(Z)\eta_{charge}(Z)\Omega_{DMA}(Z)\eta_{det,DMA-CPC}(Z)] dZ}, \quad (6.2)$$

where  $n_s$  is the source particle mobility distribution,  $\eta_{charge}$  is the Fuchs/Hoppel-Frick/Wiedensohler steady-state bipolar charging probability (Fuchs 1963; Hoppel and Frick 1986; Wiedensohler 1988), which we use in this study to compare later inverted particle size distributions with those returned by the TSI Scanning Mobility

Particle Sizer (SMPS) software used by Aerosol Dynamics Inc.,  $\Omega_{\text{DMA}}$  is the DMA transfer function (M. R. Stolzenburg 1988),  $\Omega_{\text{OMAC}}$  is the OMAC transfer function derived by Mai and Flagan (2017) and implemented by Mui, Mai, et al. (2017) with correction factors,  $\eta_{\text{trans,OMAC}}$  is the OMAC transmission efficiency,  $\eta_{\text{det,OMAC-CPC}}$  is the detection efficiency of the CPC downstream of the OMAC, and  $\eta_{\text{det,DMA-CPC}}$  is the detection efficiency of the CPC downstream of the DMA providing reference particle concentrations.

The OMAC correction factors used by Mui, Mai, et al. (2017) to characterize the ROMIAC were a mobility correction factor  $f_Z = Z_{\text{eff}}^*/Z^*$ , where  $Z_{\text{eff}}^*$  is the observed peak mobility of the calibration particle; a flow-rate ratio correction factor  $f_\beta = \beta_{\text{eff}}/\beta$ , where  $\beta_{\text{eff}}$  is the flow-rate ratio that would result in the observed transfer function resolution; and a diffusional-broadening correction factor  $f_{\tilde{\sigma}} = \tilde{\sigma}_{\text{eff}}/\tilde{\sigma}$ , where  $\tilde{\sigma}_{\text{eff}}$  is the observed diffusional broadening that would result in the observed transfer function tails. The diffusional broadening parameter is defined by Mai and Flagan (2017) as  $\tilde{\sigma}^2 = G\tilde{Z}/(\mathcal{R}_{\text{nd}}\text{Pe}_{\text{mig}})$ , where  $\tilde{Z} = Z/Z^*$  is the dimensionless particle mobility,  $\text{Pe}_{\text{mig}} = eVf/kT$  is the migration Péclet number (ratio of transport by electrophoretic migration to that by diffusion),  $f$  is a factor that accounts for nonuniformities in the electric field (unity in the case of radial classifiers),  $k$  is the Boltzmann constant, and  $T$  is the temperature. Assuming simple shear flow, the geometry factor  $G$  according to Mai and Flagan (2017) is

$$G = \begin{cases} \frac{8}{3}, & \xi = 0 \\ \frac{4 \left\{ \frac{4}{15} \left[ (1-|\xi|^{5/2}) - (1-|\xi|)^{5/2} \right] + \frac{1}{3} \left( \frac{\xi}{\alpha} \right)^2 \left[ (1-|\xi|^{3/2}) - (1-|\xi|)^{3/2} \right] \right\}}{|\xi|(1-|\xi|)}, & 0 < |\xi| < 1 \\ 2 \left[ \frac{4}{3} + \left( \frac{1}{\alpha} \right)^2 \right], & |\xi| \geq 1, \end{cases} \quad (6.3)$$

where  $\xi = \beta^{-1}(\tilde{Z} - 1) = \mathcal{R}_{\text{nd}}(\tilde{Z} - 1)$  and  $\alpha = L/b$  is the aspect ratio.

Fitting of the calibration data to Eq. (6.2) is carried out following the approach used by M. R. Stolzenburg (1988) (see also S.-H. Zhang and Flagan 1996, Hagwood, Sivathanu, and Mulholland 1999, and Mui, Mai, et al. (2017)). First, using the fact that the ROMIAC or POMAC (operating at  $\mathcal{R}_{\text{nd}} = 2.25$  and 1.5, respectively) transfer function is broad compared to the transfer function of the preceding DMA, an approximated Dirac delta effective source aerosol distribution  $n_{\text{s,eff}}(Z) = n_{\text{s}}(Z)\eta_{\text{charge}}(Z)$  is inferred from the reference CPC number concentration

values, well-established DMA transfer function, and reference CPC efficiency function, i.e.,  $n_{s,\text{eff}} = [c_{\text{out,DMA}}(V_1)]^{-1} \int [\Omega_{\text{DMA}}(Z) \eta_{\text{det,DMA-CPC}}(Z)] dZ \approx \text{constant}$ . The inferred  $n_{s,\text{eff}}$  was then used to solve for the OMAC correction factors ( $f_Z$ ,  $f_\beta$ , and  $f_{\tilde{\sigma}}$ ) and OMAC transmission efficiency ( $\eta_{\text{trans,OMAC}}$ ) using the Matlab<sup>TM</sup> nonlinear least-squares solver (“lsqcurvefit” function) with multiple local minima optimization, for the problem posed as

$$\frac{c_{\text{out,OMAC}}(V_1, V_2)}{c_{\text{out,DMA}}(V_1)} = \frac{\int [\Omega_{\text{DMA}}(Z) \Omega_{\text{eff}}(\tilde{Z}_{\text{eff}}(f_Z), \beta, \delta, \tilde{\sigma}, f_\beta, f_{\tilde{\sigma}}) \eta_{\text{trans,OMAC}}(Z) \eta_{\text{det,OMAC-CPC}}(Z)] dZ}{\int [\Omega_{\text{DMA}}(Z) \eta_{\text{det,DMA-CPC}}(Z)] dZ}, \quad (6.4)$$

where  $\tilde{Z}_{\text{eff}} = Z/Z_{\text{eff}}^*$  is the effective dimensionless mobility and the effective OMAC transfer function is

$$\begin{aligned} \Omega_{\text{eff}}(\tilde{Z}_{\text{eff}}(f_Z), \beta, \delta, \tilde{\sigma}, f_\beta, f_{\tilde{\sigma}}) = & \frac{\tilde{\sigma} f_{\tilde{\sigma}}}{\sqrt{2} \beta f_\beta (1 - \delta)} \\ & \left[ \mathcal{E} \left( \frac{\tilde{Z}_{\text{eff}} - (1 + \beta f_\beta)}{\sqrt{2} \tilde{\sigma} f_{\tilde{\sigma}}} \right) \right. \\ & + \mathcal{E} \left( \frac{\tilde{Z}_{\text{eff}} - (1 - \beta f_\beta)}{\sqrt{2} \tilde{\sigma} f_{\tilde{\sigma}}} \right) \\ & - \mathcal{E} \left( \frac{\tilde{Z}_{\text{eff}} - (1 + \delta \beta f_\beta)}{\sqrt{2} \tilde{\sigma} f_{\tilde{\sigma}}} \right) \\ & \left. - \mathcal{E} \left( \frac{\tilde{Z}_{\text{eff}} - (1 - \delta \beta f_\beta)}{\sqrt{2} \tilde{\sigma} f_{\tilde{\sigma}}} \right) \right], \quad (6.5) \end{aligned}$$

where  $\mathcal{E}(y) = y \operatorname{erf}(y) + \pi^{-1/2} e^{-y^2}$ . Finally, as was done by M. R. Stolzenburg (1988), Flagan (1999), Jiang et al. (2011), and Mui, Mai, et al. (2017), the correction factor  $f_{\tilde{\sigma}}$  is recast as a particle-size-independent dispersion contribution,  $\tilde{\sigma}_{\text{distor}}$ , that is an additive distortion term to  $\tilde{\sigma}$  (as  $\tilde{\sigma}$  should already account for the observed particle-size-dependent dispersion) through the relationships

$$\tilde{\sigma}_{\text{eff}}^2 = \tilde{\sigma}^2 + \tilde{\sigma}_{\text{distor}}^2 \quad (6.6)$$

$$\tilde{\sigma}_{\text{distor}}^2 = \tilde{\sigma}^2 (f_{\tilde{\sigma}} - 1). \quad (6.7)$$



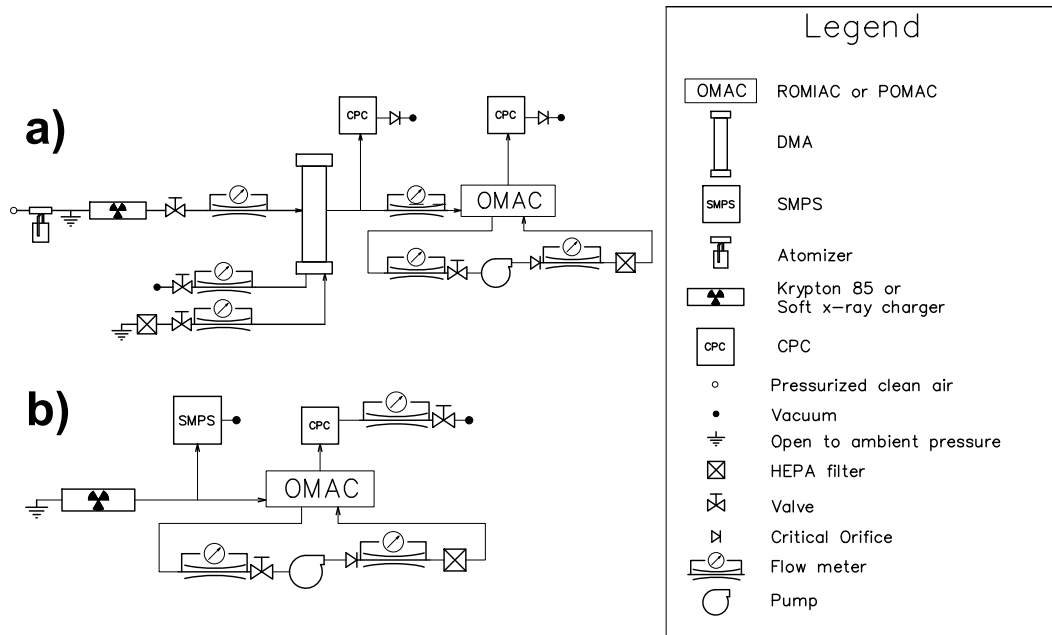


Figure 6.6: Experimental setup for a) transfer function calibrations of OMACs and b) SMPS vs. OMAC comparison ambient measurements.

## Ambient measurements

### ROMIAC-MAGIC

Ambient measurements were conducted by continuously sampling the air outside of the Aerosol Dynamics Inc. laboratory in Berkeley, CA from Thursday 2014-Jan-23 18:10:00 to Saturday 2014-Jan-25 17:10:00 local time (Pacific Standard Time; UTC-8:00), for a total sampling time of 47 hours. The sample air was transported into the laboratory and sent through a TSI 3087 soft x-ray charger before being split into two flows. The first flow was sent to the Aerosol Dynamics Inc. SMPS using the HF-DMA column ( $Q_a/Q_{sh}/R_{nd} = 1.5 \text{ lpm} / 15 \text{ lpm} / 10$ ) and a TSI 3787 CPC running at  $Q_{det} = 1.5 \text{ lpm}$ . The second flow was sent to the ROMIAC ( $Q_a/Q_{cf}/R_{nd} = 0.2 \text{ lpm} / 0.4 \text{ lpm} / 2.25$ ) stepping through 7 voltage channels, to nominally classify particles from  $10 < D_p < 190 \text{ nm}$ , and measuring 6 seconds per channel, for detection by the MAGIC detector running at  $Q_{det} = 0.2 \text{ lpm}$ . The flow configuration and high voltage power supply for the ROMIAC was identical to that used in the ROMIAC calibrations. The maximum combined power consumption by the ROMIAC pump,

flow meters, and high voltage power supply was 50 W, while the power requirements of MAGIC are 2.5 W. The MAGIC detector was not replenished with water during this measurement. The tubing lengths from the sample flow split to the SMPS and the ROMIAC-MAGIC system were such that diffusive losses would be equivalent between the two classifiers. This setup is illustrated in Fig. 6.6b.

### POMAC-MAGIC

The ambient measurements using the POMAC were conducted from Saturday 2015-Dec-12 10:30:00 to Sunday 2015-Dec-13 00:00:00 local time, for a total sampling time of 13.5 hours. The SMPS vs. POMAC-MAGIC measurements were conducted in identical manner as those with the SMPS vs. ROMIAC-MAGIC. The POMAC operated at  $Q_a/Q_{cf}/R_{nd} = 0.4 \text{ lpm} / 0.6 \text{ lpm} / 1.5$  and stepped through 14 voltage channels, to nominally classify particles from  $10 < D_p < 1000 \text{ nm}$ , and measured for 13 seconds per channel, with the MAGIC detector running at  $Q_{det} = 0.4 \text{ lpm}$ . The flow configuration and high voltage power supply for the POMAC was identical to that used in the POMAC calibrations. The maximum combined power consumption by the POMAC pump, flow meters, and high voltage power supply was 4.28 W. The MAGIC detector was not replenished with water during this measurement. This setup is illustrated in Fig. 6.6b.

## 6.3 Results and Discussion

### Calibrations

#### ROMIAC

The ROMIAC calibration data for  $D_p = 12, 15, 20, 50, 100, \text{ and } 150 \text{ nm}$  is shown in Fig. 6.7a. The fitted transfer functions describe the  $D_p = 150 \text{ nm}$  measurements with high fidelity, but are notably shifted to  $\sim 5\%$  higher mobilities for the remaining calibration diameters. The best-fit values for the correction factors and ROMIAC transmission efficiency are shown in Figs. 6.7b-e, and can be well-described as empirical functions of  $Pe_{mig}$ :

$$f_Z = \frac{0.28}{\log_{10}(Pe_{mig})} + 1.06 \quad (6.8)$$

$$f_\beta = 0.18 \log_{10}(Pe_{mig}) + 0.14 \quad (6.9)$$

$$\tilde{\sigma}_{distor}^2 = \frac{0.1}{\log_{10}(Pe_{mig})} - 0.02, \quad (6.10)$$

while  $\eta_{trans,OMAC}$  was unity for the entire particle size range of interest. The correction factor values obtained in the calibration of the ROMIAC for sub-micron

aerosol particles are generally consistent with those obtained in earlier calibrations of the ROMIAC with sub-20 nm particles (Mui, Mai, et al. 2017). The resolution achieved by the ROMIAC in calibration measurements is shown in Fig. 6.7f. The relative resolution  $\mathcal{R}/\mathcal{R}_{\text{nd}}$  ranged from 0.66 for  $D_p = 12$  nm to unity for  $D_p = 150$  nm. Resolution degradation of the ROMIAC when classifying sub-micron aerosol particles appears to degrade more rapidly than even an ideal DMA, though the observed  $\mathcal{R}/\mathcal{R}_{\text{nd}}$  values in this study were not outside the range observed in the ROMIAC characterization with sub-20 nm particles (Mui, Mai, et al. 2017).

## POMAC

The POMAC calibration data for  $D_p = 20, 30, 40, 60, 85, 120, 170, 240, 360,$  and  $500$  nm is shown in Fig. 6.8a. The fitted transfer functions describe the  $D_p = 20$  nm measurements with high fidelity, but are notably shifted to  $\sim 20\%$  higher mobilities for the remaining calibration diameters. The best-fit values for the correction factors and POMAC transmission efficiency are shown in Figs. 6.7b-e, and can be well-described as empirical functions of  $\text{Pe}_{\text{mig}}$  in the case of  $f_Z$ ,  $f_\beta$ , and  $\tilde{\sigma}_{\text{distor}}$ , or with a modified three-parameter model by Wiedensohler et al. (1997) in the case of  $\eta_{\text{trans,OMAC}}$ :

$$f_Z = \frac{-0.41}{\log_{10}(\text{Pe}_{\text{mig}})} + 0.52 \quad (6.11)$$

$$f_\beta = 0.32 \log_{10}(\text{Pe}_{\text{mig}}) - 0.29 \quad (6.12)$$

$$\tilde{\sigma}_{\text{distor}}^2 = \frac{1.22}{\log_{10}(\text{Pe}_{\text{mig}})} - 0.27 \quad (6.13)$$

$$\eta_{\text{trans,OMAC}} = 1 - \exp((13.6 \text{ nm} - D_p) / 5.7 \text{ nm}), \quad (6.14)$$

The correction factor values obtained for the POMAC, especially those for  $f_Z$ , are very different from those obtained for the ROMIAC in this study and an earlier study by Mui, Mai, et al. (2017). The resolution achieved by the POMAC in calibration measurements is shown in Fig. 6.7f. The relative resolution  $\mathcal{R}/\mathcal{R}_{\text{nd}}$  ranged from  $\sim 0.1$  for  $D_p = 20$  nm to unity for  $D_p = 500$  nm. Resolution degradation of the POMAC when classifying sub-micron aerosol particles appears to degrade very rapidly with decreasing particle size. The severe deviation of  $\mathcal{R}/\mathcal{R}_{\text{nd}}$  from the ideal OMAC limit, along with the substantial mobility correction factor deviation from unity, indicate an extremely non-ideal classification region in the POMAC. One possible source of the non-ideal behavior demonstrated is the metal filter paper used as the POMAC electrodes. Although earlier finite element simulations suggested

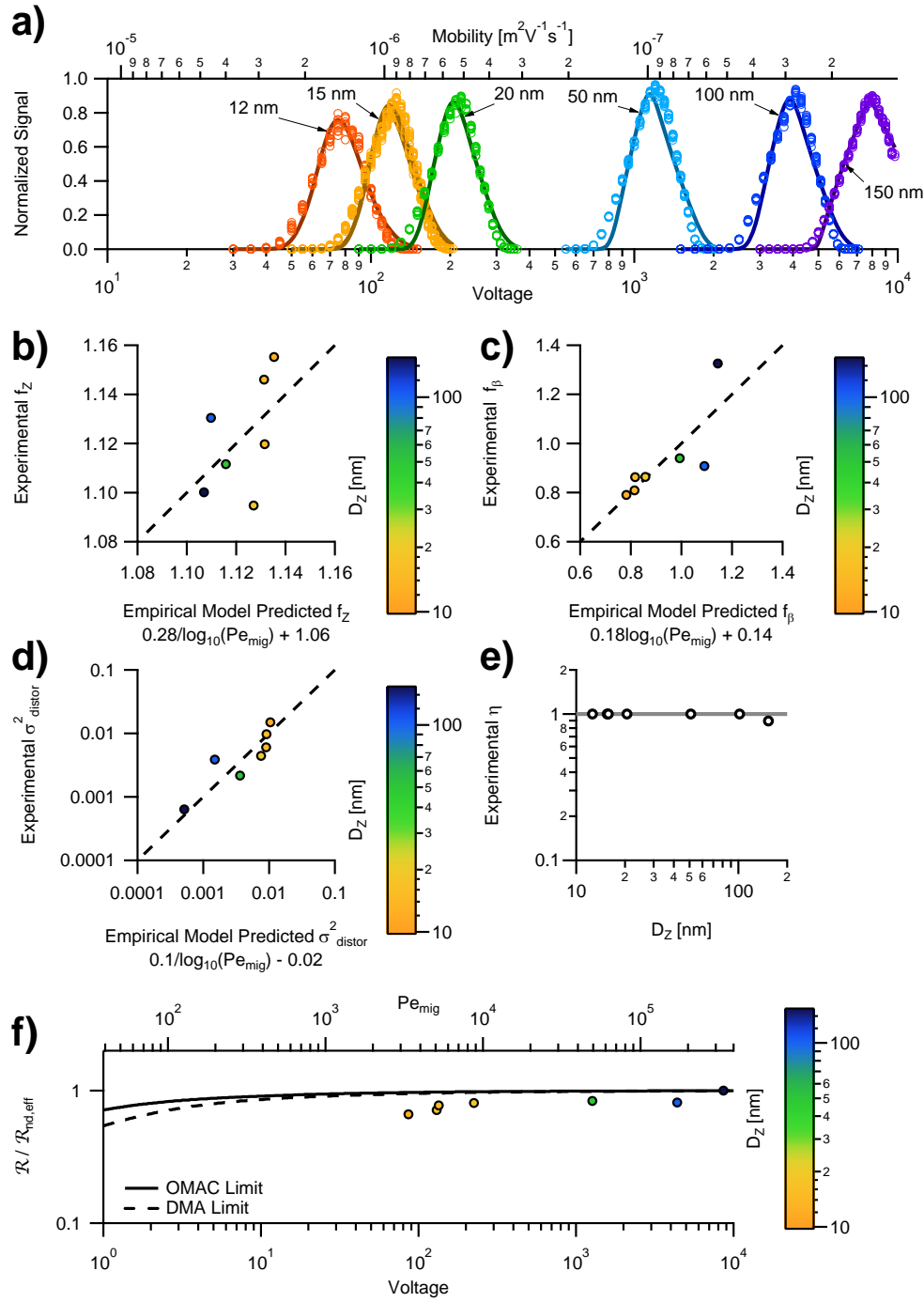


Figure 6.7: a) ROMIAC calibration data (markers) and transfer function model fits (lines) for  $12 < D_p < 150$  nm. Empirical model fits for correction factors b)  $f_z$ , c)  $f_\beta$ , and d)  $\tilde{\sigma}_{\text{distor}}^2$  as functions of  $\text{Pe}_{\text{mig}}$ . Dashed lines are a one-to-one line. e) Best-fit  $\eta_{\text{trans,OMAC}}$  values (markers) and unity line. f) Relative resolution achieved in ROMIAC calibration measurements, with theoretical relative resolution limits for the OMAC and DMA shown in solid and dashed lines, respectively.

that sparse cross-flow velocity inhomogeneities of up to  $\pm 100\%$  from the nominal cross-flow velocity would not impact the transmission of particles (Fig. 6.2), the POMAC electrodes could have pore inhomogeneities that would result in particles experiencing much greater cross-flow velocity deviations from the nominal value, and for a much greater duration of their transit along the POMAC classification region. This is a probable explanation for why this POMAC prototype was not able to classify up to the maximum  $D_p = 1000$  nm for which it was designed. Additionally, the planar configuration of an OMAC-type classifier would present non-ideal edge effects in the electric field, which likely contributed to the drastic resolution degradation for smaller particles.

## MAGIC

The detection efficiency of MAGIC in this study is shown in Fig. 6.9; at the aerosol flow rates employed by the ROMIAC and POMAC, the MAGIC detection efficiency is  $\sim 0.87$  and unity, respectively, for particles of  $D_p > 10$  nm. For inversion purposes, the MAGIC detection efficiency was described by a modified three-parameter model by Wiedensohler et al. (1997):

$$\eta_{\text{det}} = a \left[ 1 - \exp \left( (D_0 - D_p) / D_2 \right) \right], \quad (6.15)$$

where  $a$  is a coefficient representing the maximum detection efficiency and  $D_0$  and  $D_2$  are free parameters. The fitted values for MAGIC at the ROMIAC (POMAC) aerosol flow rate condition were  $a = 0.87$  (1),  $D_0 = D_2 = 1.62$  nm (3.67 nm), represented by the dashed lines in Fig. 6.9.

## Ambient measurements

### ROMIAC-MAGIC

The ROMIAC-MAGIC 47-hour ambient measurements of the particle number size distribution is shown in Fig. 6.10a, and accounted for the 5% peak mobility overestimation from the calibration transfer function fitting, while the concurrent SMPS measurement is in Fig. 6.10b. The two distributions are in good agreement in terms of the size, concentration, occurrence, and duration of particle enhancement episodes. Such episodes are evident as the Friday morning rush hour (2014-Jan-24 6:00–12:00), Friday afternoon rush hour (2014-Jan-24 18:00–23:59), a lingering signal from the Friday afternoon rush hour lasting until approximately 2014-Jan-25

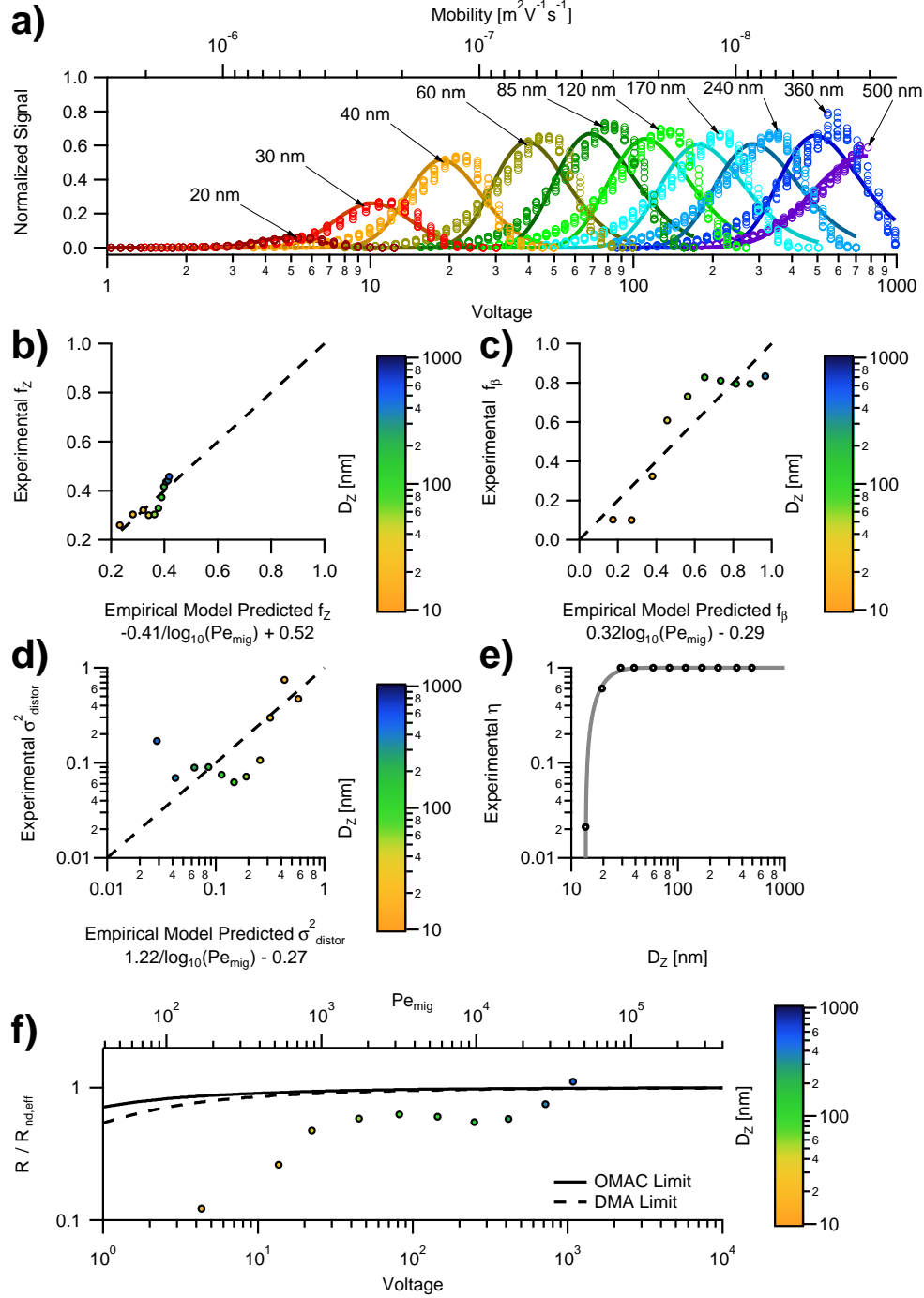


Figure 6.8: a) POMAC calibration data (markers) and transfer function model fits (lines) for  $20 < D_p < 500$  nm. Empirical model fits for correction factors b)  $f_z$ , c)  $f_\beta$ , and d)  $\sigma_{\text{distor}}^2$  as functions of  $\text{Pe}_{\text{mig}}$ . Dashed lines are a one-to-one line. e) Best-fit  $\eta_{\text{trans,OMAC}}$  values (markers) and detection efficiency model (line). f) Relative resolution achieved in POMAC calibration measurements, with theoretical relative resolution limits for the OMAC and DMA shown in solid and dashed lines, respectively.

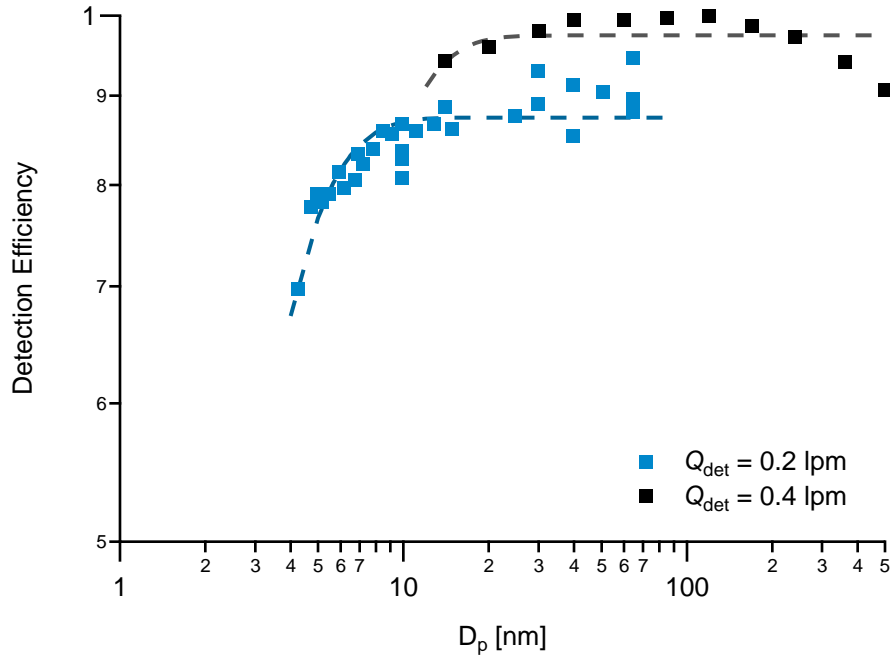


Figure 6.9: Detection efficiency of the MAGIC CPC for the aerosol flow rates of the ROMIAC ( $Q_a = 0.2$  lpm) and the POMAC ( $Q_a = 0.4$  lpm) used in this study. The dashed lines represent fits to a modified three-parameter model by Mertes, Schröder, and Wiedensohler (1995) for describing CPC efficiency.

03:00 on the next day, and a Saturday morning rush hour (2014-Jan-25 6:00–12:00). The ROMIAC-MAGIC system achieves a greater time resolution by about a factor of 4, as a ROMIAC-MAGIC scan takes  $\sim 1$  minute, while the required 4 minutes per scan.

The particle number size distributions were analyzed and integrated from 10 to 200 nm to obtain four metrics to compare the ROMIAC-MAGIC system against the SMPS. These metrics are the geometric mean diameter  $D_{p,geo}$ , total particle number concentration  $N_{tot}$ , total particle volume concentration  $V_{tot}$ , and total particle surface area concentration  $SA_{tot}$ . The time series of the metrics are shown in Figs. 6.11a, c, e, and g, showing excellent agreement of the metric values, changes, and duration between the two systems.

Since the two systems completed scan measurements at different times due to the different time resolutions, the higher time resolution ROMIAC-MAGIC metric values were interpolated at the scan measurement times of the SMPS to obtain directly comparable values. These values are plotted against those of the SMPS in Figs. 6.11b, d, f, and h. The geometric mean diameter measured by the SMPS

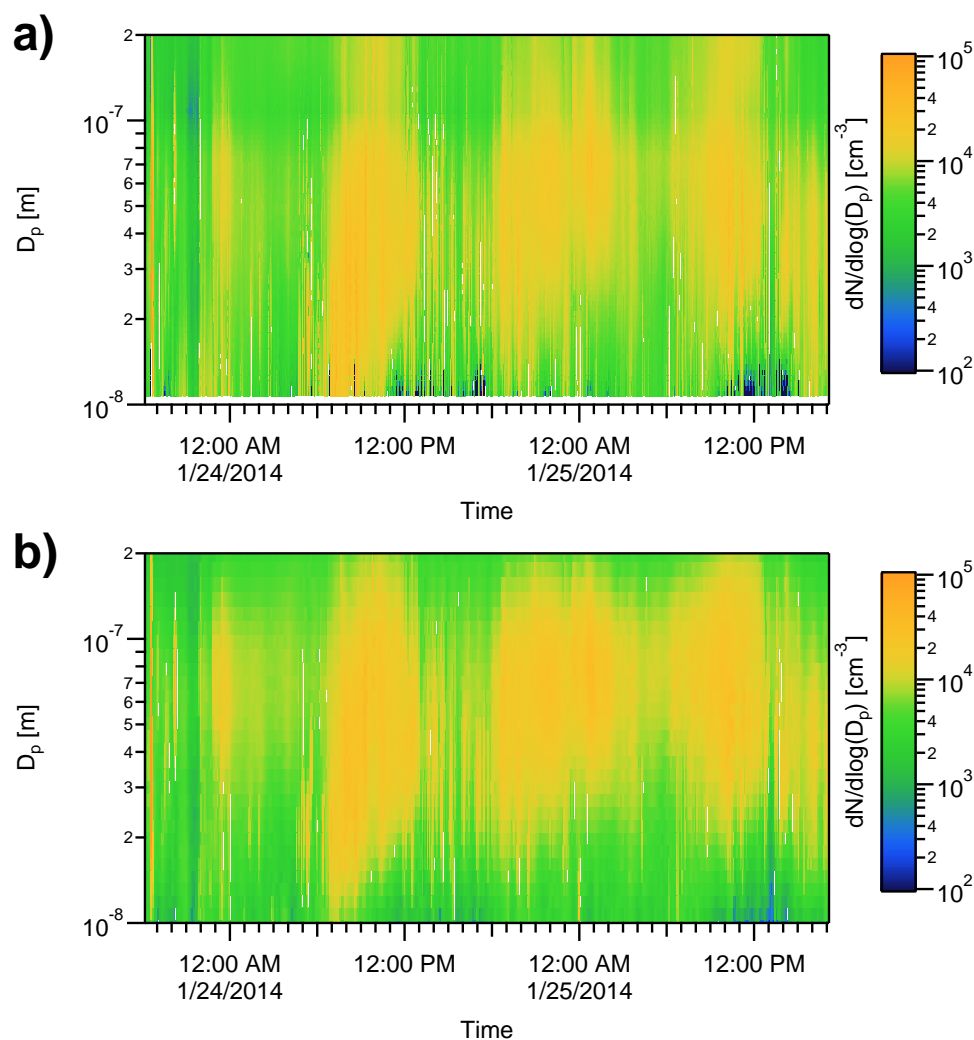


Figure 6.10: Particle number size distributions for the 47-hour measurement outside the Aerosol Dynamics Inc. laboratory in Berkeley, CA reported by the a) ROMIAC-MAGIC system and b) SMPS.



ranged from 34 to 76 nm through the sampling period, with the ROMIAC-MAGIC system obtaining a  $D_{p,geo}$  value that was, on average, 8% below that of the SMPS ( $r^2 = 0.78$ ). The SMPS  $N_{tot}$  values ranged from about 1700 to  $10^5 \text{ cm}^{-3}$ , with the ROMIAC-MAGIC system obtaining total particle number concentrations that were 3% below that of the SMPS ( $r^2 = 0.86$ ). The ROMIAC-MAGIC system obtained, on average, 10% higher  $V_{tot}$  values than the SMPS values ( $r^2 = 0.92$ ), which ranged from 1.1 to  $27 \mu\text{m}^3\text{cm}^{-3}$ . There was excellent agreement for the  $SA_{tot}$  metric, ranging from 45 to  $1300 \mu\text{m}^2\text{cm}^{-3}$ , with only a 2% disagreement between the two systems ( $r^2 = 0.91$ ).

Figure 6.12 shows the hourly deposited dose of UFP number and surface area to the pulmonary and alveolar regions of the lung, calculated from the ROMIAC-MAGIC distributions and the International Commission on Radiological Protection regional depositional model (ICRP 1994), and assuming a volumetric breathing rate of  $0.54 \text{ m}^3\text{h}^{-1}$ , as given for males, sitting and awake, by ICRP (1994) and Holmes (1994). During high UFP concentration periods, the deposited surface area dose increases two- to four-fold, while the deposited number dose increases two- to five-fold, from background levels. During episodes of elevated UFP exposure, the number dose peaks before the surface area dose. The earlier number dose elevations likely result from freshly formed particles from traffic emissions, which proceed to undergo growth and coagulation processes that lead to later increases in surface doses.

### POMAC-MAGIC

The POMAC-MAGIC 13.5-hour ambient measurements of the particle number size distribution is shown in Fig. 6.13a, and accounted for the 20% peak mobility overestimation from the calibration transfer function fitting, while the concurrent SMPS measurement is in Fig. 6.13b. There are two brief periods of missing data from the POMAC measurements when the data acquisition program stalled. The two images generally agree in terms of the size, concentration, occurrence, and duration of particle concentrations for  $D_p > 100 \text{ nm}$ , but the SMPS reports as much as an order of magnitude higher concentration for smaller particles. At approximately 2015-Dec-12 22:30, the POMAC-MAGIC system gradually stopped reporting any counts, possibly due to the MAGIC wick having dried out. The POMAC-MAGIC system and the SMPS had the same time resolution of 5 minutes per distribution scan, but were not synchronized to start and end scans concurrently.

The particle number size distributions were analyzed and integrated from 30 to 500

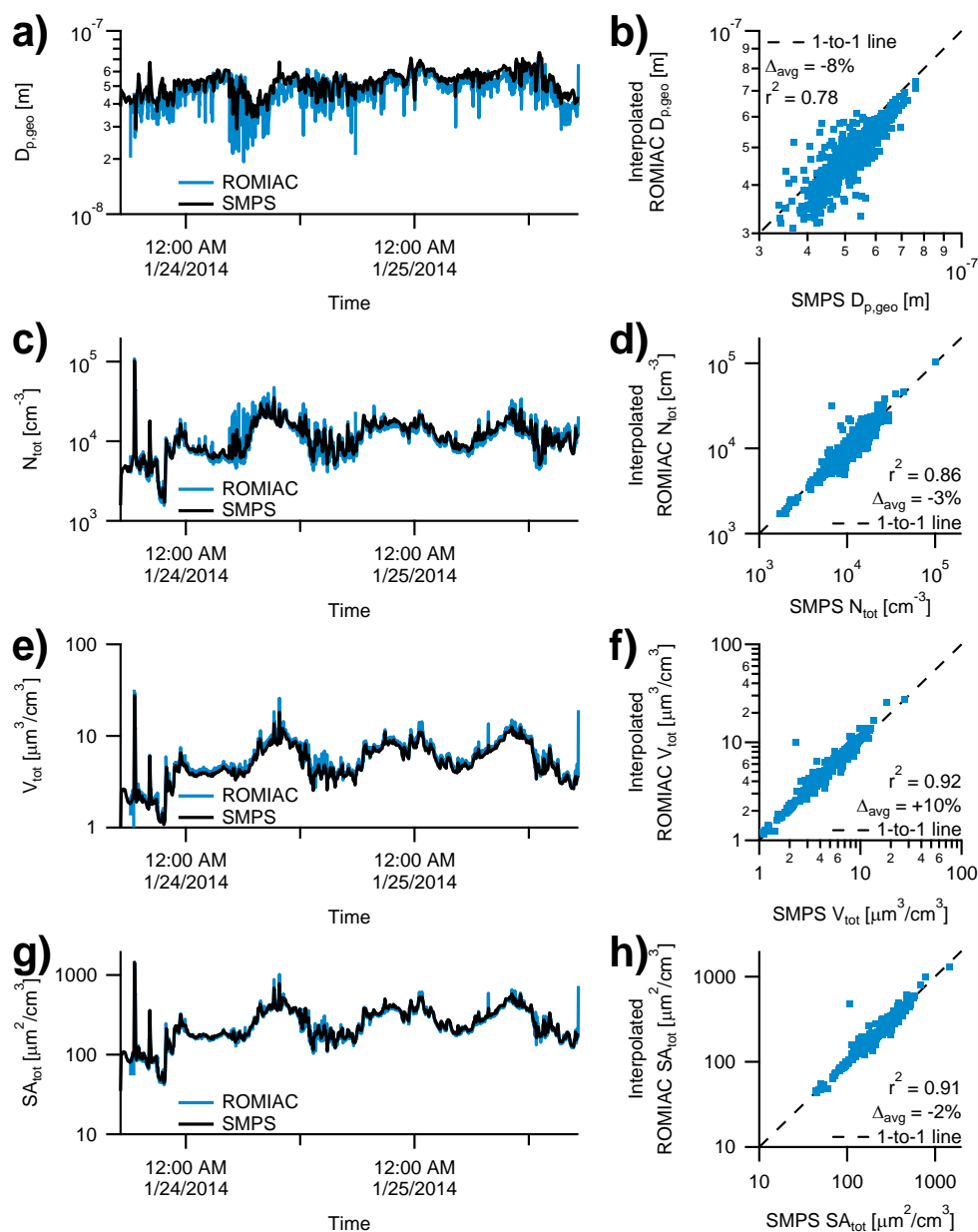


Figure 6.11: Comparison metrics for the ROMIAC-MAGIC and SMPS 47-hour ambient sampling period calculated from the distributions in Fig. 6.10. a) Time series of geometric mean diameter. b) Time series of total particle number concentration. c) Time series of total particle volume concentration. d) Time series of total particle surface area concentration. e) One-to-one comparison of geometric mean diameter. f) One-to-one comparison of total particle number concentration. g) One-to-one comparison of total particle volume concentration. h) One-to-one comparison of total particle surface area concentration. The notation  $\Delta_{avg}$  denotes the mean percent difference of the ROMIAC-MAGIC value from the SMPS value.

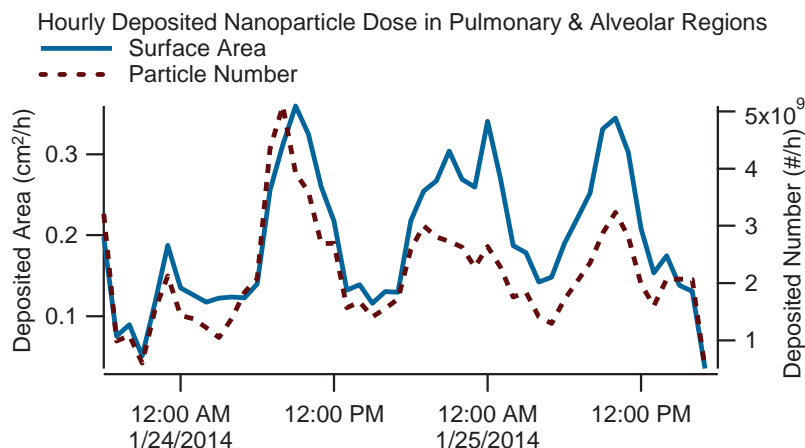


Figure 6.12: Total surface area and number of particles per hour delivered to the pulmonary/alveolar regions of the lung for the particle size distributions of Fig. 6.10a.

nm to obtain the same four metrics, as was done with ROMIAC-MAGIC, to compare the POMAC-MAGIC system against the SMPS. The time series of the metrics are shown in Figs. 6.14a, c, e, and g, showing qualitative agreement of metric changes and duration between the two systems.

The POMAC-MAGIC metric values were interpolated at the scan measurement times of the SMPS to obtain directly comparable values. These values are plotted against those of the SMPS in Figs. 6.14b, d, f, and h. The SMPS geometric mean diameter ranged from 42 to 120 nm through the sampling period, with the ROMIAC-MAGIC system obtaining a  $D_{p,geo}$  value that was, on average, 26% above that of the SMPS ( $r^2 = 0.38$ ). The SMPS  $N_{tot}$  values ranged from about 680 to 7200  $\text{cm}^{-3}$ , with the ROMIAC-MAGIC system obtaining total particle number concentrations that were 42% below that of the SMPS ( $r^2 = 0.34$ ). The ROMIAC-MAGIC system obtained, on average, 82% higher  $V_{tot}$  values than the SMPS values ( $r^2 = 0.65$ ), which ranged from 0.4 to 14  $\mu\text{m}^3\text{cm}^{-3}$ . There was good agreement for the  $SA_{tot}$  metric, ranging from 15 to 360  $\mu\text{m}^2\text{cm}^{-3}$ , with a 12% disagreement between the two systems ( $r^2 = 0.75$ ).

#### 6.4 Conclusions

Two prototype miniature particle classification systems, ROMIAC-MAGIC and POMAC-MAGIC, were calibrated and then used to concurrently obtain ambient aerosol particle number size distributions with a SMPS. Good agreement among key metrics was obtained with the two prototypes.

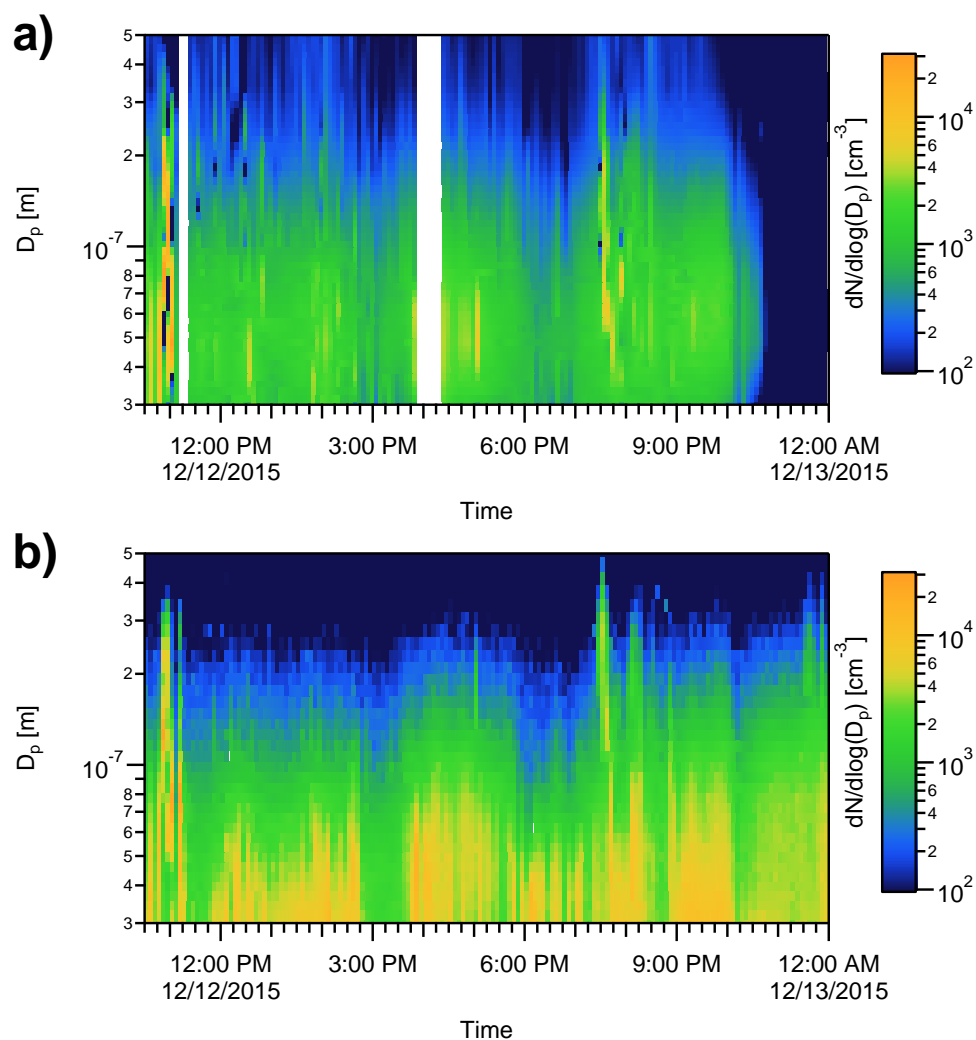


Figure 6.13: Particle number size distributions for the 13.5-hour measurement outside the Aerosol Dynamics Inc. laboratory in Berkeley, CA reported by the a) POMAC-MAGIC system and b) SMPS.

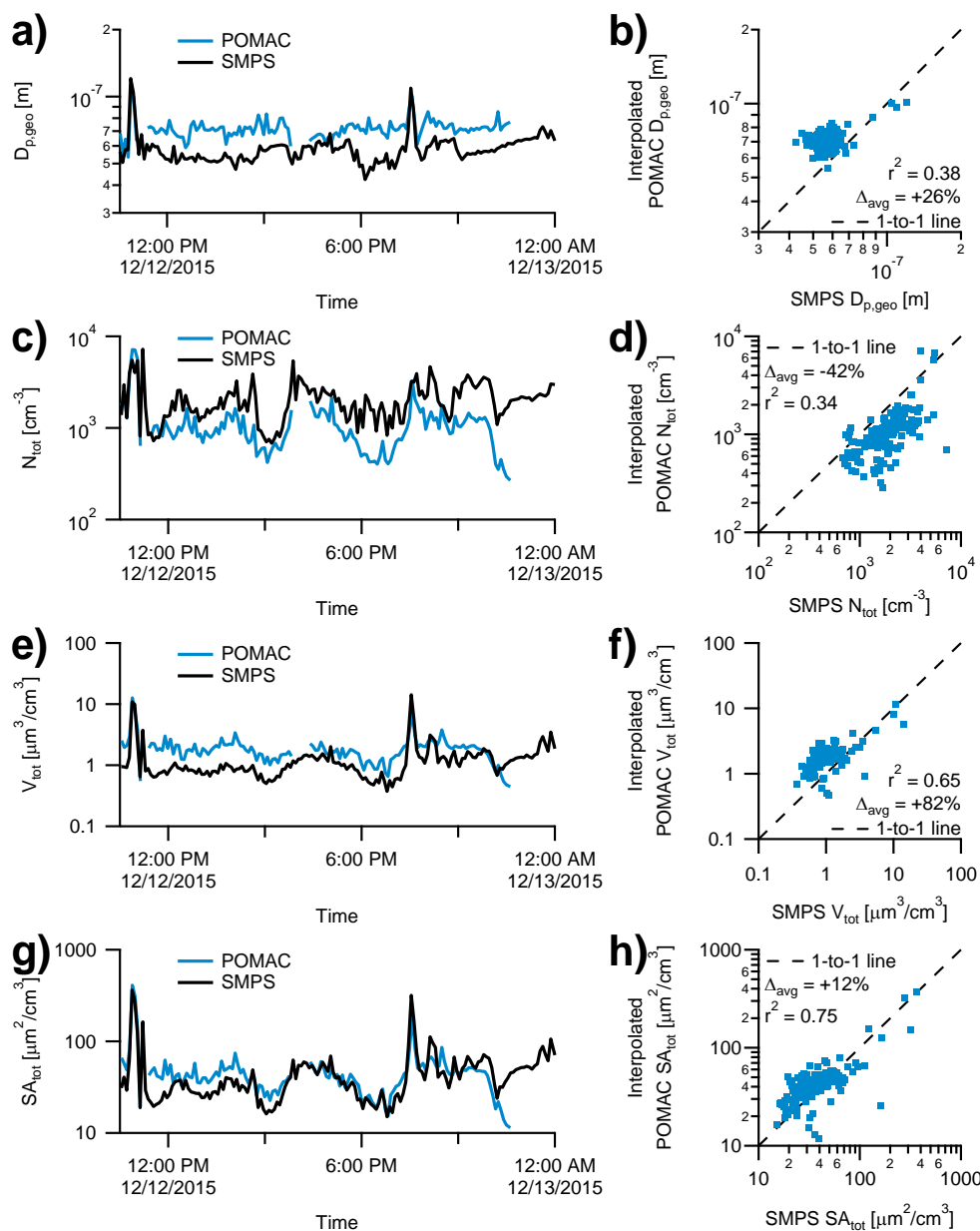


Figure 6.14: Comparison metrics for the POMAC-MAGIC and SMPS 13.5-hour ambient sampling period calculated from the distributions in Fig. 6.13. Data collected after 2015-Dec-12 22:30 was omitted for comparison purposes since the MAGIC wick appeared to have dried out. a) Time series of geometric mean diameter. b) Time series of total particle number concentration. c) Time series of total particle volume concentration. d) Time series of total particle surface area concentration. e) One-to-one comparison of geometric mean diameter. f) One-to-one comparison of total particle number concentration. g) One-to-one comparison of total particle volume concentration. h) One-to-one comparison of total particle surface area concentration. The notation  $\Delta_{avg}$  denotes the mean percent difference of the POMAC-MAGIC value from the SMPS value.

Despite being designed for nucleation mode particle classification (and thus having smaller electrodes and shorter particle residence times), the ROMIAC-MAGIC system demonstrated excellent fidelity to the SMPS for ultrafine mode particles, deviating from key aerosol distribution metrics by less than  $\pm 10\%$  compared to the SMPS. The POMAC-MAGIC system, which was designed to accommodate the lower cross-flow velocities required for accumulation mode particle classification, reported total particle surface area concentrations 12% greater than the SMPS, on average, but also deviated from the SMPS total particle volume concentrations by +82%.

The disagreement between the SMPS and POMAC-MAGIC systems for the  $D_{p,geo}$ ,  $N_{tot}$ , and  $V_{tot}$  metrics is quite substantial and likely due to the non-ideal mobility classification behavior of this prototype POMAC. However, this analysis has provided valuable insight for design and construction improvements for future iterations of OMACs intended for accumulation mode aerosol classification.

First, it is of utmost importance that the porous, conductive electrode material have the rigidity to span distances  $\sim 10$  cm without deflection while having a near-homogeneous porosity. Stainless steel wire woven mesh falters in the former requirement, while metal filter paper and sintered metal frits falter in the latter. A potential solution would be layered metal screens of progressively increasing fineness made from thin metal sheets via photo-etching, electrical discharge machining, or laser cutting. A fine stainless steel woven mesh can then be brazed taut onto the finest metal sheet screen to provide a final opening size that is smaller than can be achieved through the aforementioned machining techniques.

Second, the cross-flow should be introduced in a manner such that it is not initially introduced into the OMAC perpendicular to, and thus impinging on, the electrodes. This contributes to the cross-flow velocity inhomogeneity. Rather, the cross-flow should be introduced along  $L$  or  $W$ , or even through a distribution channel along the perimeter, to eliminate cross-flow impinging on the electrodes.

Third, the classification region  $L/W$  ratio (unity in the present POMAC prototype) should be increased to reduce the variability in particle transit distances and residence times, which increases the probability that a counted particle is “smeared” into incorrect mobility channels as shorter channel counting times are approached. An increased  $L/W$  ratio would also reduce the distance across which an electrode must span, reducing electrode deflection and aiding the maintenance of a consistent electrode separation distance through the entire classification region.

Fourth, further work must be done to better introduce the aerosol sample such that the aerosol fills the entire space between the OMAC electrodes across the entire length of the classification region, which is the assumption made in theoretical calculations of OMAC performance made by Flagan (2004), Downard, Dama, and Flagan (2011), and Mai and Flagan (2017). Current realizations of the OMAC distribute the aerosol sample into the classification region through a narrow, flow resisting gap. As a result, the aerosol particles only occupy a small fraction of the electrode separation distance, especially in the case of larger particles for which diffusion is negligible. This maldistribution of aerosol particles across the electrode gap contributes to deviations from the ideal behavior of the OMAC mobility-voltage relationship and theoretically attainable resolution.

Finally, both the ROMIAC and POMAC can be made much smaller in physical size and mass through the use of custom fittings and reduced casing material. Much of the ROMIAC's heft is the result of an initial design feature that allowed for interchangeable components to vary the electrode separation distance. The POMAC required substantial case material to ensure proper compression of gasket material, as well as clearance for electrodes that were initially composed of stainless steel wire woven mesh stretched taut over a frame. The use of a higher  $L/W$  ratio with an elliptical casing may allow for the use of an o-ring for sealing instead of gasket material, which would greatly reduce the compression requirements, while the development of a layered machined screen electrode with brazed stainless steel wire woven mesh would greatly reduce the clearance volume required.

The optimal miniature aerosol mobility classifier system may consist of two OMAC-MAGIC components that are designed and operated to excel in the measurement of different size ranges. One OMAC-MAGIC would be designed to probe the ultrafine particle regime and would have classification region dimensions and operation flow rates similar to that of the ROMIAC, while the other OMAC-MAGIC would be designed to probe the  $100 < D_p < 1000$  nm regime and have dimensions and operation flow rates similar to that of the prototype POMAC in this study.

Nonetheless, the prototype classifiers and detector in this study demonstrate the potential for miniaturized, lightweight systems to attain high fidelity aerosol particle number size distributions. Such systems will be critical for decreasing the costs and increasing the viability of portable personal exposure monitoring, regional network monitoring, and UAV-based measurements.

## **6.5 Acknowledgments**

We thank Arantzazu Eiguren-Fernandez, Nathan M. Kreisberg, and Gregory S. Lewis of Aerosol Dynamics Inc. for their technical assistance. This work was supported by National Institutes of Health under Grant No. 1R43OH010515-01 and the Department of Energy under Grant No. DE-SC0013152.



## References

- Asbach, C. et al. (2009). “Conceptual limitations and extensions of lung-deposited Nanoparticle Surface Area Monitor (NSAM)”. In: *J. Nanopart. Res.* 11.1, pp. 101–109. DOI: 10.1007/s11051-008-9479-8.
- Bräuner, E. V. et al. (2007). “Exposure to ultrafine particles from ambient air and oxidative stress-induced DNA damage”. In: *Environ. Health Persp.* 115.8, pp. 1177–1182. DOI: 10.1289/ehp.9984.
- Carlson, C. et al. (2008). “Unique cellular interaction of silver nanoparticles: Size-dependent generation of reactive oxygen species”. In: *J. Phys. Chem. B* 112.43, pp. 13608–13619. DOI: 10.1021/jp712087m.
- Carpentieri, M. and P. Kumar (2011). “Ground-fixed and on-board measurements of nanoparticles in the wake of a moving vehicle”. In: *Atmos. Env.* 45.32, pp. 5837–5852. DOI: 10.1016/j.atmosenv.2011.06.079.
- Carpentieri, M., P. Kumar, and A. Robins (2011). “An overview of experimental results and dispersion modelling of nanoparticles in the wake of moving vehicles”. In: *Environ. Pollut.* 159.3, pp. 685–693. DOI: 10.1016/j.envpol.2010.11.041.
- Colomina, I. and P. Molina (2014). “Unmanned aerial systems for photogrammetry and remote sensing: A review”. In: *Int. Soc. Photogramme.* 92, pp. 79–97. DOI: 10.1016/j.isprsjprs.2014.02.013.
- Delfino, R. J., C. Sioutas, and S. Malik (2005). “Potential role of ultrafine particles in associations between airborne particle mass and cardiovascular health”. In: *Environ. Health Persp.* 113.8, pp. 934–946. DOI: 10.1289/ehp.7938.
- Donaldson, K., X. Y. Li, and W. MacNee (1998). “Ultrafine (nanometre) particle mediated lung injury”. In: *J. Aerosol Sci.* 29.5-6, pp. 553–560. DOI: 10.1016/S0021-8502(97)00464-3.
- Downard, A. J., J. F. Dama, and R. C. Flagan (2011). “An asymptotic analysis of differential electrical mobility classifiers”. In: *Aerosol Sci. Technol.* 45.6, pp. 717–729. DOI: 10.1080/02786826.2011.558136.
- Dusek, U. et al. (2006). “Size matters more than chemistry aerosol particles”. In: *Science* 312.5778, pp. 1375–1378. DOI: 10.1126/science.1125261.
- Ervens, B. et al. (2007). “Prediction of cloud condensation nucleus number concentration using measurements of aerosol size distributions and composition and light scattering enhancement due to humidity”. In: *J. Geophys. Res.* 112.10, D10S32. DOI: 10.1029/2006JD007426.
- Fierz, M. et al. (2014). “Aerosol measurement by induced currents”. In: *Aerosol Sci. Technol.* 48.4, pp. 350–357. DOI: 10.1080/02786826.2013.875981.

- Fissan, H. et al. (2007). “Rationale and principle of an instrument measuring lung deposited nanoparticle surface area”. In: *J. Nanopart. Res.* 9.1, pp. 53–59. DOI: 10.1007/s11051-006-9156-8.
- Flagan, R. C. (1999). “On differential mobility analyzer resolution”. In: *Aerosol Sci. Technol.* 30.6, pp. 556–570. DOI: 10.1080/027868299304417.
- (2004). “Opposed migration aerosol classifier (OMAC)”. In: *Aerosol Sci. Technol.* 38.9, pp. 890–899. DOI: 10.1080/027868290505242.
- Fuchs, N. A. (1963). “On the stationary charge distribution on aerosol particles in a bipolar ionic environment”. In: *Geofisica pura e applicata* 56.1, pp. 185–193.
- Hagwood, C., Y. Sivathanu, and G. Mulholland (1999). “The DMA transfer function with Brownian motion a trajectory/Monte-Carlo approach”. In: *Aerosol Sci. Technol.* 30.1, pp. 40–61. DOI: 10.1080/027868299304877.
- Hering, S. V., S. R. Spielman, and G. S. Lewis (2014). “Moderated water-based condensational particle growth in a laminar flow”. In: *Aerosol Sci. Technol.* 48.4, pp. 401–408. DOI: 10.1080/02786826.2014.881460.
- Hering, S. V. and M. R. Stolzenburg (2005). “A method for particle size amplification by water condensation in a laminar, thermally diffusive flow”. In: *Aerosol Sci. Technol.* 39.5, pp. 428–436. DOI: 10.1080/027868290953416.
- Hering, S. V., M. R. Stolzenburg, et al. (2005). “A laminar-flow, water-based condensation particle counter (WCPC)”. In: *Aerosol Sci. Technol.* 39.7, pp. 659–672. DOI: 10.1080/02786820500182123.
- Hoek, G. et al. (2002). “Association between mortality and indicators of traffic-related air pollution in the Netherlands: A cohort study”. In: *Lancet* 360.9341, pp. 1203–1209. DOI: 10.1016/S0140-6736(02)11280-3.
- Holguin, F. (2008). “Traffic, outdoor air pollution, and asthma”. In: *Immunol. Allergy Clin. N. Am.* 28.3, pp. 577–588. DOI: 10.1016/j.iac.2008.03.008.
- Holmes, J. R. (1994). *How much air do we breathe? Measurement of breathing rate and volume in routinely performed activities*. Tech. rep. 94-11. Sacramento, CA: California Environmental Protection Agency. URL: <https://www.arb.ca.gov/research/resnotes/notes/94-11.htm>.
- Hoppel, W. A. and G. M. Frick (1986). “Ion-aerosol attachment coefficients and the steady-state charge distribution on aerosols in a bipolar ion environment”. In: *Aerosol Sci. Technol.* 5.1, pp. 1–21. DOI: 10.1080/02786828608959073.
- ICRP (1994). *Human respiratory tract model for radiological protection. ICRP publication 66*. Tech. rep. 1-3. International Commission on Radiological Protection, p. 482.

- IPCC (2013). *Climate change 2013: The physical science basis. Contribution of Working Group I to the Fifth Assessment report of the Intergovernmental Panel on Climate Change*. Ed. by T. F. Stocker et al. Cambridge, UK and New York, NY, USA: Cambridge University Press, p. 1535.
- Jiang, J. et al. (2011). “Transfer functions and penetrations of five differential mobility analyzers for sub-2 nm particle classification”. In: *Aerosol Sci. Technol.* 45.4, pp. 480–492. DOI: 10.1080/02786826.2010.546819.
- Joodatnia, P., P. Kumar, and A. Robins (2013). “The behaviour of traffic produced nanoparticles in a car cabin and resulting exposure rates”. In: *Atmos. Env.* 65, pp. 40–51. DOI: 10.1016/j.atmosenv.2012.10.025.
- Ketzel, M. and R. Berkowicz (2004). “Modelling the fate of ultrafine particles from exhaust pipe to rural background: An analysis of time scales for dilution, coagulation and deposition”. In: *Atmos. Env.* 38.17, pp. 2639–2652. DOI: 10.1016/j.atmosenv.2004.02.020.
- Knutson, E. O. and K. T. Whitby (1975). “Aerosol classification by electrical mobility: apparatus, theory, and applications”. In: *J. Aerosol Sci.* 6, pp. 443–451. DOI: 10.1016/0021-8502(75)90060-9.
- Kreyling, W. G. et al. (2011). “Translocation of inhaled nanoparticles”. In: *Cardio-vascular effects of inhaled ultrafine and nanosized particles*. Ed. by F. R. Cassee, N. L. Mills, and D. E. Newby. Hoboken, NJ, USA: John Wiley & Sons, Inc. Chap. 7, pp. 25–143.
- Li, N., J. R. Harkema, et al. (2010). “Ambient ultrafine particles provide a strong adjuvant effect in the secondary immune response: implication for traffic-related asthma flares”. In: *Am. J. Physiol. Lung Cell Mol. Physiol.* 299.3, pp. L374–83. DOI: 10.1152/ajplung.00115.2010.
- Li, N., C. Sioutas, et al. (2003). “Ultrafine particulate pollutants induce oxidative stress and mitochondrial damage”. In: *Environ. Health Persp.* 111.4, pp. 455–460. DOI: 10.1289/ehp.6000.
- Liu, Q. and D.-R. Chen (2016). “Experimental evaluation of miniature plate DMAs (mini-plate DMAs) for future ultrafine particle (UFP) sensor network”. In: *Aerosol Sci. Technol.* 50.3, pp. 297–307.
- Mai, H. and R. C. Flagan (2017). “Opposed migration aerosol classifier transfer function”. In: *Aerosol Sci. Technol.* In prep.
- Marra, J., M. Voetz, and H.-J. Kiesling (2010). “Monitor for detecting and assessing exposure to airborne nanoparticles”. In: *J. Nanopart. Res.* 12.1, pp. 21–37. DOI: 10.1007/s11051-009-9695-x.
- Maynard, A. D. and E. D. Kuempel (2005). “Airborne nanostructured particles and occupational health”. In: *J. Nanopart. Res.* 7.6, pp. 587–614. DOI: 10.1007/s11051-005-6770-9.

- Mertes, S., F. Schröder, and A. Wiedensohler (1995). "The particle detection efficiency curve of the TSI-3010 CPC as a function of the temperature difference between saturator and condenser". In: *Aerosol Sci. Technol.* 23.2, pp. 257–261. DOI: 10.1080/02786829508965310.
- Mui, W., H. Mai, et al. (2017). "Design, simulation, and characterization of a radial opposed migration ion and aerosol classifier (ROMIAC)". In: *Aerosol Sci. Technol.* In review.
- Mui, W., D. A. Thomas, et al. (2013). "Ion mobility-mass spectrometry with a radial opposed migration ion and aerosol classifier (ROMIAC)". In: *Anal. Chem.* 85, pp. 6319–6326. DOI: 10.1021/ac400580u.
- Oberdörster, G., E. Oberdörster, and J. Oberdörster (2005). "Nanotoxicology: An Emerging Discipline Evolving from Studies of Ultrafine Particles". In: *Environ. Health Persp.* 113.7, pp. 823–839. DOI: 10.1289/ehp.7339.
- Oberdörster, G., Z. Sharp, et al. (2004). "Translocation of inhaled ultrafine particles to the brain". In: *Inhal. Toxicol.* 16.6-7, pp. 437–445. DOI: 10.1080/08958370490439597.
- Patel, M. M. and R. L. Miller (2009). "Air pollution and childhood asthma: recent advances and future directions". In: *Curr. Opin. Pediatr.* 21.2, pp. 235–242. DOI: 10.1097/MOP.0b013e3283267726.
- Peters, A. et al. (2004). "Exposure to traffic and the onset of myocardial infarction". In: *New Engl. J. Med.* 351.17, pp. 1721–1730. DOI: 10.1056/NEJMoa0810625.
- Salam, M. T., T. Islam, and F. D. Gilliland (2008). "Recent evidence for adverse effects of residential proximity to traffic sources on asthma proximity". In: *Curr. Opin. Pulm. Med.* 14.1, pp. 3–8. DOI: 10.1097/MCP.0b013e3282f1987a.
- Samet, J. M. et al. (2000). "Fine particulate air pollution and mortality in 20 U.S. cities, 1987-1994". In: *New Engl. J. Med.* 343.24, pp. 1742–1749. DOI: 10.1056/NEJMoa012295. arXiv: NIHMS183007.
- Seinfeld, J. H. and S. N. Pandis (2006). *Atmospheric Chemistry and Physics: From air pollution to climate change*. 2nd. New York: John Wiley & Sons.
- Shah, A. P. et al. (2008). "Effect of inhaled carbon ultrafine particles on reactive hyperemia in healthy human subjects". In: *Environ. Health Persp.* 116.3, pp. 375–380. DOI: 10.1289/ehp.10323.
- Steer, B. et al. (2014). "Portable Planar DMA: Development and Tests". In: *Aerosol Sci. Technol.* 48.3, pp. 251–260. DOI: 10.1080/02786826.2013.868863.
- Stewart, J. C. et al. (2010). "Vascular effects of ultrafine particles in persons with type 2 diabetes". In: *Environ. Health Persp.* 118.12, pp. 1692–1698. DOI: 10.1289/ehp.1002237.
- Stolzenburg, M. R. (1988). "An ultrafine aerosol size distribution measuring system". Ph.D. Thesis. University of Minnesota.

- Stolzenburg, M., N. Kreisberg, and S. V. Hering (1998). "Atmospheric size distributions measured by differential mobility optical particle size spectrometry". In: *Aerosol Sci. Technol.* 29.5, pp. 402–418. DOI: 10.1080/02786829808965579.
- USEPA (2015). *NAAQS Table*. URL: <https://www.epa.gov/criteria-air-pollutants/naaqs-table>.
- Wiedensohler, A. (1988). "An approximation of the bipolar charge distribution for particles in the submicron size range". In: *J. Aerosol Sci.* 19.3, pp. 387–389.
- Wiedensohler, A. et al. (1997). "Intercomparison study of the size-dependent counting efficiency of 26 condensation particle counters". In: *Aerosol Sci. Technol.* 27.2, pp. 224–242. DOI: 10.1080/02786829708965469.
- Wilson, R. and J. D. Spengler, eds. (1996). *Particles in our air: concentrations and health effects*. Harvard University Press, p. 265.
- Zhang, K. M. and A. S. Wexler (2004). "Evolution of particle number distribution near roadways—Part I: analysis of aerosol dynamics and its implications for engine emission measurement". In: *Atmos. Env.* 38.38, pp. 6643–6653. DOI: 10.1016/j.atmosenv.2004.06.043.
- Zhang, K. M., A. S. Wexler, D. A. Niemeier, et al. (2005). "Evolution of particle number distribution near roadways. Part III: Traffic analysis and on-road size resolved particulate emission factors". In: *Atmos. Env.* 39.22, pp. 4155–4166. DOI: 10.1016/j.atmosenv.2005.04.003.
- Zhang, K. M., A. S. Wexler, Y. F. Zhu, et al. (2004). "Evolution of particle number distribution near roadways. Part II: the 'Road-to-Ambient' process". In: *Atmos. Env.* 38.38, pp. 6655–6665. DOI: 10.1016/j.atmosenv.2004.06.044.
- Zhang, S.-H. and R. C. Flagan (1996). "Resolution of the radial differential mobility analyzer for ultrafine particles". In: *J. Aerosol Sci.* 27.8, pp. 1179–1200.
- Zhu, Y., W. C. Hinds, S. Kim, S. Shen, et al. (2002). "Study of ultrafine particles near a major highway with heavy-duty diesel traffic". In: *Atmos. Env.* 36.27, pp. 4323–4335. DOI: 10.1016/S1352-2310(02)00354-0.
- Zhu, Y., W. C. Hinds, S. Kim, and C. Sioutas (2002). "Concentration and size distribution of ultrafine particles near a major highway". In: *J. Air Waste Manage.* 52.9, pp. 1032–1042. DOI: 10.1080/10473289.2002.10470842.
- Zhu, Y., W. C. Hinds, S. Shen, et al. (2004). "Seasonal trends of concentration and size distribution of ultrafine particles near major highways in Los Angeles Special Issue of Aerosol Science and Technology on Findings from the Fine Particulate Matter Supersites Program". In: *Aerosol Sci. Technol.* 38.S1, pp. 5–13. DOI: 10.1080/02786820390229156.
- Zhu, Y., T. Kuhn, et al. (2006). "Comparison of daytime and nighttime concentration profiles and size distributions of ultrafine particles near a major highway". In: *Environ. Sci. Technol.* 40.8, pp. 2531–6.

## *Appendix A*

### SUPPLEMENTARY INFORMATION FOR DESIGN, SIMULATION, AND CHARACTERIZATION OF A RADIAL OPPOSED MIGRATION ION AND AEROSOL CLASSIFIER (ROMIAC)

#### **A.1 Preliminary electrode mesh comparisons**

##### **Performance similarity between 325-mesh and 200-mesh electrodes**

As stated in the main text, the two prototype ROMIACs are deemed “nearly identical”. The only difference between the two instruments in the final study is the fineness of mesh used for the electrodes. In the final study, ROMIAC1 used 325-mesh for its electrodes, while ROMIAC2 used 200-mesh for its electrodes.

Initially, both ROMIACs had 325-mesh electrodes, but one pair of 325-mesh electrodes was damaged during assembly. Consequently, there were only enough available pairs of 325-mesh electrode for one ROMIAC. There were not enough available pairs of other meshes for both ROMIACs to have the same electrode mesh fineness, so preliminary measurements were made to see if there would be a large difference in transmission efficiency (in the same given ROMIAC) between using a pair of 325-mesh and 200-mesh electrodes. The transmission efficiency of TDDAB monomer (1.70 nm mobility-equivalent diameter) was measured for ROMIAC1 using 325-mesh electrodes and 200-mesh electrodes. The results in Fig. A.1 show that ROMIAC1 would achieve ~13% transmission efficiency of TDDAB monomer whether it used 200-mesh or 325-mesh electrodes. Since there was not a large observed difference in performance, it was deemed acceptable for ROMIAC1 to use 325-mesh and ROMIAC2 to use 200-mesh in the final study.

##### **Performance similarity between upper electrodes with and without hole**

Preliminary measurements also sought to answer the question of whether the aerosol outlet tubing resting directly on a mesh would negatively impact transmission efficiency. It was thought that the mesh would act like a fine screen filter, causing particle losses as particles exit the classification region and pass through the mesh into the outlet tubing. A pair of 500-mesh electrodes were used in these measurements. First, ROMIAC1 was outfitted with the 500-mesh electrodes as originally constructed, with no hole (Fig. A.2a) and then TDDAB monomer transmission

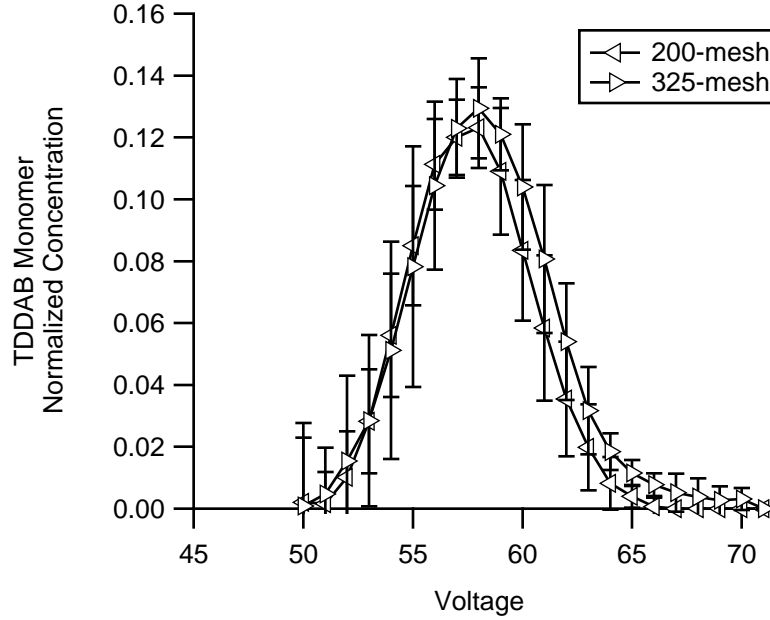


Figure A.1: Transmission efficiency measurements of TDDAB monomer through ROMIAC1 using 200-mesh and 325-mesh. Error bars represent 2 standard deviations of triplicate measurements.

efficiency measurements were conducted. Then a hole was cut out in the 500-mesh upper electrode for the aerosol outlet tubing (Fig. A.2b) and the transmission efficiency of TDDAB monomer was measured again. The results in Fig. A.3 show that ROMIAC1 would achieve  $\sim 10.5\%$  transmission efficiency of TDDAB monomer whether or not a 500-mesh upper electrode had a hole cut out for the aerosol outlet tubing.

## A.2 Detailed results

The following tables list detailed results from every measurement from the simulations and the experiments. The subscript “ref” pertains to the reference properties of the particle coming out of the source (first) classifier in tandem classifier setups. The subscript “avg” means average. “RSD” means relative standard deviation. RSD values represent precision, not accuracy. The RSD values for flow rates were calculated from repeated measurements during the course of an experiment. RSD values for  $\beta$ ,  $\delta$ ,  $\mathcal{R}_{nd,nom}$  are calculated from propagation of the flow rate RSD values.

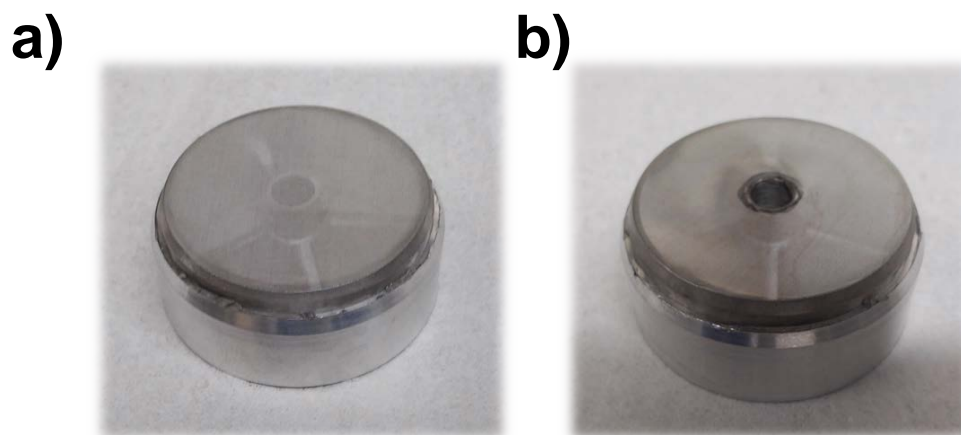


Figure A.2: 500-mesh upper electrode with (a) no hole cut out for the aerosol outlet tubing and (b) with hole cut out for aerosol outlet tubing.

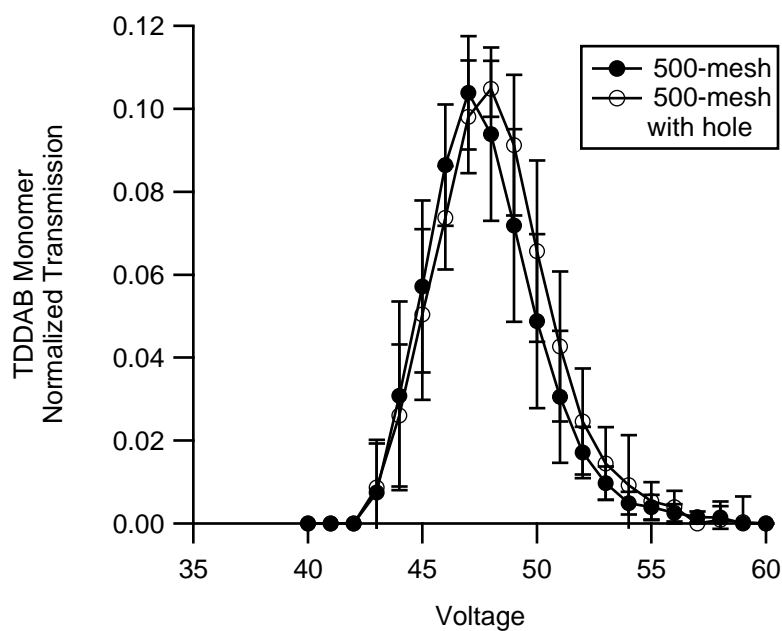


Figure A.3: Transmission efficiency measurements of TDDAB monomer through ROMIAC1 using 500-mesh electrodes without and with a hole cut in the upper electrode for the aerosol outlet tubing. Error bars represent 2 standard deviations of triplicate measurements.



RSD values for  $f_Z$ ,  $f_\beta$ ,  $\sigma_{\text{distor}}^2$ ,  $\eta_{\text{trans}}$ ,  $\mathcal{R}$ , and  $\mathcal{R}/\mathcal{R}_{\text{nd}}$  were calculated from repeated measurements (at least 3) of a given  $Q_{\text{a}}/Q_{\text{cf}}/D_Z$  combination.

Table A.1: Detailed simulation results.

| $D_{z,nom}$ | $Z_{nom}$ | $1/Z_{nom}$          | $D_{nom}$           | $V_{nom}$ | $P_{mig}$ | $Q_{a,nom}$ | $Q_{cf,nom}$ | $R_{nd,nom}$ | $\beta_{nom}$ | $\eta_{trans}$ | $f_{\beta}$ | $f_z$ | $\sigma^2_{theo}$ | $\sigma^2_{distor}$ | $R_{avg}$ | $R/R_{nd,nom}$ |
|-------------|-----------|----------------------|---------------------|-----------|-----------|-------------|--------------|--------------|---------------|----------------|-------------|-------|-------------------|---------------------|-----------|----------------|
| [m]         | [m/Vs]    | [Vs/m <sup>2</sup> ] | [m <sup>2</sup> /s] | [V]       |           | [lpn]       | [lpn]        |              |               |                |             |       |                   |                     |           |                |
| 1.16E-09    | 1.52E-04  | 6.58E+03             | 3.90E-06            | 5.64E+01  | 2.20E+03  | 1.7         | 34.3         | 20.18        | 0.05          | 0.01           | 0.91        | 1.06  | 3.92E-04          | 5.02E-04            | 13.06     | 0.65           |
| 1.47E-09    | 9.47E-05  | 1.06E+04             | 2.43E-06            | 9.06E+01  | 3.53E+03  | 1.7         | 34.3         | 20.18        | 0.05          | 0.03           | 1.00        | 1.06  | 2.33E-04          | 3.83E-04            | 13.91     | 0.69           |
| 1.70E-09    | 7.08E-05  | 1.41E+04             | 1.82E-06            | 1.21E+02  | 4.71E+03  | 1.7         | 34.3         | 20.18        | 0.05          | 0.05           | 1.00        | 1.06  | 1.70E-04          | 3.52E-04            | 14.30     | 0.71           |
| 5.00E-09    | 8.26E-06  | 1.21E+05             | 2.12E-07            | 1.04E+03  | 4.04E+04  | 1.7         | 34.3         | 20.18        | 0.05          | 0.18           | 1.00        | 1.06  | 1.81E-05          | 3.15E-04            | 15.68     | 0.78           |
| 1.00E-08    | 2.09E-06  | 4.78E+05             | 5.37E-08            | 4.10E+03  | 1.60E+05  | 1.7         | 34.3         | 20.18        | 0.05          | 0.23           | 1.00        | 1.06  | 4.63E-06          | 2.15E-04            | 15.68     | 0.78           |
| 1.20E-08    | 1.46E-06  | 6.85E+05             | 3.75E-08            | 5.87E+03  | 2.29E+05  | 1.7         | 34.3         | 20.18        | 0.05          | 0.23           | 1.00        | 1.06  | 1.19E-06          | 2.30E-04            | 15.58     | 0.77           |
| 1.16E-09    | 1.52E-04  | 6.58E+03             | 3.90E-06            | 2.19E+01  | 8.52E+02  | 2           | 13.3         | 6.65         | 0.15          | 0.06           | 0.83        | 1.07  | 4.55E-04          | 7.11E-04            | 6.46      | 0.97           |
| 1.47E-09    | 9.47E-05  | 1.06E+04             | 2.43E-06            | 3.51E+01  | 1.37E+03  | 2           | 13.3         | 6.65         | 0.15          | 0.12           | 0.79        | 1.07  | 2.71E-04          | 6.23E-04            | 6.91      | 1.04           |
| 1.70E-09    | 7.08E-05  | 1.41E+04             | 1.82E-06            | 4.69E+01  | 1.83E+03  | 2           | 13.3         | 6.65         | 0.15          | 0.17           | 0.77        | 1.07  | 1.98E-04          | 5.83E-04            | 7.07      | 1.06           |
| 5.00E-09    | 8.26E-06  | 1.21E+05             | 2.12E-07            | 4.03E+02  | 1.57E+04  | 2           | 13.3         | 6.65         | 0.15          | 0.51           | 0.71        | 1.06  | 2.18E-05          | 4.50E-04            | 7.78      | 1.17           |
| 1.00E-08    | 2.09E-06  | 4.78E+05             | 5.37E-08            | 1.59E+03  | 6.19E+04  | 2           | 13.3         | 6.65         | 0.15          | 0.58           | 0.71        | 1.06  | 5.54E-06          | 4.18E-04            | 7.70      | 1.16           |
| 2.00E-08    | 5.37E-07  | 1.86E+06             | 1.38E-08            | 6.19E+03  | 2.41E+05  | 2           | 13.3         | 6.65         | 0.15          | 0.61           | 0.72        | 1.06  | 1.43E-06          | 3.84E-04            | 7.72      | 1.16           |
| 1.16E-09    | 1.52E-04  | 6.58E+03             | 3.90E-06            | 2.73E+01  | 1.06E+03  | 2           | 16.6         | 8.30         | 0.12          | 0.05           | 0.83        | 1.07  | 5.21E-04          | 9.18E-04            | 7.40      | 0.89           |
| 1.47E-09    | 9.47E-05  | 1.06E+04             | 2.43E-06            | 4.38E+01  | 1.71E+03  | 2           | 16.6         | 8.30         | 0.12          | 0.11           | 0.85        | 1.07  | 3.12E-04          | 8.70E-04            | 7.86      | 0.95           |
| 1.70E-09    | 7.08E-05  | 1.41E+04             | 1.82E-06            | 5.86E+01  | 2.28E+03  | 2           | 16.6         | 8.30         | 0.12          | 0.15           | 0.82        | 1.07  | 2.28E-04          | 8.62E-04            | 8.23      | 0.99           |
| 5.00E-09    | 8.26E-06  | 1.21E+05             | 2.12E-07            | 5.03E+02  | 1.96E+04  | 2           | 16.6         | 8.30         | 0.12          | 0.46           | 0.74        | 1.07  | 2.53E-05          | 7.55E-04            | 9.44      | 1.14           |
| 1.00E-08    | 2.09E-06  | 4.78E+05             | 5.37E-08            | 1.98E+03  | 7.73E+04  | 2           | 16.6         | 8.30         | 0.12          | 0.53           | 0.76        | 1.07  | 6.50E-06          | 6.18E-04            | 9.32      | 1.12           |
| 1.80E-08    | 6.60E-07  | 1.52E+06             | 1.69E-08            | 6.29E+03  | 2.45E+05  | 2           | 16.6         | 8.30         | 0.12          | 0.56           | 0.76        | 1.07  | 1.66E-06          | 7.08E-04            | 9.31      | 1.12           |
| 1.16E-09    | 1.52E-04  | 6.58E+03             | 3.90E-06            | 3.29E+01  | 1.28E+03  | 2           | 20           | 10.00        | 0.10          | 0.04           | 0.92        | 1.06  | 3.76E-04          | 5.04E-04            | 8.78      | 0.88           |
| 1.47E-09    | 9.47E-05  | 1.06E+04             | 2.43E-06            | 5.28E+01  | 2.06E+03  | 2           | 20           | 10.00        | 0.10          | 0.09           | 0.88        | 1.06  | 2.24E-04          | 3.71E-04            | 9.36      | 0.94           |
| 1.70E-09    | 7.08E-05  | 1.41E+04             | 1.82E-06            | 7.06E+01  | 2.75E+03  | 2           | 20           | 10.00        | 0.10          | 0.13           | 0.87        | 1.06  | 1.63E-04          | 3.38E-04            | 9.50      | 0.95           |
| 5.00E-09    | 8.26E-06  | 1.21E+05             | 2.12E-07            | 6.05E+02  | 2.36E+04  | 2           | 20           | 10.00        | 0.10          | 0.41           | 0.80        | 1.06  | 1.73E-05          | 3.67E-04            | 10.69     | 1.07           |
| 1.00E-08    | 2.09E-06  | 4.78E+05             | 5.37E-08            | 2.39E+03  | 9.31E+04  | 2           | 20           | 10.00        | 0.10          | 0.50           | 0.77        | 1.06  | 4.45E-06          | 2.62E-04            | 10.93     | 1.09           |
| 1.50E-08    | 9.42E-07  | 1.06E+06             | 2.42E-08            | 5.31E+03  | 2.07E+05  | 2           | 20           | 10.00        | 0.10          | 0.50           | 0.79        | 1.06  | 1.14E-06          | 2.83E-04            | 10.70     | 1.07           |
| 1.16E-09    | 1.52E-04  | 6.58E+03             | 3.90E-06            | 4.94E+01  | 1.92E+03  | 2           | 30           | 15.00        | 0.07          | 0.03           | 1.00        | 1.06  | 2.52E-04          | 5.44E-04            | 11.38     | 0.76           |
| 1.47E-09    | 9.47E-05  | 1.06E+04             | 2.43E-06            | 7.92E+01  | 3.09E+03  | 2           | 30           | 15.00        | 0.07          | 0.06           | 1.00        | 1.06  | 1.59E-04          | 2.06E-04            | 12.20     | 0.81           |
| 1.70E-09    | 7.08E-05  | 1.41E+04             | 1.82E-06            | 1.06E+02  | 4.12E+03  | 2           | 30           | 15.00        | 0.07          | 0.09           | 1.00        | 1.06  | 1.16E-04          | 1.77E-04            | 12.72     | 0.85           |
| 5.00E-09    | 8.26E-06  | 1.21E+05             | 2.12E-07            | 9.08E+02  | 3.54E+04  | 2           | 30           | 15.00        | 0.07          | 0.29           | 0.92        | 1.06  | 1.21E-05          | 2.21E-04            | 13.82     | 0.92           |
| 1.00E-08    | 2.09E-06  | 4.78E+05             | 5.37E-08            | 3.59E+03  | 1.40E+05  | 2           | 30           | 15.00        | 0.07          | 0.35           | 0.90        | 1.06  | 3.16E-06          | 9.83E-05            | 14.06     | 0.94           |
| 1.20E-08    | 1.46E-06  | 6.85E+05             | 3.75E-08            | 5.14E+03  | 2.00E+05  | 2           | 30           | 15.00        | 0.07          | 0.36           | 0.91        | 1.06  | 9.95E-07          | 1.00E-04            | 13.84     | 0.92           |
| 1.16E-09    | 1.52E-04  | 6.58E+03             | 3.90E-06            | 2.29E+01  | 8.91E+02  | 2.1         | 13.9         | 6.62         | 0.15          | 0.06           | 0.83        | 1.06  | 3.05E-04          | 4.61E-04            | 6.42      | 0.97           |
| 1.47E-09    | 9.47E-05  | 1.06E+04             | 2.43E-06            | 3.67E+01  | 1.43E+03  | 2.1         | 13.9         | 6.62         | 0.15          | 0.13           | 0.79        | 1.06  | 1.81E-04          | 3.84E-04            | 6.61      | 1.00           |
| 1.70E-09    | 7.08E-05  | 1.41E+04             | 1.82E-06            | 4.91E+01  | 1.91E+03  | 2.1         | 13.9         | 6.62         | 0.15          | 0.18           | 0.77        | 1.06  | 1.33E-04          | 3.12E-04            | 6.89      | 1.04           |
| 5.00E-09    | 8.26E-06  | 1.21E+05             | 2.12E-07            | 4.21E+02  | 1.64E+04  | 2.1         | 13.9         | 6.62         | 0.15          | 0.52           | 0.70        | 1.06  | 1.43E-05          | 3.59E-04            | 7.91      | 1.20           |
| 1.00E-08    | 2.09E-06  | 4.78E+05             | 5.37E-08            | 1.66E+03  | 6.47E+04  | 2.1         | 13.9         | 6.62         | 0.15          | 0.60           | 0.71        | 1.06  | 3.72E-06          | 1.83E-04            | 7.67      | 1.16           |
| 2.00E-08    | 5.37E-07  | 1.86E+06             | 1.38E-08            | 6.47E+03  | 2.52E+05  | 2.1         | 13.9         | 6.62         | 0.15          | 0.63           | 0.71        | 1.06  | 1.17E-06          | 1.95E-04            | 7.72      | 1.17           |
| 1.16E-09    | 1.52E-04  | 6.58E+03             | 3.90E-06            | 3.29E+01  | 1.28E+03  | 2.25        | 20           | 8.89         | 0.11          | 0.06           | 0.88        | 1.07  | 3.44E-04          | 6.45E-04            | 8.32      | 0.94           |
| 1.47E-09    | 9.47E-05  | 1.06E+04             | 2.43E-06            | 5.28E+01  | 2.06E+03  | 2.25        | 20           | 8.89         | 0.11          | 0.12           | 0.85        | 1.07  | 2.07E-04          | 4.96E-04            | 8.70      | 0.98           |
| 1.70E-09    | 7.08E-05  | 1.41E+04             | 1.82E-06            | 7.06E+01  | 2.75E+03  | 2.25        | 20           | 8.89         | 0.11          | 0.16           | 0.83        | 1.07  | 1.50E-04          | 5.52E-04            | 8.84      | 0.99           |
| 5.00E-09    | 8.26E-06  | 1.21E+05             | 2.12E-07            | 6.05E+02  | 2.36E+04  | 2.25        | 20           | 8.89         | 0.11          | 0.47           | 0.74        | 1.06  | 1.67E-05          | 4.33E-04            | 10.21     | 1.15           |
| 1.00E-08    | 2.09E-06  | 4.78E+05             | 5.37E-08            | 2.39E+03  | 9.31E+04  | 2.25        | 20           | 8.89         | 0.11          | 0.54           | 0.74        | 1.06  | 4.28E-06          | 3.58E-04            | 10.04     | 1.13           |
| 1.50E-08    | 9.42E-07  | 1.06E+06             | 2.42E-08            | 5.31E+03  | 2.07E+05  | 2.25        | 20           | 8.89         | 0.11          | 0.55           | 0.76        | 1.06  | 1.35E-06          | 3.76E-04            | 9.87      | 1.11           |
| 1.16E-09    | 1.52E-04  | 6.58E+03             | 3.90E-06            | 2.19E+01  | 8.52E+02  | 2.5         | 13.3         | 5.32         | 0.19          | 0.09           | 0.77        | 1.06  | 1.91E-04          | 2.71E-04            | 5.61      | 1.05           |
| 1.47E-09    | 9.47E-05  | 1.06E+04             | 2.43E-06            | 3.51E+01  | 1.37E+03  | 2.5         | 13.3         | 5.32         | 0.19          | 0.17           | 0.74        | 1.06  | 1.15E-04          | 1.70E-04            | 5.90      | 1.11           |
| 1.70E-09    | 7.08E-05  | 1.41E+04             | 1.82E-06            | 4.69E+01  | 1.83E+03  | 2.5         | 13.3         | 5.32         | 0.19          | 0.22           | 0.72        | 1.06  | 8.42E-05          | 1.24E-04            | 6.03      | 1.13           |
| 5.00E-09    | 8.26E-06  | 1.21E+05             | 2.12E-07            | 4.03E+02  | 1.57E+04  | 2.5         | 13.3         | 5.32         | 0.19          | 0.55           | 0.68        | 1.05  | 8.99E-06          | 8.93E-05            | 6.48      | 1.22           |
| 1.00E-08    | 2.09E-06  | 4.78E+05             | 5.37E-08            | 1.59E+03  | 6.19E+04  | 2.5         | 13.3         | 5.32         | 0.19          | 0.63           | 0.68        | 1.05  | 2.20E-06          | 1.71E-04            | 6.35      | 1.19           |
| 2.00E-08    | 5.37E-07  | 1.86E+06             | 1.38E-08            | 6.19E+03  | 2.41E+05  | 2.5         | 13.3         | 5.32         | 0.19          | 0.65           | 0.69        | 1.05  | 1.02E-06          | 8.05E-05            | 6.33      | 1.19           |
| 1.16E-09    | 1.52E-04  | 6.58E+03             | 3.90E-06            | 2.73E+01  | 1.06E+03  | 2.5         | 16.6         | 6.64         | 0.15          | 0.08           | 0.81        | 1.06  | 2.06E-04          | 2.87E-04            | 6.83      | 1.03           |
| 1.47E-09    | 9.47E-05  | 1.06E+04             | 2.43E-06            | 4.38E+01  | 1.71E+03  | 2.5         | 16.6         | 6.64         | 0.15          | 0.15           | 0.77        | 1.06  | 1.24E-04          | 1.87E-04            | 7.20      | 1.08           |
| 1.70E-09    | 7.08E-05  | 1.41E+04             | 1.82E-06            | 5.86E+01  | 2.28E+03  | 2.5         | 16.6         | 6.64         | 0.15          | 0.20           | 0.76        | 1.06  | 9.02E-05          | 1.67E-04            | 7.19      | 1.08           |
| 5.00E-09    | 8.26E-06  | 1.21E+05             | 2.12E-07            | 5.03E+02  | 1.96E+04  | 2.5         | 16.6         | 6.64         | 0.15          | 0.53           | 0.70        | 1.06  | 9.44E-06          | 2.19E-04            | 7.86      | 1.18           |
| 1.00E-08    | 2.09E-06  | 4.78E+05             | 5.37E-08            | 1.98E+03  | 7.73E+04  | 2.5         | 16.6         | 6.64         | 0.15          | 0.58           | 0.72        | 1.05  | 2.39E-06          | 2.08E-04            | 7.61      | 1.15           |
| 1.80E-08    | 6.60E-07  | 1.52E+06             | 1.69E-08            | 6.29E+03  | 2.45E+05  | 2.5         | 16.6         | 6.64         | 0.15          | 0.61           | 0.72        | 1.05  | 1.11E-06          | 1.20E-04            | 7.66      | 1.15           |
| 1.16E-09    | 1.52E-04  | 6.58E+03             | 3.90E-06            | 3.29E+01  | 1.28E+03  | 2.5         | 20           | 8.00         | 0.13          | 0.07           | 0.84        | 1.06  | 2.20E-04          | 3.04E-04            | 7.85      | 0.98           |
| 1.47E-09    | 9.47E-05  | 1.06E+04             | 2.43E-06            | 5.28E+01  | 2.06E+03  | 2.5         | 20           | 8.00         | 0.13          | 0.14           | 0.81        | 1.06  | 1.32E-04          | 2.03E-04            | 7.94      | 0.99           |
| 1.70E-09    | 7.08E-05  | 1.41E+04             | 1.82E-06            | 7.06E+01  | 2.75E+03  | 2.5         | 20           | 8.00         | 0.13          | 0.19           | 0.79        | 1.06  | 9.56E-05          | 2.16E-04            | 8.36      | 1.05           |
| 5.00E-09    | 8.26E-06  | 1.21E+05             | 2.12E-07            | 6.05E+02  | 2.36E+04  | 2.5         | 20           | 8.00         | 0.13          | 0.48           | 0.75        | 1.06  | 1.05E-05          | 1.26E-04            | 8.85      | 1.11           |
| 1.00E-08    | 2.09E-06  | 4.78E+05             | 5.37E-08            | 2.39E+03  | 9.31E+04  | 2.5         | 20           | 8.00         | 0.13          | 0.56           | 0.73        | 1.06  | 2.62E-06          | 1.79E-04            | 9.11      | 1.14           |
| 1.50E-08    | 9.42E-07  | 1.06E+06             | 2.42E-08            | 5.31E+03  | 2.07E+05  | 2.5         | 20           | 8.00         | 0.13          | 0.57           | 0.74        | 1.06  | 1.20E-06          | 1.35E-04            | 8.92      | 1.11           |
| 1.16E-09    | 1.52E-04  | 6.58E+03             | 3.90E-06            | 2.19E+01  | 8.52E+02  | 3           | 13.3         | 4.43         | 0.23          | 0.12           | 0.74        | 1.06  | 2.47E-04          | 4.31E-04            | 4.59      | 1.04           |
| 1.47E-09    | 9.47E-05  | 1.06E+04             | 2.43E-06            | 3.51E+01  | 1.37E+03  | 3           | 13.3         | 4.43         | 0.23          | 0.20           | 0.71        | 1.06  | 1.47E-04          | 3.83E-04            | 5.13      | 1.16           |
| 1.70E-09    | 7.08E-05  | 1.41E+04             | 1.82E-06            | 4.69E+01  | 1.83E+03  | 3           | 13.3         | 4.43         | 0.23          | 0.26           | 0.69        | 1.06  | 1.08E-04          | 3.35E-04            | 5.24      | 1.18           |
| 5.00E-09    | 8.26E-06  | 1.21E+05             | 2.12E-07            | 4.03E+02  | 1.57E+04  | 3           | 13.3         | 4.43         | 0.23          |                |             |       |                   |                     |           |                |





## Appendix B

SUPPLEMENTARY INFORMATION FOR ION  
MOBILITY–MASS SPECTROMETRY WITH A RADIAL  
OPPOSED MIGRATION ION AND AEROSOL CLASSIFIER  
(ROMIAC)

**B.1 Introduction to FRIPS**

Free radical initiated peptide sequencing (FRIPS) is an alternative method for the gas-phase sequencing that gives information complementary to that obtained by traditional CID or ECD/ETD experiments (Hodyss, Cox, and Beauchamp 2005). In this technique, a free radical precursor is attached to the N-terminus of a peptide or protein via standard NHS-activated coupling. When the derivatized peptide is subjected to collisional activation, loss of the free radical precursor via homolytic bond cleavage generates an acetyl radical at the N-terminus of the peptide. This radical then abstracts a hydrogen atom from various sites along the peptide, yielding side chain loss or cleavage of the  $C_\alpha$ –C backbone bond through  $\beta$ -elimination. The product ions formed are highly sensitive to the  $C_\beta$ –H bond dissociation energy (BDE) of each amino acid residue, with residues possessing high  $C_\beta$ –H preferentially generating side chain loss and those with low  $C_\beta$ –H leading to backbone dissociation (Sun et al. 2009). Figure B.1 shows a general schematic of the current generation of FRIPS reagent, which utilizes the 2,5-dioxopyrrolidin-1-yl 2-(2,2,6,6-tetramethylpiperidin-1-yloxy)acetate (TEMPO–NHS) as the free radical precursor. Free radical product ions may also be generated in the  $MS^2$  spectrum via reaction of generated acetyl radical without further collisional activation.

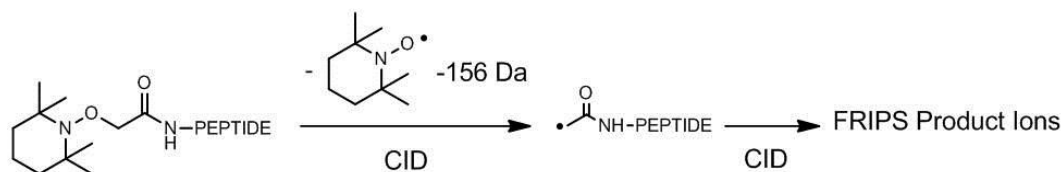


Figure B.1: Schematic of FRIPS methodology; the TEMPO precursor is coupled to the N-terminus of the peptide, and subsequent collisional activation leads to loss of the TEMPO moiety, generating an acetyl radical. CID of this radical then leads to hydrogen atom abstraction and followed by dissociation of the amino acid side chain or backbone.

## B.2 Materials and Methods

### Synthesis of TEMPO-based FRIPS Reagent

The TEMPO-based FRIPS reagent recently developed by Sohn and coworkers in the Beauchamp group, based upon the procedure outlined by Lee and coworkers (Lee et al. 2009), was synthesized and employed for free radical generation (Sohn 2011). Briefly, the FRIPS reagent was synthesized from a methyl 2-bromoacetate starting compound, to which the TEMPO (2,2,6,6-Tetramethylpiperidine-1-oxyl) reagent was coupled to give methyl 2-(2,2,6,6-tetramethylpiperidin-1-yloxy)acetate. This compound was then converted to 2-(2,2,6,6-tetramethylpiperidin-1-yloxy)acetic acid by stirring in 2M KOH in THF for 24 h. The free acid was then activated by mixing with trifluoroacetic N-hydroxysuccinimide ester in dry DMF for 24 h to yield 2,5-dioxopyrrolidin-1-yl 2-(2,2,6,6-tetramethylpiperidin-1-yloxy)acetate, the desired TEMPO-based FRIPS reagent.

### Model Peptide Derivatization

To derivatize the model peptides, ~1 mg of a peptide was dissolved in 1 mL of a 50/50 (v/v) mixture of acetonitrile and water, vortexed for 3 min, sonicated for 15 min, and centrifuged at 4500 rpm for 5 min. A reaction mixture of 50  $\mu$ L of peptide supernatant and 10  $\mu$ L of a 10  $\mu$ g/ $\mu$ L solution of FRIPS reagent in acetonitrile in a 100 mM triethylammonium bicarbonate buffer (pH 8.5) was prepared. The reaction was allowed to proceed for 2 hr and then quenched by addition of 2  $\mu$ L of formic acid. The solvent was removed with use of a rotary evaporator, and the sample was resuspended in 10  $\mu$ L of 0.1% trifluoroacetic acid and purified using a C18 ZipTip (Millipore, Billerica, MA) according to manufacturer protocol. The eluted sample was increased to a final volume of 500  $\mu$ L in 49% methanol, 49% water, and 2% acetic acid (v/v).

### Experimental Setup

The experimental setup consists of an electrospray ion source (ESI), the ROMIAC, and a Finnigan LTQ-MS (Thermo Electron Corp.); a detailed schematic is shown in Fig. B.2. A syringe pump fitted with a 250  $\mu$ L syringe (Hamilton Co., GASTIGHT 1725) supplies solution at a rate of 5  $\mu$ L  $\cdot$  min<sup>-1</sup> to the ESI, which is maintained at 5 kV potential relative to ground by a high voltage power supply (Acopian PO10HD6). Two equal flows of compressed N<sub>2</sub> gas are cleaned through a HEPA filter (Pall Life Sciences HEPA Capsule) and enter the ESI chamber perpendicular to the spray needle and convey ions to the ROMIAC. The ESI N<sub>2</sub> flow is measured by monitoring

the pressure drop through a laminar flow element (LFE) using a differential pressure transducer; the ESI gas temperature,  $T_{\text{ESI}}$ , is heated for some experiments via heating tape wrapped around the two gas inlet tubes to the ESI chamber, controlled by a variable autotransformer (Variat Type W5MT3) and measured with a thermocouple (Omega 871 Digital Thermometer). All TAAX, UB, and model peptide measurements were performed at  $T_{\text{ESI}} = 298$  K, while BK, AT1, and AT2 measurements were done at both  $T_{\text{ESI}} = 298$  K and 400 K.

The cross-flow gas through the ROMIAC is also compressed  $\text{N}_2$  that is cleaned through a HEPA filter and regulated with a proportioning solenoid valve (MKS Instruments Inc. 0248-20000SV). The cross-flow is exhausted through a vacuum pump (GAST 1023-101Q-G608X), with the flow rate kept constant by a critical orifice at the inlet to the vacuum pump. The flow rate of the classified ion flow leaving the ROMIAC is also monitored with a LFE. All experiments were run at  $Q_x = 34.3$  lpm and  $Q_s = 1.70$  lpm, resulting in  $\mathcal{R}_{\text{nd}} = 20.2$ , and the cross-flow gas temperature,  $T_x$ , was 298 K. Analytes were at atmospheric pressure the entire journey from the ESI spray needle to the LTQ-MS inlet, the duration of which is estimated to be on the order of tens to hundreds of milliseconds.

A proportional-integral-differential (PID) algorithm written in LabView provided feedback control of the sample and classified flow based on signals from the differential pressure transducers that monitor the pressure drops across the LFEs. Since the exiting cross-flow is held constant via a critical orifice, the incoming and exiting cross-flows were matched by the proportioning solenoid valve until the sample and classified flows were balanced. The LabView program also controlled the high voltage supply (EMCO High Voltage CA12N) to select the target ion mobility. Ion mobility spectra were obtained by stepping through a range of voltages and monitoring the LTQ-MS signal.

### Calibration Procedure

C2-C8 and C12 TAAX monomer ions were used as instrument calibration standards, as their reduced mobilities are unaffected by trace carrier gas contaminants and temperature (Fernández-Maestre et al. 2010; Viidanoja et al. 2005; Kaur-Atwal et al. 2009). TAAX monomer ion mobility values are from Viidanoja et al. 2005. There is a linear relationship ( $R^2 > 0.999$ ) between  $K_i^{-1}$  and  $\phi_i^*$  of the TAAX monomer standards (Fig. B.3). This relationship is used to determine  $K_i$  and reduced mobilities,  $K_{0,i}$ , of C2-C8 and C12 anion-coordinated multimer species.

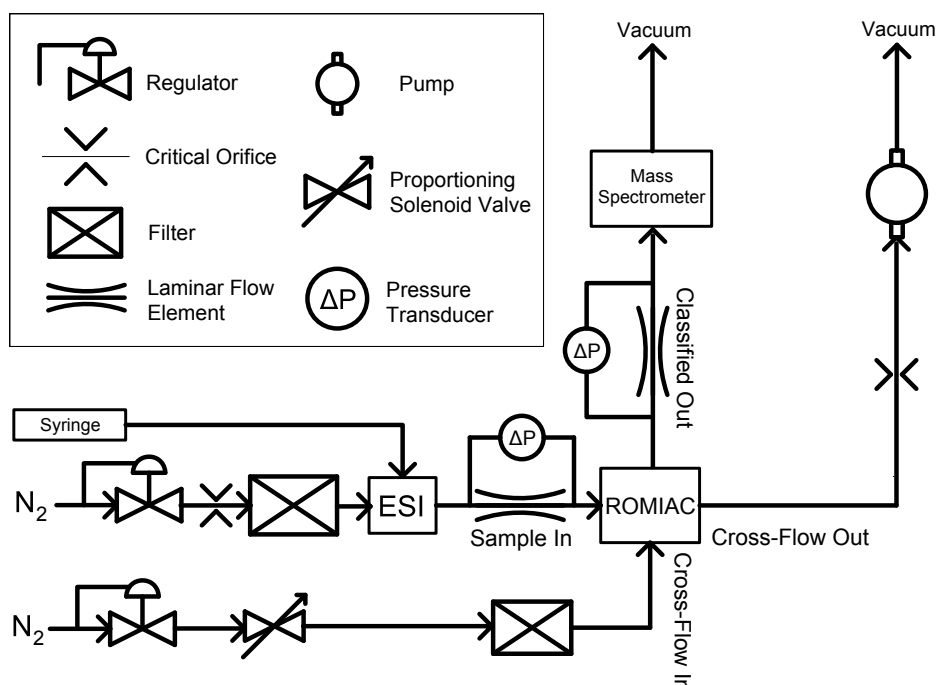


Figure B.2: Diagram of ESI-ROMIAC-LTQ-MS setup used to measure TAAX ion and peptide mobilities and cross sections. Flows were controlled both manually (with regulators and critical orifices) and automatically (with P-I-D input to solenoid valves) via a custom LabView program that responded to measured gas flows through the laminar flow elements. The program also varied the voltage across the ROMIAC electrodes.

The  $\Omega_i$  values of  $BK^{+1}$ ,  $BK^{+2}$ ,  $AT2^{+1}$ ,  $AT2^{+2}$ ,  $UB^{+7}$ , and  $UB^{+8}$  from Bush et al. 2010 and Wu, Klasmeier, and Hill 1999 were used for mobility calibration of the ROMIAC. A linear relationship exists between  $\phi_i^*$  and  $K_i^{-1}$ , and  $K_i^{-1}$  is related to  $\Omega_i$  via the Mason-Schamp equation (Revercomb and Mason 1975). For a mobility calibrant displaying multiple gas-phase conformers, the conformer making up the greatest proportion of the total signal in the classification spectrum was taken as the conformer corresponding to  $\phi_i^*$  for the calibrant. The relationship between  $\Omega_i$  and a coefficient  $\beta$  (a grouping of constants from the Mason-Schamp equation), is linear ( $R^2 > 0.996$ ; Fig. B.4). Each mobility spectrum was deconvoluted and peaks corresponding to a species were fitted to a Gaussian function. The contribution of each species to the total signal was estimated by calculating the integral under the Gaussian function.



Table B.1: LTQ–MS settings.

|                          |                      |
|--------------------------|----------------------|
| Electrospray Voltage     | 5 kV                 |
| Sheath Gas Flow Rate     | 1.7 lpm              |
| Cross Flow Rate          | 34.3 lpm             |
| Capillary Voltage        | 0 V                  |
| Capillary Temp           | 50° C                |
| Tube Lens Voltage        | 88 V                 |
| Multipole 00 Offset      | -3.7 V               |
| Lens 0 Voltage           | -4.3 V               |
| Multipole 0 Offset       | -4.6 V               |
| Gate Lens Voltage        | -38.5 V              |
| Multipole 1 Offset       | -8.9 V               |
| Multipole RF Amplitude   | 400 V <sub>p-p</sub> |
| Front Lens               | -4.9 V               |
| Front Section            | -8.8 V               |
| Center Section           | -11.9 V              |
| Back Section             | -6.75 V              |
| Back Lens                | 0 V                  |
| Trap Eject Offset        | 0 V                  |
| q value                  | 0.25                 |
| Activation Time          | 30 ms                |
| % Collisional Activation | 10%                  |

### B.3 Calculations

#### Reduced Mobility and Collisional Cross–Section

Calculated mobilities were converted to reduced mobilities,  $K_{0,i}$ , by the relationship

$$K_{0,i} = K_i \left( \frac{273.15 \text{ K}}{T} \right) \left( \frac{p}{101325 \text{ Pa}} \right), \quad (\text{B.1})$$

where  $T$  is the carrier gas temperature and  $p$  is the carrier gas pressure.

Collisional cross–section values of  $\text{BK}^{+1}$ ,  $\text{BK}^{+2}$ ,  $\text{AT2}^{+1}$ ,  $\text{AT2}^{+2}$ ,  $\text{UB}^{+7}$ , and  $\text{UB}^{+8}$  from Bush et al. 2010 and Wu, Klasmeier, and Hill 1999 were used in the mobility calibration of the ROMIAC. There is a linear relationship between  $\phi_i^*$  and  $K_i^{-1}$ , and  $K_i^{-1}$  is related to  $\Omega_i$  via the Mason–Schamp equation (Revercomb and Mason 1975):

$$K_i = \frac{3}{16} \frac{q_i}{N} \left( \frac{1}{m_i} + \frac{1}{M} \right)^{1/2} \left( \frac{2\pi}{kT} \right)^{1/2} \frac{1}{\Omega_i}, \quad (\text{B.2})$$

where  $q_i = z_i e$  is the ionic charge,  $N = \frac{p}{kT}$  is the carrier gas number density via the ideal gas law,  $k$  is the Boltzmann constant,  $m_i$  is the ion mass, and  $M$  is the carrier

Table B.2:  $m/z$  ranges used for mass-resolving ions.<sup>a</sup>

| Species                   | $m/z$ range | Species   | $m/z$ range |
|---------------------------|-------------|---|-------------|
| C2 monomer <sup>+1</sup>  | 129–134     | BK <sup>+1</sup>  | 1059–1064   |
| C2 dimer <sup>+1</sup>    | 339–344     | BK <sup>+2</sup>  | 529–534     |
| C2 trimer <sup>+1</sup>   | 549–554     | AT1 <sup>+1</sup>                                       | 1296–1301   |
| C2 tetramer <sup>+1</sup> | 759–764     | AT1 <sup>+2</sup>                                       | 647–652     |
| C2 pentamer <sup>+1</sup> | 969–974     | AT1 <sup>+3</sup>                                       | 431–436     |
| C2 hexamer <sup>+1</sup>  | 1180–1185   | AT2 <sup>+1</sup>                                       | 1045–1050   |
| C2 heptamer <sup>+1</sup> | 1390–1395   | AT2 <sup>+2</sup>                                       | 522–527     |
| C2 octamer <sup>+1</sup>  | 1600–1605   | UB <sup>+5</sup>  | 1712–1717   |
| C2 nonamer <sup>+1</sup>  | 1810–1815   | UB <sup>+6</sup>  | 1426–1431   |
| C3 monomer <sup>+1</sup>  | 185–190     | UB <sup>+7</sup>  | 1222–1227   |
| C3 dimer <sup>+1</sup>    | 498–503     | UB <sup>+8</sup>  | 1069–1074   |
| C3 trimer <sup>+1</sup>   | 811–816     | AARAAATAA b <sub>3</sub> –NH <sub>3</sub> fragment      | 281.5       |
| C3 tetramer <sup>+1</sup> | 1124–1129   | AARAAATAA b <sub>4</sub> –NH <sub>3</sub> fragment      | 352.5       |
| C3 pentamer <sup>+1</sup> | 1437–1442   | AARAAATAA b <sub>5</sub> –NH <sub>3</sub> fragment      | 423.5       |
| C3 hexamer <sup>+1</sup>  | 1750–1755   | AATAAARAA b <sub>5</sub> –H <sub>2</sub> O fragment     | 367.5       |
| C4 monomer <sup>+1</sup>  | 241–246     | AATAAARAA b <sub>6</sub> –H <sub>2</sub> O fragment     | 438.5       |
| C4 dimer <sup>+1</sup>    | 563–568     | AATAAARAA y <sub>6</sub> fragment                       | 529.6       |
| C4 trimer <sup>+1</sup>   | 886–891     | TEMPO–AARAAATAA a <sub>6</sub> +H <sup>•</sup> fragment | 526         |
| C4 tetramer <sup>+1</sup> | 1208–1213   | TEMPO–AARAAATAA c <sub>6</sub> fragment                 | 570         |
| C4 pentamer <sup>+1</sup> | 1530–1535   | TEMPO–AATAAARAA y <sub>6</sub> fragment                 | 530         |
| C4 hexamer <sup>+1</sup>  | 1853–1558   | TEMPO–AATAAARAA z <sub>7</sub> –H fragment              | 613         |
| C5 monomer <sup>+1</sup>  | 297–302     | AARA AHAMA b <sub>7</sub> –NH <sub>3</sub> fragment     | 631.5       |
| C5 dimer <sup>+1</sup>    | 676–681     | AARA AMAHA b <sub>7</sub> fragment                      | 642.5       |
| C5 trimer <sup>+1</sup>   | 1054–1059   | TEMPO–AARA AHAMA a <sub>6</sub> fragment                | 591         |
| C5 tetramer <sup>+1</sup> | 1432–1437   | TEMPO–AARA AMAHA a <sub>8</sub> fragment                | 793.8       |
| C5 pentamer <sup>+1</sup> | 1811–1816   |   |             |
| C6 monomer <sup>+1</sup>  | 353–358     |   |             |
| C6 dimer <sup>+1</sup>    | 788–793     |   |             |
| C6 trimer <sup>+1</sup>   | 1222–1227   |   |             |
| C6 tetramer <sup>+1</sup> | 1657–1662   |   |             |
| C7 monomer <sup>+1</sup>  | 409–414     |   |             |
| C7 dimer <sup>+1</sup>    | 899–904     |   |             |
| C7 trimer <sup>+1</sup>   | 1389–1394   |   |             |
| C7 tetramer <sup>+1</sup> | 1879–1884   |   |             |
| C8 monomer <sup>+1</sup>  | 465–470     |   |             |
| C8 dimer <sup>+1</sup>    | 1012–1017   |   |             |
| C8 trimer <sup>+1</sup>   | 1559–1564   |   |             |
| C12 monomer <sup>+1</sup> | 690–695     |   |             |
| C12 dimer <sup>+1</sup>   | 1461–1466   |   |             |

<sup>a</sup>C2–C8 and C12 TAAX ions are brominated, except for C3 ions, which are iodinated.  $m/z$  ranges across 5 Da to include C isotopes.

gas mass. Therefore,  $\phi_i^*$  can be related to  $\Omega_i$  via a coefficient,  $\beta$ :

$$\Omega_i \sim \beta K_i^{-1} \sim \beta \phi_i^* = \left( q_i \left( \frac{m_i + M}{m_i M} \right)^{1/2} T^{1/2} \right) \phi_i^*. \quad (\text{B.3})$$

In the case of a mobility calibrant displaying a multi-peaked signal, the peak making up the greatest proportion of the total signal was taken as the peak corresponding to  $\phi_i^*$  for the calibrant. The relationship between  $\Omega_i$  and  $\beta$  is linear ( $R^2 > 0.996$ ), as shown in Fig. B.4. It must be noted that there is a very large standard error of the intercept relative to the intercept value (see Fig. B.4) due to a limited range of  $\Omega$  covered by only nine mobility calibrant ions (i.e. non of the calibrant ions had a mobility near zero), which can result in large uncertainties when using the calibration to determine a  $\Omega$  value for other biomolecules.

### Signal Deconvolution and Fitting

Each classification signal,  $S$ , for TAAX ions, peptides, and model peptides was fitted to a Gaussian function of the form

$$S = \sum_{j=1}^n a_j e^{\left[ -\left( \frac{\phi - b_j}{c_j} \right)^2 \right]}, \quad (\text{B.4})$$

where  $a$  is the peak amplitude,  $b$  is the centroid,  $c$  is related to the peak width, and  $n$  is the number of peaks. The value  $\Delta\phi_{\text{FWHM}}$  is then calculated as:

$$\Delta\phi_{\text{FWHM},j} = 2 (\ln(2))^{1/2} c_j. \quad (\text{B.5})$$

A single peak was fitted to the signal if it appeared to be composed of one peak and the resulting value of  $R$  was no more than  $\mathcal{R}_{\text{nd}}$ . If the signal appeared to be composed of multiple peaks, additional Gaussian terms were attempted to be fitted to where they were visually evident, with consideration that the values of  $R$  could not surpass  $\mathcal{R}_{\text{nd}}$ .

In the case of multi-peaked signals, the proportion of each species' contribution to the total signal was estimated by calculating the integral under each Gaussian term,  $A_j$ ,

$$A_j = a_j c_j \pi^{1/2} \quad (\text{B.6})$$

and then calculating the fraction  $\frac{A_j}{\sum_{j=1}^n A_j}$ .

## B.4 Results

### Discussion of Effect of Field-Induced Heating

An ion's mobility, and therefore its cross section, is dependent on the ratio of the electric field,  $E$ , to the concentration of neutral particles,  $N$  (Eiceman and Karpas 1994). Inside the classification region of the ROMIAC, the electric field is  $\sim 100$  V/cm, the pressure,  $p$ , is 101,325 Pa, and the temperature,  $T$ , is 298 K. Under these conditions, the  $E/N$  ratio is  $\sim 3 \times 10^{-19}$  Townsends, which means that field-induced heating is negligible in this study.

In addition, note that  $N_2$  molecule collisions in the ROMIAC orthogonal cross-flow classification region are unlikely to significantly increase the internal energy of analyte ions since the mean velocity of molecules in the cross-flow is only  $\sim 10^{-1}$  m/s, much smaller than the background mean velocity of the bath molecules at 298 or 400 K ( $\sim 10^1$  to  $10^3$  m/s).

### Calibrations

Instrument and mobility calibrations show a linear response in  $K_{0,i}$  to  $\phi$  with TAAX ion standards ( $R^2 > 0.999$ ; Fig. B.3) and  $\Omega_i$  to  $\beta$  with calibrant peptides ( $R^2 > 0.996$ ; Fig. B.4). The ROMIAC also demonstrates high resolution with the TAAX standards (close to  $\mathcal{R}_{nd}$ ; Table B.4), though resolution of the calibrant peptides and proteins were generally not as high as those of the TAAX standards (Table B.6). This reduced resolution for peptides is fairly typical and is often assigned to the existence of multiple conformers within the mobility envelope (Wytenbach, Helden, and Bowers 1996; Counterman et al. 1998; Shvartsburg et al. 2006a; Shvartsburg et al. 2006b; Pierson et al. 2011; Wytenbach and Bowers 2011). The instrument calibration linearity demonstrates that the ROMIAC provides accurate  $K_{0,i}$  and  $\Omega_i$  values for small ions unaffected by either ESI solvents (e.g. water and methanol) in the carrier gas or concave surfaces that increase the momentum transfer cross section, while the mobility calibration linearity suggests that drag factors and/or trace solvents affected the observed calibrant peptide  $\Omega_i$  values in a similar fashion. Such solvents can complex with analyte ions (Wu, Siems, et al. 1998; Fernández-Maestre et al. 2010) and make complete desolvation of ions a challenge, thereby resulting in larger apparent  $\Omega_i$  values. In addition, large peptides and proteins can present more surface area than a spherical particle of similar size, due to concavity

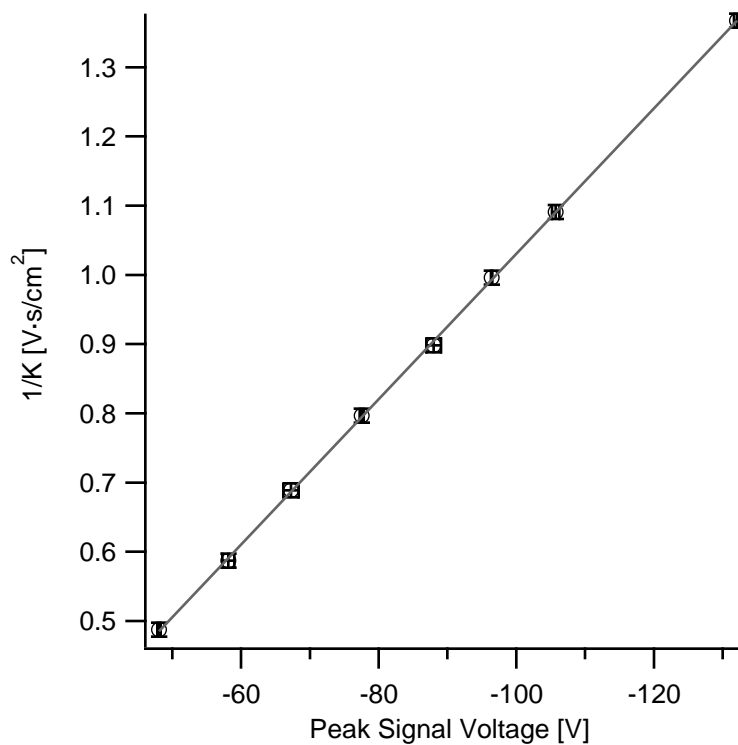


Figure B.3: ROMIAC instrument calibration with TAAX salts. Vertical error bars represent 1 standard deviation of  $K_i$  values from Viidanoja et al. 2005. Horizontal error bars represent 1 standard deviation of  $\phi_i^*$  for a TAAX ion. Fit is linear with  $R^2 > 0.999$ . Slope is  $-0.0105 \pm (4.89 \times 10^{-5})$ . Intercept is  $-0.0195 \pm 0.00430$ .

and interior cavities, thereby increasing ion–buffer gas interactions and observed  $\Omega_i$  values (Wytenbach, Bleiholder, and Bowers 2013).

Table B.3: Instrument calibration tetra-alkyl ammonium halide (TAAX) anion-coordinated singly-charged multimer  $\Omega_i$  and  $K_{0,i}$ .<sup>a</sup>

| TAAX | $k$<br>Number<br>of<br>TAAX<br>Units | $\Omega_i$<br>[Å <sup>2</sup> ] | $K_{0,i}$<br>[cm <sup>2</sup> V <sup>-1</sup> s <sup>-1</sup> ] |
|------|--------------------------------------|---------------------------------|---|
| C2   | 2                                    | 225±2.7                         | 0.94±0.011  |
| C2   | 3                                    | 256±7.3                         | 0.81±0.023  |
| C2   | 4                                    | 251±3.2                         | 0.82±0.010  |
| C2   | 5                                    | 298±2.7                         | 0.69±0.006  |
| C2   | 6                                    | 325±3.3                         | 0.63±0.007  |
| C2   | 7                                    | 353±4.0                         | 0.58±0.007  |
| C2   | 8                                    | 377±3.4                         | 0.54±0.005  |
| C2   | 9                                    | 405±4.3                         | 0.50±0.005  |
| C3   | 2                                    | 222±3.1                         | 0.94±0.013  |
| C3   | 3                                    | 289±5.8                         | 0.71±0.014  |
| C3   | 4                                    | 333±8.0                         | 0.62±0.015  |
| C3   | 5                                    | 369±4.0                         | 0.56±0.006  |
| C3   | 6                                    | 430±4.1                         | 0.48±0.005  |
| C4   | 2                                    | 250±2.7                         | 0.83±0.009  |
| C4   | 3                                    | 321±3.6                         | 0.64±0.007  |
| C4   | 4                                    | 353±4.8                         | 0.58±0.008  |
| C4   | 5                                    | 399±6.6                         | 0.51±0.008  |
| C4   | 6                                    | 461±5.3                         | 0.44±0.005  |
| C5   | 2                                    | 282±2.5                         | 0.73±0.007  |
| C5   | 3                                    | 354±3.2                         | 0.58±0.005  |
| C5   | 4                                    | 409±4.7                         | 0.50±0.006  |
| C5   | 5                                    | 440±6.1                         | 0.46±0.006  |
| C6   | 2                                    | 310±3.0                         | 0.67±0.006  |
| C6   | 3                                    | 386±3.5                         | 0.53±0.005  |
| C6   | 4                                    | 449±3.8                         | 0.46±0.004  |
| C7   | 2                                    | 335±2.8                         | 0.61±0.005  |
| C7   | 3                                    | 419±3.0                         | 0.49±0.004  |
| C7   | 4                                    | 491±3.7                         | 0.42±0.003  |
| C8   | 2                                    | 361±2.9                         | 0.57±0.005  |
| C8   | 3                                    | 454±3.4                         | 0.45±0.003  |
| C12  | 2                                    | 445±3.7                         | 0.46±0.004  |

<sup>a</sup>In N<sub>2</sub> at atmospheric pressure and  $T_{\text{ESI}} = T_x = 298$  K. Values are the average of three scans. Note that C3 species are iodinated while all other TAAX species are brominated. Detailed signal, Gaussian fit, and resolution values are found in Table B.4.

Supplementary Table B.4: TAAX instrument calibration detailed results.<sup>a</sup>

| TAAX | Trial | <sup>b</sup> $K_{0,i}$ | Start $\phi$<br>[V] | End $\phi$<br>[V] | $a_j$ | $a_j$<br>95%<br>CI | $b_j$   | $b_j$<br>95%<br>CI | $c_j$ | $c_j$<br>95%<br>CI | FWHM<br>[V] | $E$ (FWHM)<br>[V] | $R$   | $E(R)$ | $\bar{\phi}_i^+$ [V] | $\sigma_{\phi_i^+}$<br>[V] | $\bar{K}_i$ | $\bar{K}_i^{-1}$ |
|------|-------|------------------------|---------------------|-------------------|-------|--------------------|---------|--------------------|-------|--------------------|-------------|-------------------|-------|--------|----------------------|----------------------------|-------------|------------------|
|      |       |                        |                     |                   |       |                    |         |                    |       |                    |             |                   |       |        |                      |                            |             |                  |
| C2   | 1     | 1.88                   | 40                  | 60                | 1.043 | 0.033              | -48.29  | 0.03               | 1.399 | 0.051              | 2.3303      | 0.0852            | 20.72 | 0.77   | -48.06               | 0.23                       | 2.052       | 0.487            |
| C2   | 2     | 1.88                   | 40                  | 60                | 1.024 | 0.084              | -48.08  | 0.10               | 1.634 | 0.155              | 2.7222      | 0.2583            | 17.66 | 1.71   |                      |                            |             |                  |
| C2   | 3     | 1.88                   | 40                  | 60                | 1.040 | 0.039              | -47.82  | 0.05               | 1.632 | 0.071              | 2.7176      | 0.1191            | 17.59 | 0.79   |                      |                            |             |                  |
| C3   | 1     | 1.56                   | 45                  | 205               | 0.966 | 0.026              | -57.84  | 0.04               | 1.986 | 0.062              | 3.3068      | 0.104             | 17.49 | 0.56   | -58.16               | 0.86                       | 1.702       | 0.587            |
| C3   | 2     | 1.56                   | 45                  | 205               | 1.006 | 0.027              | -57.51  | 0.05               | 2.203 | 0.070              | 3.6689      | 0.1176            | 15.67 | 0.51   |                      |                            |             |                  |
| C3   | 3     | 1.56                   | 45                  | 205               | 0.957 | 0.036              | -59.14  | 0.05               | 1.818 | 0.079              | 3.0271      | 0.1319            | 19.53 | 0.86   |                      |                            |             |                  |
| C4   | 1     | 1.33                   | 60                  | 240               | 1.029 | 0.029              | -66.22  | 0.06               | 2.742 | 0.089              | 4.566       | 0.1491            | 14.50 | 0.48   | -67.26               | 1.09                       | 1.451       | 0.688            |
| C4   | 2     | 1.33                   | 60                  | 240               | 1.017 | 0.022              | -67.15  | 0.04               | 2.421 | 0.062              | 4.0327      | 0.1035            | 16.65 | 0.43   |                      |                            |             |                  |
| C4   | 3     | 1.33                   | 60                  | 240               | 1.023 | 0.027              | -68.41  | 0.04               | 2.215 | 0.068              | 3.6883      | 0.1145            | 18.54 | 0.58   |                      |                            |             |                  |
| C5   | 1     | 1.15                   | 60                  | 240               | 1.025 | 0.014              | -77.90  | 0.02               | 2.619 | 0.041              | 4.3617      | 0.0696            | 17.86 | 0.29   | -77.54               | 0.31                       | 1.255       | 0.796            |
| C5   | 2     | 1.15                   | 60                  | 240               | 1.032 | 0.016              | -77.40  | 0.03               | 2.679 | 0.050              | 4.4612      | 0.0832            | 17.35 | 0.33   |                      |                            |             |                  |
| C5   | 3     | 1.15                   | 60                  | 240               | 1.039 | 0.016              | -77.32  | 0.03               | 2.712 | 0.050              | 4.517       | 0.0842            | 17.11 | 0.32   |                      |                            |             |                  |
| C6   | 1     | 1.02                   | 75                  | 225               | 1.050 | 0.097              | -86.88  | 0.12               | 1.629 | 0.173              | 2.7131      | 0.2896            | 32.02 | 3.46   | -87.98               | 1.08                       | 1.113       | 0.898            |
| C6   | 2     | 1.02                   | 75                  | 225               | 1.015 | 0.113              | -87.21  | 0.34               | 3.750 | 0.483              | 6.2457      | 0.805             | 13.96 | 1.85   |                      |                            |             |                  |
| C6   | 3     | 1.02                   | 75                  | 225               | 0.861 | 0.144              | -88.75  | 0.40               | 2.918 | 0.566              | 4.8593      | 0.943             | 18.26 | 3.62   |                      |                            |             |                  |
| C7   | 1     | 0.92                   | 85                  | 235               | 1.036 | 0.010              | -96.43  | 0.02               | 3.326 | 0.040              | 5.5381      | 0.0671            | 17.41 | 0.21   | -96.41               | 0.08                       | 1.004       | 0.995            |
| C7   | 2     | 0.92                   | 85                  | 235               | 1.028 | 0.010              | -96.31  | 0.02               | 3.305 | 0.037              | 5.5031      | 0.0628            | 17.50 | 0.20   |                      |                            |             |                  |
| C7   | 3     | 0.92                   | 85                  | 235               | 1.007 | 0.012              | -96.48  | 0.03               | 3.284 | 0.046              | 5.4696      | 0.0781            | 17.64 | 0.25   |                      |                            |             |                  |
| C8   | 1     | 0.84                   | 90                  | 240               | 1.041 | 0.009              | -105.48 | 0.02               | 3.775 | 0.041              | 6.2871      | 0.0684            | 16.77 | 0.18   | -105.73              | 0.54                       | 0.916       | 1.090            |
| C8   | 2     | 0.84                   | 90                  | 240               | 1.036 | 0.007              | -105.36 | 0.02               | 3.736 | 0.030              | 6.2213      | 0.051             | 16.93 | 0.14   |                      |                            |             |                  |
| C8   | 3     | 0.84                   | 90                  | 240               | 1.030 | 0.007              | -106.36 | 0.02               | 3.625 | 0.028              | 6.0362      | 0.0473            | 17.62 | 0.14   |                      |                            |             |                  |
| C12  | 1     | 0.67                   | 120                 | 220               | 1.013 | 0.013              | -132.53 | 0.04               | 4.359 | 0.065              | 7.2593      | 0.1089            | 18.25 | 0.28   | -132.08              | 0.42                       | 0.731       | 1.367            |
| C12  | 2     | 0.67                   | 120                 | 220               | 1.012 | 0.015              | -131.70 | 0.06               | 4.782 | 0.085              | 7.9633      | 0.1418            | 16.53 | 0.30   |                      |                            |             |                  |
| C12  | 3     | 0.67                   | 120                 | 220               | 1.033 | 0.015              | -132.02 | 0.05               | 4.351 | 0.077              | 7.2464      | 0.1286            | 18.21 | 0.33   |                      |                            |             |                  |

<sup>a</sup>C2–C8 and C12 TAAX ions are brominated, except for C3 ions, which are iodinated.  $T_x = T_{\text{ESI}} = 298$  K.<sup>b</sup>Values from Viidanoja et al. 2005. Mobility values are in units of  $[\text{cm}^2 \cdot \text{V}^{-1} \cdot \text{s}^{-1}]$ .

Table B.5: TAAX salt ions detailed results.

[illegible]



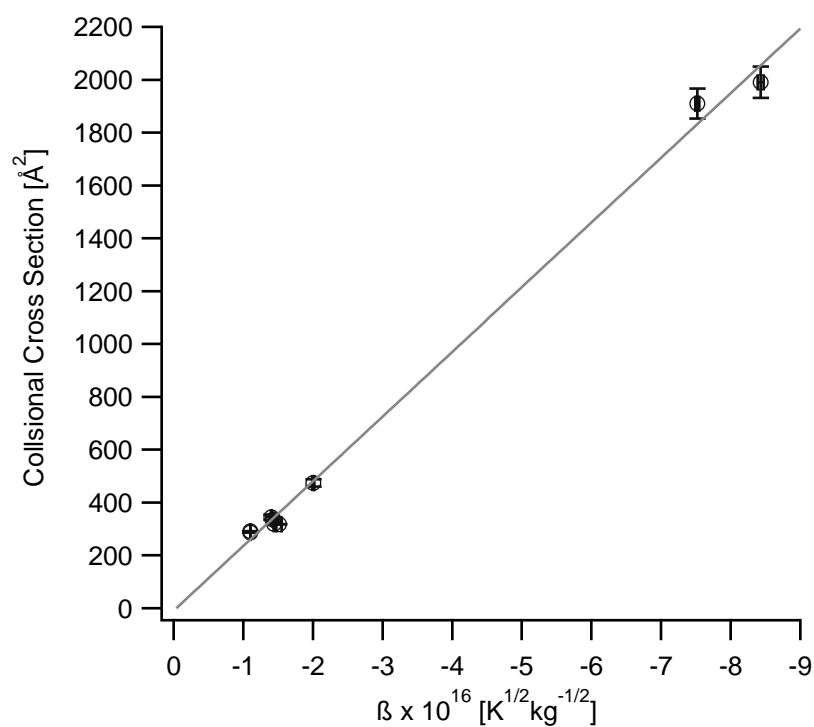


Figure B.4: ROMIAC mobility calibration with peptides. Vertical error bars represent 3% error in  $\Omega_i$  values from Bush et al. 2010. Horizontal error bars represent 1 standard deviation of  $\phi_i^*$  for a peptide ion. Fit is linear with  $R^2 > 0.996$ . Slope is  $-244.779 \pm (5.573)$ . Intercept is  $-9.145 \pm 22.171$ .

Table B.6: Peptide mobility calibration detailed results.<sup>a</sup>

| Peptide | Trial | +Charge | Start $\phi$<br>[V] | End $\phi$<br>[V] | $a_j$ | $a_j$<br>95% | $b_j$   | $b_j$<br>95% | $c_j$ | $c_j$<br>95% | FWHM<br>[V] | $E$ (FWHM)<br>[V] | $R$   | $E(R)$ | $\overline{\phi}_i^*$ [V] | $\sigma_{\phi_i^*}^*$ [V] | $\Omega$ [Å <sup>2</sup> ] | $E(\Omega)$<br>[Å <sup>2</sup> ] | $\beta$ | $E(\beta)$ |
|---------|-------|---------|---------------------|-------------------|-------|--------------|---------|--------------|-------|--------------|-------------|-------------------|-------|--------|---------------------------|---------------------------|----------------------------|----------------------------------|---------|------------|
|         |       |         |                     |                   |       | CI           |         | CI           |       | CI           |             |                   |       |        |                           |                           |                            |                                  |         |            |
| BK      | 1     | 1       | 75                  | 175               | 1.00  | 0.02         | -135.67 | 0.11         | 4.06  | 0.09         | 6.75        | 0.15              | 20.09 | 0.46   | -135.69                   | 0.20                      | c <sub>292</sub>           |                                  | -1.101  | 0.002      |
| BK      | 2     | 1       | 75                  | 175               | 0.99  | 0.01         | -135.89 | 0.08         | 4.27  | 0.08         | 7.11        | 0.14              | 19.10 | 0.38   |                           |                           |                            |                                  |         |            |
| BK      | 3     | 1       | 75                  | 175               | 0.97  | 0.02         | -135.50 | 0.09         | 4.02  | 0.08         | 6.69        | 0.13              | 20.26 | 0.42   |                           |                           |                            |                                  |         |            |
| BK      | 1     | 2       | 75                  | 175               | 0.66  | 0.58         | -89.19  | 0.83         | 5.97  | 1.32         | 9.94        | 2.20              | 8.97  | 2.07   | -88.73                    | 0.41                      | c <sub>319</sub>           |                                  | -1.439  | 0.007      |
| BK      | 2     | 2       | 75                  | 175               | 0.47  | 0.11         | -88.45  | 0.24         | 3.62  | 0.63         | 6.03        | 1.04              | 14.66 | 2.57   |                           |                           |                            |                                  |         |            |
| BK      | 3     | 2       | 75                  | 175               | 0.61  | 0.26         | -88.55  | 0.35         | 5.08  | 0.81         | 8.47        | 1.35              | 10.46 | 1.70   |                           |                           |                            |                                  |         |            |
| AT2     | 1     | 1       | 75                  | 180               | 0.98  | 0.01         | -135.72 | 0.04         | 4.18  | 0.06         | 6.96        | 0.11              | 19.51 | 0.31   | -135.76                   | 0.15                      | c <sub>286</sub>           |                                  | -1.101  | 0.001      |
| AT2     | 2     | 1       | 75                  | 180               | 1.01  | 0.01         | -135.64 | 0.04         | 4.36  | 0.06         | 7.25        | 0.10              | 18.70 | 0.27   |                           |                           |                            |                                  |         |            |
| AT2     | 3     | 1       | 75                  | 180               | 1.01  | 0.01         | -135.93 | 0.04         | 4.19  | 0.06         | 6.98        | 0.10              | 19.48 | 0.28   |                           |                           |                            |                                  |         |            |
| AT2     | 1     | 2       | 75                  | 180               | 0.72  | 0.42         | -91.71  | 0.98         | 5.67  | 1.56         | 9.45        | 2.60              | 9.71  | 2.78   | -93.36                    | 2.32                      | c <sub>318</sub>           |                                  | -1.515  | 0.038      |
| BK      | 1     | 2       | 75                  | 110               | 0.93  | 0.06         | -86.77  | 0.21         | 4.05  | 0.21         | 6.74        | 0.34              | 12.87 | 0.69   | -86.53                    | 0.21                      | d <sub>344</sub>           | 10.32                            | -1.404  | 0.003      |
| BK      | 2     | 2       | 75                  | 110               | 0.91  | 0.05         | -86.45  | 0.16         | 3.81  | 0.17         | 6.35        | 0.28              | 13.62 | 0.64   |                           |                           |                            |                                  |         |            |
| BK      | 3     | 2       | 75                  | 110               | 0.85  | 0.07         | -86.37  | 0.20         | 3.98  | 0.21         | 6.63        | 0.35              | 13.02 | 0.71   |                           |                           |                            |                                  |         |            |
| UB      | 1     | 7       | 80                  | 160               | 0.93  | 0.04         | -134.49 | 0.19         | 5.70  | 0.27         | 9.48        | 0.44              | 14.18 | 0.68   | -133.94                   | 0.52                      | d <sub>1910</sub>          | 57.3                             | -7.518  | 0.029      |
| UB      | 2     | 7       | 80                  | 160               | 0.96  | 0.03         | -133.88 | 0.12         | 5.41  | 0.17         | 9.01        | 0.29              | 14.85 | 0.49   |                           |                           |                            |                                  |         |            |
| UB      | 3     | 7       | 80                  | 160               | 0.96  | 0.04         | -133.46 | 0.17         | 5.14  | 0.25         | 8.56        | 0.41              | 15.60 | 0.77   |                           |                           |                            |                                  |         |            |
| UB      | 1     | 8       | 80                  | 160               | 0.85  | 0.04         | -132.18 | 0.15         | 4.29  | 0.21         | 7.15        | 0.36              | 18.50 | 0.94   | -131.43                   | 0.68                      | d <sub>1990</sub>          | 59.7                             | -8.431  | 0.043      |
| UB      | 2     | 8       | 80                  | 160               | 1.01  | 0.05         | -130.88 | 0.18         | 4.30  | 0.25         | 7.16        | 0.41              | 18.27 | 1.08   |                           |                           |                            |                                  |         |            |
| UB      | 3     | 8       | 80                  | 160               | 0.76  | 0.06         | -131.22 | 0.32         | 5.17  | 0.45         | 8.62        | 0.75              | 15.23 | 1.36   |                           |                           |                            |                                  |         |            |
| AT1     | 1     | 3       | 75                  | 115               | 0.83  | 0.05         | -83.33  | 0.19         | 4.32  | 0.27         | 7.20        | 0.46              | 11.57 | 0.76   | -82.65                    | 0.61                      | d <sub>474</sub>           | 14.22                            | -2.006  | 0.015      |
| AT1     | 2     | 3       | 75                  | 95                | 0.72  | 0.07         | -82.43  | 0.41         | 5.30  | 0.61         | 8.83        | 1.01              | 9.34  | 1.11   |                           |                           |                            |                                  |         |            |
| AT1     | 3     | 3       | 75                  | 95                | 0.79  | 0.07         | -82.17  | 0.32         | 4.25  | 0.46         | 7.07        | 0.77              | 11.62 | 1.31   |                           |                           |                            |                                  |         |            |
| AT2     | 1     | 2       | 80                  | 120               | 0.66  | 0.18         | -88.17  | 0.19         | 3.31  | 0.51         | 5.51        | 0.85              | 16.00 | 2.51   | -88.02                    | 0.24                      | d <sub>335</sub>           | 10.05                            | -1.428  | 0.004      |
| AT2     | 2     | 2       | 80                  | 120               | 0.73  | 0.20         | -88.16  | 0.16         | 3.39  | 0.45         | 5.65        | 0.74              | 15.61 | 2.08   |                           |                           |                            |                                  |         |            |
| AT2     | 3     | 2       | 80                  | 120               | 0.75  | 0.15         | -87.74  | 0.14         | 3.55  | 0.36         | 5.91        | 0.60              | 14.85 | 1.53   |                           |                           |                            |                                  |         |            |

<sup>a</sup>C2–C8 and C12 TAAX ions are brominated, except for C3 ions, which are iodinated.  $T_x = T_{\text{ESI}} = 298$  K.<sup>b</sup>Values from Viidanoja et al. 2005. Mobility values are in units of  $[\text{cm}^2 \cdot \text{V}^{-1} \cdot \text{s}^{-1}]$ .<sup>c</sup>Values from Wu, Klasmeier, and Hill 1999.<sup>d</sup>Values from Bush et al. 2010.

Table B.7: Mobility calibration bradykinin (BK), angiotensin I (AT1), angiotensin II (AT2), and bovine ubiquitin (UB)  $\Omega_i$  at  $T_{\text{ESI}} = 298$  K, and comparison to literature values.<sup>a</sup>

| Peptide             | Peak # | $\Omega_i$ [ $\text{\AA}^2$ ] | $^b\% \Delta$ | $^c\% \Delta$ | $^d\% \Delta$ |
|---------------------|--------|-------------------------------|---------------|---------------|---------------|
| BK <sup>+1</sup>    | 1      | 172±29.3                      | -40.9%        |               |               |
| BK <sup>+1</sup>    | 2      | 207±32.5                      | -29.0%        |               |               |
| *BK <sup>+1</sup>   | 3      | 261±29.5                      | -10.6%        |               |               |
| **BK <sup>+2</sup>  | 9      | 334±30.8                      | 4.8%          |               | -2.8%         |
| BK <sup>+2</sup>    | 10     | 365±32.7                      | 14.5%         |               | 6.2%          |
| *AT1 <sup>+1</sup>  | 13     | 292±30.0                      |               |               |               |
| *AT1 <sup>+2</sup>  | 18     | 365±34.8                      |               | -5.0%         |               |
| AT1 <sup>+2</sup>   | 19     | 380±34.3                      |               | -1.2%         |               |
| **AT1 <sup>+3</sup> | 24     | 482±37.0                      |               | 1.9%          | 1.7%          |
| *AT2 <sup>+1</sup>  | 26     | 258±28.5                      | -9.8%         |               |               |
| AT2 <sup>+1</sup>   | 27     | 278±29.3                      | -2.8%         |               |               |
| **AT2 <sup>+2</sup> | 32     | 340±31.1                      | 7.0%          | -4.1%         | 1.6%          |
| AT2 <sup>+2</sup>   | 33     | 362±31.8                      | 13.8%         | 1.9%          | 8.0%          |
| *UB <sup>+5</sup>   | 36     | 1390±57.3                     |               |               |               |
| *UB <sup>+6</sup>   | 37     | 1613±65.3                     |               |               |               |
| **UB <sup>+7</sup>  | 38     | 1831±71.2                     |               |               | -4.1%         |
| **UB <sup>+8</sup>  | 39     | 2055±79.8                     |               |               | 3.2%          |

<sup>a</sup>In N<sub>2</sub> at atmospheric pressure,  $T_{\text{ESI}} = T_x = 298$  K. Values are the average of three scans. Peak numbers correspond to those labeled in Fig. 3.3 and Fig. B.5. Detailed signal, Gaussian fit, proportion, and resolution values are found in Table B.9.

\*Indicates parent/dominant conformation for that species.

#Indicates peak was also used as a mobility calibrant.

References: <sup>b</sup>Wu, Klasmeier, and Hill 1999 <sup>c</sup>Baykut, Halem, and Raether 2009

<sup>d</sup>Bush et al. 2010.

Table B.8: Mobility calibration bradykinin (BK), angiotensin I (AT1), and angiotensin II (AT2)  $\Omega_i$  at  $T_{\text{ESI}} = 400$  K, and comparison to literature values.<sup>a</sup>

| Peptide             | Peak # | $\Omega_i$ [ $\text{\AA}^2$ ] | $^b\% \Delta$ | $^c\% \Delta$ | $^d\% \Delta$ |
|---------------------|--------|-------------------------------|---------------|---------------|---------------|
| BK <sup>+1</sup>    | 4      | 216±25.3                      | -26.0%        |               |               |
| *#BK <sup>+1</sup>  | 5      | 260±27.9                      | -10.9%        |               |               |
| BK <sup>+1</sup>    | 6      | 277±28.0                      | -5.2%         |               |               |
| BK <sup>+1</sup>    | 7      | 294±28.3                      | 0.7%          |               |               |
| BK <sup>+1</sup>    | 8      | 319±26.1                      | 9.2%          |               |               |
| *#BK <sup>+2</sup>  | 11     | 343±28.6                      | 7.6%          |               | -0.2%         |
| BK <sup>+2</sup>    | 12     | 370±29.1                      | 15.8%         |               | 7.4%          |
| AT1 <sup>+1</sup>   | 14     | 243±20.3                      |               |               |               |
| *AT1 <sup>+1</sup>  | 15     | 294±28.8                      |               |               |               |
| AT1 <sup>+1</sup>   | 16     | 326±28.8                      |               |               |               |
| AT1 <sup>+1</sup>   | 17     | 348±29.6                      |               |               |               |
| *AT1 <sup>+2</sup>  | 20     | 369±30.5                      |               | -4.0%         |               |
| AT1 <sup>+2</sup>   | 21     | 392±28.3                      |               | 2.1%          |               |
| AT1 <sup>+2</sup>   | 22     | 424±20.1                      |               | 10.4%         |               |
| AT1 <sup>+2</sup>   | 23     | 465±23.3                      |               | 21.1%         |               |
| *AT1 <sup>+3</sup>  | 25     | 510±31.7                      |               | 7.9%          | 7.7%          |
| AT2 <sup>+1</sup>   | 28     | 221±25.9                      | -22.7%        |               |               |
| *#AT2 <sup>+1</sup> | 29     | 260±28.0                      | -8.9%         |               |               |
| AT2 <sup>+1</sup>   | 30     | 289±28.6                      | 1.0%          |               |               |
| AT2 <sup>+1</sup>   | 31     | 309±28.6                      | 7.9%          |               |               |
| *#AT2 <sup>+2</sup> | 34     | 362±21.4                      | 13.7%         | 1.9%          | 7.9%          |
| AT2 <sup>+2</sup>   | 35     | 396±26.4                      | 24.6%         | 11.6%         | 18.3%         |

<sup>a</sup>In N<sub>2</sub> at atmospheric pressure,  $T_{\text{ESI}} = 400$  K and  $T_x = 298$  K. Values are the average of three scans. Peak numbers correspond to those labeled in Fig. 3.3. Detailed signal, Gaussian fit, proportion, and resolution values are found in Table B.10.

\*Indicates parent/dominant conformation for that species.

#Indicates peak was also used as a mobility calibrant.

References: <sup>b</sup>Wu, Klasmeier, and Hill 1999 <sup>c</sup>Baykut, Halem, and Raether 2009

<sup>d</sup>Bush et al. 2010.

Table B.9: Peptides: detailed results at  $T_{\text{ESI}} = 298 \text{ K}$ .

| Species | TriL | Charge | Peak | Start $\phi$ [V] | End $\phi$ [V] | $\sigma$ | $\alpha$ | 95%CI   | $b$   | $\beta$ | 95%CI | $c$   | $\gamma$ | 95%CI | $R$   | $E(R)$ | $A$   | avg. $A$ | $E(A)$ | Fraction | Effraction | avg. $c$ [V] | clews. $c$ | Ion Mass [kg] | Red. Mass [kg] | $\delta \cdot 10^{10}$ | $E(\delta \cdot 10^{10})$ | $G$ [ $\text{\AA}^{-1}$ ] | Hill1999 | Raether2009 | Robinson2010 | $\delta$ diff Hill | % diff Raether | % diff Robinson |       |        |
|---------|------|--------|------|------------------|----------------|----------|----------|---------|-------|---------|-------|-------|----------|-------|-------|--------|-------|----------|--------|----------|------------|--------------|------------|---------------|----------------|------------------------|---------------------------|---------------------------|----------|-------------|--------------|--------------------|----------------|-----------------|-------|--------|
| BK      | 1    | 1      | 0    | 50               | 160            | 0.11     | 0.02     | -91.49  | 1.51  | 6.67    | 1.86  | 11.10 | 3.09     | 8.24  | 2.43  | 0.73   | 0.33  | 0.12     | 0.05   | -91.49   | 1.51       | 1.76E-24     | 4.53E-26   | -0.74         | 0.01           | 172                    | 29.3                      | 292                       | -        | -           | -            | -40.93%            | -              | -               |       |        |
| BK      | 3    | 1      | 0    | 110              | 160            | 0.08     | 0.02     | -106.42 | 1.53  | 8.16    | 3.17  | 13.75 | 5.61     | 7.74  | 3.14  | 0.63   | 0.47  | 0.24     | 0.08   | -106.98  | 2.70       | 1.76E-24     | 4.53E-26   | -0.88         | 0.02           | 207                    | 32.5                      | 292                       | -        | -           | -29.04%      | -                  | -              |                 |       |        |
| BK      | 1    | 1      | 1    | 100              | 160            | 0.05     | 0.04     | -110.80 | 4.47  | 3.99    | 6.45  | 6.65  | 10.74    | 16.82 | 27.88 | 0.19   | -     | -        | -      | 0.04     | -          | -            | 1.76E-24   | 4.53E-26      | -              | 0.02                   | 207                       | 32.5                      | 292      | -           | -            | -29.04%            | -              | -               |       |        |
| BK      | 3    | 1      | 1    | 110              | 160            | 0.10     | 0.18     | -108.70 | 18.98 | 5.90    | 14.03 | 9.83  | 23.36    | 11.06 | 28.23 | 0.58   | -     | -        | -      | 0.10     | -136.15    | 0.57         | 1.76E-24   | 4.53E-26      | -1.10          | 0.00                   | 261                       | 29.5                      | 292      | -           | -            | -10.56%            | -              | -               |       |        |
| BK      | 1    | 2      | 50   | 160              | 0.95           | 0.02     | -135.60  | 0.08    | 4.42  | 0.11    | 7.35  | 0.18  | 18.44    | 0.47  | 4.22  | 4.93   | 0.62  | 0.80     | 0.10   | -136.15  | 0.57       | 1.76E-24     | 4.53E-26   | -1.10         | 0.00           | 261                    | 29.5                      | 292                       | -        | -           | -10.56%      | -                  | -              |                 |       |        |
| BK      | 2    | 1      | 2    | 160              | 0.91           | 0.03     | -136.73  | 0.16    | 5.84  | 0.23    | 9.72  | 0.38  | 14.07    | 0.57  | 5.33  | -      | -     | -        | 0.03   | -86.53   | 0.21       | 1.76E-24     | 4.53E-26   | -1.40         | 0.00           | 334                    | 30.8                      | 319                       | -        | -           | 344          | 4.84%              | -              | -2.78%          |       |        |
| BK      | 3    | 1      | 2    | 110              | 0.97           | 0.04     | -136.11  | 0.18    | 5.42  | 0.26    | 9.03  | 0.43  | 15.08    | 0.73  | 5.24  | 0.34   | 12.87 | 0.69     | 3.75   | 0.56     | 0.03       | -86.53       | 0.21       | 1.76E-24      | 4.53E-26       | -1.40                  | 0.00                      | 334                       | 30.8     | 319         | -            | -                  | 344            | 4.84%           | -     | -2.78% |
| BK      | 1    | 2      | 1    | 75               | 110            | 0.93     | 0.06     | -86.77  | 0.21  | 4.05    | 0.21  | 6.74  | 0.28     | 13.62 | 0.64  | 3.47   | -     | -        | -      | 0.09     | -94.31     | 0.49         | 1.76E-24   | 4.53E-26      | -1.53          | 0.01                   | 365                       | 32.7                      | 319      | -           | -            | 344                | 14.52%         | -               | 6.20% |        |
| BK      | 3    | 2      | 1    | 75               | 110            | 0.85     | 0.07     | -86.37  | 0.20  | 3.98    | 0.21  | 6.63  | 0.35     | 13.02 | 0.71  | 3.39   | -     | -        | -      | 0.09     | -94.31     | 0.49         | 1.76E-24   | 4.53E-26      | -1.53          | 0.01                   | 365                       | 32.7                      | 319      | -           | -            | 344                | 14.52%         | -               | 6.20% |        |
| BK      | 1    | 2      | 1    | 75               | 110            | 0.92     | 0.05     | -86.45  | 0.16  | 3.81    | 0.17  | 6.35  | 0.28     | 13.62 | 0.64  | 3.47   | -     | -        | -      | 0.09     | -94.31     | 0.49         | 1.76E-24   | 4.53E-26      | -1.53          | 0.01                   | 365                       | 32.7                      | 319      | -           | -            | 344                | 14.52%         | -               | 6.20% |        |
| BK      | 3    | 2      | 1    | 75               | 110            | 0.84     | 0.06     | -86.45  | 0.16  | 3.81    | 0.17  | 6.35  | 0.28     | 13.62 | 0.64  | 3.47   | -     | -        | -      | 0.09     | -94.31     | 0.49         | 1.76E-24   | 4.53E-26      | -1.53          | 0.01                   | 365                       | 32.7                      | 319      | -           | -            | 344                | 14.52%         | -               | 6.20% |        |
| BK      | 1    | 2      | 2    | 75               | 110            | 0.46     | 0.03     | -93.78  | 0.66  | 6.25    | 0.62  | 10.41 | 1.02     | 9.01  | 0.95  | 3.47   | -     | -        | -      | 0.10     | -151.79    | 0.51         | 2.1587E-24 | 4.55E-26      | -1.23          | 0.00                   | 292                       | 30.0                      | -        | -           | -            | -                  | -              | -               | -     |        |
| AT1     | 1    | 1      | 1    | 140              | 180            | 1.02     | 0.02     | -152.18 | 0.07  | 4.41    | 0.09  | 7.34  | 0.15     | 20.72 | 0.44  | 4.49   | 4.68  | 0.47     | 1.00   | 0.10     | -151.79    | 0.51         | 2.1587E-24 | 4.55E-26      | -1.23          | 0.00                   | 292                       | 30.0                      | -        | -           | -            | -                  | -              | -               | -     |        |
| AT1     | 2    | 1      | 1    | 140              | 180            | 0.91     | 0.03     | -151.98 | 0.15  | 4.77    | 0.21  | 7.95  | 0.35     | 19.12 | 0.86  | 4.33   | -     | -        | -      | 0.09     | -94.42     | 1.05         | 2.16E-24   | 4.55E-26      | -1.53          | 0.02                   | 365                       | 34.8                      | -        | -           | 384          | -                  | -              | -4.99%          | -     | -      |
| AT1     | 3    | 1      | 1    | 140              | 180            | 0.99     | 0.02     | -151.22 | 0.11  | 5.25    | 0.15  | 8.74  | 0.25     | 17.31 | 0.51  | 5.21   | -     | -        | -      | 0.09     | -94.42     | 1.05         | 2.16E-24   | 4.55E-26      | -1.53          | 0.02                   | 365                       | 34.8                      | -        | -           | 384          | -                  | -              | -4.99%          | -     | -      |
| AT1     | 1    | 2      | 1    | 75               | 115            | 0.67     | 0.07     | -93.54  | 0.12  | 3.92    | 0.25  | 6.53  | 0.41     | 14.31 | 0.92  | 2.63   | 2.14  | 0.49     | 0.39   | 0.09     | -94.42     | 1.05         | 2.16E-24   | 4.55E-26      | -1.53          | 0.02                   | 365                       | 34.8                      | -        | -           | 384          | -                  | -              | -4.99%          | -     | -      |
| AT1     | 2    | 2      | 1    | 75               | 115            | 0.58     | 0.15     | -95.99  | 0.22  | 3.62    | 0.48  | 6.08  | 0.79     | 15.86 | 2.13  | 2.12   | -     | -        | -      | 0.10     | -98.13     | 0.83         | 2.16E-24   | 4.55E-26      | -1.59          | 0.01                   | 380                       | 34.3                      | -        | -           | 384          | -                  | -              | -1.15%          | -     | -      |
| AT1     | 1    | 2      | 1    | 75               | 115            | 0.39     | 0.06     | -97.40  | 0.72  | 7.30    | 0.35  | 12.15 | 0.59     | 8.02  | 0.45  | 2.87   | 3.35  | 0.55     | 0.61   | 0.10     | -98.13     | 0.83         | 2.16E-24   | 4.55E-26      | -1.59          | 0.01                   | 380                       | 34.3                      | -        | -           | 384          | -                  | -              | -1.15%          | -     | -      |
| AT1     | 2    | 2      | 2    | 75               | 115            | 0.50     | 0.11     | -99.04  | 1.00  | 6.40    | 0.46  | 10.66 | 0.76     | 9.29  | 0.75  | 3.23   | -     | -        | -      | 0.10     | -98.13     | 0.83         | 2.16E-24   | 4.55E-26      | -1.59          | 0.01                   | 380                       | 34.3                      | -        | -           | 384          | -                  | -              | -1.15%          | -     | -      |
| AT1     | 3    | 2      | 2    | 75               | 115            | 0.63     | 0.20     | -97.94  | 1.63  | 6.28    | 0.71  | 10.45 | 1.18     | 9.37  | 1.21  | 3.96   | -     | -        | -      | 0.06     | -82.65     | 0.61         | 2.16E-24   | 4.55E-26      | -2.01          | 0.01                   | 482                       | 37.0                      | -        | -           | 473          | -                  | -              | 1.89%           | -     | 1.67%  |
| AT1     | 1    | 3      | 1    | 75               | 115            | 0.83     | 0.05     | -83.33  | 0.19  | 4.32    | 0.27  | 7.20  | 0.46     | 11.57 | 0.76  | 3.60   | 3.59  | 0.22     | 1.00   | 0.06     | -82.65     | 0.61         | 2.16E-24   | 4.55E-26      | -2.01          | 0.01                   | 482                       | 37.0                      | -        | -           | 473          | -                  | -              | 1.89%           | -     | 1.67%  |
| AT1     | 2    | 3      | 1    | 75               | 95             | 0.72     | 0.07     | -82.43  | 0.41  | 5.30    | 0.61  | 8.83  | 1.01     | 9.34  | 1.11  | 3.80   | -     | -        | -      | 0.05     | -134.50    | 0.10         | 1.74E-24   | 4.53E-26      | -1.09          | 0.00                   | 258                       | 28.5                      | 286      | -           | -            | -                  | -9.82%         | -               | -     |        |
| AT2     | 1    | 1      | 1    | 120              | 160            | 1.00     | 0.02     | -134.44 | 0.09  | 3.86    | 0.12  | 6.42  | 0.21     | 20.94 | 0.69  | 3.84   | 4.09  | 0.22     | 0.93   | 0.05     | -134.50    | 0.10         | 1.74E-24   | 4.53E-26      | -1.09          | 0.00                   | 258                       | 28.5                      | 286      | -           | -            | -                  | -9.82%         | -               | -     |        |
| AT2     | 2    | 1      | 1    | 120              | 160            | 0.98     | 0.03     | -134.43 | 0.11  | 4.28    | 0.13  | 7.13  | 0.22     | 18.85 | 0.60  | 4.19   | -     | -        | -      | 0.02     | -144.61    | 0.29         | 1.74E-24   | 4.53E-26      | -1.17          | 0.00                   | 278                       | 29.3                      | 286      | -           | -            | -                  | -2.80%         | -               | -     |        |
| AT2     | 1    | 2      | 1    | 120              | 160            | 0.96     | 0.02     | -144.28 | 1.85  | 5.19    | 2.75  | 8.64  | 4.58     | 16.70 | 0.90  | 0.30   | 0.30  | 0.08     | 0.07   | 0.02     | -144.61    | 0.29         | 1.74E-24   | 4.53E-26      | -1.17          | 0.00                   | 278                       | 29.3                      | 286      | -           | -            | -                  | -2.80%         | -               | -     |        |
| AT2     | 2    | 2      | 1    | 120              | 160            | 0.06     | 0.01     | -144.76 | 2.94  | 6.96    | 3.85  | 11.59 | 6.41     | 12.49 | 7.16  | 0.39   | -     | -        | -      | 0.02     | -144.61    | 0.29         | 1.74E-24   | 4.53E-26      | -1.17          | 0.00                   | 278                       | 29.3                      | 286      | -           | -            | -                  | -2.80%         | -               | -     |        |
| AT2     | 3    | 1      | 2    | 120              | 160            | 0.05     | 0.01     | -144.80 | 1.32  | 4.62    | 1.97  | 7.70  | 3.28     | 18.81 | 8.19  | 0.22   | -     | -        | -      | 0.04     | -88.02     | 0.24         | 1.74E-24   | 4.53E-26      | -1.43          | 0.00                   | 340                       | 31.1                      | 318      | -           | -            | 355                | 7.05%          | -4.11%          | 1.62% |        |
| AT2     | 1    | 2      | 1    | 80               | 120            | 0.66     | 0.18     | -88.17  | 0.19  | 3.31    | 0.51  | 5.51  | 0.85     | 16.00 | 2.51  | 2.20   | 2.45  | 0.23     | 0.43   | 0.04     | -88.02     | 0.24         | 1.74E-24   | 4.53E-26      | -1.43          | 0.00                   | 340                       | 31.1                      | 318      | -           | -            | 355                | 7.05%          | -4.11%          | 1.62% |        |
| AT2     | 2    | 2      | 1    | 80               | 120            | 0.73     | 0.20     | -88.16  | 0.16  | 3.39    | 0.45  | 5.65  | 0.74     | 15.61 | 2.08  | 2.48   | -     | -        | -      | 0.04     | -88.02     | 0.24         | 1.74E-24   | 4.53E-26      | -1.43          | 0.00                   | 340                       | 31.1                      | 318      | -           | -            | 355                | 7.05%          | -4.11%          | 1.62% |        |
| AT2     | 3    | 2      | 1    | 80               | 120            | 0.75     | 0.15     | -87.74  | 0.14  | 3.55    | 0.36  | 5.91  | 0.60     | 14.85 | 1.53  | 2.66   | -     | -        | -      | 0.12     | -93.41     | 0.30         | 1.74E-24   | 4.53E-26      | -1.52          | 0.00                   | 362                       | 31.8                      | 318      | -           | -            | 355                | 13.78%         | 1.92%           | 8.01% |        |
| AT2     | 1    | 2      | 2    | 80               | 120            | 0.62     | 0.07     | -92.74  | 1.25  | 6.51    | 0.96  | 10.84 | 1.60     | 8.64  | 1.39  | 4.01   | 3.26  | 0.66     | 0.57   | 0.12     | -93.41     | 0.30         | 1.74E-24   | 4.53E-26      | -1.52          | 0.00                   | 362                       | 31.8                      | 318      | -           | -            | 355                | 13.78%         | 1.92%           | 8.01% |        |
| AT2     | 2    | 2      | 2    | 80               | 120            | 0.68     | 0.08     | -93.66  | 1.13  | 6.48    | 1.03  | 10.85 | 1.70     | 8.55  | 1.27  | 3.01   | -     | -        | -      | 0.15     | -142.60    | 0.33         | 1.42E-23   | 4.68E-26      | -5.72          | 0.01                   | 1390                      | 57.3                      | -        | -           | -            | -                  | -              | -               | -     |        |
| AT2     | 3    | 2      | 2    | 80               | 120            | 0.46     | 0.06     | -93.34  | 1.43  | 6.58    | 1.03  | 10.85 | 1.70     | 8.55  | 1.27  | 3.01   | -     | -        | -      | 0.15     | -142.60    | 0.33         | 1.42E-23   | 4.68E-26      | -5.72          | 0.01                   | 1390                      | 57.3                      | -        | -           | -            | -                  | -              | -               | -     | -      |
| U8      | 1    | 5      | 1    | 80               | 160            | 0.87     | 0.04     | -142.94 | 0.34  | 10.18   | 0.49  | 16.94 | 0.82     | 8.44  | 0.43  | 8.83   | 8.18  | 1.26     | 1.00   | 0.15     | -142.60    | 0.33         | 1.42E-23   | 4.68E-26      | -5.72          | 0.01                   | 1390                      | 57.3                      | -        | -           | -            | -                  | -              | -               | -     |        |
| U8      | 2    | 5      | 1    | 80               | 160            | 0.76     | 0.04     | -142.28 | 0.41  | 8.90    | 0.58  | 14.82 | 0.96     | 9.60  | 0.65  | 6.72   | -     | -        | -      | 0.03     | -137.76    | 0.52         | 1.42E-23   | 4.68E-26      | -6.63          | 0.03                   | 1613                      | 65.3                      | -        | -           | -            | -                  | -              | -               | -     |        |
| U8      | 3    | 5      | 1    | 80               | 160            | 0.96     | 0.04     | -142.57 | 0.33  | 9.39    | 0.47  | 15.64 | 0.78     | 9.12  | 0.47  | 8.98   | -     | -        | -      | 0.03     | -137.76    | 0.52         | 1.42E-23   | 4.68E-26      | -6.63          | 0.03                   | 1613                      | 65.3                      | -        | -           | -            | -                  | -              | -               | -     |        |
| U8      | 1    | 6      | 1    | 80               | 160            | 0.95     | 0.02     | -138.34 | 0.11  | 6.09    | 0.16  | 10.15 | 0.26     | 13.63 | 0.36  | 5.78   | 5.98  | 0.19     | 1.00   | 0.03     | -137.76    | 0.52         | 1.42E-23   | 4.68E-26      | -6.63          | 0.03                   | 1613                      | 65.3                      | -        | -           | -            | -                  | -              | -               | -     |        |
| U8      | 2    | 6      | 1    | 80               | 160            | 0.99     | 0.03     | -137.31 | 0.13  | 6.23    | 0.18  | 10.37 | 0.31     | 13.24 | 0.40  | 6.16   | -     | -        | -      | 0.04     | -135.94    | 0.52         | 1.42E-23   | 4.68E-26      | -7.52          | 0.03                   | 1831                      | 71.2                      | -        | -           | -            | -                  | 1910           | -               | -     | -4.13% |
| U8      | 3    | 6      | 1    | 80               | 160            | 0.95     | 0.02     | -137.63 | 0.12  | 6.30    | 0.17  | 10.48 | 0.28     | 13.13 | 0.37  | 6.00   | -     | -        | -      | 0.04     | -135.94    | 0.52         | 1.42E-23   | 4.68E-26      | -7.52          | 0.03                   | 1831                      | 71.2                      | -        | -           | -            | -                  | 1910           | -               | -     | -4.13% |
| U8      | 1    | 7      | 1    | 80               | 160            | 0.93     | 0.04     | -134.49 | 0.19  | 5.70    | 0.27  | 9.48  | 0.44     | 14.18 | 0.68  | 5.30   | -     | -        | -      | 0.09     | -131.43    | 0.68         | 1.42E-23   | 4.68E-26      | -8.43          | 0.04                   | 2055                      |                           |          |             |              |                    |                |                 |       |        |

Table B.10: Peptides: detailed results at  $T_{\text{ESI}} = 400$  K.

| Species | Total | Charge | Peak | Start $\Delta$ [V] | End $\Delta$ [V] | $\alpha$ | $\alpha$ 95%CI | $\beta$ | $\beta$ 95%CI | $c$   | $c$ 95%CI | $\gamma$ WMA | $\gamma$ WMA | $\delta$ | $\delta$ 95%CI | $\epsilon$ | $\epsilon$ 95%CI | Fraction | F(Fraction) | $\Delta E$ [V] | $\Delta E$ [V] | $\Delta E$ [V] | Ion Mass [u] | Red. Mass [u] | $\delta x_{\text{ion}}^{\text{ion}}$ | $O$ [Å] | $H$ [Å] | $D$ [Å] | Robinson2009 | Robinson2010 | Self-Hell | % diff Barber | % diff Robinson |   |
|---------|-------|--------|------|--------------------|------------------|----------|----------------|---------|---------------|-------|-----------|--------------|--------------|----------|----------------|------------|------------------|----------|-------------|----------------|----------------|----------------|--------------|---------------|--------------------------------------|---------|---------|---------|--------------|--------------|-----------|---------------|-----------------|---|
| BK      | 1     | 1      | 1    | 75                 | 175              | 0.02     | 0.01           | -112.43 | 2.35          | 9.26  | 3.36      | 15.42        | 15.42        | 7.29     | 2.79           | 0.15       | 0.14             | 0.01     | 0.02        | 0.00           | -113.45        | 1.00           | 216          | 25.3          | 292                                  | -       | -       | -       | -            | -            | -         | -             |                 |   |
| BK      | 2     | 1      | 1    | 75                 | 175              | 0.02     | 0.01           | -113.49 | 2.49          | 7.87  | 2.98      | 13.10        | 13.10        | 4.95     | 8.67           | 3.44       | 0.13             |          |             |                | -135.69        | 0.20           | 260          | 27.9          | 292                                  | -       | -       | -       | -            | -            | -         | -             |                 |   |
| BK      | 3     | 1      | 1    | 75                 | 175              | 0.02     | 0.01           | -114.43 | 2.49          | 9.01  | 3.61      | 15.00        | 15.00        | 6.01     | 7.63           | 3.22       | 0.14             |          |             |                | -135.69        | 0.20           | 260          | 27.9          | 292                                  | -       | -       | -       | -            | -            | -         | -             |                 |   |
| BK      | 1     | 2      | 1    | 75                 | 175              | 0.09     | 0.01           | -135.89 | 0.08          | 4.27  | 0.08      | 7.11         | 7.11         | 0.15     | 19.10          | 0.38       | 4.23             |          |             |                | -135.69        | 0.20           | 260          | 27.9          | 292                                  | -       | -       | -       | -            | -            | -         | -             | -               |   |
| BK      | 3     | 1      | 2    | 75                 | 175              | 0.09     | 0.02           | -135.90 | 0.09          | 4.02  | 0.08      | 6.69         | 6.69         | 0.13     | 20.26          | 0.42       | 3.92             |          |             |                | -135.69        | 0.20           | 260          | 27.9          | 292                                  | -       | -       | -       | -            | -            | -         | -             | -               |   |
| BK      | 1     | 1      | 3    | 75                 | 175              | 0.31     | 0.02           | -143.71 | 0.39          | 4.94  | 0.95      | 8.22         | 8.22         | 1.58     | 17.48          | 3.41       | 1.51             | 0.14     | 0.21        | 0.02           | -143.97        | 0.37           | 277          | 28.0          | 292                                  | -       | -       | -       | -            | -            | -         | -             | -               |   |
| BK      | 2     | 1      | 3    | 75                 | 175              | 0.30     | 0.04           | -143.80 | 0.27          | 4.16  | 0.52      | 6.93         | 6.93         | 0.86     | 20.76          | 2.63       | 1.24             |          |             |                | -143.97        | 0.37           | 277          | 28.0          | 292                                  | -       | -       | -       | -            | -            | -         | -             | -               |   |
| BK      | 3     | 1      | 3    | 75                 | 175              | 0.30     | 0.04           | -143.80 | 0.27          | 4.16  | 0.52      | 6.93         | 6.93         | 0.86     | 20.76          | 2.63       | 1.24             |          |             |                | -143.97        | 0.37           | 277          | 28.0          | 292                                  | -       | -       | -       | -            | -            | -         | -             | -               |   |
| BK      | 1     | 1      | 4    | 75                 | 175              | 0.14     | 0.02           | -152.73 | 1.22          | 5.40  | 1.58      | 8.99         | 8.99         | 2.63     | 17.00          | 5.12       | 0.75             | 0.22     | 0.12        | 0.03           | -152.72        | 0.38           | 294          | 28.3          | 292                                  | -       | -       | -       | -            | -            | -         | -             | -               |   |
| BK      | 2     | 1      | 4    | 75                 | 175              | 0.14     | 0.01           | -152.35 | 1.21          | 6.86  | 1.94      | 11.42        | 11.42        | 3.23     | 13.34          | 3.88       | 0.99             |          |             |                | -152.72        | 0.38           | 294          | 28.3          | 292                                  | -       | -       | -       | -            | -            | -         | -             | -               |   |
| BK      | 3     | 1      | 4    | 75                 | 175              | 0.13     | 0.03           | -153.10 | 0.76          | 4.22  | 1.01      | 7.03         | 7.03         | 1.69     | 21.79          | 5.33       | 0.56             |          |             |                | -152.72        | 0.38           | 294          | 28.3          | 292                                  | -       | -       | -       | -            | -            | -         | -             | -               |   |
| BK      | 1     | 1      | 5    | 75                 | 175              | 0.03     | 0.01           | -165.81 | 2.05          | 6.32  | 2.93      | 10.53        | 10.53        | 4.88     | 12.73          | 4.48       | 0.19             | 0.22     | 0.08        | 0.01           | -165.29        | 1.77           | 319          | 29.1          | 319                                  | -       | -       | -       | -            | -            | -         | -             | -               |   |
| BK      | 2     | 1      | 5    | 75                 | 175              | 0.04     | 0.01           | -163.38 | 2.63          | 7.83  | 3.32      | 13.05        | 13.05        | 5.52     | 12.52          | 5.51       | 0.30             |          |             |                | -165.29        | 1.77           | 319          | 29.1          | 319                                  | -       | -       | -       | -            | -            | -         | -             | -               |   |
| BK      | 3     | 1      | 5    | 75                 | 175              | 0.06     | 0.58           | -89.19  | 0.83          | 5.97  | 1.32      | 9.94         | 9.94         | 2.20     | 8.57           | 2.07       | 3.96             | 2.92     | 1.14        | 0.35           | 0.14           | -88.73         | 0.41         | 343           | 28.6                                 | 319     | -       | -       | -            | -            | -         | -             | -               | - |
| BK      | 2     | 2      | 1    | 75                 | 175              | 0.47     | 0.11           | -88.45  | 0.24          | 3.62  | 0.63      | 6.03         | 6.03         | 1.04     | 16.66          | 2.57       | 1.71             |          |             |                | -88.73         | 0.41           | 343          | 28.6          | 319                                  | -       | -       | -       | -            | -            | -         | -             | -               |   |
| BK      | 3     | 2      | 1    | 75                 | 175              | 0.61     | 0.26           | -88.55  | 0.35          | 5.08  | 0.81      | 8.47         | 8.47         | 1.35     | 10.46          | 2.70       | 3.09             |          |             |                | -88.73         | 0.41           | 343          | 28.6          | 319                                  | -       | -       | -       | -            | -            | -         | -             | -               |   |
| BK      | 1     | 2      | 2    | 75                 | 175              | 0.83     | 0.04           | -94.99  | 0.71          | 8.15  | 0.56      | 13.58        | 13.58        | 0.94     | 7.00           | 0.54       | 6.75             | 5.39     | 1.24        | 0.65           | 0.15           | -95.37         | 0.43         | 370           | 29.1                                 | 319     | -       | -       | -            | -            | -         | -             | -               | - |
| BK      | 3     | 2      | 2    | 75                 | 175              | 0.61     | 0.13           | -95.27  | 2.26          | 8.39  | 1.36      | 13.86        | 13.86        | 2.27     | 6.82           | 1.27       | 5.08             |          |             |                | -95.37         | 0.43           | 370          | 29.1          | 319                                  | -       | -       | -       | -            | -            | -         | -             | -               |   |
| BK      | 2     | 2      | 2    | 75                 | 175              | 0.01     | 0.00           | -126.24 | 5.01          | 13.29 | 7.32      | 22.12        | 22.12        | 12.19    | 5.71           | 3.37       | 0.10             | 0.07     | 0.03        | 0.01           | -127.32        | 3.84           | 243          | 20.3          | -                                    | -       | -       | -       | -            | -            | -         | -             | -               |   |
| AT1     | 1     | 1      | 1    | 70                 | 200              | 0.01     | 0.01           | -131.31 | 0.03          | 4.49  | 0.04      | 7.48         | 7.48         | 0.07     | 20.50          | 0.15       | 4.54             | 4.54     | 0.03        | 0.74           | 0.00           | -153.25        | 0.15         | 215           | 24                                   | -       | -       | -       | -            | -            | -         | -             | -               |   |
| AT1     | 2     | 1      | 1    | 70                 | 200              | 0.01     | 0.01           | -131.31 | 0.03          | 4.49  | 0.04      | 7.48         | 7.48         | 0.07     | 20.50          | 0.15       | 4.54             | 4.54     | 0.03        | 0.74           | 0.00           | -153.25        | 0.15         | 215           | 24                                   | -       | -       | -       | -            | -            | -         | -             | -               | - |
| AT1     | 3     | 1      | 1    | 70                 | 200              | 0.01     | 0.01           | -131.31 | 0.03          | 4.49  | 0.04      | 7.48         | 7.48         | 0.07     | 20.50          | 0.15       | 4.54             | 4.54     | 0.03        | 0.74           | 0.00           | -153.25        | 0.15         | 215           | 24                                   | -       | -       | -       | -            | -            | -         | -             | -               | - |
| AT1     | 1     | 2      | 1    | 70                 | 200              | 1.02     | 0.01           | -153.37 | 0.03          | 4.49  | 0.04      | 7.48         | 7.48         | 0.07     | 20.50          | 0.15       | 4.54             | 4.54     | 0.03        | 0.74           | 0.00           | -153.25        | 0.15         | 215           | 24                                   | -       | -       | -       | -            | -            | -         | -             | -               | - |
| AT1     | 2     | 2      | 1    | 70                 | 200              | 1.01     | 0.01           | -153.08 | 0.03          | 4.47  | 0.04      | 7.44         | 7.44         | 0.07     | 20.57          | 0.20       | 4.51             |          |             |                | -169.20        | 0.53           | 215          | 24            | -                                    | -       | -       | -       | -            | -            | -         | -             | -               |   |
| AT1     | 3     | 1      | 2    | 70                 | 200              | 0.15     | 0.01           | -153.08 | 0.03          | 4.47  | 0.04      | 7.44         | 7.44         | 0.07     | 20.57          | 0.20       | 4.51             |          |             |                | -169.20        | 0.53           | 215          | 24            | -                                    | -       | -       | -       | -            | -            | -         | -             | -               |   |
| AT1     | 1     | 3      | 1    | 70                 | 200              | 0.14     | 0.01           | -168.68 | 0.52          | 5.85  | 0.65      | 9.67         | 9.67         | 1.07     | 12.44          | 1.99       | 0.82             | 0.85     | 0.04        | 0.14           | 0.01           | -169.20        | 0.53         | 215           | 24                                   | -       | -       | -       | -            | -            | -         | -             | -               | - |
| AT1     | 2     | 1      | 3    | 70                 | 200              | 0.16     | 0.01           | -168.68 | 0.52          | 5.85  | 0.65      | 9.67         | 9.67         | 1.07     | 12.44          | 1.99       | 0.82             |          |             |                | -169.20        | 0.53           | 215          | 24            | -                                    | -       | -       | -       | -            | -            | -         | -             | -               |   |
| AT1     | 3     | 1      | 3    | 70                 | 200              | 0.16     | 0.01           | -168.68 | 0.52          | 5.85  | 0.65      | 9.67         | 9.67         | 1.07     | 12.44          | 1.99       | 0.82             |          |             |                | -169.20        | 0.53           | 215          | 24            | -                                    | -       | -       | -       | -            | -            | -         | -             | -               |   |
| AT1     | 1     | 1      | 4    | 70                 | 200              | 0.11     | 0.01           | -180.46 | 0.57          | 5.60  | 0.62      | 9.33         | 9.33         | 1.04     | 19.35          | 2.21       | 0.62             | 0.67     | 0.08        | 0.11           | 0.01           | -180.07        | 0.35         | 215           | 24                                   | -       | -       | -       | -            | -            | -         | -             | -               | - |
| AT1     | 2     | 1      | 4    | 70                 | 200              | 0.10     | 0.01           | -179.96 | 0.77          | 6.12  | 0.89      | 10.19        | 10.19        | 1.48     | 17.67          | 2.64       | 0.62             |          |             |                | -180.07        | 0.35           | 215          | 24            | -                                    | -       | -       | -       | -            | -            | -         | -             | -               |   |
| AT1     | 3     | 1      | 4    | 70                 | 200              | 0.10     | 0.01           | -179.96 | 0.77          | 6.12  | 0.89      | 10.19        | 10.19        | 1.48     | 17.67          | 2.64       | 0.62             |          |             |                | -180.07        | 0.35           | 215          | 24            | -                                    | -       | -       | -       | -            | -            | -         | -             | -               |   |
| AT1     | 1     | 2      | 1    | 70                 | 200              | 0.48     | 0.08           | -95.31  | 0.17          | 2.83  | 0.42      | 4.72         | 4.72         | 0.70     | 20.19          | 3.04       | 1.37             | 1.96     | 1.18        | 0.21           | 0.13           | -95.37         | 0.06         | 369           | 30.5                                 | -       | -       | -       | -            | -            | -         | -             | -               | - |
| AT1     | 2     | 2      | 1    | 70                 | 200              | 0.87     | 0.21           | -95.37  | 1.02          | 3.82  | 0.64      | 6.36         | 6.36         | 1.06     | 15.00          | 2.67       | 3.32             |          |             |                | -95.37         | 0.06           | 369          | 30.5          | -                                    | -       | -       | -       | -            | -            | -         | -             | -               | - |
| AT1     | 3     | 2      | 1    | 70                 | 200              | 0.53     | 0.12           | -95.42  | 0.25          | 2.24  | 0.51      | 3.74         | 3.74         | 0.85     | 25.54          | 5.90       | 1.19             |          |             |                | -180.07        | 0.35           | 215          | 24            | -                                    | -       | -       | -       | -            | -            | -         | -             | -               |   |
| AT1     | 1     | 2      | 2    | 70                 | 200              | 0.88     | 0.02           | -102.15 | 0.42          | 7.56  | 0.52      | 12.59        | 12.59        | 0.86     | 8.11           | 0.59       | 6.62             | 4.72     | 2.21        | 0.52           | 0.24           | -101.32        | 0.75         | 216           | 24                                   | -       | -       | -       | -            | -            | -         | -             | -               | - |
| AT1     | 2     | 2      | 2    | 70                 | 200              | 0.88     | 0.02           | -102.15 | 0.42          | 7.56  | 0.52      | 12.59        | 12.59        | 0.86     | 8.11           | 0.59       | 6.62             |          |             |                | -101.32        | 0.75           | 216          | 24            | -                                    | -       | -       | -       | -            | -            | -         | -             | -               |   |
| AT1     | 3     | 2      | 2    | 70                 | 200              | 0.88     | 0.02           | -102.15 | 0.42          | 7.56  | 0.52      | 12.59        | 12.59        | 0.86     | 8.11           | 0.59       | 6.62             |          |             |                | -101.32        | 0.75           | 216          | 24            | -                                    | -       | -       | -       | -            | -            | -         | -             | -               |   |
| AT1     | 1     | 2      | 3    | 70                 | 200              | 0.87     | 0.07           | -101.13 | 1.15          | 6.35  | 1.26      | 10.57        | 10.57        | 2.11     | 9.57           | 2.02       | 5.25             |          |             |                | -109.31        | 3.02           | 216          | 24            | -                                    | -       | -       | -       | -            | -            | -         | -             | -               |   |
| AT1     | 2     | 2      | 3    | 70                 | 200              | 0.87     | 0.07           | -101.13 | 1.15          | 6.35  | 1.26      | 10.57        | 10.57        | 2.11     | 9.57           | 2.02       | 5.25             |          |             |                | -109.31        | 3.02           | 216          | 24            | -                                    | -       | -       | -       | -            | -            | -         | -             | -               |   |
| AT1     | 3     | 2      | 3    | 70                 | 200              | 0.87     | 0.07           | -101.13 | 1.15          | 6.35  | 1.26      | 10.57        | 10.57        | 2.11     | 9.57           | 2.02       | 5.25             |          |             |                | -109.31        | 3.02           | 216          | 24            | -                                    | -       | -       | -       | -            | -            | -         | -             | -               |   |
| AT1     | 1     | 2      | 3    | 70                 | 200              | 0.52     | 0.09           | -107.18 | 1.73          | 4.96  | 1.93      | 8.26         | 8.26         | 3.21     | 12.97          | 5.26       | 2.59             |          |             |                | -109.31        | 3.02           | 216          | 24            | -                                    | -       | -       | -       | -            | -            | -         | -             | -               |   |
| AT1     | 2     | 2      | 3    | 70                 | 200              | 0.52     | 0.09           | -107.18 | 1.73          | 4.96  | 1.93      | 8.26         | 8.26         | 3.21     | 12.97          | 5.26       | 2.59             |          |             |                | -109.31        | 3.02           | 216          | 24            | -                                    | -       | -       | -       | -            | -            | -         | -             | -               |   |
| AT1     | 3     | 2      | 3    | 70                 | 200              | 0.52     | 0.09           | -107.18 | 1.73          | 4.96  | 1.93      | 8.26         | 8.26         | 3.21     | 12.97          | 5.26       | 2.59             |          |             |                | -109.31        | 3.02           | 216          | 24            | -                                    | -       | -       | -       | -            | -            | -         | -             | -               |   |
| AT1     | 1     | 2      | 4    | 70                 | 200              | 0.08     | 0.03           | -116.87 | 1.84          | 3.33  | 2.22      | 5.54         | 5.54         | 3.69     | 21.09          | 14.37      | 0.25             | 0.38     | 0.09        | 0.03           | 0.01           | -119.87        | 2.45         | 216           | 24                                   | -       | -       | -       | -            | -            | -         | -             | -               | - |
| AT1     | 2     | 2      | 4    | 70                 | 200              | 0.08     | 0.03           | -116.87 | 1.84          | 3.33  | 2.22      | 5.54         | 5.54         | 3.69     | 21.09          | 14.37      | 0.25             |          |             |                | -119.87        | 2.45           | 216          | 24            | -                                    | -       | -       | -       | -            | -            | -         | -             | -               |   |
| AT1     | 3     | 2      | 4    | 70                 | 200              | 0.08     | 0.03           | -116.87 | 1.84          | 3.33  | 2.22      | 5.54         | 5.54         | 3.69     | 21.09          | 14.37      | 0.25             |          |             |                | -119.87        | 2.45           | 216          | 24            | -                                    | -       | -       | -       | -            | -            | -         | -             | -               |   |
| AT1     | 1     | 3      | 1    | 70                 | 200              | 0.06     | 0.05           | -121.41 | 3.27          | 3.30  | 4.23</    |              |              |          |                |            |                  |          |             |                |                |                |              |               |                                      |         |         |         |              |              |           |               |                 |   |

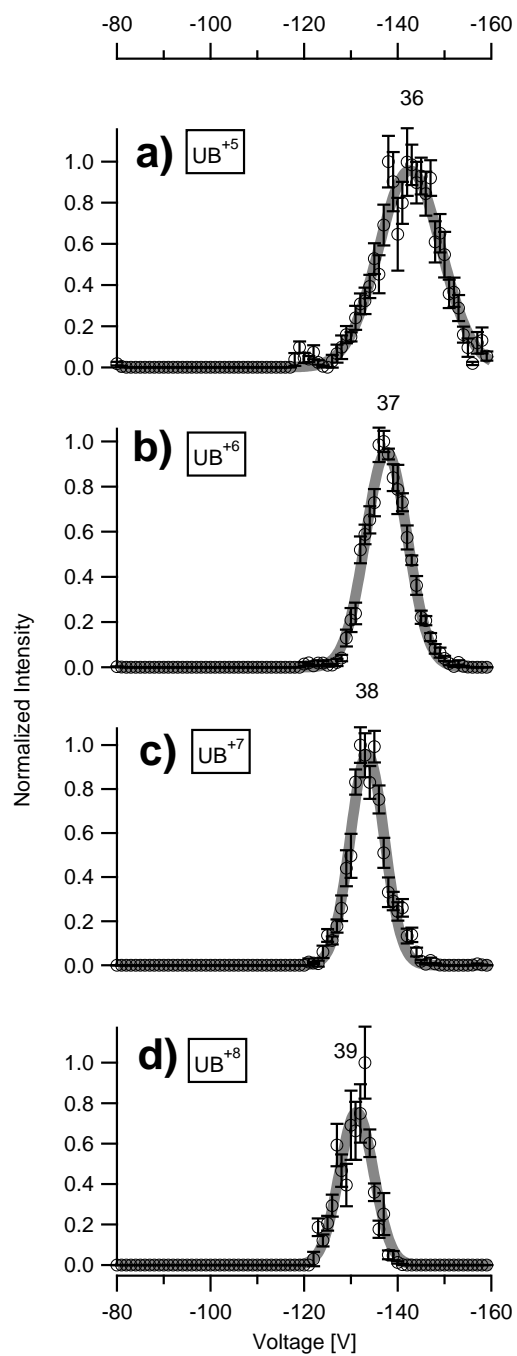


Figure B.5: A single experimental classification of UB, showing mass-resolved, normalized signal as a function of  $\phi$ . Error bars on the circular markers indicate 1 standard deviation of the normalized signal at that  $\phi$  for that one scan. Each resolvable Gaussian peak is labeled with a unique identifier number. The thick gray line is the Gaussian-fitted function to the signal. a)  $\text{UB}^{+5}$  at  $T_{\text{ESI}} = 298$  K. b)  $\text{UB}^{+6}$  at  $T_{\text{ESI}} = 298$  K. c)  $\text{UB}^{+7}$  at  $T_{\text{ESI}} = 298$  K. d)  $\text{UB}^{+8}$  at  $T_{\text{ESI}} = 298$  K.

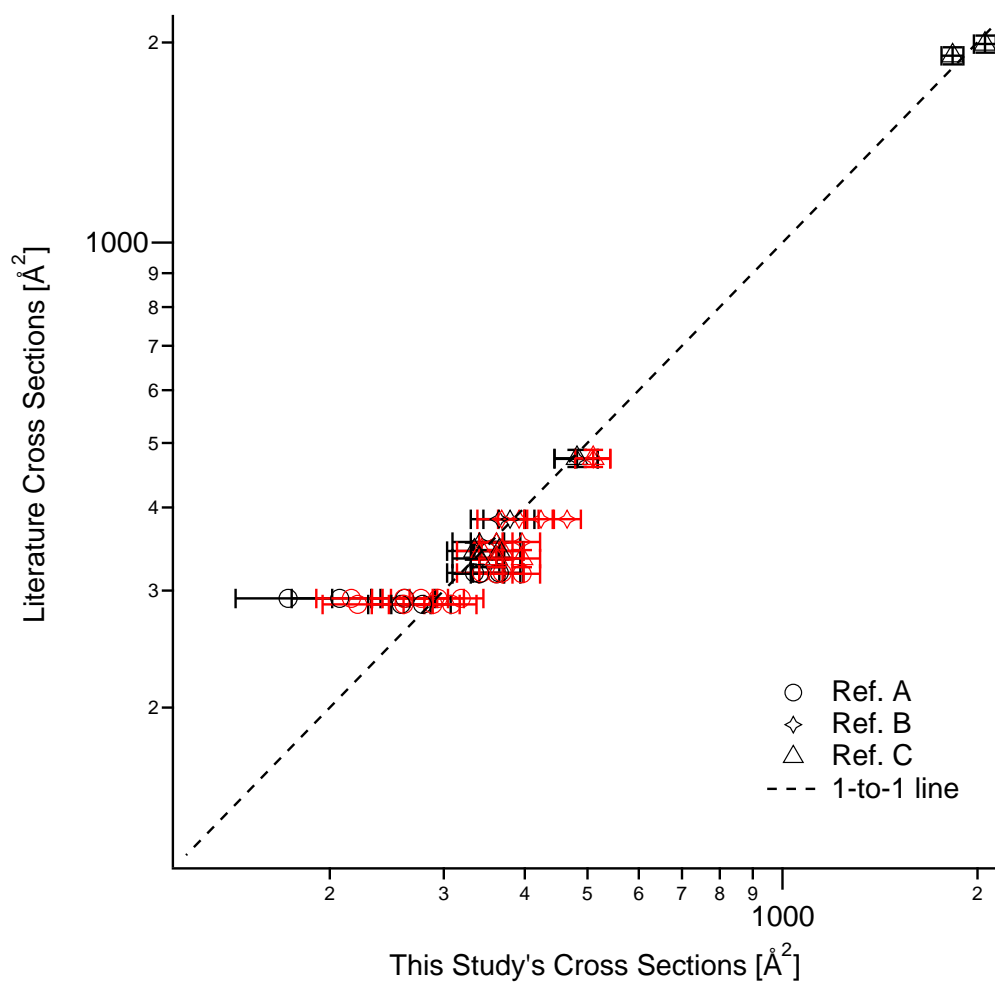


Figure B.6: Measured cross sections values in this study against those from other studies. Black markers indicate  $T_{\text{ESI}} = 298$  K and red markers indicate  $T_{\text{ESI}} = 400$  K. Horizontal error bars denote 1 standard deviation of triplicates. Vertical error bars indicate that study's estimated error, if provided. Ref. A: Wu, Klasmeier, and Hill 1999. Ref. B: Baykut, Halem, and Raether 2009. Ref. C: Bush et al. 2010.



Table B.11: Model peptides: detailed results at  $T_{\text{ESI}} = 298 \text{ K}$ .

| Sequence  | TEMPO | CID | charge | $m/z$       | Start $\phi$ [V] | End $\phi$ [V] | $\sigma$ | $\sigma$ 95%CI | $b$     | $b$ 95%CI | $c$  | $c$ 95%CI | FWHM | E(FWHM) | $R$   | E(R) | Ion Mass [kg] | Red. Mass [kg] | $\theta \times 10^{-16}$ | E( $\theta$ ) $\times 10^{-16}$ | $\Omega$ [ $\text{\AA}^2$ ] | E( $\Omega$ ) |
|-----------|-------|-----|--------|-------------|------------------|----------------|----------|----------------|---------|-----------|------|-----------|------|---------|-------|------|---------------|----------------|--------------------------|---------------------------------|-----------------------------|---------------|
| AA_AAA_AA | no    | no  | 1      | 969.5-974   | 100              | 120            | 0.92     | 0.04           | -110.20 | 0.15      | 3.97 | 0.21      | 6.62 | 0.35    | 16.65 | 0.90 | 1.61E-24      | 4.52E-26       | -0.89                    | 0.001                           | 210                         | 26.9          |
| AARAAATAA | no    | yes | 1      | 281.5-283.7 | 100              | 120            | 0.90     | 0.06           | -111.65 | 0.23      | 4.10 | 0.32      | 6.83 | 0.54    | 16.34 | 1.32 | 4.69E-25      | 4.23E-26       | -0.94                    | 0.002                           | 220                         | 26.9          |
| AARAAATAA | no    | yes | 1      | 352.5-355   | 100              | 120            | 0.87     | 0.07           | -112.01 | 0.21      | 3.48 | 0.30      | 5.79 | 0.51    | 19.35 | 1.73 | 5.87E-25      | 4.31E-26       | -0.93                    | 0.002                           | 219                         | 26.9          |
| AARAAATAA | no    | yes | 1      | 423.5-425.7 | 100              | 120            | 0.94     | 0.08           | -111.12 | 0.22      | 3.21 | 0.31      | 5.34 | 0.51    | 20.81 | 2.02 | 7.05E-25      | 4.36E-26       | -0.92                    | 0.002                           | 216                         | 26.9          |
| AATAAARAA | no    | yes | 1      | 367.5-369.5 | 100              | 120            | 0.82     | 0.09           | -112.07 | 0.35      | 4.01 | 0.49      | 6.68 | 0.82    | 16.78 | 2.11 | 6.12E-25      | 4.32E-26       | -0.93                    | 0.003                           | 219                         | 26.7          |
| AATAAARAA | no    | yes | 1      | 438.5-440.7 | 100              | 120            | 0.89     | 0.07           | -111.90 | 0.24      | 3.68 | 0.34      | 6.12 | 0.57    | 18.27 | 1.74 | 7.30E-25      | 4.37E-26       | -0.92                    | 0.002                           | 217                         | 26.8          |
| AATAAARAA | no    | yes | 1      | 529.6-531.8 | 100              | 120            | 0.84     | 0.07           | -112.18 | 0.26      | 3.57 | 0.36      | 5.94 | 0.60    | 18.87 | 1.96 | 8.81E-25      | 4.42E-26       | -0.92                    | 0.002                           | 216                         | 26.8          |
| AARAAATAA | yes   | yes | 1      | 526-529     | 120              | 150            | 0.96     | 0.02           | -128.48 | 0.07      | 3.81 | 0.10      | 6.35 | 0.17    | 20.23 | 0.56 | 8.76E-25      | 4.42E-26       | -1.06                    | 0.001                           | 249                         | 27.9          |
| AARAAATAA | yes   | yes | 1      | 570-575     | 120              | 150            | 0.96     | 0.03           | -128.63 | 0.10      | 4.00 | 0.15      | 6.67 | 0.24    | 19.30 | 0.72 | 9.50E-25      | 4.43E-26       | -1.05                    | 0.001                           | 249                         | 27.8          |
| AATAAARAA | yes   | yes | 1      | 529.8-534   | 120              | 150            | 0.97     | 0.02           | -135.66 | 0.09      | 4.20 | 0.12      | 7.00 | 0.20    | 19.39 | 0.58 | 8.83E-25      | 4.42E-26       | -1.11                    | 0.001                           | 264                         | 28.2          |
| AATAAARAA | yes   | yes | 1      | 613-617     | 120              | 150            | 0.98     | 0.02           | -135.72 | 0.07      | 4.19 | 0.11      | 6.98 | 0.18    | 19.45 | 0.50 | 1.02E-24      | 4.45E-26       | -1.11                    | 0.001                           | 263                         | 28.2          |
| AARAA_A_A | no    | no  | 1      | 868-873     | 115              | 135            | 0.97     | 0.02           | -120.34 | 0.07      | 3.42 | 0.10      | 5.69 | 0.17    | 21.13 | 0.65 | 1.45E-24      | 4.50E-26       | -0.98                    | 0.001                           | 230                         | 27.5          |
| AARAAHAMA | no    | yes | 1      | 631.5-635   | 110              | 130            | 0.91     | 0.05           | -119.66 | 0.16      | 3.80 | 0.23      | 6.32 | 0.38    | 18.93 | 1.17 | 1.05E-24      | 4.45E-26       | -0.98                    | 0.001                           | 230                         | 27.3          |
| AARAAHAMA | no    | yes | 1      | 642.5-646   | 110              | 130            | 0.89     | 0.06           | -120.96 | 0.20      | 3.75 | 0.29      | 6.24 | 0.48    | 19.37 | 1.53 | 1.07E-24      | 4.46E-26       | -0.99                    | 0.002                           | 233                         | 27.3          |
| AARAA_A_A | yes   | no  | 1      | 1065.5-1070 | 130              | 160            | 0.87     | 0.05           | -141.97 | 0.21      | 4.72 | 0.30      | 7.85 | 0.50    | 18.08 | 1.18 | 1.77E-24      | 4.53E-26       | -1.15                    | 0.002                           | 273                         | 28.2          |
| AARAAHAMA | yes   | yes | 1      | 591.5-594   | 130              | 160            | 0.94     | 0.05           | -140.28 | 0.18      | 4.05 | 0.25      | 6.75 | 0.42    | 20.78 | 1.31 | 9.84E-25      | 4.44E-26       | -1.15                    | 0.001                           | 272                         | 28.2          |
| AARAAHAMA | yes   | yes | 1      | 793.8-795.9 | 130              | 160            | 0.95     | 0.04           | -143.05 | 0.14      | 3.73 | 0.20      | 6.22 | 0.33    | 23.00 | 1.23 | 1.32E-24      | 4.49E-26       | -1.17                    | 0.001                           | 276                         | 28.4          |

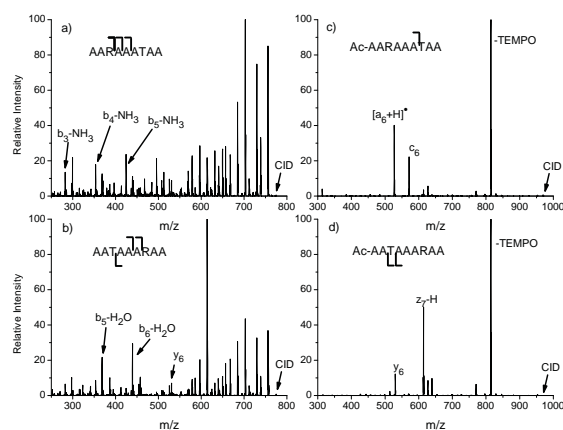


Figure B.7: CID spectra of the peptide isomers a) AARAAATAA and b) AATAAARAA. Corresponding FRIPS spectra are shown in c) and d). Labeled peaks are product ions specific to each isomer used for identification during separation by the ROMIAC; other peaks common to both isomers are not labeled for clarity. Product ions in the FRIPS spectrum are referenced to the acetyl radical generated by loss of the TEMPO moiety.

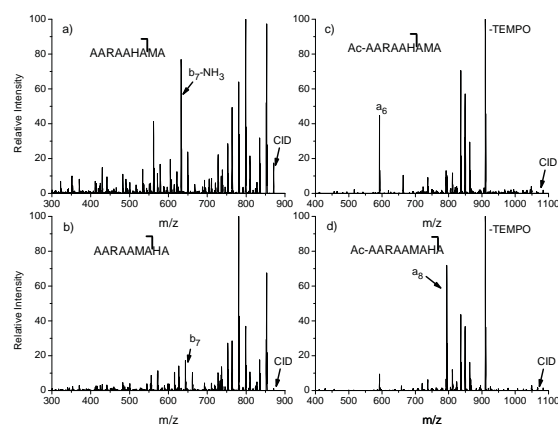


Figure B.8: Same as Fig. B.7, but for a) AARAAHAMA and b) AARAAMAHA. Corresponding FRIPS spectra are shown in c) and d).

## References

- Baykut, G., O. von Halem, and O. Raether (2009). "Applying a dynamic method to the measurement of ion mobility". In: *J. Am. Soc. Mass Spectrom.* 20.11, pp. 2070–81. doi: 10.1016/j.jasms.2009.07.013.
- Bush, M. F. et al. (2010). "Collision cross sections of proteins and their complexes: a calibration framework and database for gas-phase structural biology." In: *Anal. Chem.* 82.22, pp. 9557–65. doi: 10.1021/ac1022953.
- Counterman, A. E. et al. (1998). "High-order structure and dissociation of gaseous peptide aggregates that are hidden in mass spectra". In: *J. Am. Soc. Mass Spectrom.* 9.8, pp. 743–59. doi: 10.1016/S1044-0305(98)00052-X.
- Eiceman, G. A. and Z. Karpas (1994). *Ion mobility spectrometry*. CRC Press.
- Fernández-Maestre, R. et al. (2010). "Chemical standards in ion mobility spectrometry". In: *Analyst* 135.6, pp. 1433–42. doi: 10.1039/b915202d.
- Hodyss, R., H. A. Cox, and J. L. Beauchamp (2005). "Bioconjugates for tunable peptide fragmentation: free radical initiated peptide sequencing (FRIPS)." In: *J. Am. Chem. Soc.* 127.36, pp. 12436–7. doi: 10.1021/ja052042z.
- Kaur-Atwal, G. et al. (2009). "Chemical standards for ion mobility spectrometry: a review". In: *Int. J. Mobil. Spectrom.* 12.1, pp. 1–14. doi: 10.1007/s12127-009-0021-1.
- Lee, M. et al. (2009). "Gas-phase peptide sequencing by TEMPO-mediated radical generation." In: *Analyst* 134.8, pp. 1706–12. doi: 10.1039/b904115j.
- Pierson, N. A. et al. (2011). "Number of solution states of bradykinin from ion mobility and mass spectrometry measurements". In: *J. Am. Chem. Soc.* 133.35, pp. 13810–13813. doi: 10.1021/ja203895j.
- Revercomb, H. E. and E. A. Mason (1975). "Theory of plasma chromatography/gaseous electrophoresis - a review". In: *Anal. Chem.* 47.7, pp. 970–983. doi: 10.1021/ac60357a043.
- Shvartsburg, A. A. et al. (2006a). "Characterizing the structures and folding of free proteins using 2-D gas-phase separations: observation of multiple unfolded conformers". In: *Anal. Chem.* 78.10, pp. 3304–3315. doi: 10.1021/ac060283z.
- (2006b). "High-resolution field asymmetric waveform ion mobility spectrometry using new planar geometry analyzers". In: *Anal. Chem.* 78.11, pp. 3706–14. doi: 10.1021/ac052020v.
- Sohn, C. H. (2011). "New reagents and methods for mass spectrometry-based proteomics investigations". Dissertation (Ph.D.) California Institute of Technology, p. 199.
- Sun, Q. et al. (2009). "Side chain chemistry mediates backbone fragmentation in hydrogen deficient peptide radicals". In: *J. Proteome Res.* 8, pp. 958–966. doi: 10.1021/pr800592t.

- Viidanoja, J. et al. (2005). "Tetraalkylammonium halides as chemical standards for positive electrospray ionization with ion mobility spectrometry/mass spectrometry". In: *Rapid Comm. Mass Sp.* 19.21, pp. 3051–5. DOI: 10.1002/rcm.2172.
- Wu, C., J. Klasmeier, and H. H. Hill (1999). "Atmospheric pressure ion mobility spectrometry of protonated and sodiated peptides". In: *Rapid Comm. Mass Sp.* 13.12, pp. 1138–42. DOI: 10.1002/(SICI)1097-0231(19990630)13:12<1138::AID-RCM625>3.0.CO;2-8.
- Wu, C., W. F. Siems, et al. (1998). "Electrospray ionization high-resolution ion mobility spectrometry-mass spectrometry". In: *Anal. Chem.* 70.23, pp. 4929–4938. DOI: 10.1021/ac980414z.
- Wytenbach, T., C. Bleiholder, and M. T. Bowers (2013). "Factors contributing to the collision cross section of polyatomic ions in the kilodalton to gigadalton range: application to ion mobility measurements". In: *Anal. Chem.* Article ASAP. DOI: 10.1021/ac3029008.
- Wytenbach, T. and M. T. Bowers (2011). "Structural stability from solution to the gas phase: native solution structure of ubiquitin survives analysis in a solvent-free ion mobility-mass spectrometry environment". In: *J. Phys. Chem. B* 115.42, pp. 12266–75. DOI: 10.1021/jp206867a.
- Wytenbach, T., G. von Helden, and M. T. Bowers (1996). "Gas-phase conformation of biological molecules: Bradykinin". In: *J. Am. Chem. Soc.* 118.35, pp. 8355–8364. DOI: 10.1021/ja9535928.

## Appendix C

### SUPPLEMENTARY INFORMATION FOR CHARGE DISTRIBUTION UNCERTAINTY IN DIFFERENTIAL MOBILITY ANALYSIS OF AEROSOLS

#### Ion mobility distributions

The mobility distribution of the ions produced in a TSI 3077 bipolar  $^{85}\text{Kr}$  aerosol charger was measured in laboratory conditions at Caltech in Pasadena, CA ( $T = 298.15$ ,  $p = 96757$  Pa). HEPA-filtered, particle-free, room air was directed into the charger and the ions exiting the charger were segregated according to their electrical mobility using a Radial Opposed Migration Ion and Aerosol Classifier, ROMIAC (Mui, Thomas, et al. 2013; Mui, Mai, et al. 2017), with a TSI 3068 electrometer used for detecting the ions. The measurement covered the mobility range from  $0.1 \text{ cm}^2\text{V}^{-1}\text{s}^{-1}$  to  $5.9 \text{ cm}^2\text{V}^{-1}\text{s}^{-1}$ . All the plumbing of the instrumentation setup was stainless steel. The sample flow rate was 2.25 lpm and the cross-flow rate was 20 lpm, for a non-dispersive resolution of 8.9.

The data was inverted using a transfer function derived for a rectilinear opposed migration aerosol classifier (OMAC; Flagan 2004) following the flux coordinate method of Stolzenburg (1988) for deriving the transfer function for a cylindrical differential mobility analyzer. The derivation of the OMAC transfer function is described in detail by Mai and Flagan (2017) and is applied by Mui, Mai, et al. (2017) in a comprehensive characterization of the instrument using high mobility electrosprayed tetralkyl ammonium halide ions as small as 1.16 nm in mobility diameter. The ROMIAC transfer function, with explicit correction factors for the ROMIAC, is

$$\Omega = \frac{\sqrt{\tilde{\sigma}^2 + \tilde{\sigma}_{\text{distor}}^2}}{\sqrt{2}B\gamma_B(1 - \delta)} \left[ \mathcal{E} \left( \frac{\tilde{Z} - (1 + B\gamma_B)}{\sqrt{2}\sqrt{\tilde{\sigma}^2 + \tilde{\sigma}_{\text{distor}}^2}} \right) + \mathcal{E} \left( \frac{\tilde{Z} - (1 - B\gamma_B)}{\sqrt{2}\sqrt{\tilde{\sigma}^2 + \tilde{\sigma}_{\text{distor}}^2}} \right) - \mathcal{E} \left( \frac{\tilde{Z} - (1 + \delta B\gamma_B)}{\sqrt{2}\sqrt{\tilde{\sigma}^2 + \tilde{\sigma}_{\text{distor}}^2}} \right) - \mathcal{E} \left( \frac{\tilde{Z} - (1 - \delta B\gamma_B)}{\sqrt{2}\sqrt{\tilde{\sigma}^2 + \tilde{\sigma}_{\text{distor}}^2}} \right) \right], \quad (\text{C.1})$$

where  $\tilde{\sigma}$  is a dimensionless measure of diffusional broadening, evaluated as an

integral (which is a function of the operating flow rates, voltage, and classifier geometry) along the ion migration path,  $B$  is the ratio of the sample flow rate to the cross-flow rate,  $\delta$  is the flow rate ratio imbalance,  $\tilde{Z} = Z/Z^*$  is the dimensionless mobility, where  $Z$  is the mobility and  $Z^*$  is the nominal ion mobility transmitted by the ROMIAC at a given cross-flow rate and voltage setting,  $\tilde{\sigma}_{\text{distor}}^2$  and  $\gamma_B$  are correction factors for  $\tilde{\sigma}$  and  $B$ , respectively, for the ROMIAC due in part to its radial geometry, and

$$\mathcal{E}(y) = y \operatorname{erf}(y) + \pi^{-1/2} e^{-y^2}. \quad (\text{C.2})$$

The electrosprayed ions were also used to characterize the ROMIAC efficiency, which has been found to empirically follow a function of the ion mobility and flow rate ratio. Mui, Mai, et al. (2017) also measured the transmission efficiency of high mobility ions in the ROMIAC; for the flow rate ratio in this work, the transmission efficiency of 1–2 nm ions ranges from 6–23%.

The inversion algorithm used for obtaining the ion mobility distribution is the same as that used for inferring particle size distributions from the synthetic signals in Section 2.4 in the main text, with the difference being that the ROMIAC transfer function and measured transmission efficiencies were incorporated into the inversion algorithm, as opposed to using the pseudo-instrument transfer function.

In the measured mobility distribution of the negative charger ions,  $n_i^-(Z_i)$ , we observed one major peak, at the mobility of  $\sim 1.5 \text{ cm}^2\text{V}^{-1}\text{s}^{-1}$ , which contributed over 99 % of the negative ions (Figure C.1). The observed mean and median mobilities were  $Z_{i,\text{ave}}^- = 1.53$  and  $Z_{i,\text{med}}^- = 1.56 \text{ cm}^2\text{V}^{-1}\text{s}^{-1}$ , respectively. The mobility distribution of positive ions,  $n_i^+(Z_i)$ , however, was considerably more continuous, with the major peak, at mobility of  $\sim 1.2 \text{ cm}^2\text{V}^{-1}\text{s}^{-1}$ , contributing  $\sim 84$  % of the negative ions. The observed mean and median mobilities were  $Z_{i,\text{ave}}^+ = 1.12$  and  $Z_{i,\text{med}}^+ = 1.12 \text{ cm}^2\text{V}^{-1}\text{s}^{-1}$ , respectively. The signal from particles with  $d_p > 1.9 \text{ nm}$  would not be affected due to charger ions being detected in addition to the particles, but a slightly more conservative lower limit of 2 nm was used for the particle size distribution in this study.

Filtered ambient lab air was transported through stainless steel tubing in this study, but another choice of sampled gas mixture or plumbing material used would have likely resulted in a different  $n_i^\pm(Z_i)$  (G. Steiner and Reischl 2012; Gerhard Steiner et al. 2014; Maißer et al. 2015). In order to probe the effect of ion mobility

distribution on the charge distribution, and, consequently, on the biases in the particle size distribution measurements due to inaccurate assumptions of the charge distribution acquired in the charger, we conducted the simulations using two different ion mobility distributions: the one according to our measurements and another based on the measurements by G. Steiner and Reischl (2012), which are referred to as measured and SR distributions, respectively (Figure C.1).

Since Steiner and Reischl used different relation between ion mobility and size, the SR distribution is based on the values of electrometer current as a function of electrical mobility as reported by G. Steiner and Reischl (2012), but the conversion of those mobility values to diameter and mass was according to Eq. (1). For the SR distribution, the mean and median mobility of negative (positive) ions were  $Z_{i,ave}^- = 2.14$  and  $Z_{i,med}^- = 2.19 \text{ cm}^2\text{V}^{-1}\text{s}^{-1}$  ( $Z_{i,ave}^+ = 1.66$  and  $Z_{i,med}^+ = 1.66 \text{ cm}^2\text{V}^{-1}\text{s}^{-1}$ ), respectively. These mean mobilities differ slightly from the corresponding values reported by Steiner and Reischl, which were 2.09 and  $1.65 \text{ cm}^2\text{V}^{-1}\text{s}^{-1}$  for negative and positive ions, respectively. This minor difference has no effect on the conclusions of this study, as the purpose of using both the measured and SR distributions is to cover the extremes of very low (measured) and high (SR) charger ion mobilities using realistic ion mobility distributions.

## Flux coefficients and charge distributions

### Calculation of charge distributions using effective flux coefficients

The bipolar steady-state charge distribution of an aerosol can be deduced from the ion-to-particle flux coefficients by solving a system of population balance equations (Hussin et al. 1983). A detailed derivation of the model employed in this study is given in López-Yglesias and Flagan (2013b), except that we account for the polarization of air in the ion mass-mobility relation and that, instead of considering only one type of negative and positive ion, we follow the approach taken by Lee et al. (2005) to describe the ions using a discrete mobility distribution,  $n_i^\pm(Z_i)$ . For discrete distribution

$$n_{i,T}^\pm = \sum_{m=1}^x n_{i,m}^\pm(Z_{i,m}), \quad (\text{C.3})$$

where  $n_{i,T}$  is the total concentration of ions,  $n_{i,m}^\pm(Z_{i,m})$  is the concentration of ions with electrical mobility  $Z_{i,m}$ ,  $x$  is the number of mobility bins in the distribution and “+” and “-” refer to positive and negative polarity, respectively. In this case,

the balance equation describing the variation of concentration of particles having charge state  $k$ ,  $n_k$ , becomes

$$\begin{aligned} \frac{dn_k(d_p)}{dt} = & \sum_{m=1}^x \beta_{k-1}^+(d_p, Z_{i,m}) n_{i,m}^+(Z_{i,m}) n_{k-1}(d_p) \\ & - \sum_{m=1}^x \beta_k^+(d_p, Z_{i,m}) n_{i,m}^+(Z_{i,m}) n_k(d_p) \\ & + \sum_{m=1}^x \beta_{k+1}^-(d_p, Z_{i,m}) n_{i,m}^-(Z_{i,m}) n_{k+1}(d_p) \\ & - \sum_{m=1}^x \beta_k^-(d_p, Z_{i,m}) n_{i,m}^-(Z_{i,m}) n_k(d_p), \end{aligned} \quad (C.4)$$

where  $t$  is time and  $\beta_k^\pm(d_p, Z_i)$  is the flux coefficient of ions with mobility  $Z_i$  to particles with diameter  $d_p$ . We can now define an effective flux coefficient of the total ion mobility distribution,  $\beta_{\text{eff},k}^\pm(d_p)$ , as

$$\beta_{\text{eff},k}^\pm(d_p) = \frac{\sum_{m=1}^x \beta_k^\pm(d_p, Z_{i,m}) n_{i,m}^\pm(Z_{i,m})}{\sum_{m=1}^x n_{i,m}^\pm(Z_{i,m})} = \frac{\sum_{m=1}^x \beta_k^\pm(d_p, Z_{i,m}) n_{i,m}^\pm(Z_{i,m})}{n_{i,T}^\pm}. \quad (C.5)$$

By using the effective flux coefficient, the balance equation simplifies to

$$\begin{aligned} \frac{dn_k(d_p)}{dt} = & \beta_{\text{eff},k-1}^+(d_p) n_{i,T}^+ n_{k-1}(d_p) \\ & - \beta_{\text{eff},k}^+(d_p) n_{i,T}^+ n_k(d_p) \\ & + \beta_{\text{eff},k+1}^-(d_p) n_{i,T}^- n_{k+1}(d_p) \\ & - \beta_{\text{eff},k}^-(d_p) n_{i,T}^- n_k(d_p). \end{aligned} \quad (C.6)$$

In other words, with the definition of the effective flux coefficients, Eq. (C.5), the balance equation accounting for the whole ion mobility distribution, Eq. (C.4), reduces to a balance equation with only one type of ions, Eq. (C.6). By specifying the maximum number of charges that a particle can acquire,  $k_{\text{max}}$ , the Eq. (C.6) can be written for each charge state considered, and the fraction of particles with a diameter,  $d_p$ , that have the charge state  $k$ ,  $f_k(d_p)$ , can be solved for each  $k$  from that set of balance equations (e.g.,  $k_{\text{max}} = 5$  for Hoppel and Frick (1986),  $k_{\text{max}}$



= 100 for López-Yglesias and Flagan (2013b), and  $k_{\max} = 30$  in this study). The definition of the effective flux coefficient allows for a simplified visualization of the flux coefficients of the ion mobility distribution, as the coefficients for each ion type need not to be depicted separately, though, on the other hand, the effective flux coefficients do not correspond to any specific ion type.

### **Variation in flux coefficients due to ion mobility distribution**

Figure C.2 shows the effective flux coefficients calculated according to Eq. (C.5). For the simplicity of presentation, only the flux coefficients to particles with up to three charges are shown. While the flux coefficients are qualitatively similar for the measured and SR distributions, there are considerable differences in the values throughout the diameter range considered. Except for the fluxes to particles with  $d_p < 10$  nm and charge state opposite to that of the ion, the flux coefficients for the SR distribution were higher than those of the measured distribution (Figure C.3).

Particles with  $d_p < 10$  nm carry at most a single charge, so their charge distribution depends only on the flux coefficients of ions to particles that are either neutral or carry a charge opposite to that of the ion. As the ion fluxes to neutral and oppositely-charged particles were higher and lower, respectively, for the SR distribution than for the measured distribution, i.e., there was more charging of neutral particles and less neutralization of charged particles, the fraction of singly-charged particles with  $d_p < 10$  nm was higher for the SR distribution than for the measured distribution (Figure C.4). If the charge distribution according the measured distribution was acquired in the charger, but the higher charged fraction corresponding to the SR distribution was assumed in the inversion, the concentrations of particles  $< 10$  nm in diameter were underestimated (Figure 4.4).

The probability of a particle carrying multiple charges increases with increasing particle size (Figure C.4). At particle sizes with considerable fractions of multiply-charged particles, it becomes complicated to interpret how the changes in the flux coefficients affect the charge distribution, since the number of equations in the form of Eq. (C.6) in the system of balance equations increases with increasing  $k_{\max}$ . For particles larger than 10 nm in diameter the flux coefficients were higher for the ions characterized by the SR distribution than the corresponding flux coefficients of the measured ions for vast majority of particle sizes and charge states (Figure C.3). Those differences in the flux coefficients resulted in differences in the charge distribution (Figure C.4). Consequently, if the charge distribution based on the

measured ions was acquired in the charger, but the one according to SR distribution was assumed in the inversion, the concentrations of particles with  $10 \text{ nm} < d_p < 100 \text{ nm}$  were underestimated if negative particles were counted, while both over- and underestimation was observed for particles with  $d_p > 10 \text{ nm}$ , if positive particles were counted.

### **Variation in flux coefficients due to temperature and pressure**

As expected based on the results by López-Yglesias and Flagan (2013a), the flux coefficients at the  $T$  and  $p$  corresponding to 10 km altitude differ significantly from those at laboratory conditions. Moreover, since the chemical composition of the air going into the charger affects the mobility distribution of the ions (Gerhard Steiner et al. 2014; Maißer et al. 2015), the actual mobility distribution of the ions at 10 km altitude would likely differ from those in the laboratory. Assessing this difference requires data that are beyond the scope of this study.

In general, at 10 km altitude, when the measured distribution was used, the flux coefficient of ions to oppositely- and similarly-charged particles were higher and lower, respectively, than at the laboratory, and the flux coefficients at different conditions approached a different asymptote with increasing particle size (Figure C.2). The variation of the flux coefficients with altitude conditions altered the charge distributions calculated for these conditions (Figure C.4). Furthermore, charge distributions calculated for both conditions differed from that predicted using the parameterization by Wiedensohler (1988), which was based on the Hoppel and Frick (1986) calculations at standard temperature and pressure.

For particles with  $d_p < 10$  the ion fluxes to neutral particles were approximately the same both in the laboratory conditions and at 10 km altitude, so the observed difference in the charge distributions in those conditions were due to variation in the ion flux to oppositely-charged particles (Figure C.5). As the flux of positive ions to negative particles was consistently higher at 10 km than at laboratory, the negative particles were more rapidly neutralized resulting to lower steady-state fraction (Figure C.4). Failure to take that lower fraction of negatively-charged particles into account in the inversion resulted in underestimation of concentrations of particles with  $d_p < 10 \text{ nm}$  (Figure 4.5). The flux of negative ions to positive particles, however, was either smaller or larger at 10 km altitude than at laboratory, depending on particle size, which resulted in particle concentrations being either over- or underestimated, respectively.

### Variation in flux coefficients due to ion mass

Regardless of whether the measured or SR distribution was used, when the mass of ions was considerably decreased, the largest changes in the effective flux coefficients were the increases in the ion fluxes to neutral particles and to particles with charge similar to the ions, especially for particles with  $d_p < 20$  nm (Figure C.6). As those fluxes increase the net charge of the aerosol population, the decrease in the ion masses resulted in higher fractions of singly-charged particles with  $d_p < 20$  nm, which, if not taken into account in the inversion, resulted in overestimation of the particle concentrations (Figure 4.6). When the measured distribution was used, this overestimation switched to underestimation at  $d_p = 21$  nm, if positive particles were counted. The reason for this switch was that, at that size, the increase in the flux of positive ions to neutral particles was overtaken by the increase in the flux of negative ions to positive particles, which resulted in decrease in the fraction of singly-charged positive particles. The same phenomenon was observed also when the SR distribution was used, though the switch occurred at  $d_p = 60$  nm, and the magnitude of the underestimation of concentrations of particles with  $d_p > 60$  nm was less pronounced than in the case of the measured distribution. The effects of more massive ions on the flux coefficients were opposite to the effects of less massive ions (Figure C.7).

### Variation in flux coefficients due to relative permittivity of the particle

If the particles were made of material with low relative permittivity, such as polystyrene with  $\chi_p = 2.6$ , the ion-to-particle fluxes were smaller than corresponding fluxes to conductive particles (Figure C.8). The flux coefficients were smaller regardless of the particle charge state, as the decrease in the relative permittivity of the particle decreased the potential related to image charges induced on the particle, which is always an attractive potential for the system of a point charge outside of a sphere. The fluxes of ions to oppositely-charged particles, for which the Coulombic force between the net charges of the ion and the particle was attractive, were less affected than the fluxes of ions to similarly-charged particles, for which the Coulombic force between the net charges is repulsive. As a result, for particles with  $d_p < 30$  nm, the fractions of charged polystyrene particles were lower than the corresponding fractions of charged conductive particles, which, if not accounted for in the inversion, resulted in underestimation of the particle concentrations (Figure 4.7).

### **Additional sources of uncertainty in the inferred particle size distribution**

#### **Bias in the inferred particle size distribution due to using mean or median mobility instead of the whole ion mobility distribution**

While studies using the Brownian dynamics method to estimate the charge distribution have accounted for multiple ion species (Gopalakrishnan, Meredith, et al. 2013; Maißer et al. 2015; Gopalakrishnan, McMurry, and Hogan 2015), in most previous studies (e.g., Hoppel and Frick 1986; López-Yglesias and Flagan 2013a) estimating the charge distribution from the ion-to-particle flux coefficients, the ions have been modeled using a single characteristic positive and negative ion. We conducted simulations to examine the effect of this simplification. When calculating  $f_{\text{cha}}$  using the whole measured ion mobility distribution, but  $f_{\text{inv}}$  using only the mean,  $Z_{i,\text{ave}}$ , or median,  $Z_{i,\text{med}}$ , value of the mobility, little bias was observed in the particle size distribution (Figure C.9). Using  $Z_{i,\text{ave}}$  caused less bias than using  $Z_{i,\text{med}}$ : the value of  $R_{\text{ave}}^*(d_p)$  was within a factor of 1.05 from unity when  $Z_{i,\text{ave}}$  was used, and mostly within a factor of 1.1 from unity when  $Z_{i,\text{med}}$  was used. For negative particle measurements, differences were found primarily when  $d_p > 100$  nm, but for positive particles, there was also a noticeable difference for particles smaller than 10 nm. This difference between the two polarities was likely caused by the negative ion mobility distribution being much more monodisperse than the positive one (Figure C.1).

When the SR distribution was used, the observed biases in the inferred particle size distribution due to using  $Z_{i,\text{ave}}$  or  $Z_{i,\text{med}}$ , instead of the whole ion mobility distribution were even smaller than when the measured distribution was used (Figure C.9); The value of value of  $R_{\text{ave}}^*(d_p)$  was within a factor of 1.05 from unity almost without exception, and, in general, the bias factor was smaller when  $Z_{i,\text{ave}}$  was used than when  $Z_{i,\text{med}}$  was used.

#### **Bias in the inferred particle size distribution due to relative permittivity of charger ions**

We examined the effect of the relative permittivity of the ion on the bias in the inferred particle size distribution. With the value of  $\chi_1 = 6$  used when calculating  $f_{\text{inv}}$ , a negligible bias in particle size distribution was observed regardless of the value used when calculating  $f_{\text{cha}}$ , or whether the measured or SR distribution was used (Figure C.10).

### **Bias in the inferred size distribution due to limited value of $q_{\max}$ used in the inversion analysis**

López-Yglesias and Flagan (2013b) showed that limiting the number of charge states considered may have a considerable effect on the calculated charge distribution: In this study, we set  $k_{\max} = 30$  when calculating any charge distribution. In order to lessen the computational burden, however, we only considered particles with  $\leq 15$  charges in the inversion analysis, i.e.,  $q_{\max} = 15$ ; the effect of this truncation was negligible in comparison to calculations with  $q_{\max} = 30$ . It should be noted that truncating the inversion charge distribution at  $q_{\max} = 15$  when the original charge distribution was calculated with  $k_{\max} = 30$  is a less constrained approximation than would occur if the original charge distribution had been calculated with  $k_{\max} = 15$ : omitting charge states for which the fractional population would be considerable increases the fractional populations in the charge states that are taken into account (López-Yglesias and Flagan 2013b). The effect of reducing the  $q_{\max}$  to 9 or 6 had little effect, but limiting it to 3 introduced a noticeable bias in the size distribution for  $d_p > 100$  nm, regardless of whether the measured or SR distribution was used (Figure C.11). It should be noted that the number of charges that should be taken into account in the inversion depends on the covered particle size range, as larger particles can acquire considerably more charges than do small ones.

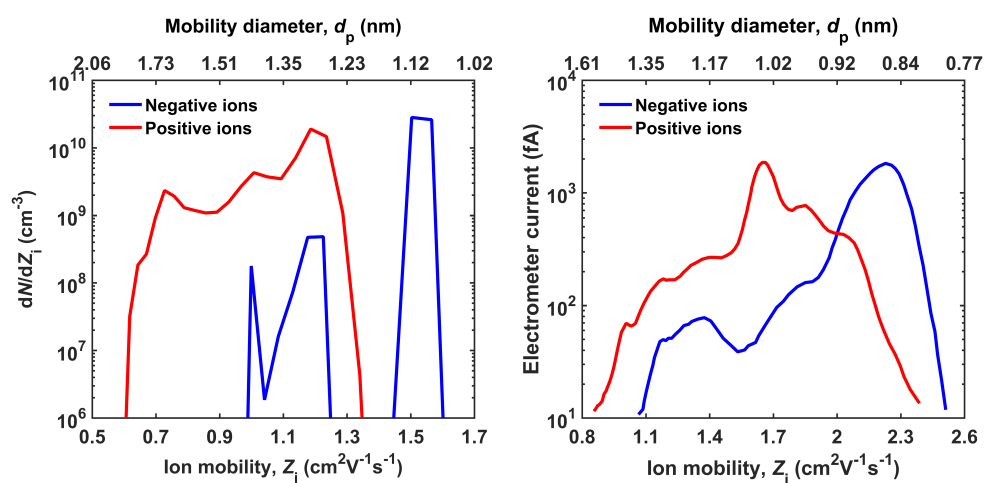


Figure C.1: Left panel: The measured mobility distribution of the ions produced by <sup>85</sup>Kr aerosol charger using particle free laboratory air as the sample. Right panel: The mobility distribution of the ions produced by <sup>241</sup>Am aerosol charger using clean and dry laboratory air as the sample (G. Steiner and Reischl 2012). It should be noted that, unlike the mobility values, the diameter values do not match those reported by Steiner and Reischl due to different relation between mobility and size used in this study.

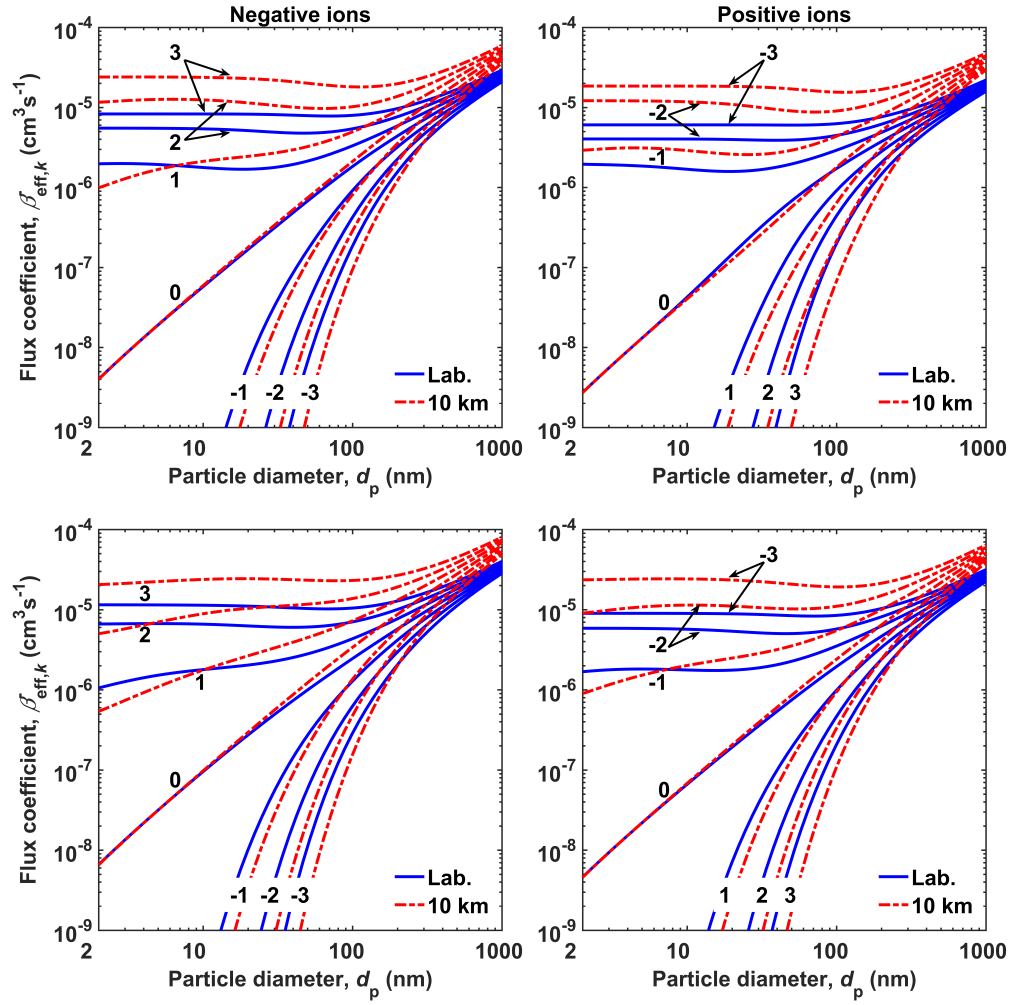


Figure C.2: The effective flux coefficients,  $\beta_{\text{eff},k}^{\pm}$ , of negative (left panels) and positive (right panels) ions to particles with  $k$  charges in  $T$  and  $p$  corresponding to the measured ion distribution (upper panels) and to the SR distribution (lower panels) at conditions at laboratory ( $T = 298.15$  K;  $p = 96757$  Pa; “Lab.”) and at 10 km altitude ( $T = 223$  K;  $p = 26500$  Pa; “10 km”).

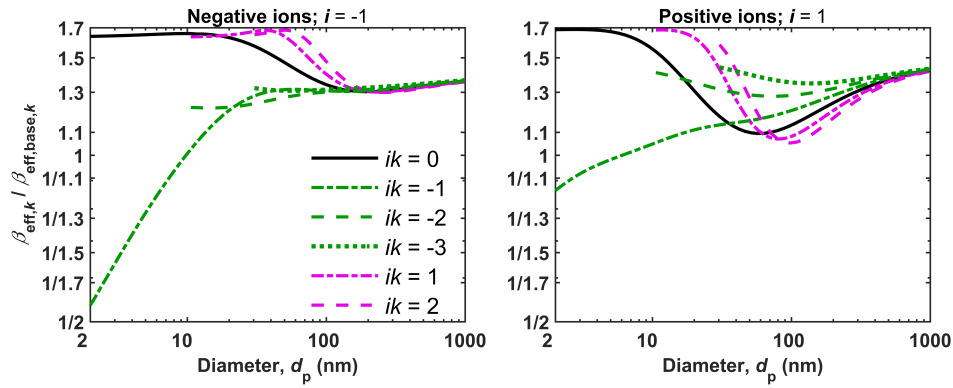


Figure C.3: The ratio of effective flux coefficients of the SR distribution,  $\beta_{\text{eff}}$ , to those of the measured distribution,  $\beta_{\text{eff,base}}$ . The particle and ion charge states are denoted by  $k$  and  $i$ , respectively, with the fluxes of negative (positive) ions shown on the left (right). The particle charge states relative to the ion polarity are denoted with line style and color as indicated in the legend. The ion fluxes to particles with one similar or two opposite charges, and with two similar or three opposite charges are depicted only for particles with  $d_p > 10$  nm and  $d_p > 30$  nm, since doubly- and triply-charged particles, respectively, are extremely rare below these thresholds.



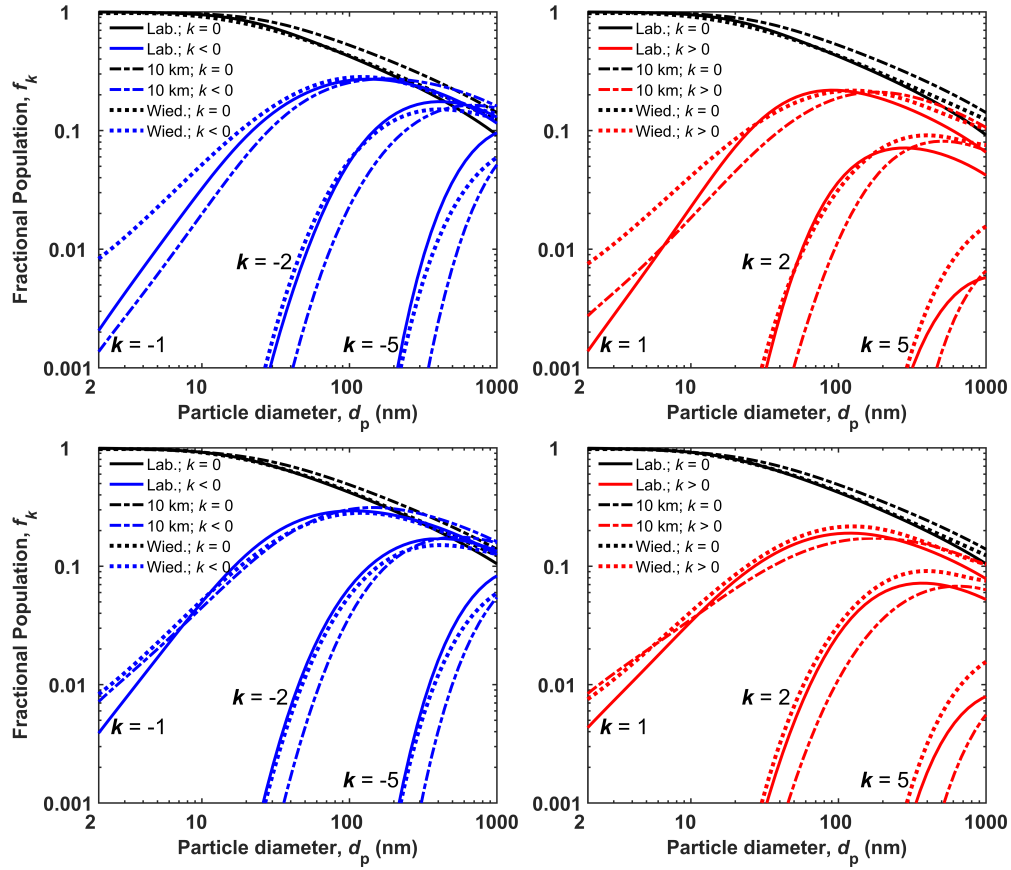


Figure C.4: The charge distributions in  $T$  and  $p$  corresponding to conditions at laboratory ( $T = 298.15$  K;  $p = 96757$  Pa; “Lab.”) and at 10 km altitude ( $T = 223$  K;  $p = 26500$  Pa; “10 km”), and the charge distribution according to Wiedensohler (1988; “Wied.”), as indicated by line style. Fractional populations of negative (positive) particles are shown on the left (right) with  $k$  denoting the particle charge state. Data is shown for the measured (upper panels) and SR (lower panels) distributions.

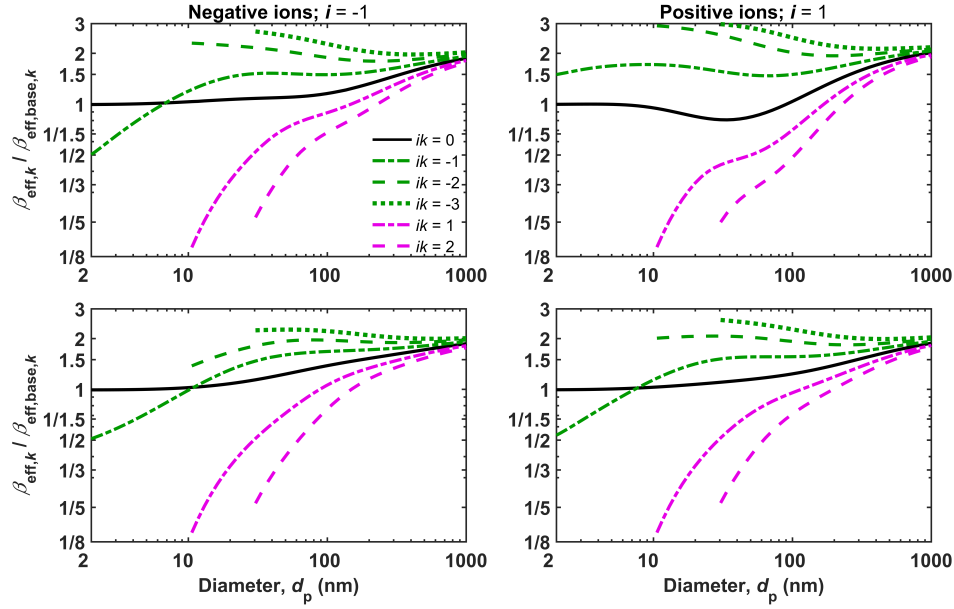


Figure C.5: The ratio of effective flux coefficients at 10 km altitude,  $\beta_{\text{eff}}$ , to those at laboratory,  $\beta_{\text{eff,base}}$ . The particle and ion charge states are denoted by  $k$  and  $i$ , respectively, with the fluxes of negative (positive) ions shown on the left (right). The particle charge states relative to the ion polarity are denoted with line style and color as indicated in the legend. Data in upper and lower panels correspond to the measured and SR distributions, respectively. The ion fluxes to particles with one similar or two opposite charges, and with two similar or three opposite charges are depicted only for particles with  $d_p > 10$  nm and  $d_p > 30$  nm, since doubly- and triply-charged particles, respectively, are extremely rare below these thresholds.

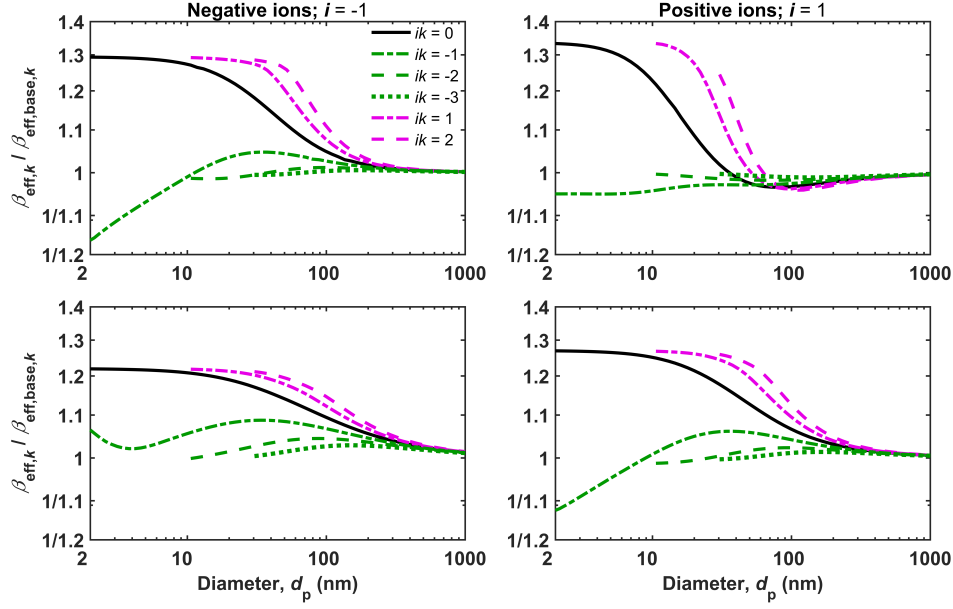


Figure C.6: The same as Figure C.5, except that  $\beta_{\text{eff}}$  and  $\beta_{\text{eff,base}}$  are the effective flux coefficients of ions with masses in the range from 130 to 1000 Da and from 220 to 1800 Da, respectively, for the measured distribution (upper panels). For SR distribution (lower panels),  $\beta_{\text{eff}}$  and  $\beta_{\text{eff,base}}$  are the effective flux coefficients of ions with masses in the range from 43 to 460 Da and from 55 to 840 Da, respectively.

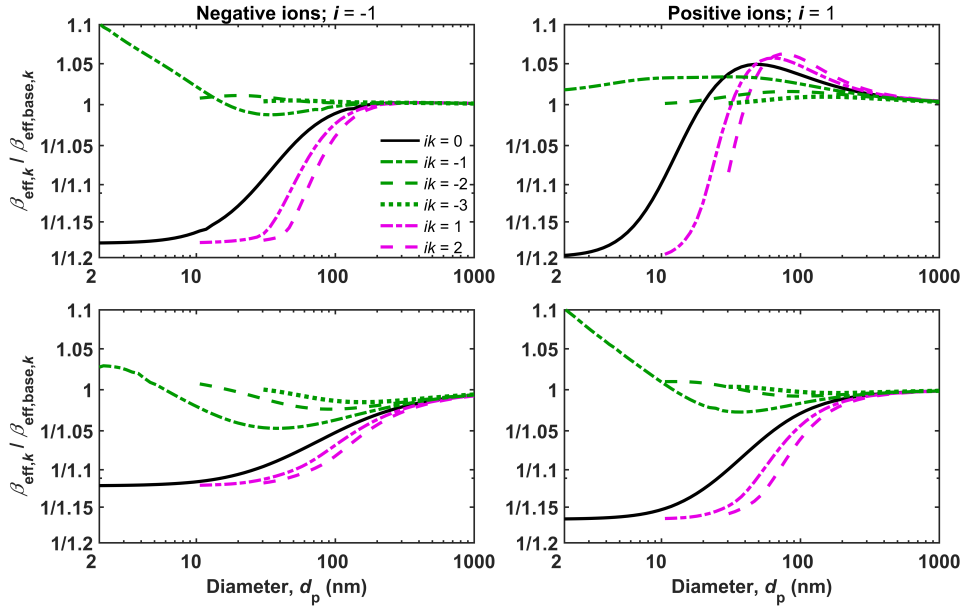


Figure C.7: The same as Figure C.5, except that  $\beta_{\text{eff}}$  and  $\beta_{\text{eff,base}}$  are the effective flux coefficients of ions with masses in the range from 300 to 2700 Da and from 220 to 1800 Da, respectively, for the measured distribution (upper panels). For SR distribution (lower panels),  $\beta_{\text{eff}}$  and  $\beta_{\text{eff,base}}$  are the effective flux coefficients of ions with masses in the range from 62 to 1200 Da and from 55 to 840 Da, respectively.

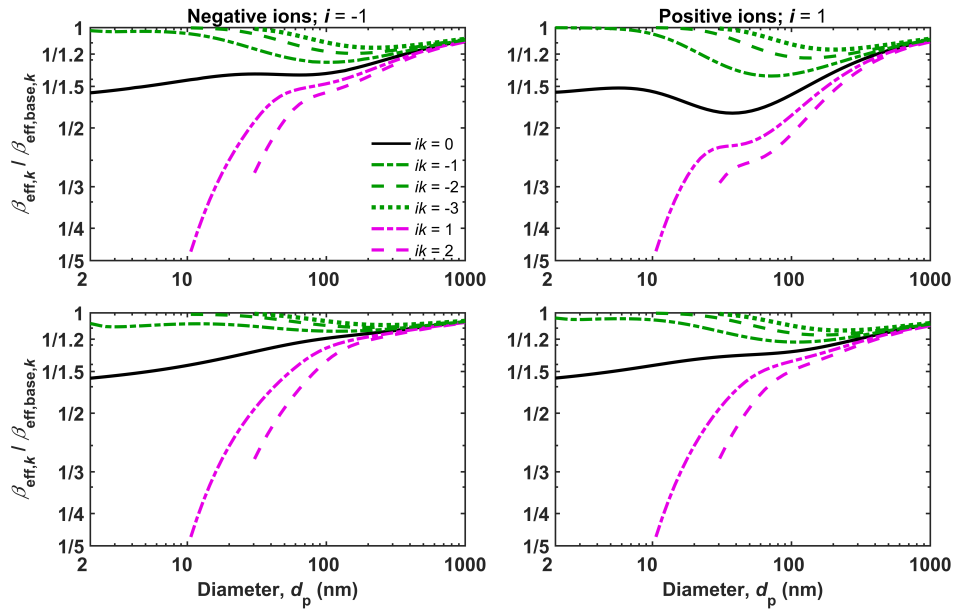


Figure C.8: The same as Figure C.5, except that  $\beta_{\text{eff}}$  and  $\beta_{\text{eff,base}}$  are the effective flux coefficients of ions to polystyrene ( $\chi_p = 2.6$ ) and conductive ( $\chi_p = \infty$ ) particles, respectively. The data for NaCl particles ( $\chi_p = 6$ ) were qualitatively the same as the data shown here for polystyrene particles, except that the ratios of  $\beta_{\text{eff}}$  and  $\beta_{\text{eff,base}}$  were closer to unity.

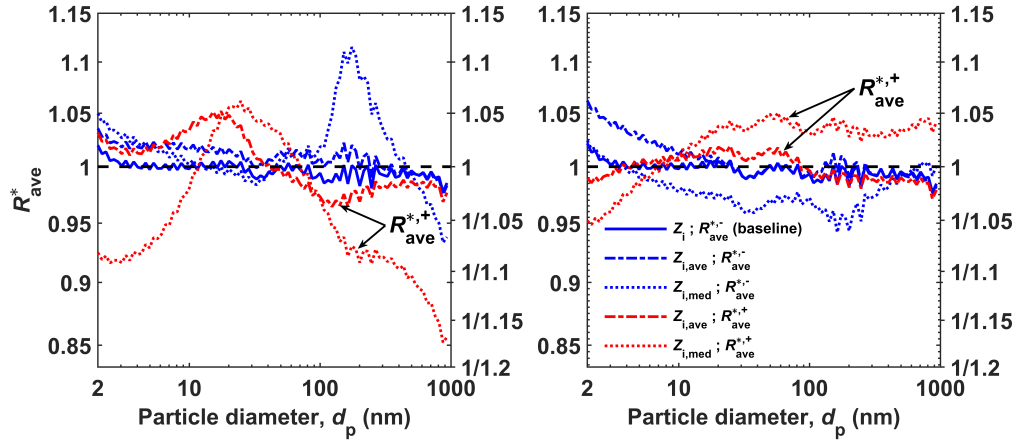


Figure C.9: Left panel: The bias observed in the inferred size distribution when the measured ion mobility distribution,  $Z_i$ , was used when calculating  $f_{\text{cha}}$ , but either the whole distribution,  $Z_i$ , mean mobility,  $Z_{i,\text{ave}}$ , or median mobility,  $Z_{i,\text{med}}$ , was used when calculating  $f_{\text{inv}}$ , as indicated in the legend. The line color denotes the signal polarity. Right panel: The same as the left panel, except that the SR distribution was used.

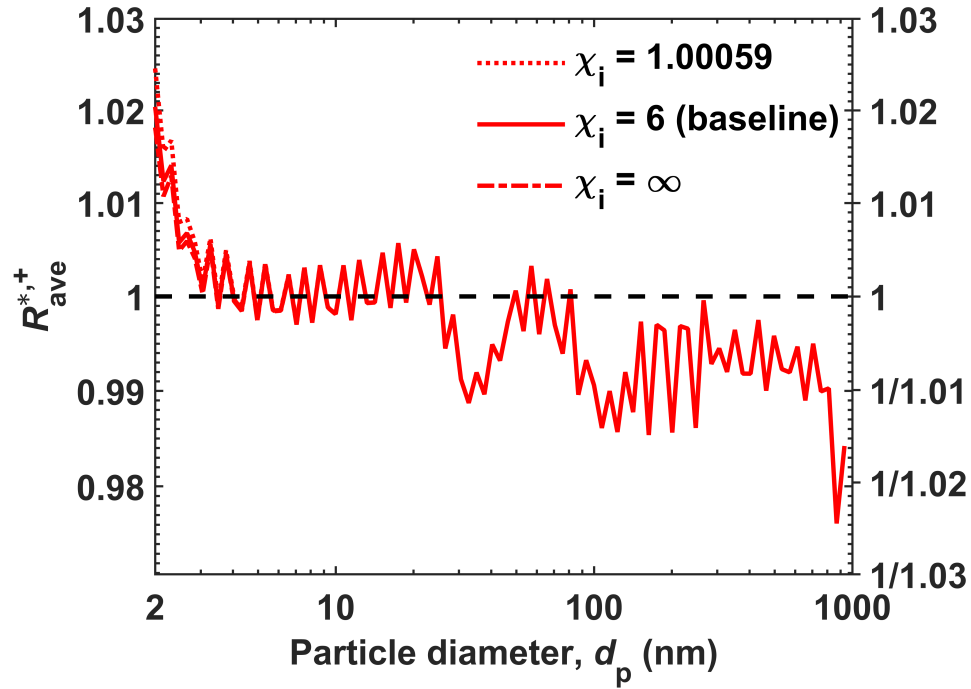


Figure C.10: The bias observed in the inferred particle size distribution when the relative permittivity of ions,  $\chi_i$ , was assumed to be  $\infty$  (conductive), 6 (dielectric), or 1.00059 (air) when calculating  $f_{\text{cha}}$ , but  $\chi_i = 6$  was assumed when calculating  $f_{\text{inv}}$ , as indicated in the legend. Only data for positive polarity when using the measured distribution is shown, as values for the negative polarity would not differ from the baseline case, and the biases observed when using the SR distribution were practically the same.

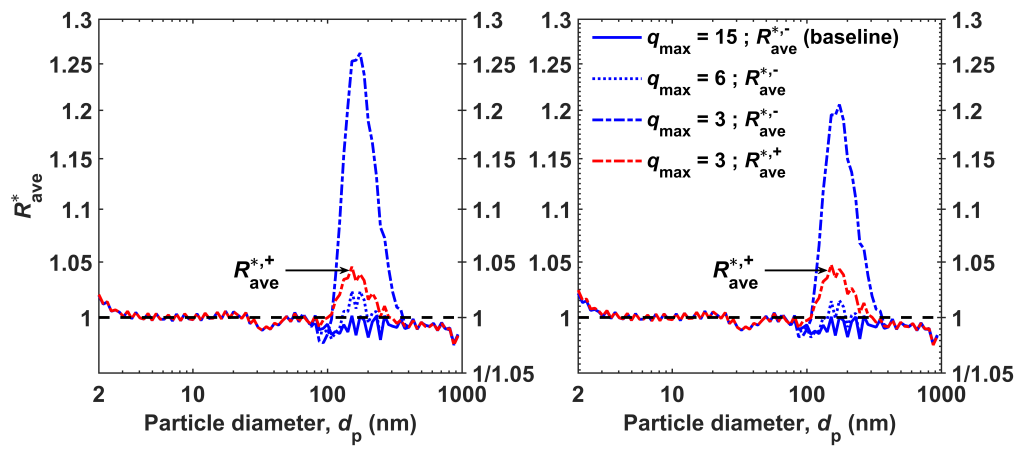


Figure C.11: The bias observed in the inferred size distribution when up to 30 charges were considered when calculating the signal, but the number of charges considered in the inversion,  $q_{max}$ , was 15, 6 or 3. The line color denotes the signal polarity, with a noticeable difference between the polarities observed only when  $q_{max} = 3$ . The bias observed when using the measured and SR distributions are depicted on the left and right, respectively.

## References

- Flagan, R. C. (2004). “Opposed migration aerosol classifier (OMAC)”. In: *Aerosol Sci. Technol.* 38.9, pp. 890–899. DOI: 10.1080/027868290505242.
- Gopalakrishnan, R., P. H. McMurry, and C. J. Hogan (2015). “The bipolar diffusion charging of nanoparticles: A review and development of approaches for non-spherical particles”. In: *Aerosol Sci. Technol.* 49.12, pp. 1181–1194. DOI: 10.1080/02786826.2015.1109053.
- Gopalakrishnan, R., M. J. Meredith, et al. (2013). “Brownian dynamics determination of the bipolar steady state charge distribution on spheres and non-spheres in the transition regime”. In: *J. Aerosol Sci.* 63, pp. 126–145. DOI: 10.1016/j.jaerosci.2013.04.007.
- Hoppel, W. A. and G. M. Frick (1986). “Ion-aerosol attachment coefficients and the steady-state charge distribution on aerosols in a bipolar ion environment”. In: *Aerosol Sci. Technol.* 5.1, pp. 1–21. DOI: 10.1080/02786828608959073.
- Hussin, A. et al. (1983). “Bipolar diffusion charging of aerosol particles-I: experimental results within the diameter range 4–30 nm”. In: *J. Aerosol Sci.* 14.5, pp. 671–677. DOI: 10.1016/0021-8502(83)90071-X.
- Lee, H. M. et al. (2005). “Effects of mobility changes and distribution of bipolar ions on aerosol nanoparticle diffusion charging”. In: *J. Chem. Eng. Jpn.* 38.7, pp. 486–496. DOI: 10.1252/jcej.38.486.
- López-Yglesias, X. and R. C. Flagan (2013a). “Ion-aerosol attachment coefficients and the steady-state charge distribution on aerosols in a bipolar ion environment”. In: *Aerosol Sci. Technol.* 47.6, pp. 688–704. DOI: 10.1080/02786828608959073.
- (2013b). “Population balances of micron-sized aerosols in a bipolar ion environment”. In: *Aerosol Sci. Technol.* 47.6, pp. 681–687. DOI: 10.1080/02786826.2013.783684.
- Mai, H. and R. C. Flagan (2017). “Opposed migration aerosol classifier transfer function”. In: *Aerosol Sci. Technol.* In prep.
- Maißer, A. et al. (2015). “The mass-mobility distributions of ions produced by a Po-210 source in air”. In: *J. Aerosol Sci.* 90, pp. 36–50. DOI: 10.1016/j.jaerosci.2015.08.004.
- Mui, W., H. Mai, et al. (2017). “Design, simulation, and characterization of a radial opposed migration ion and aerosol classifier (ROMIAC)”. In: *Aerosol Sci. Technol.* In review.
- Mui, W., D. A. Thomas, et al. (2013). “Ion mobility-mass spectrometry with a radial opposed migration ion and aerosol classifier (ROMIAC)”. In: *Anal. Chem.* 85, pp. 6319–6326. DOI: 10.1021/ac400580u.

- Steiner, G. and G. P. Reischl (2012). “The effect of carrier gas contaminants on the charging probability of aerosols under bipolar charging conditions”. In: *J. Aerosol Sci.* 54, pp. 21–31. doi: 10.1016/j.jaerosci.2012.07.008.
- Steiner, Gerhard et al. (2014). “High-resolution mobility and mass spectrometry of negative ions produced in a <sup>241</sup>Am aerosol charger”. In: *Aerosol Sci. Technol.* 48.3, pp. 261–270. doi: 10.1080/02786826.2013.870327.
- Stolzenburg, M. R. (1988). “An ultrafine aerosol size distribution measuring system”. Ph.D. Thesis. University of Minnesota.
- Wiedensohler, A. (1988). “An approximation of the bipolar charge distribution for particles in the submicron size range”. In: *J. Aerosol Sci.* 19.3, pp. 387–389.



*Appendix D*

US PATENT 9,095,793 B2: RADIAL OPPOSED MIGRATION  
AEROSOL CLASSIFIER WITH GROUNDED AEROSOL  
ENTRANCE AND EXIT

Inventors: Richard C. Flagan, Wilton Mui, Andrew J. Downard

Publication Date: August 4, 2015



US009095793B2

(12) **United States Patent**  
**Flagan et al.**

(10) **Patent No.:** **US 9,095,793 B2**

(45) **Date of Patent:** **Aug. 4, 2015**

(54) **RADIAL OPPOSED MIGRATION AEROSOL CLASSIFIER WITH GROUNDED AEROSOL ENTRANCE AND EXIT**

(71) Applicant: **California Institute of Technology**,  
Pasadena, CA (US)

(72) Inventors: **Richard C. Flagan**, Pasadena, CA (US);  
**Wilton Mui**, Pasadena, CA (US);  
**Andrew J. Downard**, Los Angeles, CA  
(US)

(73) Assignee: **California Institute of Technology**,  
Pasadena, CA (US)

(\*) Notice: Subject to any disclaimer, the term of this  
patent is extended or adjusted under 35  
U.S.C. 154(b) by 172 days.

(21) Appl. No.: **13/769,122**

(22) Filed: **Feb. 15, 2013**

(65) **Prior Publication Data**  
US 2013/0213861 A1 Aug. 22, 2013

**Related U.S. Application Data**

(60) Provisional application No. 61/600,409, filed on Feb.  
17, 2012.

(51) **Int. Cl.**  
**B07B 7/04** (2006.01)  
**B01D 21/00** (2006.01)  
**B03C 1/30** (2006.01)  
**B03C 3/017** (2006.01)  
**B03C 3/14** (2006.01)

(Continued)

(52) **U.S. Cl.**  
CPC . **B01D 21/00** (2013.01); **B03C 1/30** (2013.01);  
**B03C 3/017** (2013.01); **B03C 3/14** (2013.01);  
**B03C 3/15** (2013.01); **G01N 15/0266** (2013.01)

(58) **Field of Classification Search**  
USPC ..... 209/142, 143; 210/644, 748; 95/28, 58,  
95/71, 78  
See application file for complete search history.

(56) **References Cited**

U.S. PATENT DOCUMENTS

4,597,947 A \* 7/1986 Almaula ..... 422/603  
5,193,688 A \* 3/1993 Giddings ..... 209/155  
5,242,594 A \* 9/1993 Weinmann et al. .... 210/634

(Continued)

FOREIGN PATENT DOCUMENTS

EP 2352008 8/2011

OTHER PUBLICATIONS

PCT International Search Report and Written Opinion dated May 27,  
2013 for PCT Application No. PCT/US2013/026499.

(Continued)

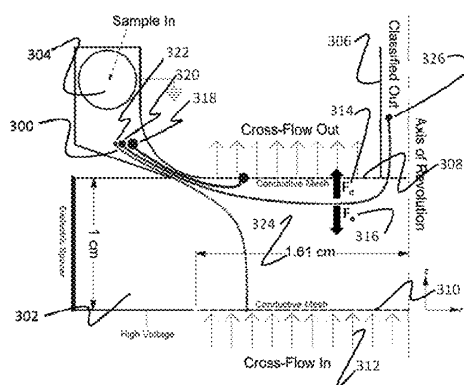
*Primary Examiner* — Terrell Matthews

(74) *Attorney, Agent, or Firm* — Gates & Cooper LLP

(57) **ABSTRACT**

A radial opposed migration classifier is provided for separating particles in a sample, introducing and removing the particles into and out of the classifier at the same potential. A sample passes through a classification channel having two circular walls. The sample is introduced and exits the classifier through the same plane as the first wall, which is at a different potential from the second wall. A cross-flow fluid enters the classification channel through one of the walls. The cross-flow fluid flows at a first velocity and exits in a first direction through the other wall. An imposed field is applied on the particles in a second direction counter to the first direction of the cross-flow. This causes the particles of a desired size and/or charge to migrate at a second velocity opposite and/or equal to a first velocity of the cross-flow. The particles that travel through the channel are discharged.

**28 Claims, 18 Drawing Sheets**



- (51) **Int. Cl.**  
**B03C 3/15** (2006.01)  
**G01N 15/02** (2006.01)

(56) **References Cited**

**U.S. PATENT DOCUMENTS**

|              |      |         |                 |           |
|--------------|------|---------|-----------------|-----------|
| 5,606,112    | A    | 2/1997  | Flagan et al.   |           |
| 6,109,119    | A *  | 8/2000  | Jiang et al.    | 73/865.5  |
| 6,276,534    | B1 * | 8/2001  | Huang et al.    | 209/139.2 |
| 6,905,029    | B2 * | 6/2005  | Flagan          | 209/210   |
| 2004/0050756 | A1   | 3/2004  | Flagan          |           |
| 2004/0159587 | A1 * | 8/2004  | Couture         | 209/132   |
| 2005/0006578 | A1   | 1/2005  | Rockwood et al. |           |
| 2006/0266132 | A1   | 11/2006 | Cheng et al.    |           |
| 2009/0173670 | A1   | 7/2009  | Okuda et al.    |           |
| 2013/0108834 | A1 * | 5/2013  | Sweetland       | 428/162   |

**OTHER PUBLICATIONS**

Bacher, G., "Charge-reduced nano electrospray ionization combined with differential mobility analysis of peptides, proteins, glycoproteins, noncovalent protein complexes and viruses", *Journal of Mass Spectrometry*, 36(9), pp. 1038-1052, Sep. 2001.

Baykut, G., et al., "Applying a Dynamic Method to the Measurement of Ion Mobility", *Journal of the American Society for Mass Spectrometry*, 20(11), pp. 2070-2081, Nov. 2009.

Brunelli, N. A., et al., "Radial Differential Mobility Analyzer for One Nanometer Particle Classification", *Aerosol Science and Technology*, 43(1), pp. 53-59, Jan. 2009.

Bush, M. F., et al., "Collision Cross Sections of Proteins and Their Complexes: a Calibration Framework and Database for Gas-Phase Structural Biology", *Analytical Chemistry*, vol. 82, No. 22, pp. 9557-9565, Nov. 15, 2010.

Chen, D. R., et al., "Design and Evaluation of a Nanometer Aerosol Differential Mobility Analyzer (Nano-DMA)", *J Aerosol Sci*, 1998, vol. 29 No. 5/6, pp. 497-509.

Counterman, A. E., et al., "High-Order Structure and Dissociation of Gaseous Peptide Aggregates that are Hidden in Mass Spectra", *Journal of the American Society for Mass Spectrometry*, 9(8), pp. 743-759, Aug. 1998.

De Juan, J., et al., "High Resolution Size Analysis of Nanoparticles and Ions: Running a Vienna DMA of Near Optimal Length at Reynolds Numbers Up to 5000", *J Aerosol Sci*, 1998, vol. 29, No. 5/6, pp. 617-626.

De La Mora, J. F., et al., "The potential of differential mobility analysis coupled to MS for the study of very large singly and multiply charged proteins and protein complexes in the gas phase", *Biotechnology Journal*, 1(9), pp. 988-997, Sep. 2006.

Downard, A. J., et al., "An Asymptotic Analysis of Differential Electrical Mobility Classifiers", *Aerosol Science and Technology*, 45(6), pp. 727-739, Apr. 2011.

Fernandez-Maestre, R., et al., "Chemical standards in ion mobility spectrometry", *The Analyst*, 135(6), pp. 1433-1442, Jun. 2010.

Flagan, R.C., "Opposed Migration Aerosol Classifier (OMAC)", *Aerosol Science and Technology*, 38(9), pp. 890-899, Jan. 2004.

Gamero-Castano, M., et al., "Mechanisms of electrospray ionization of singly and multiply charged salt clusters", *Analytica Chimica Acta*, 406, pp. 67-91, Feb. 2000.

Giles, K., et al., "Applications of a travelling wave-based radio-frequency-only stacked ring ion guide", *Rapid Communications in Mass Spectrometry*, 18(20), pp. 2401-2414, Jan. 2004.

Guevremont, R., et al., "Combined Ion Mobility/Time-of-Flight Mass Spectrometry Study of Electrospray-Generated Ions", *Analytical Chemistry*, vol. 69, No. 19, pp. 3959-3965, Oct. 1, 1997.

Hodyss, R., et al., "Bioconjugates for Tunable Peptide Fragmentation: Free Radical Initiated Peptide Sequencing (FRIPS)", *Journal of the American Chemical Society*, 127(36), pp. 12436-12437, Sep. 2005.

Hogan, Jr., C. J., et al., "Ion-Pair Evaporation from Ionic Liquid Clusters", *Journal of the American Society for Mass Spectrometry*, 21, pp. 1382-1386, Aug. 2010.

Hogan, Jr., C. J., et al., "Ion Mobility Measurements of Nondenatured 12-150 kDa Proteins and Protein Multimers by Tandem Differential Mobility Analysis-Mass Spectrometry (DMA-MS)", *Journal of the American Society for Mass Spectrometry*, 22(1), pp. 158-172, Jan. 2011.

Hogan, Jr., C. J., et al., "Tandem Differential Mobility Analysis-Mass Spectrometry Reveals Partial Gas-Phase Collapse of the GroEL Complex", *Journal of Physical Chemistry B*, 115, pp. 3614-3621, Apr. 2011.

Kaddis, C. S., "Sizing Large Proteins and Protein Complexes by Electrospray Ionization Mass Spectrometry and Ion Mobility", *Journal of the American Society for Mass Spectrometry*, 18(7), pp. 1206-1216, Jul. 2007.

Kaufman, S. L., "Macromolecule Analysis Based on Electrophoretic Mobility in Air: Globular Proteins", *Analytical Chemistry*, vol. 68, No. 11, pp. 1895-1904, Jun. 1, 1996.

Kaufman, S. L., "Analysis of Biomolecules Using Electrospray and Nanoparticle Methods: the Gas-Phase Electrophoretic Mobility Molecular Analyzer (GEMMA)", *Journal of Aerosol Science*, vol. 29, No. 5/6, pp. 537-552, 1998.

Kaur-Atwal, G., et al., "Chemical standards for ion mobility spectrometry: a review", *International Journal for Ion Mobility Spectrometry*, 12(1), pp. 1-14, May 2009.

Knutson, E. O., et al., "Aerosol Classification by Electrical Mobility: Apparatus, Theory, and Applications", *Journal of Aerosol Science*, vol. 6, pp. 443-451, 1975.

Kulmala, M., et al., "Toward Direct Measurement of Atmospheric Nucleation", *Science*, vol. 318, Oct. 5, 2007.

Labowsky, M., et al., "Novel ion mobility analyzers and filters", *Journal of Aerosol Science*, 37(3), pp. 340-362, Mar. 2006.

Lee, M., et al., "Gas-phase peptide sequencing by TEMPO-mediated radical generation", *Analyst*, 134(8), pp. 1706-1712, Aug. 2009.

Martinez-Lozano, P., et al., "Experimental tests of a nano-DMA with no voltage change between aerosol inlet and outlet slits", *J Aerosol Sci*, 2006, 37(11), pp. 1629-1642.

Purves, R. W., "Investigation of Bovine Ubiquitin Conformers Separated by High-Field Asymmetric Waveform Ion Mobility Spectrometry: Cross Section Measurements Using Energy-Loss Experiments With a Triple Quadrupole Mass Spectrometer", *Journal of the American Society for Mass Spectrometry*, 11(8), pp. 738-745, Aug. 2000.

Ramiro, E., et al., "Experimental Validation of a High Resolution Nano-DMA", *Journal of Aerosol Science*, 35, S749-S758, European Aerosol Conference 2004.

Revercomb, H. E., "Theory of Plasma Chromatography/Gaseous Electrophoresis—a Review", *Analytical Chemistry*, vol. 47, No. 7, pp. 970-983, Jun. 1975.

Rosser, S., et al., "Vienna-Type DMA of High Resolution and High Flow Rate", *Aerosol Science and Technology*, 39 (12), pp. 1191-1200, Dec. 2005.

Shvartsburg, A. A., et al., "Separation of Peptide Isomers with Variant Modified Sites by High-Resolution Differential Ion Mobility Spectrometry", *Analytical Chemistry*, vol. 82, No. 19, pp. 8327-8334, Oct. 1, 2010.

Sohn, C.H., "New Reagents and Methods for Mass Spectrometry-Based Proteomics Investigations", Dissertation (Ph. D.), California Institute of Technology, Pasadena, CA, 2011.

Sun, Q., et al., "Side Chain Chemistry Mediates Backbone Fragmentation in Hydrogen Deficient Peptide Radicals", *Journal of Proteome Research*, 8, pp. 958-966, 2009.

Tammet, H., "Symmetric Inclined Grid Mobility Analyzer for the Measurement of Charged Clusters and Fine Nanoparticles in Atmospheric Air", *Aerosol Science and Technology*, 45(4), pp. 468-479, Mar. 2011.

Ude, S., et al., "Molecular monodisperse mobility and mass standards from electrosprays of tetra-alkyl ammonium halides", *Journal of Aerosol Science*, 36(10), pp. 1224-1237, Oct. 2005.

Viidanoja, J., et al., "Tetraalkylammonium halides as chemical standards for positive electrospray ionization with ion mobility spectrometry/mass spectrometry", *Rapid Communications in Mass Spectrometry*, 19(21), pp. 3051-3055, Jan. 2005.

Winklmayr, W., et al., "A New Electromobility Spectrometer for the Measurement of Aerosol Size Distributions in the Size Range from 1 to 1000 nm", *J Aerosol Sci*, 1991, vol. 22, No. 3, pp. 289-296.

**US 9,095,793 B2**

Page 3

(56)

**References Cited****OTHER PUBLICATIONS**

Wittmer, D., "Electrospray Ionization Ion Mobility Spectrometry", *Analytical Chemistry*, vol. 66, No. 14, pp. 2348-2355, 1994.

Wu, C., et al., "Atmospheric Pressure Ion Mobility Spectrometry of Protonated and Sodiated Peptides", *Rapid Communications in Mass Spectrometry*, 13(12), pp. 1138-1142, Jan. 1999.

Wu, C., et al., "Electrospray Ionization High-Resolution Ion Mobility Spectrometry-Mass Spectrometry", *Analytical Chemistry*, vol. 70, No. 23, pp. 4929-4938, Dec. 1, 1998.

Wytenbach, T., et al., "Gas-Phase Conformation of Biological Molecules: Bradykinin", *Journal of the American Chemical Society*, 118(35), pp. 8355-8364, 1996.

Zhang, S.-H., et al., "Radial Differential Mobility Analyzer", *Aerosol Science and Technology*, 1995, 23(3), pp. 357-372.

Zhang, S.-H., et al., "Resolution of the Radial Differential Mobility Analyzer for Ultrafine Particles", *J Aerosol Sci*, 1996, vol. 27, No. 8, pp. 1179-1200.

\* cited by examiner

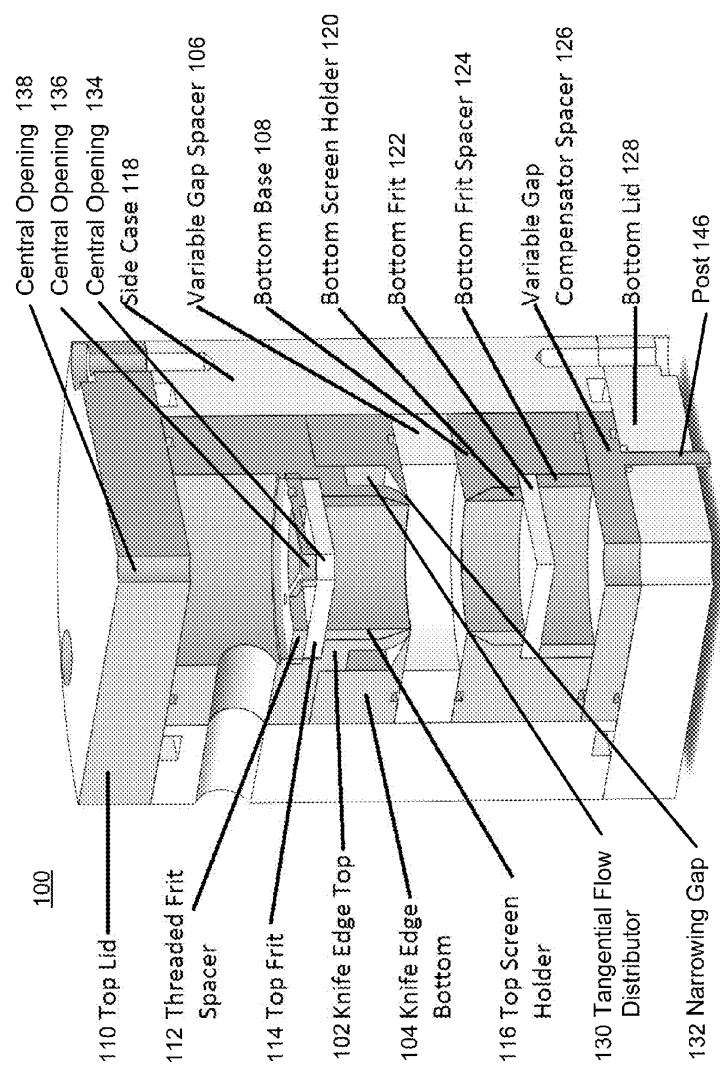


FIG. 1A

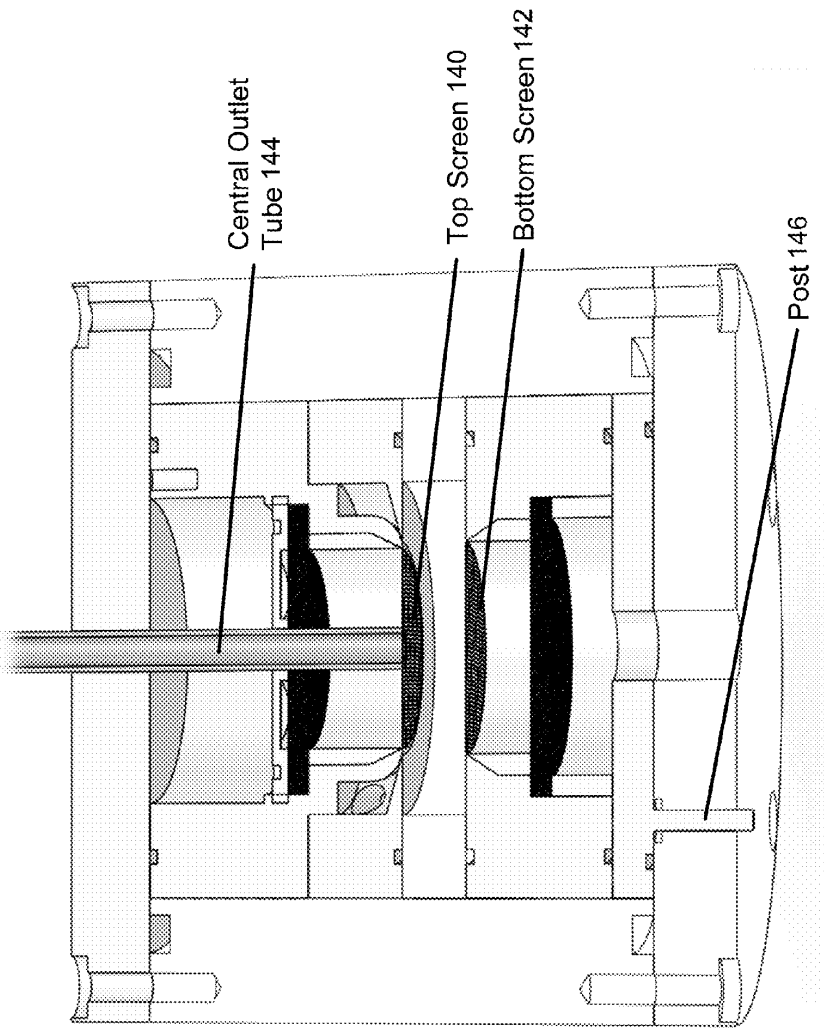


FIG. 1B

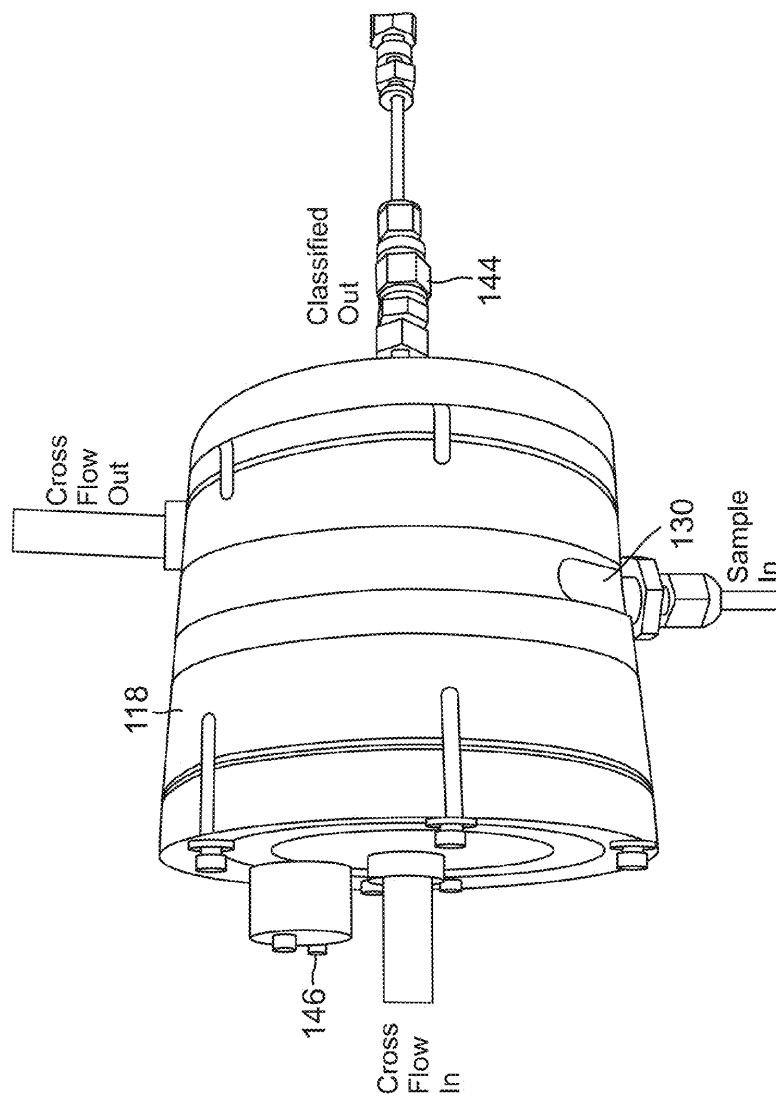


FIG. 1C

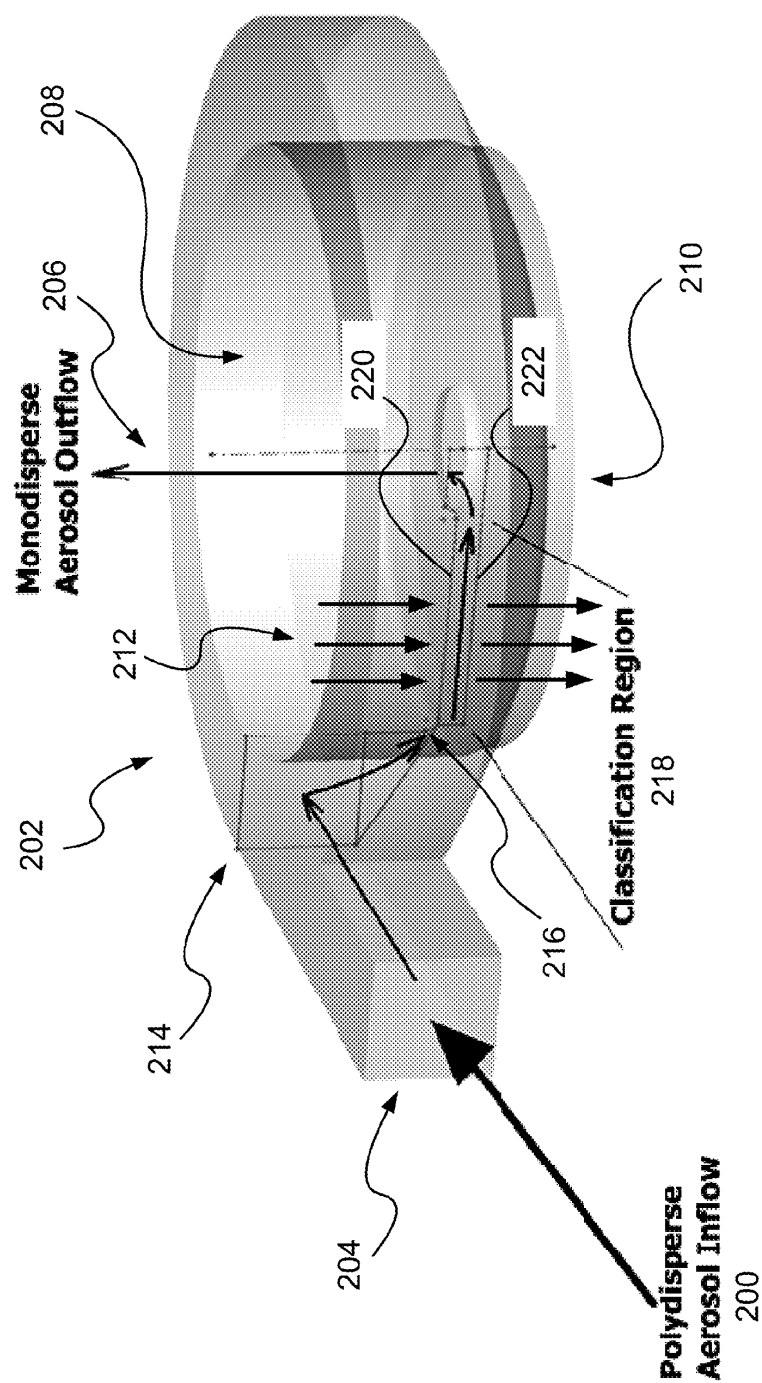


FIG. 2





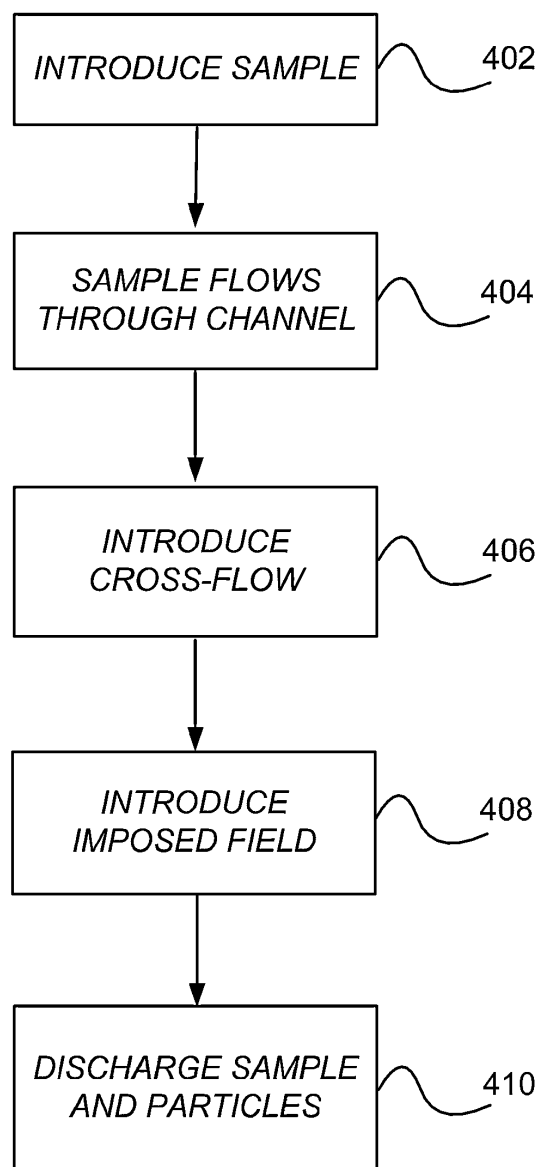
400

FIG. 4



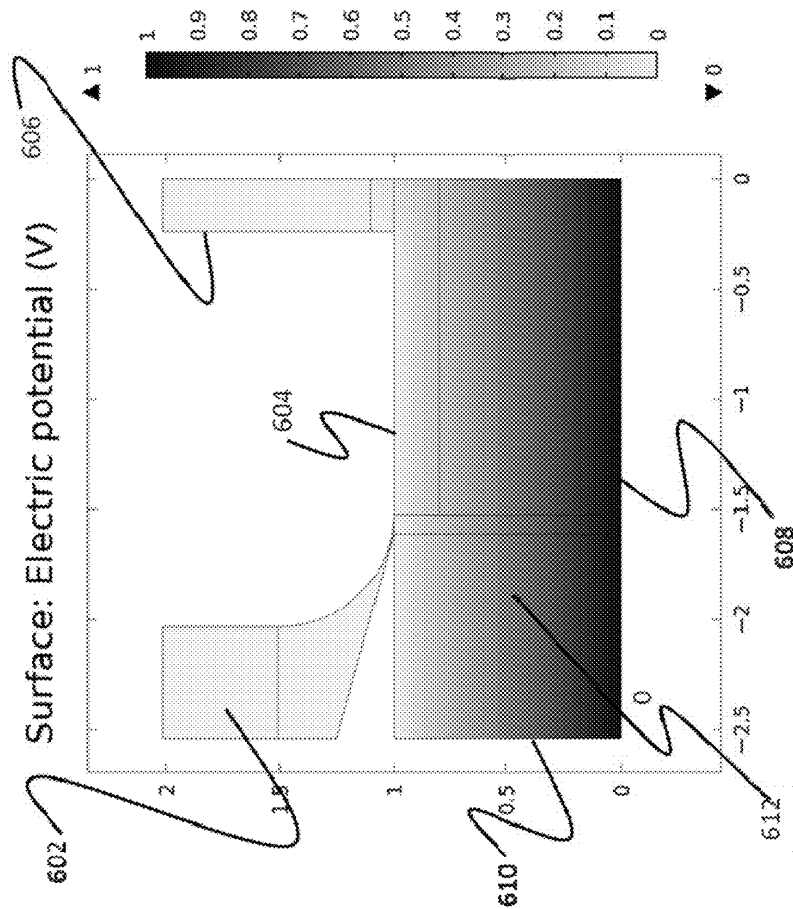


FIG. 6

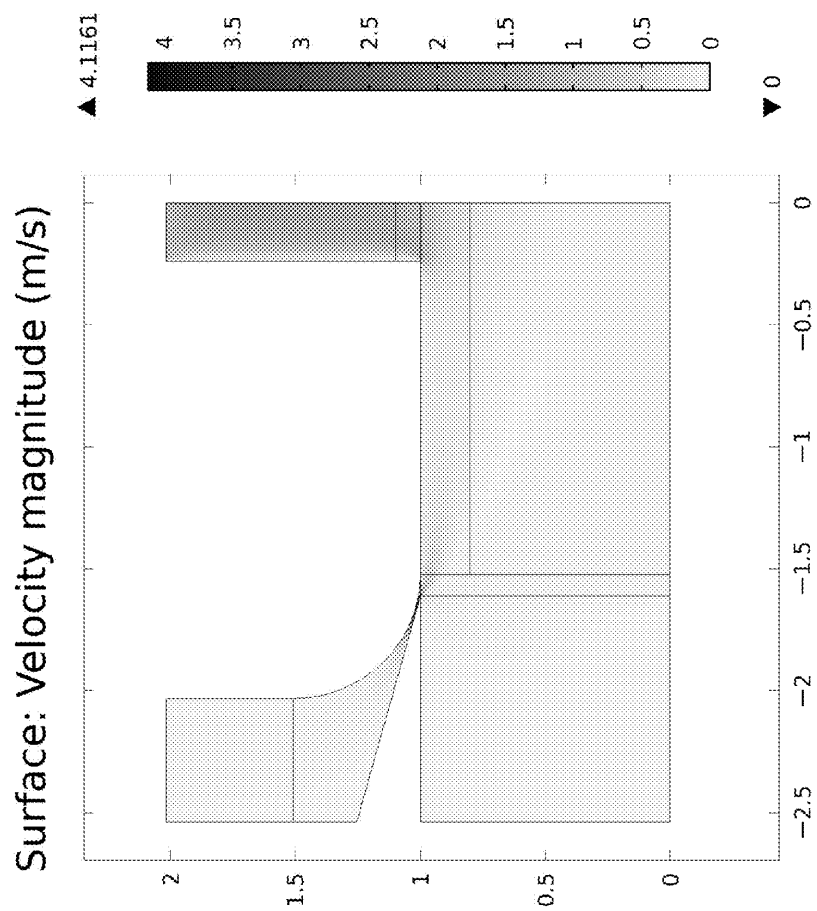


FIG. 7

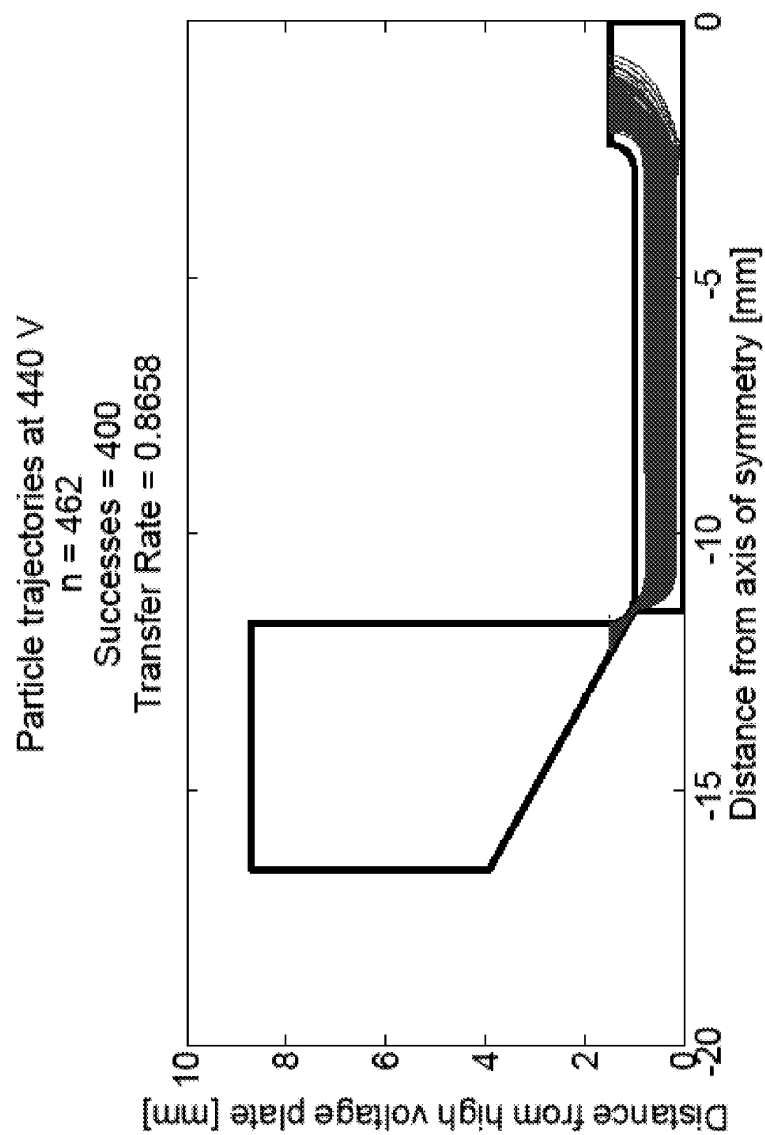


FIG. 8

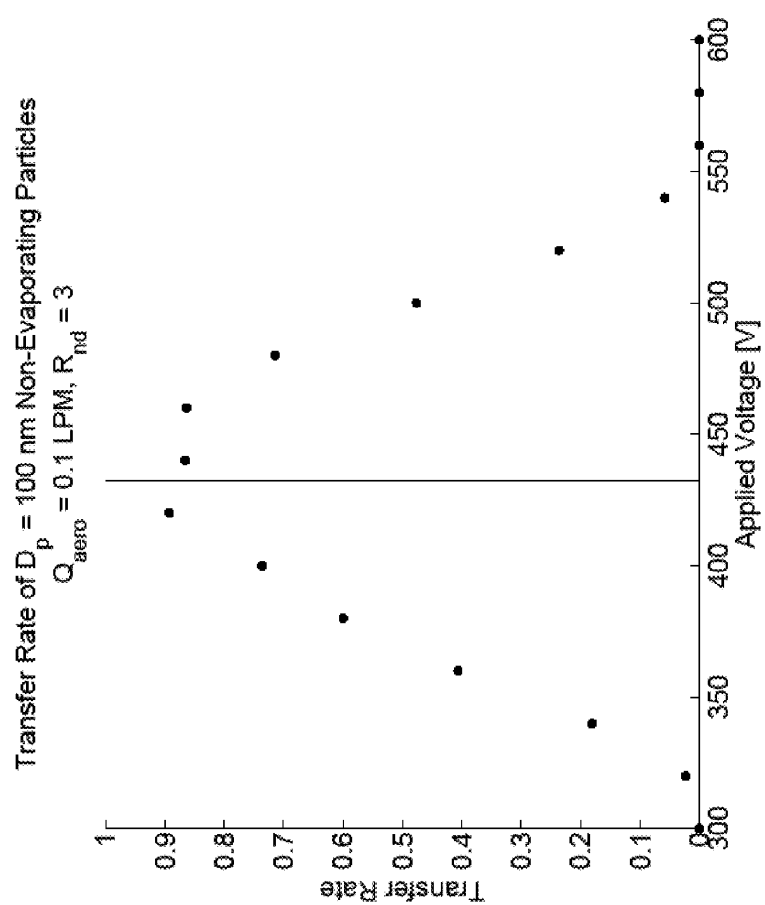
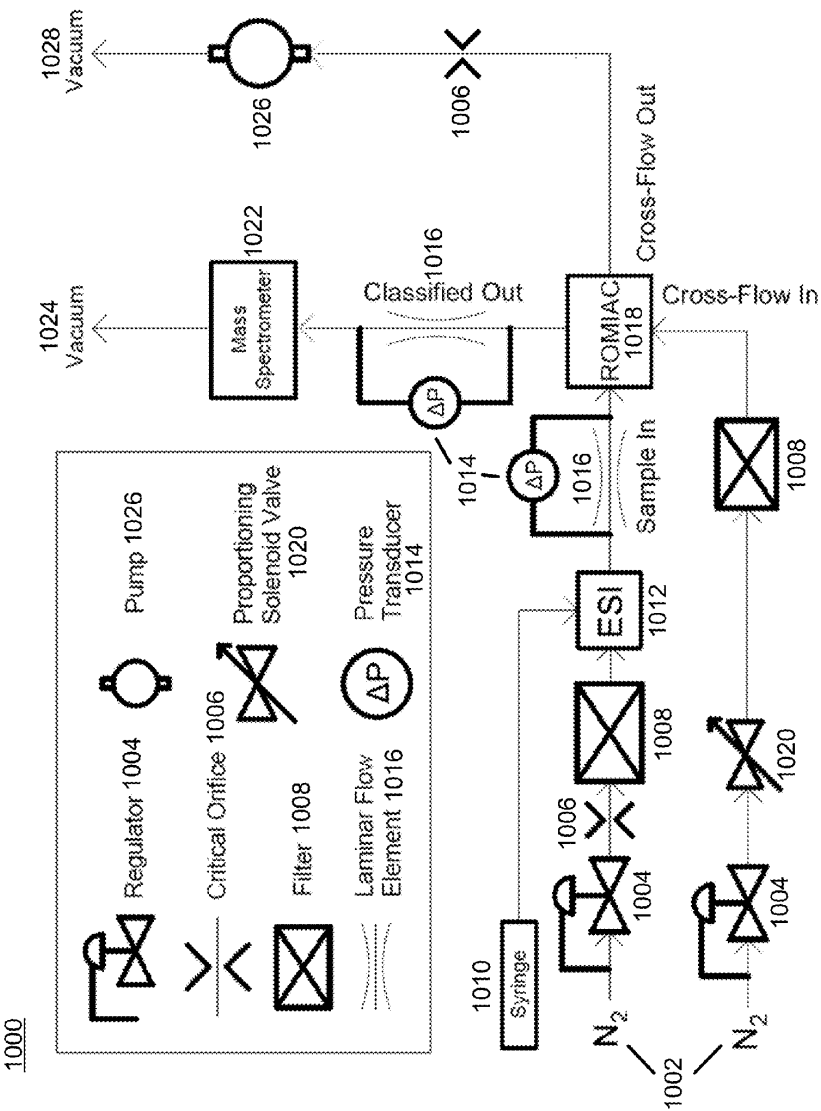


FIG. 9





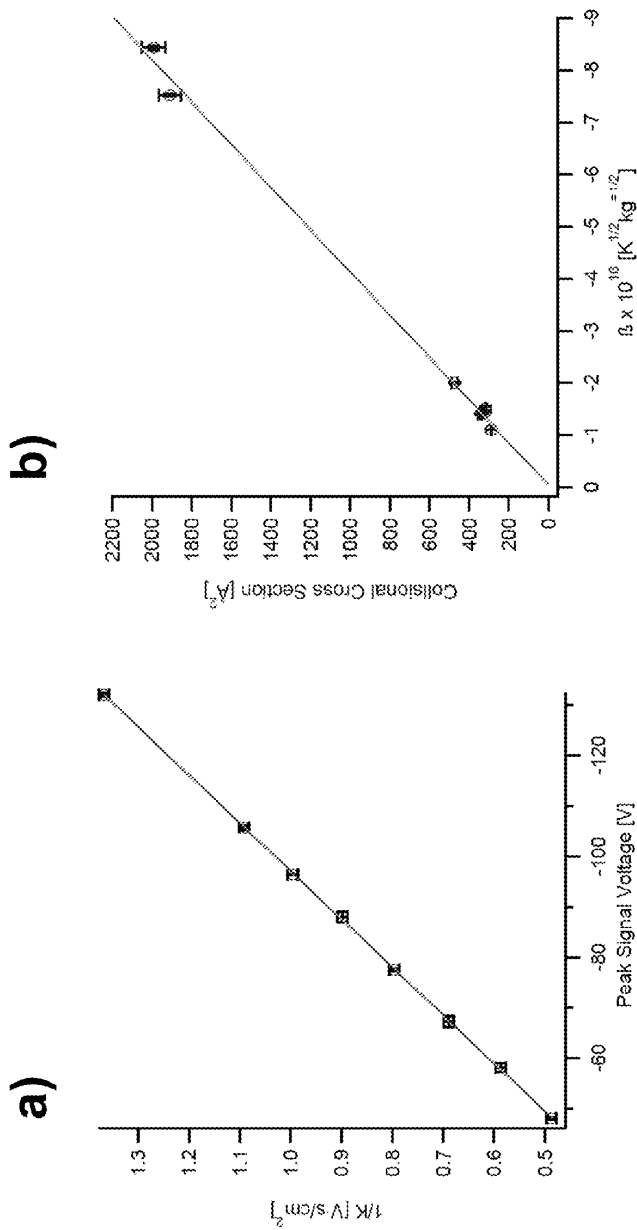


FIG. 11

multimer  $\Omega_i$  and  $K_{0,i}$ ,<sup>a</sup> Tetra-alkyl ammonium halide (TAAX) anion-coordinated singly-charged

| TAAX | k<br>Number<br>of<br>TAAX<br>Units | $\Omega_i$<br>[Å <sup>2</sup> ] | $K_{0,i}$<br>[cm <sup>2</sup> V <sup>-1</sup> s <sup>-1</sup> ] |
|------|------------------------------------|---------------------------------|---|
| C2   | 2                                  | 235±2.7                         | 0.94±0.011  |
| C2   | 3                                  | 256±7.3                         | 0.81±0.023  |
| C2   | 4                                  | 251±3.2                         | 0.82±0.010  |
| C2   | 5                                  | 208±2.7                         | 0.69±0.006  |
| C2   | 6                                  | 325±3.3                         | 0.63±0.007  |
| C2   | 7                                  | 353±4.0                         | 0.58±0.007  |
| C2   | 8                                  | 377±3.4                         | 0.54±0.005  |
| C2   | 9                                  | 405±4.3                         | 0.50±0.005  |
| C3   | 2                                  | 222±3.1                         | 0.94±0.013  |
| C3   | 3                                  | 289±5.8                         | 0.71±0.014  |
| C3   | 4                                  | 333±8.0                         | 0.62±0.015  |
| C3   | 5                                  | 369±4.0                         | 0.56±0.006  |
| C3   | 6                                  | 430±4.1                         | 0.48±0.005  |
| C4   | 2                                  | 250±2.7                         | 0.83±0.009  |
| C4   | 3                                  | 321±3.6                         | 0.64±0.007  |
| C4   | 4                                  | 353±4.8                         | 0.58±0.008  |
| C4   | 5                                  | 399±6.6                         | 0.51±0.008  |
| C4   | 6                                  | 461±5.3                         | 0.44±0.005  |
| C5   | 2                                  | 282±2.5                         | 0.73±0.007  |
| C5   | 3                                  | 354±3.2                         | 0.58±0.005  |
| C5   | 4                                  | 409±4.7                         | 0.50±0.006  |
| C5   | 5                                  | 440±6.1                         | 0.46±0.006  |
| C6   | 2                                  | 310±3.0                         | 0.67±0.006  |
| C6   | 3                                  | 386±3.5                         | 0.53±0.005  |
| C6   | 4                                  | 449±3.8                         | 0.46±0.004  |
| C7   | 2                                  | 335±2.8                         | 0.61±0.005  |
| C7   | 3                                  | 419±3.0                         | 0.49±0.004  |
| C7   | 4                                  | 491±3.7                         | 0.42±0.003  |
| C8   | 2                                  | 361±2.9                         | 0.57±0.005  |
| C8   | 3                                  | 454±3.4                         | 0.45±0.003  |
| Cl2  | 2                                  | 445±3.7                         | 0.46±0.004  |

<sup>a</sup>In N<sub>2</sub> at atmospheric pressure and  $T_{\text{EVT}} = T_s = 298$  K. Values are the average of three scans. Note that C3 species are iodinated while all other TAAX species are brominated.

FIG. 12

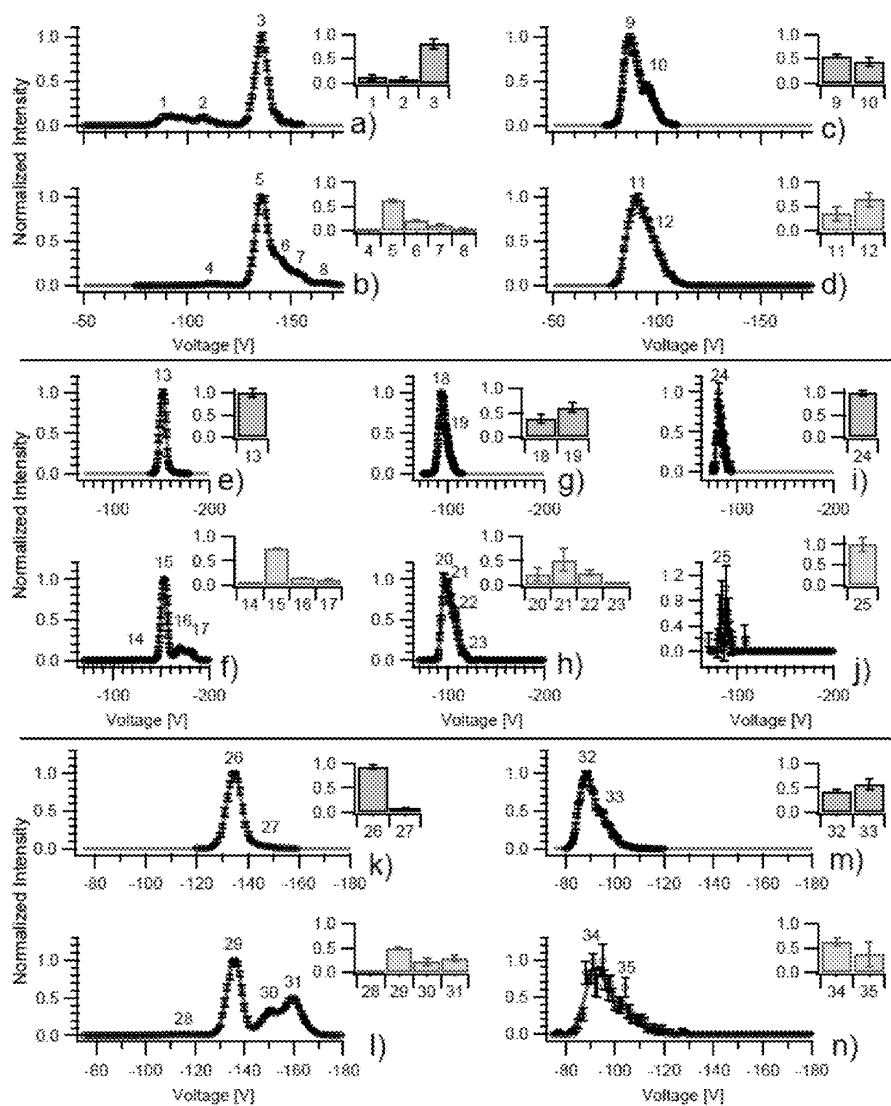


FIG. 13

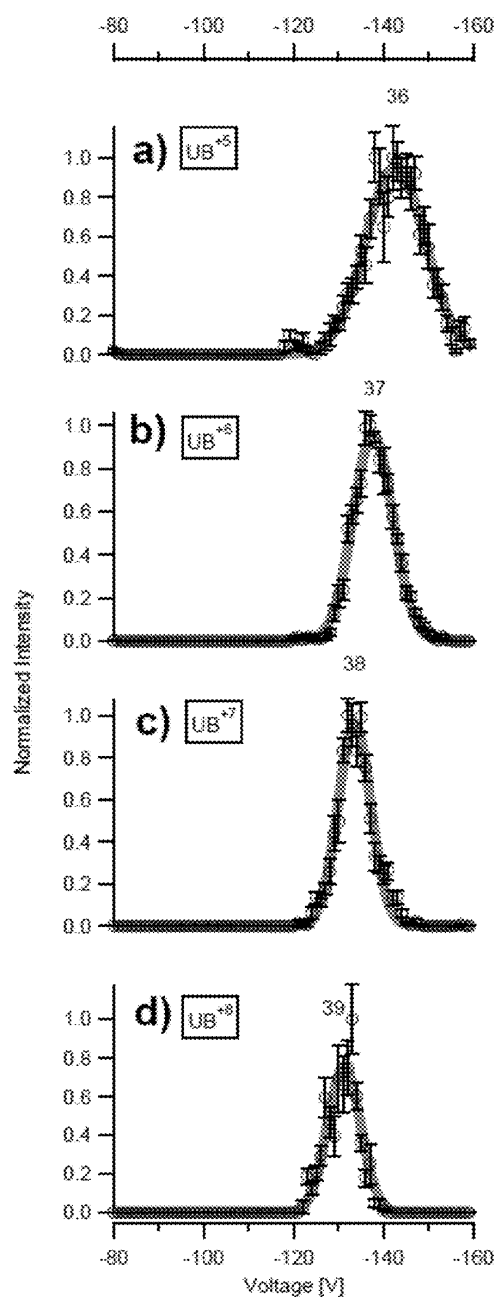


FIG. 14

Dominant conformation bradykinin (BK), angiotensin I (AT1), angiotensin II (AT2), and bovine ubiquitin (UB)  $\Omega_x$  values.<sup>a</sup>

| Peptide            | Peak No. | <sup>b</sup> $\Omega_x$ [ $\text{\AA}^2$ ] | <sup>c</sup> $\Omega_x$ [ $\text{\AA}^2$ ] | <sup>d</sup> % $\Delta$ | <sup>e</sup> % $\Delta$ | <sup>f</sup> % $\Delta$ |
|--------------------|----------|--|--|-------------------------|-------------------------|-------------------------|
| *BK <sup>+1</sup>  | 3        | 316 $\pm$ 3.8                              | 261 $\pm$ 29.5                             | -10.6%                  |                         |                         |
| #BK <sup>+1</sup>  | 5        | 315 $\pm$ 2.9                              | 260 $\pm$ 27.9                             | -10.9%                  |                         |                         |
| *BK <sup>+2</sup>  | 9        | 398 $\pm$ 4.8                              | 334 $\pm$ 30.8                             | 4.8%                    |                         | -2.8%                   |
| #BK <sup>+2</sup>  | 11       | 409 $\pm$ 5.78                             | 343 $\pm$ 28.6                             | 7.6%                    |                         | -0.2%                   |
| *AT1 <sup>+1</sup> | 13       | 352 $\pm$ 3.8                              | 292 $\pm$ 30.0                             |                         |                         |                         |
| #AT1 <sup>+1</sup> | 15       | 355 $\pm$ 3.0                              | 294 $\pm$ 28.8                             |                         |                         |                         |
| *AT1 <sup>+2</sup> | 18       | 434 $\pm$ 8.9                              | 365 $\pm$ 34.8                             |                         | -5.0%                   |                         |
| #AT1 <sup>+2</sup> | 20       | 439 $\pm$ 4.3                              | 369 $\pm$ 30.5                             |                         | -4.0%                   |                         |
| *AT1 <sup>+3</sup> | 24       | 568 $\pm$ 9.0                              | 482 $\pm$ 37.0                             |                         | 1.9%                    | 1.7%                    |
| #AT1 <sup>+3</sup> | 25       | 602 $\pm$ 8.5                              | 510 $\pm$ 31.7                             |                         | 7.9%                    | 7.7%                    |
| *AT2 <sup>+1</sup> | 26       | 312 $\pm$ 2.7                              | 258 $\pm$ 28.5                             | -9.8%                   |                         |                         |
| #AT2 <sup>+1</sup> | 29       | 315 $\pm$ 2.8                              | 260 $\pm$ 28.0                             | -8.9%                   |                         |                         |
| *AT2 <sup>+2</sup> | 32       | 405 $\pm$ 5.0                              | 340 $\pm$ 31.1                             | 7.0%                    | -4.1%                   | 1.6%                    |
| #AT2 <sup>+2</sup> | 34       | 430 $\pm$ 14.9                             | 362 $\pm$ 21.4                             | 13.7%                   | 1.9%                    | 7.9%                    |
| *UB <sup>+5</sup>  | 36       | 1636 $\pm$ 16.3                            | 1390 $\pm$ 57.3                            |                         |                         |                         |
| *UB <sup>+6</sup>  | 37       | 1895 $\pm$ 22.0                            | 1613 $\pm$ 65.3                            |                         |                         |                         |
| *UB <sup>+7</sup>  | 38       | 2149 $\pm$ 25.3                            | 1831 $\pm$ 71.2                            |                         |                         | -4.1%                   |
| *UB <sup>+8</sup>  | 39       | 2409 $\pm$ 231.6                           | 2055 $\pm$ 79.8                            |                         |                         | 3.2%                    |

<sup>a</sup>In N<sub>2</sub> at atmospheric pressure and  $T_x = 298$  K. Values are the average of three scans.

<sup>b</sup> $T_{ESI} = 298$  K.

<sup>c</sup> $T_{ESI} = 400$  K.

<sup>d</sup>Peak was used for mobility calibration.

<sup>e</sup>Cross section estimated from instrument calibration (using TAAX ions)

<sup>f</sup>Cross section estimated from mobility calibration (using peptides and proteins)

<sup>g</sup>% Percent difference between this study's mobility calibration  $\Omega_x$  value and that published

in (i) C. Wu, J. Klemm, and M. H. Hill, *Atmospheric pressure ion mobility spectrometry of protonated and solvated peptides*, *Rapid Communications in Mass Spectrometry*, 13(12):1138-42, January 1999  
(ii) G. Baykut, O. von Helden, and O. Raether, *Applying a dynamic method to the measurement of ion mobility*, *Journal of the American Society for Mass Spectrometry*, 20(11):2070-81, November 2009  
(iii) M.F. Bush, Z. Hall, K. Giles, J. Heyes, C.V. Robinson, and B.T. Rustolo, *Collision cross sections of proteins and their complexes: a calibration from crank and database for gas-phase structural biology*, *Analytical Chemistry*, 82(22):9557-65, November 2010

FIG. 15

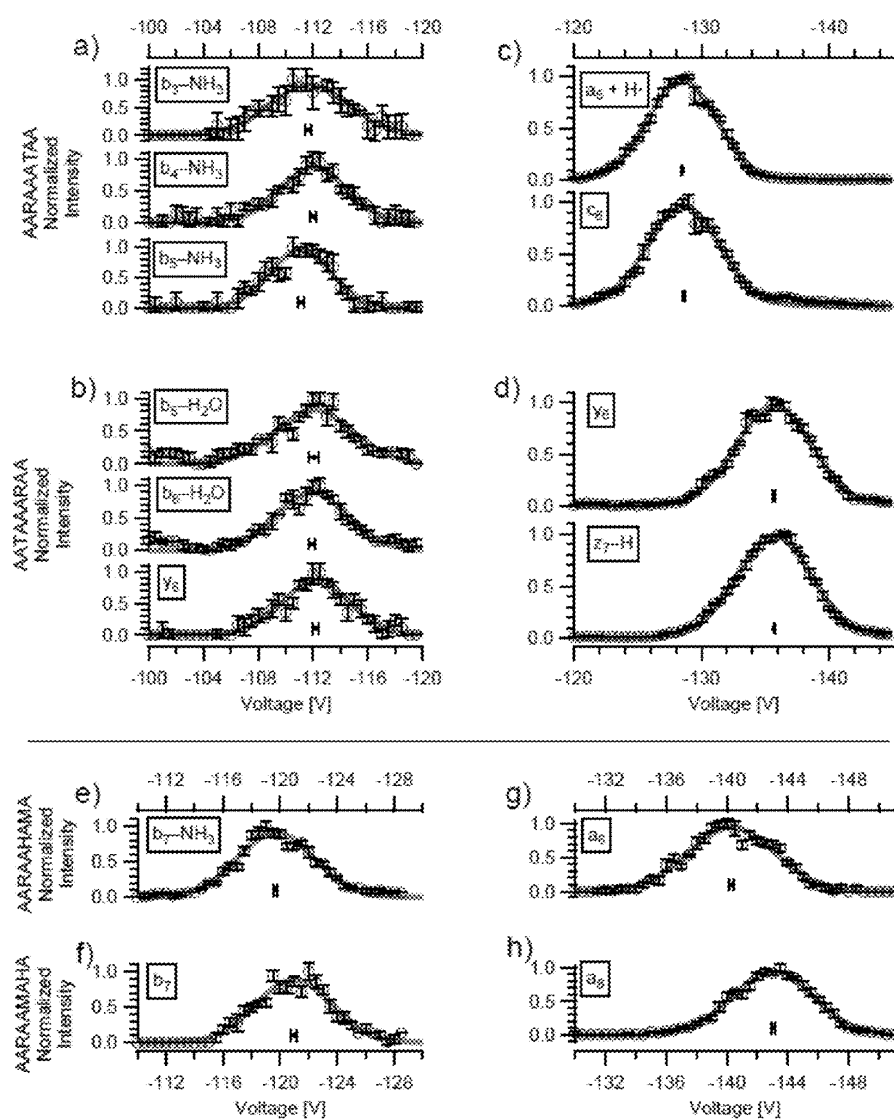


FIG. 16

US 9,095,793 B2

1

# **RADIAL OPPOSED MIGRATION AEROSOL CLASSIFIER WITH GROUNDED AEROSOL ENTRANCE AND EXIT**

## **CROSS-REFERENCE TO RELATED APPLICATIONS**

This application claims the benefit under 35 U.S.C. Section 119(e) of the following co-pending and commonly-assigned U.S. provisional patent application, which is incorporated by reference herein:

Provisional Application Ser. No. 61/600,409, filed on Feb. 17, 2012, by Richard C. Flagan et al., entitled "RADIAL OPPOSED MIGRATION AEROSOL CLASSIFIER WITH GROUNDED AEROSOL ENTRANCE AND EXIT."

This application is also related to the following commonly-assigned patent and patent applications, which are incorporated by reference herein:

U.S. Pat. No. 6,905,029, issued on Jun. 14, 2005, by Richard C. Flagan, entitled "CROSS-FLOW DIFFERENTIAL MIGRATION CLASSIFIER;" and

U.S. patent application Ser. No. 13/768,817, filed on Feb. 15, 2013, by Richard C. Flagan et al., entitled "OPPOSED MIGRATION AEROSOL CLASSIFIER GAS AND HEAT EXCHANGER," which claims priority to Provisional Application Ser. No. 61/600,434, filed on Feb. 17, 2012, by Richard C. Flagan et al., entitled "OPPOSED MIGRATION AEROSOL CLASSIFIER GAS AND HEAT EXCHANGER."

## **BACKGROUND OF THE INVENTION**

### **1. Field of the Invention**

The present invention relates generally to separating and measuring particles and molecules in fluids, and in particular, to using a radial cross-flow differential migration classifier to separate and/or measure particles.

### **2. Description of the Related Art**

(Note: This application references a number of different publications as indicated throughout the specification by reference numbers enclosed in brackets, e.g., [x]. A list of these different publications ordered according to these reference numbers can be found below in the section entitled "References." Each of these publications is incorporated by reference herein.)

For four decades, the long column differential mobility analyzer (DMA) has been the instrument of choice for the classification of aerosol particles in the 10 nm to 1 micron range [1]. However, there are currently no particle classifiers that are optimal in the sub-10 nm range. One reason is the residence time required for a classifier to effectively separate the particles.

The reduction of column length and the increase of flow rates have led to decreased residence times of samples in a classifier. This has enabled custom instruments to classify particles and gas ions in the range of 1 to 10 nm, where diffusive losses had hampered the performance of standard long column instruments [2-4]. Reductions in residence time have also been obtained by using a radial geometry, which has an inwardly accelerating flow [5-9].

However, in addition to residence time, another important consideration for mobility classifying instruments is its transport efficiency, which is the actual number of particles transmitted divided by the number of particles transmitted if there were no diffusive losses. A major cause for losses is the unfavorable field arising from the voltage transition that nearly all DMAs share [6]. The charged particles have an increased residence time in the neighborhood of the voltage

2

transition. Parasitic fields resulting from static buildups on the dielectric can also further increase losses. Clever instruments have been developed that have eliminated the voltage transition altogether [10,11], but they have not been widely adopted; perhaps partially because of the complexity of determining their transfer function [10].

Altogether, current mobility classification instruments are generally bulky, require expensive blowers or pumps to achieve large flow rates, and require an unfavorable voltage transition at the inlet or outlet that hampers performance and transfer efficiency.

In view of the above, what is needed is a method, apparatus, and article of manufacture for continuously separating particles with enhanced transport efficiency and reduced loss of particles. In particular, there is a need for a method, apparatus, and article of manufacture for separating particles that reduces the diffusive loss of particles due to factors such as voltage transitions and static buildups.

## **SUMMARY OF THE INVENTION**

The invention provided herein has a number of embodiments useful, for example, in separating and measuring particles and molecules in fluids. According to one or more embodiments of the present invention, a radial opposed migration aerosol classifier (ROMAC) is provided for separating and/or measuring particles and molecules in fluids.

In one aspect of the present invention, a radial opposed migration classifier is provided. The radial opposed migration classifier comprises a classification channel through which passes a sample, comprising one or more particles suspended within a sample fluid. The classification channel comprises a first circular wall and a second circular wall that are both permeable to a flow of fluid. The radial opposed migration classifier also comprises a flow distributor channel for introducing the sample into the classification channel. In one or more embodiments, the flow distributor channel comprises a narrowing gap leading into the classification channel. In one or more further embodiments, the sample is introduced tangentially into the flow distributor channel.

A cross-flow fluid enters the classification channel through one of the permeable circular walls. The cross-flow fluid flows at a first velocity and exits in a first direction through the other permeable circular wall. Additionally, an imposed field, including but not limited to an electric, magnetic, thermal, or gravitational field, is applied on the one or more particles in a second direction counter to the first direction of the cross-flow. The imposed field causes the one or more of the particles of a desired size and/or charge to migrate at a second velocity opposite and/or equal to a first velocity of the cross-flow. The particles that travel through the channel are discharged from the radial opposed migration classifier.

In one or more embodiments, the flow distributor channel introduces the sample into the classification channel in the same plane as the first circular wall. Furthermore, the particles that travel through the channel are discharged through a central outlet on the first circular wall.

In further embodiments, the imposed field is an electric field. Particles are introduced into the classification channel through an entrance at an electric potential and discharged from the radial opposed migration classifier through an exit at the same electric potential. In one exemplary application, the particles are discharged at an electrical ground voltage.

In other embodiments, the discharged particles that travel through the channel are classified based on a property of the discharged particles, including but not limited to a size, mass or charge of the discharged particles. In additional embodi-

3

ments, distributions of the particles with respect to a property of the particles are determined by stepping a strength of the imposed field through a range of values and measuring a concentration of the discharged particles. In other embodiments, distributions of the particles with respect to a property of the particles are determined by stepping a rate of the cross flow through a range of values and measuring a concentration of the discharged particles.

#### BRIEF DESCRIPTION OF THE DRAWINGS

Referring now to the drawings in which like reference numbers represent corresponding parts throughout:

FIGS. 1A-C illustrates various perspective views of an assembled radial migration aerosol classifier (ROMAC) in accordance with one or more embodiments of the invention. FIG. 1A is a perspective view of a 2-plane sectional cut of a radial opposed migration aerosol classifier (ROMAC). FIG. 1B is a cross-sectional side view of an assembled ROMAC. FIG. 1C is a photograph of an assembled ROMAC;

FIG. 2 illustrates a revolved volume of the classification region of a radial opposed migration aerosol classifier (ROMAC) in accordance with one or more embodiments of the invention;

FIG. 3 illustrates a classification region of a radial opposed migration aerosol classifier (ROMAC) in accordance with one or more embodiments of the invention;

FIG. 4 is a flow chart illustrating a logical flow for separating/classifying particles in a fluid sample in accordance with one or more embodiments of the invention;

FIG. 5 illustrates a radial opposed migration aerosol classifier (ROMAC) in accordance with one or more embodiments of the invention;

FIG. 6 illustrates an electric potential field distribution model of a solution flowing through a section of a radial opposed migration aerosol classifier (ROMAC) in accordance with one or more embodiments of the invention;

FIG. 7 illustrates a fluid velocity field distribution model of a solution flowing through a section of a radial opposed migration aerosol classifier (OMAC) in accordance with one or more embodiments of the invention;

FIG. 8 illustrates a particle trajectories simulation model of a solution flowing through a section of a radial opposed migration aerosol classifier (ROMAC) in accordance with one or more embodiments of the invention;

FIG. 9 illustrates a particle transfer simulation model of a solution flowing through a section of a radial opposed migration aerosol classifier (ROMAC) in accordance with one or more embodiments of the invention;

FIG. 10 illustrates a schematic of a system setup using the radial opposed migration ion/aerosol classifier (ROMIAC) for ion mobility-mass spectrometry, in accordance with one or more embodiments of the invention;

FIGS. 11(a)-(b) illustrate a 2-part calibration of a radial opposed migration ion/aerosol classifier (ROMIAC). FIG. 11(a) is a graph depicting the instrument calibration with tetraalkylammonium halides (TAAX), which was not affected by carrier gas contaminants and/or analyte surface concavities. FIG. 11(b) is a graph depicting the mobility calibration with peptides, which was affected by carrier gas contaminants and/or analyte surface concavities;

FIG. 12 is a table detailing the mobility of various TAAX multimers successfully classified with the ROMIAC;

FIGS. 13(a)-(n) are a series of graphs showing the detection of bradykinin, angiotensin I, and angiotensin II at various electrospray ionization chamber carrier gas temperatures (i.e. 298K and 400K) and charge states (i.e. +1, +2, +3);

4

FIGS. 14(a)-(d) are a series of graphs showing the detection of bovine ubiquitin at various charge states (i.e. +5, +6, +7, +8);

FIG. 15 is a table illustrating the collisional cross-section,  $\Omega_c$ , as well as the comparison to literature values of the various peptides, bradykinin (BK), angiotensin I (AT1), angiotensin II (AT2), and bovine ubiquitin (UB);

FIGS. 16(a)-(h) illustrate the separation by ion mobility-mass spectrometry of model peptide isomers AARAAATAA vs. AATAAARAA and of AARAAHAMA vs. AARAAMAHA, as separated by the ROMIAC. FIGS. 16(a-b, e-f) shows the separation with no 2,2,6,6-Tetramethylpiperidin-1-yl)oxyl (TEMPO) tag attached. FIGS. 16(c-d, g-h) shows the separation with TEMPO tagged on the peptides.

#### DETAILED DESCRIPTION OF THE PREFERRED EMBODIMENTS

In the following description, reference is made to the accompanying drawings which form a part hereof, and which is shown, by way of illustration, several embodiments of the present invention. It is understood that other embodiments may be utilized and structural changes may be made without departing from the scope of the present invention.

##### Overview

Opposed migration aerosol classifiers (OMAC) [5] and related inclined grid mobility analyzers (IGMA) [11] scale favorably in their performance relative to DMAs. OMACs in particular can be made much more compact than DMAs and can also classify a broader range of particle diameters than a DMA for fixed flows [12]. For example, a planar-geometry OMAC has been found to be able to differentiate between a bi-disperse mixture of 1.47 nm tetraheptylammonium monomer ions and 1.78 nm tetraheptylammonium dimer ions, with a resolving power of 4.

The OMAC was conceived of as a planar device, and implementations of the related IGMA have all been planar. However, for planar OMACs, some difficulty has been found in obtaining satisfactory internal seals around the rectangular-shaped porous media (i.e., frits, screens) that distribute the cross-flow and serve as the electrodes. Additionally, considerable particle losses have been found in the inlet and outlet regions, on either end of the classification region, owing to the presence of an imposed field without a counteracting cross-flow at these regions. These complications have prevented the instrument from realizing its full potential.

The innovative design features of the radial opposed migration classifier provided herein overcome these complications. In particular, the radial opposed migration classifier addresses the unanticipated difficulties with the fluid flow and electrical field associated with a planar geometry, particularly the unfavorable voltage transitions at the inlet and outlet regions. In one aspect, the radial geometry provides a reduction in the residence time of the particles within the system. In other aspects, the inlet and outlet edge effects and diffusive losses are considerably smaller for a radial geometry when compared to a planar geometry.

In one or more embodiments, both the sample inlet from the flow distributor channel ("race track") and the outlet/classified sample exit are located on the same side of the upper plane of the classification region. In one or more embodiments, the radial opposed migration classifier is a radial opposed migration aerosol classifier (ROMAC) for separating and/or measuring particles in an aerosol. In an exemplary application, the ROMAC allows for aerosol introduction and collection at the same wall/plane. Conventional mobility analysis (e.g. DMA) relies on differential displace-



5

ment of particles in an electrical field, and thus most initial DMA instrument designers were inclined to locate the aerosol inlet and classified outlet at locations with different potentials. Systems and methods are provided herein where the aerosol is introduced and collected at the same potential, which in one exemplary application is at electric ground voltage for safety reasons. This enhances transport efficiency over alternatives that achieve aerosol classification using a sample inlet and outlet at different voltages.

It should be noted that even though a radial opposed migration aerosol classifier (ROMAC) is used to describe various embodiments of the invention as follows, the radial opposed migration classifier provided herein may be used to separate and measure particles contained in any fluid, including liquids (e.g. colloids or suspensions) and other gases (e.g. atmospheric ultrafine particles), and using any kind of field (e.g. electric, magnetic, thermal, or gravitational).

Details of the Radial Opposed Migration Classifier

FIGS. 1A-C provide examples of a general structure of a radial opposed migration classifier. FIG. 1A shows a perspective view of a 2-plane sectional cut of an assembled ROMAC system 100 in accordance with one or more embodiments of the invention. A top lid 110, a bottom lid 128, and a side case 118 form an outer enclosure for the system 100. FIG. 1B shows a cross-sectional side view of the assembled ROMAC system 100. FIG. 1C is a photograph of an assembled ROMAC. The modular assembly of the ROMAC allows for fine control of key geometric parameters.

A classification region, similar to the classification channel 218 illustrated in FIG. 2 and classification channel 302 illustrated in FIG. 3, is created by a knife edge top 102, knife edge bottom 104, variable gap spacer 106, bottom base 108, and conductive, porous circular screens 140 and 142 respectively stretched across top screen holder 116 and bottom screen holder 120. An embroidery hoop-inspired method may be used for stretching a conductive porous screen/electrode. The thickness dimension of variable gap spacer 106 may be adjusted to change the space between the knife edge top 102 and bottom base 108. A top screen holder 116 and a bottom screen holder 120 are used to hold respective top and bottom permeable circular walls/screens 140 and 142, such as stretched stainless steel mesh. A top frit 114 and bottom frit 122 serve to laminarize the cross-flow before it enters the classification region. The top frit 114 is held in place and may be positionally adjusted within the system 100 by a threaded frit spacer 112. Similarly, bottom frit 122 is held in place and may be positionally adjusted within the system 100 by a bottom frit spacer 124.

Additionally, the top frit 114, threaded frit spacer 112, and top lid 110 all include respective central openings 134, 136, and 138 for a central outlet tube 144 to pass through and rest on the circular screen 140 stretched across top screen holder 116. The central outlet tube 144 is connected to the classification region and provides a negative pressure that allows particles that are balanced by both the drag and imposed field forces to be discharged from the system 100 through the central outlet tube 144.

A flow distributor channel 130 includes a narrowing gap 132, similar to the narrow knife gap 216 illustrated in FIG. 2, which leads to the classification region. The narrowing gap 132 is created by the knife edge top 102 and knife edge bottom 104.

In one or more embodiments, top lid 110, knife edge top 102, knife edge bottom 104, top screen holder 116, top frit 114, threaded frit spacer 112, and the outlet tube 144 that passes through central openings 134-138 and rests on the conductive circular screen 140 stretched across top screen

6

holder 116 are at electrical ground. Side case 118, variable gap spacer 106, and bottom lid 128 are electrical insulators. Bottom base 108, bottom screen holder 120, bottom frit 122, bottom frit spacer 124, variable gap compensator spacer 126, and the conductive circular screen 142 stretched across bottom screen holder 120 are at a non-ground electrical potential. A post 146 extends from variable gap compensator spacer 126 through bottom lid 128 and serves as a means to apply a non-ground electric potential.

FIG. 2 is an illustrative diagram of how a sample 200 would traverse the interior sample volume of a ROMAC 202. ROMAC volume 202 has an inlet port 204 and outlet port 206 for a sample 200, such as polydisperse, positively charged aerosol, and an inlet port 208 and outlet port 210 for a vapor-free cross-flow 212. The aerosol inlet port 204 of the ROMAC volume 202 would receive the sample 200, which would enter a flow distributor channel 214 ("racetrack"). Typically, the flow distributor channel 214 forms a ring or "racetrack" that is concentric to the circular walls 220, 222. In one or more embodiments, the sample 200 enters the flow distributor channel 214 tangentially. The tangential introduction of sample 200 to the flow distributor channel 214 reduces particle loss by impaction, as well as assists in uniform sample distribution in a radial manner. Due to the pressure difference between the racetrack 214 and the sample outlet 206, the sample 200 will be uniformly and radially drawn toward the center outlet port 206 through a narrow knife edge gap 216. After passing through the narrow knife edge gap 216, the sample 200 is now in the classification region 218, where only the particles that are balanced by both the drag and imposed field forces imparted on them will successfully traverse the classification region 218 and exit the ROMAC volume 202 through the central outlet port 206.

The aerosol inlet port 204 may be open to ambient fluid or be connected to an apparatus that would provide the sample 200, such as a reaction chamber, electrospray ionization chamber, or nebulizer. The aerosol outlet port 206 may be connected to an apparatus that would provide negative pressure, such as a condensation nuclei counter pulling a vacuum. The cross-flow inlet port 208 may be connected to an apparatus that would provide vapor-free clean air at a controlled temperature and flow rate, while the cross-flow outlet port 210 may be connected to a vacuum that would result in a matched flow rate to the cross-flow inlet 208. In one or more embodiments, the upper circular wall 220 of the classification region is at electrical ground voltage, while the bottom circular wall 222 of the classification region is at a high positive voltage.

Details of the Classification Region of the Radial Opposed Migration Classifier

FIG. 3 is an illustrative diagram of how particles in a fluid sample are separated/classified in the classification region of a radial opposed migration classifier in accordance with one or more embodiments of the present invention. A particulate-laden fluid sample 300 is pumped or injected into a classification channel 302 from a tangential inlet port 304, similar to the aerosol inlet port 204 in FIG. 2. A pressure difference between the inlet/entrance 304 (i.e. where the sample is injected) and outlet/exit 306 (i.e. where the sample is discharged) regions of the classification channel 302 causes the sample 300 to flow in one direction through classification channel 302. The particulate-laden sample 300 may be a polydisperse sample (i.e. comprising particles of various size, shape, and/or mass) or may be a monodisperse sample (i.e. comprising particles of uniform size, shape, and/or mass). FIG. 3 shows, for example, a polydisperse sample 300 comprising particles of various sizes, 318, 320, and 322.

The sample 300 travels between two circular walls 308 and 310 of classification channel 302 that are permeable to the flow of gases or liquids. The permeable circular walls 308 and 310 may include filters that can capture particles or may be made of a mesh, screen, foam, frit, honeycomb, or porous material (e.g., a porous metal such as sintered metal) that allows particles to pass through it.

A fluid cross-flow 312 enters the classification channel 302 through a circular wall 310, and exits through the opposing circular wall 308. The fluid cross-flow 312 may be a gas or liquid and imparts a drag force 314 ( $F_d$ ) on the particles suspended within the sample fluid. The drag force 314 is strong enough to potentially cause all the particles in sample 300 to be lost by passing through the circular wall 308 or by deposition onto the circular wall 308.

In one or more embodiments, the cross-flow 312 is at a desired temperature predetermined by a user. As the cross-flow fluid 312 replaces the sample fluid by forcing the sample fluid out of the channel 302 through the opposing wall 308, the predetermined temperature of the cross-flow 312 rapidly replaces and changes the temperature of the sample and its particles.

In one or more further embodiments, the cross-flow 312 is vapor-less. By forcing the sample fluid out of the channel 302 through opposing wall 308, a sample fluid that includes trace vapors is replaced with a cross-flow fluid 312 that is vapor-less. Thus, any trace vapors that are introduced when the sample 300 is injected into the channel 302 are removed/replaced with the vapor-less cross-flow.

Additionally, an imposed field imparts a force 316 counter to the drag force 314. The imposed field can take several forms. For example, the particles 318-322 may be first charged or may already carry a charge and the imposed field may be an electric field that causes the particles 318-322 to move counter to the cross-flow 312.

Likewise, the imposed field may be a magnetic field that is imposed on magnetic particles. In another example, the classification channel 302 is horizontal or inclined at an angle so that gravitational sedimentation counters an upward cross-flow. The classification channel 302 may also be arranged in a drum and spun so that centrifugal forces are imposed on the particles 318-322. Temperature differences between the two circular walls 308 and 310 may also be used to create a thermophoretic migration of the particles 318-322 that is counter to the cross-flow 312.

In one or more embodiments, as illustrated in FIG. 3, the imposed field is an electric field created by a conductive circular wall 310 at a high voltage and a conductive circular wall 308 at ground voltage. The voltage difference imparts an electric force ( $F_e$ ) 316 on the particles 318-322 in a direction that is counter and opposite to the drag force 314. Depending on certain properties/characteristics of the particles 318-322, such as the size, shape, and/or mass, the electric force 316 will cause each particle 318-322 to migrate at a specific velocity towards circular wall 310.

Due to the advective flow of the sample 300 through classification channel 302, particles 318-322 of a certain property/characteristic (e.g. size, shape, mass, charge) that are substantially balanced by the drag force 314 and the force 316 created by the imposed field will traverse the classification region, while particles 318-322 that are different and subject to unbalanced forces will impact one of the circular walls 308 or 310. In other words, if the cross-flow 312 velocity is exactly equal but opposite to the migration velocity of the particles 318-322 due to the imposed field, the particles 318-322 will remain entrained in the sample and be carried straight through classification channel 302. Particles 318-322

that migrate at a higher or lower velocity than the velocity of the cross-flow 312 are transmitted to one of the circular walls 308 or 310. These particles 318-322 are lost through the circular walls 308/310 or may be disposed of, for example by deposition on and adhesion to the circular walls 308/310.

FIG. 3 illustrates a polydisperse sample 300, comprising particles 318, 320, and 322 of varying sizes that migrate at different velocities, which result in varying mobility separations. By adjusting the cross-flow velocity and the imposed field, a particle of a desired size 320 will remain in the classification channel 302 while the other particles 318 and 322 are removed. Specifically, a smaller particle 322 exits the classification channel 302 through circular wall 310 and a larger particle 318 exits through circular wall 308, while a particle of the desired size 320 exits through the outlet region 306 of classification channel 302. In other embodiments, for example when the imposed field is gravity-based, the respective directions of larger and smaller particles 318 and 322 are opposite of that for an imposed electric field.

Note however, that for the particle 320 to reach the outlet 306 of the classification channel 302, the velocity of the cross flow 312 need not be exactly equal and opposite the particle migration velocity caused by the imposed field. Particles 318-322 subject to slightly unbalanced counteracting velocities may still successfully traverse the classification channel 302 due to the finite length of classification channel 302. Particles 318-322 migrating at a velocity that is sufficiently close to and opposite the cross-flow 312 may possibly remain entrained in the sample 300 for a sufficient amount of time to travel through classification channel 302 and be discharged before impacting circular wall 308 or 310. Thus, the diameter 324 of the classification channel 302 may be changed depending on the desired level of specificity for particles 318-322 of particular properties/characteristics (e.g., size, shape, mass, charge). Successful particle travel through a classification channel 302 with a longer diameter would require more balanced counteracting forces on the particle 318-322, which means a smaller range of variability in the properties/characteristics (e.g., size, shape, mass, charge) of the particles 318-322 discharged. On the other hand, successful particle travel through a classification channel 302 with a shorter diameter would require less balancing of the counteracting forces on the particle 318-322, which means a greater range of variability in the properties/characteristics (e.g., size, shape, mass, charge) of the particles 318-322 discharged.

The sample 300 comprising classified particles 318-322 of a certain property is continuously discharged from classification channel 302 as a classified sample flow 326. The cross-flow 312 exiting through circular wall 308 or the sample flow 326 exiting the classification channel 302 through outlet 306 may be analyzed or scanned continuously to determine particle property/characteristic (e.g., size, mass, charge) distributions. For example, knowledge of the particle size dependence for migration velocity or mobility and the strength of the cross-flow 312 and the imposed field would enable a determination of the particle size distributions.

In embodiments of the invention, the distribution of particles with respect to the appropriate migration (electrophoretic for charged particles in an electric field, magnetophoretic for magnetic particles in a magnetic field, thermophoretic in the presence of a temperature gradient, sedimentation for gravitational separations) can be determined by stepping either the imposed field strength, or the cross-flow 312 rate through a range of values, and measuring the concentration of particles 318-322 that is transmitted (i.e., particles 318-322 that exit the classification channel 302 in the classified-sample flow 326). Accordingly, the migration

for the particles **318-322** in the sample flow may be determined by slowly increasing/decreasing the cross-flow **312** or the imposed field in a stepwise fashion while measuring the particle concentration in the classified-sample flow **326**.

In addition, if the particles **318** and **322** are allowed to migrate through the circular walls **308** and **310**, provision may be taken to remove the particles **318** and **322** from the cross flow **312** so that the cross-flow **312** can be re-circulated. Such provisions may include filtration of the cross-flow **312** after it exits the classification channel **302**.

#### Logical Flow

FIG. 4 is a flow chart illustrating a logical flow **400** for separating/classifying particles in a fluid sample in accordance with one or more embodiments of the invention as shown in FIG. 5. At block **402**, a sample **500**, comprising one or more particles **502** suspended within a sample fluid **504**, is introduced into a flow distributor channel **506** which subsequently introduces the sample **500** into a classification channel **510**. The sample **500** may be a variety of substances in a variety of forms. For example, the sample **500** may take the form of an aerosol, gas mixture, colloid, suspension of particles in a fluid, or liquid solution. Furthermore, the sample **500** may be a polydisperse sample (i.e. comprising particles of various size, shape, and/or mass) or may be a monodisperse sample (i.e. comprising particles of uniform size, shape, and/or mass). The sample **500** may also include trace vapors that are also introduced when the sample **500** is introduced (e.g. injected or pumped) into the flow distributor **506** and/or classification channel **510**.

An inlet port first receives the sample **500**, which then enters the flow distributor channel **506**. In one or more embodiments, the sample **500** is introduced tangentially into the flow distributor channel **506**. In one or more further embodiments, the flow distributor channel **506** comprises a narrowing gap **508** leading into the classification channel **510**. Due to a pressure difference between the flow distributor channel **506** and the sample outlet **512**, the sample **500** is uniformly drawn and/or pushed from the flow distributor channel **506** into the classification channel **510** through the narrowing gap **508**.

At block **404**, the sample **500** is introduced to the classification channel **510** through the flow distributor channel **506** and flows through the classification channel **510**. The classification channel **510** has a first circular wall **514** and a second circular wall **516** that are both permeable to a flow of fluid (liquid or gas). The pressure difference between the inlet/entrance region (i.e. where the sample **500** is introduced by the flow distributor channel) and outlet/exit region (i.e. central outlet port **512** where the sample **500** is discharged) of the classification channel **510** causes the sample **500** to flow in one general direction through the classification channel **510** (i.e. radially drawn towards the center or axis of revolution **530** of the permeable circular walls **514** and **516**). In one or more embodiments the sample flow is laminar. In one or more other embodiments, the classification channel **510** is part of a classification region of a radial opposed migration aerosol classifier (ROMAC).

At block **406**, a cross-flow fluid **518** is introduced to the classification channel **510** through one of the permeable circular walls **516**. This results in a drag force **528** on the sample **500** and particles **502**. The cross-flow **518** may also be a variety of substances in a variety of forms. For example, the cross-flow **518** may be a liquid, gas, or comprise solids suspended in a fluid, etc. The cross-flow **518** flows at a first velocity and exits in a first direction through the other permeable circular wall **514**. In one or more embodiments, a top frit **114** and/or a bottom frit **122** respectively above and below the

first and second permeable circular walls **514**, **516** are used to laminarize the cross-flow **518** before it enters the classification channel **510**.

At block **408**, an imposed field is applied in a second direction that is counter to the first direction of the cross-flow **518**. In one or more embodiments, the direction of the imposed field is orthogonal to the direction of the flow of the sample particles **502** through classification channel **510**. The imposed field causes the targeted particles **502** in the sample to migrate at a velocity that is opposite and/or equal in magnitude to the velocity of the cross-flow **518**. Therefore, as the cross-flow **518** forces the sample fluid **504** to exit along with it through the permeable circular wall **514**, the particles **502** that are balanced by the imposed field and cross-flow **518** remain within the classification channel **510** and are retained in the sample **500**. For particles where the imposed field subjects a force that is not equal to the cross-flow, the particles will move in an overall direction towards one of the permeable circular walls **514**, **516** rather than remain between the circular walls **514**, **516**. In one or more embodiments, as shown in FIG. 5, a dielectric **520** creates an electric potential by having the conductive circular wall **514** be at electrical ground voltage **522** and conductive circular wall be at a high voltage **524**. This results in an electric force **526** on the particles **502**.

At block **410**, the particles **502** remaining in the classification channel **510** (i.e., those particles whose field migration velocity is opposite and equal to the cross-flow velocity) are discharged through the central outlet port **512**. It should be noted that the particles **502** may migrate within a range of migration velocities that may not be exactly equal to the cross-flow **518** but still travel through the classification channel **510** and be discharged.

Subsequent actions may then process and/or use the discharged particles **502**. In one or more embodiments, the discharged particles **502** may be collected as a classified and/or purified sample. In one or more other embodiments, the discharged particles **502** that travel through the classification channel **510** are classified based on a property of the discharged particles **502**, for example a size, mass or charge of the discharged particles **502**.

While particles **502** that remain in the flow through the classification channel **510** are discharged, various other particles may be removed from the flow. For example, particles that reach the permeable walls **514**, **516** may be removed from the flow through the classification channel **510** either by deposition on and adhesion to the walls **514**, **516** or by passing through the walls **514**, **516**.

It should be noted that the functions noted in the blocks may occur out of the order noted in FIG. 4. For example, in one or more embodiments, blocks **406** and **408** which are shown in succession may in fact occur concurrently/in parallel. In other embodiments, due to the positioning of the cross-flow **518**, blocks **406** and **408** may occur in the reverse order, where the particles **502** are subject to the imposed field before coming into contact with the cross-flow **518**.

#### Illustrative Models and Simulations

As illustrative examples, the invention was modeled as a radially symmetric space similar to the ROMAC **202** depicted in FIG. 2 in COMSOL<sup>TM</sup> Multiphysics 4.1<sup>TM</sup> to obtain values for fluid properties, fluid flows, and electric fields in the region of the ROMAC through which aerosol particles will flow through. The electric potential solution is shown in FIG. 6 and the combined sample and cross-flow fluid velocity magnitude solution is shown in FIG. 7. More specifically, FIG. 6 illustrates that the introduction region **602**, similar to flow distributor channel **506** in FIG. 5, wall **604**, similar to

## 11

permeable circular wall **514** in FIG. 5, and outlet **606**, similar to central outlet port **512** in FIG. 5, are at ground potential, while wall **608**, similar to permeable circular wall **516** in FIG. 5, is at some non-ground potential. Wall **610** represents a dielectric spacer, similar to dielectric **520** in FIG. 5, which separates walls **604** and **608**, allowing for a potential field to exist in classification region **612**, similar to classification region **510** in FIG. 5. Additionally, FIG. 7 shows that the high flow velocity regions are in the knife edge gap and sample outlet, similar to knife edge gap **508** and sample outlet **512**, respectively, in FIG. 5. This is due to a pressure difference between sample outlet **512** and flow distributor channel **506** that draws the sample from the flow distributor channel **506** toward the sample outlet **512**. The sample thus flows radially inward toward the sample outlet **512**, in a direction that is orthogonal to the potential field in FIG. 6.

The COMSOL™ solutions were then used as inputs for a MATLAB™ script developed to simulate the trajectories of particles of a particular size when released into the ROMAC aerosol space. The trajectories used inputs of fluid velocity, density, viscosity, temperature, and electric potential to simulate the movement of particles in finite time steps. In addition, the diffusional movement of the particles was simulated as well.

FIG. 8 illustrates a simulation of 100 nm particles traversing the ROMAC at a voltage that was predicted to yield the maximum transmission of particles through the classification region. The aerosol flowrate was set at 0.1 lpm, cross-flow rate at 0.3 lpm, temperature at 298 K, and voltage at 440 V. The results demonstrate the feasibility of the invention, as the numerical simulations were executed with well-reputed software and relied on the established knowledge of mechanisms of particle movement. In addition, FIG. 8 demonstrates that the use of a sample inlet and outlet at the same electric potential greatly reduces particle losses, since 400 out of 462, or 87%, simulated particles were transmitted through the ROMAC. FIG. 8 shows a reduction of particle diffusion to the walls of the classification region that would otherwise result from unfavorable voltage transitions that occur in nearly all other DMA designs.

The type of simulation illustrated in FIG. 8 was repeated at various voltages to obtain a predicted transfer function (FIG. 9) for the ROMAC in the case of 100 nm particles at an aerosol flow rate of 0.1 lpm, a cross-flow rate of 0.3 lpm, and temperature of 298 K. The vertical line in FIG. 9 is the theoretical voltage that would result in a balance of the drag force and electric force imparted on the particles (which would result in maximum transmission, i.e. 100% transmission of the particles). The peak of the simulated transfer function is in very good agreement with the theoretical voltage for 100% transmission. The resolution of the ROMAC in this simulation is estimated to be roughly 3, which compares favorably to the maximum theoretical non-diffusive resolution of 3. Thus, FIG. 9 also shows that the introduction and extraction of the sample from an inlet and outlet at the same electric potential greatly reduces diffusive particle losses that would otherwise degrade the resolution from the maximum theoretical non-diffusive resolution.

#### Illustrative Experimental Results and Discussion

#### Ion Mobility Spectrometry: Exemplary Application of the ROMIAC

TSI™ classic DMAs are able to classify particles in the range of 10-1000 nm. Even TSI™ nano-DMAs only have a range of 2-150 nm. Thus, there is a need for a particle classifier that is optimal in the sub-10 nm regime, not just touching

## 12

it. This is important due to the persistent 1-2 nm cluster mode in the background atmosphere and because particle formation takes place below 3 nm [13].

In an exemplary application, ion mobility spectrometry was performed with a radial opposed migratory ion/aerosol classifier (ROMIAC) to demonstrate the ability of the ROMIAC in separating particles in the sub-10 nm regime. Even though no condensation particle counters (CPC) were available to detect 1 nm particles and no polystyrene latex (PSL) standards were that small, there still existed other size standards (and quasi-standards) that could be detected with a mass-spectrometer, in this instance, tetraalkylammonium halides (TAAX) and peptides.

FIG. 10 illustrates a schematic of a radial opposed migration ion/aerosol classifier (ROMIAC) system in accordance with one or more embodiments of the invention. More specifically, the schematic of FIG. 10 shows an experimental set-up of a system **1000** used to separate/classify particles.

An inert nitrogen gas **1002** ( $N_2$ ) is used as both the sample fluid and the cross-flow fluid. For the sample fluid, nitrogen gas **1002** passes through a regulator **1004** which has a critical orifice **1006** leading to a filter **1008**. The filter **1008** removes any undesired particulates in the nitrogen gas **1002**. A syringe **1010** with solution containing the analytes of interest is used to transport the solvated analyte to an electrospray ionization (ESI) spray chamber **1012**, which disperses the analyte as a charged, fine aerosol, benefiting from the additional nebulization by the inert nitrogen gas **1002**. A pressure transducer **1014** measures the flow rate of the sample aerosol passing through a laminar flow element **1016**, where it is then introduced into the ROMIAC **1018**. Additionally, inert nitrogen gas **1002** ( $N_2$ ) passes through a regulator **1004** and is controllably released by a proportioning solenoid valve **1020**. After being filtered by filter **1008**, the nitrogen gas **1002** is introduced into the ROMIAC **1018** as the cross-flow.

After the separation process as described above, the desired particles are discharged from the ROMIAC **1018** due to the pressure difference created by vacuum **1024**. A pressure transducer **1014** measures the flow rate of the classified aerosol passing through a laminar flow element **1016** prior to being introduced to a mass spectrometer **1022**. The cross-flow also exits the ROMIAC **1018** and passes through a critical orifice **1006** where it is pumped by pump **1026** to a vacuum **1028**. The flow rates measured by pressure transducers **1014** are balanced by adjusting regulator **1004** until the pressure transducers **1014** report the same flow rate values. Due to critical orifice **1006**, it can be assured that the cross-flows entering and exiting ROMIAC **1018** are balanced as well.

As illustrated in FIG. 11, a 2-part calibration was first performed [15]. FIG. 11(a) is a graph depicting the instrument calibration with TAAX [16], which was not affected by ESI solvent contaminants or analyte surface concavities. FIG. 11(a) shows a relatively linear relationship between the peak signal voltage and the inverse mobility of the analyte. FIG. 11(b) is a graph depicting the mobility calibration with peptides [17,18], which was affected by ESI solvent contaminants or analyte surface concavities. FIG. 11(b) shows a relatively linear relationship between collisional cross-section and a relational coefficient  $\beta$  (which is a grouping of variables relating to analyte mass, charge, and temperature in the Mason-Schamp equation).

FIG. 12 is a table detailing the mobility of various TAAX multimers, which are singly-charged anion-coordinated multimers. Generally, as more monomer units are added to a TAAX ion, the cross section increases and the mobility of the TAAX multimer decreases. The superscript is defined as fol-

## 13

lows: <sup>a</sup>In N<sub>2</sub> at atmospheric pressure and T<sub>ESI</sub>=T<sub>x</sub>=298 K. Values are the average of three scans. Note that C3 species are iodinated while all other TAAX species are brominated.

FIG. 13 contains graphs illustrating the detection by mass spectrometry of various peptides separated by the ROMIAC. The vertical axis for the graphs represents the normalized intensity of the signal from a mass spectrometer and the horizontal axis for the graphs represents the applied voltage. FIGS. 13(a)-(d) are a series of graphs showing the detection of bradykinin at various temperatures (i.e. 298K (FIGS. 13(a), 13(c)) and 400K (FIGS. 13(b), 13(d))) and charge states (i.e. +1 (FIGS. 13(a)-(b)), +2 (FIGS. 13(c)-(d))). FIGS. 13(e)-(j) are a series of graphs showing the detection of angiotensin I at various temperatures (i.e. 298K (FIGS. 13(e), 13(g), 13(i)) and 400K (FIGS. 13(f), 13(h), 13(j))) and charge states (i.e. +1 (FIGS. 13(e)-(f)), +2 (FIGS. 13(g)-(h)), +3 (FIGS. 13(i)-(j))). FIGS. 13(k)-(n) are a series of graphs showing the detection of angiotensin II at various temperatures (i.e. 298K (FIGS. 13(k), 13(m)) and 400K (FIGS. 13(l), 13(n))) and charge states (i.e. +1 (FIGS. 13(k)-(l)), +2 (FIGS. 13(m)-(n))). FIG. 14(a)-(d) are a series of graphs showing the detection of bovine ubiquitin at various charge states (i.e. +5, +6, +7, +8).

FIG. 15 is a table illustrating the collisional cross-sections,  $\Omega_i$ , from the two different calibrations, as well as the comparison of the mobility calibration to literature values of the various peptides, bradykinin (BK), angiotensin I (AT1), angiotensin II (AT2), and bovine ubiquitin (UB). The superscripts are defined as follows: <sup>a</sup>In N<sub>2</sub> at atmospheric pressure and T<sub>x</sub>=298 K. Values are the average of three scans; <sup>b</sup>T<sub>ESI</sub>=298 K; <sup>c</sup>T<sub>ESI</sub>=400 K; <sup>d</sup>Peak was used for mobility calibration; <sup>e</sup>Cross section estimated from instrument calibration (using TAAX ions); <sup>f</sup>Cross section estimated from mobility calibration (using peptides and proteins); and <sup>g</sup>, <sup>h</sup>, <sup>i</sup>Percent difference between this study's mobility calibration  $\Omega_i$  value and that published in [17-19].

#### Model Peptide Isomer Separation

In an exemplary application, a radial opposed migratory ion/aerosol classifier (ROMIAC) was used to see if model peptides whose sequences differed by only one pair switch could be separated. In this instance, the sequences tested were AARAAATAA vs. AATAAARAA and AARAAHAMA vs. AARAAMAHA. Additionally, a TEMPO tag (2,2,6,6-Tetramethylpiperidin-1-yl)oxyl) was added to see if the tag would modify the structures of the sequences to enhance separation by the ROMIAC.

FIGS. 16(a)-(d) illustrate the detection by mass spectrometry of model peptides AARAAATAA vs. AATAAARAA as separated by the ROMIAC. FIG. 16(a)-(b) shows the separation with no TEMPO tag attached. FIG. 16(c)-(d) shows the separation with TEMPO tagged on the peptides. Similarly, FIGS. 16(e)-(h) illustrate the detection by mass spectrometry of model peptides AARAAHAMA vs. AARAAMAHA as separated by the ROMIAC. FIG. 16(e)-(f) shows the separation with no TEMPO tag attached. FIG. 16(g)-(h) shows the separation with TEMPO tagged on the peptides.

These results demonstrate ROMIAC's ability to classify ions/particles. Ions and peptides were successfully classified at the 1-2 nm size range. Resolutions achieved were close to the maximum theoretical resolution based on flow rate ratios (~20). There was also a very linear response in mobility to voltage changes. Furthermore, ROMIAC was able to resolve isomers with small structural differences.

#### Conclusion

The foregoing description of the preferred embodiment of the invention has been presented for the purposes of illustration and description. It is not intended to be exhaustive or to

## 14

limit the invention to the precise form disclosed. Many modifications and variations are possible in light of the above teaching. It is intended that the scope of the invention be limited not by this detailed description, but rather by the claims appended hereto. All publications, patents, and patent applications cited herein are hereby incorporated by reference in their entirety for all purposes.

#### REFERENCES

- [1] Knutson, E. and K. Whitby, Aerosol classification by electric mobility: apparatus, theory, and applications, *J Aerosol Sci*, 1975, p. 443-451.
- [2] Winklmayr, W., et al. A New Electromobility Spectrometer for the Measurement of Aerosol Size Distributions in the Size Range from 1 to 1000 nm. *J Aerosol Sci*, 1991, 22(3): p. 289-296.
- [3] Chen, D., et al. Design and Evaluation of a Nanometer Aerosol Differential Mobility Analyzer (Nano-DMA). *J. Aerosol Sci*, 1998, 29(5-6): p. 497-509.
- [4] de Juan, L. and J. de la Mora, High Resolution Size Analysis of Nanoparticles and Ions: Running a Vienna DMA of Near Optimal Length at Reynolds Numbers Up to 5000. *J Aerosol Sci*, 1998, 29(5-6): p. 617-626.
- [5] Flagan, R. C., Cross-flow Differential Migration Classifier, U.S. Pat. No. 6,905,029.
- [6] Zhang, S., et al., Radial Differential Mobility Analyzer. *Aerosol Science and Technology*, 1995, 23(3): p. 357-372.
- [7] Zhang, S. and R. Flagan, Resolution of the Radial Differential Mobility Analyzer for Ultrafine Particles. *J Aerosol Sci*, 1996, 27(8): p. 1179-1200.
- [8] Brunelli, N. A., R. C. Flagan, and K. P. Giapis, Radial Differential Mobility Analyzer for One Nanometer Particle Classification. *Aerosol Science and Technology*, 2009, 43(1): p. 53-59.
- [9] Flagan, R. C. and S. H. Zhang, Radial Differential Mobility Analyzer, U.S. Pat. No. 5,606,112.
- [10] Martinez-Lozano, P., M. Labowsky, and J. F. de la Mora, Experimental Tests of a Nano-DMA with No Voltage Change Between Aerosol Inlet and Outlet Slits. *J Aerosol Sci*, 2006, 37(11): p. 1629-1642.
- [11] Tammiet, H., Symmetric Inclined Grid Mobility Analyzer for the Measurement of Charged Clusters and Fine Nanoparticles in Atmospheric Air. *Aerosol Science and Technology*, 2011, p. 468-479.
- [12] Downard, A., J. Dama, and R. Flagan, An Asymptotic Analysis of Differential Electrical Mobility Classifiers. *Aerosol Science and Technology*, 2011, p. 717-729.
- [13] Kulmala, M. et al. Toward Direct Measurement of Atmospheric Nucleation. *Science*, 2007.
- [14] Flagan, R. C. Opposed Migration Aerosol Classifier (OMAC). *Aerosol Science and Technology*, 2004, 38:890-899.
- [15] Fernandez-Maestre, R., et al. Chemical Standards in Ion Mobility Spectrometry. *The Analyst*, 2010.
- [16] Viidanoja, J., et al. Tetraalkylammonium Halides as Chemical Standards for Positive Electrospray Ionization with Ion Mobility Spectrometry/Mass Spectrometry. *RCMS*, 2005.
- [17] Bush, M., et al. Collision Cross Sections of Proteins and Their Complexes: A Calibration Framework and Database for Gas-Phase Structural Biology. *Anal. Chem.*, 2010, 82(22):9557-65.
- [18] Wu., C., et al. Atmospheric Pressure Ion Mobility Spectrometry of Protonated and Sodiated Peptides. *RCMS*, 1999, 13(12):1138-42.

## US 9,095,793 B2

15

[19] Baykut, G., O. von Halem, and O. Raether. Applying a Dynamic Method to the Measurement of Ion Mobility. *Journal of the American Society for Mass Spectrometry*, 2009, 20(11):2070-81.

What is claimed is:

1. A radial opposed migration classifier comprising:

a classification channel through which passes a sample comprising one or more particles suspended within a sample fluid, the classification channel comprising a first circular wall and a second circular wall that are both permeable to a flow of fluid;

a flow distributor channel for introducing the sample into the classification channel wherein the flow distributor channel comprises a narrowing gap leading into the classification channel;

a cross-flow fluid that enters the classification channel through one of the permeable circular walls, wherein the cross-flow fluid flows at a first velocity and exits in a first direction through the other permeable circular wall;

an imposed field that is applied on the one or more particles in a second direction counter to the first direction of the cross-flow fluid, wherein the imposed field causes the one or more of the particles to migrate at a second velocity opposite and/or equal to a first velocity of the cross-flow fluid; and

wherein the particles that travel through the channel are discharged from the radial opposed migration classifier.

2. The radial opposed migration classifier of claim 1, wherein the sample is introduced tangentially into the flow distributor channel.

3. The radial opposed migration classifier of claim 1, wherein the flow distributor channel introduces the sample into the classification channel through a same plane as the first circular wall and further wherein the particles that travel through the channel are discharged through a central outlet on the same plane as the first circular wall.

4. The radial opposed migration classifier of claim 1, wherein the imposed field is an electric field.

5. The radial opposed migration classifier of claim 4, wherein the particles are introduced into the classification channel at an electric potential and discharged from the radial opposed migration classifier at the same electric potential.

6. The radial opposed migration classifier of claim 4, wherein the particles are discharged at an electrical ground voltage.

7. The radial opposed migration classifier of claim 1, wherein the discharged particles that travel through the channel are classified based on a property of the discharged particles.

8. The radial opposed migration classifier of claim 7, wherein the property of the discharged particles is a size, mass or charge of the discharged particles.

9. A method for separating particles comprising:

introducing a sample, comprising one or more particles suspended within a sample fluid, from a flow distributor channel into to a classification channel wherein the flow distributor channel comprises a narrowing gap leading into the classification channel;

passing the sample through the classification channel, wherein the classification channel comprises a first circular wall and a second circular wall that are both permeable to a flow of fluid;

introducing a cross-flow fluid to the classification channel through one of the permeable circular walls, wherein the cross-flow fluid flows at a first velocity and exits in a first direction through the other permeable circular wall;

16

applying an imposed field on the one or more particles in a second direction counter to the first direction of the cross-flow fluid, wherein the imposed field causes the one or more particles to migrate at a second velocity opposite and/or equal to the first velocity of the cross-flow fluid; and

discharging the particles that travel through the channel.

10. The method of claim 9, wherein the sample is introduced tangentially into the flow distributor channel.

11. The method of claim 9, wherein the flow distributor channel introduces the sample into the classification channel through a same plane as the first circular wall and further wherein the particles that travel through the channel are discharged through a central outlet on the same plane as the first circular wall.

12. The method of claim 9, wherein the imposed field is an electric field.

13. The method of claim 12, wherein the particles are introduced into the classification channel at an electric potential and discharged from the radial opposed migration classifier at the same electric potential.

14. The method of claim 12, wherein the particles are discharged at an electrical ground voltage.

15. The method of claim 9, further comprising classifying the discharged particles that travel through the channel based on a property of the discharged particles.

16. The method of claim 15, wherein the property of the discharged particles is a size, mass or charge of the discharged particles.

17. The radial opposed migration classifier of claim 1, wherein classified particles pass through a permeable screen when output from the radial opposed migration classifier.

18. The method of claim 9, wherein the discharged particles pass through a permeable screen when output from classification channel.

19. The radial opposed migration classifier of claim 1, wherein:

a temperature of the sample fluid is changed by changing a temperature of the cross-flow fluid.

20. The method of claim 9, wherein a temperature of the sample fluid is changed by changing a temperature of the cross-flow fluid.

21. The radial opposed migration classifier of claim 1, wherein:

vapors in the sample fluid are replaced with a vapor-less cross-flow fluid.

22. The method of claim 9, wherein:

vapors in the sample fluid are replaced with a vapor-less cross-flow fluid.

23. The radial opposed migration classifier of claim 1, wherein:

one or more of the particles that reach the first circular wall or the second circular wall are removed from the sample fluid by:

deposition on and adhesion to the first circular wall or the second circular wall; or

passing through the first circular wall or the second circular wall.

24. The method of claim 9, further comprising:

removing one or more of the particles that reach the first circular wall or the second circular from the sample fluid by:

deposition on and adhesion to the first circular wall or the second circular wall; or

passing through the first circular wall or the second circular wall.

## US 9,095,793 B2

17

25. A radial opposed migration classifier comprising:  
 a classification channel through which passes a sample  
 comprising one or more gas ions suspended in a gas  
 mixture, the classification channel comprising a first  
 circular wall and a second circular wall that are both  
 permeable to a flow of gas;  
 a flow distributor channel for introducing the gas mixture  
 into the classification channel;  
 a cross-flow gas that enters the classification channel  
 through one of the permeable circular walls, wherein the  
 cross-flow gas flows at a first velocity and exits in a first  
 direction through the other permeable circular wall, and  
 wherein a temperature of the gas mixture is changed by  
 changing a temperature of the cross-flow gas;  
 an imposed field that is applied on the one or more gas ions  
 in a second direction counter to the first direction of the  
 cross-flow gas, wherein the imposed field causes the one  
 or more of the gas ions to migrate at a second velocity  
 opposite and/or equal to a first velocity of the cross-flow  
 gas; and  
 wherein the gas ions that travel through the channel are  
 discharged from the radial opposed migration classifier.  
 26. The radial opposed migration classifier of claim 25,  
 further comprising:

18

a first flow measuring device that measures a first flow rate  
 of the sample into the radial opposed migration classi-  
 fier;  
 a second flow measuring device that measures a second  
 flow rate of classified gas ions output from the radial  
 opposed migration classifier;  
 wherein the first flow rate and the second flow rate are  
 balanced by adjusting a regulator; and  
 wherein the classified gas ions output from the radial  
 opposed migration classifier are input into a mass spec-  
 trometer to detect and analyze the classified gas ions.  
 27. The radial opposed migration classifier of claim 25,  
 wherein:  
 vapors in the gas mixture are replaced with a vapor-less  
 cross-flow gas.  
 28. The radial opposed migration classifier of claim 25,  
 wherein:  
 one or more of the gas ions that reach the first circular wall  
 or the second circular wall are removed from the gas  
 mixture by:  
 deposition on and adhesion to the first circular wall or  
 the second circular wall; or  
 passing through the first circular wall or the second  
 circular wall.

\* \* \* \* \*

*Appendix E***US PATENT 9,138,663 B2: OPPOSED MIGRATION AEROSOL  
CLASSIFIER GAS AND HEAT EXCHANGER**

Inventors: Richard C. Flagan, Wilton Mui, Andrew J. Downard

Publication Date: September 22, 2015





US009138663B2

(12) **United States Patent**  
**Flagan et al.**

(10) **Patent No.:** **US 9,138,663 B2**

(45) **Date of Patent:** **Sep. 22, 2015**

(54) **OPPOSED MIGRATION AEROSOL  
CLASSIFIER GAS AND HEAT EXCHANGER**

(71) Applicant: **California Institute of Technology**,  
Pasadena, CA (US)

(72) Inventors: **Richard C. Flagan**, Pasadena, CA (US);  
**Wilton Mui**, Pasadena, CA (US);  
**Andrew J. Downard**, Los Angeles, CA  
(US)

(73) Assignee: **California Institute of Technology**,  
Pasadena, CA (US)

(\*) Notice: Subject to any disclaimer, the term of this  
patent is extended or adjusted under 35  
U.S.C. 154(b) by 283 days.

(21) Appl. No.: **13/768,817**

(22) Filed: **Feb. 15, 2013**

(65) **Prior Publication Data**  
US 2013/0213860 A1 Aug. 22, 2013

#### Related U.S. Application Data

(60) Provisional application No. 61/600,434, filed on Feb.  
17, 2012.

(51) **Int. Cl.**  
**G01N 15/00** (2006.01)  
**G01N 1/40** (2006.01)  
**B01D 21/00** (2006.01)  
**G01N 15/02** (2006.01)

(52) **U.S. Cl.**  
CPC ..... **B01D 21/00** (2013.01); **G01N 15/0266**  
(2013.01); **G01N 2015/0046** (2013.01)

(58) **Field of Classification Search**  
USPC ..... 95/57–81; 96/3, 52, 64; 209/132–734  
See application file for complete search history.

(56) **References Cited**

#### U.S. PATENT DOCUMENTS

|           |     |        |          |          |
|-----------|-----|--------|----------|----------|
| 4,147,621 | A * | 4/1979 | Giddings | 210/637  |
| 4,214,981 | A * | 7/1980 | Giddings | 209/155  |
| 4,737,268 | A * | 4/1988 | Giddings | 209/12.2 |
| 4,830,756 | A * | 5/1989 | Giddings | 210/239  |

(Continued)

#### FOREIGN PATENT DOCUMENTS

EP 2352008 8/2011

#### OTHER PUBLICATIONS

PCT International Search Report and Written Opinion dated May 27,  
2013 for PCT Application No. PCT/US2013/026499.

(Continued)

*Primary Examiner* — Duane Smith

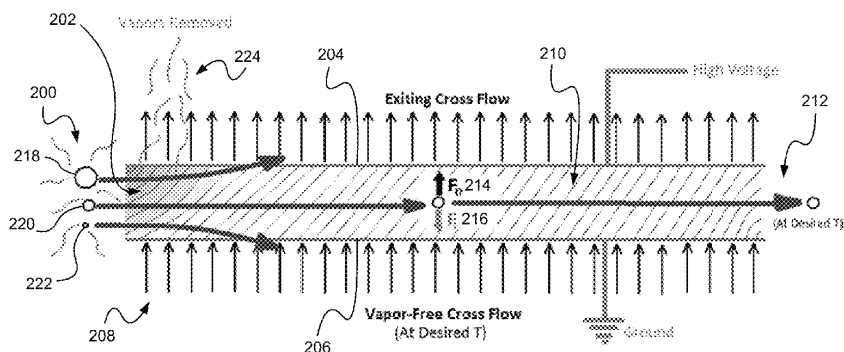
*Assistant Examiner* — Sonji Turner

(74) *Attorney, Agent, or Firm* — Gates & Cooper LLP

(57) **ABSTRACT**

A method is provided for changing a property of a sample. A sample, comprising particles suspended within a sample fluid, is introduced into a channel which comprises two walls that are permeable to a flow of fluid. A cross-flow is introduced at a predetermined temperature and of a predetermined chemical composition into the channel through a wall. This cross-flow flows at a first velocity and exits in a first direction through the other wall. An imposed field is applied on the particles in a second direction counter to the first direction of the cross-flow. The imposed field causes the particles to migrate at a second velocity opposite and/or equal to the first velocity of the cross-flow. Particles that are approximately balanced by the first and second velocities travel through the channel and are discharged in a fluid of predetermined chemical composition and at the predetermined temperature of the cross-flow.

**20 Claims, 12 Drawing Sheets**



## US 9,138,663 B2

Page 2

(56)

## References Cited

## U.S. PATENT DOCUMENTS

|              |      |         |                 |            |
|--------------|------|---------|-----------------|------------|
| 4,894,146    | A *  | 1/1990  | Giddings        | 209/12.2   |
| 4,894,172    | A *  | 1/1990  | Williams        | 210/748.01 |
| 5,133,844    | A *  | 7/1992  | Stevens         | 204/549    |
| 6,365,050    | B1 * | 4/2002  | Cauchon         | 210/635    |
| 6,905,029    | B2 * | 6/2005  | Flagan          | 209/210    |
| 7,141,152    | B2 * | 11/2006 | Le Febre        | 204/450    |
| 7,199,362    | B2 * | 4/2007  | Rockwood et al. | 250/286    |
| 8,360,244    | B2 * | 1/2013  | Wyatt et al.    | 209/156    |
| 8,384,897    | B2 * | 2/2013  | Mizukami et al. | 356/335    |
| 2003/0226754 | A1 * | 12/2003 | Le Febre        | 204/451    |
| 2004/0050756 | A1 * | 3/2004  | Flagan          | 209/156    |
| 2005/0006578 | A1 * | 1/2005  | Rockwood et al. | 250/289    |
| 2006/0266132 | A1   | 11/2006 | Cheng et al.    |            |
| 2008/0060457 | A1 * | 3/2008  | Liu et al.      | 73/863.31  |
| 2009/0173670 | A1   | 7/2009  | Okuda et al.    |            |
| 2011/0019187 | A1 * | 1/2011  | Mizukami et al. | 356/335    |
| 2011/0155650 | A1 * | 6/2011  | McNeil-Watson   | 209/155    |

## OTHER PUBLICATIONS

Liu, B., et al., Aerosol Mobility Chromatograph—New Detector for Sulfuric-Acid Aerosols. *Atmos Environ*, 1978, 12 (1-3): p. 99-104.

Rader, D. et al., Application of the Tandem Differential Mobility Analyzer to Studies of Droplet Growth or Evaporation. *J Aerosol Sci*, 1986, 17(5): p. 771-787.

Flagan, R., Opposed migration aerosol classifier (OMAC), *Aerosol Science and Technology*, 2004, 38(9): p. 890.

Downard, A. et al., An Asymptotic Analysis of Differential Electrical Mobility Classifiers, *Aerosol Science and Technology*, 2011, p. 717-729.

Knutson, E. et al., Aerosol classification by electric mobility: apparatus, theory, and applications, *J Aerosol Sci*, 1975, p. 443-451.

Tammet, H., Symmetric Inclined Grid Mobility Analyzer for the Measurement of Charged Clusters and Fine Nanoparticles in Atmospheric Air, *Aerosol Science and Technology*, 2011, p. 468-479.

\* cited by examiner

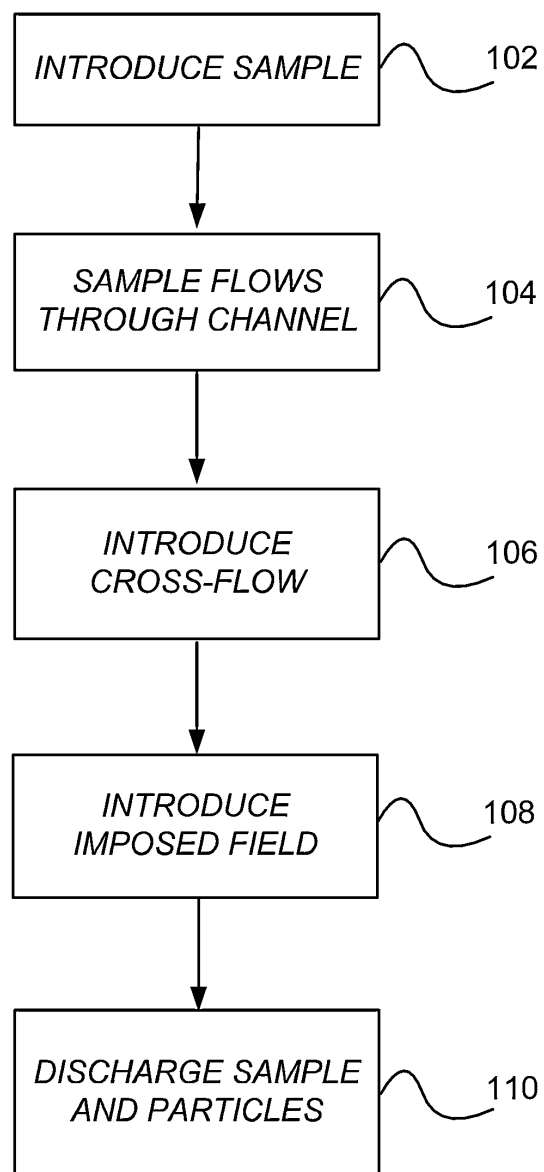
100

FIG. 1

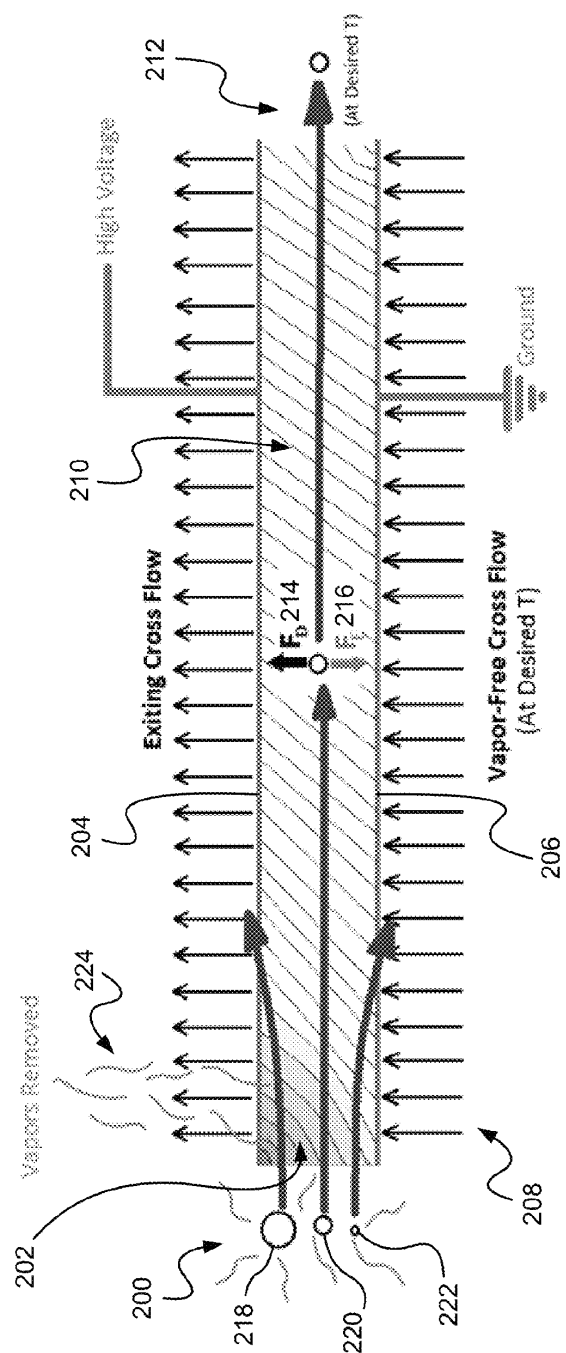


FIG. 2

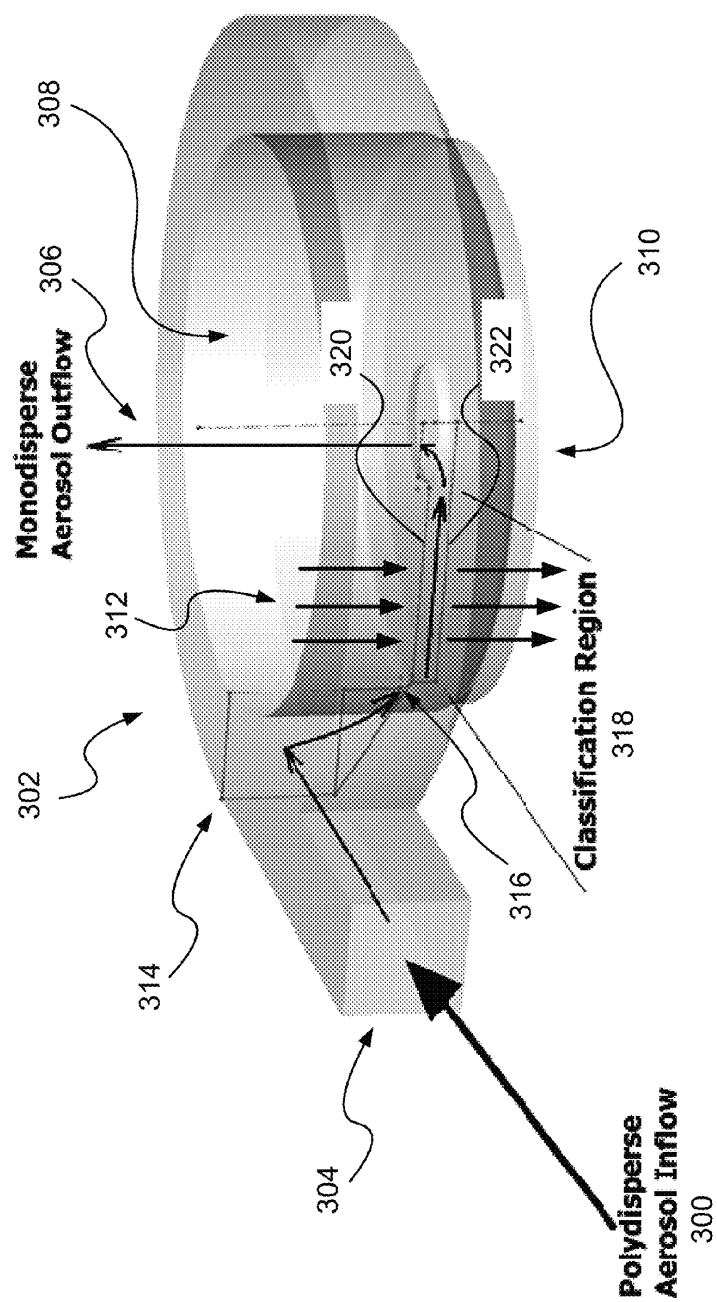


FIG. 3

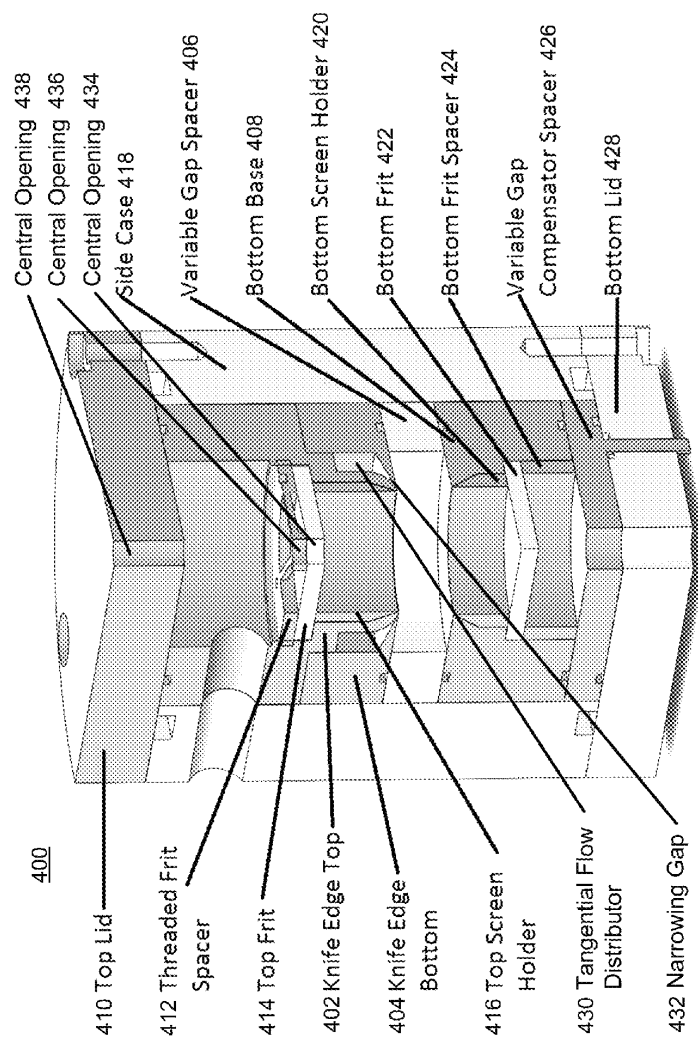


FIG. 4

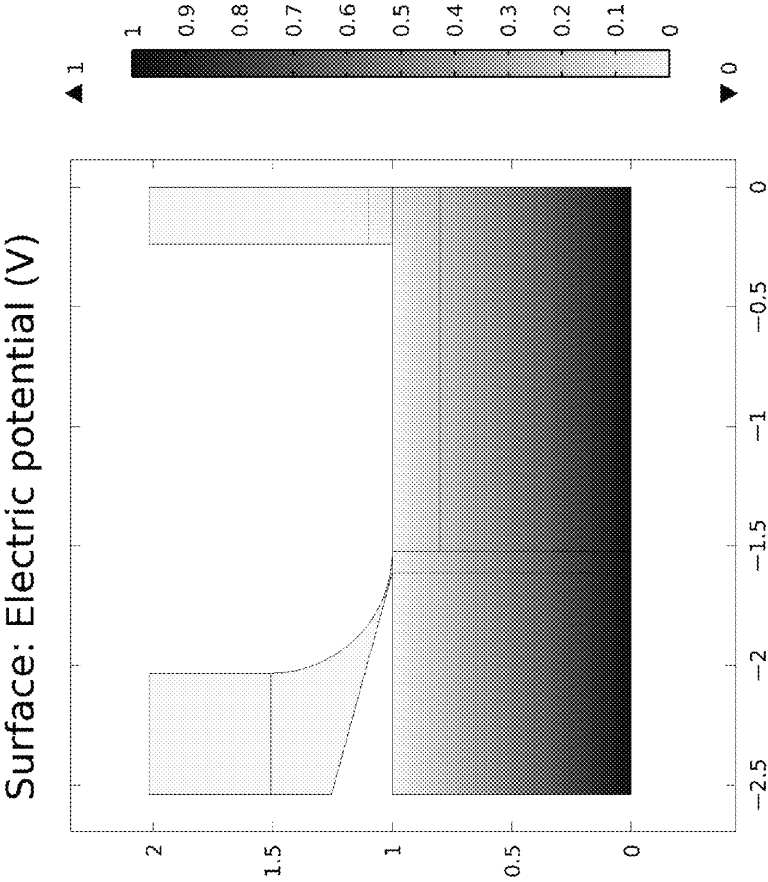


FIG. 5

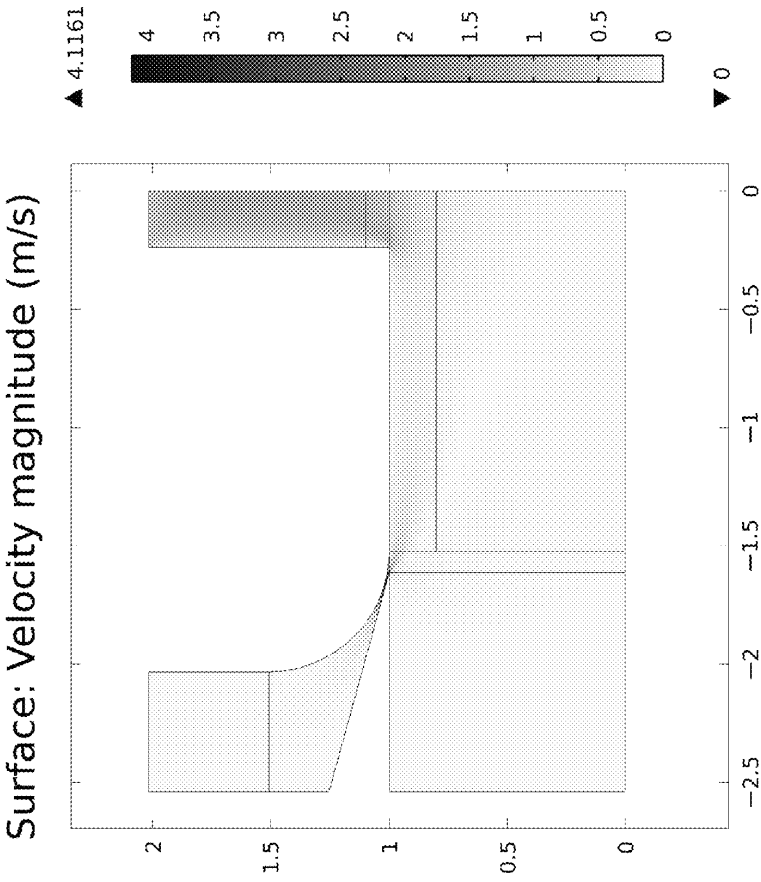


FIG. 6



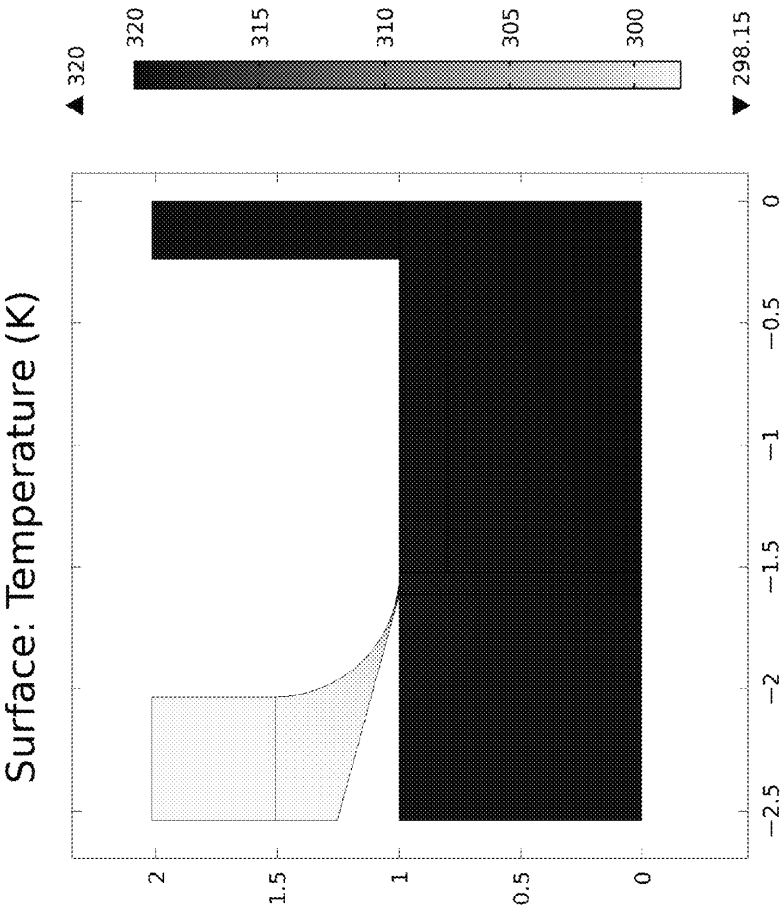


FIG. 7

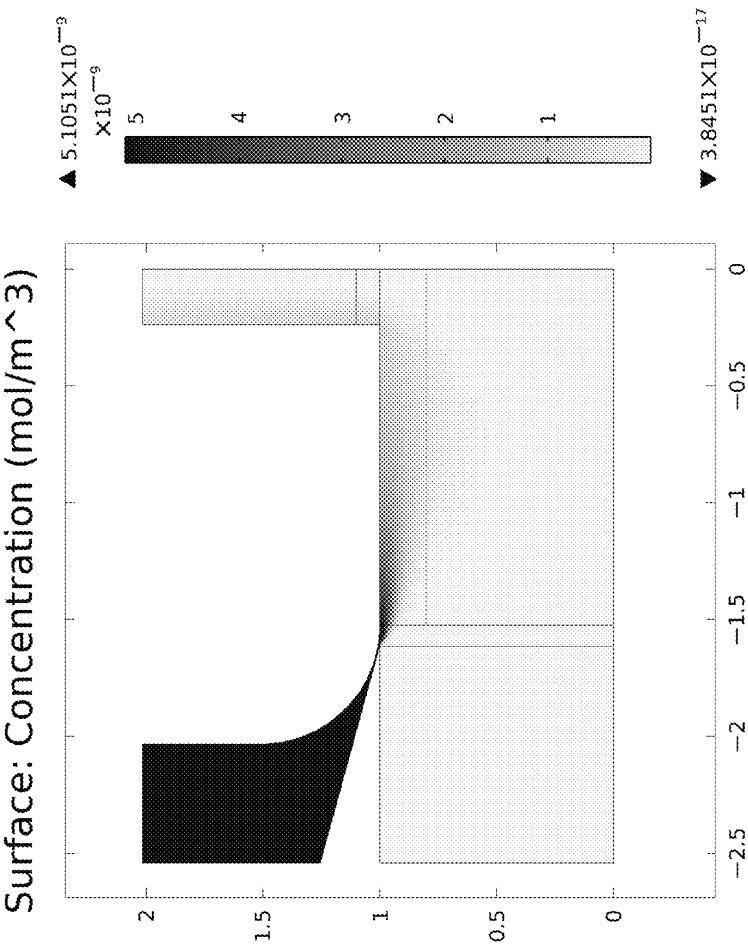


FIG. 8

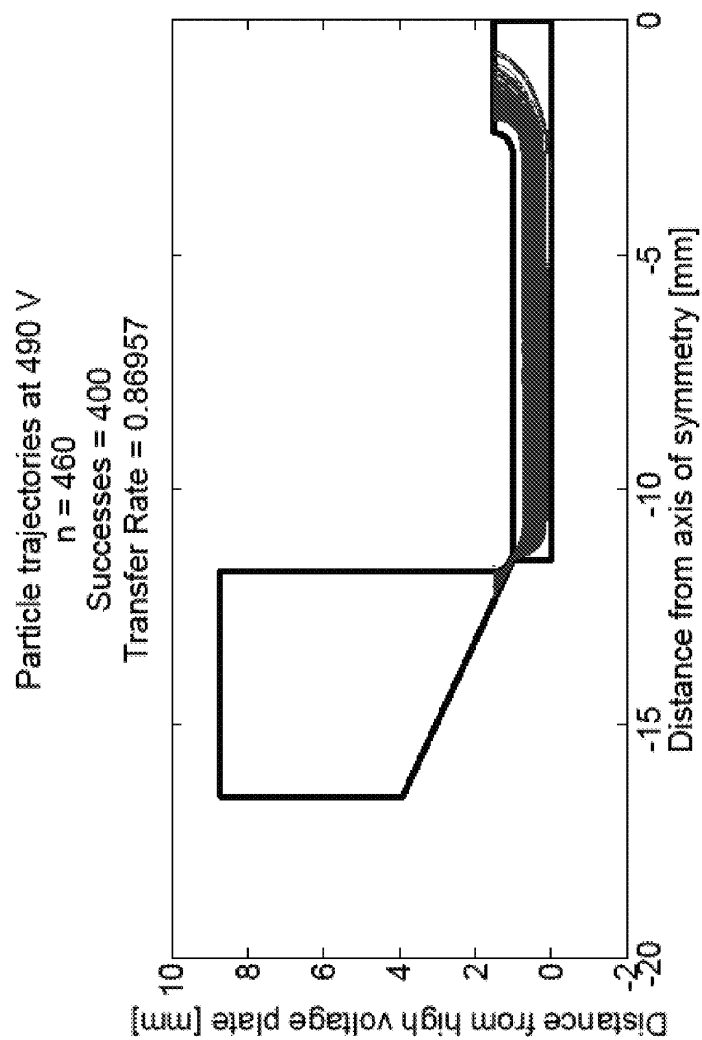


FIG. 9

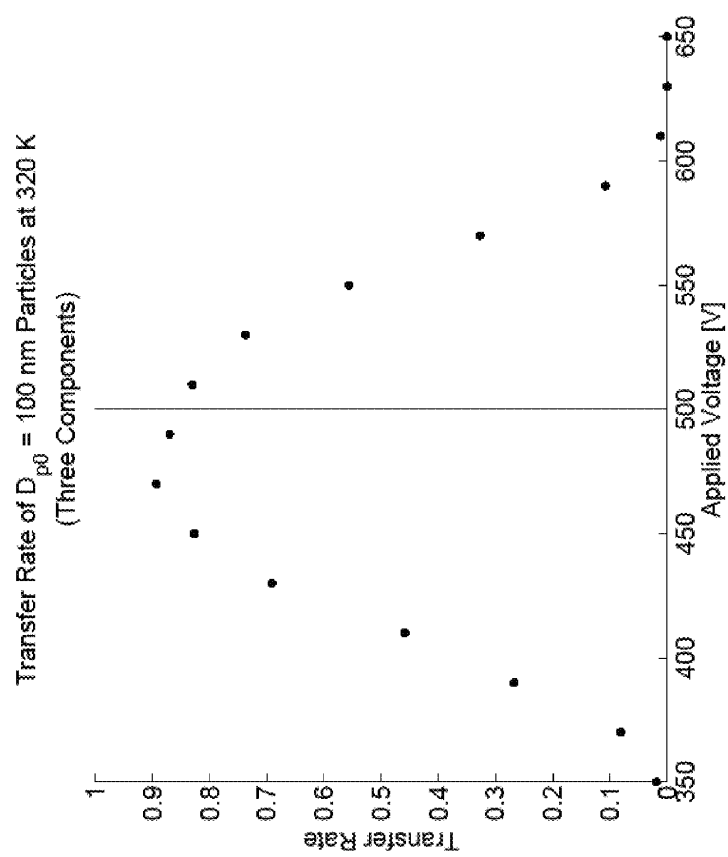


FIG. 10

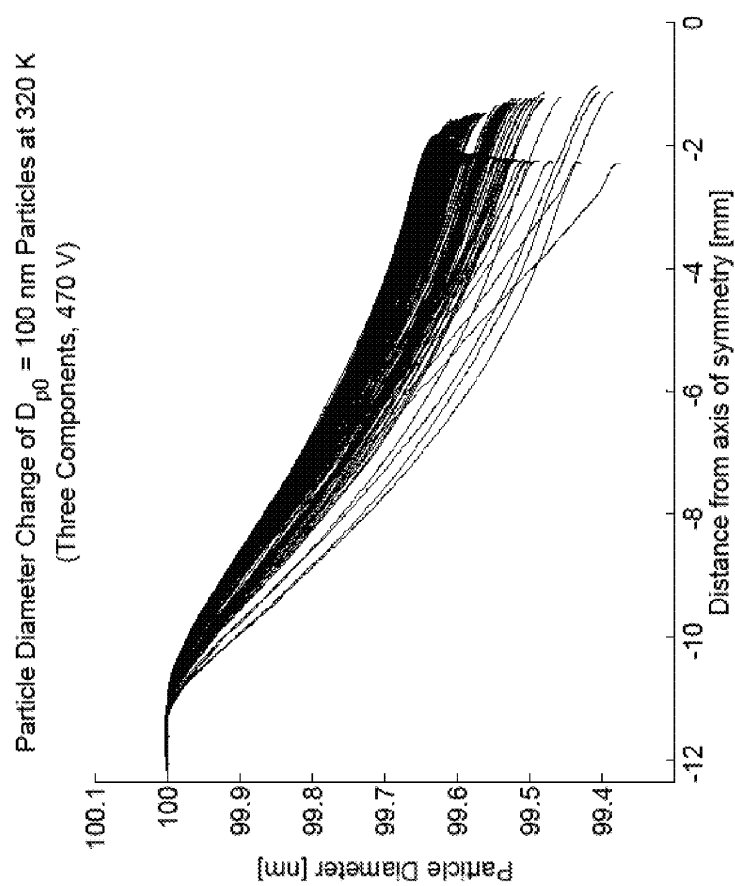


FIG. 11

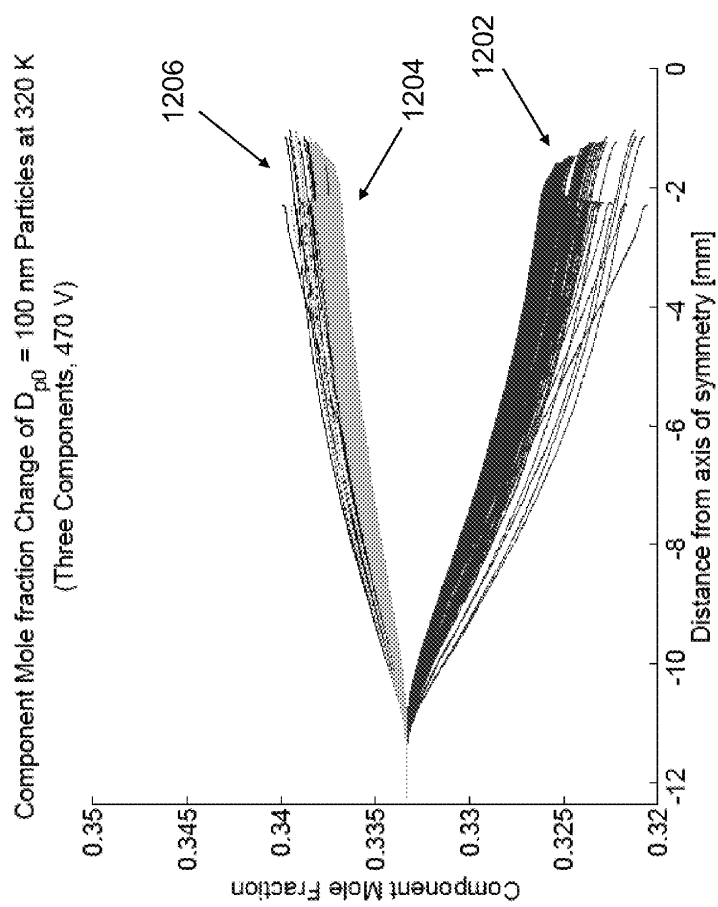


FIG. 12

US 9,138,663 B2

1

# OPPOSED MIGRATION AEROSOL CLASSIFIER GAS AND HEAT EXCHANGER

## CROSS-REFERENCE TO RELATED APPLICATIONS

This application claims the benefit under 35 U.S.C. Section 119(e) of the following commonly-assigned U.S. provisional patent application, which is incorporated by reference herein:

Provisional Application Ser. No. 61/600,434, filed on Feb. 17, 2012, by Richard C. Flagan et al., entitled "OPPOSED MIGRATION AEROSOL CLASSIFIER GAS AND HEAT EXCHANGER,".

This application is also related to the following commonly-assigned patent and patent applications, which are incorporated by reference herein:

U.S. Pat. No. 6,905,029, issued on Jun. 14, 2005, by Richard C. Flagan, entitled "CROSS-FLOW DIFFERENTIAL MIGRATION CLASSIFIER,"; and

U.S. patent application Ser. No. 13/769,122, filed on Feb. 15, 2013, by Richard C. Flagan et al., entitled "RADIAL OPPOSED MIGRATION AEROSOL CLASSIFIER WITH GROUNDED AEROSOL ENTRANCE AND EXIT," which claims priority to Provisional Application Ser. No. 61/600,409, filed on Feb. 17, 2012, by Richard C. Flagan et al., entitled "RADIAL OPPOSED MIGRATION AEROSOL CLASSIFIER WITH GROUNDED AEROSOL ENTRANCE AND EXIT,".

## BACKGROUND OF THE INVENTION

### 1. Field of the Invention

The present invention relates generally to methods, apparatuses, and articles of manufacture for changing a property of a sample, and in particular, for changing a temperature, particle size, and/or chemical composition of a fluidic sample with an opposed migration aerosol classifier (OMAC).

### 2. Description of the Related Art

(Note: This application references a number of different publications as indicated throughout the specification by reference numbers enclosed in brackets, e.g., [x]. A list of these different publications ordered according to these reference numbers can be found below in the section entitled "References." Each of these publications is incorporated by reference herein.)

A number of different systems and techniques have been developed for separating and measuring particles contained in fluids such as gases (e.g. aerosols or atmospheric ultrafine particles) and liquids (e.g. colloids or suspensions). Common systems and techniques in the art include the usage of condensation particle counters (CPC) and differential electrical mobility classifiers (DEMC) such as differential mobility analyzers (DMA) and inclined grid mobility analyzers (IGMA). Such systems separate and measure particles according to specific particle properties/characteristics, for example a size, mass or charge of the particle. The systems may also separate and measure particles based on a change in a specific property/characteristic of the particles (e.g. size, mass, charge) when the particles are subjected to certain conditions and environments.

One exemplary application for DMAs in tandem measurements (i.e. tandem differential mobility analysis) is to probe for particle properties such as hygroscopicity and volatility [1, 2]. A typical tandem DMA setup comprises a fixed-voltage DMA that supplies a substantially monodisperse aerosol sample. The temperature and/or vapor composition is then changed, typically by flowing the sample through a denuder

2

or a heated tube. The particles respond to this changed environment, and the extent to which they grow or shrink is determined by using a second DMA operating in scanning mode.

Independent of the system used, oftentimes the greatest difficulty in separating and measuring particles with changing environments is the different time histories of the particles as they traverse the intermediate step where a sample property, such as the temperature or composition, is changed. For example, temperature and vapor changes respectively rely on diffusion from and to the walls of the system, which is often a comparatively slow process relative to the sample flow through the system. Furthermore, particles that are near the walls may experience a substantially different environment as compared to those further away from the walls of the system. Thus, a final measured signal is often an amalgamation of particles subject to inconsistent conditions and environments under a wide range of time histories. Therefore, the effect of changing a property of a sample is difficult to measure and quantify with great certainty and the separation or measurement of specific particles is equally frustrated.

In view of the above, there is a need for a method, apparatus, and article of manufacture for rapidly changing sample properties, such as the fluid temperature, particle size, and/or fluid chemical composition. Furthermore, there is a need for a method, apparatus, and article of manufacture for performing tandem mobility analysis that subjects particles in a sample to uniform conditions and environments under more consistent time histories, which will allow for more easily quantifiable separations and measurements.

## SUMMARY OF THE INVENTION

The invention provided herein has a number of embodiments useful, for example, in changing a property of a sample. According to one or more embodiments of the present invention, a method, apparatus, and article of manufacture are provided for rapidly changing a sample property, such as the fluid temperature, particle size, and/or fluid chemical composition, using an opposed migration aerosol classifier (OMAC).

In one aspect of the present invention, a method for changing a property of a sample is provided. The method comprises introducing a sample, comprising one or more particles suspended within a sample fluid, through a channel. The channel comprises two walls that are permeable to a flow of fluid. A fluid cross-flow of predetermined chemical composition is introduced at a predetermined temperature to the channel through one of the permeable walls. This cross-flow flows at a first velocity and exits in a first direction through the other permeable wall. An imposed field (where the field can be an electric, magnetic, thermal, gravitational field, amongst others) is applied on the one or more particles in the sample in a second direction counter to the first direction of the cross-flow. The imposed field causes the one or more of the particles of desired size and/or charge to migrate at a second velocity opposite and/or equal to a first velocity of the cross-flow. The particles that travel through the channel are discharged. Furthermore, the particles that travel through the channel are discharged at the predetermined temperature of the cross-flow fluid. In one or more embodiments, the sample fluid is substantially replaced by the cross-flow fluid as the sample flows through the channel. Therefore, the discharged particles that travel through the channel are no longer suspended within the sample fluid but are rather suspended within the cross-flow fluid.

## US 9,138,663 B2

3

In certain embodiments of the invention, the cross-flow fluid, which may contain one or more trace vapors, replaces a trace vapor in the sample fluid. In further embodiments of the invention, a size of the one or more particles of the sample is changed while the one or more particles travel through the channel due to a difference in the sample fluid and cross-flow fluid temperatures and/or a difference in the concentration of one or more vapors in the sample fluid and the cross-flow fluid. In still other embodiments, the chemical composition of the sample fluid is changed while the one or more particles of the sample travel through the channel.

## BRIEF DESCRIPTION OF THE DRAWINGS

Referring now to the drawings in which like reference numbers represent corresponding parts throughout:

FIG. 1 is a flow chart illustrating a logical flow for changing a property of a sample in accordance with one or more embodiments of the invention.

FIG. 2 illustrates the changing of various properties of a sample in accordance with one or more embodiments of the invention;

FIG. 3 illustrates a radial opposed migration aerosol classifier (ROMAC) in accordance with one or more embodiments of the invention;

FIG. 4 illustrates a perspective view of a 2-plane sectional cut of a radial opposed migration aerosol classifier (ROMAC) in accordance with one or more embodiments of the invention;

FIG. 5 illustrates an electric potential distribution model of a solution flowing through a section of a radial opposed migration aerosol classifier (ROMAC) in accordance with one or more embodiments of the invention;

FIG. 6 illustrates a fluid velocity distribution model of a solution flowing through a section of a radial opposed migration aerosol classifier (ROMAC) in accordance with one or more embodiments of the invention;

FIG. 7 illustrates a fluid temperature distribution model of a solution flowing through a section of a radial opposed migration aerosol classifier (ROMAC) in accordance with one or more embodiments of the invention;

FIG. 8 illustrates a trace vapor concentration distribution model of a solution flowing through a section of a radial opposed migration aerosol classifier (ROMAC) in accordance with one or more embodiments of the invention;

FIG. 9 illustrates a particle trajectories simulation model of a solution flowing through a section of a radial opposed migration aerosol classifier (ROMAC) in accordance with one or more embodiments of the invention;

FIG. 10 illustrates a particle transfer simulation model of a solution flowing through a section of a radial opposed migration aerosol classifier (ROMAC) in accordance with one or more embodiments of the invention;

FIG. 11 illustrates a particle diameter change simulation model of a solution flowing through a section of a radial opposed migration aerosol classifier (ROMAC) in accordance with one or more embodiments of the invention; and

FIG. 12 illustrates a particle chemical composition change simulation model of a solution flowing through a section of a radial opposed migration aerosol classifier (ROMAC) in accordance with one or more embodiments of the invention.

## DETAILED DESCRIPTION OF THE PREFERRED EMBODIMENTS

In the following description, reference is made to the accompanying drawings which form a part hereof, and which

4

is shown, by way of illustration, several embodiments of the present invention. It is understood that other embodiments may be utilized and structural changes may be made without departing from the scope of the present invention.

## Overview

An opposed migration aerosol classifier (OMAC) is an excellent option for nanoparticle classification in the gas phase [3]. Its performance is favorable relative to other alternatives in that it is well suited for classifying sub-10 nm aerosol and gas ions. Additionally, OMAC instruments may be made with a more compact footprint than the commonly used alternative of differential mobility analyzers (DMA) [4-6]. Thus, in one exemplary implementation, an OMAC may be used in tandem mobility analysis as a replacement to a first stage DMA. An OMAC may also be used as a replacement to a second stage DMA, though the design of a scanning OMAC is more complex.

In one aspect of the present invention, methods and systems are provided using an OMAC for replacing the diffusion-based methods currently used for changing fluid sample properties. These methods and systems that are related to the OMAC rely on the advection of a fluid sample through cross-flows and imposed fields, which are both considerably faster than diffusion, to change various properties of the sample and the particles within the sample. Thus, for example, OMACs are excellent for rapid gas exchange when compared to other mobility analyzers. For an aerosol sample, the aerosol inlet gas is rejected from the system almost immediately and replaced by a desired cross-flow gas, thereby rapidly changing the properties of the sample.

Though the usage of an OMAC is described in various embodiments of the invention as follows, other differential electrical mobility classifiers (DEMC) may also be used for changing the properties of a sample, such as rapidly changing the gas temperature and/or composition in which a charged aerosol is suspended. Suitable DEMCs include, but are not limited to, OMACs, DMAs, and IGMAs of planar, radial, coaxial cylindrical, conical, and other geometries. For example, an inclined grid mobility analysis (IGMA) may be used since, similar to an OMAC, it also shares favorable up-scaling in performance metrics when compared to DMAs [7].

## Logical Flow

FIG. 1 is a flow chart illustrating a logical flow 100 for changing a property of a sample in accordance with one or more embodiments of the invention. At block 102, a sample, comprising one or more particles suspended within a sample fluid, is introduced into a channel. The sample may be a variety of substances in a variety of forms. For example, the sample may take the form of an aerosol, gas mixture, colloid, suspension of particles in a fluid, or liquid solution. Furthermore, the sample may be a polydisperse sample (i.e. comprising particles of various size, shape, and/or mass) or may be a monodisperse sample (i.e. comprising particles of uniform size, shape, and/or mass). The sample may also include trace vapors that are also introduced when the sample is injected or pumped into the channel. The channel has two or more walls that are permeable to the flow of fluid (liquid or gas). In one or more embodiments, the channel is part of a classification region of an opposed migration aerosol classifier (OMAC) or radial opposed migration aerosol classifier (ROMAC).

At block 104, the sample flows through the channel between the two or more permeable walls. A pressure difference between the inlet/entrance region (i.e. where the sample is introduced) and outlet/exit region (i.e. where the sample is discharged) of the channel causes the sample to flow in one



5

general direction through the channel. In one or more embodiments the sample flow is laminar.

At block 106, a cross-flow at a predetermined temperature is introduced to the channel through one of the permeable walls. The cross-flow may also be a variety of substances in a variety of forms. For example, the cross-flow may be a liquid, gas, or comprise solids suspended in a fluid, etc. The cross-flow flows at a first velocity and exits in a first direction through the other permeable wall. In one or more embodiments, the cross-flow exits the channel through a wall directly opposite the wall it is introduced through. As the cross-flow exits the channel, the cross-flow forces the initial sample fluid to exit along with it through the permeable wall. Therefore, the sample fluid of the sample is replaced by the cross-flow as the sample flows through the channel. By replacing the sample fluid with the cross-flow, any trace vapors that were introduced along with the sample will also be forced out through the permeable wall. Moreover, the predetermined temperature of the cross-flow replaces and changes the temperature of the sample and its particles.

At block 108, an imposed field is applied in a second direction that is counter to the first direction of the cross-flow. In one or more embodiments, the direction of the imposed field is orthogonal to the direction of the flow of the cross-flow. The imposed field causes the targeted particles in the sample to migrate at a velocity that is opposite and/or equal in magnitude to the velocity of the cross-flow. Therefore, as the cross-flow forces the sample fluid to exit along with it through the permeable wall, the particles that are balanced by the imposed field and cross-flow remain within the channel and are retained in the sample. For particles where the imposed field subjects a force that is not equal to the cross-flow, the particles will move in an overall direction towards one of the permeable walls rather than remain between the walls.

At block 110, the particles remaining in the channel (i.e., those particles whose field migration velocity is opposite and equal to the cross-flow velocity) are discharged. It should be noted that the particles may migrate within a range of migration velocities that may not be exactly equal to the cross-flow but still travel through the channel and be discharged.

Since the temperature of the sample may be changed by the predetermined temperature of the cross-flow, the particles that travel through the channel are at the predetermined temperature of the cross-flow when they are discharged. Further, in one or more embodiments, a vapor-free cross-flow removes the trace vapors in the sample and thus the trace vapors are not included with the discharged particles that travel through the channel.

Subsequent actions may then process and/or use the discharged particles. In one or more embodiments, the discharged particles that travel through the channel are analyzed or scanned to determine a change in a property/characteristic of the discharged particles resulting from changing a property of the sample. In one exemplary application, a differential mobility analyzer (DMA) is used to scan the discharged particles. The discharged particles may also be collected as a classified and/or purified sample. In one or more other embodiments, the discharged particles that travel through the channel are classified based on a property of the discharged particles, for example a size, mass or charge of the discharged particles.

While particles that remain in the flow through the channel are discharged, various other particles may be removed from the flow. For example, particles that reach the permeable walls may be removed from the flow through the channel either by deposition on and adhesion to the walls or by passing through the walls.

6

It should be noted that the functions noted in the blocks may occur out of the order noted in FIG. 1. For example, in one or more embodiments, blocks 106 and 108 which are shown in succession may in fact occur concurrently/in parallel. In other embodiments, due to the positioning of the cross-flow, blocks 106 and 108 may occur in the reverse order, where the particles are subject to the imposed field before coming into contact with the cross-flow.

Illustrative System for Changing Sample Properties

FIG. 2 is an illustrative diagram of how properties of a sample are changed in accordance with one or more embodiments of the present invention. A particulate-laden fluid sample 200 is pumped or injected into a channel 202. A pressure difference between the inlet/entrance (i.e. where the sample is injected) and outlet/exit (i.e. where the sample is discharged) regions of the channel 202 causes the sample 200 to flow in one direction through channel 202. In various embodiments, this channel 202 is part of the classification region of an OMAC. The particulate-laden sample 200 may be a polydisperse sample (i.e. comprising particles of various size, shape, and/or mass) or may be a monodisperse sample (i.e. comprising particles of uniform size, shape, and/or mass). FIG. 2 shows, for example, a polydisperse sample 200 comprising particles of various sizes, 218, 220, and 222.

The sample 200 travels between two walls 204 and 206 of channel 202 that are permeable to the flow of gases or liquids. The permeable walls 204 and 206 may include filters that can capture particles or may be made of a mesh, screen, foam, frit, honeycomb, or porous material (e.g., a porous metal such as sintered metal) that allows particles to pass through it.

A fluid cross-flow 208 enters the channel 202 through a wall 206, and exits through the opposing wall 204. The fluid cross-flow 208 follows streamlines 210 due to the orthogonal velocity of sample 200 relative to the initial velocity of cross-flow 208. The fluid cross-flow 208 may be a gas or liquid and imparts a drag force 214 ( $F_D$ ) on the particles suspended within the sample fluid. The drag force 214 is strong enough to potentially cause all the particles in sample 200 to be lost by passing through the wall 204 or by deposition onto the wall 204.

In one or more embodiments, the cross-flow 208 is at a desired temperature predetermined by a user. As the cross-flow fluid 208 replaces the sample fluid by forcing the sample fluid out of the channel 202 through the opposing wall 204 along streamlines 210, the predetermined temperature of the cross-flow 208 rapidly replaces and changes the temperature of the sample and its particles.

In one or more further embodiments, the cross-flow 208 is vapor-less. By forcing the sample fluid out of the channel 202 through opposing wall 204 along streamlines 210, a sample fluid that includes trace vapors 224 is replaced with a cross-flow fluid 208 that is vapor-less. Thus, any trace vapors 224 that are introduced when the sample 200 is injected into the channel 202 are removed/replaced with the vapor-less cross-flow.

Additionally, an imposed field imparts a force 216 counter to the drag force 214. The imposed field can take several forms. For example, the particles 218-222 may be first charged or may already carry a charge and the imposed field may be an electric field that causes the particles 218-222 to move counter to the cross-flow 208. Likewise, the imposed field may be a magnetic field that is imposed on magnetic particles. In another example, the channel 202 is horizontal or inclined at an angle so that gravitational sedimentation counters an upward cross-flow. The channel 202 may also be arranged in a drum and spun so that centrifugal forces are imposed on the particles 218-222. Temperature differences

between the two walls **204** and **206** may also be used to create a thermophoretic migration of the particles **218-222** that is counter to the cross-flow **208**.

In one or more embodiments, as illustrated in FIG. 2, the imposed field is an electric field created by a conductive wall **204** at a high voltage and a conductive wall **206** at ground voltage. The voltage difference imparts an electric force ( $F_E$ ) **216** on the particles **218-222** in a direction that is counter and opposite to the drag force **214**. Depending on certain properties/characteristics of the particles **218-222**, such as the size, shape, and/or mass, the electric force **216** will cause each particle **218-222** to migrate at a specific velocity towards wall **206**.

Due to the advective flow of the sample **200** through channel **202**, particles **218-222** of a certain property/characteristic (e.g. size, shape, mass, charge) that are substantially balanced by the drag force **214** and the force **216** created by the imposed field will traverse the classification region, while particles **218-222** that are different and subject to unbalanced forces will impact one of the walls **204** or **206**. In other words, if the cross-flow **208** velocity is exactly equal but opposite to the migration velocity of the particles **218-222** due to the imposed field, the particles **218-222** will remain entrained in the sample and be carried straight through channel **202**. Particles **218-222** that migrate at a higher or lower velocity than the velocity of the cross-flow **208** are transmitted to one of the walls **204** or **206**. These particles **218-222** are lost through the walls **204/206** or may be disposed of, for example by deposition on and adhesion to the walls **204/206**.

FIG. 2 illustrates a polydisperse sample **200**, comprising particles **218**, **220**, and **222** of varying sizes that migrate at different velocities, which result in varying mobility separations. By adjusting the cross-flow velocity and the imposed field, a particle of a desired size **220** will remain in the channel **202** while the other particles **218** and **222** are removed. Specifically, a smaller particle **222** exits the channel **202** through wall **206** and a larger particle **218** exits through wall **204**, while a particle of the desired size **220** exits through the outlet region of channel **202**. In other embodiments, for example when the imposed field is gravity-based, the respective directions of larger and smaller particles **218** and **222** are opposite of that for an imposed electric field.

Note however, that for the particle **220** to reach the outlet of the channel **202**, the velocity of the cross flow **208** need not be exactly equal and opposite the particle migration velocity caused by the imposed field. Particles **218-222** subject to slightly unbalanced counteracting velocities may still successfully traverse the channel **202** due to the finite length of channel **202**. Particles **218-222** migrating at a velocity that is sufficiently close to and opposite the cross-flow **208** may possibly remain entrained in the sample **200** for a sufficient amount of time to travel through channel **202** and be discharged before impacting wall **204** or **206**. Thus, the length of the channel **202** may be changed depending on the desired level of specificity for particles **218-222** of particular properties/characteristics (e.g., size, shape, mass, charge). Successful particle travel through a longer channel **202** would require more balanced counteracting forces on the particle **218-222**, which means a smaller range of variability in the properties/characteristics (e.g., size, shape, mass, charge) of the particles **218-222** discharged. On the other hand, successful particle travel through a shorter channel **202** would require less balancing of the counteracting forces on the particle **218-222**, which means a greater range of variability in the properties/characteristics (e.g., size, shape, mass, charge) of the particles **218-222** discharged.

The sample **200** comprising classified particles **218-222** of a certain property is continuously discharged from channel **202** as a classified sample flow **212**. As described previously, the cross-flow **208** is able to rapidly change the temperature of the sample **200** and its particles **218-222** as well as remove any trace vapors **224** within the sample **200**. Thus, as shown in FIG. 2, the discharged classified sample flow **212** is at a desired temperature, vapor-less, and comprising particles **218-222** of a desired characteristic.

Furthermore in one or more embodiments, the invention is able to change the size of the particles **218-222** within a sample **200**. By changing the temperature of the sample **200**, the particles **218-222** within the sample **200** are rapidly and uniformly heated or cooled as they travel through the channel **202**. With the heating or cooling of the particles **218-222**, the size of the particles **218-222** may be respectively increased or decreased through thermal expansion or contraction. Thus, by controlling the predetermined temperature of the cross-flow **208**, the size of the discharged particles **218-222** may be controlled.

In further embodiments, the invention is able to change the chemical composition of the sample **200**. In addition to removing trace vapors **224** with a vapor-free cross-flow **208**, the fluid cross-flow **208** is able to remove and/or replace other compositions, vapors, and gases within a sample **200** depending on the composition of the replacement cross-flow **208**. Moreover, volatile particles **218-222** or components within the sample **200** may be evaporated from the sample by heating the sample **200** with a predetermined cross-flow temperature and/or removing vapors within the sample **200**, thereby decreasing in size particles **218-222**. Additionally, particles **218-222** may be increased in size if the replacement cross-flow **208** is composed of vapors that can condense onto particles **218-222** and the temperature of cross-flow **208** does not prevent these additional vapors from condensing onto particles **218-222**. The composition of a sample **200** may be finely controlled due to the different evaporation or condensation rates of the particles or components. If certain volatile compounds are desired in the classified sample flow **212**, the cross-flow **208** will contain these compounds in the desired concentrations. These concentrations can be set at a level to condense onto and grow particles **218-222**, or at a level to cause no change in the size of particles **218-222** and maintain the particle size after exiting the invention in the classified sample flow **212**.

The cross-flow **208** exiting through wall **204** or the sample flow **212** exiting the channel **202** may be analyzed or scanned continuously to determine particle property/characteristic (e.g., size, mass, charge) distributions. For example, knowledge of the particle size dependence for migration velocity or mobility and the strength of the cross-flow **208** and the imposed field would enable a determination of the particle size distributions.

To allow even larger flows, multiple channels **202** may be arranged in parallel, with a single cross-flow **208** passing through the successive channels **202**. In the case of electrophoretic migration, the electric potential on successive walls may be alternated, which would enable large volumetric flows to be separated without having to resort to unreasonably high voltages.

In addition, if the particles **218** and **222** are allowed to migrate through the walls **204** or **206**, provision may be taken to remove the particles **218** and **222** from the cross flow **208** so that the cross-flow **208** can be re-circulated. Such provisions may include filtration of the cross-flow **208** after it exits the channel **202**.

Details of Changing Sample Properties with a Radial Opposed Migration Aerosol Classifier (ROMAC)

In one or more embodiments of the invention, a radial opposed migration classifier (ROMAC) is used to change the properties of a sample. FIG. 3 is an illustrative diagram of how a sample 300 would traverse a ROMAC 302.

ROMAC 302 has an inlet port 304 and outlet port 306 for a sample 300, such as polydisperse, positively charged aerosol, and an inlet port 308 and outlet port 310 for a vapor-free cross-flow 312. The aerosol inlet port 304 of the ROMAC 302 would receive the sample 300, which would enter a flow distributor 314 ("racetrack"). In one or more embodiments, the sample 300 enters the flow distributor 314 tangentially. Due to the pressure difference between the racetrack 314 and the sample outlet 306, the sample 300 will be uniformly and radially drawn toward the center outlet port 306 through a narrow knife edge gap 316. After passing through the narrow knife edge gap 316, the sample 300 is now in the classification region 318, where only the particles that are balanced by both the drag and imposed field forces imparted on them will successfully traverse the classification region 318 and exit the ROMAC 302 through the central outlet port 306.

The aerosol inlet port 304 may be open to ambient fluid or connected to an apparatus that would provide the sample, such as a reaction chamber, electrospray ionization chamber, or nebulizer. The aerosol outlet port 306 may be connected to an apparatus that would provide negative pressure, such as a condensation nuclei counter pulling a vacuum. The cross-flow inlet port 308 may be connected to an apparatus that would provide vapor-free clean air at a controlled temperature and flow rate, while the cross-flow outlet port 310 may be connected to a vacuum that would result in a matched flow rate to the cross-flow inlet. In one or more embodiments, the upper plate 320 of the classification region is at electrical ground voltage, while the bottom plate 322 of the classification region is at a high positive voltage.

FIG. 4 shows a perspective view of a 2-plane sectional cut of an assembled ROMAC system 400 in accordance with one or more embodiments of the invention. A top lid 410, a bottom lid 428, and a side case 418 form an outer enclosure for the system 400.

A classification region, similar to the channel 202 illustrated in FIG. 2 and channel 318 illustrated in FIG. 3, is created by a knife edge top 402, knife edge bottom 404, variable gap spacer 406, bottom base 408, and conductive, porous screens (not shown) stretched across top screen holder 416 and bottom screen holder 420. The thickness dimension of variable gap spacer 406 may be adjusted to change the space between the knife edge top 402 and bottom base 408. A top screen holder 416 and a bottom screen holder 420 are used to hold respective top and bottom permeable walls, such as stretched stainless steel mesh (not shown). A top frit 414 and bottom frit 422 serve to laminarize the cross-flow before it enters the classification region. The top frit 414 is held in place and may be positionally adjusted within the system 400 by a threaded frit spacer 412. Similarly, bottom frit 422 is held in place and may be positionally adjusted within the system 400 by a bottom frit spacer 424.

Additionally, the top frit 414, threaded frit spacer 412, and top lid 410 all include central openings 434, 436, and 438 for a single outlet tube (not shown) to pass through the respective central openings 434, 436, and 438 and rest on a screen stretched across top screen holder 416. The single outlet tube is connected to the classification region and provides a negative pressure that allows particles that are balanced by both the drag and imposed field forces to be discharged from the system 400 through the single outlet tube (not shown).

A flow distributor 430 includes a narrowing gap 432, similar to the narrow knife gap 316 illustrated in FIG. 3, which leads to the classification region. The narrowing gap 432 is created by the knife edge top 402 and knife edge bottom 404. In one or more embodiments, the sample is introduced tangentially into the flow distributor 430.

In one or more embodiments, top lid 410, knife edge top 402, knife edge bottom 404, top screen holder 416, top frit 414, threaded frit spacer 412, and the outlet tube (not shown) that passes through central openings 434-438 and rests on a conductive screen (not shown) stretched across top screen holder 416 are at electrical ground. Side case 418, variable gap spacer 406, and bottom lid 428 are electrical insulators. Bottom base 408, bottom screen holder 420, bottom frit 422, bottom frit spacer 424, variable gap compensator spacer 426, and a conductive screen (not shown) stretched across bottom screen holder 420 are at a non-ground electrical potential. A post 446 extends from variable gap compensator spacer 426 through bottom lid 428 serves as a means to apply a non-ground electric potential.

#### Illustrative Models and Simulations

As illustrative examples, the invention was modeled as a radially symmetric space similar to the ROMAC 302 depicted in FIG. 3 in COMSOL<sup>TM</sup> Multiphysics 4.1<sup>TM</sup> to obtain values for fluid properties, fluid flows, electric fields, and concentrations of dilute vapors in the region of the invention through which aerosol particles will flow through. The electric potential solution is shown in FIG. 5, the combined sample and cross-flow fluid velocity magnitude solution is shown in FIG. 6, the fluid temperature solution is shown in FIG. 7, and the dilute species vapor concentration is shown in FIG. 8. All four of the figures were modeled at an aerosol flow rate of 1 lpm and a cross-flow rate of 2 lpm, with a cross-flow temperature of 320 K, an incoming aerosol vapor concentration of 5.1 mol/m<sup>3</sup>, and an incoming sample vapor diffusivity of 5.8 × 10<sup>-6</sup> m<sup>2</sup>/s.

FIG. 7 demonstrates that the invention as modeled sufficiently exchanges the gas such that it is rapidly and uniformly heated to the desired temperature (in this case, 320 K) by the time the particles reach the aerosol outlet.

FIG. 8 demonstrates that the invention as modeled sufficiently removes the trace vapors present in the original incoming aerosol gas, such that by the time the particles reach the aerosol outlet, they are surrounded in vapor-free fluid.

The COMSOL<sup>TM</sup> solutions were then used as inputs for a MATLAB<sup>TM</sup> script developed to simulate the trajectories of particles of a particular size when released into the invention. The trajectories used inputs of fluid velocity, density, viscosity, temperature, and electric potential to simulate the movement of particles, their change in size, and the change in chemical composition in finite time steps. In addition, diffusional movement of the particles was simulated as well.

FIG. 9 shows a simulation of 100 nm particles composed of three organic substances with different volatilities traversing the invention with the porous, conductive walls having a voltage difference that was predicted to yield the maximum transmission of particles through the classification region. The aerosol flowrate was set at 0.1 lpm, cross-flow rate at 0.3 lpm, temperature at 320 K, and voltage at 490 V. The type of simulation illustrated in FIG. 9 was repeated at various voltages to obtain a predicted transfer function (FIG. 10) for the invention. The results demonstrate the feasibility of the invention, as the numerical simulations were executed with well-reputed software and relied on the established knowledge of mechanisms of particle movement.

FIG. 10 illustrates a simulated transfer function of 100 nm particles traversing through the invention at an aerosol flow

## US 9,138,663 B2

## 11

rate of 0.1 lpm, cross-flow rate of 0.3 lpm, and temperature at 320 K. The vertical line indicates the theoretical voltage that would result in a balance of the drag force and electric force imparted on the particles (which would result in maximum transmission, i.e. 100% transmission of the particles). The peak of the simulated transfer function is in very good agreement with the theoretical voltage for 100% transmission, but is slightly shifted to the left, since particles were slowly evaporating and shrinking as they were traversing the classification region, due to the heat and gas exchanging functions of the instrument.

FIG. 11 illustrates the simulated diameter change of each individual 100 nm particle, showing each particle's size evolution as it traverses the invention. The aerosol flow rate is set at 0.1 lpm, cross-flow rate at 0.3 lpm, temperature at 320 K, and voltage at 470 V.

FIG. 12 illustrates the simulated chemical composition change of 100 nm particles traversing through the invention an aerosol flow rate of 0.1 lpm, cross-flow rate of 0.3 lpm, temperature of 320 K, and voltage of 470 V. Initial chemical composition is 33% of each of 3 species 1202, 1204, and 1206. 1202 is the most volatile species, followed by 1204, followed by 1206 being the least volatile species. The chemical composition change of each particle is shown as different components of the particles evaporate at different rates due to the heat and vapor removal functions of the invention.

## CONCLUSION

The foregoing description of the preferred embodiment of the invention has been presented for the purposes of illustration and description. It is not intended to be exhaustive or to limit the invention to the precise form disclosed. Many modifications and variations are possible in light of the above teaching. It is intended that the scope of the invention be limited not by this detailed description, but rather by the claims appended hereto. All publications, patents, and patent applications cited herein are hereby incorporated by reference in their entirety for all purposes.

## REFERENCES

- [1] Liu, B., et al., Aerosol Mobility Chromatograph-New Detector for Sulfuric-Acid Aerosols. *Atmos Environ*, 1978, 12(1-3): p. 99-104.
- [2] Rader, D. and P. McMurry, Application of the Tandem Differential Mobility Analyzer to Studies of Droplet Growth or Evaporation. *J Aerosol Sci*, 1986, 17(5): p. 771-787.
- [3] Flagan, R., Cross-flow differential migration classifier. U.S. Pat. No. 6,905,029.
- [4] Flagan, R., Opposed migration aerosol classifier (OMAC), *Aerosol Science and Technology*, 2004, 38(9): p. 890.
- [5] Downard, A., J. Dama, and R. Flagan, An Asymptotic Analysis of Differential Electrical Mobility Classifiers, *Aerosol Science and Technology*, 2011, p. 717-729.
- [6] Knutson, E. and K. Whitby, Aerosol classification by electric mobility: apparatus, theory, and applications, *J Aerosol Sci*, 1975, p. 443-451.
- [7] Tammet, H., Symmetric Inclined Grid Mobility Analyzer for the Measurement of Charged Clusters and Fine Nanoparticles in Atmospheric Air, *Aerosol Science and Technology*, 2011, p. 468-479.

What is claimed is:

1. A method for changing a property of a sample comprising:

## 12

introducing a sample, comprising one or more particles suspended within a sample fluid, through a channel, wherein the channel comprises two walls that are permeable to a flow of fluid;

introducing a fluid cross-flow of a predetermined chemical composition and at a predetermined temperature to the channel through one of the permeable walls, wherein the fluid cross-flow flows at a first velocity and exits in a first direction through the other permeable wall;

applying an imposed field on the one or more particles in a second direction counter to the first direction of the fluid cross-flow, wherein the imposed field causes the one or more particles to migrate at a second velocity opposite and/or equal to the first velocity of the fluid cross-flow; and

continuously discharging the particles that travel through the channel, wherein the particles that travel through the channel are discharged in a fluid of the predetermined chemical composition and at the predetermined temperature of the fluid cross-flow, and wherein a size and/or chemical composition of the one or more particles of the sample is changed by the predetermined chemical composition and/or predetermined temperature of the fluid cross-flow while the one or more particles travel through the channel.

2. The method of claim 1, wherein the sample fluid is substantially replaced by the fluid cross-flow as the sample flows through the channel, whereby the discharged particles that travel through the channel are suspended within the fluid cross-flow.

3. The method of claim 1, wherein the fluid cross-flow removes a trace vapor from the sample.

4. The method of claim 1, wherein a chemical composition of the sample is changed while the one or more particles of the sample travel through the channel.

5. The method of claim 1, further comprising charging the one or more particles in the sample, wherein the imposed field is an electric field.

6. The method of claim 1, further comprising analyzing or scanning the discharged particles that travel through the channel to determine a change in a property of the discharged particles resulting from changing a property of the fluid through which the particles travel.

7. The method of claim 6, wherein a differential mobility analyzer is used to scan the discharged particles.

8. The method of claim 1, further comprising classifying the discharged particles that travel through the channel based on a property of the discharged particles.

9. The method of claim 8, wherein the property of the discharged particles is a size, mass or charge of the discharged particles.

10. An opposed migration classifier comprising:

a channel through which passes a sample comprising one or more particles suspended within a sample fluid, wherein the channel comprises two walls that are permeable to a flow of fluid;

a fluid cross-flow of a predetermined chemical composition and at a predetermined temperature that enters the channel through one of the permeable walls, wherein the fluid cross-flow flows at a first velocity and exits in a first direction through the other permeable wall;

an imposed field that is applied on the one or more particles in a second direction counter to the first direction of the fluid cross-flow, wherein the imposed field causes the one or more of the particles to migrate at a second velocity opposite and/or equal to a first velocity of the fluid cross-flow; and

## US 9,138,663 B2

## 13

wherein the particles that travel through the channel are discharged in a fluid of the predetermined chemical composition and at the predetermined temperature of the fluid cross-flow, and wherein a size and/or chemical composition of the one or more particles of the sample is changed by the predetermined chemical composition and/or predetermined temperature of the fluid cross-flow while the one or more particles travel through the channel.

11. The opposed migration classifier of claim 10, wherein the sample fluid is substantially replaced by the fluid cross-flow as the sample flows through the channel, whereby the discharged particles that travel through the channel are suspended within the fluid cross-flow.

12. The opposed migration classifier of claim 10, wherein the fluid cross-flow removes a trace vapor from the sample.

13. The opposed migration classifier of claim 10, wherein a chemical composition of the sample is changed while the one or more particles of the sample travel through the channel.

14. The opposed migration classifier of claim 10, wherein: the one or more particles in the sample is charged; and the imposed field is an electric field.

15. The opposed migration classifier of claim 10, wherein the discharged particles that travel through the channel are analyzed or scanned to determine a change in a property of the discharged particles resulting from a change in a property of the fluid through which the particles travel.

16. The opposed migration classifier of claim 15, wherein a differential mobility analyzer is used to scan the discharged particles.

17. The opposed migration classifier of claim 10, wherein the discharged particles that travel through the channel are classified based on a property of the discharged particles.

## 14

18. The opposed migration classifier of claim 17, wherein the property of the discharged particles is a size, mass or charge of the discharged particles.

19. A method for changing a property of one or more particles in a sample comprising:

introducing a sample, comprising one or more particles suspended within a sample fluid, through a channel, wherein the channel comprises two walls that are permeable to a flow of fluid;

introducing a fluid cross-flow of a predetermined chemical composition and/or at a predetermined temperature to the channel through one of the permeable walls, wherein the fluid cross-flow flows at a first velocity and exits in a first direction through the other permeable wall;

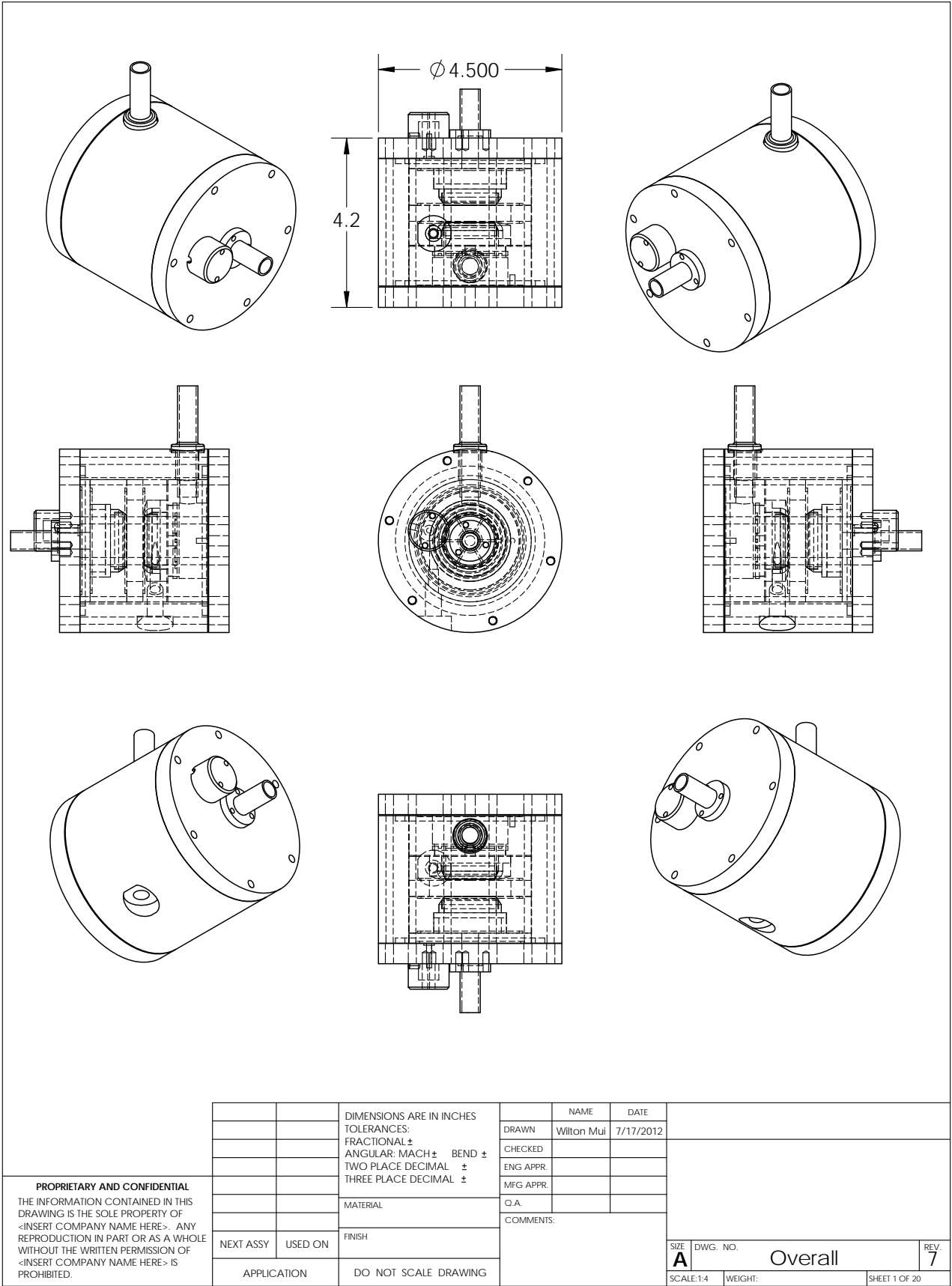
applying an imposed field on the one or more particles in a second direction counter to the first direction of the fluid cross-flow, wherein the imposed field causes the one or more particles to migrate at a second velocity opposite and/or equal to the first velocity of the fluid cross-flow; and

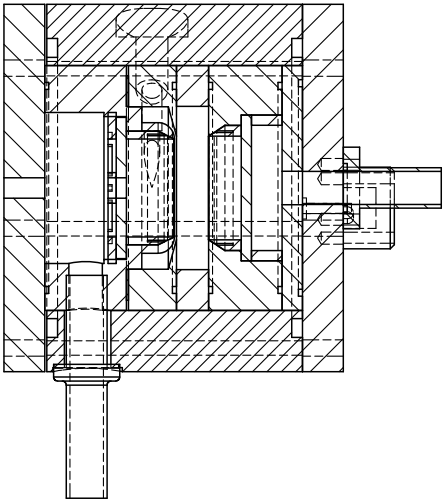
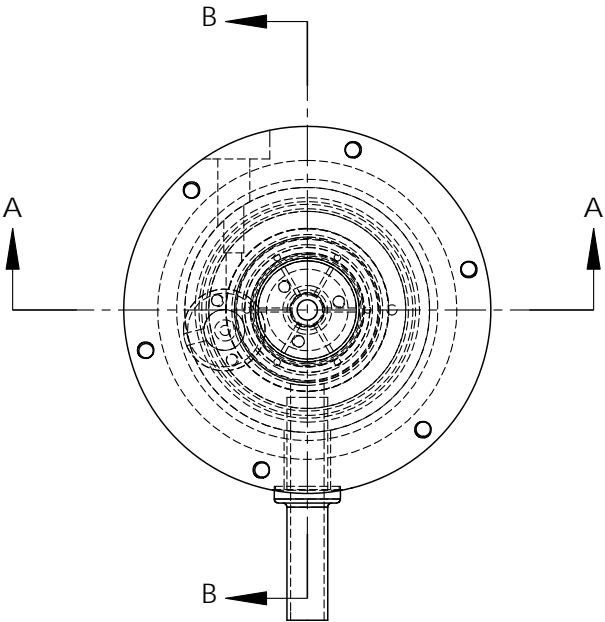
continuously discharging the particles that travel through the channel, wherein the particles that travel through the channel are discharged in a fluid of the predetermined chemical composition and at the predetermined temperature of the fluid cross-flow, and wherein a property of the one or more particles of the sample is changed by the predetermined chemical composition and/or predetermined temperature of the fluid cross-flow while the one or more particles travel through the channel.

20. The method of claim 19, wherein the property of the one or more particles is a size, mass or chemical composition of the discharged particles.

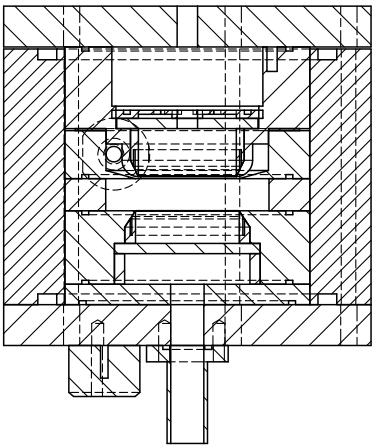
\* \* \* \* \*

*Appendix F***TECHNICAL DRAWINGS OF THE RADIAL OPPOSED  
MIGRATION ION AND AEROSOL CLASSIFIER (ROMIAC)**





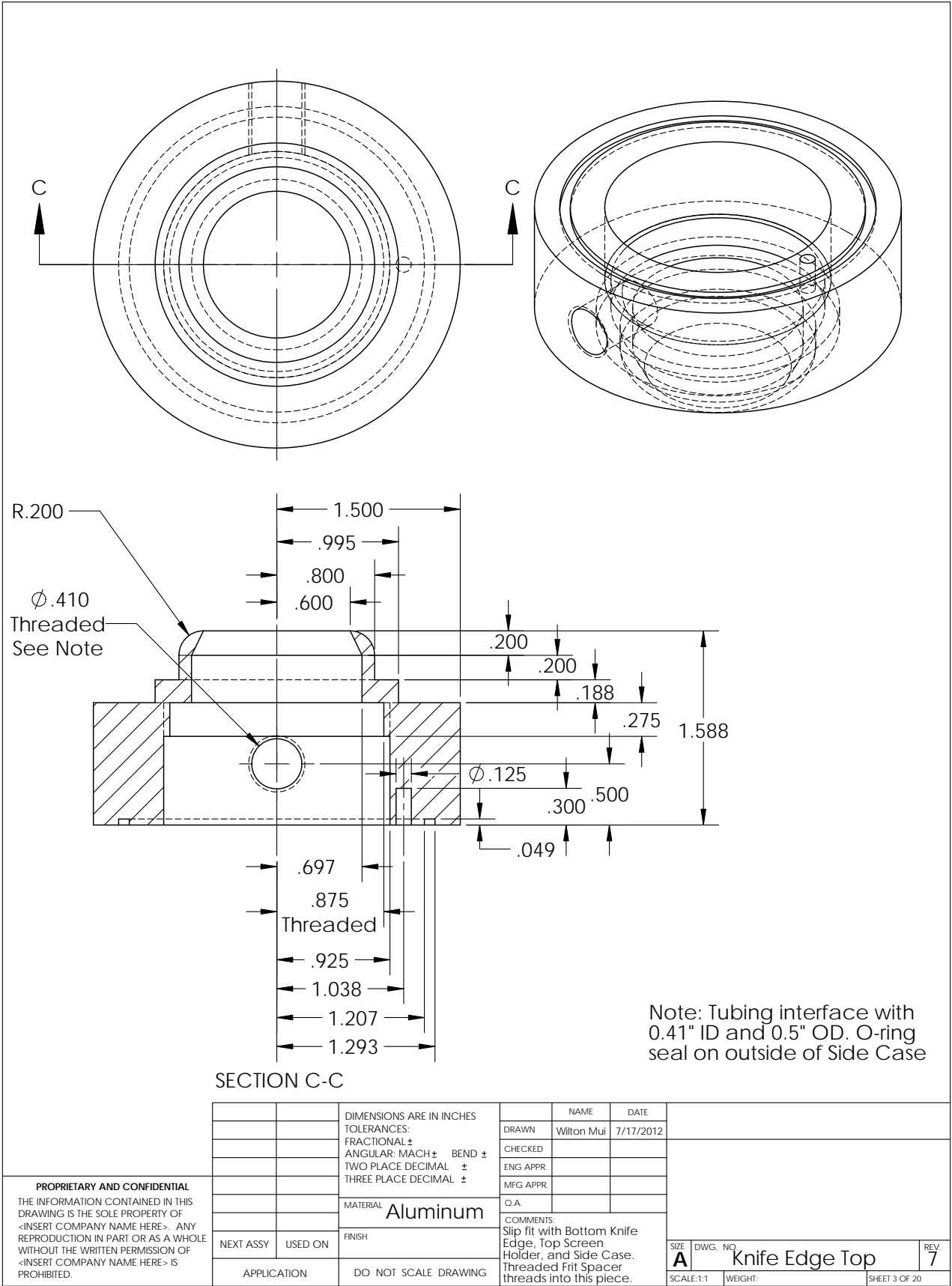
SECTION B-B  
SCALE 1 : 2

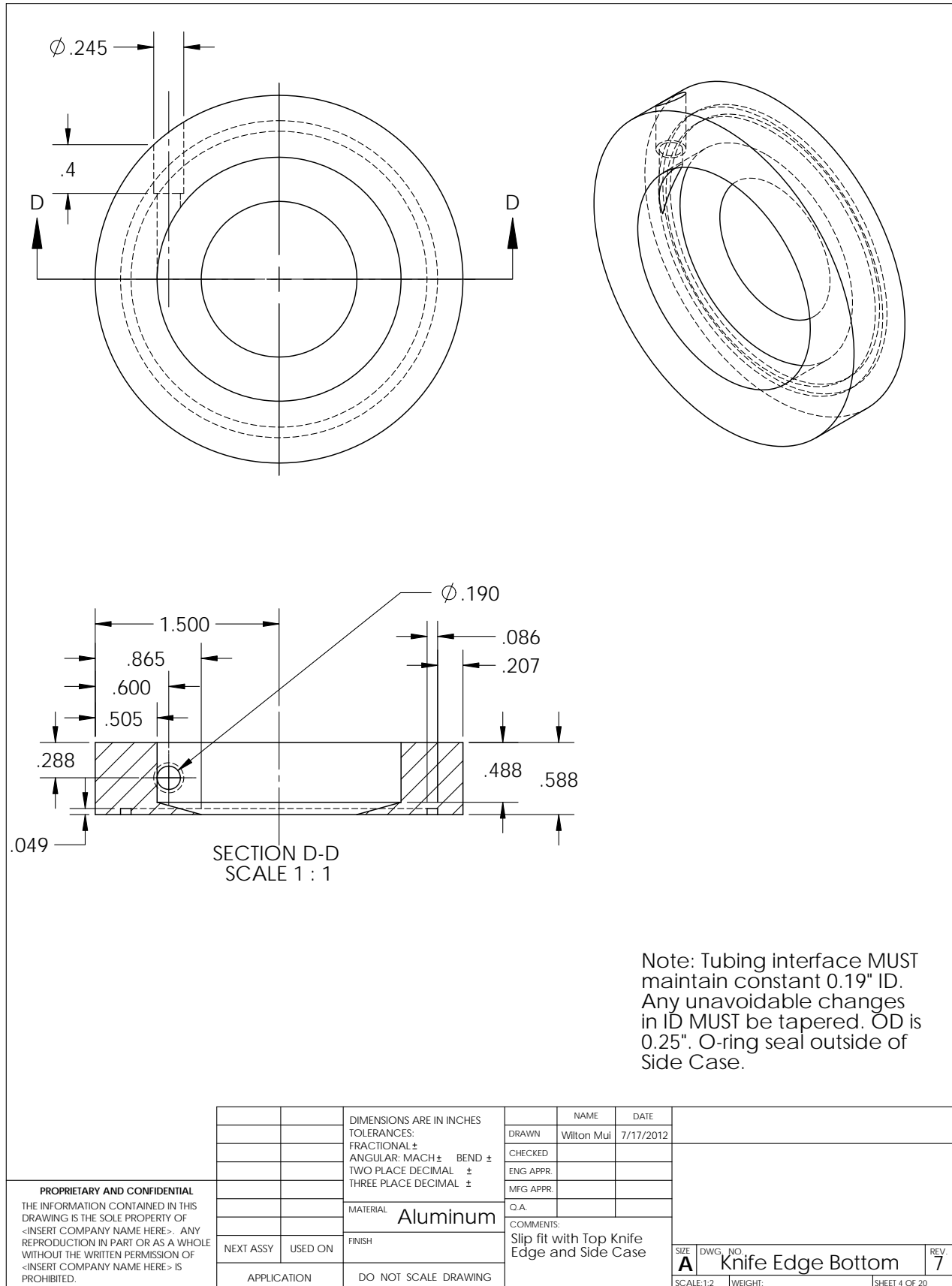


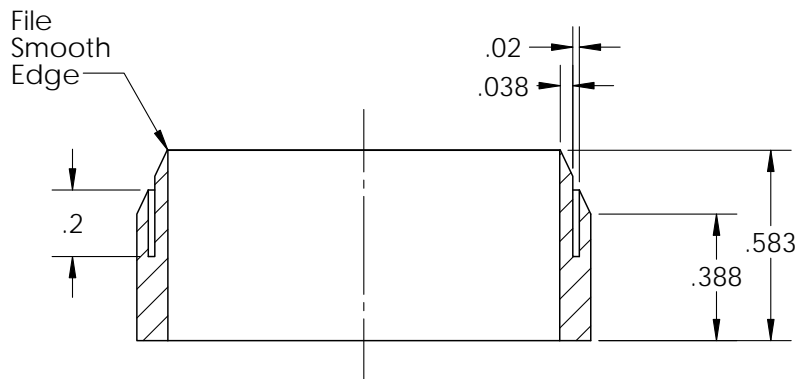
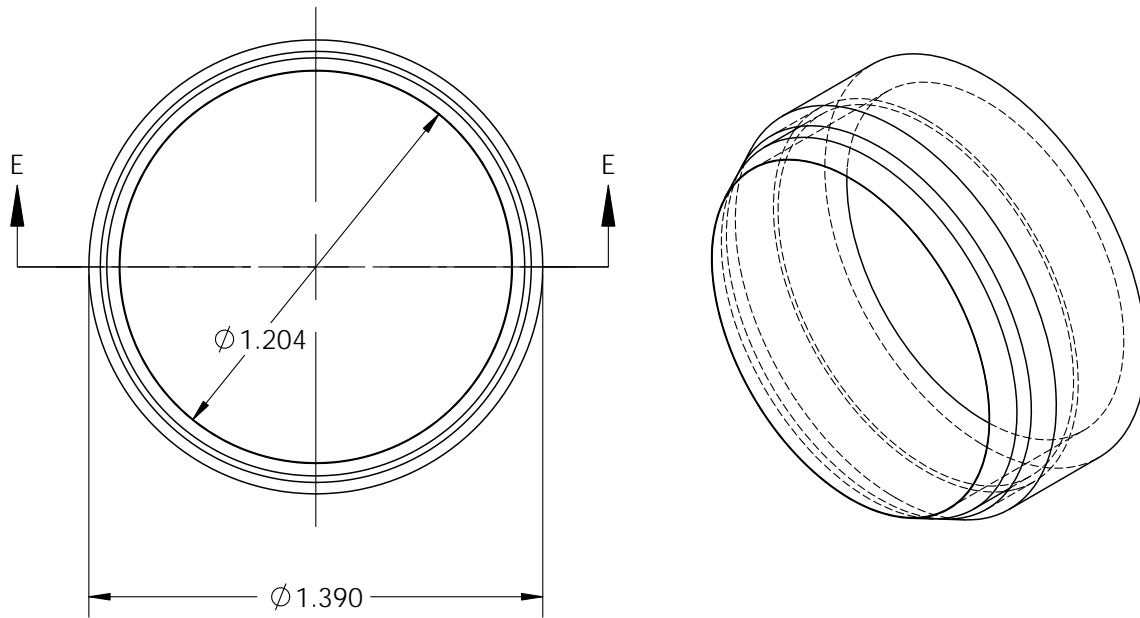
SECTION A-A  
SCALE 1 : 2

|  |           |                      |  |   |           |            |            |          |                  |      |               |
|--|-----------|----------------------|--|---|-----------|------------|------------|----------|------------------|------|---------------|
| <p><b>PROPRIETARY AND CONFIDENTIAL</b></p> <p>THE INFORMATION CONTAINED IN THIS DRAWING IS THE SOLE PROPERTY OF &lt;INSERT COMPANY NAME HERE&gt;. ANY REPRODUCTION IN PART OR AS A WHOLE WITHOUT THE WRITTEN PERMISSION OF &lt;INSERT COMPANY NAME HERE&gt; IS PROHIBITED.</p> |           |                      |  | <p>DIMENSIONS ARE IN INCHES</p> <p>TOLERANCES:</p> <p>FRACTIONAL ±</p> <p>ANGULAR: MACH ±    BEND ±</p> <p>TWO PLACE DECIMAL    ±</p> <p>THREE PLACE DECIMAL    ±</p> |           | NAME       | DATE       |          |                  |      |               |
|  |           |                      |  |   | DRAWN     | Wilton Mui | 7/17/2012  |          |                  |      |               |
|  |           |                      |  |   | CHECKED   |            |            |          |                  |      |               |
|  |           |                      |  |   | ENG APPR. |            |            |          |                  |      |               |
|  |           |                      |  |   | MFG APPR. |            |            |          |                  |      |               |
|  |           |                      |  |   | Q.A.      |            |            |          |                  |      |               |
|  |           |                      |  |   | COMMENTS: |            |            |          |                  |      |               |
|  | NEXT ASSY | USED ON              |  | FINISH  |           |            |            | SIZE     | DWG. NO.         | REV. |               |
| APPLICATION  |           | DO NOT SCALE DRAWING |  |   |           |            |            | <b>A</b> | Overall Sections |      | 7             |
|  |           |                      |  |   |           |            | SCALE: 1:4 |          | WEIGHT:          |      | SHEET 2 OF 20 |



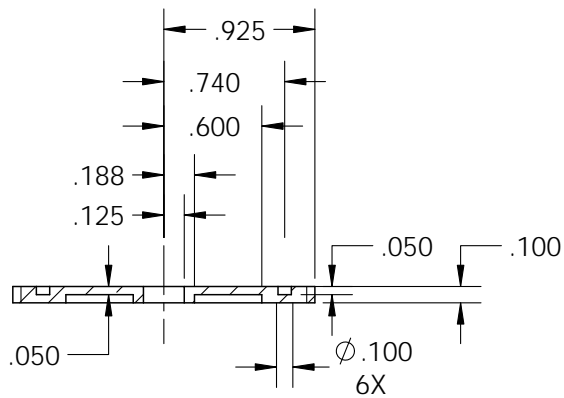
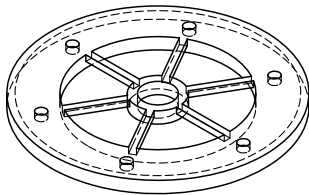
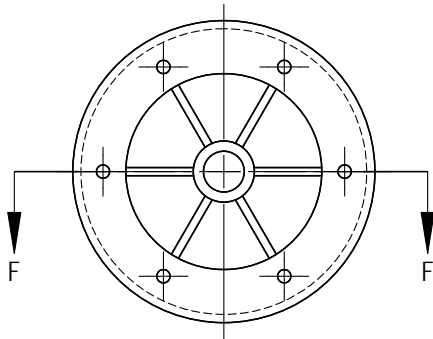






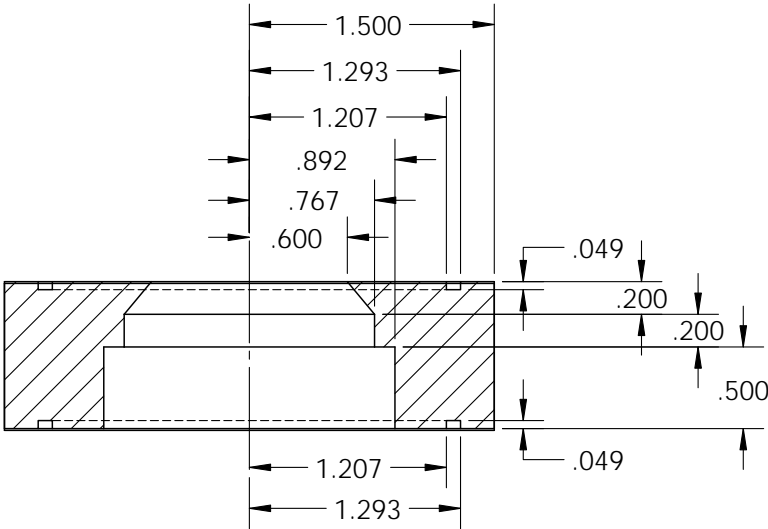
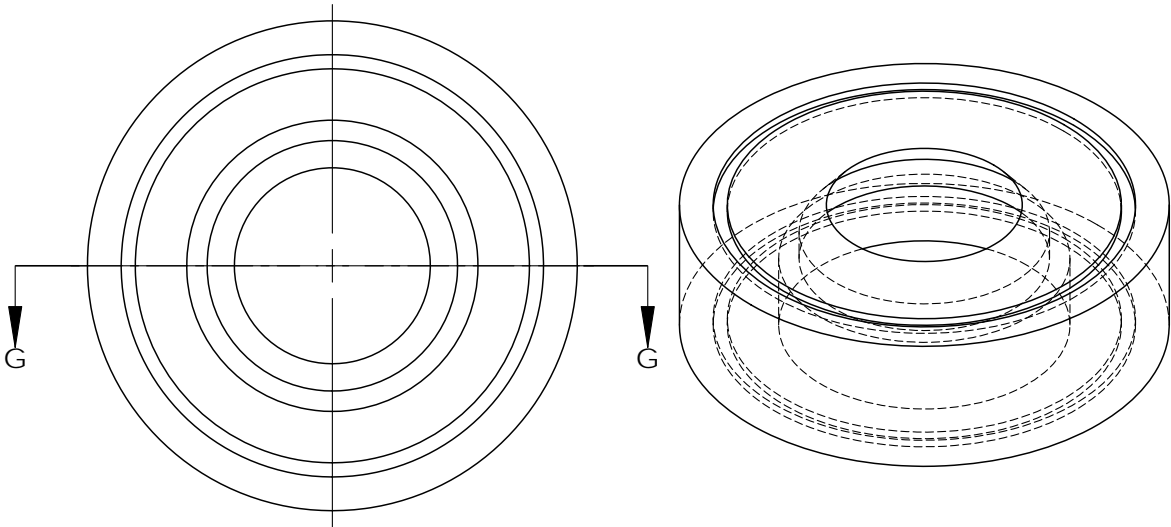
SECTION E-E  
SCALE 2 : 1

|   |  |                                     |  |   |  |   |                   |               |  |
|---|--|-------------------------------------|--|---|--|---|-------------------|---------------|--|
| <b>PROPRIETARY AND CONFIDENTIAL</b><br>THE INFORMATION CONTAINED IN THIS DRAWING IS THE SOLE PROPERTY OF <INSERT COMPANY NAME HERE>. ANY REPRODUCTION IN PART OR AS A WHOLE WITHOUT THE WRITTEN PERMISSION OF <INSERT COMPANY NAME HERE> IS PROHIBITED. |  |                                     |  | DIMENSIONS ARE IN INCHES<br>TOLERANCES:<br>FRACTIONAL ±<br>ANGULAR: MACH ± BEND ±<br>TWO PLACE DECIMAL ±<br>THREE PLACE DECIMAL ± |  | NAME<br>Wilton Mui                        | DATE<br>7/17/2012 |               |  |
|   |  |                                     |  | MATERIAL<br>Aluminum  |  | CHECKED<br>ENG APPR.<br>MFG APPR.<br>Q.A. |                   |               |  |
|   |  |                                     |  | FINISH  |  | COMMENTS:<br>Slip fit with Knife Edge Top |                   |               |  |
|   |  |                                     |  |   |  |   |                   |               |  |
|   |  |                                     |  |   |  |   |                   |               |  |
| NEXT ASSY<br>USED ON  |  | APPLICATION<br>DO NOT SCALE DRAWING |  | SIZE<br>A   |  | DWG. NO.<br>Top Screen Holder             |                   | REV.<br>7     |  |
|   |  |                                     |  | SCALE: 1:1  |  | WEIGHT:                                   |                   | SHEET 5 OF 20 |  |



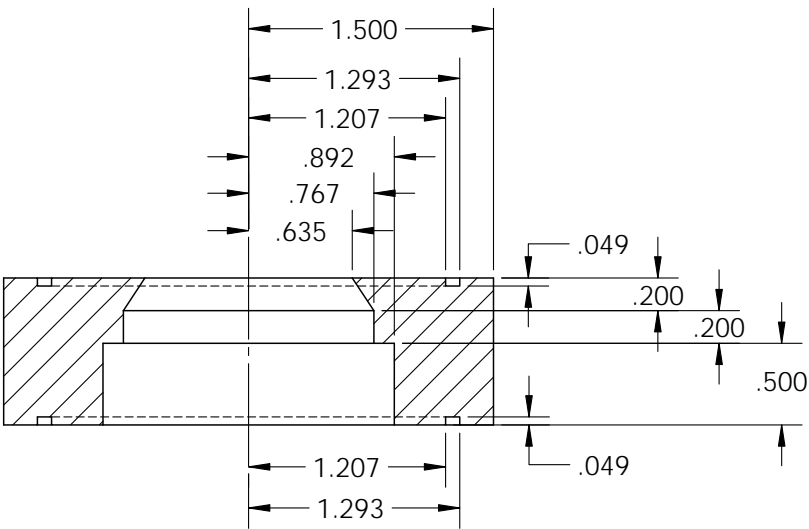
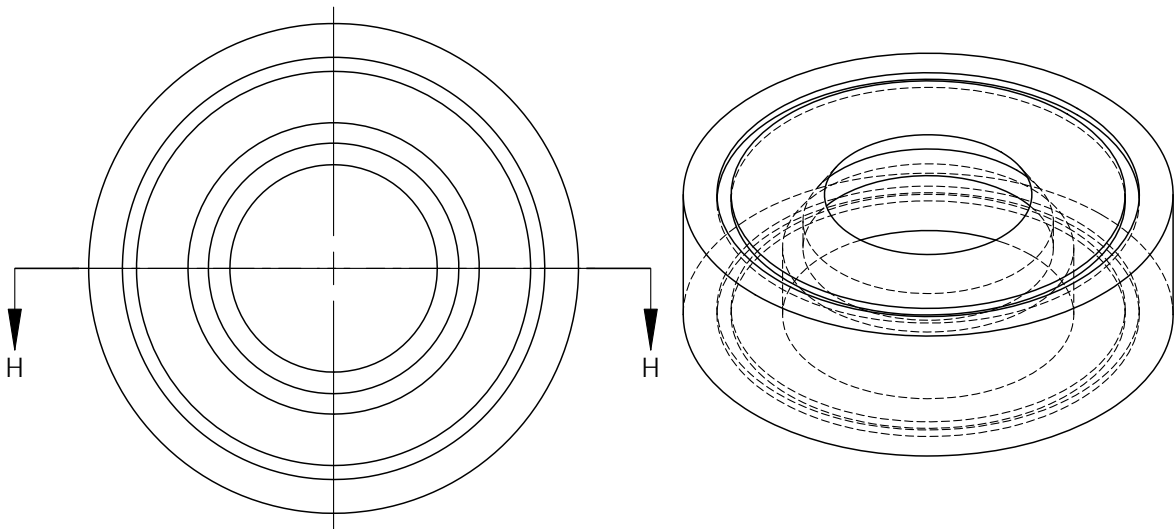
SECTION F-F

|  |  |             |          |  |           |            |                                |                      |         |               |
|--|--|-------------|----------|--|-----------|------------|--------------------------------|----------------------|---------|---------------|
| <p><b>PROPRIETARY AND CONFIDENTIAL</b></p> <p>THE INFORMATION CONTAINED IN THIS DRAWING IS THE SOLE PROPERTY OF &lt;INSERT COMPANY NAME HERE&gt;. ANY REPRODUCTION IN PART OR AS A WHOLE WITHOUT THE WRITTEN PERMISSION OF &lt;INSERT COMPANY NAME HERE&gt; IS PROHIBITED.</p> |  |             |          | DIMENSIONS ARE IN INCHES<br>TOLERANCES:<br>FRACTIONAL ±<br>ANGULAR: MACH ±    BEND ±<br>TWO PLACE DECIMAL ±<br>THREE PLACE DECIMAL ± |           | NAME       | DATE                           |                      |         |               |
|  |  |             |          |  | DRAWN     | Wilton Mui | 7/17/2012                      |                      |         |               |
|  |  |             |          |  | CHECKED   |            |                                |                      |         |               |
|  |  |             |          |  | ENG APPR. |            |                                |                      |         |               |
|  |  |             |          |  | MFG APPR. |            |                                |                      |         |               |
|  |  |             |          |  | Q.A.      |            |                                |                      |         |               |
|  |  |             |          | MATERIAL   | COMMENTS: |            | Threads into<br>Top Knife Edge |                      |         |               |
|  |  |             | Aluminum |  |           |            |                                |                      |         |               |
|  |  | NEXT ASSY   | USED ON  | FINISH   |           |            |                                |                      |         |               |
|  |  | APPLICATION |          | DO NOT SCALE DRAWING   |           |            |                                |                      |         |               |
|  |  |             |          |  |           |            | SIZE                           | DWG. NO.             | REV.    |               |
|  |  |             |          |  |           |            | A                              | Threaded Frit Spacer |         | 7             |
|  |  |             |          |  |           |            | SCALE: 1:1                     |                      | WEIGHT: | SHEET 6 OF 20 |



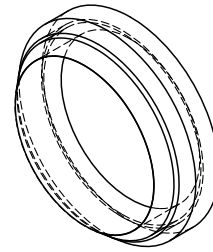
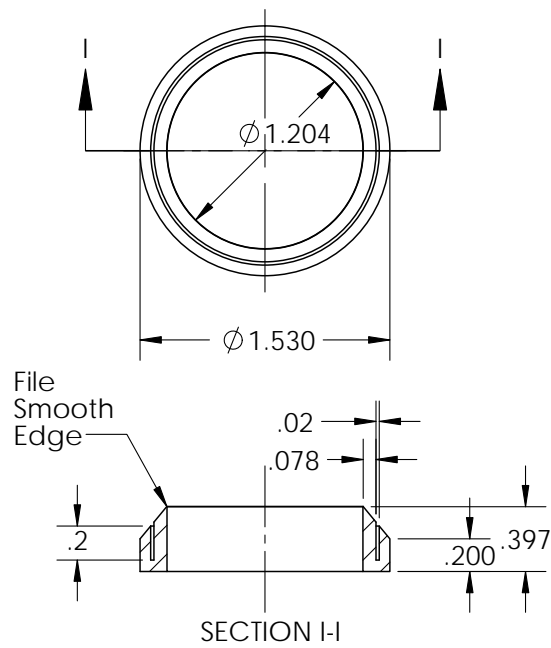
SECTION G-G

|  |         |  |  |   |                      |            |   |  |  |
|--|---------|--|--|---|----------------------|------------|---|--|--|
| <p><b>PROPRIETARY AND CONFIDENTIAL</b></p> <p>THE INFORMATION CONTAINED IN THIS DRAWING IS THE SOLE PROPERTY OF &lt;INSERT COMPANY NAME HERE&gt;. ANY REPRODUCTION IN PART OR AS A WHOLE WITHOUT THE WRITTEN PERMISSION OF &lt;INSERT COMPANY NAME HERE&gt; IS PROHIBITED.</p> |         |  |  | <p>DIMENSIONS ARE IN INCHES</p> <p>TOLERANCES:</p> <p>FRACTIONAL ±</p> <p>ANGULAR: MACH ±    BEND ±</p> <p>TWO PLACE DECIMAL   ±</p> <p>THREE PLACE DECIMAL   ±</p> |                      | NAME       | DATE  | <p>Slip fit with Bottom Screen Holder 1, Bottom Frit Spacer, Bottom Frit, and Side Case.</p> <p><b>A</b>    DWG. NO.    <b>Bottom Base 1</b>    REV.    <b>7</b></p> <p>SCALE: 1:1    WEIGHT:    SHEET 7 OF 20</p> |  |
|  |         |  |  |   | DRAWN                | Wilton Mui | 7/17/2012   |  |  |
|  |         |  |  |   | CHECKED              |            |   |  |  |
|  |         |  |  |   | ENG APPR.            |            |   |  |  |
|  |         |  |  |   | MFG APPR.            |            |   |  |  |
|  |         |  |  |   | Q.A.                 |            |   |  |  |
|  |         |  |  | MATERIAL  | Aluminum             |            | <p>COMMENTS:</p> <p>Slip fit with Bottom Screen Holder 1, Bottom Frit Spacer, Bottom Frit, and Side Case.</p> |  |  |
|  |         |  |  | FINISH  |                      |            |   |  |  |
| NEXT ASSY  | USED ON |  |  |   |                      |            |   |  |  |
|  |         |  |  | APPLICATION   | DO NOT SCALE DRAWING |            |   |  |  |

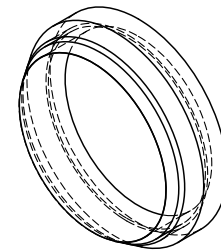
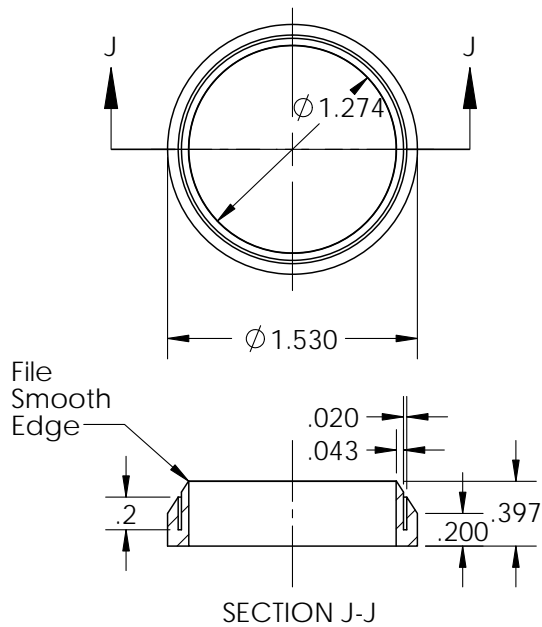


SECTION H-H

|  |  |                      |          |   |           |            |               |               |   |
|--|--|----------------------|----------|---|-----------|------------|---------------|---------------|---|
| <p><b>PROPRIETARY AND CONFIDENTIAL</b></p> <p>THE INFORMATION CONTAINED IN THIS DRAWING IS THE SOLE PROPERTY OF &lt;INSERT COMPANY NAME HERE&gt;. ANY REPRODUCTION IN PART OR AS A WHOLE WITHOUT THE WRITTEN PERMISSION OF &lt;INSERT COMPANY NAME HERE&gt; IS PROHIBITED.</p> |  |                      |          | <p>DIMENSIONS ARE IN INCHES</p> <p>TOLERANCES:</p> <p>FRACTIONAL ±</p> <p>ANGULAR: MACH ±    BEND ±</p> <p>TWO PLACE DECIMAL    ±</p> <p>THREE PLACE DECIMAL    ±</p> |           | NAME       | DATE          |               |   |
|  |  |                      |          |   | DRAWN     | Wilton Mui | 7/17/2012     |               |   |
|  |  |                      |          |   | CHECKED   |            |               |               |   |
|  |  |                      |          |   | ENG APPR. |            |               |               |   |
|  |  |                      |          |   | MFG APPR. |            |               |               |   |
|  |  |                      |          |   | Q.A.      |            |               |               |   |
|  |  |                      |          | MATERIAL  | COMMENTS: |            |               |               |   |
|  |  |                      | Aluminum |   |           |            |               |               |   |
|  |  |                      | FINISH   |   |           |            |               |               |   |
| NEXT ASSY  |  | USED ON              |          | Slip fit with Bottom Screen Holder 2, Bottom Frit Spacer, Bottom Frit, and Side Case.   |           | SIZE       | DWG. NO       | REV.          |   |
| APPLICATION  |  | DO NOT SCALE DRAWING |          |   |           | A          | Bottom Base 2 |               | 7 |
|  |  |                      |          |   |           | SCALE:1:1  | WEIGHT:       | SHEET 8 OF 20 |   |

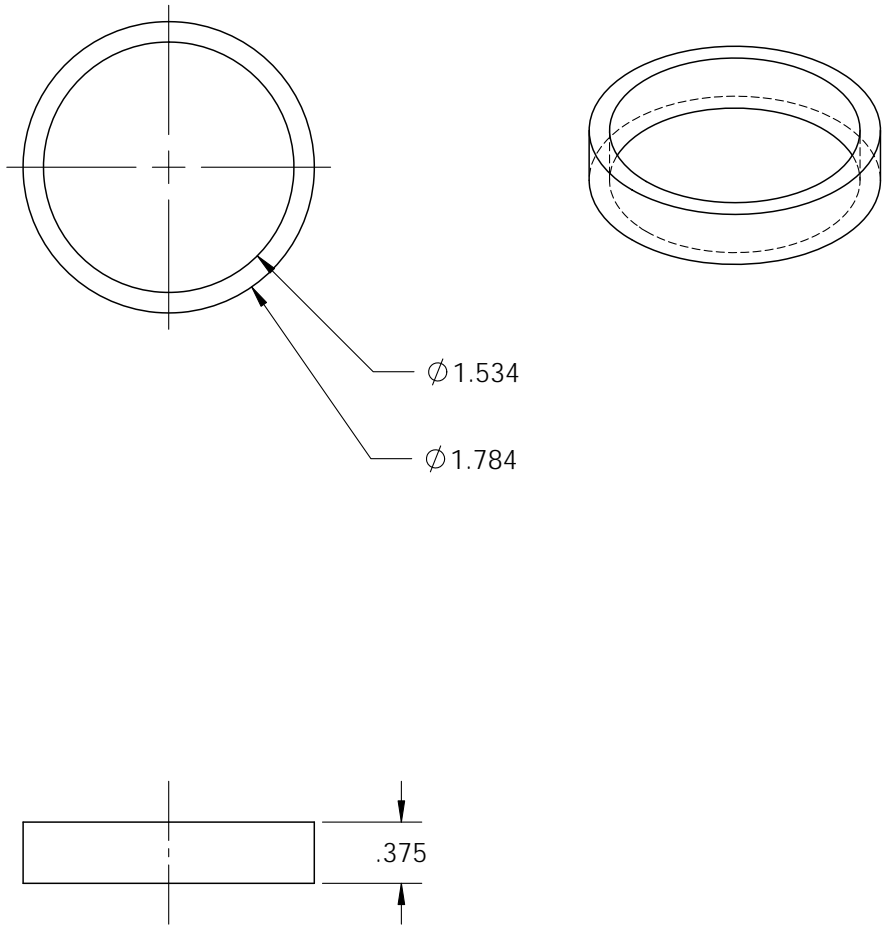


Bottom Screen Holder 1



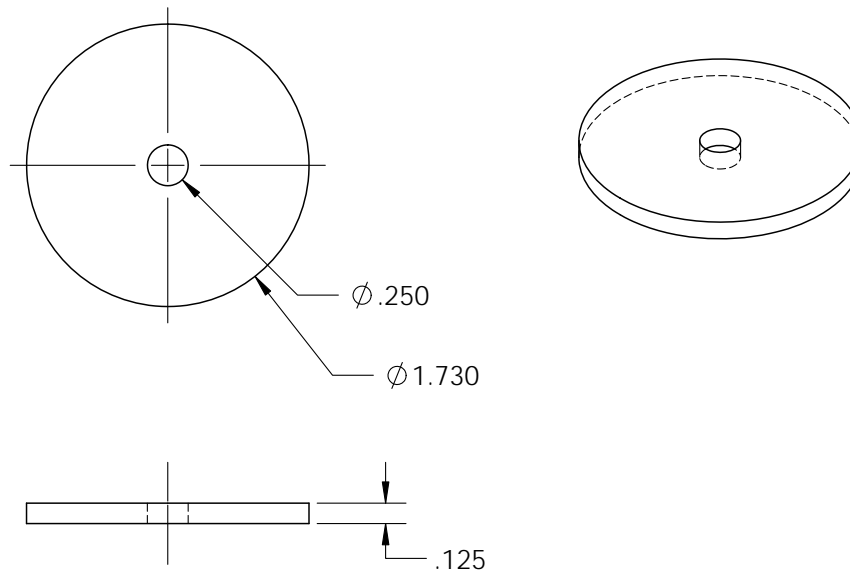
Bottom Screen Holder 2

|   |  |                      |  |                                  |  |  |  |   |  |
|---|--|----------------------|--|----------------------------------|--|--|--|---|--|
| <b>PROPRIETARY AND CONFIDENTIAL</b><br>THE INFORMATION CONTAINED IN THIS DRAWING IS THE SOLE PROPERTY OF <INSERT COMPANY NAME HERE>. ANY REPRODUCTION IN PART OR AS A WHOLE WITHOUT THE WRITTEN PERMISSION OF <INSERT COMPANY NAME HERE> IS PROHIBITED. |  |                      |  | DIMENSIONS ARE IN INCHES         |  | NAME                                       |  | DATE  |  |
|   |  |                      |  | TOLERANCES:                      |  | DRAWN                                      |  | Wilton Mui 7/17/2012                            |  |
|   |  |                      |  | FRACTIONAL ±                     |  | CHECKED                                    |  |   |  |
|   |  |                      |  | ANGULAR: MACH ± BEND ±           |  | ENG APPR                                   |  |   |  |
|   |  |                      |  | TWO PLACE DECIMAL ±              |  | MFG APPR                                   |  |   |  |
|   |  |                      |  | THREE PLACE DECIMAL ±            |  | Q.A.                                       |  |   |  |
|   |  | MATERIAL             |  | Aluminum                         |  | COMMENTS:                                  |  |   |  |
| NEXT ASSY   |  | USED ON              |  | FINISH                           |  | Slip fit with<br>respective<br>Bottom Base |  | SIZE DWG. NO.<br><b>A</b> Bottom Screen Holders |  |
| APPLICATION   |  | DO NOT SCALE DRAWING |  | SCALE: 1:1 WEIGHT: SHEET 9 OF 20 |  |  |  |   |  |
|   |  |                      |  |                                  |  |  |  | REV. 7  |  |

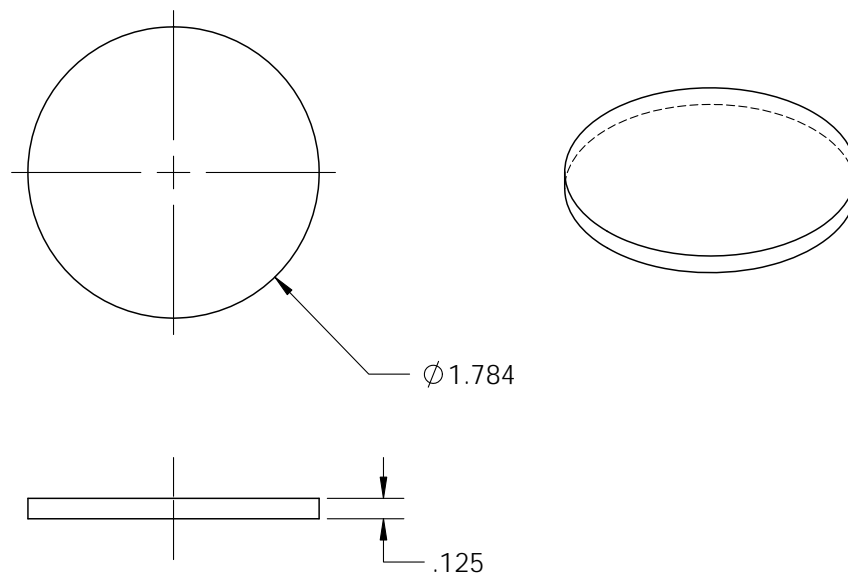


|   |           |         |   |   |            |            |                  |                                |                |
|---|-----------|---------|---|---|------------|------------|------------------|--------------------------------|----------------|
| <b>PROPRIETARY AND CONFIDENTIAL</b><br>THE INFORMATION CONTAINED IN THIS DRAWING IS THE SOLE PROPERTY OF <INSERT COMPANY NAME HERE>. ANY REPRODUCTION IN PART OR AS A WHOLE WITHOUT THE WRITTEN PERMISSION OF <INSERT COMPANY NAME HERE> IS PROHIBITED. |           |         | DIMENSIONS ARE IN INCHES<br>TOLERANCES:<br>FRACTIONAL ±<br>ANGULAR: MACH ± BEND ±<br>TWO PLACE DECIMAL ±<br>THREE PLACE DECIMAL ± |   | NAME       | DATE       |                  |                                |                |
|   |           |         |   | DRAWN                                   | Wilton Mui | 7/17/2012  |                  |                                |                |
|   |           |         |   | CHECKED                                 |            |            |                  |                                |                |
|   |           |         |   | ENG APPR.                               |            |            |                  |                                |                |
|   |           |         | MATERIAL<br>Aluminum  | MFG APPR.                               |            |            |                  |                                |                |
|   |           |         |   | Q.A.                                    |            |            |                  |                                |                |
|   | NEXT ASSY | USED ON | FINISH  | COMMENTS:<br>Slip fit with Bottom Bases |            |            | SIZE<br><b>A</b> | DWG. NO.<br>Bottom Frit Spacer | REV.<br>7      |
| APPLICATION   |           |         | DO NOT SCALE DRAWING  |   |            | SCALE: 1:1 |                  | WEIGHT:                        | SHEET 10 OF 20 |



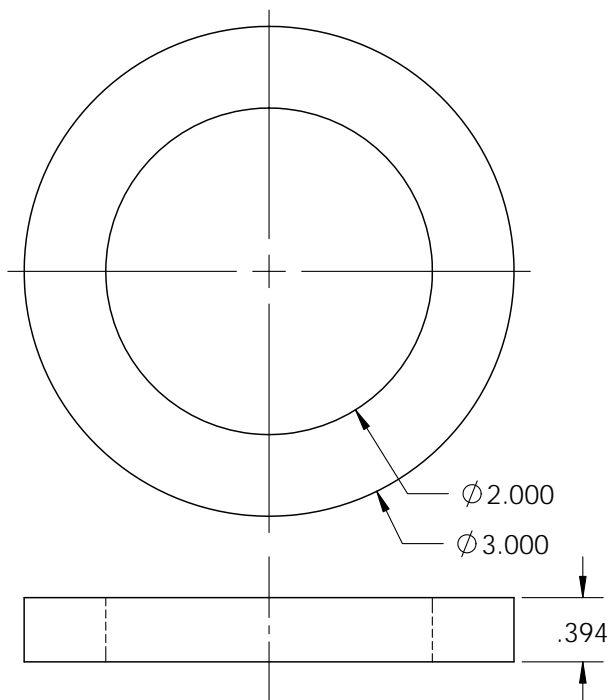


Top Frit



### Bottom Frit

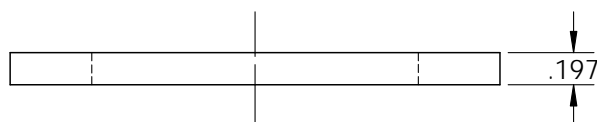
|  |             |           |  |   |            |           |                  |                              |                 |
|--|-------------|-----------|--|---|------------|-----------|------------------|------------------------------|-----------------|
| <p><b>PROPRIETARY AND CONFIDENTIAL</b></p> <p>THE INFORMATION CONTAINED IN THIS DRAWING IS THE SOLE PROPERTY OF &lt;INSERT COMPANY NAME HERE&gt;. ANY REPRODUCTION IN PART OR AS A WHOLE WITHOUT THE WRITTEN PERMISSION OF &lt;INSERT COMPANY NAME HERE&gt; IS PROHIBITED.</p> |             |           | DIMENSIONS ARE IN INCHES<br>TOLERANCES:<br>FRACTIONAL ±<br>ANGULAR: MACH ±    BEND ±<br>TWO PLACE DECIMAL    ±<br>THREE PLACE DECIMAL    ± | NAME  | DATE       |           |                  |                              |                 |
|  |             |           |  | DRAWN   | Wilton Mui | 7/17/2012 |                  |                              |                 |
|  |             |           |  | CHECKED   |            |           |                  |                              |                 |
|  |             |           |  | ENG APPR.                                       |            |           |                  |                              |                 |
|  |             |           |  | MFG APPR.                                       |            |           |                  |                              |                 |
|  |             |           |  | MATERIAL  |            |           |                  |                              |                 |
|  |             |           |  | Mott Porous 316L SS Disc                        |            |           |                  |                              |                 |
|  |             |           |  | COMMENTS:                                       |            |           |                  |                              |                 |
|  |             |           |  | Slip fit Bottom Frit<br>with Bottom Base 1 & 2. |            |           |                  |                              |                 |
|  |             | NEXT ASSY | USED ON  | FINISH  |            |           |                  |                              |                 |
|  | APPLICATION |           | DO NOT SCALE DRAWING   |   |            |           | SIZE<br><b>A</b> | DWG. NO.<br><br><b>Frits</b> | REV<br><b>7</b> |
|  |             |           |  | SCALE: 1:1                                      | WEIGHT:    |           | SHEET 11 OF 20   |                              |                 |



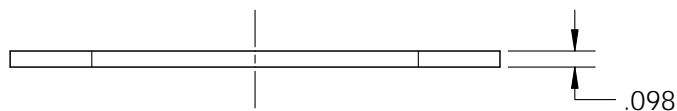
1 cm spacer



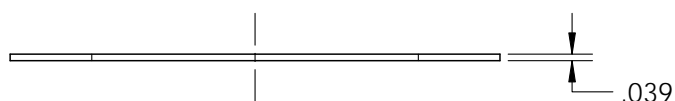
0.75 cm spacer



0.50 cm spacer

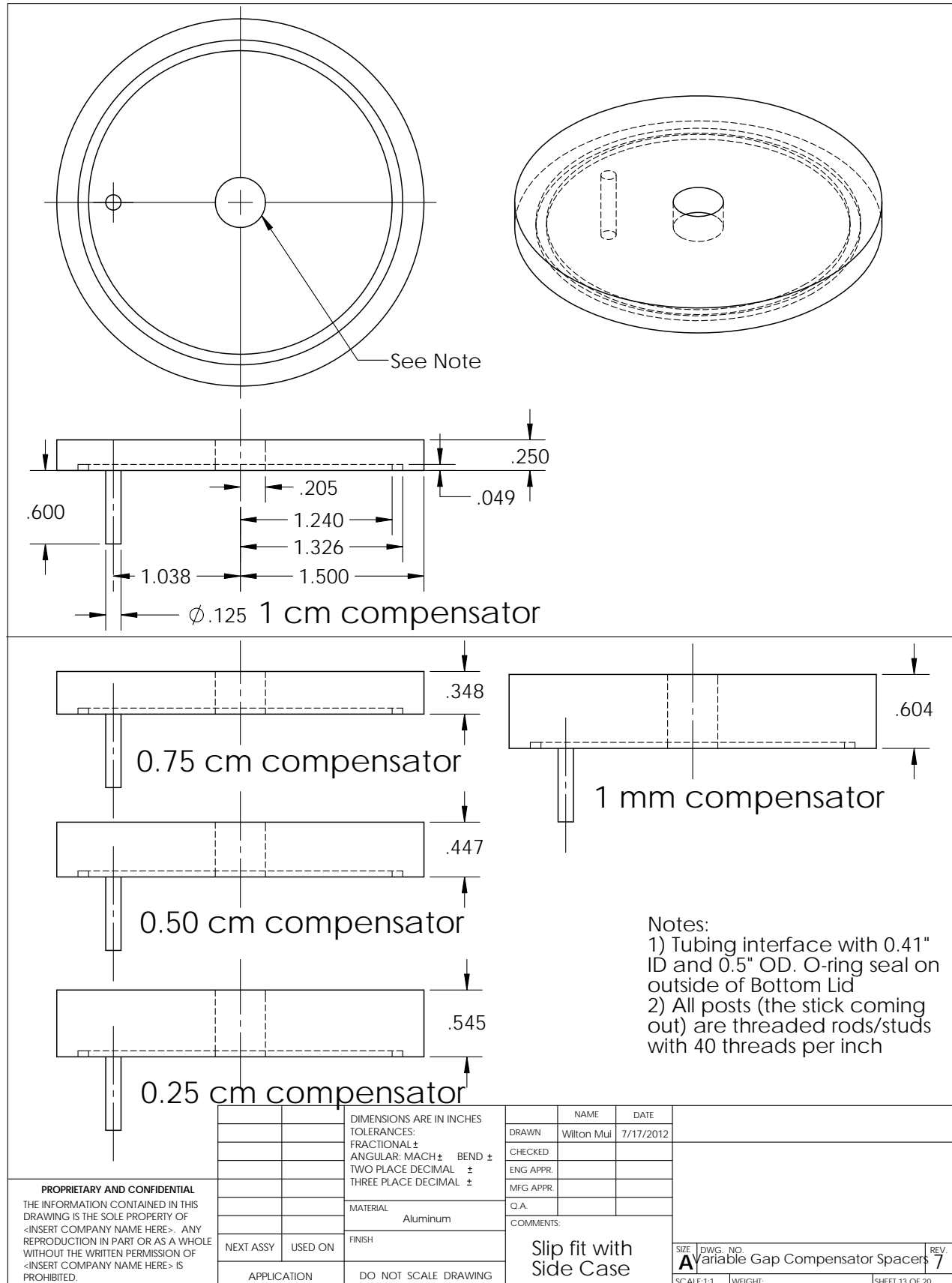


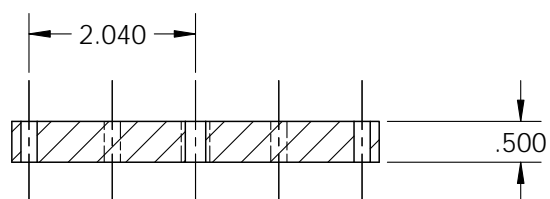
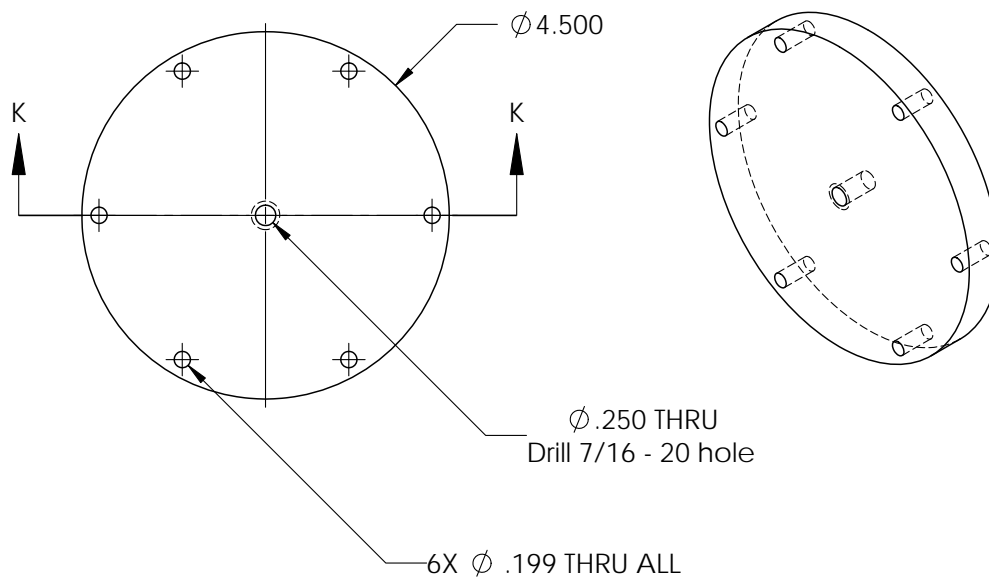
0.25 cm spacer



1 mm spacer

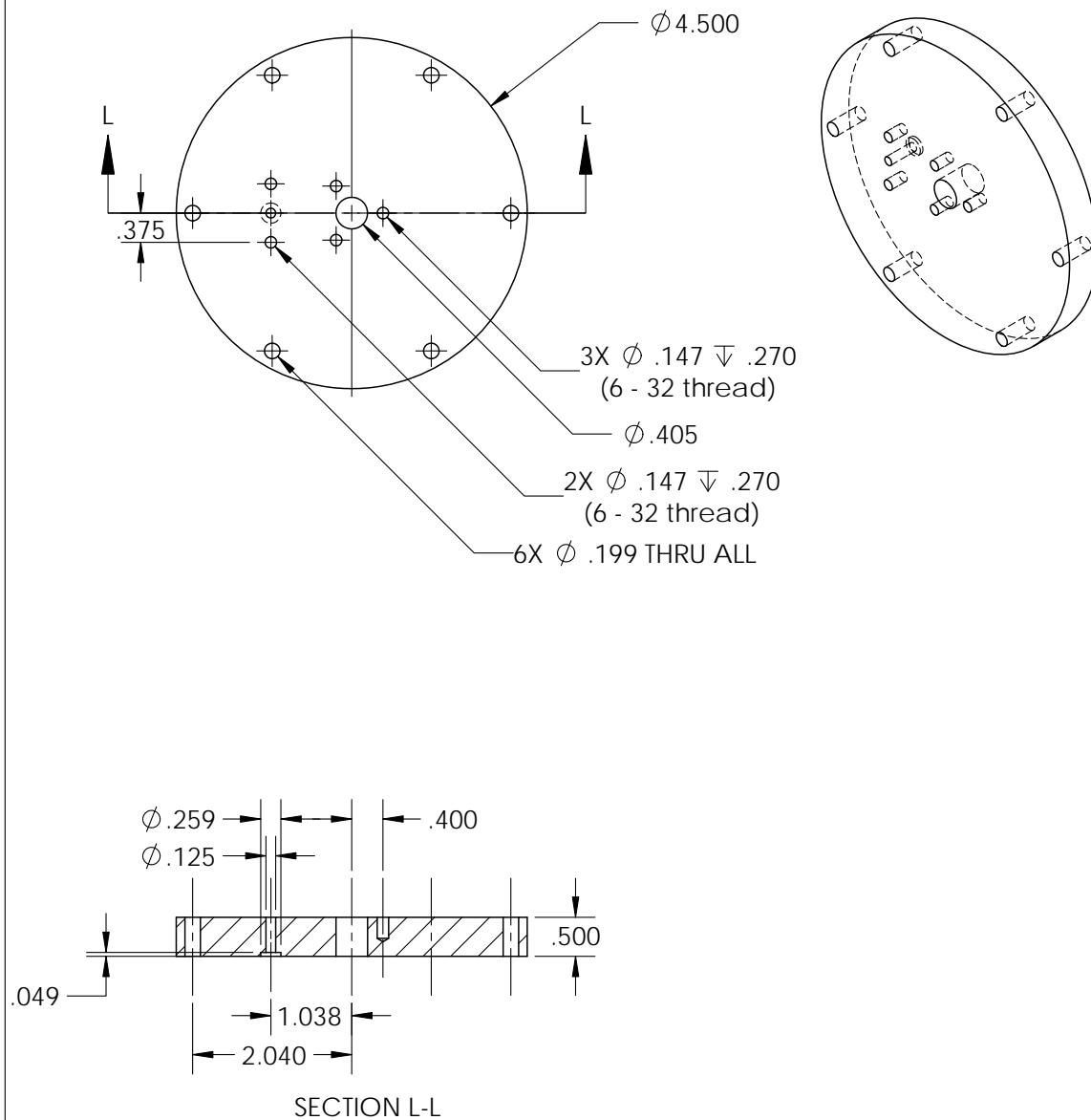
|   |             |         |   |           |            |           |                                      |            |          |                |
|---|-------------|---------|---|-----------|------------|-----------|--------------------------------------|------------|----------|----------------|
| <b>PROPRIETARY AND CONFIDENTIAL</b><br>THE INFORMATION CONTAINED IN THIS DRAWING IS THE SOLE PROPERTY OF <INSERT COMPANY NAME HERE>. ANY REPRODUCTION IN PART OR AS A WHOLE WITHOUT THE WRITTEN PERMISSION OF <INSERT COMPANY NAME HERE> IS PROHIBITED. |             |         | DIMENSIONS ARE IN INCHES<br>TOLERANCES:<br>FRACTIONAL ±<br>ANGULAR: MACH ± BEND ±<br>TWO PLACE DECIMAL ±<br>THREE PLACE DECIMAL ± |           | NAME       | DATE      | COMMENTS:<br>Slip fit with Side Case | SIZE       | DWG. NO. | REV.           |
|   |             |         |   | DRAWN     | Wilton Mui | 7/17/2012 |                                      |            |          |                |
|   |             |         |   | CHECKED   |            |           |                                      |            |          |                |
|   |             |         |   | ENG APPR. |            |           |                                      |            |          |                |
|   |             |         |   | MFG APPR. |            |           |                                      |            |          |                |
|   |             |         |   | Q.A.      |            |           |                                      |            |          |                |
|   |             |         | MATERIAL  | Delrin    |            |           |                                      |            |          |                |
|   |             |         | FINISH  |           |            |           |                                      |            |          |                |
|   | NEXT ASSY   | USED ON |   |           |            |           |                                      |            |          |                |
|   | APPLICATION |         | DO NOT SCALE DRAWING  |           |            |           |                                      | SCALE: 1:1 | WEIGHT:  | SHEET 12 OF 20 |



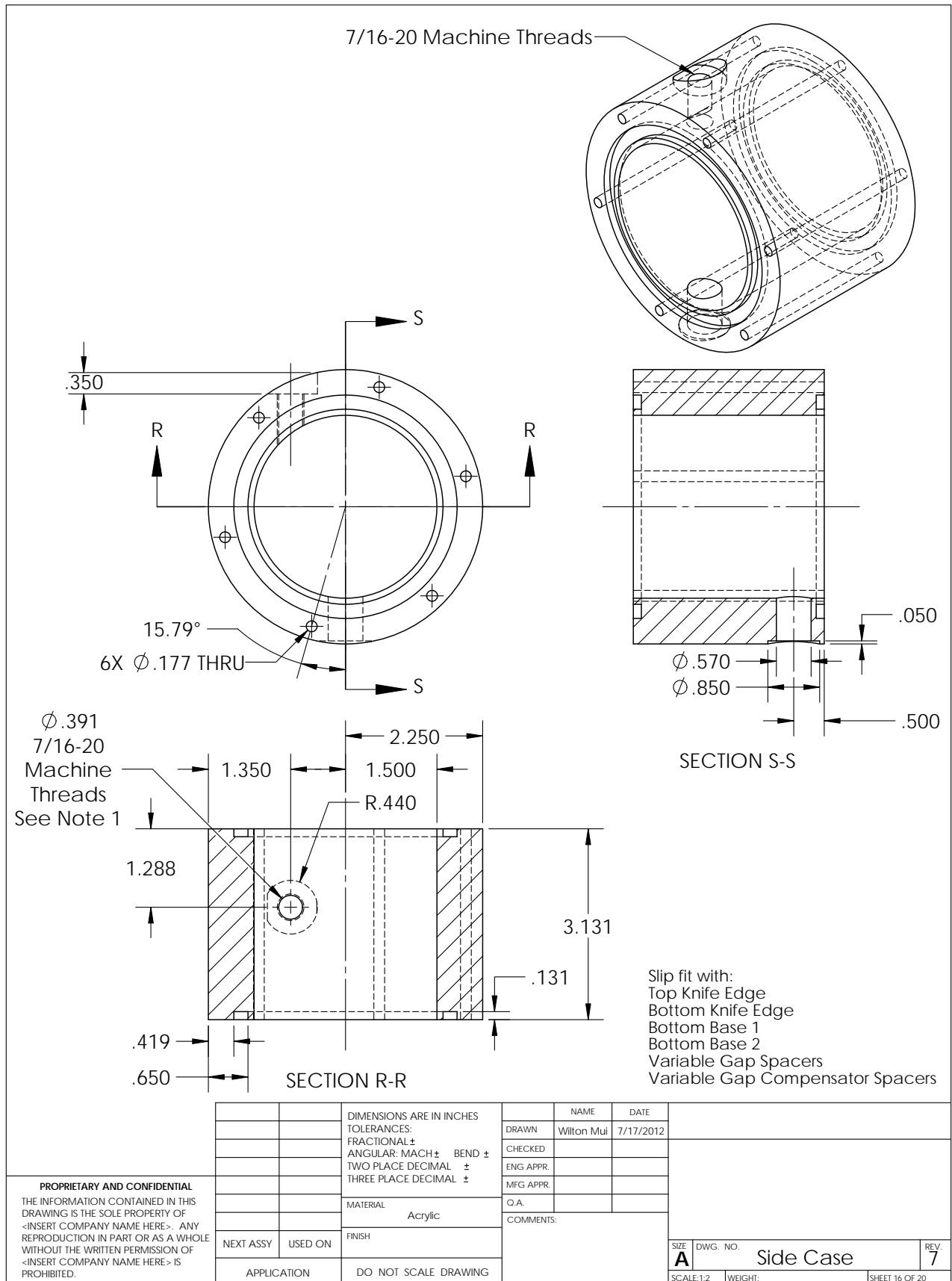


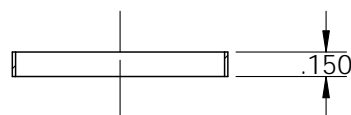
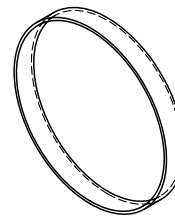
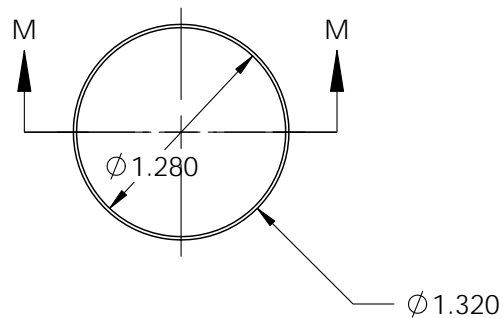
SECTION K-K

|   |           |             |                                |            |           |            |                |
|---|-----------|-------------|--------------------------------|------------|-----------|------------|----------------|
| <b>PROPRIETARY AND CONFIDENTIAL</b><br>THE INFORMATION CONTAINED IN THIS DRAWING IS THE SOLE PROPERTY OF <INSERT COMPANY NAME HERE>. ANY REPRODUCTION IN PART OR AS A WHOLE WITHOUT THE WRITTEN PERMISSION OF <INSERT COMPANY NAME HERE> IS PROHIBITED. |           |             | DIMENSIONS ARE IN INCHES       |            | NAME      | DATE       |                |
|   |           |             | TOLERANCES:                    |            | DRAWN     | Wilton Mui | 7/17/2012      |
|   |           |             | FRACTIONAL $\pm$               |            | CHECKED   |            |                |
|   |           |             | ANGULAR: MACH $\pm$ BEND $\pm$ |            | ENG APPR. |            |                |
|   |           |             | TWO PLACE DECIMAL $\pm$        |            | MFG APPR. |            |                |
|   |           |             | THREE PLACE DECIMAL $\pm$      |            | Q.A.      |            |                |
|   |           |             | MATERIAL                       | Aluminum   | COMMENTS: |            |                |
|   |           |             | FINISH                         |            |           |            |                |
|   | NEXT ASSY | USED ON     |                                |            |           |            |                |
|   |           | APPLICATION | DO NOT SCALE DRAWING           |            | SIZE      | DWG. NO.   | Top Lid        |
|   |           |             |                                | A          |           |            | 7              |
|   |           |             |                                | SCALE: 1:2 | WEIGHT:   |            | SHEET 14 OF 20 |



|  |             |                |  |           |            |      |           |     |   |            |   |           |         |                |
|--|-------------|----------------|--|-----------|------------|------|-----------|-----|---|------------|---|-----------|---------|----------------|
| <p><b>PROPRIETARY AND CONFIDENTIAL</b></p> <p>THE INFORMATION CONTAINED IN THIS DRAWING IS THE SOLE PROPERTY OF &lt;INSERT COMPANY NAME HERE&gt;. ANY REPRODUCTION IN PART OR AS A WHOLE WITHOUT THE WRITTEN PERMISSION OF &lt;INSERT COMPANY NAME HERE&gt; IS PROHIBITED.</p> |             |                | DIMENSIONS ARE IN INCHES<br>TOLERANCES:<br>FRACTIONAL ±<br>ANGULAR: MACH ±    BEND ±<br>TWO PLACE DECIMAL    ±<br>THREE PLACE DECIMAL    ± | NAME      | DATE       |      |           |     |   |            |   |           |         |                |
|  |             |                |  | DRAWN     | Wilton Mui |      | 7/17/2012 |     |   |            |   |           |         |                |
|  |             |                |  | CHECKED   |            |      |           |     |   |            |   |           |         |                |
|  |             |                |  | ENG APPR. |            |      |           |     |   |            |   |           |         |                |
|  |             |                |  | MFG APPR. |            |      |           |     |   |            |   |           |         |                |
|  |             |                |  | Q.A.      |            |      |           |     |   |            |   |           |         |                |
|  |             |                |  | COMMENTS: |            |      |           |     |   |            |   |           |         |                |
|  | NEXT ASSY   | USED ON        | FINISH   |           |            |      |           |     |   |            |   |           |         |                |
|  | APPLICATION |                | DO NOT SCALE DRAWING   |           |            |      |           |     |   |            |   |           |         |                |
|  |             |                |  |           |            |      |           |     |   |            |   |           |         |                |
| <table><tr><td>SIZE</td><td>DWG. NO.</td><td>REV</td></tr><tr><td>A</td><td>Bottom Lid</td><td>7</td></tr><tr><td>SCALE:1:2</td><td>WEIGHT:</td><td>SHEET 15 OF 20</td></tr></table>   |             |                |  |           |            | SIZE | DWG. NO.  | REV | A | Bottom Lid | 7 | SCALE:1:2 | WEIGHT: | SHEET 15 OF 20 |
| SIZE   | DWG. NO.    | REV            |  |           |            |      |           |     |   |            |   |           |         |                |
| A  | Bottom Lid  | 7              |  |           |            |      |           |     |   |            |   |           |         |                |
| SCALE:1:2  | WEIGHT:     | SHEET 15 OF 20 |  |           |            |      |           |     |   |            |   |           |         |                |

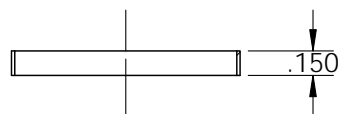
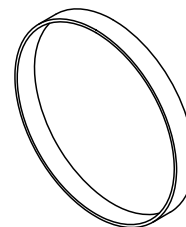
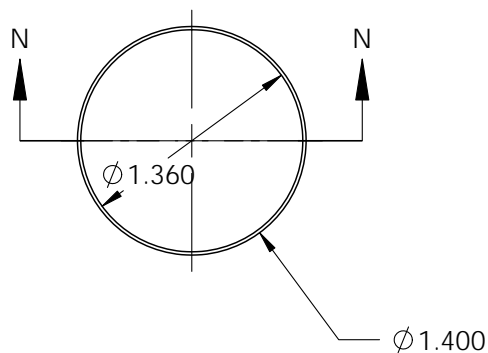




SECTION M-M  
SCALE 1 : 1

Note: Slip fit with  
Top Screen Holder

## Top Mesh Holder Complement



SECTION N-N  
SCALE 1 : 1

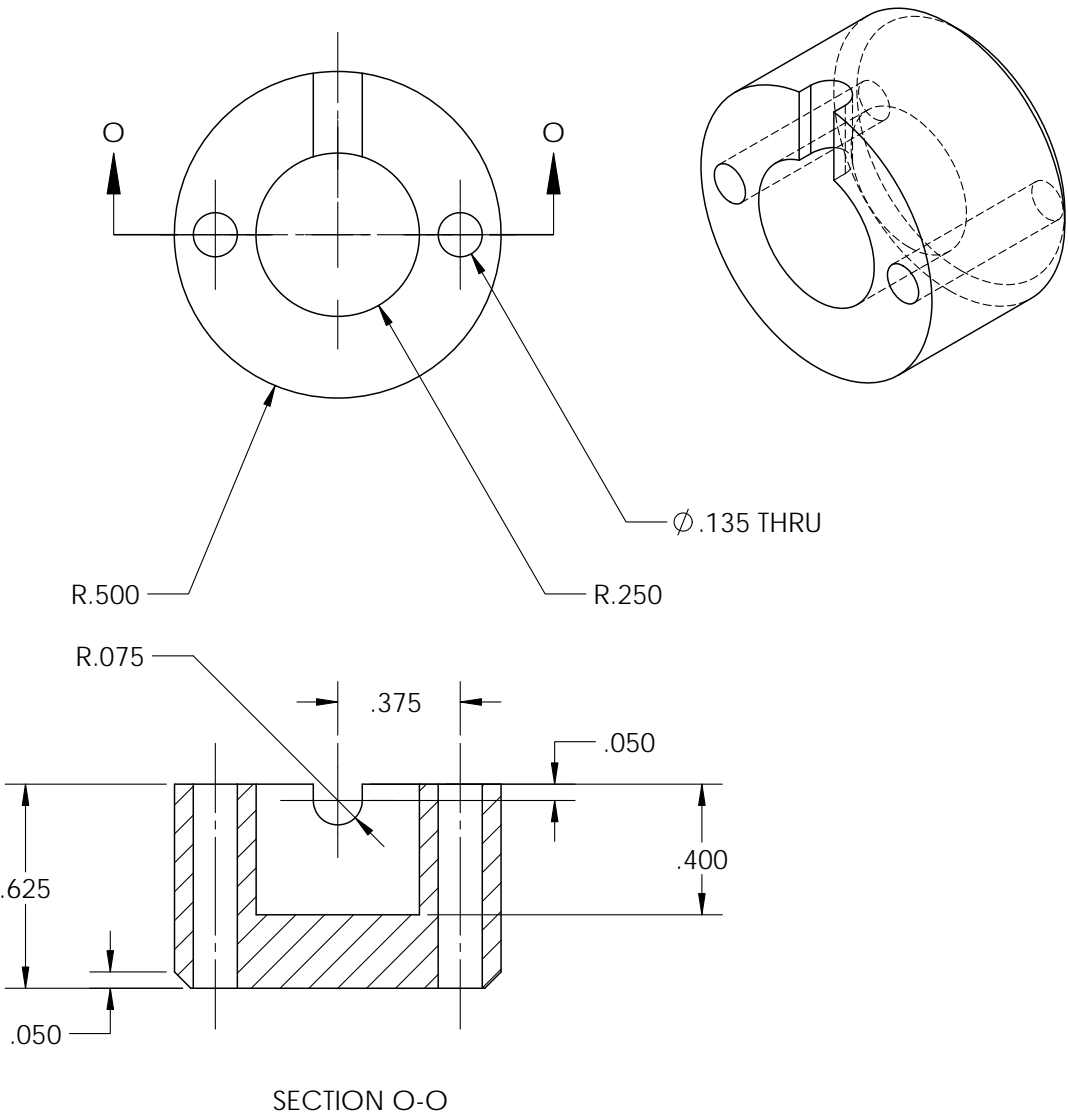
Note: Slip fit with  
Bottom Screen Holder

## Bottom Mesh Holder Complement

### PROPRIETARY AND CONFIDENTIAL

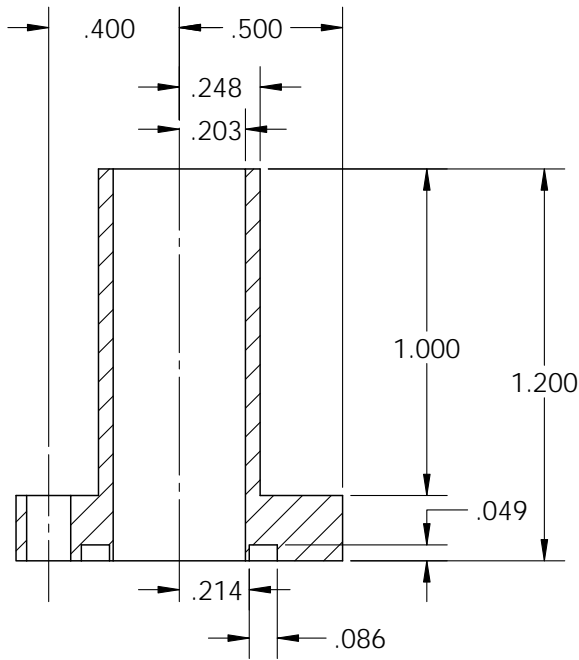
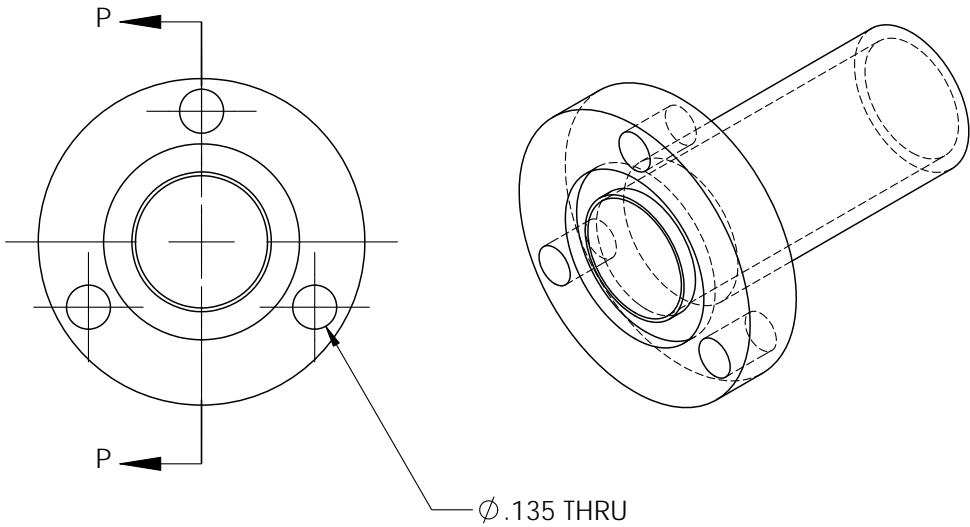
THE INFORMATION CONTAINED IN THIS DRAWING IS THE SOLE PROPERTY OF <INSERT COMPANY NAME HERE>. ANY REPRODUCTION IN PART OR AS A WHOLE WITHOUT THE WRITTEN PERMISSION OF <INSERT COMPANY NAME HERE> IS PROHIBITED.

|             |                      |  |  |            |                |  |              |
|-------------|----------------------|--|--|------------|----------------|--|--------------|
|             |                      | DIMENSIONS ARE IN INCHES<br>TOLERANCES:<br>FRACTIONAL ±<br>ANGULAR: MACH ±    BEND ±<br>TWO PLACE DECIMAL    ±<br>THREE PLACE DECIMAL    ± |  | NAME       | DATE           |  |              |
|             |                      |  | DRAWN  | Wilton Mui | 7/17/2012      |  |              |
|             |                      |  | CHECKED  |            |                |  |              |
|             |                      |  | ENG APPR.                                      |            |                |  |              |
|             |                      |  | MFG APPR.                                      |            |                |  |              |
|             |                      | MATERIAL<br><br>Aluminum   | Q.A.   |            |                |  |              |
|             |                      |  | COMMENTS:                                      |            |                |  |              |
| NEXT ASSY   | USED ON              | FINISH   |  |            |                |  |              |
| APPLICATION | DO NOT SCALE DRAWING |  | SIZE <b>A</b> DWG. NO. Mesh Holder Complements |            |                |  | REV <b>7</b> |
|             |                      |  | SCALE:1:2    WEIGHT:                           |            | SHEET 17 OF 20 |  |              |



|  |         |  |         |  |                      |            |            |                    |                |
|--|---------|--|---------|--|----------------------|------------|------------|--------------------|----------------|
| <p><b>PROPRIETARY AND CONFIDENTIAL</b></p> <p>THE INFORMATION CONTAINED IN THIS DRAWING IS THE SOLE PROPERTY OF &lt;INSERT COMPANY NAME HERE&gt;. ANY REPRODUCTION IN PART OR AS A WHOLE WITHOUT THE WRITTEN PERMISSION OF &lt;INSERT COMPANY NAME HERE&gt; IS PROHIBITED.</p> |         |  |         | DIMENSIONS ARE IN INCHES<br>TOLERANCES:<br>FRACTIONAL ±<br>ANGULAR: MACH ±    BEND ±<br>TWO PLACE DECIMAL    ±<br>THREE PLACE DECIMAL    ± |                      | NAME       | DATE       | <div></div>        |                |
|  |         |  |         |  | DRAWN                | Wilton Mui | 7/17/2012  |                    |                |
|  |         |  |         |  | CHECKED              |            |            |                    |                |
|  |         |  |         |  | ENG APPR.            |            |            |                    |                |
|  |         |  |         |  | MFG APPR.            |            |            |                    |                |
|  |         |  |         |  | Q.A.                 |            |            |                    |                |
|  |         |  |         | MATERIAL   | COMMENTS:            |            |            |                    |                |
|  |         |  | Plastic |  |                      |            |            |                    |                |
|  |         |  | FINISH  |  |                      |            |            |                    |                |
| NEXT ASSY  | USED ON |  |         |  |                      |            |            |                    |                |
|  |         |  |         | APPLICATION  | DO NOT SCALE DRAWING |            |            |                    |                |
|  |         |  |         |  |                      |            | SIZE       | DWG. NO            | REV.           |
|  |         |  |         |  |                      |            | A          | High Voltage Cover | 7              |
|  |         |  |         |  |                      |            | SCALE: 2:1 |                    | WEIGHT:        |
|  |         |  |         |  |                      |            |            |                    | SHEET 18 OF 20 |

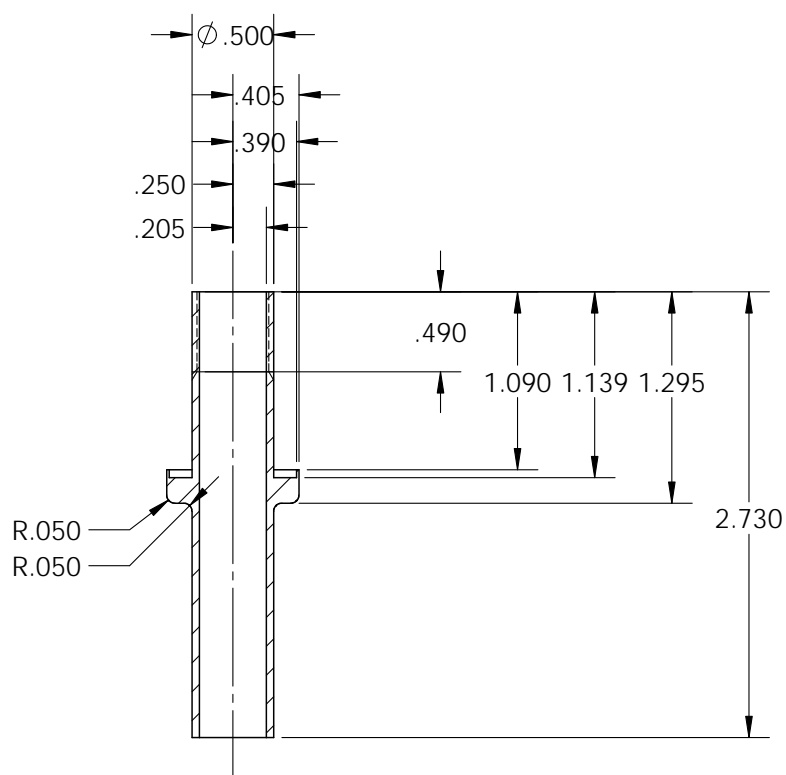
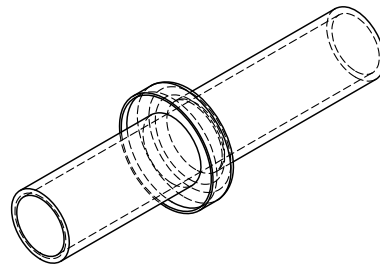
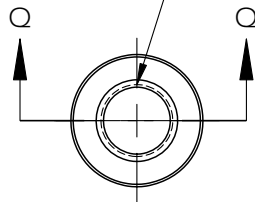




SECTION P-P

|  |  |  |  |  |           |            |           |  |  |
|--|--|--|--|--|-----------|------------|-----------|--|--|
| <p><b>PROPRIETARY AND CONFIDENTIAL</b></p> <p>THE INFORMATION CONTAINED IN THIS DRAWING IS THE SOLE PROPERTY OF &lt;INSERT COMPANY NAME HERE&gt;. ANY REPRODUCTION IN PART OR AS A WHOLE WITHOUT THE WRITTEN PERMISSION OF &lt;INSERT COMPANY NAME HERE&gt; IS PROHIBITED.</p> |  |  |  | DIMENSIONS ARE IN INCHES<br>TOLERANCES:<br>FRACTIONAL ±<br>ANGULAR: MACH ±    BEND ±<br>TWO PLACE DECIMAL    ±<br>THREE PLACE DECIMAL    ± |           | NAME       | DATE      |  |  |
|  |  |  |  |  | DRAWN     | Wilton Mui | 7/17/2012 |  |  |
|  |  |  |  |  | CHECKED   |            |           |  |  |
|  |  |  |  |  | ENG APPR. |            |           |  |  |
|  |  |  |  |  | MFG APPR. |            |           |  |  |
|  |  |  |  |  | Q.A.      |            |           |  |  |
|  |  |  |  |  | COMMENTS: |            |           |  |  |
|  |  |  |  |  |           |            |           |  |  |
|  |  |  |  |  |           |            |           |  |  |
|  |  |  |  |  |           |            |           |  |  |
|  |  |  |  |  |           |            |           |  |  |
|  |  |  |  |  |           |            |           |  |  |
|  |  |  |  |  |           |            |           |  |  |
|  |  |  |  |  |           |            |           |  |  |
|  |  |  |  |  |           |            |           |  |  |
|  |  |  |  |  |           |            |           |  |  |
|  |  |  |  |  |           |            |           |  |  |
|  |  |  |  |  |           |            |           |  |  |
|  |  |  |  |  |           |            |           |  |  |
|  |  |  |  |  |           |            |           |  |  |
|  |  |  |  |  |           |            |           |  |  |
|  |  |  |  |  |           |            |           |  |  |
|  |  |  |  |  |           |            |           |  |  |
|  |  |  |  |  |           |            |           |  |  |
|  |  |  |  |  |           |            |           |  |  |
|  |  |  |  |  |           |            |           |  |  |
|  |  |  |  |  |           |            |           |  |  |
|  |  |  |  |  |           |            |           |  |  |
|  |  |  |  |  |           |            |           |  |  |
|  |  |  |  |  |           |            |           |  |  |
|  |  |  |  |  |           |            |           |  |  |
|  |  |  |  |  |           |            |           |  |  |
|  |  |  |  |  |           |            |           |  |  |
|  |  |  |  |  |           |            |           |  |  |
|  |  |  |  |  |           |            |           |  |  |
|  |  |  |  |  |           |            |           |  |  |
|  |  |  |  |  |           |            |           |  |  |
|  |  |  |  |  |           |            |           |  |  |
|  |  |  |  |  |           |            |           |  |  |
|  |  |  |  |  |           |            |           |  |  |
|  |  |  |  |  |           |            |           |  |  |
|  |  |  |  |  |           |            |           |  |  |
|  |  |  |  |  |           |            |           |  |  |
|  |  |  |  |  |           |            |           |  |  |
|  |  |  |  |  |           |            |           |  |  |
|  |  |  |  |  |           |            |           |  |  |
|  |  |  |  |  |           |            |           |  |  |
|  |  |  |  |  |           |            |           |  |  |
|  |  |  |  |  |           |            |           |  |  |
|  |  |  |  |  |           |            |           |  |  |
|  |  |  |  |  |           |            |           |  |  |
|  |  |  |  |  |           |            |           |  |  |
|  |  |  |  |  |           |            |           |  |  |
|  |  |  |  |  |           |            |           |  |  |
|  |  |  |  |  |           |            |           |  |  |
|  |  |  |  |  |           |            |           |  |  |
|  |  |  |  |  |           |            |           |  |  |
|  |  |  |  |  |           |            |           |  |  |
|  |  |  |  |  |           |            |           |  |  |
|  |  |  |  |  |           |            |           |  |  |
|  |  |  |  |  |           |            |           |  |  |
|  |  |  |  |  |           |            |           |  |  |
|  |  |  |  |  |           |            |           |  |  |
|  |  |  |  |  |           |            |           |  |  |
|  |  |  |  |  |           |            |           |  |  |
|  |  |  |  |  |           |            |           |  |  |
|  |  |  |  |  |           |            |           |  |  |
|  |  |  |  |  |           |            |           |  |  |
|  |  |  |  |  |           |            |           |  |  |
|  |  |  |  |  |           |            |           |  |  |
|  |  |  |  |  |           |            |           |  |  |
|  |  |  |  |  |           |            |           |  |  |
|  |  |  |  |  |           |            |           |  |  |
|  |  |  |  |  |           |            |           |  |  |
|  |  |  |  |  |           |            |           |  |  |
|  |  |  |  |  |           |            |           |  |  |
|  |  |  |  |  |           |            |           |  |  |
|  |  |  |  |  |           |            |           |  |  |
|  |  |  |  |  |           |            |           |  |  |
|  |  |  |  |  |           |            |           |  |  |
|  |  |  |  |  |           |            |           |  |  |
|  |  |  |  |  |           |            |           |  |  |
|  |  |  |  |  |           |            |           |  |  |
|  |  |  |  |  |           |            |           |  |  |
|  |  |  |  |  |           |            |           |  |  |
|  |  |  |  |  |           |            |           |  |  |
|  |  |  |  |  |           |            |           |  |  |
|  |  |  |  |  |           |            |           |  |  |
|  |  |  |  |  |           |            |           |  |  |
|  |  |  |  |  |           |            |           |  |  |
|  |  |  |  |  |           |            |           |  |  |
|  |  |  |  |  |           |            |           |  |  |
|  |  |  |  |  |           |            |           |  |  |
|  |  |  |  |  |           |            |           |  |  |
|  |  |  |  |  |           |            |           |  |  |
|  |  |  |  |  |           |            |           |  |  |
|  |  |  |  |  |           |            |           |  |  |
|  |  |  |  |  |           |            |           |  |  |
|  |  |  |  |  |           |            |           |  |  |
|  |  |  |  |  |           |            |           |  |  |
|  |  |  |  |  |           |            |           |  |  |
|  |  |  |  |  |           |            |           |  |  |
|  |  |  |  |  |           |            |           |  |  |
|  |  |  |  |  |           |            |           |  |  |
|  |  |  |  |  |           |            |           |  |  |
|  |  |  |  |  |           |            |           |  |  |
|  |  |  |  |  |           |            |           |  |  |
|  |  |  |  |  |           |            |           |  |  |
|  |  |  |  |  |           |            |           |  |  |
|  |  |  |  |  |           |            |           |  |  |
|  |  |  |  |  |           |            |           |  |  |
|  |  |  |  |  |           |            |           |  |  |
|  |  |  |  |  |           |            |           |  |  |
|  |  |  |  |  |           |            |           |  |  |
|  |  |  |  |  |           |            |           |  |  |
|  |  |  |  |  |           |            |           |  |  |
|  |  |  |  |  |           |            |           |  |  |
|  |  |  |  |  |           |            |           |  |  |
|  |  |  |  |  |           |            |           |  |  |
|  |  |  |  |  |           |            |           |  |  |
|  |  |  |  |  |           |            |           |  |  |
|  |  |  |  |  |           |            |           |  |  |

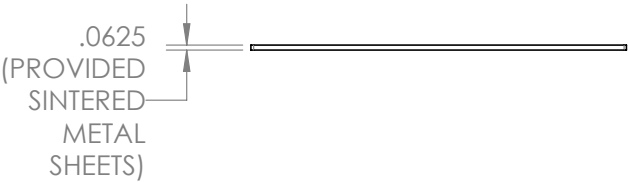
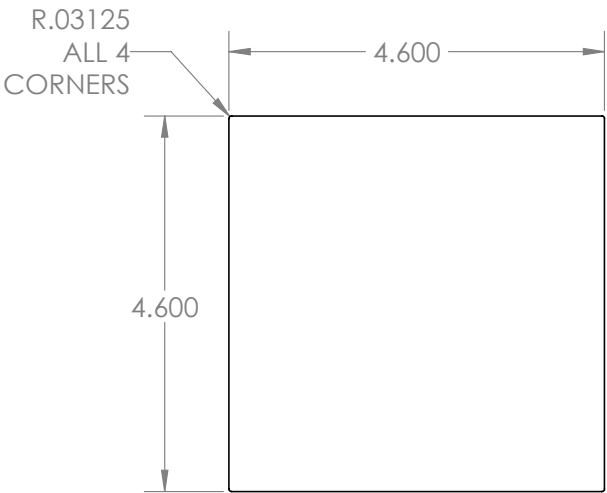
1/2-20 Machine Threads  
On Outside  
0.490 inch from end



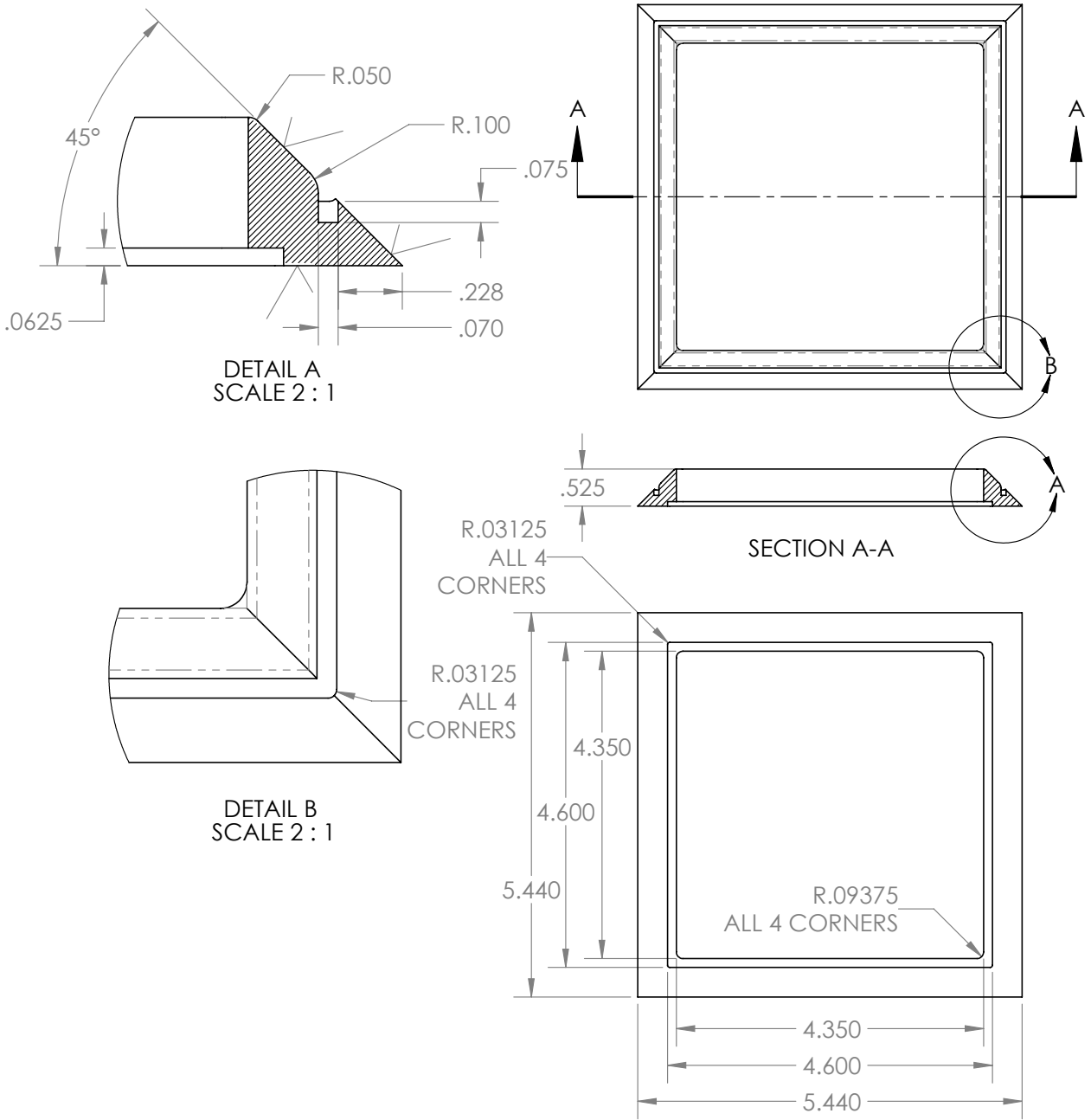
SECTION Q-Q

|   |  |                      |  |                          |  |  |  |                      |  |
|---|--|----------------------|--|--------------------------|--|--|--|----------------------|--|
| <b>PROPRIETARY AND CONFIDENTIAL</b><br>THE INFORMATION CONTAINED IN THIS DRAWING IS THE SOLE PROPERTY OF <INSERT COMPANY NAME HERE>. ANY REPRODUCTION IN PART OR AS A WHOLE WITHOUT THE WRITTEN PERMISSION OF <INSERT COMPANY NAME HERE> IS PROHIBITED. |  |                      |  | DIMENSIONS ARE IN INCHES |  | NAME   |  | DATE                 |  |
|   |  |                      |  | TOLERANCES:              |  | DRAWN  |  | Wilton Mui 7/17/2012 |  |
|   |  |                      |  | FRACTIONAL ±             |  | CHECKED                                      |  |                      |  |
|   |  |                      |  | ANGULAR: MACH ± BEND ±   |  | ENG APPR                                     |  |                      |  |
|   |  |                      |  | TWO PLACE DECIMAL ±      |  | MFG APPR                                     |  |                      |  |
|   |  |                      |  | THREE PLACE DECIMAL ±    |  | Q.A.   |  |                      |  |
|   |  | MATERIAL             |  | Aluminum                 |  | COMMENTS:                                    |  |                      |  |
|   |  | FINISH               |  |                          |  | Screws into larger port on side of Side Case |  |                      |  |
| NEXT ASSY   |  | USED ON              |  |                          |  | SIZE   |  | DWG. NO.             |  |
| APPLICATION   |  | DO NOT SCALE DRAWING |  |                          |  | A  |  | Side Case Port       |  |
|   |  |                      |  |                          |  | SCALE: 1:1                                   |  | WEIGHT:              |  |
|   |  |                      |  |                          |  |  |  | REV. 7               |  |
|   |  |                      |  |                          |  |  |  | SHEET 20 OF 20       |  |

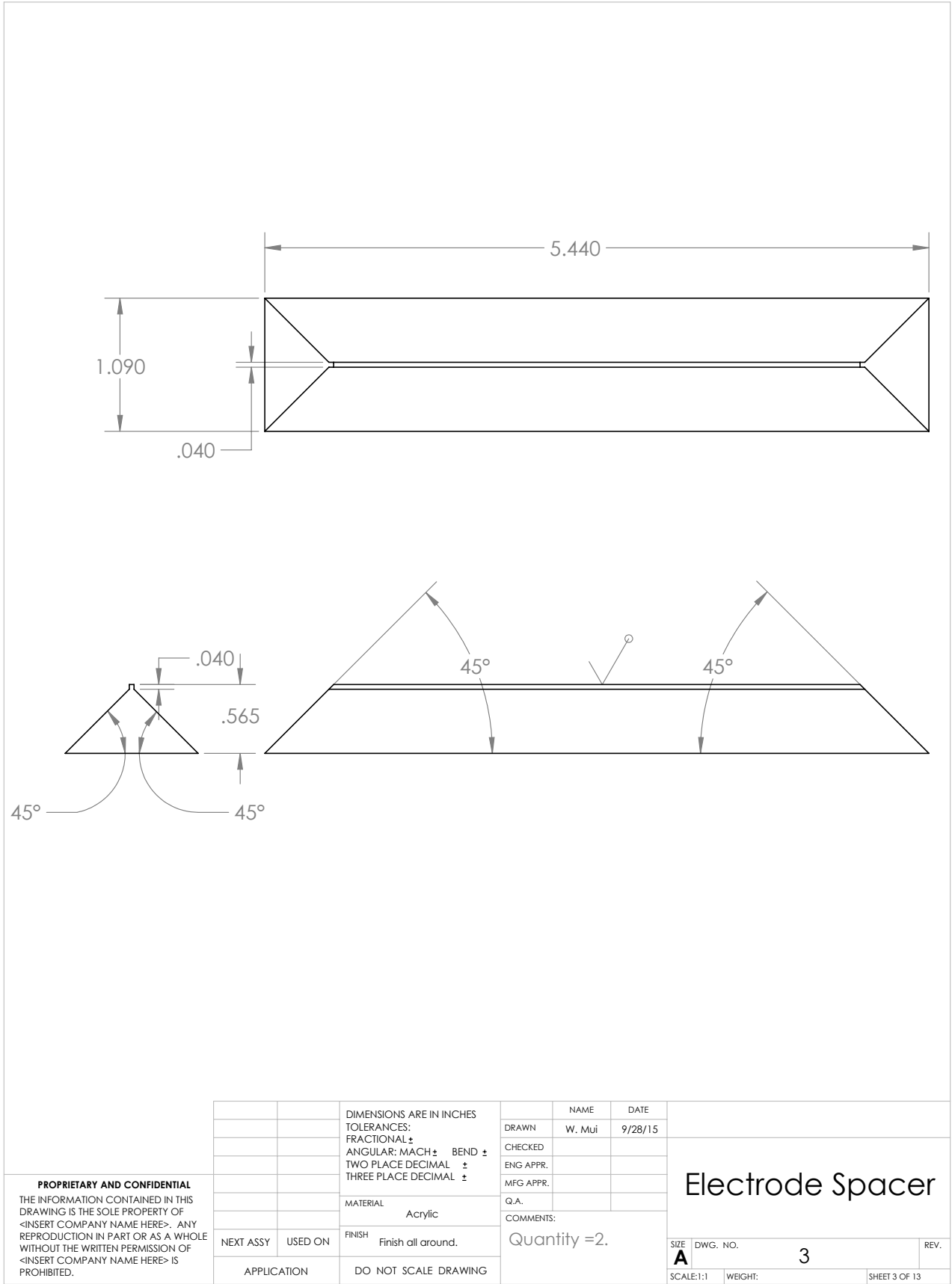
*Appendix G***TECHNICAL DRAWINGS OF THE PLANAR OPPOSED  
MIGRATION AEROSOL CLASSIFIER (POMAC)**

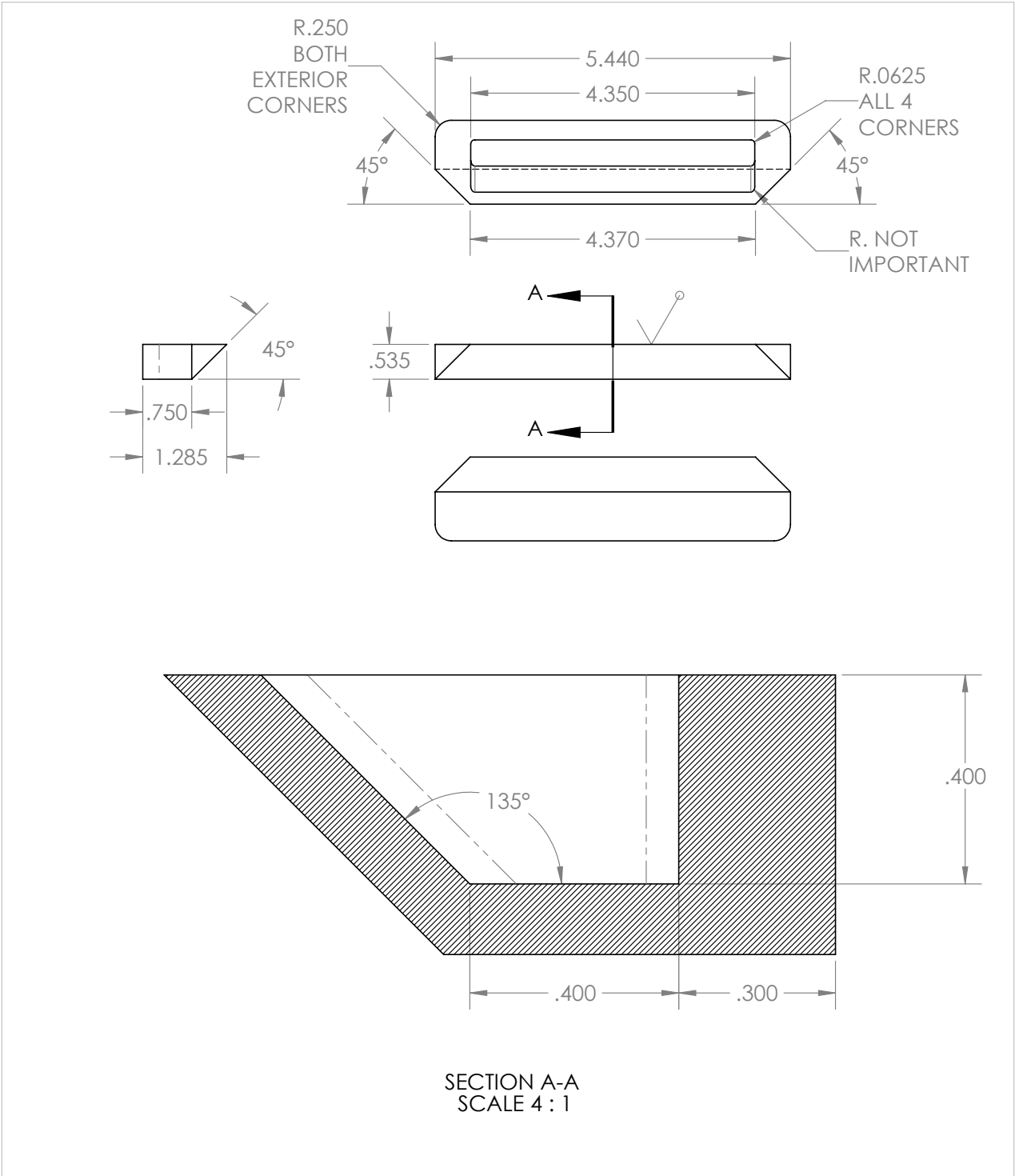


|   |             |         |                             |   |        |         |                                    |               |      |
|---|-------------|---------|-----------------------------|---|--------|---------|------------------------------------|---------------|------|
| <div>PROPRIETARY AND CONFIDENTIAL</div> <div>THE INFORMATION CONTAINED IN THIS DRAWING IS THE SOLE PROPERTY OF &lt;INSERT COMPANY NAME HERE&gt;. ANY REPRODUCTION IN PART OR AS A WHOLE WITHOUT THE WRITTEN PERMISSION OF &lt;INSERT COMPANY NAME HERE&gt; IS PROHIBITED.</div> |             |         | DIMENSIONS ARE IN INCHES    |   | NAME   | DATE    | <div>Sintered Metal Diffuser</div> |               |      |
|   |             |         | TOLERANCES:                 | DRAWN   | W. Mui | 9/28/15 |                                    |               |      |
|   |             |         | FRACTIONAL ±                | CHECKED   |        |         |                                    |               |      |
|   |             |         | ANGULAR: MACH ±    BEND ±   | ENG APPR.   |        |         |                                    |               |      |
|   |             |         | TWO PLACE DECIMAL   ±       | MFG APPR.   |        |         |                                    |               |      |
|   |             |         | THREE PLACE DECIMAL   ±     | Q.A.  |        |         |                                    |               |      |
|   |             |         | MATERIAL                    | COMMENTS:<br>Quantity = 2.<br>Use water soluble cutting fluid.<br>Slip fits into 'Mesh Frame' piece,<br>or as well as possible. |        |         | SIZE                               | DWG. NO.      | REV. |
|   |             |         | 316LSS Sintered Metal Sheet |   |        |         | <b>A</b>                           | 1             |      |
|   | NEXT ASSY   | USED ON | FINISH                      |   |        |         |                                    |               |      |
|   | APPLICATION |         | DO NOT SCALE DRAWING        |   |        |         |                                    |               |      |
|   |             |         | SCALE:1:2                   |   |        | WEIGHT: |                                    | SHEET 1 OF 13 |      |

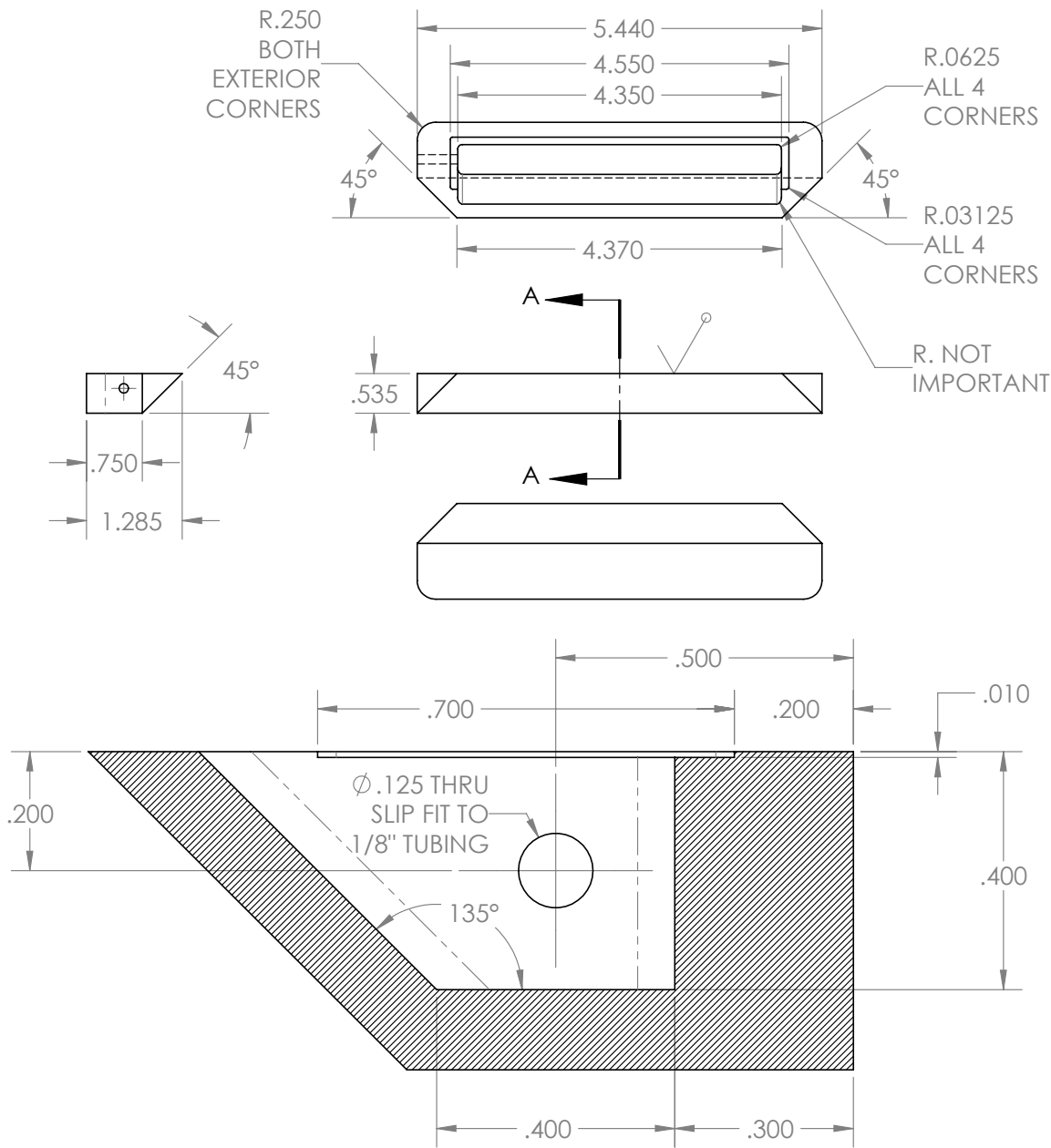


|   |  |   |  |  |         |                                 |  |
|---|--|---|--|--|---------|---------------------------------|--|
| <b>PROPRIETARY AND CONFIDENTIAL</b><br>THE INFORMATION CONTAINED IN THIS DRAWING IS THE SOLE PROPERTY OF <INSERT COMPANY NAME HERE>. ANY REPRODUCTION IN PART OR AS A WHOLE WITHOUT THE WRITTEN PERMISSION OF <INSERT COMPANY NAME HERE> IS PROHIBITED. |  | DIMENSIONS ARE IN INCHES<br>TOLERANCES:<br>FRACTIONAL ±<br>ANGULAR: MACH ± BEND ±<br>TWO PLACE DECIMAL ±<br>THREE PLACE DECIMAL ± |  | NAME   | DATE    | <b>Mesh Frame</b>               |  |
|   |  | MATERIAL<br>Aluminum  |  | DRAWN<br>W. Mui  | 9/28/15 |                                 |  |
|   |  | FINISH<br>As marked.  |  | CHECKED  |         |                                 |  |
|   |  | NEXT ASSY   |  | USED ON  |         |                                 |  |
|   |  | APPLICATION<br>DO NOT SCALE DRAWING   |  | ENG APPR.  |         |                                 |  |
|   |  |   |  | MFG APPR.  |         | SIZE<br><b>A</b>                |  |
|   |  |   |  | Q.A.   |         | DWG. NO.<br><b>2</b>            |  |
|   |  |   |  | COMMENTS:<br>Quantity =2.<br>Slip fits with 'Sintered Metal Diffuser' piece, or as best as possible. |         | REV.                            |  |
|   |  |   |  |  |         | SCALE:1:2 WEIGHT: SHEET 2 OF 13 |  |





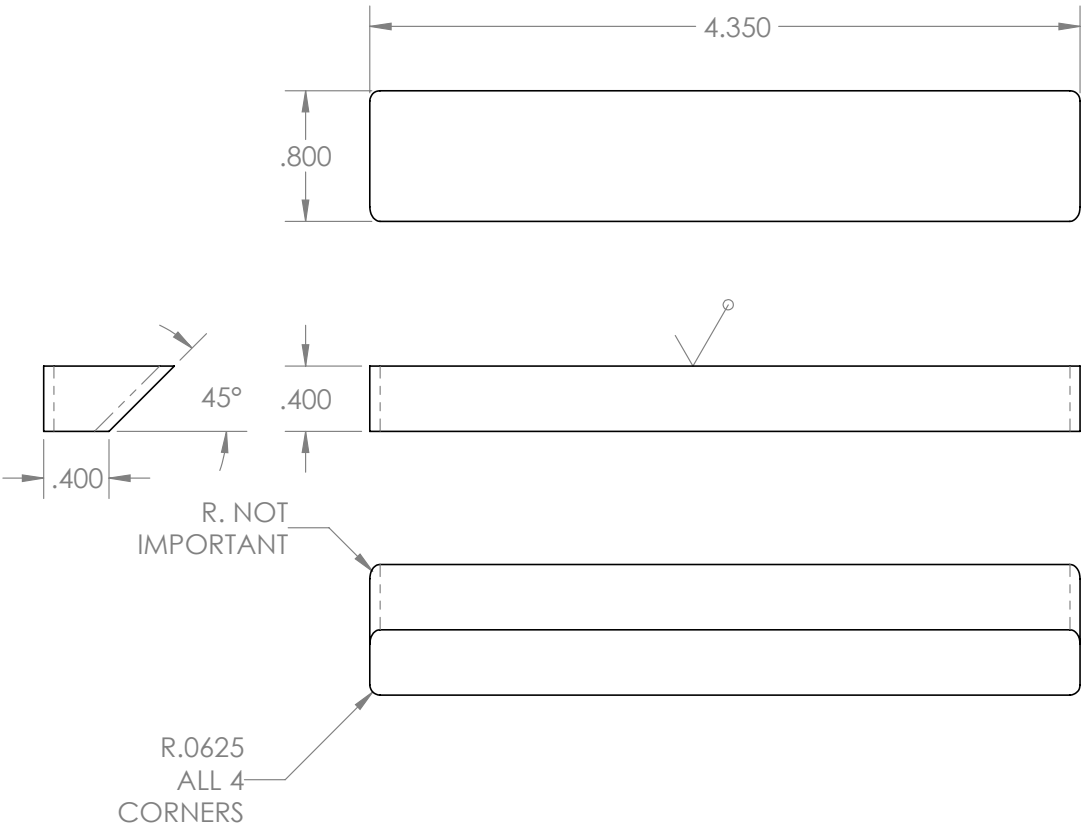
|   |         |   |  |  |                  |                              |               |
|---|---------|---|--|--|------------------|------------------------------|---------------|
| <b>PROPRIETARY AND CONFIDENTIAL</b><br>THE INFORMATION CONTAINED IN THIS DRAWING IS THE SOLE PROPERTY OF <INSERT COMPANY NAME HERE>. ANY REPRODUCTION IN PART OR AS A WHOLE WITHOUT THE WRITTEN PERMISSION OF <INSERT COMPANY NAME HERE> IS PROHIBITED. |         | DIMENSIONS ARE IN INCHES<br>TOLERANCES:<br>FRACTIONAL ±<br>ANGULAR: MACH ± BEND ±<br>TWO PLACE DECIMAL ±<br>THREE PLACE DECIMAL ± |  | NAME   | DATE             | <b>Plastic Inlet Channel</b> |               |
|   |         | MATERIAL Delrin   |  | DRAWN  | W. Mui 9/29/2015 |                              |               |
|   |         | FINISH Finish all around.   |  | CHECKED  |                  |                              |               |
|   |         | DO NOT SCALE DRAWING  |  | ENG APPR.  |                  |                              |               |
|   |         |   |  | MFG APPR.  |                  |                              |               |
| NEXT ASSY   | USED ON |   |  | Q.A.   |                  | SIZE DWG. NO. 4              |               |
| APPLICATION   |         |   |  | COMMENTS:<br>Quantity = 2.<br>Slip fits with 'Metal Inlet Lining' piece. |                  | REV.                         |               |
|   |         |   |  | SCALE: 1:2   |                  | WEIGHT:                      | SHEET 4 OF 13 |



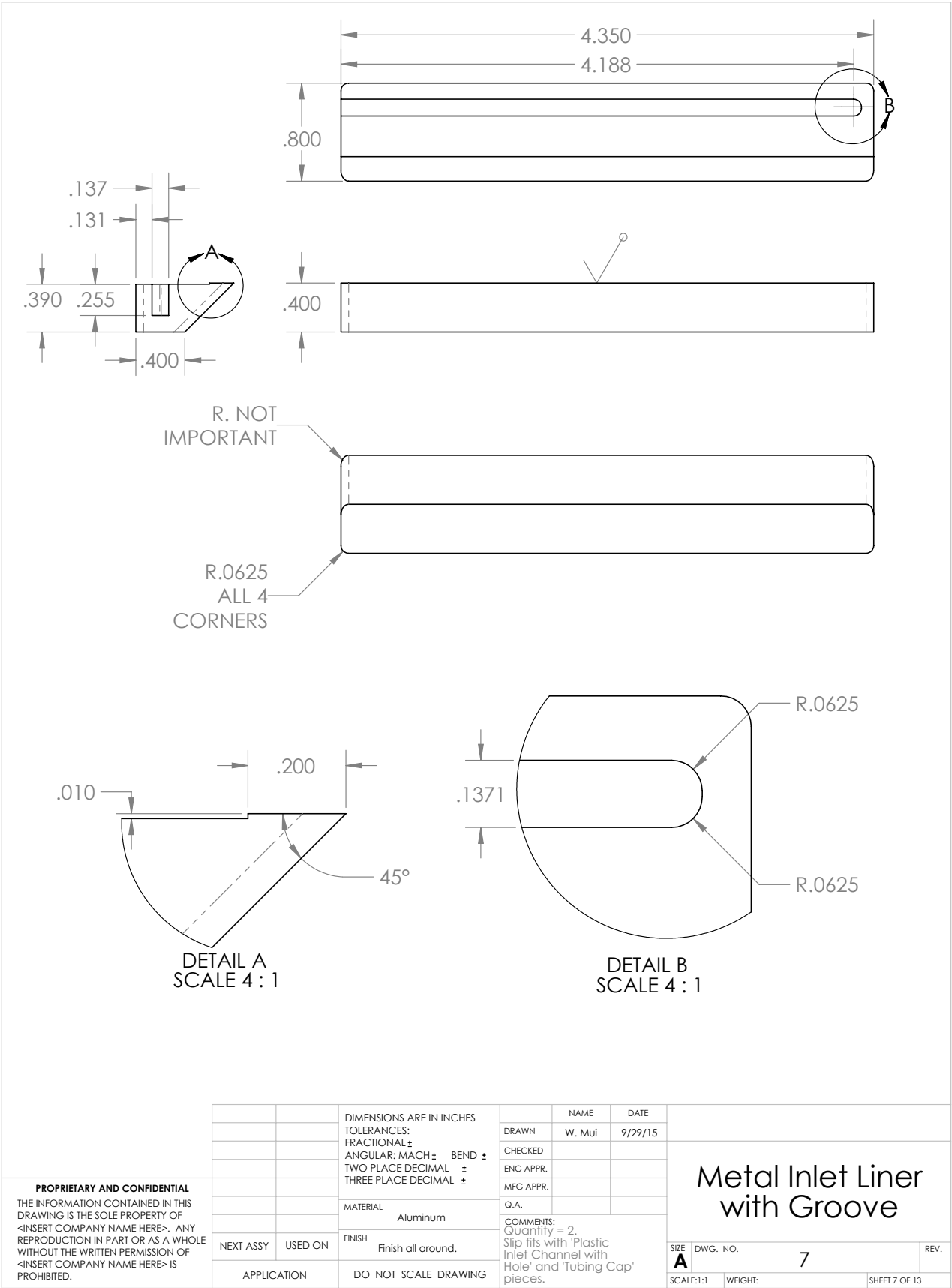
SECTION A-A  
SCALE 4 : 1

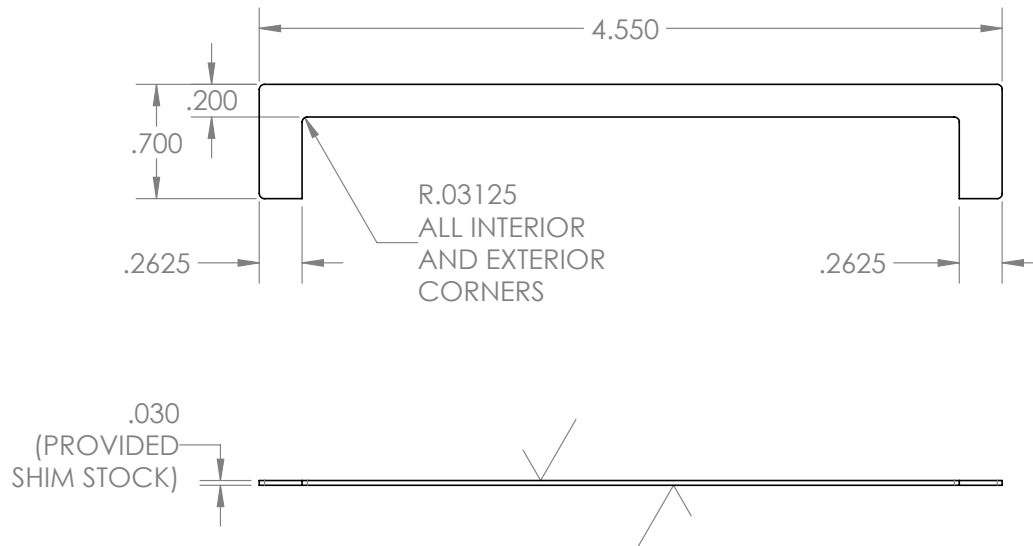
|   |  |  |  |  |         |  |  |
|---|--|--|--|--|---------|--|--|
| <b>PROPRIETARY AND CONFIDENTIAL</b><br>THE INFORMATION CONTAINED IN THIS DRAWING IS THE SOLE PROPERTY OF <INSERT COMPANY NAME HERE>. ANY REPRODUCTION IN PART OR AS A WHOLE WITHOUT THE WRITTEN PERMISSION OF <INSERT COMPANY NAME HERE> IS PROHIBITED. |  | DIMENSIONS ARE IN INCHES<br>TOLERANCES:<br>FRACTIONAL ±<br>ANGULAR: MACH ±    BEND ±<br>TWO PLACE DECIMAL ±<br>THREE PLACE DECIMAL ± |  | NAME   | DATE    | <h1>Plastic Inlet Channel with Hole</h1> |  |
|   |  | MATERIAL<br>Delrin   |  | DRAWN<br>W. Mui  | 9/28/15 |  |  |
|   |  | FINISH<br>Finish all around.   |  | CHECKED  |         |  |  |
|   |  | NEXT ASSY    USED ON   |  | ENG APPR.  |         |  |  |
|   |  | APPLICATION    DO NOT SCALE DRAWING  |  | MFG APPR.  |         |  |  |
|   |  |  |  | Q.A.   |         | SIZE   DWG. NO.    5    REV.             |  |
|   |  |  |  | COMMENTS:<br>Quantity = 2, Slip fits with 1/8" tubing and with 'Metal Inlet Lining with Groove' piece. |         | SCALE:1:2    WEIGHT:    SHEET 5 OF 13    |  |



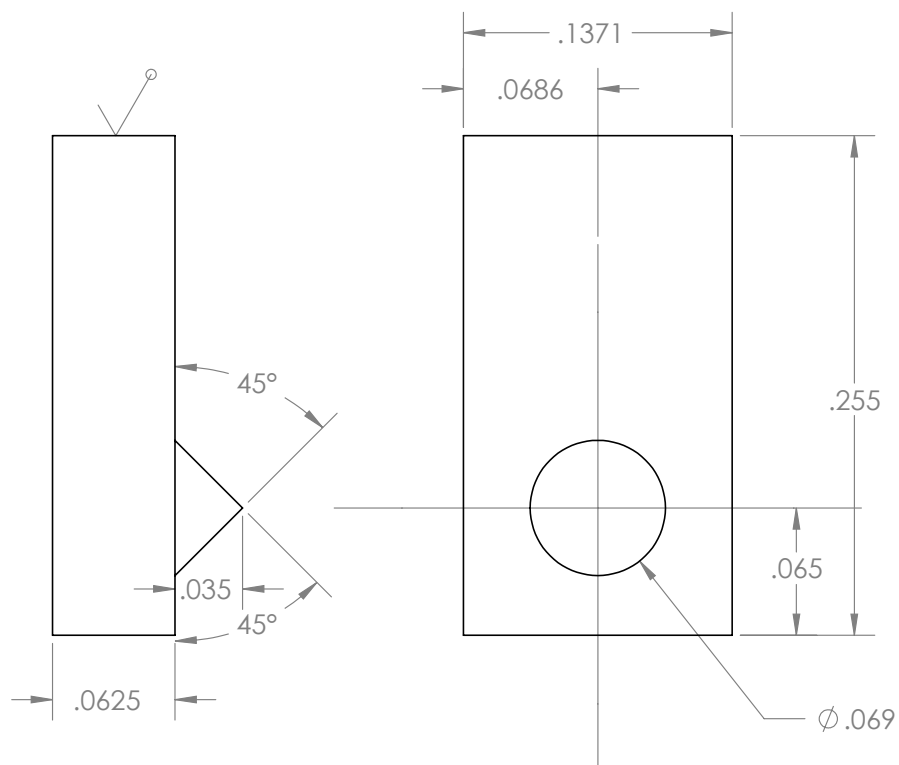


|   |             |         |   |                    |        |            |   |               |      |
|---|-------------|---------|---|--------------------|--------|------------|---|---------------|------|
| <b>PROPRIETARY AND CONFIDENTIAL</b><br>THE INFORMATION CONTAINED IN THIS DRAWING IS THE SOLE PROPERTY OF <INSERT COMPANY NAME HERE>. ANY REPRODUCTION IN PART OR AS A WHOLE WITHOUT THE WRITTEN PERMISSION OF <INSERT COMPANY NAME HERE> IS PROHIBITED. |             |         | DIMENSIONS ARE IN INCHES<br>TOLERANCES:<br>FRACTIONAL ±<br>ANGULAR: MACH ± BEND ±<br>TWO PLACE DECIMAL ±<br>THREE PLACE DECIMAL ± |                    | NAME   | DATE       | Metal Inlet Liner   |               |      |
|   |             |         |   | DRAWN              | W. Mui | 9/29/2015  |   |               |      |
|   |             |         |   | CHECKED            |        |            |   |               |      |
|   |             |         |   | ENG APPR.          |        |            |   |               |      |
|   |             |         |   | MFG APPR.          |        |            |   |               |      |
|   |             |         | MATERIAL  | Aluminum           | Q.A.   |            | Quantity = 2.<br>Slip fits with<br>'Plastic Inlet' piece. |               |      |
|   |             |         | FINISH  | Finish all around. |        |            |   |               |      |
|   | NEXT ASSY   | USED ON |   |                    |        | SIZE       | DWG. NO.  | 6             | REV. |
|   | APPLICATION |         | DO NOT SCALE DRAWING  |                    |        | SCALE: 1:1 | WEIGHT:   | SHEET 6 OF 13 |      |

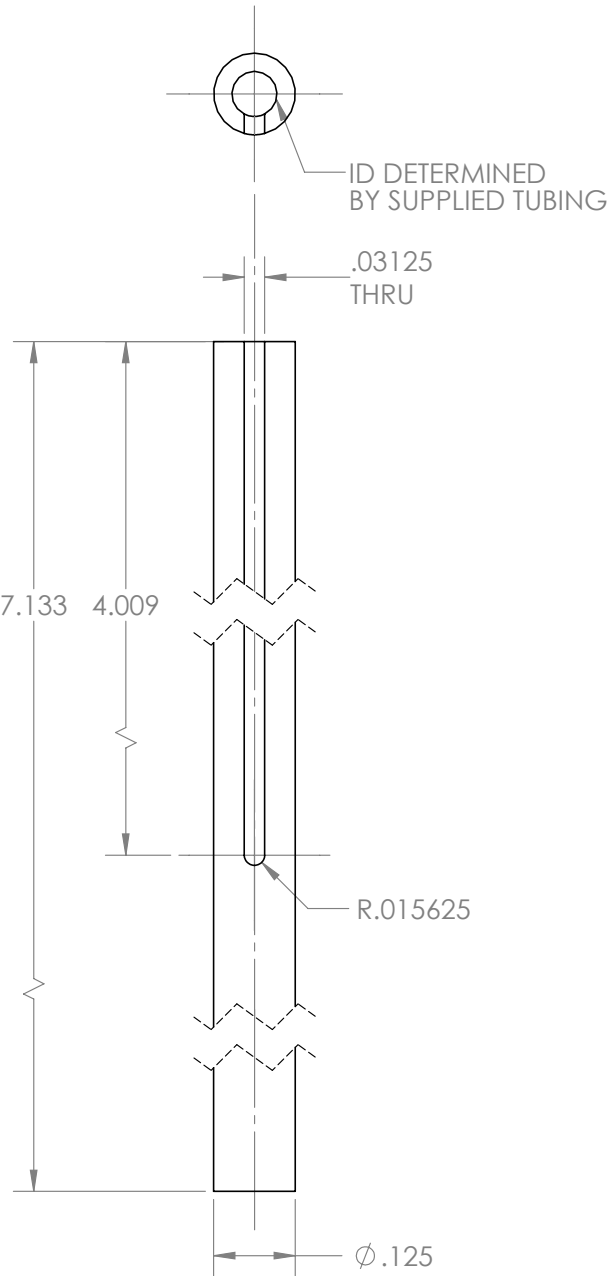




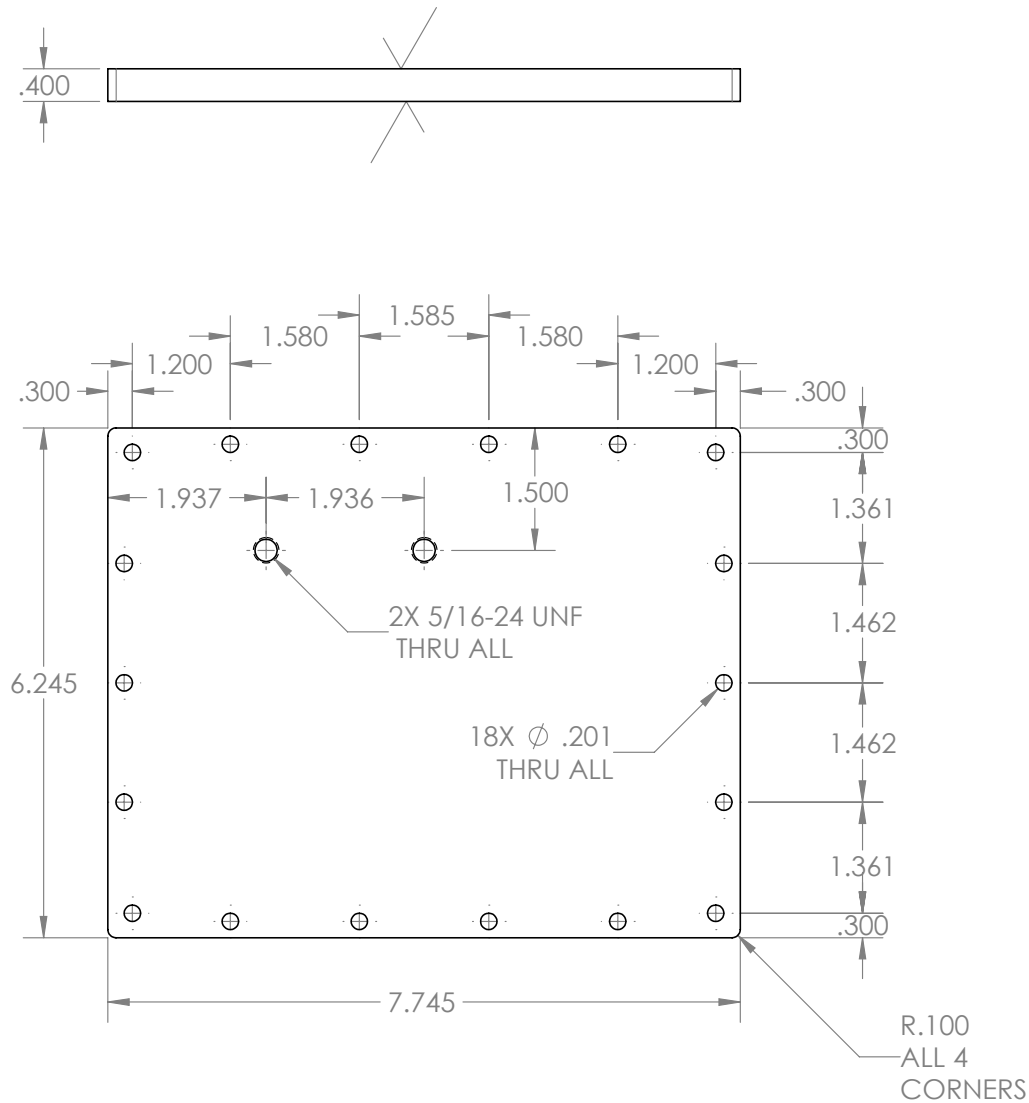
|  |         |                      |            |  |               |                   |   |           |
|--|---------|----------------------|------------|--|---------------|-------------------|---|-----------|
| <p><b>PROPRIETARY AND CONFIDENTIAL</b></p> <p>THE INFORMATION CONTAINED IN THIS DRAWING IS THE SOLE PROPERTY OF &lt;INSERT COMPANY NAME HERE&gt;. ANY REPRODUCTION IN PART OR AS A WHOLE WITHOUT THE WRITTEN PERMISSION OF &lt;INSERT COMPANY NAME HERE&gt; IS PROHIBITED.</p> |         |                      |            | DIMENSIONS ARE IN INCHES<br>TOLERANCES:<br>FRACTIONAL ±<br>ANGULAR: MACH ±    BEND ±<br>TWO PLACE DECIMAL ±<br>THREE PLACE DECIMAL ± | NAME          | DATE              | <h1>Shim</h1>   |           |
|  |         |                      |            |  | DRAWN         | W. Mui            |   | 9/29/2015 |
|  |         |                      |            |  | CHECKED       |                   |   |           |
|  |         |                      |            |  | ENG APPR.     |                   |   |           |
|  |         |                      |            |  | MFG APPR.     |                   |   |           |
|  |         |                      |            | MATERIAL<br>30 mil Shim Stock  | Q.A.          |                   | <p>COMMENTS:</p> <p>Quantity = 2.<br/>Use provided shim stock.<br/>Fits into 'Plastic Inlet Channel with Hole' piece.</p> |           |
| NEXT ASSY  | USED ON | FINISH               | As marked. |  |               |                   |   |           |
| APPLICATION  |         | DO NOT SCALE DRAWING |            |  |               |                   |   |           |
|  |         |                      |            |  | SIZE <b>A</b> | DWG. NO. <b>8</b> | REV.  |           |
|  |         |                      |            |  | SCALE:1:1     | WEIGHT:           | SHEET 8 OF 13   |           |



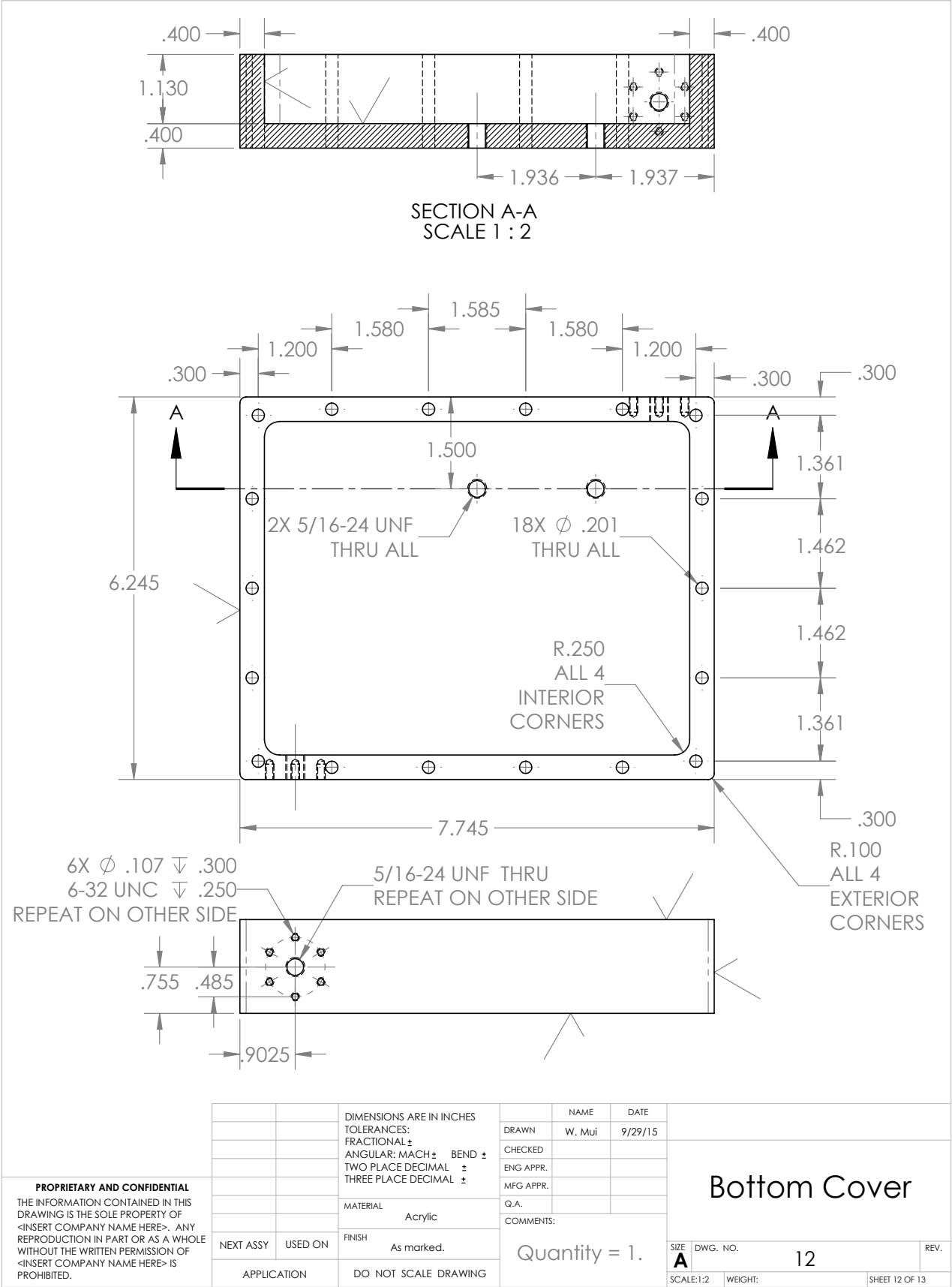
|  |             |         |  |  |                          |   |             |
|--|-------------|---------|--|--|--------------------------|---|-------------|
| <p><b>PROPRIETARY AND CONFIDENTIAL</b></p> <p>THE INFORMATION CONTAINED IN THIS DRAWING IS THE SOLE PROPERTY OF &lt;INSERT COMPANY NAME HERE&gt;. ANY REPRODUCTION IN PART OR AS A WHOLE WITHOUT THE WRITTEN PERMISSION OF &lt;INSERT COMPANY NAME HERE&gt; IS PROHIBITED.</p> |             |         | <p>DIMENSIONS ARE IN INCHES</p> <p>TOLERANCES:</p> <p>FRACTIONAL ±</p> <p>ANGULAR: MACH ± BEND ±</p> <p>TWO PLACE DECIMAL ±</p> <p>THREE PLACE DECIMAL ±</p> | <p>NAME</p> <p>DRAWN W. Muji</p> <p>CHECKED</p> <p>ENG APPR.</p> <p>MFG APPR.</p> <p>Q.A.</p> <p>DATE</p> <p>9/29/15</p> | <p><b>Tubing Cap</b></p> | <p>SIZE DWG. NO. 9</p> <p>SCALE: 12:1 WEIGHT: SHEET 9 OF 13</p> | <p>REV.</p> |
|  |             |         | <p>MATERIAL</p> <p>Aluminum</p>  | <p>COMMENTS:</p> <p>Quantity = 2.</p> <p>Slip fits with 'Metal Inlet Liner with 'Groove' piece.</p>                      |                          |   |             |
|  | NEXT ASSY   | USED ON | <p>FINISH</p> <p>Finish all around.</p>  |  |                          |   |             |
|  | APPLICATION |         | DO NOT SCALE DRAWING   |  |                          |   |             |
|  |             |         |  |  |                          |   |             |
|  |             |         |  |  |                          |   |             |
|  |             |         |  |  |                          |   |             |
|  |             |         |  |  |                          |   |             |

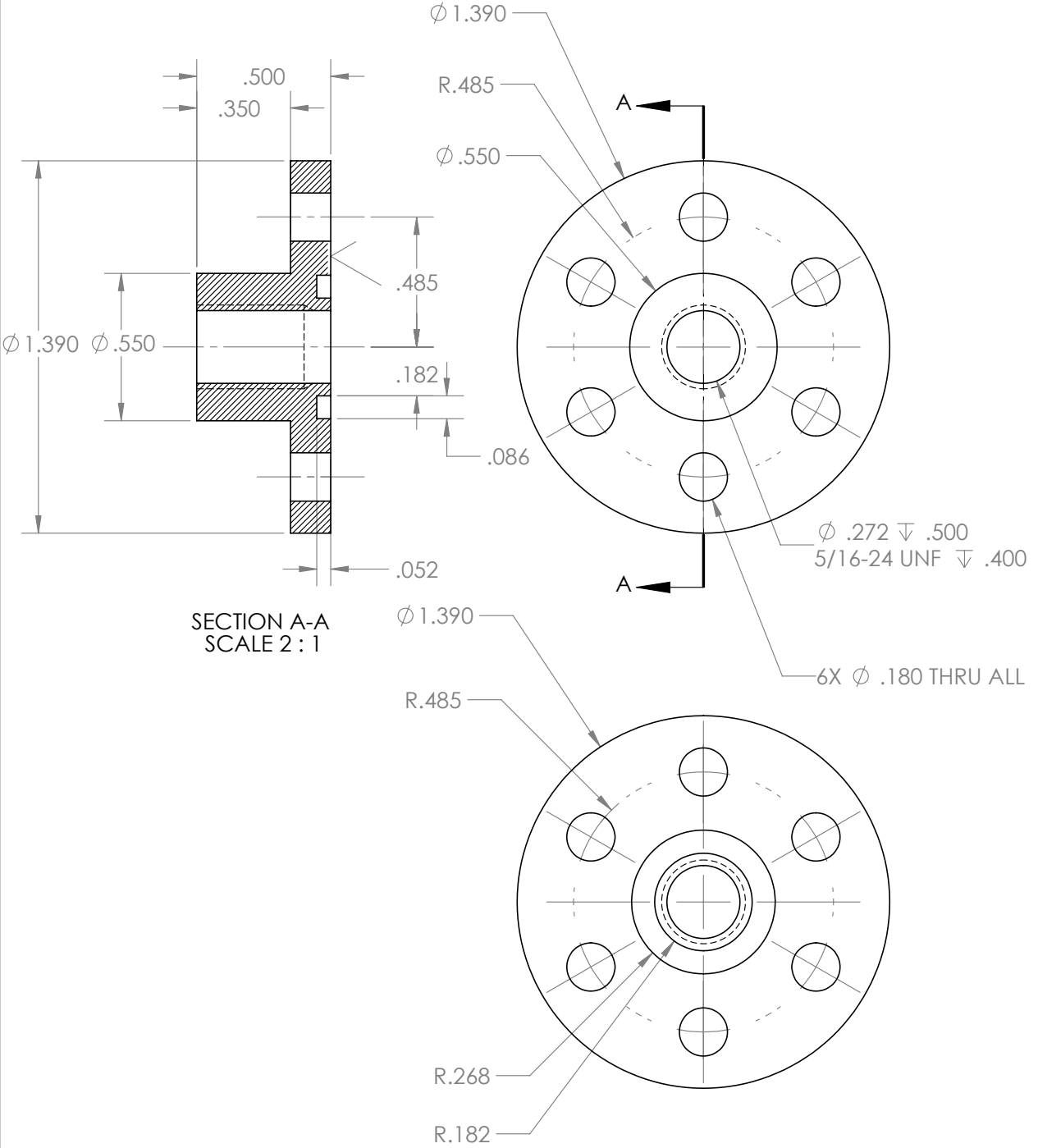


|   |             |         |  |   |   |        |           |  |  |  |
|---|-------------|---------|--|---|---|--------|-----------|--|--|--|
| <div>PROPRIETARY AND CONFIDENTIAL</div> <div>THE INFORMATION CONTAINED IN THIS DRAWING IS THE SOLE PROPERTY OF &lt;INSERT COMPANY NAME HERE&gt;. ANY REPRODUCTION IN PART OR AS A WHOLE WITHOUT THE WRITTEN PERMISSION OF &lt;INSERT COMPANY NAME HERE&gt; IS PROHIBITED.</div> |             |         | DIMENSIONS ARE IN INCHES<br>TOLERANCES:<br>FRACTIONAL ±<br>ANGULAR: MACH ±    BEND ±<br>TWO PLACE DECIMAL   ±<br>THREE PLACE DECIMAL   ± |   | NAME  | DATE   |           |  |  |  |
|   |             |         |  |   | DRAWN   | W. Mui | 9/29/2015 |  |  |  |
|   |             |         |  |   | CHECKED   |        |           |  |  |  |
|   |             |         |  |   | ENG APPR.   |        |           |  |  |  |
|   |             |         |  |   | MFG APPR.   |        |           |  |  |  |
|   |             |         |  |   | Q.A.  |        |           |  |  |  |
|   |             |         |  | MATERIAL<br>1/8" Stainless Steel Tubing | COMMENTS:<br>Quantity = 2.<br>Slip fits into 'Plastic Inlet Channel with Hole' piece. |        |           |  |  |  |
|   | NEXT ASSY   | USED ON | FINISH<br>None   |   |   |        |           |  |  |  |
|   | APPLICATION |         | DO NOT SCALE DRAWING   |   |   |        |           |  |  |  |
|   |             |         |  |   |   |        |           |  |  |  |
|   |             |         |  |   |   |        |           |  |  |  |
|   |             |         |  |   |   |        |           |  |  |  |
|   |             |         |  |   |   |        |           |  |  |  |
|   |             |         |  |   |   |        |           |  |  |  |
|   |             |         |  |   |   |        |           |  |  |  |
|   |             |         |  |   |   |        |           |  |  |  |
|   |             |         |  |   |   |        |           |  |  |  |
|   |             |         |  |   |   |        |           |  |  |  |
|   |             |         |  |   |   |        |           |  |  |  |
|   |             |         |  |   |   |        |           |  |  |  |
|   |             |         |  |   |   |        |           |  |  |  |
|   |             |         |  |   |   |        |           |  |  |  |
|   |             |         |  |   |   |        |           |  |  |  |
|   |             |         |  |   |   |        |           |  |  |  |
|   |             |         |  |   |   |        |           |  |  |  |
|   |             |         |  |   |   |        |           |  |  |  |
|   |             |         |  |   |   |        |           |  |  |  |
|   |             |         |  |   |   |        |           |  |  |  |
|   |             |         |  |   |   |        |           |  |  |  |
|   |             |         |  |   |   |        |           |  |  |  |
|   |             |         |  |   |   |        |           |  |  |  |
|   |             |         |  |   |   |        |           |  |  |  |
|   |             |         |  |   |   |        |           |  |  |  |
|   |             |         |  |   |   |        |           |  |  |  |
|   |             |         |  |   |   |        |           |  |  |  |
|   |             |         |  |   |   |        |           |  |  |  |
|   |             |         |  |   |   |        |           |  |  |  |
|   |             |         |  |   |   |        |           |  |  |  |
|   |             |         |  |   |   |        |           |  |  |  |
|   |             |         |  |   |   |        |           |  |  |  |
|   |             |         |  |   |   |        |           |  |  |  |
|   |             |         |  |   |   |        |           |  |  |  |
|   |             |         |  |   |   |        |           |  |  |  |
|   |             |         |  |   |   |        |           |  |  |  |
|   |             |         |  |   |   |        |           |  |  |  |
|   |             |         |  |   |   |        |           |  |  |  |
|   |             |         |  |   |   |        |           |  |  |  |
|   |             |         |  |   |   |        |           |  |  |  |
|   |             |         |  |   |   |        |           |  |  |  |
|   |             |         |  |   |   |        |           |  |  |  |
|   |             |         |  |   |   |        |           |  |  |  |
|   |             |         |  |   |   |        |           |  |  |  |
|   |             |         |  |   |   |        |           |  |  |  |
|   |             |         |  |   |   |        |           |  |  |  |
|   |             |         |  |   |   |        |           |  |  |  |
|   |             |         |  |   |   |        |           |  |  |  |
|   |             |         |  |   |   |        |           |  |  |  |
|   |             |         |  |   |   |        |           |  |  |  |
|   |             |         |  |   |   |        |           |  |  |  |
|   |             |         |  |   |   |        |           |  |  |  |
|   |             |         |  |   |   |        |           |  |  |  |
|   |             |         |  |   |   |        |           |  |  |  |
|   |             |         |  |   |   |        |           |  |  |  |
|   |             |         |  |   |   |        |           |  |  |  |
|   |             |         |  |   |   |        |           |  |  |  |
|   |             |         |  |   |   |        |           |  |  |  |
|   |             |         |  |   |   |        |           |  |  |  |
|   |             |         |  |   |   |        |           |  |  |  |
|   |             |         |  |   |   |        |           |  |  |  |
|   |             |         |  |   |   |        |           |  |  |  |
|   |             |         |  |   |   |        |           |  |  |  |
|   |             |         |  |   |   |        |           |  |  |  |
|   |             |         |  |   |   |        |           |  |  |  |
|   |             |         |  |   |   |        |           |  |  |  |
|   |             |         |  |   |   |        |           |  |  |  |
|   |             |         |  |   |   |        |           |  |  |  |
|   |             |         |  |   |   |        |           |  |  |  |
|   |             |         |  |   |   |        |           |  |  |  |
|   |             |         |  |   |   |        |           |  |  |  |
|   |             |         |  |   |   |        |           |  |  |  |
|   |             |         |  |   |   |        |           |  |  |  |
|   |             |         |  |   |   |        |           |  |  |  |
|   |             |         |  |   |   |        |           |  |  |  |
|   |             |         |  |   |   |        |           |  |  |  |
|   |             |         |  |   |   |        |           |  |  |  |
|   |             |         |  |   |   |        |           |  |  |  |
|   |             |         |  |   |   |        |           |  |  |  |
|   |             |         |  |   |   |        |           |  |  |  |
|   |             |         |  |   |   |        |           |  |  |  |
|   |             |         |  |   |   |        |           |  |  |  |
|   |             |         |  |   |   |        |           |  |  |  |
|   |             |         |  |   |   |        |           |  |  |  |
|   |             |         |  |   |   |        |           |  |  |  |
|   |             |         |  |   |   |        |           |  |  |  |
|   |             |         |  |   |   |        |           |  |  |  |
|   |             |         |  |   |   |        |           |  |  |  |
|   |             |         |  |   |   |        |           |  |  |  |
|   |             |         |  |   |   |        |           |  |  |  |
|   |             |         |  |   |   |        |           |  |  |  |
|   |             |         |  |   |   |        |           |  |  |  |
|   |             |         |  |   |   |        |           |  |  |  |
|   |             |         |  |   |   |        |           |  |  |  |
|   |             |         |  |   |   |        |           |  |  |  |
|   |             |         |  |   |   |        |           |  |  |  |
|   |             |         |  |   |   |        |           |  |  |  |
|   |             |         |  |   |   |        |           |  |  |  |
|   |             |         |  |   |   |        |           |  |  |  |
|   |             |         |  |   |   |        |           |  |  |  |
|   |             |         |  |   |   |        |           |  |  |  |
|   |             |         |  |   |   |        |           |  |  |  |
|   |             |         |  |   |   |        |           |  |  |  |
|   |             |         |  |   |   |        |           |  |  |  |
|   |             |         |  |   |   |        |           |  |  |  |
|   |             |         |  |   |   |        |           |  |  |  |
|   |             |         |  |   |   |        |           |  |  |  |
|   |             |         |  |   |   |        |           |  |  |  |
|   |             |         |  |   |   |        |           |  |  |  |
|   |             |         |  |   |   |        |           |  |  |  |
|   |             |         |  |   |   |        |           |  |  |  |
|   |             |         |  |   |   |        |           |  |  |  |
|   |             |         |  |   |   |        |           |  |  |  |
|   |             |         |  |   |   |        |           |  |  |  |
|   |             |         |  |   |   |        |           |  |  |  |
|   |             |         |  |   |   |        |           |  |  |  |
|   |             |         |  |   |   |        |           |  |  |  |
|   |             |         |  |   |   |        |           |  |  |  |
|   |             |         |  |   |   |        |           |  |  |  |
|   |             |         |  |   |   |        |           |  |  |  |
|   |             |         |  |   |   |        |           |  |  |  |
|   |             |         |  |   |   |        |           |  |  |  |
|   |             |         |  |   |   |        |           |  |  |  |
|   |             |         |  |   |   |        |           |  |  |  |
|   |             |         |  |   |   |        |           |  |  |  |
|   |             |         |  |   |   |        |           |  |  |  |
|   |             |         |  |   |   |        |           |  |  |  |
|   |             |         |  |   |   |        |           |  |  |  |
|   |             |         |  |   |   |        |           |  |  |  |
|   |             |         |  |   |   |        |           |  |  |  |
|   |             |         |  |   |   |        |           |  |  |  |
|   |             |         |  |   |   |        |           |  |  |  |
|   |             |         |  |   |   |        |           |  |  |  |
|   |             |         |  |   |   |        |           |  |  |  |
|   |             |         |  |   |   |        |           |  |  |  |
|   |             |         |  |   |   |        |           |  |  |  |
|   |             |         |  |   |   |        |           |  |  |  |
|   |             |         |  |   |   |        |           |  |  |  |
|   |             |         |  |   |   |        |           |  |  |  |
|   |             |         |  |   |   |        |           |  |  |  |
|   |             |         |  |   |   |        |           |  |  |  |
|   |             |         |  |   |   |        |           |  |  |  |
|   |             |         |  |   |   |        |           |  |  |  |
|   |             |         |  |   |   |        |           |  |  |  |
|   |             |         |  |   |   |        |           |  |  |  |
|   |             |         |  |   |   |        |           |  |  |  |
|   |             |         |  |   |   |        |           |  |  |  |
|   |             |         |  |   |   |        |           |  |  |  |
|   |             |         |  |   |   |        |           |  |  |  |
|   |             |         |  |   |   |        |           |  |  |  |
|   |             |         |  |   |   |        |           |  |  |  |
|   |             |         |  |   |   |        |           |  |  |  |
|   |             |         |  |   |   |        |           |  |  |  |
|   |             |         |  |   |   |        |           |  |  |  |
|   |             |         |  |   |   |        |           |  |  |  |
|   |             |         |  |   |   |        |           |  |  |  |
|   |             |         |  |   |   |        |           |  |  |  |
|   |             |         |  |   |   |        |           |  |  |  |
|   |             |         |  |   |   |        |           |  |  |  |
|   |             |         |  |   |   |        |           |  |  |  |
|   |             |         |  |   |   |        |           |  |  |  |
|   |             |         |  |   |   |        |           |  |  |  |
|   |             |         |  |   |   |        |           |  |  |  |
|   |             |         |  |   |   |        |           |  |  |  |
|   |             |         |  |   |   |        |           |  |  |  |
|   |             |         |  |   |   |        |           |  |  |  |
|   |             |         |  |   |   |        |           |  |  |  |
|   |             |         |  |   |   |        |           |  |  |  |
|   |             |         |  |   |   |        |           |  |  |  |
|   |             |         |  |   |   |        |           |  |  |  |
|   |             |         |  |   |   |        |           |  |  |  |
|   |             |         |  |   |   |        |           |  |  |  |
|   |             |         |  |   |   |        |           |  |  |  |
|   |             |         |  |   |   |        |           |  |  |  |
|   |             |         |  |   |   |        |           |  |  |  |
|   |             |         |  |   |   |        |           |  |  |  |
|   |             |         |  |   |   |        |           |  |  |  |
|   |             |         |  |   |   |        |           |  |  |  |
|   |             |         |  |   |   |        |           |  |  |  |
|   |             |         |  |   |   |        |           |  |  |  |
|   |             |         |  |   |   |        |           |  |  |  |
|   |             |         |  |   |   |        |           |  |  |  |
|   |             |         |  |   |   |        |           |  |  |  |
|   |             |         |  |   |   |        |           |  |  |  |
|   |             |         |  |   |   |        |           |  |  |  |
|   |             |         |  |   |   |        |           |  |  |  |
|   |             |         |  |   |   |        |           |  |  |  |
|   |             |         |  |   |   |        |           |  |  |  |
|   |             |         |  |   |   |        |           |  |  |  |
|   |             |         |  |   |   |        |           |  |  |  |
|   |             |         |  |   |   |        |           |  |  |  |
|   |             |         |  |   |   |        |           |  |  |  |
|   |             |         |  |   |   |        |           |  |  |  |
|   |             |         |  |   |   |        |           |  |  |  |
|   |             |         |  |   |   |        |           |  |  |  |
|   |             |         |  |   |   |        |           |  |  |  |
|   |             |         |  |   |   |        |           |  |  |  |
|   |             |         |  |   |   |        |           |  |  |  |
|   |             |         |  |   |   |        |           |  |  |  |
|   |             |         |  |   |   |        |           |  |  |  |
|   |             |         |  |   |   |        |           |  |  |  |
|   |             |         |  |   |   |        |           |  |  |  |
|   |             |         |  |   |   |        |           |  |  |  |
|   |             |         |  |   |   |        |           |  |  |  |
|   |             |         |  |   |   |        |           |  |  |  |
|   |             |         |  |   |   |        |           |  |  |  |
|   |             |         |  |   |   |        |           |  |  |  |
|   |             |         |  |   |   |        |           |  |  |  |
|   |             |         |  |   |   |        |           |  |  |  |
|   |             |         |  |   |   |        |           |  |  |  |
|   |             |         |  |   |   |        |           |  |  |  |
|   |             |         |  |   |   |        |           |  |  |  |
|   |             |         |  |   |   |        |           |  |  |  |
|   |             |         |  |   |   |        |           |  |  |  |
|   |             |         |  |   |   |        |           |  |  |  |
|   |             |         |  |   |   |        |           |  |  |  |
|   |             |         |  |   |   |        |           |  |  |  |
|   |             |         |  |   |   |        |           |  |  |  |
|   |             |         |  |   |   |        |           |  |  |  |
|   |             |         |  |   |   |        |           |  |  |  |
|   |             |         |  |   |   |        |           |  |  |  |
|   |             |         |  |   |   |        |           |  |  |  |
|   |             |         |  |   |   |        |           |  |  |  |
|   |             |         |  |   |   |        |           |  |  |  |
|   |             |         |  |   |   |        |           |  |  |  |
|   |             |         |  |   |   |        |           |  |  |  |
|   |             |         |  |   |   |        |           |  |  |  |
|   |             |         |  |   |   |        |           |  |  |  |
|   |             |         |  |   |   |        |           |  |  |  |
|   |             |         |  |   |   |        |           |  |  |  |
|   |             |         |  |   |   |        |           |  |  |  |
|   |             |         |  |   |   |        |           |  |  |  |
|   |             |         |  |   |   |        |           |  |  |  |
|   |             |         |  |   |   |        |           |  |  |  |
|   |             |         |  |   |   |        |           |  |  |  |
|   |             |         |  |   |   |        |           |  |  |  |
|   |             |         |  |   |   |        |           |  |  |  |
|   |             |         |  |   |   |        |           |  |  |  |
|   |             |         |  |   |   |        |           |  |  |  |
|   |             |         |  |   |   |        |           |  |  |  |
|   |             |         |  |   |   |        |           |  |  |  |
|   |             |         |  |   |   |        |           |  |  |  |
|   |             |         |  |   |   |        |           |  |  |  |
|   |             |         |  |   |   |        |           |  |  |  |
|   |             |         |  |   |   |        |           |  |  |  |
|   |             |         |  |   |   |        |           |  |  |  |
|   |             |         |  |   |   |        |           |  |  |  |
|   |             |         |  |   |   |        |           |  |  |  |
|   |             |         |  |   |   |        |           |  |  |  |
|   |             |         |  |   |   |        |           |  |  |  |
|   |             |         |  |   |   |        |           |  |  |  |
|   |             |         |  |   |   |        |           |  |  |  |
|   |             |         |  |   |   |        |           |  |  |  |
|   |             |         |  |   |   |        |           |  |  |  |
|   |             |         |  |   |   |        |           |  |  |  |
|   |             |         |  |   |   |        |           |  |  |  |
|   |             |         |  |   |   |        |           |  |  |  |
|   |             |         |  |   |   |        |           |  |  |  |
|   |             |         |  |   |   |        |           |  |  |  |
|   |             |         |  |   |   |        |           |  |  |  |
|   |             |         |  |   |   |        |           |  |  |  |
|   |             |         |  |   |   |        |           |  |  |  |
|   |             |         |  |   |   |        |           |  |  |  |
|   |             |         |  |   |   |        |           |  |  |  |
|   |             |         |  |   |   |        |           |  |  |  |
|   |             |         |  |   |   |        |           |  |  |  |
|   |             |         |  |   |   |        |           |  |  |  |



|   |         |   |  |               |        |                  |          |
|---|---------|---|--|---------------|--------|------------------|----------|
| <b>PROPRIETARY AND CONFIDENTIAL</b><br>THE INFORMATION CONTAINED IN THIS DRAWING IS THE SOLE PROPERTY OF <INSERT COMPANY NAME HERE>. ANY REPRODUCTION IN PART OR AS A WHOLE WITHOUT THE WRITTEN PERMISSION OF <INSERT COMPANY NAME HERE> IS PROHIBITED. |         | DIMENSIONS ARE IN INCHES<br>TOLERANCES:<br>FRACTIONAL ±<br>ANGULAR: MACH ± BEND ±<br>TWO PLACE DECIMAL ±<br>THREE PLACE DECIMAL ± |  | NAME          | DATE   | <b>Top Cover</b> |          |
|   |         | MATERIAL  |  | DRAWN         | W. Mui |                  |          |
|   |         | Acrylic   |  | CHECKED       |        |                  |          |
|   |         | FINISH  |  | ENG APPR.     |        |                  |          |
|   |         | As marked.  |  | MFG APPR.     |        |                  |          |
| NEXT ASSY   | USED ON | COMMENTS:   |  | Q.A.          |        | SIZE             | DWG. NO. |
| APPLICATION   |         | DO NOT SCALE DRAWING  |  | Quantity = 1. |        | <b>A</b>         | 11       |
|   |         |   |  |               |        | SCALE:1:2        | WEIGHT:  |
|   |         |   |  |               |        | SHEET 11 OF 13   |          |





|   |  |   |  |               |        |                                   |  |
|---|--|---|--|---------------|--------|-----------------------------------|--|
| <b>PROPRIETARY AND CONFIDENTIAL</b><br>THE INFORMATION CONTAINED IN THIS DRAWING IS THE SOLE PROPERTY OF <INSERT COMPANY NAME HERE>. ANY REPRODUCTION IN PART OR AS A WHOLE WITHOUT THE WRITTEN PERMISSION OF <INSERT COMPANY NAME HERE> IS PROHIBITED. |  | DIMENSIONS ARE IN INCHES<br>TOLERANCES:<br>FRACTIONAL $\pm$<br>ANGULAR: MACH $\pm$ BEND $\pm$<br>TWO PLACE DECIMAL $\pm$<br>THREE PLACE DECIMAL $\pm$ |  | NAME          | DATE   | <h1>Flange</h1>                   |  |
|   |  | MATERIAL  |  | DRAWN         | W. Mui |                                   |  |
|   |  | FINISH  |  | CHECKED       |        |                                   |  |
|   |  | NEXT ASSY   |  | ENG APPR.     |        |                                   |  |
|   |  | USED ON   |  | MFG APPR.     |        |                                   |  |
| APPLICATION   |  | DO NOT SCALE DRAWING  |  | Q.A.          |        | COMMENTS:                         |  |
|   |  |   |  | Quantity = 2. |        | SIZE DWG. NO. 13                  |  |
|   |  |   |  |               |        | SCALE: 2:1 WEIGHT: SHEET 13 OF 13 |  |



*Appendix H*ON THE SOURCES OF METHANE TO THE LOS ANGELES  
ATMOSPHERE

By Paul O. Wennberg, Wilton Mui, Debra Wunch, Eric A. Kort, Donald R. Blake, Elliot L. Atlas, Gregory W. Santoni, Steven C. Wofsy, Glenn S. Diskin, Seongeun Jueong, and Marc L. Fischer

This chapter is was originally published in *Environmental Science and Technology* as:

Wennberg, P. O. et al. (2012). “On the sources of methane to the Los Angeles atmosphere”. In: *Environ. Sci. Technol.* 46.17, pp. 9282–9. DOI: 10.1021/es301138y.

## On the Sources of Methane to the Los Angeles Atmosphere

Paul O. Wennberg,<sup>\*,†,‡</sup> Wilton Mui,<sup>†</sup> Debra Wunch,<sup>‡</sup> Eric A. Kort,<sup>§</sup> Donald R. Blake,<sup>||</sup> Elliot L. Atlas,<sup>⊥</sup> Gregory W. Santoni,<sup>#</sup> Steven C. Wofsy,<sup>#</sup> Glenn S. Diskin,<sup>∇</sup> Seongeun Jeong,<sup>○</sup> and Marc L. Fischer<sup>○</sup>

<sup>†</sup>Division of Engineering and Applied Science, California Institute of Technology, Pasadena, California 91125, United States

<sup>‡</sup>Division of Geological and Planetary Sciences, California Institute of Technology, Pasadena, California 91125, United States

<sup>§</sup>Keck Institute for Space Studies, California Institute of Technology, Pasadena, California 91125, United States

<sup>||</sup>School of Physical Sciences, University of California – Irvine, Irvine, California 92697, United States

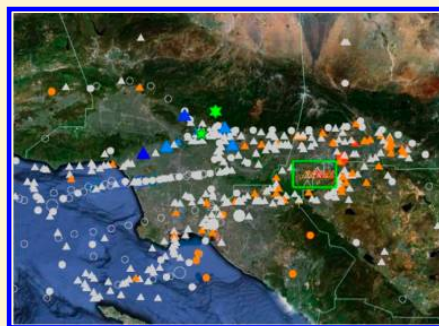
<sup>⊥</sup>Rosenstiel School of Marine and Atmospheric Science, University of Miami, Miami, Florida 33149, United States

<sup>#</sup>School of Engineering and Applied Sciences and Department of Earth and Planetary Sciences, Harvard University, Cambridge, Massachusetts 02138, United States

<sup>∇</sup>NASA Langley Research Center, Hampton, Virginia 23681, United States

<sup>○</sup>Environmental Energy Technologies Division, Lawrence Berkeley National Laboratory, Berkeley, California 94720, United States

**ABSTRACT:** We use historical and new atmospheric trace gas observations to refine the estimated source of methane ( $\text{CH}_4$ ) emitted into California's South Coast Air Basin (the larger Los Angeles metropolitan region). Referenced to the California Air Resources Board (CARB) CO emissions inventory, total  $\text{CH}_4$  emissions are  $0.44 \pm 0.15$  Tg each year. To investigate the possible contribution of fossil fuel emissions, we use ambient air observations of methane ( $\text{CH}_4$ ), ethane ( $\text{C}_2\text{H}_6$ ), and carbon monoxide (CO), together with measured  $\text{C}_2\text{H}_6$  to  $\text{CH}_4$  enhancement ratios in the Los Angeles natural gas supply. The observed atmospheric  $\text{C}_2\text{H}_6$  to  $\text{CH}_4$  ratio during the ARCTAS (2008) and CalNex (2010) aircraft campaigns is similar to the ratio of these gases in the natural gas supplied to the basin during both these campaigns. Thus, at the upper limit (assuming that the only major source of atmospheric  $\text{C}_2\text{H}_6$  is fugitive emissions from the natural gas infrastructure) these data are consistent with the attribution of most ( $0.39 \pm 0.15$  Tg  $\text{yr}^{-1}$ ) of the excess  $\text{CH}_4$  in the basin to uncombusted losses from the natural gas system (approximately 2.5–6% of natural gas delivered to basin customers). However, there are other sources of  $\text{C}_2\text{H}_6$  in the region. In particular, emissions of  $\text{C}_2\text{H}_6$  (and  $\text{CH}_4$ ) from natural gas seeps as well as those associated with petroleum production, both of which are poorly known, will reduce the inferred contribution of the natural gas infrastructure to the total  $\text{CH}_4$  emissions, potentially significantly. This study highlights both the value and challenges associated with the use of ethane as a tracer for fugitive emissions from the natural gas production and distribution system.



### ■ INTRODUCTION

Five to six hundred teragrams (Tg) of methane ( $\text{CH}_4$ ) are currently released into the atmosphere each year.<sup>1</sup> Since 1750, the atmospheric abundance of  $\text{CH}_4$  has increased from ~700 to 1800 ppb, yielding an increase in the globally averaged radiative forcing of ~0.5 W  $\text{m}^{-2}$ , or nearly 1/3 of the total estimated change.<sup>1</sup> The large change in the abundance of  $\text{CH}_4$  has likely also altered the concentrations of atmospheric oxidants such as ozone and the hydroxyl radical.<sup>2</sup> While the total  $\text{CH}_4$  budget and its trend are well constrained by atmospheric data recorded in situ or from air trapped in polar ice and snow, the individual contributions from its many sources (agriculture, natural wetlands, landfill gas release, energy production, and biomass burning) remain uncertain.<sup>3</sup>

Based on inventory analysis, or bottom-up methods, the United States Environmental Protection Agency (USEPA) estimates that US anthropogenic emissions of  $\text{CH}_4$  to the atmosphere in 2009 were 32 Tg.<sup>4</sup> Top-down estimates using

measurements of atmospheric  $\text{CH}_4$  over the US suggest this number is likely too low by 20% or more.<sup>5</sup> Even using the lower USEPA number,  $\text{CH}_4$  accounts for approximately 10% of all US greenhouse gas (GHG) emissions under EPA's assumption that  $\text{CH}_4$  has a 100-year radiative forcing 21 times that of  $\text{CO}_2$  by mass (~12% using IPCC's estimate of 25<sup>1</sup>).

One of the largest sources of  $\text{CH}_4$  in the US are fugitive emissions from natural gas production and use (estimated to be 10 Tg or approximately 3% of the total gas produced).<sup>4</sup> Because  $\text{CH}_4$  has such a large radiative forcing relative to  $\text{CO}_2$ , relatively small losses of  $\text{CH}_4$  to the atmosphere can substantially increase the GHG forcing associated with this sector (e.g., 11% fugitive emission (mol/mol) doubles the 100-

**Received:** March 23, 2012

**Revised:** July 19, 2012

**Accepted:** August 1, 2012

**Published:** August 1, 2012



year radiative forcing compared to a system in which  $\text{CH}_4$  is completely combusted to  $\text{CO}_2$ ). To date, USEPA's evaluation of these fugitive emissions has focused primarily on losses sustained during energy production, while little attention has been paid to its storage, distribution, and end use.<sup>4</sup> Current inventory analysis suggests less than 1% is lost from transmission, storage, and distribution.<sup>4</sup> The California Air Resources Board (CARB) estimates fugitive emissions from the natural gas infrastructure account for only 0.093 Tg/yr or roughly 7% of the total CA  $\text{CH}_4$  source of 1.36 Tg/yr.<sup>6</sup>

In this study, we follow up on the studies of Wunch et al. (2009)<sup>7</sup> and Hsu et al. (2010)<sup>8</sup> that pointed to large  $\text{CH}_4$  emissions from within the greater Los Angeles basin. These reports add to a growing body of evidence for significant  $\text{CH}_4$  emissions from urban regions.<sup>9,10,11</sup>

There are many possible sources of  $\text{CH}_4$  within the greater Los Angeles metropolitan area. There are numerous landfills, some still active. In addition, the dairy industry in the east of the basin, wastewater treatment plants, and petroleum production and refineries as well as seeps of natural geogenic  $\text{CH}_4$ <sup>12</sup> contribute to the total emissions of  $\text{CH}_4$  to the Los Angeles atmosphere. Previous measurements of  $\text{CH}_4$ ,  $\text{CO}$ , and  $\text{CO}_2$ <sup>7,8</sup> cannot distinguish between the sources. Recent measurements of  $\text{CH}_4$  isotopologues by Townsend-Small et al.<sup>13</sup> suggest, however, that fossil fuels are the main source of  $\text{CH}_4$  to the Los Angeles atmosphere.

Most of fossil  $\text{CH}_4$  is derived from thermal decomposition of larger hydrocarbons. As a result, a suite of other gases, including  $\text{C}_2\text{H}_6$ , is typically associated with fossil  $\text{CH}_4$ . With few sources beyond fossil fuel emissions,  $\text{C}_2\text{H}_6$  has been used extensively as a tracer of such emissions.<sup>3,14</sup> Over the past forty years large and increasing quantities of  $\text{C}_2\text{H}_6$  have been removed from the US and Middle East natural gas for production of ethylene (which in turn is used as a chemical feedstock). As described below,  $\text{C}_2\text{H}_6$  is declining in the natural gas supply in Los Angeles and now comprises ~2% of the volume. The low and declining ratio of  $\text{C}_2\text{H}_6$  to  $\text{CH}_4$  in the natural gas reflects the increasing value of  $\text{C}_2\text{H}_6$  whose price is more closely tied with crude oil than natural gas. For example, between 1980 and 2010, US natural gas production increased by 35%, while US production of  $\text{C}_2\text{H}_6$  increased by more than 300%.<sup>15</sup> In 2010,  $\text{C}_2\text{H}_6$  production equaled 6% by mass or 3% by volume of natural gas  $\text{CH}_4$ .<sup>16</sup> As a result, reduction in the amount of  $\text{C}_2\text{H}_6$  in natural gas supplied to consumers has been significant. Xiao et al. (2008)<sup>14</sup> estimated that US natural gas contains ~5%  $\text{C}_2\text{H}_6$  at the wellhead. This suggests that 60% of the  $\text{C}_2\text{H}_6$  is now removed prior to distribution. Thus, uncombusted losses from the natural gas infrastructure post liquid fuel processing (i.e., after the extraction of ethane, propane, etc.) may be an important contributor to the observed decrease in the atmospheric concentration of ethane.<sup>3,17</sup>

In contrast to fossil  $\text{CH}_4$ , biogenic production of  $\text{CH}_4$  by anaerobic methanogens in landfills, wastewater treatment facilities, or in the guts of ruminants has essentially no associated  $\text{C}_2\text{H}_6$  production.<sup>14</sup> Thus, simultaneous measurements of  $\text{CH}_4$  and  $\text{C}_2\text{H}_6$  offer one possible tool to partition enhanced  $\text{CH}_4$  to either fossil or biogenic sources. Here, we use measurements of  $\text{C}_2\text{H}_6$  and  $\text{CH}_4$  as well as other tracers to investigate the sources of excess  $\text{CH}_4$  within the greater Los Angeles Basin.

## DATA SOURCES

**In Situ Atmospheric Data.** The aircraft in situ data used in this analysis were obtained during two sampling studies performed over the Los Angeles basin in 2008 and 2010. In June of 2008, air samples were collected from the NASA DC-8 aircraft during the California portion of the NASA Arctic Research of the Composition of the Troposphere from Aircraft and Satellites (ARCTAS) field experiment.<sup>18</sup> The four ARCTAS flights included in this study (18, 22, 24, and 26 June) occurred during daytime hours and sampled the basin as illustrated in Figure 1. In May and June of 2010, samples were

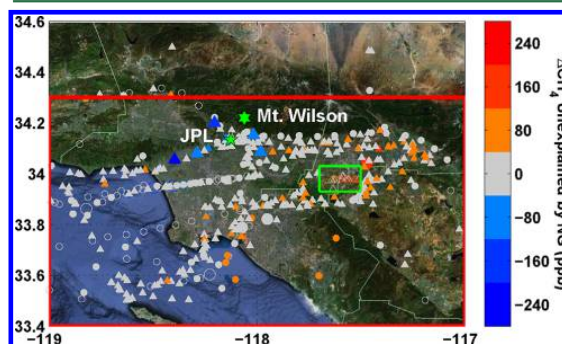


**Figure 1.** The locations of the ARCTAS (circles) and CalNex (triangles) measurements in the greater Los Angeles Basin overlaid on a Google Earth satellite image. The open symbols are measurements excluded from this analysis, either because they are samples that explicitly targeted dairy farms (green box), or because they were obtained in air with markedly different ratios of  $\Delta\text{CO}$  to  $\Delta\text{CO}_2$  than the basin as a whole (see text). The colors represent the amount of  $\Delta\text{CH}_4$  'unexplained' by the putative source from natural gas (see text). Yellow and red colors represent an excess of  $\Delta\text{CH}_4$ . The larger symbol sizes are measurements with  $\Delta\text{C}_2\text{H}_6$  in excess of 4 ppb. The green pentagon and hexagon are the locations of JPL and Mt. Wilson, respectively. The region bounding emission map sums is shown in red.

collected from NOAA's WP-3D aircraft during the California Research at the Nexus of Air Quality and Climate Change (CalNex) study as shown in Figure 1.

$\text{C}_2\text{H}_6$  and other hydrocarbons were measured in so-called "whole-air canisters" collected in both campaigns and analyzed at the University of California – Irvine. The instrumentation and analysis methods are described by Colman et al.<sup>19</sup>  $\text{CH}_4$  and  $\text{CO}$  were measured by tunable diode laser spectroscopy during ARCTAS,<sup>20</sup> while  $\text{CO}_2$  was measured by a nondispersive IR instrument.<sup>21</sup> During CalNex,  $\text{CO}$ ,  $\text{CO}_2$ , and  $\text{CH}_4$  were measured by quantum-cascade laser absorption spectroscopy.<sup>22</sup>

We also make use of measurements from Mt. Wilson (34.22N, 118.06W, elevation 1735 m) previously reported by Hsu et al.<sup>8</sup> and Gorham et al.<sup>23</sup> In four campaigns in 2007 and 2008, continuous real-time monitoring of  $\text{CH}_4$  and meteorological conditions, along with whole-air sampling of organic gases and  $\text{CO}$  analyzed at the University of California – Irvine, were obtained.

**Remote Sensing Atmospheric Data.** Total column measurement of atmospheric  $\text{CO}_2$ ,  $\text{CO}$ , and  $\text{CH}_4$  were measured with a ground-based Fourier transform spectrometer (FTS) located in Pasadena (on the campus of NASA's Jet Propulsion Laboratory) from the fall of 2007 through summer 2008. These data and the method of analysis are described in

Wunch et al.<sup>7</sup> Here, we extend the analysis to examine the seasonal variations in the ratio of CH<sub>4</sub> to CO (and CO<sub>2</sub>).

**Natural Gas Composition Analysis.** The chemical composition of natural gas arriving to the Los Angeles Basin in the major pipelines is measured in situ semicontinuously by gas chromatography using Danalyzers (Daniel Division Headquarters - Houston, Texas, USA). Monthly averages of these data were provided to us by the dominant natural gas supplier to Los Angeles, Southern California Gas Company (May Lew, personal communication). Because we do not know the location of the monitors (each from a different pipeline feeding the basin), we have simply averaged the data for each sampling period to produce an estimate of the ratio of C<sub>2</sub>H<sub>6</sub> to CH<sub>4</sub> in the supply gas. We use the mean reported ratio and assume that the true ratio in the natural gas supply as a whole is within 66% of the range of all the measured values (Table 1). During the

**Table 1. Ratio of Ethane to Methane in Natural Gas (Mol:Mol) Delivered to Southern California Gas Company from Major Pipelines**

| SoCalGas sample ID# | June 2007 (%) | May–July 2008 (%) | April–June 2010 (%) |
|---------------------|---------------|-------------------|---------------------|
| 36817               | 1.76          | 2.14              | 1.36                |
| 36821               | 2.00          | 1.88              | 1.67                |
| 36824               | 1.72          | 1.74              | 1.33                |
| 36825               | 2.14          | 2.14              | 1.80                |
| 36836               | 2.59          | 2.56              | 2.10                |
| mean                | 2.04          | 2.09              | 1.65                |
| 66% of range        | ±0.29         | ±0.27             | ±0.25               |

period of ARCTAS, this ratio was  $2.09 \pm 0.27\%$  while during CalNex the ratio was  $1.65 \pm 0.25\%$ . Despite the large uncertainty in the absolute ratio, the reduction between 2008 and 2010 is a robust result as C<sub>2</sub>H<sub>6</sub> to CH<sub>4</sub> decreased at all pipeline locations sampled ( $-20 \pm 10\%$ ) while the fraction of total natural gas received from each pipeline was similar in 2008 and 2010.<sup>24</sup>

**Analysis.** All the aircraft data used in our analysis are obtained at altitudes less than 1.5 km within the basin (33.5–34.5° N; 117–119° W). To avoid the influence of fire, we only include data where the biomass burning tracer acetonitrile (CH<sub>3</sub>CN) is less than 300 ppt. We define background concentrations for CO, CO<sub>2</sub>, C<sub>2</sub>H<sub>6</sub>, and CH<sub>4</sub> for each flight using the average of the five samples with the lowest values of C<sub>2</sub>H<sub>6</sub>. These 'background' samples are typically from either offshore or at altitudes above the local boundary layer. For C<sub>2</sub>H<sub>6</sub>, the mean standard deviation of the background values (<110 ppt) is much smaller than the enhancements observed

over the basin (1000s ppt). For all the samples taken in each flight, we determine the excess concentration of each gas,  $\Delta X$ , relative to the background value

$$\Delta X = [X] - [X]_0$$

where  $X = \text{CO}, \text{CO}_2, \text{C}_2\text{H}_6$ , or  $\text{CH}_4$ , and  $[X]_0$  denotes the background concentration of  $X$ . While improving the precision of the analysis, the calculation of anomalies relative to these background samples does not alter (within error) the slopes of the gas correlations.

To estimate basin-wide emissions of CH<sub>4</sub> we use the slope of the correlation between  $\Delta \text{CH}_4$  and  $\Delta \text{CO}$  together with estimates of the CO emissions from CARB.<sup>25</sup> This method of estimating the emissions of a gas (using the correlation with CO) does not require that the same source is emitting both gases or even that emissions are geographically colocated. When the lifetimes of gases are long compared to the mixing time within the basin, gases whose sources are distinct will nonetheless be well correlated. Both CH<sub>4</sub> and CO are long-lived, and thus we expect that they will be well correlated - particularly in the afternoon after vertical mixing has helped homogenize the air in the basin. Indeed, previous excess ground-based remote sensing and in situ data from Mt. Wilson have demonstrated that CH<sub>4</sub> (and C<sub>2</sub>H<sub>6</sub>) are highly correlated with CO in the basin.<sup>7,8,23</sup>

To test for spatial representativeness in the aircraft data (i.e., well mixed air masses), we use the ratio of  $\Delta \text{CO}$  to  $\Delta \text{CO}_2$ . The sources of CO are overwhelmingly from automobiles, while those of CO<sub>2</sub> include all sectors in the basin (industrial, residential, mobile). During CalNex, the correlation of  $\Delta \text{CO}$  with  $\Delta \text{CO}_2$  is high ( $R^2=75\%$ ) and  $\Delta \text{CO}/\Delta \text{CO}_2 = 0.82 \pm 0.03\%$ , a value broadly consistent with expectation from the basin-wide estimates of the emissions of these gases.<sup>7</sup> In contrast, the correlation of  $\Delta \text{CO}$  with  $\Delta \text{CO}_2$  in the ARCTAS measurements that are colocated with the whole air samples are bifurcated ( $R^2=51\%$ ). Many of the ARCTAS samples were obtained in the morning at low altitude (<600 m) just offshore. This highly polluted air has a much lower  $\Delta \text{CO}/\Delta \text{CO}_2$  ( $0.28 \pm 0.05\%$ ). We believe this offshore plume results from advection of the shallow and highly polluted nocturnal boundary layer from the basin. This plume has very high concentrations of numerous hydrocarbons including very short-lived alkenes as well as CFCs and HCFCs. To avoid biasing our analysis by these nonrepresentative samples, we filter the data for  $\Delta \text{CO}/\Delta \text{CO}_2 > 0.70\%$ . The locations of the samples that are removed from our analysis are shown as the open circles in Figure 1. The rest of the ARCTAS samples have a  $\Delta \text{CO}/\Delta \text{CO}_2$  broadly consistent with the basin-wide emissions ( $0.86 \pm 0.06\%$ ;  $R^2=88\%$ ). The ratio  $\Delta \text{CO}/\Delta \text{CO}_2$  in 2007/8 is slightly larger

**Table 2. Trace Gas Ratios and Estimated Emissions in Los Angeles**

| year   | location                | $\Delta \text{CH}_4/\Delta \text{CO}_2$ (%) | $\Delta \text{CH}_4/\Delta \text{CO}$ | $\Delta \text{C}_2\text{H}_6/\Delta \text{CO}$ (%) | $\Delta \text{C}_2\text{H}_6/\Delta \text{CH}_4$ (%) | $E_{\text{CO}} (\text{Tg yr}^{-1})^b$ | $E_{\text{C}_2\text{H}_6} (\text{Gg yr}^{-1})$ | $E_{\text{CH}_4} (\text{Tg yr}^{-1})$ | $E_{\text{max CH}_4 \text{ NG}} (\text{Tg yr}^{-1})$ |
|--------|-------------------------|---|---------------------------------------|--|--|---------------------------------------|--|---------------------------------------|--|
| 2007/8 | Pasadena <sup>7</sup>   | $0.78 \pm 0.08$                             | $0.66 \pm 0.12^a$                     |  |  | 1.20                                  |  | $0.4 \pm 0.1$                         |  |
| 2007/8 | Mt. Wilson <sup>8</sup> | ---   | $0.55 \pm 0.03$                       | $1.13 \pm 0.19$                                    | $2.05 \pm 0.30^c$                                    | 1.20                                  | 14.5   | $0.38 \pm 0.1$                        | $0.38 \pm 0.15$                                      |
| 2008   | ARCTAS                  | $0.674 \pm 0.058$                           | $0.761 \pm 0.038$                     | $1.37 \pm 0.12$                                    | $1.70 \pm 0.16$                                      | 1.13                                  | 16.6   | $0.47 \pm 0.1$                        | $0.38 \pm 0.15$                                      |
| 2010   | CalNex                  | $0.655 \pm 0.029$                           | $0.743 \pm 0.031$                     | $1.17 \pm 0.08$                                    | $1.50 \pm 0.11$                                      | 1.03                                  | 12.9   | $0.44 \pm 0.1$                        | $0.40 \pm 0.15$                                      |

<sup>a</sup>The ratio and uncertainty are derived from the variation of the monthly data shown in Figure 2. <sup>b</sup>We use the inventory from the California Air Resources Board for 2008 and 2010. Estimate of the emissions in 2007 are interpolated between the 2005 and 2008 inventory.<sup>32</sup> <sup>c</sup>Hsu et al.<sup>8</sup> reported the ratio of methane to CO in flask samples obtained from Mt. Wilson; Gorham et al.<sup>23</sup> reported the ratio of ethane to methane in the same samples. Here we report the ratio of these ratios for the 4 sample periods described in Hsu et al.<sup>8</sup>

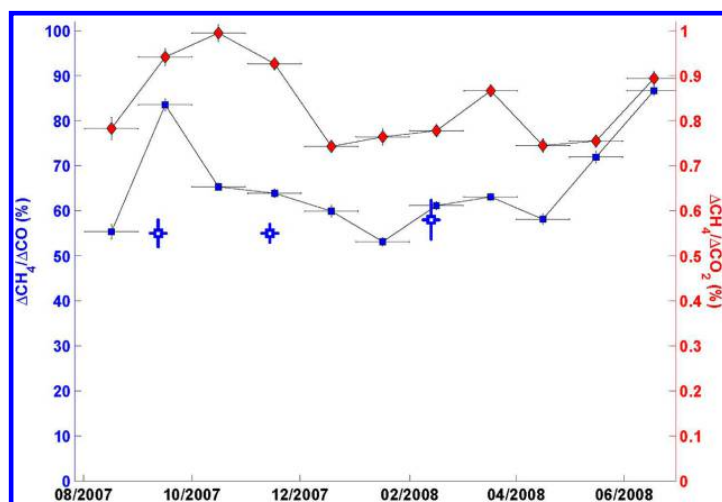


**Figure 2.** The monthly ratio of  $\Delta\text{CH}_4/\Delta\text{CO}$  (blue squares, left axis) and  $\Delta\text{CH}_4/\Delta\text{CO}_2$  (red diamonds, right axis) measured by a remote sensing technique at the campus of NASA's Jet Propulsion Laboratory (closed symbols) and at the top of Mt. Wilson (open symbols) by in situ sampling.

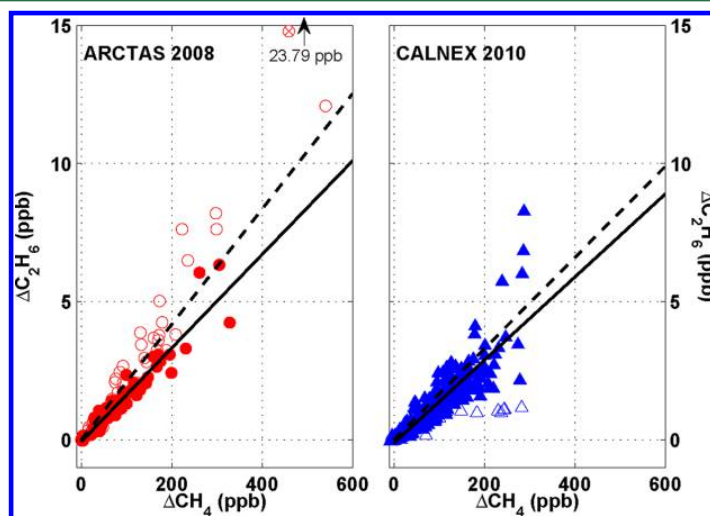


**Figure 3.**  $\Delta\text{C}_2\text{H}_6$  and  $\Delta\text{CH}_4$  during the ARCTAS 2008 and CalNex 2010 aircraft campaigns. The solid lines are the best fit lines to the data, and the dashed lines are the ratios of  $\text{C}_2\text{H}_6$  to  $\text{CH}_4$  in the natural gas delivered to the greater Los Angeles basin at the times of the measurements. The open symbols are measurements excluded from this analysis, either because they are samples that explicitly targeted dairy farms or because they were obtained in air with markedly different ratios of  $\Delta\text{CO}$  to  $\Delta\text{CO}_2$  (see text).

than in 2010, not inconsistent with the CARB inventory which suggests that CO emissions declined by  $\sim 6\text{--}8\%$  per year between 2005 and 2008 and by  $\sim 5\%$  per year between 2008 and 2010 (see Table 2).

During CalNex, the aircraft heavily sampled the dairy area near Chino, CA ( $33.98 \pm 0.05$  N;  $117.6 \pm 0.10$  W), shown in the small green box in Figure 1. This area is home to approximately 150,000 dairy cows, approximately 8% of the California dairy.<sup>26</sup> We excluded these data (shown as open symbols in Figure 1 and Figure 3) from our analysis to avoid spatial representativeness bias (e.g., to produce a sample set in 2008 and 2010 with a similar geographical distribution).

For a temporal representativeness test, we rely on the nearly continuous year-long total column measurements obtained at JPL in 2007/2008.<sup>7</sup> The slopes of  $\Delta\text{CH}_4$  vs  $\Delta\text{CO}$  and  $\Delta\text{CO}_2$

(monthly average) are shown in Figure 2. There is little ( $\pm 15\%$ ) variability in the slope of  $\Delta\text{CH}_4$  to  $\Delta\text{CO}$  seasonally. Further, we see no difference in the correlation between weekdays and weekends (not shown). Thus, consistent with the Hsu et al. and Gorham et al. studies from Mt. Wilson, it appears that the  $\text{CH}_4$  emissions do not have strong temporal variations. A similar lack of temporal variability in urban  $\text{CH}_4$  emissions was noted by Gioli et al. in their study of Florence, Italy.<sup>9</sup>

In Table 2, we tabulate the observed slope of  $\Delta\text{CH}_4$  vs  $\Delta\text{CO}$  and  $\Delta\text{C}_2\text{H}_6$  vs  $\Delta\text{CO}$  (as well as slopes to  $\Delta\text{CO}_2$ ). We include in this table the previously reported data including ground-based in situ measurements obtained on Mt. Wilson, just north of Pasadena,<sup>8</sup> and ground-based remote sensing measurements.<sup>7</sup> For the remote sensing data, the error is derived from



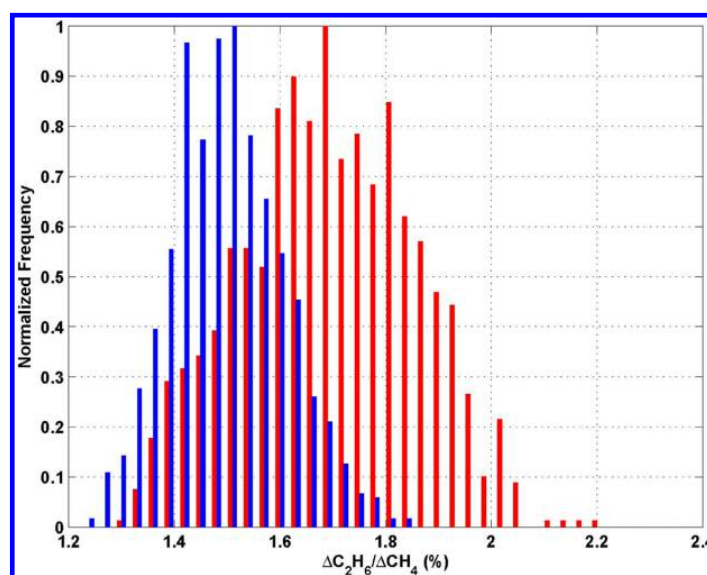


**Figure 4.** Histograms of the distributions of the slopes of the possible linear fits to the data in Figure 3 from the bootstrap analysis. The data in red (to the right) are computed from the ARCTAS measurements, and the data in blue (to the left) are from CalNex.

the observed month-to-month variability shown in Figure 2. Uncertainty in the Mt. Wilson data is as reported by the authors of these studies.

Using the CARB CO inventory, the unweighted mean and standard deviation of the resulting  $\text{CH}_4$  emissions estimates are  $0.44 \pm 0.04$  Tg. Additional sources of error include unaccounted for spatial and temporal representation error (perhaps <10% given the consistency of these different approaches) and uncertainty in the emissions of CO (~10%), suggesting that total annual emissions of  $\text{CH}_4$  to the basin are  $0.44 \pm 0.15$  Tg. Similarly,  $\text{C}_2\text{H}_6$  annual emissions are estimated to be  $14 \pm 4$  Gg.

A scatter plot of  $\Delta\text{C}_2\text{H}_6$  plotted as a function of the  $\Delta\text{CH}_4$  is shown in Figure 3 for both the ARCTAS and CalNex campaigns. The observed slopes of  $\Delta\text{C}_2\text{H}_6$  vs  $\Delta\text{CH}_4$  are listed in Table 2 and shown as the solid line on Figure 3. Errors, listed in Table 2 and illustrated in Figure 4, are calculated using the bootstrap method.<sup>27</sup>

## DISCUSSION

**Bottom Up Inventory.** Shown in Table 3 is an estimate of the sources for  $\text{CH}_4$  and  $\text{C}_2\text{H}_6$  to the Los Angeles Air Basin by sector for 2008. The basin-level  $\text{CH}_4$  emissions are estimates calculated by summing 0.1 degree (~10 km) spatial resolution maps of California's estimated annual average emissions<sup>28</sup> for

**Table 3.** 2008 Sector Based Inventory for Emissions of  $\text{CH}_4$  and  $\text{C}_2\text{H}_6$  into the Atmosphere of the South Coast Air Basin

| sector      | $\text{CH}_4$ emissions (Tg/yr) | $\text{C}_2\text{H}_6$ emissions (Gg/yr) |
|-------------|---------------------------------|--|
| landfills   | 0.086                           | —  |
| livestock   | 0.076                           | —  |
| wastewater  | 0.020                           | —  |
| petroleum   | 0.007                           | 1.3                                      |
| wetlands    | 0.001                           | —  |
| natural gas | 0.022                           | 0.9                                      |
| SUM         | 0.212                           | 2.2                                      |

different source sectors over the red box ( $-119 < \text{longitude} < -117$ ,  $33.4 < \text{latitude} < 34.3$ ) that captures the LA Basin (Figure 1). The emissions from landfills are derived from estimates of individual landfills following established methods.<sup>29</sup> Emissions from livestock are estimated by scaling livestock density to 2008 total emissions reported of California livestock.<sup>6,30</sup> Emissions from wetlands are derived from Potter et al.<sup>31</sup> For wastewater, we use the CARB inventory<sup>32</sup> for statewide domestic wastewater treatment multiplied by the fraction of state residents using either septic systems or central waste treatment.<sup>33</sup> Of the 3.5 million California residents using septic systems, 28% live in the Los Angeles basin (mostly in the east of the basin) yielding 0.010 Tg/yr, while 45% of the California residents using central waste treatment live in the basin yielding 0.009 Tg/yr. In addition, we add 50% of the emission due to statewide wastewater treatment associated with petroleum refining (0.001 Tg/yr). The remainder of the statewide wastewater inventory is associated with agriculture, particularly paper pulp processing; we assume none of the emissions are in the basin. As we have filtered our atmospheric data to avoid biomass burning, we do not include any such emissions here.

For petroleum, the inventory is derived from mandatory reporting of oil extraction and refining to the CARB. In addition, we include the CARB statewide mobile emissions associated with the basin.<sup>30</sup> For natural gas, we use an estimate of the fraction of the "Lost-and-Unaccounted-For Gas" from either known fugitive emissions or unaccounted for losses as communicated to us by the Southern California Gas Company (0.02 Tg  $\text{CH}_4$ /yr or approximately 0.1% of deliveries, M.A. Bermel, Southern California Gas Company, personal communication). As only 0.01 Tg of natural gas was produced in the basin in 2009 (in production not associated with petroleum extraction), we neglect this sector.

For  $\text{C}_2\text{H}_6$ , we assume that only the petroleum and natural gas sectors have associated emissions. For petroleum, we assume that the ratio of  $\text{C}_2\text{H}_6$  to  $\text{CH}_4$  is 10%,<sup>14,34</sup> while for the natural

gas sector we use the measured  $C_2H_6:CH_4$  ratio in 2008 from the Southern California Gas Company (Table 1).

In sum, while the bottom-up  $CH_4$  inventory (0.212 Tg/yr) accounts for 35–73% of the inferred total emissions to the basin, these sources explain a much smaller fraction of the excess  $C_2H_6$  (~15%). To simultaneously close the budget of both gases requires a 0.23 Tg source of  $CH_4$  with a  $C_2H_6:CH_4$  molar ratio of 2.6%, a ratio consistent with a source from fossil fuels.

**Fossil Fuel Emissions of Methane and Ethane in the Basin.** There are two fossil  $CH_4$  sources to the basin that need to be better quantified: 1) emissions from underlying geological resource and 2) emissions associated with the imported natural gas.

The Los Angeles Basin overlays a large number of petroleum and gas rich sediments.<sup>12b</sup> In 2009, 0.22 Tg of natural gas was produced in the basin (approximately 2% of the gas consumed) – the vast majority associated with petroleum production.<sup>35</sup> In addition, there are numerous capped wells from historical gas and oil production.<sup>34</sup> The CARB inventory suggests, however, that the methane (and, by inference, the  $C_2H_6$ ) emissions from this sector are small (Table 3).<sup>8</sup> If the emissions from petroleum production or from emissions of capped wells are much higher than reported, this sector could be an important contributor to both the  $C_2H_6$  and  $CH_4$  budgets.

In a heterogeneous environment such as Los Angeles, it is not straightforward to find unique tracers of the geological gas emissions. For example, while the ratio of propane to  $C_2H_6$  in Los Angeles air<sup>23</sup> (~1) is similar to the ratio measured in many of the gas and petroleum fields<sup>34</sup> and much higher than in the natural gas supply (~0.17), large amounts of propane are sold in Los Angeles (~0.6 Tg/yr).<sup>36</sup> Gorham et al. estimate of 71 tons of propane emitted into the basin each day<sup>23</sup> thus represents only ~4% of the supply. Indeed, elevated propane is found in many cities that have no known geological sources.<sup>37</sup>

Emissions from the natural gas infrastructure are estimated by the Southern California Gas Company to be very small. Nevertheless, it is striking how similar the slope of  $\Delta C_2H_6$  vs  $\Delta CH_4$  is to the ratio of these gases in the natural gas supply (shown as dashed lines in Figure 3). In addition, the change in the observed ratio between 2008 (ARCTAS) and 2010 (CalNex) is of the same sign and magnitude as the reduction in the amount of  $C_2H_6$  in the natural gas.

To estimate the upper limit to the contribution of emissions from the imported natural gas to the total sources of methane, we use the ratio of ethane to methane in ambient air and in the gas supply. Assuming that the only significant source of  $C_2H_6$  to the Los Angeles atmosphere is fugitive emissions of natural gas, the maximum emissions of  $CH_4$  into the atmosphere from natural gas, NG, are

$$E_{\max}(CH_{4,NG}) = E(CH_4) \times (\beta/\alpha)$$

where  $\alpha$  is the ratio of  $C_2H_6$  to  $CH_4$  in the natural gas (Table 1), and  $\beta$  is the same ratio in ambient air. The values of  $\beta$  are reported in Table 2. Clearly, if the only emissions of  $C_2H_6$  are from uncombusted natural gas supplied to the basin, most of the  $\Delta CH_4$  in the basin is also derived from this source. The average  $E_{\max}(CH_{4,NG})$  is  $0.39 \pm 0.15$  Tg where the error is dominated by the systematic uncertainty in  $\alpha$  (Table 2).

We show in Figure 1 the mixing ratio of  $\Delta CH_4$  not explained by  $\Delta C_2H_6$ ,  $[\Delta CH_4]^*$

$$[\Delta CH_4]^* = \Delta CH_4 - 1/\alpha(\Delta C_2H_6)$$

The circles are from 2008 while the triangles are from 2010. The larger symbols are locations where  $\Delta C_2H_6$  is greater than 4 ppb. The only obvious source of  $CH_4$  not associated with  $\Delta C_2H_6$  is in the east of the basin near Chino, California (red open triangles within the green box), where a large concentration of dairy farms is located. Samples obtained near landfills (e.g., Scholl Canyon (34.16N,118.19W)) and near the large Hyperion wastewater treatment plant (33.92N,118.43W) show no obvious  $CH_4$  enhancements above those explained by  $C_2H_6$ , though the sampling is admittedly sparse and wind will certainly advect these emissions away from their source.

Southern California Gas Company delivers natural gas to the Los Angeles Basin and the surrounding area. Approximately 30% of its gas is delivered to residential customers (5.4 Tg/yr), 30% to industrial and commercial customers (5.6 Tg/yr), 37% to electric utilities (6.9 Tg/yr), and the remainder to natural gas vehicles and enhanced oil recovery steaming (0.5 Tg/yr).<sup>38</sup> Assuming that this distribution of gas is the same inside the Los Angeles Basin (which includes Los Angeles, San Bernardino, Orange, and Riverside Counties), an emission of 0.39 Tg represents approximately 3.5% of the gas delivered to customers in the basin (~11 Tg in 2007).<sup>38</sup> Southern California Gas Company also delivers to Fresno, Imperial, Kern, Kings, Santa Barbara, San Luis Obispo, Tulare, and Ventura Counties, which are less densely populated, are not located in the basin, and consume an additional 1 Tg for residential customers and 6 Tg for nonresidential customers. Southern California Gas Company,<sup>24</sup> however, operates several large storage facilities within the basin. Thus, using the total volume flowing through pipelines in the basin as a denominator, 0.39 Tg represents approximately 2% of the gas flowing into the basin.

As mentioned above, however, mass balance estimates by Southern California Gas Company suggest that only ~0.1% of the natural gas is lost between the city gates and the customer meters (M. A. Bermel, Southern California Gas Company, personal communication). This suggests that if the methane emissions in Los Angeles are associated with the natural gas infrastructure, such losses must occur post consumer metering. Losses of gas within both homes and businesses are certainly one possible explanation for our findings. Steady but very small leaks from gas fittings and valves could contribute a significant fraction of the total gas used in these settings. Indeed, it is highly likely that the vast majority of all valves and fittings between the gas wells and the end-use gas appliances are located at the very end of the delivery system, e.g. in customers' homes and businesses. For example, the first author's home (constructed in 1914) contains no fewer than 100 gas fittings, seven ball valves, and, within the appliances themselves, eight control/throttle valves; several had obvious leaks. Yet, the duty cycle of appliance use is very low – just a few percent of the time is any gas appliance in use. Thus, small steady leaks could amount to a few percent of the total consumed. Such leaks would produce only a small enhancement in methane in the home and would not be detectable by smell or constitute, in any way, a health or fire hazard. For example, consider a 150 m<sup>2</sup> home that uses 1000 m<sup>3</sup> of gas annually and has one air exchange each hour. If 5% of the annual natural gas usage is lost unburned into the home (less than the use of a typical pilot light), methane concentrations would only be about 12 ppm higher than in the ambient air outside the home; the odorant concentration would be orders of magnitude below the threshold necessary to smell the gas. If such high leakage

rates occurred across the US, losses within the distribution system would represent a source of more than 6 Tg/year.<sup>4</sup> This additional source of CH<sub>4</sub> would go a substantial way toward reconciling the top-down and inventory estimates of total US CH<sub>4</sub> sources.<sup>39</sup> Electronic gas metering is currently being installed throughout Southern California Gas Company's service area, and these data may provide a rapid and noninvasive method of evaluating whether some or many customers have unrealistically large and steady natural gas consumption.

**Outlook for Future Studies.** Emissions of methane from Los Angeles are substantial and considerably larger than current inventories suggest. The correlation between methane and ethane within the basin point suggest fossil fuel emissions as the likely source of much of the unaccounted for source. We are unable, however, to definitively determine whether these emissions are associated with imported gas or emissions from the underlying geological resource. The obvious next step is to undertake in situ sampling to seek out sources of methane within Los Angeles and more broadly in a cross section of urban centers, in an extended version of the work by Baker et al.<sup>26</sup> These measurements should include a suite of hydrocarbons and perhaps sulfur compounds together with an associated inventory of possible sources, including natural gas.

## AUTHOR INFORMATION

### Corresponding Author

\*Phone: 626-395-2447. E-mail: wennberg@caltech.edu.

### Notes

The authors declare no competing financial interest.

## ACKNOWLEDGMENTS

Data used in this analysis were obtained with support of NASA, NOAA, and the California Air Resources Board. We thank Stephanie A. Vay for her efforts to obtain the CO<sub>2</sub> data during ARCTAS. We thank the Southern California Gas Company for their interest and support in this study. The analysis was supported by the California Institute of Technology. Support for the analysis of the remote sensing data was provided by NASA's Terrestrial Ecology Program. W.M. acknowledges support from a NSF Graduate Research Fellowship. This work was funded in part by the W. M. Keck Institute for Space Studies. G.S. acknowledges support from NSF and EPA STAR graduate fellowships. We thank Joseph Fischer, Larry Hunsaker, Webster Tassat, Marc Vayssières, and Ying-Kang Hsu for sharing advice and data. This work was supported by the California Energy Commission's Public Interest Environmental Research (CEC-PIER) program, the California Air Resources Board, and the US Dept. of Energy through the LBNL Laboratory Directed Research and Development, under contract No. DE-AC02-05CH11231.

## REFERENCES

- (1) Solomon, S. Intergovernmental Panel on Climate Change; Intergovernmental Panel on Climate Change. Working Group I, Climate Change 2007: The Physical Science Basis: Contribution of Working Group I to the Fourth Assessment Report of the Intergovernmental Panel on Climate Change. Cambridge University Press: Cambridge, New York, 2007; p viii, 996 p.
- (2) Shindell, D. T.; Faluvegi, G.; Koch, D. M.; Schmidt, G. A.; Unger, N.; Bauer, S. E. Improved Attribution of Climate Forcing to Emissions. *Science* **2009**, 326 (5953), 716–718, DOI: 10.1126/Science.1174760.

- (3) Aydin, M.; Verhulst, K. R.; Saltzman, E. S.; Battle, M. O.; Montzka, S. A.; Blake, D. R.; Tang, Q.; Prather, M. J. Recent decreases in fossil-fuel emissions of ethane and methane derived from firm air. *Nature* **2011**, 476 (7359), 198–201, DOI: 10.1038/Nature10352.
- (4) United States Environmental Protection Agency, 2011 U.S. Greenhouse Gas Inventory Report; Inventory of U.S. Greenhouse Gas Emissions and Sinks: 1990–2009. 2011.
- (5) Kort, E. A.; Eluszkiewicz, J.; Stephens, B. B.; Miller, J. B.; Gerbig, C.; Nehrkorn, T.; Daube, B. C.; Kaplan, J. O.; Houweling, S.; Wofsy, S. C. Emissions of CH<sub>4</sub> and N<sub>2</sub>O over the United States and Canada based on a receptor-oriented modeling framework and COBRA-NA atmospheric observations. *Geophys. Res. Lett.* **2008**, 35 (18), Art. L18808 DOI: 10.1029/2008gl034031.
- (6) California Air Resources Board Greenhouse Gas Inventory Data - 2000 to 2009. <http://www.arb.ca.gov/cc/inventory/data/data.htm> (accessed June 2012).
- (7) Wunch, D.; Wennberg, P. O.; Toon, G. C.; Keppel-Aleks, G.; Yavin, Y. G. Emissions of greenhouse gases from a North American megacity. *Geophys. Res. Lett.* **2009**, 36, Art. L15810 DOI: 10.1029/2009gl039825.
- (8) Hsu, Y. K.; VanCuren, T.; Park, S.; Jakober, C.; Herner, J.; FitzGibbon, M.; Blake, D. R.; Parrish, D. D. Methane emissions inventory verification in southern California. *Atmos. Environ.* **2010**, 44 (1), 1–7, DOI: 10.1016/J.Atmosenv.2009.10.002.
- (9) Gioli, B.; Toscano, P.; Lugato, E.; Matese, A.; Miglietta, F.; Zaldei, A.; Vaccari, F. P. Methane and carbon dioxide fluxes and source partitioning in urban areas: The case study of Florence, Italy. *Environ. Pollut.* **2012**, 164, 125–131, DOI: 10.1016/J.Envpol.2012.01.019.
- (10) Lowry, D.; Holmes, C. W.; Rata, N. D.; O'Brien, P.; Nisbet, E. G. London methane emissions: Use of diurnal changes in concentration and delta C-13 to identify urban sources and verify inventories. *J. Geophys. Res., [Atmos.]* **2001**, 106 (D7), 7427–7448.
- (11) Mays, K. L.; Shepson, P. B.; Stirr, B. H.; Karion, A.; Sweeney, C.; Gurney, K. R. Aircraft-based measurements of the carbon footprint of Indianapolis. *Environ. Sci. Technol.* **2009**, 43 (20), 7816–7823, DOI: 10.1021/Es901326b.
- (12) (a) Clark, J. F.; Washburn, L.; Hornafius, J. S.; Luyendyk, B. P. Dissolved hydrocarbon flux from natural marine seeps to the southern California Bight. *J. Geophys. Res., [Oceans]* **2000**, 105 (C5), 11509–11522. (b) Biddle, K. T. The Los Angeles Basin: An Overview. In *Active Margin Basins*; Biddle, K. T., Ed.; American Association of Petroleum Geologists: Tulsa, OK, 1991; pp 5–24.
- (13) Townsend-Small, A.; Tyler, S. C.; Pataki, D. E.; Xu, X. M.; Christensen, L. E. Isotopic measurements of atmospheric methane in Los Angeles, California, USA: influence of "fugitive" fossil fuel emissions. *J. Geophys. Res., [Atmos.]* **2012**, 117, Art. D07308 DOI: 10.1029/2011jd016826.
- (14) Xiao, Y. P.; Logan, J. A.; Jacob, D. J.; Hudman, R. C.; Yantosca, R.; Blake, D. R. Global budget of ethane and regional constraints on US sources. *J. Geophys. Res., [Atmos.]* **2008**, 113 (D21), Art. D21306 DOI: 10.1029/2007jd009415.
- (15) U.S. Energy Information Administration; U.S. Gas Plant Production of Ethane. <http://www.eia.gov/dnav/pet/hist/LeafHandler.ashx?n=PET&s=METFPUS1&f=A> (accessed Dec. 15, 2011).
- (16) U.S. Energy Information Administration, Natural Gas Gross Withdrawals. <http://www.eia.gov/dnav/ng/hist/n9010us2A.htm> (accessed Dec. 15, 2011).
- (17) Rinsland, C. P.; Jones, N. B.; Connor, B. J.; Logan, J. A.; Pougatchev, N. S.; Goldman, A.; Murcray, F. J.; Stephen, T. M.; Pine, A. S.; Zander, R.; Mahieu, E.; Demoulin, P. Northern and southern hemisphere ground-based infrared spectroscopic measurements of tropospheric carbon monoxide and ethane. *J. Geophys. Res., [Atmos.]* **1998**, 103 (D21), 28197–28217.
- (18) Jacob, D. J.; Crawford, J. H.; Maring, H.; Clarke, A. D.; Dibb, J. E.; Emmons, L. K.; Ferrare, R. A.; Hostetler, C. A.; Russell, P. B.; Singh, H. B.; Thompson, A. M.; Shaw, G. E.; McCauley, E.; Pederson, J. R.; Fisher, J. A. The Arctic research of the composition of the troposphere from aircraft and satellites (ARCTAS) mission: Design,



execution, and first results. *Atmos. Chem. Phys.* **2010**, *10* (11), 5191–5212, DOI: 10.5194/Acp-10-5191-2010.

(19) Colman, J. J.; Swanson, A. L.; Meinardi, S.; Sive, B. C.; Blake, D. R.; Rowland, F. S. Description of the analysis of a wide range of volatile organic compounds in whole air samples collected during PEM-Tropics A and B. *Anal. Chem.* **2001**, *73* (15), 3723–3731.

(20) Sachse, G. W.; Collins, J. E.; Hill, G. F.; Wade, L. O.; Burney, L. G.; Ritter, J. A. Airborne tunable diode-laser sensor for high-precision concentration and flux measurements of carbon-monoxide and methane. *P. Soc. Photo-Opt. Ins.* **1991**, *1433*, 157–166.

(21) Vay, S. A.; Anderson, B. E.; Conway, T. J.; Sachse, G. W.; Collins, J. E.; Blake, D. R.; Westberg, D. J. Airborne observations of the tropospheric CO<sub>2</sub> distribution and its controlling factors over the South Pacific Basin. *J. Geophys. Res., [Atmos.]* **1999**, *104* (D5), 5663–5676.

(22) Kort, E. A.; Patra, P. K.; Ishijima, K.; Daube, B. C.; Jimenez, R.; Elkins, J.; Hurst, D.; Moore, F. L.; Sweeney, C.; Wofsy, S. C. Tropospheric distribution and variability of N<sub>2</sub>O: Evidence for strong tropical emissions. *Geophys. Res. Lett.* **2011**, *38*, Art. L15806 DOI: 10.1029/2011gl047612.

(23) Gorham, K. A.; Blake, N. J.; VanCuren, R. A.; Fuelberg, H. E.; Meinardi, S.; Blake, D. R. Seasonal and diurnal measurements of carbon monoxide and nonmethane hydrocarbons at Mt. Wilson, California: Indirect evidence of atomic Cl in the Los Angeles basin. *Atmos. Environ.* **2010**, *44* (19), 2271–2279, DOI: 10.1016/J.Atmos-env.2010.04.019.

(24) Semptra SoCalGas Envoy. [http://scgenvoy.semptra.com/#nav=/Public/ViewExternalArchive.showArchive%3FarchiveType%3DDaily\\_operations%26rand%3D179](http://scgenvoy.semptra.com/#nav=/Public/ViewExternalArchive.showArchive%3FarchiveType%3DDaily_operations%26rand%3D179) (accessed Dec. 15, 2011).

(25) California Air Resources Board; 2008 Estimated Annual Average Emissions; South Coast Air Basin. [http://www.arb.ca.gov/app/emsinv/emseic1\\_query.php?F\\_DIV=-4&F\\_YR=2008&F\\_SEASON=A&SP=2009&F\\_AREA=AB&F\\_AB=SC&F\\_DD=Y](http://www.arb.ca.gov/app/emsinv/emseic1_query.php?F_DIV=-4&F_YR=2008&F_SEASON=A&SP=2009&F_AREA=AB&F_AB=SC&F_DD=Y) (accessed Dec. 15, 2011).

(26) California Livestock County Estimates. [http://www.nass.usda.gov/Statistics\\_by\\_State/California/Publications/County\\_Estimates](http://www.nass.usda.gov/Statistics_by_State/California/Publications/County_Estimates) (accessed July 10, 2012).

(27) Efron, B. 1977 Rietz Lecture - Bootstrap methods: Another look at the jackknife. *Ann. Stat.* **1979**, *7* (1), 1–26, DOI: 10.1214/aos/1176344552.

(28) CALGEM. <http://calgem.lbl.gov/> (accessed June 2012).

(29) 2006 IPCC Guidelines for National Greenhouse Gas Inventories; IPCC: Hayama, Kanagawa, Japan, 2006.

(30) Jeong, S.; Zhao, C. F.; Andrews, A. E.; Bianco, L.; Wilczak, J. M.; Fischer, M. L. Seasonal variation of CH<sub>4</sub> emissions from central California. *J. Geophys. Res., [Atmos.]* **2012**, *117*, Art. D11306 DOI: 10.1029/2011jd016896.

(31) Potter, C.; Klooster, S.; Hiatt, S.; Fladeland, M.; Genovese, V.; Gross, P. Wetlands in the United States: Satellite-derived estimation based on ecosystem carbon. *Earth Interact.* **2006**, *10*.

(32) California Air Resources Board 2009 Almanac Emission Projection Data. <http://www.arb.ca.gov/app/emsinv/emssumcat.php> (accessed March 19, 2012).

(33) Status Report: Onsite Wastewater Treatment Systems in California, 2003. [www.swrcb.ca.gov/water\\_issues/programs/owts/docs/stat\\_rpt0803.pdf](http://www.swrcb.ca.gov/water_issues/programs/owts/docs/stat_rpt0803.pdf) (accessed Aug. 14, 2012).

(34) Jeffrey, A. W. A. A., H. A.; Jenden, P. D. Geochemistry of Los Angeles Basin Oil and Gas Systems. In *Active Margin Basins*; Biddle, K. T., Ed.; American Association of Petroleum Geologists: Tulsa, OK, 1991; pp 197–219.

(35) Miller, E. M. 2009 Annual Report of the State Oil & Gas Supervisor; Sacramento, CA, 2010.

(36) Radlein, B. *Final Environmental Assessment for Proposed Rule 1177 – Liquefied Petroleum Gas Transfer and Dispensing*; Los Angeles, 2012.

(37) Baker, A. K.; Beyersdorf, A. J.; Doeze, L. A.; Katzenstein, A.; Meinardi, S.; Simpson, I. J.; Blake, D. R.; Rowland, F. S. Measurements of nonmethane hydrocarbons in 28 United States cities. *Atmos.*

*Environ.* **2008**, *42* (1), 170–182, DOI: 10.1016/J.Atmos-env.2007.09.007.

(38) 2008 California Gas Report, California Gas and Electric Utilities, 2008. [www.socalgas.com/regulatory/documents/cgr/2008\\_CGR.pdf](http://www.socalgas.com/regulatory/documents/cgr/2008_CGR.pdf) accessed Aug. 14, 2012.

(39) Kort, E. A.; Andrews, A. E.; Dlugokencky, E.; Sweeney, C.; Hirsch, A.; Eluszkiewicz, J.; Nehrkorn, T.; Michalak, A.; Stephens, B.; Gerbig, C.; Miller, J. B.; Kaplan, J.; Houweling, S.; Daube, B. C.; Tans, P.; Wofsy, S. C. Atmospheric constraints on 2004 emissions of methane and nitrous oxide in North America from atmospheric measurements and a receptor-oriented modeling framework. *J. Integrative Environ. Sci.* **2010**, *7* (2), 125–133, DOI: 10.1080/19438151003767483.

## NOTE ADDED IN PROOF

A recent study for the California Air Resources Board suggests that the CARB inventory of emissions from the petroleum industry is underestimated by a factor of two. (Y. K. Hsu, personal communication).

## NOTE ADDED AFTER ASAP PUBLICATION

Reference 25 was modified in the version of this paper published August 20, 2012. The correct version published August 21, 2012.

*Appendix I*BRINGING THE OCEAN INTO THE LABORATORY TO PROBE  
THE CHEMICAL COMPLEXITY OF SEA SPRAY AEROSOL

By Kimberly A. Prather, Timothy H. Bertram, Vicki H. Grassian, Grant B. Deane, M. Dale Stokes, Paul J. DeMott, Lihini I. Aluwihare, Brian P. Palenik, Farooq Azam, John H. Seinfeld, Ryan C. Moffet, Mario J. Molina, Christopher D. Cappa, Franz M. Geiger, Gregory C. Roberts, i, Lynn M. Russell, Andrew P. Ault, Jonas Baltrusaitis, Douglas B. Collins, Craig E. Corrigan, Luis A. Cuadra-Rodriguez, Carlena J. Ebben, Sara D. Forestieri, Timothy L. Guasco, Scott P. Hersey, Michelle J. Kim, William F. Lambert, Robin L. Modini, Wilton Mui, Byron E. Pedler, Matthew J. Ruppel, Olivia S. Ryder, Nathan G. Schoepp, Ryan C. Sullivan, and Defeng Zhao

This chapter is was originally published in the *Proceedings of the National Academy of Sciences of the United States of America* as:

Prather, K. A. et al. (2013). “Bringing the ocean into the laboratory to probe the chemical complexity of sea spray aerosol”. In: *Proc. Natl. Acad. Sci. USA* 110.19, pp. 7550–5. doi: 10.1073/pnas.1300262110.

# Bringing the ocean into the laboratory to probe the chemical complexity of sea spray aerosol

Kimberly A. Prather<sup>a,b,1</sup>, Timothy H. Bertram<sup>a</sup>, Vicki H. Grassian<sup>c</sup>, Grant B. Deane<sup>b</sup>, M. Dale Stokes<sup>b</sup>, Paul J. DeMott<sup>d</sup>, Lihini I. Aluwihare<sup>b</sup>, Brian P. Palenik<sup>b</sup>, Farooq Azam<sup>b</sup>, John H. Seinfeld<sup>e</sup>, Ryan C. Moffet<sup>f</sup>, Mario J. Molina<sup>a,b</sup>, Christopher D. Cappa<sup>g</sup>, Franz M. Geiger<sup>h</sup>, Gregory C. Roberts<sup>b,i</sup>, Lynn M. Russell<sup>b</sup>, Andrew P. Ault<sup>c</sup>, Jonas Baltrusaitis<sup>c,2</sup>, Douglas B. Collins<sup>a</sup>, Craig E. Corrigan<sup>b</sup>, Luis A. Cuadra-Rodriguez<sup>a</sup>, Carlena J. Ebben<sup>h</sup>, Sara D. Forestieri<sup>g</sup>, Timothy L. Guasco<sup>a</sup>, Scott P. Hersey<sup>e</sup>, Michelle J. Kim<sup>b</sup>, William F. Lambert<sup>b</sup>, Robin L. Modini<sup>b</sup>, Wilton Mui<sup>e</sup>, Byron E. Pedler<sup>b</sup>, Matthew J. Ruppel<sup>a</sup>, Olivia S. Ryder<sup>a</sup>, Nathan G. Schoepp<sup>a</sup>, Ryan C. Sullivan<sup>d,3</sup>, and Defeng Zhao<sup>a,4</sup>

<sup>a</sup>Department of Chemistry and Biochemistry and <sup>b</sup>Scripps Institution of Oceanography, University of California at San Diego, La Jolla, CA 92093; <sup>c</sup>Department of Chemistry, University of Iowa, Iowa City, IA 52242; <sup>d</sup>Department of Atmospheric Science, Colorado State University, Fort Collins, CO 80523; <sup>e</sup>Division of Chemistry and Chemical Engineering, California Institute of Technology, Pasadena, CA 91125; <sup>f</sup>Department of Chemistry, University of the Pacific, Stockton, CA 95211; <sup>g</sup>Department of Civil and Environmental Engineering, University of California, Davis, CA 95616; <sup>h</sup>Department of Chemistry, Northwestern University, Evanston, IL 60208; and <sup>i</sup>Centre National de Recherches Météorologiques, 31057 Toulouse, France

Edited\* by Mark H. Thiemens, University of California at San Diego, La Jolla, CA, and approved March 21, 2013 (received for review January 10, 2013)

The production, size, and chemical composition of sea spray aerosol (SSA) particles strongly depend on seawater chemistry, which is controlled by physical, chemical, and biological processes. Despite decades of studies in marine environments, a direct relationship has yet to be established between ocean biology and the physicochemical properties of SSA. The ability to establish such relationships is hindered by the fact that SSA measurements are typically dominated by overwhelming background aerosol concentrations even in remote marine environments. Herein, we describe a newly developed approach for reproducing the chemical complexity of SSA in a laboratory setting, comprising a unique ocean-atmosphere facility equipped with actual breaking waves. A mesocosm experiment was performed in natural seawater, using controlled phytoplankton and heterotrophic bacteria concentrations, which showed SSA size and chemical mixing state are acutely sensitive to the aerosol production mechanism, as well as to the type of biological species present. The largest reduction in the hygroscopicity of SSA occurred as heterotrophic bacteria concentrations increased, whereas phytoplankton and chlorophyll-*a* concentrations decreased, directly corresponding to a change in mixing state in the smallest (60–180 nm) size range. Using this newly developed approach to generate realistic SSA, systematic studies can now be performed to advance our fundamental understanding of the impact of ocean biology on SSA chemical mixing state, heterogeneous reactivity, and the resulting climate-relevant properties.

clouds | marine aerosols | biologically active | cloud condensation nuclei | ice nucleation

Atmospheric aerosols have a profound impact on climate by directly interacting with incoming solar radiation, as well as by serving as the seeds that nucleate clouds (1). Natural aerosol sources, which include the oceans, deserts, and wildfires, contribute 90% (mass/mass) to atmospheric aerosols, with sea spray and dust representing the two largest contributors. Given the vast coverage of the Earth's surface by the oceans, the impact of sea spray aerosol (SSA) on the Earth's radiation budget is a critical area of ongoing climate investigations. The current uncertainties associated with the total radiative forcing by anthropogenic aerosols are much larger than those for greenhouse gases (2). To reduce these uncertainties, the impact of large natural sources, such as sea spray, must be better understood, because the difference between the total forcing and the forcing from natural sources will provide a critical constraint on the forcing from anthropogenic aerosols (3). Primary SSA, formed at the air/sea interface through bubble-mediated processes (4), dominates the natural aerosol burden in most marine environments. However, it has become increasingly difficult to unravel contributions

from anthropogenic and marine sources even in remote marine environments (3, 5). Global models that parameterize nascent SSA disagree by more than two orders of magnitude in the absolute number flux (global, annual average) (6–8) and require major assumptions regarding nascent SSA size and single particle mixing state (6). Currently, accurate representation of SSA in climate models is limited by an incomplete understanding of the dependence of SSA properties on physical, biological, and chemical processes occurring in the ocean (8).

Previous field and laboratory studies have shown that SSA is a complex mixture of sea salt (SS) and an array of organic species with differing solubilities (4, 9, 10). Most SSA field and laboratory measurements focus on absolute mass concentrations and the enrichment of organic compounds relative to salts (e.g., ref. 11), with the assumption that salts and organic species are equally distributed among all particles of a given size (internally mixed). The chemical associations between species within individual SSA particles (or chemical mixing state) is directly influenced by ocean physics, biology, and chemistry, and ultimately control both particle hygroscopicity (12) and the number of particles that can act as cloud condensation nuclei (CCN) and ice nuclei (IN) (13). The few studies that focus on single particle measurements suggest that SSA cannot be completely described as internally mixed (9, 14, 15) but, rather, as a distribution of chemically distinct particle types (externally mixed). The current view of SSA particle mixing state in the size range most important for cloud formation (<200 nm) is controversial (16). Although some studies suggest a large fraction of salt particles below 200 nm, others report salts are nearly absent and SSA becomes increasingly enriched with organic species at these small sizes (e.g., ref. 11). Some suggest individual SSA

Author contributions: K.A.P., T.H.B., V.H.G., and M.J.M. designed research; G.B.D., M.D.S., P.J.D., A.P.A., D.B.C., C.E.C., L.A.C.-R., C.J.E., S.D.F., T.L.G., M.J.K., R.L.M., W.M., M.J.R., O.S.R., R.C.S., and D.Z. performed research; G.B.D., M.D.S., L.I.A., B.P.P., F.A., J.H.S., G.C.R., L.M.R., W.F.L., B.E.P., and N.G.S. contributed new reagents/analytic tools; K.A.P., G.B.D., M.D.S., P.J.D., J.H.S., R.C.M., C.D.C., F.M.G., A.P.A., J.B., D.B.C., C.E.C., L.A.C.-R., C.J.E., T.L.G., S.P.H., W.M., M.J.R., R.C.S., and D.Z. analyzed data; and K.A.P., T.H.B., V.H.G., and C.D.C. wrote the paper.

The authors declare no conflict of interest.

\*This Direct Submission article had a prearranged editor.

<sup>1</sup>To whom correspondence should be addressed. E-mail: kprather@ucsd.edu.

<sup>2</sup>Present address: PhotoCatalytic Synthesis Group, Faculty of Science and Engineering, University of Twente, 7522 NB, Enschede, The Netherlands.

<sup>3</sup>Present address: Center for Atmospheric Particle Studies, Carnegie Mellon University, Pittsburgh, PA 15213.

<sup>4</sup>Present address: Institute of Energy and Climate: Troposphere (IEK-8), Forschungszentrum Juelich, D-52428 Juelich, Germany.

This article contains supporting information online at [www.pnas.org/lookup/suppl/doi:10.1073/pnas.1300262110/-DCSupplemental](http://www.pnas.org/lookup/suppl/doi:10.1073/pnas.1300262110/-DCSupplemental).

particles may be even more complex and composed of organized structures formed by the complexation of inorganic salts with organic species produced by biological processes (17, 18). Even though climate impacts of SSA are expected to depend on particle composition as a function of size, no study to date has probed how SSA mixing state changes as a function of seawater conditions, a major focus of this investigation.

The goal of this study is to develop a unique approach that will allow us to bridge results from laboratory and field studies of SSA by accurately reproducing the chemical complexity and associations (i.e., mixing state) of real-world SSA for controlled studies of reactivity, water uptake, and climate-relevant properties. Here, we describe a newly developed approach that brings the chemical complexity of the ocean-atmosphere system into the laboratory (Fig. S1). Simultaneous measurements of seawater, SSA size distributions, and size-resolved single particle chemical composition are made in an enclosed ocean-atmosphere wave channel equipped with breaking waves and natural seawater. This facility permits studies of the impact of seawater composition on SSA properties under controlled and well-characterized biological conditions (19). This paper is divided into three sections, each detailing the progression of advances: (i) measurements of nascent SSA produced by breaking waves in a laboratory setting, demonstrating the extreme sensitivity of the SSA size distribution to the bubble size distribution, and hence the SSA production mechanism; (ii) size-resolved associations between inorganic and organic species within individual SSA particles (i.e., chemical mixing state), covering two orders of magnitude in size from 30 nm to 3  $\mu\text{m}$ , by integrating the results from several single particle techniques, including aerosol TOF mass spectrometry (ATOFMS), scanning tunneling X-ray microscopy (STXM), and transmission electron microscopy (TEM); and (iii) a mesocosm seawater experiment to explore the dependence of SSA chemical mixing state and physicochemical properties on ocean biology over a range of conditions representative of the open ocean, by adding well-characterized phytoplankton and bacteria mixtures and allowing the chemistry to evolve over a 5-d period (20–22).

### Generation and Reproduction of SSA Size Distributions

In the SSA particle production process, several key interfaces ultimately determine the surface species and morphology of SSA. As a bubble rises through the water column, different hydrophobic molecules are attracted to the air/bubble interface, offering the first level of chemical selectivity (4, 23). Because a bubble bursts at the ocean surface, the sea surface microlayer represents a second critical interface where chemical partitioning occurs (24). Finally, as individual droplets undergo drying under lower relative humidity (RH) conditions, the resulting SSA particle morphology will depend on surface interactions. Biological processes play a significant role in forming the species that each bubble encounters in the water column as well as those residing in the sea surface microlayer (4, 23). Thus, each step of the SSA production process must be properly replicated or erroneous conclusions will be drawn in any subsequent heterogeneous reactivity and water uptake studies on SSA.

SSA is created when bubbles entrained by breaking waves burst at the ocean surface (4). Two distinct mechanisms control aerosol production: the rapid retraction and disintegration of the thin fluid film that caps the bubble (film drops) and the breakup of a reactionary jet (jet drops), with their relative contributions depending on the size spectrum of the bubbles (8). Accurate representation of these mechanisms in the laboratory is a critical requirement for reproducing the size distribution and chemical composition of nascent SSA. However, the majority of previous laboratory studies generated SSA using sintered glass filters and typically did not measure bubble size distributions (25). In the experiments described herein, SSA was generated using three different interchangeable systems: (i) sintered glass filters (25), (ii) a pulsed-plunging waterfall, and (iii) continuous wave breaking at 0.6 Hz, all operating within a sealed 33-m wave channel filled with natural seawater pumped directly from the Pacific Ocean (SI Text, section 1).

In situ acoustic and optical measurements of bubble size distributions ( $dN/dr_B$ , where  $r_B$  = bubble radius; Fig. 1A) show consistency between generation mechanisms up to approximately  $r_B = 0.7$  mm but deviate above 1 mm. Aerosol production is sensitive to total foam area and the distribution of cell sizes within the foam (26). Multiplying the bubble size distribution by the potential to generate surface film (roughly  $2\pi r_B^2$ ) yields a peak in the distribution at the Hinze scale, as observed in previous open ocean studies ( $a_H = 1.3$  mm;  $a$  is the bubble radius and  $H$  stands for Hinze, Fig. 1A) (19). Because most foam from breaking waves comes from bubbles around this scale, the level and slope of the bubble distribution at this scale must be reproduced by any generation mechanism used as a surrogate for natural wave breaking. It has been reported that the vast majority of submicrometer SSA particles that can act as CCN emanate from film drops that are produced by larger bubbles with sizes above 1 mm (27–29). Importantly, the measured bubble spectrum for the breaking waves used in this study matches the shape and Hinze scale of bubble spectra measured previously for open ocean breaking waves (19). Previous studies using plunging jets have produced similar bubble size distributions only up to radii of 0.57 mm (30). Thus, herein breaking waves with bubble size distributions representative of open ocean conditions are used to produce nascent SSA with atmospherically representative size distributions and chemical mixing states, as described below.

Nascent SSA size distribution ( $dN/d\log d_p$ , where  $d_p$  is particle physical diameter) from the three production mechanisms were measured at  $15 \pm 10\%$  RH (Fig. 1B). The mode of the probability density function of the particle number distribution is  $162 \pm 21$  nm (1 $\sigma$ ) for SSA generated using breaking waves. The number distribution is broad, extending from 10 nm to 5  $\mu\text{m}$ . The plunging waterfall produces SSA with a similar size distribution to that produced by breaking waves, which is expected, given the similar bubble spectra produced by the two generation methods. In contrast, SSA produced using two sizes of sintered glass filters or frits commonly used in previous experiments (25) exhibits a much narrower size distribution, reflecting the different bubble size spectrum produced by this method (compare with Fig. 1A).

The measured size distribution peaks at the lower end of the accumulation mode ( $\sim 162$  nm) as observed in previous studies in marine environments (6, 8). This distribution shows only a small contribution from particles in the smaller Aitken mode in the sub-100-nm size range. This distribution is in contrast to previous marine field studies, including those that used frits to produce SSA, which show another mode below 100 nm (8, 25, 31–33). As described, it is extremely difficult to separate out contributions

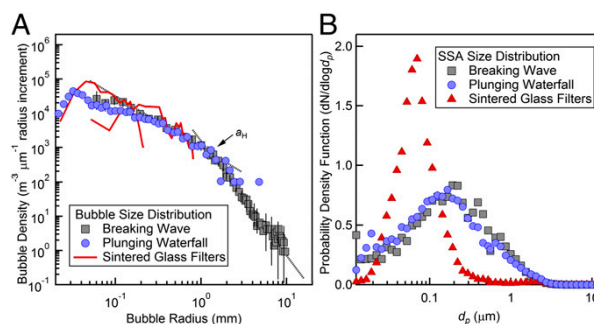


**Fig. 1.** (A) Bubble radius distributions for breaking waves (gray squares), plunging waterfall (blue circles), and sintered glass filters (red line). [Reproduced with permission from ref. 19 (Copyright 2002, Macmillan Publishers)]. (B) Probability density function of the resulting SSA number distributions ( $dN/d\log d_p$ , with the  $d_p$  at  $15 \pm 10\%$  RH) produced by these three methods. The SSA distribution recovered from the plunging waterfall is consistent with that produced by breaking waves, whereas the SSA distribution by the sintered glass filters (red triangles) is considerably narrower.



from background aerosols and other secondary particle formation processes that have been shown to occur in marine environments (3, 5, 34). The ability to produce and measure an extremely stable nascent SSA size distribution over a broad range of biological conditions demonstrates the advantage of performing these experiments in a laboratory setting, where contributions from other sources and secondary processes can be eliminated. Thus, future studies will probe the effects of seawater temperature, wind, and biological conditions to determine if the Aitken mode can be produced under different conditions (i.e., phytoplankton bloom) or whether it is entirely attributable to background and secondary processes.

The motivation for the development of this unique ocean-atmosphere facility is to be able to perform systematic control studies that help provide a better understanding of the large observed variability in SSA size and composition distributions measured over the ocean, as well as associated variations in cloud properties (6). Thus, it is critical to use a production process that replicates the full bubble size distributions, including larger sizes, to generate SSA with a realistic distribution of particle sizes and compositions.

### SSA Chemical Mixing State

Our first experiments used natural seawater drawn directly from Pacific coastal waters into the wave channel. Over the course of 10 d, after adding multiple varieties of phytoplankton cultures and filling the tank on different days with natural seawater, very little change was observed in the overall SSA composition or hygroscopicity. To explore the influence of ocean biological and chemical complexity on emitted SSA properties, a 5-d mesocosm experiment was then conducted wherein natural seawater was doped sequentially with well-characterized ZoBell growth medium, bacteria (*Alteromonas* spp. and *Pseudoalteromonas atlantica*), and phytoplankton (*Dunaliella tertiolecta*) cultures (Table S1). The time series for heterotrophic bacteria, phytoplankton, chlorophyll-*a*, and total organic carbon (TOC) concentrations are shown in Fig. 2. The primary objective of these experiments was not to simulate large-scale oceanic phytoplankton blooms that occur in limited regions of the ocean (11) but, instead, to detail how variations in and interactions between biological species alter SSA properties under conditions generally representative of the mean ocean state [i.e., TOC = 60–70  $\mu\text{M}$  (20), bacteria concentrations of  $5 \times 10^5$ – $3 \times 10^6$  cells·mL<sup>-1</sup> (21), chlorophyll-*a* concentrations of 0.15–1 mg·m<sup>-3</sup> (22)]. SSA was produced using continuous wave breaking, where measurements of background particle levels within the wave channel indicate that contamination from background aerosol contributed ~10% on average (up to 20% for short isolated periods) to the measured particle number concentrations (Fig. S2). Both SSA number concentrations and size distributions were exceptionally stable

[ $N_{\text{total}} = 145 \pm 20$  particles·cm<sup>-3</sup> and  $d_p$  (mode) =  $162 \pm 21$  nm (1 $\sigma$ )] across the entire 5-d mesocosm experiment (Figs. S2 and S3) and showed very little variation even as bacteria, phytoplankton, chlorophyll-*a*, and TOC concentrations changed (Fig. 2).

The mixing state of nascent SSA during the mesocosm experiment was examined using a combination of particle morphology and chemical heterogeneity measurements of individual particles, determining the size-resolved number fractions of chemically distinct particle types. Integration of microscopy and MS data of individual SSA particles reveals four predominant SSAs that persist throughout all experiments conducted (Fig. 3A), although the size-dependent relative number fractions vary over time (Fig. 4A and B). The four individual particle types were defined based on both physical shape and chemical signatures (SI Text, section 4). They can be categorized as inorganic salts (types 1 and 2), biological (type 3), and organic (type 4) particles (Table S2), where the labels reflect the most dominant signals in the individual particles. A minor fraction of particles composed of unique signatures, each in negligible (<1%) abundance, and background aerosols were also detected. These particles were grouped together as a separate category referred to as Other (gray; Fig. 3A and SI Text, section 4.3.3). The relative fractions of the four major particle types show a strong size dependence [aerodynamic diameter ( $d_a$ ) = 30–3,000 nm], with externally mixed particle populations spanning from inorganic salts dominating the largest sizes to mostly organic particles at the smallest sizes (Fig. 3A). It is important to note that all particle measurements discussed here describe nascent SSA, sampled less than 30 s following production, thus eliminating subsequent chemical and atmospheric processing of these particles, which are processes that have been shown to make major contributions in field observations to the composition of marine aerosols (35).

Supermicrometer particles are dominated by SS particles, with one type containing the typical inorganic salts dominated by NaCl (SS, type 1) and a second type (type 2) in which SS is mixed with organic carbon (SS-OC; Fig. S4). Individual SS-containing particles display spatial heterogeneity, with clear structural differences in the surface vs. inner regions of the particles. Larger type 1 particles show a cubic NaCl structure in microscopy analysis, and many type 2 (SS-OC) particles have an additional visible ring of Mg<sup>2+</sup> on their surface, which becomes more common in smaller submicrometer particles (Fig. S5). One explanation for these rings is that they form when more soluble species, such as magnesium chloride, dehydrate last under vacuum in the electron microscope; however, this layered structure is also observed in the ATOFMS, which does not completely dry out the particles. We hypothesize that these rings serve as indicators of surface interactions between organic species and inorganic cations, as shown previously in laboratory studies of model inorganic/organic systems (36). A unique finding in this study is the presence of two distinct populations of nascent SS particles, supermicrometer particles dominated by NaCl showing cubic structures and smaller submicrometer salt particles relatively enriched in Mg<sup>2+</sup> and organic species. This finding has significant ramifications for heterogeneous reactivity and water uptake studies. Additionally, a notable fraction of supermicrometer particles (type 3) had common biological markers, including organic-nitrogen species and phosphate in the negative ion mass spectra, coupled with Mg<sup>2+</sup> and oftentimes transition metals in the positive ion mass spectra (37). Type 3 particles are likely biological particles, possibly bacteria, which have been shown to become enriched in the bubble bursting process (4, 23). These represented up to 17% of the supermicrometer particles, similar to the abundances previously reported for biological particles in marine environments (38).

Submicrometer SSA particles were composed of two externally mixed particle types, SS-OC (type 2) and organic dominated particles with no detectable chloride (type 4), as determined by TEM energy-dispersive X-ray analysis. Further details on the mixing state of organic and inorganic species within smaller type 4

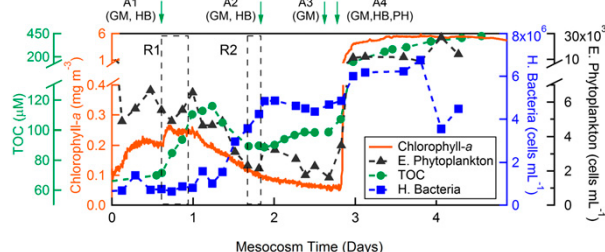


**Fig. 2.** Concentrations of seawater TOC (green circles), chlorophyll-*a* (orange line), heterotrophic bacteria (blue squares), and photosynthetic eukaryotic phytoplankton (black triangles) measured over the 5-d mesocosm experiment. Times for the four major additions of growth medium (GM), heterotrophic bacteria (HB), and phytoplankton (PH) are noted (A1–A4) with green arrows (SI Text, section 2.1 and Table S1). Dashed boxes mark two sampling regions (R1 and R2).

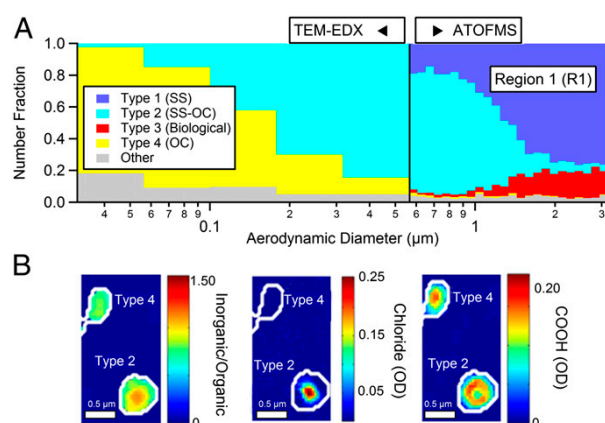


**Fig. 3.** (A) Size-resolved chemical mixing state for R1 (Fig. 2). Integration of two single particle analysis methods [TEM with energy-dispersive X-ray (EDX) analysis < 562 nm and ATOFMS > 562 nm] shows the existence of four major submicrometer particle types. (B) STXM chemical spatial maps of the two most dominant submicrometer particle types (types 2 and 4) highlight the differences in the inorganic-to-organic ratios (Left), abundance of chloride (Center), and carboxylates (Right).

submicrometer individual particles were obtained with STXM (Fig. 3B). These particles were composed of homogeneously mixed organic species (e.g., carboxylate) combined with  $\text{Na}^+$ ,  $\text{Ca}^{2+}$ , sulfur, and  $\text{Mg}^{2+}$  but distinctly lacking chloride. These type 4 particles represent the most abundant type below 180 nm, consistent with previous observations showing an increase in insoluble organic species at the smallest sizes (39), and are believed to be hydrophobic colloidal or gel particles (40). Particles composed primarily of insoluble organic compounds have been hypothesized to form when long-chain polymeric bioorganic species, such as carbohydrates, proteins, and lipids, bridge with divalent ions, including  $\text{Ca}^{2+}$  and  $\text{Mg}^{2+}$ , to form stable collapsed structures (40).

### Chemical Biology Impacts on SSA Chemical Mixing State

During the first 2 d of the mesocosm experiment, an increase occurred in the relative fraction of type 4 OC-dominated particles in the 60–180 nm ( $d_a$ ) range (Fig. 4A; 0.26–0.85). Such a dramatic shift illustrates the influence of ocean biology on the chemical composition of particles in the size window most critical for aerosol–cloud interactions. Notably, this major shift occurred at modest TOC, chlorophyll-*a*, and phytoplankton levels (< 0.3  $\text{mg}\cdot\text{m}^{-3}$  and <  $7 \times 10^5$  cells· $\text{mL}^{-1}$ ). The transition was anticorrelated with chlorophyll-*a* and phytoplankton concentrations, and it was correlated with the onset of increasing bacteria concentrations ( $4 \times 10^6$  cells· $\text{mL}^{-1}$ ). In contrast, the chemical mixing state of SSA in larger sizes (180–320 nm) (Fig. 4B) showed less sensitivity to changes in bacteria, phytoplankton, and TOC concentrations. This result highlights the size-dependent response of SSA chemical composition and mixing state to changes in the distribution of and interactions between biological species in seawater. It also suggests that commonly used metrics for biological productivity in global atmospheric models and SSA parameterizations, such as ocean color and/or chlorophyll-*a* concentration, may not always represent adequate indicators of changes in SSA chemical composition and the associated climate-relevant properties that could be occurring under more typical ocean conditions (41, 42).

### Impact of SSA Mixing State on Particle Hygroscopicity

Hygroscopicity measurements under both sub- and supersaturated conditions were performed during the mesocosm experiment. These measurement techniques probe water uptake of particles in different size ranges in the submicrometer mode. The

ability of an individual particle to scatter radiation and/or serve as CCN depends on size, the degree of supersaturation, and the overall ability of a particle to uptake water, which depends on the single particle chemical mixing state. In general, particles composed mostly of water-soluble or hygroscopic salts will activate into cloud drops at relatively small sizes. As less soluble organic species are added to hygroscopic salt particles, the overall hygroscopicity decreases and the size at which the particles can activate increases. Particles that are composed of purely hydrophobic organic species will activate at even larger sizes (13). In previous marine cloud studies, the mixing state in the cloud-active size range (60–200 nm) has not been directly measured as a function of biological conditions. Bulk measurements of collections of SSA particles force one to assume all particles are internal mixtures of all seawater components in equal proportions, which suggests all SSA particles will have the same affinity for water. It is important to note that this will certainly not be the case for the different populations of nascent SSA particles described herein (12). The question we address here is as follows: How do biologically induced changes in the relative proportions of the two distinct submicrometer particle types (SS-OC and insoluble OC) affect hygroscopic properties?

Before adding bacteria and/or phytoplankton to the natural seawater, the measured mean activation diameter ( $d_{act}$ ) at which particles began to serve as CCN was 63 nm (+18 nm, –4 nm; supersaturation of 0.2%), consistent with previous measurements for low biological activity seawater and the resulting hygroscopic SSA (12). Following a fivefold increase in bacteria concentrations that occurred ~24 h after the initial addition of bacteria and ZoBell growth medium, the mean  $d_{act}$  nearly doubled to  $118 \pm 13$  nm (Fig. 4D), corresponding to a factor of six decrease in the overall CCN-derived hygroscopicity (*SI Text*, section 5.2). Given the observed size distribution and relative fractions of inorganic and insoluble organic particles, this change in  $d_{act}$  values would result in a 32% decrease in the number of SSA particles that would activate as cloud droplets at 0.2% supersaturation. Because the size distribution showed very little change, the observed increase in  $d_{act}$  (Fig. 4D) directly

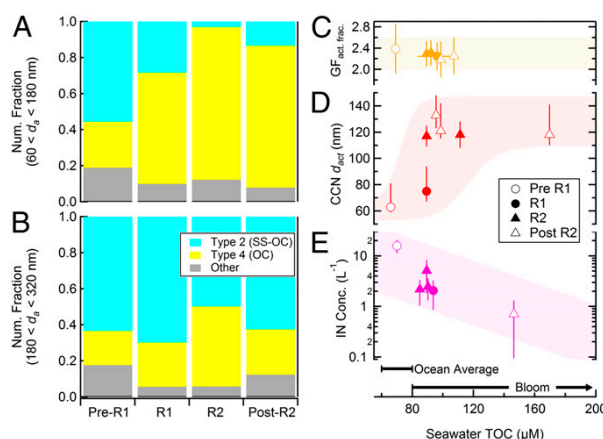


**Fig. 4.** (A) Single particle chemical mixing state for particles with a diameter between 60 and 180 nm for sampling regions indicated in Fig. 2 and Table S3 (the full dataset in these regions is discussed in *SI Text*, section 6). Num. fraction, number fraction. (B) Same as A, but for the next largest size regime (180 <  $d_p$  < 320 nm). (C) GF at 92% RH for the hygroscopic fraction of SSA ( $GF_{act, frac} = d_{wet}/d_{dry}$ , act. frac. refers to the active fraction that took up water,  $GF > 1.2$ ). (D)  $d_{act}$  measured at 0.2% supersaturation for cloud droplet formation, and (E) IN concentrations (Conc.) at –32 °C as a function of seawater TOC levels. The shaded regions are provided as a visual guide. The data represent mean values, and the vertical error bars for GF and IN are 2 $\sigma$ . For CCN, the lower error bars are 2 $\sigma$ , whereas the upper bars account for potential errors in the counting mechanism used (*SI Text*, section 5.1). The horizontal error bars represent 1 $\sigma$ .

corresponds to a change in SSA chemical composition. More specifically, based on TEM analysis, the contributions from the two externally mixed particle types in the smallest <180-nm size range change with the relative fraction of type 4 insoluble OC particles increasing (Fig. 4A; 0.26–0.85) and replacing mixed SS-OC (type 2) particles. Notably, this observed decrease in hygroscopicity, which occurred under modest changes in bacteria, phytoplankton, TOC, and chlorophyll-*a* concentrations within the range of typical open ocean conditions, is significantly larger than in laboratory studies of nascent sea spray on the addition of biogenic material in the form of a variety of phytoplankton exudates (12). This large decrease in hygroscopicity occurred as the levels of two traditional indicators of high biological activity, phytoplankton and chlorophyll-*a*, were decreasing (6, 41). Little additional change occurred in CCN activity (Table S3) after phytoplankton were added when concentrations of chlorophyll-*a* (>5.5 mg·m<sup>-3</sup>) exceeded the levels observed during most oceanic blooms (>2 mg·m<sup>-3</sup>) (43). This result highlights the fact that bacteria and the full complexity of interactions between all biological species (e.g., phytoplankton, bacteria) must be included when probing seawater composition impacts on the concentration and composition of ocean-derived organic matter in SSA. The mesocosm experiment serves as an example of how this newly developed ocean-atmosphere wave flume approach will be used to determine cause-and-effect relationships between changing seawater composition and SSA mixing state.

To obtain complementary measurements of water uptake by larger submicrometer particles, subsaturated hygroscopic growth measurements of 175 to 225-nm dry diameter particles were made. Hygroscopic growth factor ( $GF_{act, frac.} = d_{wet}/d_{dry}$ ) for the hygroscopic particle fraction ( $GF > 1.2$ ) ranged from 2.2–2.4 at 92% RH, in the same range as SS (12). The  $GF$ s appeared to be independent of seawater composition (Fig. 4C and Fig. S64). However, not all particles within this size range were hygroscopic, with  $18 \pm 4\%$  displaying  $GF < 1.2$ , corresponding to 15-fold lower hygroscopicity compared with the highly hygroscopic particles (SI Text and Fig. S64). The fraction of “nonhygroscopic” particles agrees well with the fraction of type 4 (OC) particles (0.25%) detected by TEM in the same size range (Fig. 4B), suggesting these are indeed hydrophobic (insoluble) organic particles as described by Facchini et al. (39). Additionally, despite the clear changes to the mean hygroscopicity of the smallest particles ( $d_p < d_{act}$ ), no change occurred in the mean optically weighted  $GF$ s for all measured submicrometer particles measured using a cavity ring-down aerosol extinction spectrometer (Fig. S6B). This is consistent with the finding that the mean composition of the submicrometer SSA in the size range most relevant for light scattering and the direct aerosol effect on climate (300–1,000 nm) showed little dependence on changes in seawater composition (Fig. 4B). Our results suggest that under certain conditions, such as those simulated in these experiments, which are dominated by heterotrophic bacteria, a dichotomy of climate impacts can exist wherein certain changes in ocean composition due to biology can have a minimal influence on the optical properties of submicrometer SSA, although having a substantial impact on the indirect effect through modification of the hygroscopicity of particles with  $d_p < d_{act}$ , and hence cloud properties.

The final climate-relevant property probed as part of these studies of nascent SSA particles involves their ability to form IN. IN are rare; on average, only 1 in  $10^5$  particles serves as an ice nucleus below  $-22^\circ\text{C}$  (44). Some laboratory experiments and global aerosol modeling studies have investigated marine bacteria as potential sources of IN (45, 46), although our understanding of the actual chemical species influencing ice formation in SSA remains extremely limited. Observations of IN over marine regions show broadly distributed average IN concentrations of 10–20 per cubic meter active at  $-15^\circ\text{C}$  (47), increasing an order of magnitude per  $5^\circ\text{C}$  drop in temperature, consistent with values measured in these experiments at  $-32^\circ\text{C}$ . Oceanic regions with higher IN concentrations have been suggested to be associated with higher biological activity, as indicated by chlorophyll-*a* or

phytoplankton levels (46), but no definitive identification has been made of the specific sources of IN in marine environments. In this study, the dependence of IN concentrations on seawater conditions showed less variability than the CCN concentrations over the same range of conditions. The IN concentrations initially showed a small increase as bacteria concentrations increased but ultimately decreased at higher TOC levels above 100  $\mu\text{M}$  (Fig. 4E). It is possible the high TOC levels created a sea surface film that inhibited the initial release of particles serving as IN. Our measurements showing the highest IN concentrations at the lowest TOC levels commonly observed in natural seawater suggest marine sources should be considered as a possible source of IN even outside of biologically active environments. However, further studies are needed to identify the sources leading to the modest yet globally significant marine IN source inferred from our studies and measured over a large fraction of the oceans.

### Implications for Future Aerosol-Chemistry-Climate Studies

The development of this unique ocean-atmosphere facility sets the stage for future studies focused on improving our understanding of ocean-SSA-climate interactions. A number of key findings have emanated from the studies reported herein. First, the production rate and size distribution of SSA are extremely sensitive to the production mechanism, where bubbles with radii at and above the Hinze scale ( $a_H = 1.3$  mm) are critical for SSA production, size, and composition. It is suggested that future studies aimed at producing SSA include measurements of bubble size distributions of the chosen production method to determine whether they fully emulate breaking waves, and that they include larger bubble sizes. Second, over a broad range of conditions, the mixing state of SSA is composed of varying fractions of four major externally mixed particle types, the number fractions of which are sensitive to ocean biology, and particularly the presence of heterotrophic bacteria, which have been shown to play a key role in consuming and transforming dissolved organic matter (48). Using this controlled approach, changes in the relative proportion of two externally mixed particle types (SS-OC and a second type dominated by insoluble organic species) occur, directly resulting in a change in the cloud formation potential of SSA. Interestingly, under the conditions of this experiment, the chemical composition and mixing state of particles larger than 180 nm did not demonstrate the same sensitivity to changes in seawater composition. This finding shows the importance of taking into account the size-resolved particle mixing state when predicting cloud properties in marine environments. Similar to the submicrometer hygroscopicity and optical property measurements, methods that measure bulk submicrometer mass of different chemical species will also be most strongly affected by the composition of larger, more massive particles at the upper end (>500 nm) of the submicrometer size mode (49), and thus relatively insensitive to changes in the number of particles in the size range most important for cloud formation (13).

The results of this study demonstrate the critical importance of using both the proper physical production mechanism that replicates breaking waves as well as a complete suite of biological species, including bacteria, phytoplankton, and viruses (48), to study factors controlling the concentration and composition of ocean-derived organic matter in SSA (40). Using the newly developed approach, studies will begin to study the coupling of ocean physical, biological, and chemical processes systematically, with the ultimate goal of linking seawater composition with SSA mixing state and cloud properties. This study represents a critical first step in producing and characterizing nascent SSA. Future studies will now focus on probing how rapidly these nascent SSA particles evolve by controlling a variety of atmospheric parameters, including photochemistry, aqueous phase processes, and heterogeneous chemistry with reactive trace gases. Finally, this ocean-atmosphere facility can be used to simulate how future changes in oceanic and atmospheric conditions may influence the chemical, physical, and climate-relevant properties of SSA.



## Methods

To produce SSA particles with the identical size and composition of those in the atmosphere in a low-background environment, a unique ocean-atmosphere facility was developed that involved retrofitting a  $33 \times 0.5 \times 1$ -m wave channel housed at the Hydraulics Laboratory at the Scripps Institution of Oceanography. A significant effort was dedicated to reducing background particle concentrations ( $5,000$ – $10,000 \text{ cm}^{-3}$ ) to low enough values ( $<20 \text{ cm}^{-3}$ ) so that individual SSA particles, produced in very low numbers ( $50$ – $150 \text{ cm}^{-3}$ ) by each breaking wave, could be detected. SSA, generated from natural seawater, was sampled by multiple instruments within 30 s of being produced. Fig. S1 shows the wave channel with a multitude of gas and particle instruments probing SSA size, chemical mixing state, optical properties, hygroscopicity, and IN activity. Full details on the 5-d mesocosm experiment, including the source of the seawater, the methods used for seawater analyses, a discussion of the modifications to the existing wave channel that made it possible to detect low SSA concentrations, details of each of the particle generation methods, experi-

mental procedures for measuring the bubble and aerosol size distributions, and analytical methods used for single particle measurements (including classification of particle types, supersaturated and subsaturated hygroscopicity measurements, and ice nucleation determinations) are provided in *SI Text*.

**ACKNOWLEDGMENTS.** We thank Suresh Dhaniyala, Robert Pomeroy, Paul Harvey, and the entire staff of the Scripps Institution of Oceanography Hydraulics Laboratory for helpful discussions and technical development of the sealed wave-channel. This overall study was supported by the National Science Foundation (NSF) Center for Chemical Innovation, the Center for Aerosol Impacts on Climate and the Environment (CAICE) under Grant CHE1038028. Partial support was provided to CAICE collaborators for the intensive study measurements by NSF Grant ATM0837913 (to C.D.C. and S.D.F.), Office of Naval Research Grant N00014-10-1-0200 (to J.H.S., S.P.H., and W.M.), an NSF Graduate Research Fellowship (to C.J.E.), an Irving M. Klotz professorship (to F.M.G.), NSF PO Grant OCE-1155123 (to G.B.D.), Gordon and Betty Moore Foundation Marine Microbiology Initiative (to F.A.) and NSF Grant ATM0841602 (to P.J.D. and R.C.S.).

- Haywood J, Boucher O (2000) Estimates of the direct and indirect radiative forcing due to tropospheric aerosols: A review. *Rev Geophys* 38(4):513–543.
- Intergovernmental Panel on Climate Change (2007). *Climate Change 2007: The Physical Science Basis*. Contribution of Working Group I to the Fourth Assessment Report of the Intergovernmental Panel on Climate Change, eds Solomon, S., D. Qin, M. Manning, Z. Chen, M. Marquis, K.B. Averyt, M. Tignor and H.L. Miller (Cambridge Univ Press, Cambridge, UK), pp. 129–234. Available at [http://www.cambridge.org/features/earth\\_environmental/climatechange/wg1.htm](http://www.cambridge.org/features/earth_environmental/climatechange/wg1.htm).
- Andreae MO (2007) Atmosphere. Aerosols before pollution. *Science* 315(5808):50–51.
- Blanchard DC (1989) The ejection of drops from the sea and their enrichment with bacteria and other materials—A review. *Estuaries* 12(3):127–137.
- Shank LM, et al. (2012) Organic matter and non-refractory aerosol over the remote Southeast Pacific: Oceanic and combustion sources. *Atmos Chem Phys* 12(1):557–576.
- de Leeuw G, et al. (2011) Production flux of sea spray aerosol. *Rev Geophys* 49:RG2001.
- Jaegle L, Quinn PK, Bates TS, Alexander B, Lin JT (2011) Global distribution of sea salt aerosols: New constraints from in situ and remote sensing observations. *Atmos Chem Phys* 11(7):3137–3157.
- Lewis ER, Schwartz SE (2004) *Sea Salt Aerosol Production: Mechanisms, Methods, Measurements, and Models: A Critical Review* (American Geophysical Union, Washington, DC).
- Leck C, Bigg EK (2005) Biogenic particles in the surface microlayer and overlying atmosphere in the central Arctic Ocean during summer. *Tellus B Chem Phys Meteorol* 57(4):305–316.
- Parungo FP, Nagamoto CT, Rosinski J, Haagenson PL (1986) A study of marine aerosols over the Pacific-ocean. *J Atmos Chem* 4(2):199–226.
- O'Dowd CD, et al. (2004) Biogenically driven organic contribution to marine aerosol. *Nature* 431(7009):676–680.
- Fuentes E, Coe H, Green D, McFiggans G (2011) On the impacts of phytoplankton-derived organic matter on the properties of the primary marine aerosol. Part 2. Composition, hygroscopicity and cloud condensation activity. *Atmos Chem Phys* 11(6):2585–2602.
- Andreae MO, Rosenfeld D (2008) Aerosol-cloud-precipitation interactions. Part 1. The nature and sources of cloud-active aerosols. *Earth Sci Rev* 89(1–2):13–41.
- Hawkins LN, Russell LM (2010) Polysaccharides, proteins, and phytoplankton fragments: Four chemically distinct types of marine primary organic aerosol classified by single particle spectromicroscopy. *Adv Meteorol* 2010:1–14.
- Murphy DM, et al. (1998) Influence of sea-salt on aerosol radiative properties in the Southern Ocean marine boundary layer. *Nature* 392(6671):62–65.
- Bigg EK, Leck C (2008) The composition of fragments of bubbles bursting at the ocean surface. *J Geophys Res Atmos* 113(D11):D11209.
- Ellison GB, Tuck AF, Vaida V (1999) Atmospheric processing of organic aerosols. *J Geophys Res Atmos* 104(D9):11633–11641.
- Griffith EC, Tuck AF, Vaida V (2012) Ocean-atmosphere interactions in the emergence of complexity in simple chemical systems. *Acc Chem Res* 45(12):2106–2113.
- Deane GB, Stokes MD (2002) Scale dependence of bubble creation mechanisms in breaking waves. *Nature* 418(6900):839–844.
- Hansell DA, Carlson CA, Repeta DJ, Schlitzer R (2009) Dissolved organic matter in the ocean: a controversy stimulates new insights. *Oceanography (Wash DC)* 22(4):202–211.
- Li WKW (1998) Annual average abundance of heterotrophic bacteria and Synechococcus in surface ocean waters. *Limnol Oceanogr* 43(7):1746–1753.
- Boyce DG, Lewis MR, Worm B (2010) Global phytoplankton decline over the past century. *Nature* 466(7306):591–596.
- Aller JY, Kuznetsova MR, Jahns CJ, Kemp PF (2005) The sea surface microlayer as a source of viral and bacterial enrichment in marine aerosols. *J Aerosol Sci* 36(5–6):801–812.
- Schmitt-Kopplin P, et al. (2012) Dissolved organic matter in sea spray: A transfer study from marine surface water to aerosols. *Biogeosciences* 9(4):1571–1582.
- Keene WC, et al. (2007) Chemical and physical characteristics of nascent aerosols produced by bursting bubbles at a model air-sea interface. *J Geophys Res Atmos* 112: D21202.
- Sellegrri K, O'Dowd CD, Yoon YJ, Jennings SG, de Leeuw G (2006) Surfactants and submicron sea spray generation. *J Geophys Res Atmos* 111(D22):D22215.
- Cipriano RJ, Blanchard DC (1981) *Bubble and aerosol spectra produced by a laboratory breaking wave*. *J Geophys Res C Oceans Atmos* 86(Nc9):8085–8092.
- Resch FJ, Darrozes JS, Afeti GM (1986) Marine liquid aerosol production from bursting of air bubbles. *J Geophys Res Oceans* 91(C1):1019–1029.
- Wu J (2001) Production functions of film drops by bursting bubbles. *J Phys Oceanogr* 31(11):3249–3257.
- Fuentes E, Coe H, Green D, de Leeuw G, McFiggans G (2010) Laboratory-generated primary marine aerosol via bubble-bursting and atomization. *Atmospheric Measurement Techniques* 3(1):141–162.
- Yoon YJ, et al. (2007) Seasonal characteristics of the physicochemical properties of North Atlantic marine atmospheric aerosols. *J Geophys Res Atmos* 112(D4):D04206.
- Clarke AD, Owens SR, Zhou JC (2006) An ultrafine sea-salt flux from breaking waves: Implications for cloud condensation nuclei in the remote marine atmosphere. *J Geophys Res Atmos* 111(D6):D06202.
- Bates TS, et al. (2012) Measurements of ocean derived aerosol off the coast of California. *J Geophys Res Atmos* 117:D00V15.
- Gantt B, Meskhidze N, Zhang Y, Xu J (2010) The effect of marine isoprene emissions on secondary organic aerosol and ozone formation in the coastal United States. *Atmos Environ* 44(1):115–121.
- Murphy DM, Thomson DS, Middlebrook AM, Schein ME (1998) In situ single-particle characterization at Cape Grim. *J Geophys Res Atmos* 103(D13):16485–16491.
- Tang CY, Huang ZSA, Allen HC (2010) Binding of  $\text{Mg}^{2+}$  and  $\text{Ca}^{2+}$  to palmitic acid and deprotonation of the COOH headgroup studied by vibrational sum frequency generation spectroscopy. *J Phys Chem B* 114(51):17068–17076.
- Gaston CJ, et al. (2011) Unique ocean-derived particles serve as a proxy for changes in ocean chemistry. *J Geophys Res Atmos* 116:D18310.
- Matthias-Maser S, Brinkmann J, Schneider W (1999) The size distribution of marine atmospheric aerosol with regard to primary biological aerosol particles over the South Atlantic Ocean. *Atmos Environ* 33(21):3569–3575.
- Facchini MC, et al. (2008) Primary submicron marine aerosol dominated by insoluble organic colloids and aggregates. *Geophys Res Lett* 35(17):L17814.
- Verdugo P (2012) Marine microgels. *Annu Rev Mar Sci* 4:375–400.
- Gantt B, et al. (2012) Model evaluation of marine primary organic aerosol emission schemes. *Atmos Chem Phys* 12(18):8553–8566.
- O'Dowd CD, et al. (2008) A combined organic-inorganic sea-spray source function. *Geophys Res Lett* 35(1):L01801.
- Chavez FP, Messié M, Pennington JT (2011) Marine primary production in relation to climate variability and change. *Annu Rev Mar Sci* 3:227–260.
- DeMott PJ, et al. (2010) Predicting global atmospheric ice nuclei distributions and their impacts on climate. *Proc Natl Acad Sci USA* 107(25):11217–11222.
- Burrows SM, Hoose C, Pöschl U, Lawrence MG (2012) Ice nuclei in marine air: bio-particles or dust? *Atmos Chem Phys Discuss* 12(2):4373–4416.
- Schnell RC, Vali G (1976) Biogenic ice nuclei. 1. Terrestrial and marine sources. *J Atmos Sci* 33(8):1554–1564.
- Bigg EK (1973) Ice nucleus concentrations in remote areas. *J Atmos Sci* 30(6): 1153–1157.
- Azam F (1998) Microbial control of oceanic carbon flux: The plot thickens. *Science* 280(5364):694–696.
- Ovadnevaité J, et al. (2012) On the effect of wind speed on submicron sea salt mass concentrations and source fluxes. *J Geophys Res Atmos* 117:D16201.



# Supporting Information

Prather et al. 10.1073/pnas.1300262110

## SI Text

Additional details on the Center for Aerosol Impacts on Climate and the Environment (CAICE) 5-d mesocosm experiment are provided here. In section 1, the overall experiment is described, with more details provided on the source of the seawater used throughout the experiments. In section 2, a detailed time line of the mesocosm experiment (section 2.1) is described, as well as the methods that were used for seawater analyses (section 2.2). A description of the sea spray aerosol (SSA) production mechanisms is provided in section 3, including a discussion of the modifications to the existing wave channel to make it suitable for aerosol measurements (section 3.1), details for each of the particle generation methods used (section 3.2), and experimental procedures for measuring the bubble (section 3.3) and aerosol (section 3.4) size distributions. Methods for the single particle measurements used in this study are described in section 4, which includes a discussion of how the data from the various techniques were merged and classified (section 4.3). In section 5, a description of the supersaturated (section 5.1) and subsaturated (section 5.2) hygroscopicity measurements is given, as well as details on the ice nucleation measurement technique (section 5.3). Lastly, in section 6, a table (Table S3) summarizing experimentally determined values for the different time periods of interest for the mesocosm experiment is provided.

## 1. Seawater Source

All experiments in this study were performed in a  $33 \times 0.5 \times 1$ -m (length  $\times$  width  $\times$  height, 0.6 m water depth) wave channel located in the Hydraulics Laboratory at Scripps Institution of Oceanography. A view of the wave-flume facility is shown in Fig. S1, showing all gas, aerosol, and seawater measurement instruments. This picture was taken during the intensive measurement period when the results of this study were obtained. The CAICE intensive mesocosm experiment was conducted from November 10–16, 2011. Seawater from the Pacific Ocean was pumped from the Scripps Pier, 300 m offshore, using an intake located 2 m above the ocean floor. A PVC channel delivers pumped water down the length of the pier into two  $3 \times 7$ -m coarse filter beds composed of 30 cm of No. 12 crystal sand, 20 cm of pea gravel, and 45 cm of rock. Following filtration, the water is delivered to three  $2.2 \times 10^3$ -L holding tanks. Precautions are taken, including regular cleaning, to prevent marine life from colonizing in the delivery pipes. The residence time of water in the holding tanks is relatively short because the total system provides  $\sim 6.7 \times 10^6$  L of water per day to various Scripps facilities. Seawater was filtered through an additional series of sand and diatomaceous earth filters before filling the experimental facility. Before the beginning of the campaign, we performed coincident measurements of bacteria counts at the water intake in the ocean and in the wave channel to determine the influence of the various seawater filters. These measurements confirmed that  $\sim 75\%$  of the ambient bacteria were being removed by the water handling system ( $2.33 \times 10^5$  cells·mL $^{-1}$  and  $9.822 \times 10^5$  cells·mL $^{-1}$  for the wave channel and ocean, respectively). Before filling the wave channel to a constant 60-cm depth, the channel was rinsed with fresh seawater from the holding tank.

## 2. Experimental Time Line and Seawater Analyses

**2.1. Experimental Time Line.** During the course of the 5-d mesocosm experiment, natural seawater was enriched with organic species via four separate additions at different times of various combinations of heterotrophic bacteria culture isolates (*Alteromonas*

TW2, TW7, and ALT199 and *Pseudoalteromonas atlantica* strain 19262), ZoBell 2216E (a bacterial growth medium), and a monoculture of *Dunaliella tertiolecta* (a common marine green algae). Addition 1 consisted of 100 L of seawater collected from the Scripps Pier, ZoBell growth medium, and three strains of *Alteromonas* (heterotrophic bacteria). Addition 2 was composed of the same three strains of heterotrophic bacteria and the ZoBell growth medium they were cultured in. Addition 3 was of ZoBell medium. Addition 4 contained ZoBell medium, one strain of heterotrophic bacteria (*P. atlantica*), and a monoculture of a phytoplankton (*D. tertiolecta*). A description of each addition, including approximate amounts and times when added, is provided in Table S1. Throughout the mesocosm experiment, these additions modulated the biological and organic content of the water by as much as one order of magnitude, with bacteria and phytoplankton loadings ranging from  $5.39 \times 10^5$ – $6.77 \times 10^6$  cells·mL $^{-1}$  and from  $1.61 \times 10^3$ – $2.71 \times 10^4$  cells·mL $^{-1}$ , respectively. During this same period, measured values of total organic carbon (TOC) ranged from 66–423  $\mu$ M, with  $>90\%$  composed of dissolved organic carbon (OC), whereas chlorophyll-*a* (chl-*a*) concentrations ranged from 0.048–6.9 mg·m $^{-3}$ .

**2.2. Seawater Analyses.** A variety of methods were used to determine the chemical and biological contents of the seawater in the wave flume. Seawater chl-*a* concentrations were measured in real time using a WET Labs ECO Triplet customizable fluorimeter operating at 695 nm. For determination of the TOC levels, seawater was sampled from the wave flume using syringes composed of high-density polyethylene and polypropylene, which had been washed in 10% (vol/vol) HCl and rinsed with Milli-Q water. Collected seawater was transferred into precombusted (450 °C for 6 h) 40-mL glass vials and immediately acidified with two drops of trace metal-free concentrated HCl. OC analyses were conducted as per standard high-temperature combustion procedures (Shimadzu Scientific Instruments) (1).

Heterotrophic bacteria, *Synechococcus*, and photosynthetic eukaryotes were enumerated and classified into broad groups via flow cytometry (Altra; Beckman-Coulter) at the School for Ocean, Earth Sciences, and Technology (SOEST) Flow Cytometry Facility at the University of Hawaii. Surface seawater samples were collected for biological analysis using serological graduated pipettes and ejected into sterile 1-mL polypropylene cryogenic vials (Simport Scientific), where they were fixed with 50  $\mu$ L of 0.2  $\mu$ m filtered 10% (vol/vol) paraformaldehyde. The vials were flash-frozen in liquid N $_2$  at  $-196$  °C and then transferred to a  $-80$  °C freezer for long-term storage. The vials were placed in a Styrofoam container packed with dry ice for shipment to the SOEST facility, where they were stained with Hoechst 33342 and analyzed with two collinearly aligned argon ion lasers, one tuned in the UV range to a combination of the 334-, 351-, and 364-nm laser lines and the other to 488 nm (2).

## 3. Laboratory Production of Nascent SSA

**3.1. Modification of Wave Channel for SSA Measurements.** To create a low background environment, the existing open wave channel was retrofitted to include an air filtration system capable of delivering particle-free air to the head space of the channel, resulting in an airflow velocity of 12.2 cm·s $^{-1}$  in the channel. In this application, ambient air is passed through a four-stage filtration system (Hydrosil International), consisting of a prefilter; 4-mm coal-based, pellet-activated charcoal; potassium permanganate (KMnO $_4$ ); and a  $30 \times 30 \times 29$ -cm high-efficiency particulate air

filter for the removal of volatile organic compounds, nitrogen and sulfur oxides, and aerosol particles before entering the wave channel. Filter breakthrough was monitored continuously upstream of the sea spray production region using a condensation particle counter (Fig. S2).

**3.2. Aerosol Production Mechanisms.** The wave channel was equipped with three interchangeable particle generation mechanisms. Briefly, these were as follows: (i) breaking waves generated by a hydraulic paddle within the wave channel, (ii) two sizes of sintered glass filters, and (iii) a unique pulsed-plunging waterfall constructed within the wave channel. For each of the three methods, aerosol particles were sampled within 30 s of their production using an array of sampling manifolds held 20 cm above the water surface. The relative humidity (RH) within the wave channel ranged between 58% and 78%.

**3.2.1. Breaking waves.** Breaking waves were generated in the wave channel with a computer-controlled hydraulic paddle. Uniform sinusoidal wave pulses with a frequency of 0.6 Hz were forced to break over a submerged artificial shoal. This method produced a consistent aerosol concentration of  $145 \pm 20 \text{ cm}^{-3}$  and was used for the majority of the experimentation presented herein.

**3.2.2. Sintered glass filters.** Sintered glass filters have commonly been used to form bubbles as proxies for wave breaking (3). Here, we flowed dry nitrogen gas ( $0.5 \text{ L} \cdot \text{min}^{-1}$ ) through four submerged sintered glass filters, two 90-mm-diameter type E filters and two 25-mm-diameter type A filters, similar to the setup used by Keene et al. (3). The glass filters were set at a depth of  $\sim 25 \text{ cm}$  (filter surface to water surface).

**3.2.3. Pulsed-plunging waterfall.** Plunging jets of water have recently been introduced as another artificial method for laboratory generation of SSA (4). In this technique, a water recirculation system is used to produce SSA by gravitational impingement of a waterfall. Unlike systems used previously, our scheme uses a waterfall that extends across the full width of the wave channel and “sweeps” across an  $\sim 15\text{-cm}$  section of the water surface. This modification was used because it allows surface foam to decay before bubble production resumes. The “sweeping” behavior was achieved by switching a solenoid bypass valve on the waterfall pumping system with a period of 6 s, allowing water to be delivered to the spillway in a periodic manner (5).

**3.3. Bubble Size Distribution Measurements.** Bubble size distributions were obtained using methods described previously by Deane and Stokes (6). Briefly, bubble plumes were imaged a few centimeters from the sides or top of the glass wave channel with high-speed cameras. The distribution of bubble sizes was then obtained through computer-aided analysis of the images. The air entrained by the plunging waterfall and breaking waves was monitored for consistency throughout the experiment by analyzing the underwater noise radiated by newly formed bubbles with the plumes. Acoustic measurements were conducted with hydrophones (model ITC-6050C; International Transducer Corporation) placed a few centimeters from the bubble plumes and analyzed with a Stanford Research Systems SR785 Dynamic Signal Analyzer.

The reference distribution for a laboratory plunging breaking wave by Deane and Stokes (6) is in absolute units of bubbles per  $\text{m}^{-3} \cdot \mu\text{m}^{-1}$  radius increment, which is standard for the oceanographic literature (6). The absolute levels of the distributions for sintered glass filters and plunging water were variable, depending on airflow, plunging sheet height, and roughness, among other factors. To facilitate comparison with the breaking wave, the bubble size distributions for the sintered glass filters and plunging waterfall were first converted to probability density functions (PDFs) and then scaled by  $5.6 \times 10^6$ . The scaling factor was determined to be the value that brought the plunging waterfall and breaking wave distributions into agreement at a bubble radius of 1 mm.

**3.4. SSA Size Distributions.** Particle size distributions (PSDs) were determined by a commercially available TSI scanning mobility particle sizer (SMPS) and aerodynamic particle sizer (APS). The SMPS measures particle mobility diameter ( $d_m$ ) by scanning voltages through a TSI electrostatic classifier with a differential mobility analyzer (DMA) column (model 3080). Sampled particles are directed past a 0.058-cm impactor to remove particles too large for analysis and into the DMA column, which separates particles by electrical mobility. The range of particle sizes that can be analyzed in this way is dependent on the aerosol and sheath flow rates, which were set at 0.4 and  $4.0 \text{ L} \cdot \text{min}^{-1}$ , respectively, corresponding to particle diameters of 10–600 nm. Particles selected in the DMA are injected into a condensation particle counter (model 3010; TSI), which counts the particles over a range of size bins.

The APS (model 3321; TSI) determines the aerodynamic diameter ( $d_a$ ) of particles in the range of 0.542–20  $\mu\text{m}$  by measuring particle TOF. Particles were sampled at  $5.0 \text{ L} \cdot \text{min}^{-1}$  (1.0 and  $4.0 \text{ L} \cdot \text{min}^{-1}$  aerosol and sheath flow rates, respectively). To determine  $d_a$ , particles enter the inlet of the APS and pass between two separate paths of a continuous wave (CW) laser split with a beamsplitter.

For both the SMPS and APS analyses, particles passed through silica gel diffusion driers, where they were dried to  $15 \pm 10\%$  RH. The  $d_m$  and  $d_a$  size distributions recorded were merged to obtain a geometric physical diameter ( $d_p$ ) size distribution. For the purposes of merging, particles sized by the SMPS were assumed to be of a spherical geometry, which allows for the relation:

$$d_m = d_p. \quad [\text{S1}]$$

Particles sized by the APS were assigned an effective density,  $\rho_{\text{eff}}$ , of  $1.8 \text{ g} \cdot \text{cm}^{-3}$ , a value determined experimentally, which allows for conversion based on the relation:

$$d_p = \frac{d_a}{\sqrt{\frac{\rho_{\text{eff}}}{\rho_0}}} \quad [\text{S2}]$$

with  $\rho_0$  equal to unit density (i.e.,  $1 \text{ g} \cdot \text{cm}^{-3}$ ). Both instruments had their resolution set to 32 bins per decade for consistency in merging. The SMPS tends to undercount particles at the high end of the distribution due to the cutoff from the particle impactor, whereas the APS can undercount particles at the low end due to poor scattering efficiency of the smallest particles. As a result, particle bins in the overlapping size region of the two methods were subsequently removed, excluding the largest and smallest bins of the SMPS and APS, respectively.

**3.5. Size Distribution Stability.** As noted in the main text, the overall shape of the SSA size distribution underwent subtle changes throughout the course of the 5-d mesocosm experiment (Fig. S3A), whereas TOC levels increased from 70  $\mu\text{M}$  to more than 400  $\mu\text{M}$ . Fig. S3B displays the mean PDFs of the measured SSA size distributions for region 1 (R1;  $\circ$ ) and R2 ( $\blacktriangle$ ).

#### 4. Single Particle Measurements of the Chemical Composition of SSA

**4.1. OffLine Measurements.** Samples analyzed offline and discussed herein were collected using a micro-orifice uniform deposition impactor (model 100; MSP Corp.) at  $30 \text{ L} \cdot \text{min}^{-1}$ , with 50% size cuts at 5.6, 2.5, 1.0, 0.53, 0.30, 0.18, 0.09, and 0.05  $\mu\text{m}$ . A variety of microscopy substrates were used, including the following: 400 mesh carbon type B with Formvar transmission electron microscopy (TEM) grids (part no. 01814-F; Ted Pella, Inc.) for TEM and scanning tunneling X-ray microscopy (STXM) with near edge X-ray absorption fine structure (NEXAFS) analysis

and silicon wafers (Ted Pella Inc.) for SEM and atomic force microscopy (AFM) analysis. TEM data were collected on a JEOL 2100F field emission transmission electron microscope operating at 200 kV in scanning TEM mode (STEM) using a Gatan high angle annular dark field detector and Thermo Noran energy-dispersive X-ray spectrometer detector.

**4.1.1 TEM energy-dispersive X-ray analysis.** Single particle size and chemical composition were determined for ~100 particles per stage, ranging from 2.5 to 0.05  $\mu\text{m}$ . Particles were sized using ImageJ freeware (National Institute of Health) by tracing the perimeter manually. For particles where an outer ring was present, a projected area diameter ( $d_{pa}$ ) was determined using the outer perimeter. This can then be converted to a  $d_a$  via:

$$d_a = \frac{d_{pa}}{S_v \sqrt{\frac{\rho_p}{S_D \rho_0}}}, \quad [\text{S3}]$$

where  $S_v$  is the volumetric shape factor,  $S_D$  is the aerodynamic shape factor,  $\rho_p$  is the particle density, and  $\rho_0$  is unit density ( $1 \text{ g}\cdot\text{cm}^{-3}$ ) (7, 8). The particle densities used were  $1.8 \text{ g}\cdot\text{cm}^{-3}$  for types 1 and 2 and  $1.2 \text{ g}\cdot\text{cm}^{-3}$  for type 3 (low-density organic) (9). Size distributions for each stage were determined and aligned closely with the manufacturer's  $d_a$  50% cut points. To merge the different stages, the relative contribution of each stage to a specific size bin was determined and weighted using four logarithmic bins per decade.

**4.1.2 STXM with NEXAFS.** STXM with NEXAFS spectroscopy was conducted at the advanced light source at Lawrence Berkeley National Laboratory using previously described methodology (10, 11). Briefly, soft X-ray radiation was used at the C (290 eV), Ca (352 eV), S (170 eV), and Cl (199 eV) absorption edges. X-ray energy was selected by a monochromator, and the transmitted intensity ( $I$ ) was measured as the sample was rastered using piezoelectric nanotranslators at different X-ray energies. The X-ray spectrum was converted to OD using Beer's law:

$$OD = \ln\left(\frac{I_0}{I}\right) = \mu(E)\rho t, \quad [\text{S4}]$$

where  $I_0$  is the transmitted intensity for particle-free regions of the substrate,  $I$  is the transmitted intensity for particle-containing regions,  $\mu$  is the energy-dependent mass absorption coefficient,  $\rho$  is the mass density, and  $t$  is the particle thickness. The Cl map in Fig. 3B is of the Cl L-edge. The map of the carboxylic acid group (COOH) is of the peak at 288.7 eV on the carbon K-edge. The ratio of the carbon pre-edge OD ( $OD_{pre} = 278 \text{ eV}$ ) to the OD of the carbon postedge ( $OD_{post} = 320 \text{ eV}$ ) is an indicator of inorganic material in the particle, because  $OD_{pre}$  is proportional to the number of noncarbon atoms and  $OD_{post} - OD_{pre}$  is proportional to the number of carbon atoms (12). The map of the ratio of inorganic to organic material is the ratio of  $\frac{OD_{pre}}{OD_{post}}$ , the determination of which is described elsewhere (10, 13).

**4.2. Online SSA Measurements.** **4.2.1. Aerosol TOF-MS.** Simultaneous measurements of SSA vacuum aerodynamic diameter ( $d_{va}$ ) and chemical composition were performed with two aerosol TOF mass spectrometers: one equipped with a converging nozzle ( $d_{va} = 0.2\text{--}3.0 \mu\text{m}$ ) and the other fitted with an aerodynamic lens inlet ( $d_{va} = 0.1\text{--}1.5 \mu\text{m}$ ). The description of these instruments can be found elsewhere (14–17). Briefly, aerosols were sampled through one diffusion drier and passed through the aerosol TOF-MS (ATOFMS) inlet into a differentially pumped vacuum chamber, where particles were accelerated to its size-dependent terminal velocity into the sizing region. In the sizing region, particles passed through two orthogonal continuous wave lasers ( $\lambda = 532 \text{ nm}$ , ~50 mW) located 6 cm apart, creating light scat-

tering pulses detected by photomultiplier tubes that were used to determine particle velocity. Particle velocity was then translated into  $d_a$  on comparison with a calibration curve obtained using polystyrene latex spheres of known sizes. Sized particle events were used to trigger a Q-switched neodymium:yttrium aluminium garnet laser ( $\lambda = 266 \text{ nm}$ ,  $1.2\text{--}1.5 \text{ mJ}\cdot\text{pulse}^{-1}$ ) that desorbs and ionizes individual particles. Dual polarity ions produced by individual particles were detected by two reflectron TOF mass spectrometers and stored for further analysis.

ATOFMS mass spectra and size data were compiled and analyzed using the YAADA v2.1 (<http://www.yaada.org>) software analysis toolkit for MATLAB (MathWorks). An adaptive neural network clustering algorithm (ART-2a) was used to segregate particles into distinct clusters, which were then recombined into particle types based on their mass spectral signatures and size-distributions (18). ATOFMS particle types are defined by characteristic mass-to-charge ratio distributions. Mass spectral peak assignments represent the most likely ion at a specific mass-to-charge ratio based on previous laboratory studies of particle standards, as well as field studies. One aerosol TOF mass spectrometer has better transmission at supermicrometer sizes ( $d_{va} > 1 \mu\text{m}$ ), and the other has better transmission at submicrometer sizes ( $d_{va} < 1 \mu\text{m}$ ); thus, their size-resolved chemical contributions were combined to provide data over the full ranges covered. As part of this process, the ART-2a cluster results from one aerosol TOF mass spectrometer were matched to the particles detected by the other aerosol TOF mass spectrometer using ART-2a matching algorithms before combining the clusters into particle types. This procedure ensured that the classification for the particle types was consistent for both instruments. Size-resolved number fractions were combined for the two aerosol TOF mass spectrometers using 32 logarithmic bins per decade.

**4.3. ATOFMS, TEM, and STXM particle classification.** Size-resolved chemical composition data from TEM energy-dispersive X-ray (EDX) and ATOFMS were merged at the  $0.562\text{-}\mu\text{m}$  logarithmic bin cut; particles smaller than  $0.562 \mu\text{m}$  are represented in Fig. 3A from microscopy analysis, whereas larger particles are represented by ATOFMS analysis. Table S2 describes the characteristics of the main types observed using TEM-EDX, STXM-NEXAFS, and ATOFMS. The elemental/ionic/molecular markers for each type are listed in order of intensity from highest to lowest.

**4.3.1. Identification of particles: Types 1 and 2.** Types 1 and 2, as viewed by the microscopy techniques, are aqueous internal mixtures of Na, Cl, Mg, Ca, K, S, and OC. Particles with intense Na and Cl are the dominant types above  $300 \text{ nm}$  and are easily distinguished from types 3 and 4 using TEM-EDX, STXM-NEXAFS, and ATOFMS. For the microscopy techniques, both types 1 and 2 have a well-defined cubic core of NaCl (EDX) and Cl (STXM-NEXAFS) surrounded by a ring of material [mixed cation sulfate (Na, Mg, K, Ca) and OC] (19). With ATOFMS, negative ion peaks for  $^{23}\text{Na}^+$ ,  $^{35,37}\text{Cl}^-$ , and clusters such as  $^{81,83}\text{Na}_2\text{Cl}^+$  are observed (Fig. S4). ATOFMS allows separation of types 1 and 2 based on the ion spectral patterns, distinctive size distributions, lower intensity  $^{35,37}\text{Cl}^-$  peaks, and presence of more intense alkali metal-chloride clusters, including  $^{93,95}\text{NaCl}_2^-$ ,  $^{129,131}\text{MgCl}_3^-$ , and  $^{151,153}\text{Na}_2\text{Cl}_3^-$ . Some type 2 particles (mostly in the submicrometer size range) contain signatures of biological species (e.g.,  $^{26}\text{CN}^-$ ,  $^{42}\text{CNO}^-$ ,  $^{79}\text{PO}_3$ ), which have been previously observed in field measurements (16).

**4.3.2. Identification of particles: Types 3 and 4.** Type 3 was clearly distinguished using ATOFMS mass spectral signatures and characterized by  $^{24}\text{Mg}^+$ ,  $^{39}\text{K}^+$ , and  $^{40}\text{Ca}^+ \gg ^{23}\text{Na}^+$  in these chloride- and biological-containing particles, which have been linked with oceanic biological activity in ambient measurements (15). Additionally, many type 3 particles contain transition metals, specifically  $^{52}\text{Cr}^+$ ,  $^{54,56}\text{Fe}^+$ , and  $^{107,109}\text{Ag}$ .



Type 4 particles could be distinguished from types 1–3 by all three methods. In EDX analysis, the peaks present include S and a mixture of Na, Mg, K, and Ca, with the intensities and presence of the different cations varying between particles. These particles do not have well-defined effloresced structures like types 1 and 2; rather, they appear to have a well-mixed homogeneous composition. In STXM, type 4 is identifiable by a lack of Cl and a core/shell effloresced structure, the presence of OC mixed with inorganic species (with slightly more OC), the presence of COOH in the carbon K-edge spectrum, and sulfur. The same homogeneous distribution of species is observed using STXM for the type 4 particles. In ATOFMS, type 4 is a Ca- and Mg-rich particle that contains smaller organic peaks as described in Table S2; this type has been previously observed in field measurements and linked to high biological activity and possibly microgel formation (15, 20). Type 4 particles do not produce negative ion mass spectra, suggesting that the presence of water is suppressing negative ion formation.

TEM-EDX images are shown in Fig. S5 for types 1 and 2, corresponding to the single particle mass spectra shown in Fig. S4. This figure demonstrates the chemical and structural variability of nascent SSA particle populations, which includes the Mg ring in the sea salt-OC type 2 particles.

**4.3.3. Identification of other particle types: Contamination particles.** It should also be noted that several particles, appearing to be contamination, were observed as inorganic-dominated ( $OD_{pre}/OD_{post} > 1.5$ ) and composed of sulfate without any other inorganic cations, suggesting they were ammonium sulfate particles. Their fractional contribution was roughly 10–15% in the smallest size bins, consistent with measured background concentrations (Fig. S2); thus, they are included as the Other type in Fig. 3A. A second clear contamination particle type composed of elemental carbon was also identified and excluded from subsequent analysis. These particles had graphitic ring-like structure within 15- to 30-nm spherules as identified by high resolution TEM (HR-TEM),  $sp^2$  bonding as observed with STXM-NEXAFS, and traces of sulfate (likely secondary) as identified by EDX and STXM. In addition, two ATOFMS organic particle types (accounting up to 18–30% in the smallest ATOFMS sizes detected) suspected of being contamination were also identified as the Other type: One contained sulfate signatures, and the other had no negative spectra. ATOFMS particles in the Other category also include particles that had unique OC signatures in minor abundance and accounted for 9% of all particles analyzed. The background particles were confirmed by comparing the mass spectral signatures with background air measurements in the room and by monitoring temporal trends of the different particle types when the wave flume was opened to room air.

## 5. Climate-Relevant Properties

**5.1. Supersaturated Hygroscopicity Measurements.** Measurements of cloud condensation nuclei (CCN) number concentrations were conducted using a miniaturized stream-wise thermal gradient cloud condensation nuclei counter (CCNc) (21). The aerosol is introduced to a column with continuously wetted walls. A warm-to-cold thermal gradient is generated using thermoelectric devices in three positions along the column, causing the air at the centerline of the flow to be supersaturated with respect to water vapor, causing CCN active aerosols to grow into cloud droplets. Droplets were counted using an OPC. The CCNc was operated at a constant supersaturation of  $0.20 \pm 0.02\%$  during this experiment. CCN activation diameters ( $d_{act}$ s) were calculated by iteratively integrating number size distributions for time periods corresponding to CCN measurements:

$$\int_{d_{act}}^{2 \times 10^{-4}} n(d_p) dd_p = N_{CCN}, \quad [S5]$$

where  $n(d_p)$  is the number size distribution,  $N_{CCN}$  is the number concentration of CCN at an instrumental supersaturation of 0.2%, and the  $d_p$  is expressed in units of nanometers. This technique to determine  $d_{act}$  has been compared with tandem DMA-CCN analysis and was found to be comparable in laboratory tests. Due to the diffusion driers and other unknown particle loss mechanisms, the SMPS and APS regularly undercounted particles by 15–35% in comparison to the condensation particle counter. Given the counting method used, this systematic bias could only lead to values of  $d_{act}$  that are larger than those reported. Therefore, the upper bound of the uncertainty in  $d_{act}$  is determined, assuming all particle losses occurred at diameters greater than  $d_{act}$  and recalculating the value of  $d_{act}$ . In many cases, this resulted in uncertainties greater than 2 SDs, and the larger of the two quantities is reported as the upper bound for  $d_{act}$ . The lower uncertainties represent 2 SDs. This approach produces a highly conservative estimate of uncertainty.

An increase of  $d_{act}$  by 19% between unamended seawater (pre-R1) and R1 was observed as TOC increased from  $\sim 71$  to  $89 \mu\text{M}$ . As explained in the main text,  $d_{act}$  increased by 57% between R1 and R2, whereas TOC concentrations remained constant. The  $d_{act}$  increased from  $63 (+18, -4) \text{ nm}$  for pre-R1 to  $118 \pm 13 \text{ nm}$  for R2, resulting in a 32% decrease in CCN number between these two regions. This change was calculated by taking the percent difference of raw CCN numbers of sea spray active particles between the two regions. Bacteria concentrations increased by a factor of five, whereas chl-*a* remained relatively low, suggesting the importance of bacteria in the TOC pool and its impact on cloud formation potential. The changes in CCN activity measurements can be explained by the increase in the fraction of externally mixed type 4 (OC).

**5.2. Subsaturated Hygroscopicity Measurements.** Subsaturated aerosol water uptake was measured using a differential aerosol sizing and hygroscopicity spectrometer probe (DASH-SP) (22). In this instrument, the aerosol flow first passes through a DMA to select a dry particle size. The monodisperse output of the DMA is then split into four parallel channels of different RH: <8%, 74%, 85%, and 92%. Particles are allowed to come into equilibrium with the RH in each channel, causing the particle to grow in size as it accommodates water. The size distribution of particles after humidification is measured with an optical particle counter (OPC). The  $GF$  was calculated using the ratio of the wet size ( $d_{wet}$ ) to the dry size ( $d_{dry}$ ):

$$GF = \frac{d_{wet}}{d_{dry}}. \quad [S6]$$

The  $GF$  values reported here are labeled as  $GF_{active \text{ frac}}$  because with the relatively low particle concentrations generated in these experiments, it becomes difficult for the DASH-SP to determine quantitatively the number concentration of particles that do not accommodate significant quantities of water vapor, owing to the implementation of the OPC detection system in this instrument. A subpopulation of particles exhibiting weak water uptake was observed as discussed in the main text. The 85% and 74% RH  $GF$ s, along with the 92% RH data reported in Fig. 4, are presented in Fig. S6A.

Hygroscopic  $GF$ s were also measured for submicrometer particles using the University of California, Davis cavity ring-down aerosol extinction spectrometer (CRD-AES) (23). Submicrometer

particles were selected by passing the sampled airstream through a particulate matter with a 1  $\mu\text{m}$  cutoff ( $\text{PM}_{10}$ ) impactor. In this instrument, light extinction ( $b_{\text{ext}}$ ) by particles is measured at 532 nm after drying ( $\text{RH} < 35\%$ ) and in two channels that have been humidified to RHs of  $80 \pm 2\%$  and  $85 \pm 1\%$  by passing the airstream through independent humidifiers. At the signal levels obtained during this study, the extinction measurements are accurate for submicrometer aerosol to within 3%. The ratio between the humidified and dry particle  $b_{\text{ext}}$  values gives the optical hygroscopic  $GF$ , referred to as  $f(\text{RH})$ . In the CRD-AES, RH is not actively controlled but the highest RH measurement was always within 2% of 85%. To determine  $f(\text{RH})$  at 85% exactly, the observed RH dependence of  $b_{\text{ext}}$  was used to calculate  $b_{\text{ext}}(85\%)$  by first determining the parameter  $\gamma_{\text{RH}}$ , which is determined as the slope of a graph of  $-\log[b_{\text{ext}}(\text{RH})]$  vs.  $\log(100 - \text{RH})$ , where RH is the measured RH (24). The derived  $\gamma_{\text{RH}}$  is then used to calculate  $b_{\text{ext}}(85\%)$ . Given that the measurement of RH is always within 2% of 85% and the particular sensitivity of SSA  $b_{\text{ext}}$  to changes in RH, the absolute uncertainty in the  $f(85\%)$  measurement is  $\sim 10\%$ , although the precision is likely closer to 7% (estimated based on the stability of the signals with time). The  $f(85\%)$  values are then used along with the measured PSDs to derive the physical hygroscopic  $GF$ , shown in Fig. S6B. Specifically,  $b_{\text{ext}}$  values are calculated using the Mie theory for the dry PSD and for particles of increasing diameter, where the diameter increase is assumed to occur due to water uptake. The wet particle refractive index ( $RI$ ) used in the calculations is determined using volume mixing rules assuming  $RI_{\text{H}_2\text{O}} = 1.33$  and  $RI_{\text{dry}} = 1.54$ . The  $GF(85\%)$  is determined by finding the value of the  $GF$  that gives  $f(\text{RH})_{\text{calculated}} = f(85\%)_{\text{observed}}$ . It is estimated that this conversion process leads to an overall absolute uncertainty in the optically derived  $GF(85\%)$  of  $\sim 15\%$  and a precision-based uncertainty of  $\sim 10\%$ . Importantly, the measured optically derived  $GF(85\%)$  is weighted toward the size of SSA particles with the largest extinction cross-sections (here, scattering cross-sections because the SSA particles were found to be nonabsorbing). Given the size distribution of the particles sampled in this study, the optically derived submicrometer  $GF$  was strongly weighted toward particles with  $300 \text{ nm} < d_{p,\text{dry}} < 1,000 \text{ nm}$ , with a median  $d_{p,\text{dry}}$  of  $660 \pm 50 \text{ nm}$ .

To determine the change in hygroscopicity, the measurements of particle growth by water uptake and by CCN activation were both converted to a single parameter,  $\kappa$  (25). The term  $\kappa$  describes the water activity of an aerosol particle and can be used to transform measurements of water uptake both below and above water saturation into the same linear hygroscopicity metric. Large  $\kappa$  values indicate a more hygroscopic particle chemical composition with a correspondingly larger  $GF$  or smaller  $d_{\text{act}}$  at a specific RH or water supersaturation, respectively. Soluble highly hygroscopic inorganic salts, such as those that compose SSA, have  $\kappa$  values of 1.0 or slightly larger. A  $\kappa$  value of 0 is the lower limit and describes a completely insoluble particle composition that only absorbs water through surface wetting at water saturation. Particle hygroscopicity covering the full range of  $\kappa$  values from 0–1.4 has been observed (26–28). Only particle components that have dissolved at the relevant water activity can absorb water (28).

The method for converting measured  $d_{\text{act}}$ , critical supersaturation pairs from CCN analysis to  $\kappa$ , is described by Petters and Kreidenweis (25). We assume a temperature of 298.15 K

and a surface tension of pure water for the air/water interface. Although changes in surface tension can alter the observed particle hygroscopicity, by assuming a constant surface tension, these effects are accounted for by the overall computed apparent hygroscopicity.

Converting the measured subsaturated  $GF$ s to  $\kappa$  simply involves rearranging the principle equation, where water activity is equal to the gas phase RH used in the measurement, at equilibrium (29). Surface tension effects are generally too small to alter subsaturated hygroscopicity significantly and can be ignored. A freely available lookup table was used to calculate the  $\kappa$  values for both methods. In neither method did we attempt to account explicitly for the solubility of any components in the complex, mixed particles because these are not known.

**5.3. Ice Nucleation.** Ice nuclei (IN) measurements were made using the Colorado State University continuous flow diffusion chamber (CFDC) (30, 31). The sample aerosol ( $1.5 \text{ L} \cdot \text{min}^{-1}$ ) is focused by particle-free sheath air ( $8.5 \text{ L} \cdot \text{min}^{-1}$ ) in the annular space between two cylindrical, ice-coated walls in the processing section of the CFDC. Processing temperature and humidity at the aerosol lamina are defined by the inner and outer wall temperature differences, with the temperature chosen to represent that of typical mixed-phase cloud formation conditions and the RH set at 104–105% with respect to subcooled liquid water so as to favor the condensation/immersion-freezing mechanisms predominantly in mixed-phase clouds. After roughly 5 s in the growth section, the aerosols enter ice-saturated conditions for  $\sim 3 \text{ s}$  to evaporate activated cloud droplets that did not freeze and to allow detection of only IN as ice crystals larger than 3  $\mu\text{m}$  exiting the CFDC into an OPC. An inertial impactor was used upstream of the CFDC to restrict assessment of IN to aerosols smaller than 2.5  $\mu\text{m}$  (aerodynamic diameter) and to ensure that large aerosol particles were not falsely counted as ice crystals. To improve sampling statistics for the low sample flow rates used, IN concentrations were calculated for integrated time periods for which uncertainties could be well defined based on Poisson sampling errors. The typical sample period was 3–10 min long. Sample periods were alternated with periods sampling particle-free air to correct for any background frost production. Measurements were obtained at a range of temperatures from  $-20^\circ\text{C}$  through  $-35^\circ\text{C}$ . Data presented here focused specifically on measurements performed at  $-32^\circ\text{C}$ . Throughout the mesocosm experiment, it was observed that IN numbers decreased drastically as TOC increased, dropping from 21 IN per liter in clean, unaltered seawater at a TOC of  $70.7 \mu\text{M}$  (pre-R1) to 2–4 IN per liter at a TOC of  $89.3 \mu\text{M}$  (R1 and R2).

## 6. Summary of Measurements

A brief summary of experimentally determined values of four different conditions (i.e., time periods) is presented in Table S3. Pre-R1 corresponds to a time period before the beginning of the mesocosm experiment in which the wave channel was filled with unamended seawater and breaking waves were used for particle generation. This time period was chosen because it had the full suite of particle measurements available. R1 and R2 correspond to periods of low and high seawater bacteria concentrations, respectively, as discussed in the main text. Post-R2 refers to a time period of high chl-*a* and TOC levels.

1. Alvarez-Salgado XA, Miller AEJ (1998) Simultaneous determination of dissolved organic carbon and total dissolved nitrogen in seawater by high temperature catalytic oxidation: Conditions for precise shipboard measurements. *Mar Chem* 62(3–4): 325–333.
2. Monger BC, Landry MR (1993) Flow cytometric analysis of marine bacteria with hoechst 33342. *Appl Environ Microbiol* 59(3):905–911.
3. Keene WC, et al. (2007) Chemical and physical characteristics of nascent aerosols produced by bursting bubbles at a model air-sea interface. *J Geophys Res Atmos* 112:D21202.

4. Fuentes E, Coe H, Green D, de Leeuw G, McFiggans G (2010) Laboratory-generated primary marine aerosol via bubble-bursting and atomization. *Atmospheric Measurement Techniques* 3(1):141–162.
5. Stokes MD, et al. (2012) A standard marine aerosol reference tank system as a breaking wave analogue. *Atmospheric Measurement Techniques Discussion* 5:8701–8728.
6. Deane GB, Stokes MD (2002) Scale dependence of bubble creation mechanisms in breaking waves. *Nature* 418(6900):839–844.
7. Ott DK, Cyrs W, Peters TA (2008) Passive measurement of coarse particulate matter,  $\text{PM}_{10-2.5}$ . *J Aerosol Sci* 39(2):156–167.

8. Wagner J, Leith D (2001) Passive aerosol sampler. Part I: Principle of operation. *Aerosol Sci Technol* 34(2):186–192.
9. Kuwata M, Zorn SR, Martin ST (2012) Using elemental ratios to predict the density of organic material composed of carbon, hydrogen, and oxygen. *Environ Sci Technol* 46(2):787–794.
10. Moffet RC, Henn T, Laskin A, Gilles MK (2010) Automated chemical analysis of internally mixed aerosol particles using X-ray spectromicroscopy at the carbon K-edge. *Anal Chem* 82(19):7906–7914.
11. Russell LM, Hawkins LN, Frossard AA, Quinn PK, Bates TS (2010) Carbohydrate-like composition of submicron atmospheric particles and their production from ocean bubble bursting. *Proc Natl Acad Sci USA* 107(15):6652–6657.
12. Henke BL, Gullikson EM, Davis JC (1993) X-ray interactions Photoabsorption, scattering, transmission, and reflection at E = 50–30,000 eV, Z = 1–92. *Atomic Data and Nuclear Data Tables* 54(2):181–342.
13. Hawkins LN, Russell LM (2010) Polysaccharides, proteins, and phytoplankton Fragments: Four chemically distinct types of marine primary organic aerosol classified by single particle spectromicroscopy. *Adv Meteorol* 2010:1–14.
14. Gard EE, et al. (1998) Direct observation of heterogeneous chemistry in the atmosphere. *Science* 279(5354):1184–1187.
15. Gaston CJ, et al. (2011) Unique ocean-derived particles serve as a proxy for changes in ocean chemistry. *J Geophys Res Atmos* 116:D18310.
16. Pratt KA, et al. (2009) In situ detection of biological particles in cloud ice-crystals. *Nat Geosci* 2(6):397–400.
17. Lewis ER, Schwartz SE (2004) *Sea Salt Aerosol Production: Mechanisms, Methods, Measurements, and Models: A Critical Review* (American Geophysical Union, Washington, DC).
18. Song XH, Hopke PK, Ferguson DP, Prather KA (1999) Classification of single particles analyzed by ATOFMS using an artificial neural network, ART-2A. *Anal Chem* 71(4):860–865.
19. Li J, Anderson JR, Buseck PR (2003) TEM study of aerosol particles from clean and polluted marine boundary layers over the North Atlantic. *J Geophys Res Atmos* 108(D6):4189.
20. Bigg EK, Leck C (2008) The composition of fragments of bubbles bursting at the ocean surface. *J Geophys Res Atmos* 113(D11):D11209.
21. Roberts GC, Nenes A (2005) A continuous-flow streamwise thermal-gradient CCN chamber for atmospheric measurements. *Aerosol Sci Technol* 39(3):206–221.
22. Sorooshian A, et al. (2008) Rapid, size-resolved aerosol hygroscopic growth measurements: Differential aerosol sizing and hygroscopicity spectrometer probe (DASH-SP). *Aerosol Sci Technol* 42(6):445–464.
23. Langridge JM, Richardson MS, Lack D, Law D, Murphy DM (2011) Aircraft instrument for comprehensive characterization of aerosol optical properties. Part I: Wavelength-dependent optical extinction and its relative humidity dependence measured using cavity ringdown spectroscopy. *Aerosol Sci Technol* 45(11):1305–1318.
24. Quinn PK, et al. (2005) Impact of particulate organic matter on the relative humidity dependence of light scattering: A simplified parameterization. *Geophys Res Lett* 32(22):L22809.
25. Petters MD, Kreidenweis SM (2007) A single parameter representation of hygroscopic growth and cloud condensation nucleus activity. *Atmos Chem Phys* 7(8):1961–1971.
26. Fuentes E, Coe H, Green D, McFiggans G (2011) On the impacts of phytoplankton-derived organic matter on the properties of the primary marine aerosol. Part 2: Composition, hygroscopicity and cloud condensation activity. *Atmos Chem Phys* 11(6):2585–2602.
27. Suda SR, et al. (2012) Hygroscopicity frequency distributions of secondary organic aerosols. *J Geophys Res Atmos* 117:D04207.
28. Sullivan RC, et al. (2009) Effect of chemical mixing state on the hygroscopicity and cloud nucleation properties of calcium mineral dust particles. *Atmos Chem Phys* 9(10):3303–3316.
29. Petters MD, et al. (2009) Towards closing the gap between hygroscopic growth and activation for secondary organic aerosol. Part 2: Theoretical approaches. *Atmos Chem Phys* 9(12):3999–4009.
30. DeMott PJ, et al. (2010) Predicting global atmospheric ice nuclei distributions and their impacts on climate. *Proc Natl Acad Sci USA* 107(25):11217–11222.
31. Rogers DC, DeMott PJ, Kreidenweis SM, Chen YL (2001) A continuous-flow diffusion chamber for airborne measurements of ice nuclei. *J Atmos Ocean Technol* 18(5):725–741.



Fig. S1. Birds-eye lens view of CAICE intensive campaign conducted at the ocean-atmosphere wave flume ( $33 \times 0.5 \times 1$  m) facility developed in phase I (November 2011).

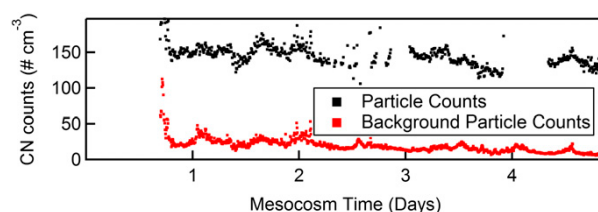
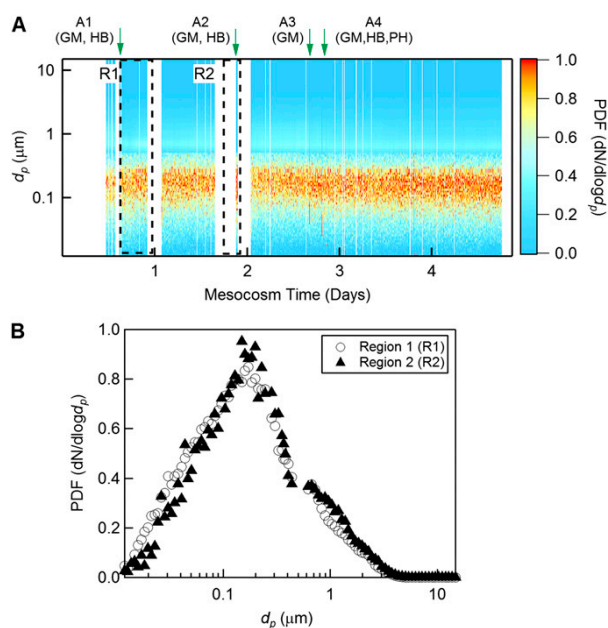
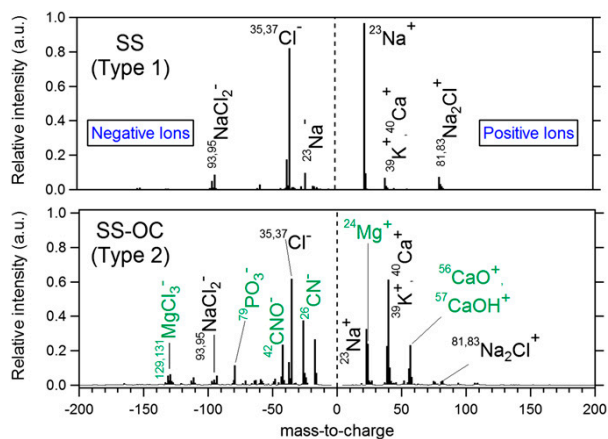


Fig. S2. SSA number concentrations measured at the primary aerosol sampling port (black) and background concentrations measured upstream of the wave breaking region (red). CN, condensation nuclei.



**Fig. S3.** (A) Time series of the PDF of the SSA number distribution ( $RH = 15 \pm 10\%$ ) shows stability over the 5-d mesocosm experiment. Times for the four major additions of growth medium (GM), heterotrophic bacteria (HB), and phytoplankton (PH) are noted (A1–A4) with green arrows (Table S1). Dashed boxes mark two sampling regions (R1 and R2). (B) Aerosol size distributions ( $dN/d\log d_p$ ) for R1 (○) and R2 (▲) shown in Fig. 2. This shows the relatively small variability observed in the sea spray size distribution despite a large change in seawater conditions.



**Fig. S4.** ATOFMS mass spectra of two distinct sea salt types (types 1 and 2). a.u., arbitrary units.





100



**Table S2. Peaks used to identify the different particle types using single particle analysis techniques (TEM-EDX, STXM-NEXAFS, and ATOFMS)**

| Type | TEM-EDX  | STXM-NEXAFS   | ATOFMS  |
|------|--|---|---|
| 1    | Na, Cl, Mg, Ca, K, S, O  | Cl, COOH, S (sulfate), Ca,  | $^{23}\text{Na}^+$ , $^{35,37}\text{Cl}^-$ , $^{39}\text{K}^+$ , $^{81,83}\text{Na}_2\text{Cl}^+$ , $^{40}\text{Ca}^+$  |
| 2    | Na, Cl, Mg, Ca, K, S, O  | Cl, COOH, S (sulfate), Ca inorganic core/organic shell                    | $^{23}\text{Na}^+$ , $^{93,95}\text{NaCl}_2^+$ , $^{81,83}\text{Na}_2\text{Cl}^+$ , $^{129,131}\text{MgCl}_3^-$ , $^{151,153}\text{Na}_2\text{Cl}_3^-$ , $^{26}\text{CN}^-$ , $^{42}\text{CNO}^-$ , $^{35,37}\text{Cl}^-$ , $^{40}\text{Ca}^+$ , $^{39}\text{K}^+$ , $^{79}\text{PO}_3^-$ |
| 3    | Mg, Ca, S, Cl  | —   | $^{24}\text{Mg}^+$ , $^{54,56}\text{Fe}^+$ , $^{39}\text{K}^+$ , $^{40}\text{Ca}^+$ , $^{52}\text{Cr}^+$ , $^{107,109}\text{Ag}^+$ , $^{35,37}\text{Cl}^-$ , $^{26}\text{CN}^-$ , $^{42}\text{CNO}^-$ , $^{79}\text{PO}_3^-$  |
| 4    | Ca, Mg, Na, K, S, (no Cl) (order of cation ion intensity varies) | COOH, S, Ca, (no Cl) homogeneous mixture of organic/inorganic (> organic) | $^{40}\text{Ca}^+$ , $^{24}\text{Mg}^+$ , $^{39}\text{K}^+$ , $^{23}\text{Na}^+$ , $^{56}\text{CaO}^+$ , $^{75}\text{CaCl}^+$ , $^{81,83}\text{Na}_2\text{Cl}^+$ , small organic peaks ( $m/z = 12, 15, 27$ )   |

For each method, the peaks identified are listed in order of intensity from highest to lowest within each particle type.

**Table S3. Summary of measurements presented in Figs. 2–4 for R1 and R2 throughout the main text**

| Measurement*                                     | Pre-R1                      | R1                          | R2                          | Post-R2                                |
|--|-----------------------------|-----------------------------|-----------------------------|--|
| Heterotrophic bacteria, cells·mL <sup>-1</sup>   | $9.4 (\pm 6.6) \times 10^5$ | $7.6 (\pm 2.0) \times 10^5$ | $3.9 (\pm 0.7) \times 10^6$ | $5.2 (4.2; 6.2)^{\dagger} \times 10^6$ |
| Eukaryotic phytoplankton, cells·mL <sup>-1</sup> | $5.7 (\pm 1.4) \times 10^3$ | $5.3 (\pm 0.6) \times 10^3$ | $2.6 (\pm 1.0) \times 10^3$ | $5.6 (1.6; 12)^{\dagger} \times 10^3$  |
| TOC, $\mu\text{M}$                               | $69.1 \pm 4.8$              | $89.3 \pm 8.9$              | $89.3 \pm 1.0$              | $137 (90; 281)^{\dagger}$              |
| Chl- <i>a</i> , mg·m <sup>-3</sup>               | $0.18 \pm 0.08$             | $0.24 \pm 0.02$             | $0.10 \pm 0.01$             | $2.11 (0.048; 5.56)^{\dagger}$         |
| CN, cm <sup>-3</sup>                             | —                           | $159 \pm 36$                | $153 \pm 11$                | $145 \pm 22$                           |
| $d_{\text{act}}$ , nm                            | $63 (+18, -4)$              | $75 (+19, -8)$              | $118 \pm 13^{\ddagger}$     | $124(+34, -14)$                        |
| IN, L  | $15.8 \pm 4.6$              | $2.1 \pm 1.2$               | $4.7 \pm 2.9$               | $0.7 \pm 0.6$                          |
| $GF$ , $d_{\text{wet}}/d_{\text{dry}}$ at 92% RH | $2.4 \pm 0.4$               | $2.2 \pm 0.2$               | $2.3 \pm 0.2$               | $2.2 \pm 0.4$                          |
| SSA chemical composition                         |                             |                             |                             |  |
| Type 2 (SS-OC, 60–180 nm)                        | $0.55 \pm 0.09$             | $0.28 \pm 0.09$             | $0.03 \pm 0.09$             | $0.16 \pm 0.12$                        |
| Type 4 (OC, 60–180 nm)                           | $0.26 \pm 0.09$             | $0.62 \pm 0.09$             | $0.85 \pm 0.09$             | $0.84 \pm 0.12$                        |
| Type 2 (SS-OC, 180–320 nm)                       | $0.63 \pm 0.10$             | $0.70 \pm 0.11$             | $0.50 \pm 0.09$             | $0.70 \pm 0.09$                        |
| Type 4 (OC, 180–320 nm)                          | $0.19 \pm 0.10$             | $0.25 \pm 0.11$             | $0.45 \pm 0.09$             | $0.30 \pm 0.09$                        |

A region for natural seawater (pre-R1) and a region for high TOC/Chl-*a* (post-R2) are also included for comparison. R1, R2, and post-R2 correspond to sampling periods of 0.62–0.91, 1.74–1.87, and 1.88–3.67 d, respectively. CN, condensation nuclei; SS, sea salt.

\*Measurements were made of heterotrophic bacteria, eukaryotic phytoplankton, TOC, chl-*a*, CN,  $d_{\text{act}}$ , IN,  $GF$ , and fractions of types 2 and 4 in the two size ranges.

<sup>†</sup>Average values reported with minimum and maximum values in parentheses.

<sup>‡</sup> $d_{\text{act}}$  is the average of two values from before R2 (at 1.3 and 1.6 d) due to the lack of sufficient size distribution data during period R2.

*Appendix J*

INFLUENCE OF PARTICLE-PHASE STATE ON THE  
HYGROSCOPIC BEHAVIOR OF MIXED  
ORGANIC-INORGANIC AEROSOLS

By Natasha Hodas, Andi Zuend, Wilton Mui, Richard C. Flagan, and John H. Seinfeld

This chapter is was originally published in *Atmospheric Chemistry and Physics* as:

Hodas, N. et al. (2015). “Influence of particle-phase state on the hygroscopic behavior of mixed organic-inorganic aerosols”. In: *Atmos. Chem. Phys.* 15.9, pp. 5027–5045. DOI: 10.5194/acp-15-5027-2015.



# Influence of particle-phase state on the hygroscopic behavior of mixed organic–inorganic aerosols

N. Hodas<sup>1</sup>, A. Zuend<sup>2</sup>, W. Mui<sup>3</sup>, R. C. Flagan<sup>1,3</sup>, and J. H. Seinfeld<sup>1,3</sup>

<sup>1</sup>Division of Chemistry and Chemical Engineering, California Institute of Technology,  
 1200 E. California Blvd., Pasadena, CA, USA

<sup>2</sup>Department of Atmospheric and Oceanic Sciences, McGill University, Montreal, Quebec, Canada

<sup>3</sup>Division of Engineering and Applied Science, California Institute of Technology, Pasadena, CA, USA

Correspondence to: N. Hodas (nhodas@caltech.edu)

Received: 20 November 2014 – Published in Atmos. Chem. Phys. Discuss.: 23 December 2014

Revised: 3 April 2015 – Accepted: 17 April 2015 – Published: 5 May 2015

**Abstract.** Recent work has demonstrated that organic and mixed organic–inorganic particles can exhibit multiple phase states depending on their chemical composition and on ambient conditions such as relative humidity (RH). To explore the extent to which water uptake varies with particle-phase behavior, hygroscopic growth factors (HGFs) of nine laboratory-generated, organic and organic–inorganic aerosol systems with physical states ranging from well-mixed liquids to phase-separated particles to viscous liquids or semi-solids were measured with the Differential Aerosol Sizing and Hygroscopicity Spectrometer Probe at RH values ranging from 40 to 90 %. Water-uptake measurements were accompanied by HGF and RH-dependent thermodynamic equilibrium calculations using the Aerosol Inorganic–Organic Mixtures Functional groups Activity Coefficients (AIOMFAC) model. In addition, AIOMFAC-predicted growth curves are compared to several simplified HGF modeling approaches: (1) representing particles as ideal, well-mixed liquids; (2) forcing a single phase but accounting for non-ideal interactions through activity coefficient calculations; and (3) a Zdanovskii–Stokes–Robinson-like calculation in which complete separation of the inorganic and organic components is assumed at all RH values, with water uptake treated separately in each of the individual phases. We observed variability in the characteristics of measured hygroscopic growth curves across aerosol systems with differing phase behaviors, with growth curves approaching smoother, more continuous water uptake with decreasing prevalence of liquid–liquid phase separation and increasing oxygen : carbon ratios of the organic aerosol components. We also observed indirect

evidence for the dehydration-induced formation of highly viscous semi-solid phases and for kinetic limitations to the crystallization of ammonium sulfate at low RH for sucrose-containing particles. AIOMFAC-predicted growth curves are generally in good agreement with the HGF measurements. The performances of the simplified modeling approaches, however, differ for particles with differing phase states. This suggests that no single simplified modeling approach can be used to capture the water-uptake behavior for the diversity of particle-phase behavior expected in the atmosphere. Errors in HGFs calculated with the simplified models are of sufficient magnitude to produce substantial errors in estimates of particle optical and radiative properties, particularly for the assumption that water uptake is driven by absorptive equilibrium partitioning with ideal particle-phase mixing.

## 1 Introduction

Atmospheric aerosols alter the Earth's radiation budget, reduce visibility, and are associated with adverse health effects (Finlayson-Pitts and Pitts, 2000; Pöschl, 2005; Seinfeld and Pandis, 2006). The magnitude of these impacts is influenced by aerosol water content, as this is a major determinant of aerosol particle size. Furthermore, aerosol water can impact gas-phase photochemistry and secondary organic aerosol (SOA) concentrations by serving as a sink for reactive gases and as a medium for aqueous-phase and heterogeneous reactions (Ervens et al., 2011, 2013). As a result, clear understanding of the hygroscopicity of atmospheric aerosols

is key to representing aerosol properties and behavior in atmospheric models and to improving our understanding of their impacts on climate and air quality.

Organic aerosol (OA) comprises a substantial fraction of total aerosol mass (20–90%; Seinfeld and Pandis, 2006). Moreover, particle formation and transformation processes commonly lead to the formation of internally mixed organic–inorganic particles (Seinfeld and Pankow, 2003; Marcolli et al., 2004; Zhang et al., 2005; Murphy et al., 2006; Goldstein and Galbally, 2007; Hallquist et al., 2009). Multiple studies have sought to elucidate the hygroscopic properties of OA, as well as the influence of organic aerosol components on the hygroscopic behavior and phase transitions of inorganic salts. Much of this work has focused on single- and multi-component aerosols comprised of carboxylic, dicarboxylic, and humic acids (e.g., Prenni et al., 2001; Choi and Chan, 2002a; Brooks et al., 2004; Chan et al., 2006; Moore and Raymond, 2008; Hatch et al., 2009; Pope et al., 2010; Lei et al., 2014), as well as mixtures of organic acids with inorganic salts (e.g., Cruz and Pandis, 2000; Choi and Chan, 2002b; Prenni et al., 2003; Wise et al., 2003; Brooks et al., 2004; Svenningsson et al., 2006; Sjogren et al., 2007; Gao et al., 2008). Recent studies have explored water uptake by sugars, higher molecular weight organics, and polymers (Gysel et al., 2004; Mochida and Kawamura, 2004; Tong et al., 2011; Zobrist et al., 2011; Lei et al., 2014; Xu et al., 2014). Such studies have aimed to characterize the hygroscopicity of biomass burning aerosols, highly oxygenated aged SOA, and oligomers. This body of research has demonstrated that the water-uptake behavior of OA components and their influence on the phase transitions of inorganics depend on multiple factors, including the composition and relative amounts of the organic and inorganic aerosol fractions, the physiochemical properties of the organic components, and ambient conditions. Controlled laboratory studies have also served as a basis for the development and evaluation of thermodynamic models (Clegg et al., 2001; Chan et al., 2005; Raatikainen and Laaksonen, 2005; Clegg and Seinfeld, 2006; Marcolli and Krieger, 2006; Svenningsson et al., 2006; Moore and Raymond, 2008; Zardini et al., 2008; Zuend et al., 2011; Lei et al., 2014), with the aim of representing water uptake by organic and mixed organic–inorganic aerosols.

Current regional and global chemical transport models include a simplified treatment of aerosol hygroscopicity. In CMAQ (Community Multi-scale Air Quality model), for example, only water uptake by the inorganic fraction is considered (Binkowski and Roselle, 2003; <http://www.epa.gov/AMD/Research/Air/aerosolModule.html>). In WRF-Chem (Weather Research and Forecasting model coupled with Chemistry), aerosol hygroscopicity depends on the aerosol module implemented. In MADE (Modal Aerosol Dynamics model for Europe) and MOSAIC (Model for Simulating Aerosol Interactions and Chemistry), only the inorganic aerosol components are considered in estimates of aerosol liquid water (Zaveri et al., 2008). In GOCART (Goddard

Chemistry Aerosol Radiation and Transport), however, the influence of water uptake on the optical properties of OA is prescribed in tabulated relative humidity (RH)-dependent growth factors (Koepke et al., 1997; <http://acmg.seas.harvard.edu/geos>). The modal aerosol module (MAM) assumes the hygroscopicity of primary and secondary organic aerosols can be described with a single parameter based on Köhler theory ( $\kappa$ ; Petters and Kreidenweis, 2007). Similarly, aerosol water associated with organic aerosol components is considered in GEOS-Chem (Goddard Earth Observing System coupled with chemistry) using a set of RH-dependent hygroscopic growth factors (HGFs) for total particulate organic carbon ([http://wiki.seas.harvard.edu/geos-chem/index.php/Aerosol\\_optical\\_properties](http://wiki.seas.harvard.edu/geos-chem/index.php/Aerosol_optical_properties)). In the advanced particle microphysics (APM) module of GEOS-Chem, hygroscopicity is again parameterized based on Köhler theory (Yu et al., 2012). When water uptake by both inorganic and organic components is taken into account in these large-scale chemical transport models, total aerosol liquid water concentrations are commonly calculated either assuming particles are externally mixed or using a volume- or mass-weighted average of the  $\kappa$  values or water contents of all simulated components (Drury et al., 2008; Yu et al., 2012). This simplified treatment of water uptake leads to substantial uncertainties in predicted direct and indirect radiative forcing of atmospheric aerosols (Chung and Seinfeld, 2002; Kanakidou et al., 2005; Liu and Wang, 2010). Furthermore, the assumption of external or additive mixing of the aerosol components fails to account for the influence that particle mixing state and particle-phase morphology can have on aerosol hygroscopicity and optical properties.

Recent work has demonstrated that organic and mixed organic–inorganic particles can exist in multiple phase states depending on their chemical composition and on ambient conditions such as RH and temperature (Cappa et al., 2008; Zobrist et al., 2008; Ciobanu et al., 2009; Virtanen et al., 2010; Bertram et al., 2011; Koop et al., 2011; Krieger et al., 2012). For example, non-ideal interactions between aerosol components can result in a liquid–liquid phase separation (LLPS) in which an inorganic–electrolyte-rich phase and an organic-rich phase co-exist within a single particle (Erdakos and Pankow, 2004; Ciobanu et al., 2009; Zuend et al., 2010; Bertram et al., 2011; Pöhlker et al., 2012; Song et al., 2012a; Zuend and Seinfeld, 2012; You et al., 2012, 2013, 2014). Laboratory studies have demonstrated that ambient OA can exist as a highly viscous liquid, semi-solid, or glass under atmospherically relevant conditions (Zobrist et al., 2008, 2011; Mikhailov et al., 2009; Koop et al., 2011; Tong et al., 2011). Amorphous solid (glassy) SOA has been observed both in a laboratory chamber and in the field (Virtanen et al., 2010; Saukko et al., 2012). Such complex phase behavior has major implications for the partitioning of water and semi-volatile organic species to the particle phase (Ciobanu et al., 2009; Koop et al., 2011; Krieger et al., 2012; Mikhailov et al., 2009; Bones et al., 2012; Song et al., 2012a, 2014; Zaveri et al.,

2014). Diffusion coefficients in solid or semi-solid particles have been estimated to be up to 7 orders of magnitude smaller than in liquids (Vaden et al., 2011; Abbatt et al., 2012), resulting in the inhibition of mass transfer through the aerosol bulk and delayed uptake and evaporation of water (Koop et al., 2011; Bones et al., 2012; Shiraiwa et al., 2011, 2013; Lienhard et al., 2014). Assuming that multi-component particles exist as well-mixed single-phase liquids when two separate phases are actually present can result in errors as large as 200 % in predicted particle mass formed through the partitioning of organic vapors to the condensed phase (Zuend et al., 2010; Zuend and Seinfeld, 2012). The present study explores the extent to which phase separations and other complex phase behavior influence the partitioning of water vapor to the particle phase.

A variety of methods have been used to characterize the factors that influence the prevalence of LLPS and amorphous solid OA. Coupling single-particle techniques with microscopy has enabled the observation of particle-phase transitions with changing ambient conditions (Krieger et al., 2012). Song et al. (2012a), for example, evaluated the prevalence of LLPS as a function of RH and characterized the chemical composition of phases present within mixed organic–inorganic aerosols using a high-speed video camera and Raman microscopy. Moisture-induced glass transitions have been observed for sucrose solutions using single-particle techniques and differential scanning calorimetry (Zobrist et al., 2008, 2011). Similarly, phase states (solid/semi-solid vs. liquid) of SOA as a function of RH have been inferred based on the fraction of particles that bounced when impacted on a steel substrate (Sauko et al., 2012). A combination of bounce-fraction measurements and electron microscopy of newly formed OA in a boreal forest provided the first evidence that SOA formed in the atmosphere can behave as amorphous solids (Virtanen et al., 2010). These analyses have also shown that phase separation and particle viscosity vary with chemical composition (e.g., the organic : inorganic mass ratio), the molecular properties of the organic fraction of the aerosols (e.g., oxygen : carbon [O : C] ratio, molar mass, hydrophilicity), and RH (Bertram et al., 2011; Song et al., 2012a, b; You et al., 2013). While these studies have provided valuable information regarding the influence of RH and particle water content on particle-phase state, investigations of the influence of complex phase behavior on water uptake are limited. Furthermore, the single-particle techniques commonly used to study particle-phase morphology generally require particle sizes on the order of 1–10  $\mu\text{m}$  (Krieger et al., 2012). There is a need for the study of the properties and behavior of submicrometer particles with complex phase morphologies. Herein, we explore variability in the hygroscopic behavior of accumulation-mode particles with phase morphologies ranging from well-mixed liquids to phase-separated particles to amorphous solids or semi-solids and evaluate the impor-

ance of accounting for such complex phase states and related phase transitions when modeling water uptake.

## 2 Methods

### 2.1 Hygroscopic growth factor measurements

Diameter hygroscopic growth factors of nine laboratory-generated aerosol systems that serve as atmospheric aerosol surrogates were measured at RHs ranging from 40 to 90 % with the Differential Aerosol Sizing and Hygroscopicity Spectrometer Probe (DASH-SP). The DASH-SP has been described in detail previously (Sorooshian et al., 2008). Briefly, in the DASH-SP, aerosols are dried in a Nafion dryer, pass through a  $^{210}\text{Po}$  neutralizer, and are then size-selected with a differential mobility analyzer, resulting in a monodisperse aerosol population. The size-selected aerosols are split into four flows in which they are exposed to humidified air in parallel Nafion humidifiers at four different controlled RH values. Residence times in the Nafion dryer and in each of the humidifiers are 1 and 4 s, respectively. The aerosols were also sent through a silica gel diffusion dryer with a residence time of  $\sim 3$ –5 s prior to entering the DASH-SP. The size distributions of the particles following humidification are measured with four dedicated optical particle counters (OPCs). A data processing algorithm that accounts for the dependence of the OPC signal on particle diameter and refractive index has been developed to calculate wet particle diameter (i.e., particle diameter after exposure to humidified air) from the OPC signal (Sorooshian et al., 2008). This calculation requires knowledge of the refractive index of the dry particle. One of the flow regions of the DASH-SP is kept dry ( $\text{RH} < 8\%$ ) to enable calculation of the effective refractive index using an empirical relationship between OPC signal height, refractive index, and particle size. This empirical relationship was developed using calibration salts with known refractive indices (Sorooshian et al., 2008). It is assumed that the particles are spherical and that they scatter, but not do absorb, light. Hygroscopic diameter growth factors are calculated as the ratio of the mode diameter of the wet particle size distribution (i.e., at a 40–90 % RH set point) to the dry-mode particle diameter ( $\text{HGF} = D_{\text{wet}}/D_{\text{dry}}$ ). In this work, HGFs were measured for particles with dry mobility diameters of 250 nm. HGF measurements were performed at room temperature ( $\sim 298\text{ K}$ ). A minimum of 1500 particles were counted and sized at each RH value to produce the dry and wet size distributions. Experiments were repeated 10 times for each aerosol system and reported growth factors were calculated as the average across those 10 runs. The overall average uncertainty in DASH-SP-measured HGFs is approximately 5 % but can approach 8 % at lower values of RH (Sorooshian et al., 2008).

With the aim of exploring the extent to which water uptake varies with particle-phase state, hygroscopic growth curves

were measured for chemical systems for which particle-phase behavior as a function of RH has previously been characterized. For all systems studied here, RH-dependent phase states had previously been observed at room temperature. Most of those studies were based on single-particle techniques, in which a single-particle (typically supermicron-sized) is isolated in a controlled environment and probed with various optical and microscopy techniques (Tong et al., 2011; Zobrist et al., 2011; Song et al., 2012a; You et al., 2013). Briefly, You et al. (2013) explored the prevalence of liquid–liquid phase separations as a function of RH for internally mixed organic–inorganic aerosol systems comprising one organic compound and one inorganic salt. Single particles were deposited on a glass slide coated with a hydrophobic substrate that was then mounted in a RH- and temperature-controlled flow cell. Phase transitions during RH cycling were observed with an optical reflectance microscope. Song et al. (2012a) studied the phase behavior of more complex particle mixtures, each consisting of three dicarboxylic acids with 5, 6, or 7 carbon atoms ( $C_5$ ,  $C_6$ ,  $C_7$ ) and ammonium sulfate, deposited on a glass slide using a Raman microscope equipped with a high-speed camera. Zobrist et al. (2011) and Tong et al. (2011) studied the phase-state and water-uptake behavior of sucrose particles using an electrodynamic balance coupled with various optical techniques and optical tweezers coupled with bright-field imaging, respectively.

Seven aerosol systems with RH-dependent phase morphologies ranging from well-mixed liquids to phase-separated particles to amorphous solids or semi-solids were chosen for study in the present work from the above-described studies. Table 1 summarizes the compositions and phase behaviors of these chemical systems as determined in these prior studies. Two additional chemical systems consisting of sucrose and ammonium sulfate with varying organic : inorganic ratios were also studied here. A concurrent study (Robinson et al., 2014) also explored the hygroscopic behavior of submicron sucrose–ammonium sulfate particles, with the aim of characterizing the influence of glassy aerosol components on the optical properties of organic–inorganic particles. Sucrose was selected as a model compound in that work and in the present study due to its high glass-transition temperature ( $T_g = 331\text{--}335.7\text{ K}$ ), as characterized by Zobrist et al. (2008) and Dette et al. (2014). The phase behavior of these systems as a function of RH, however, has only been characterized for a sucrose : ammonium sulfate dry mass ratio of 2 : 1 (You and Bertram, 2015, Table 1). The phase behavior of the 1 : 1 sucrose–ammonium sulfate system has not been characterized with single-particle techniques.

In addition to differences in phase behavior, the aerosol systems represent variations in their complexity (in terms of dry composition). Particle compositions range from single-component organic systems, to two-component systems consisting of one organic and ammonium sulfate, to more complex systems consisting of dicarboxylic acid mixtures and ammonium sulfate (Table 1). To evaluate the performance

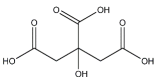
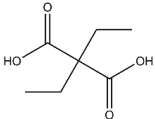
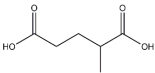
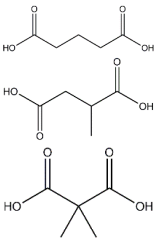
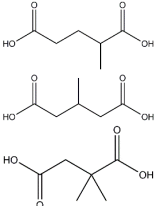
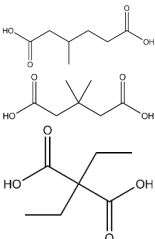
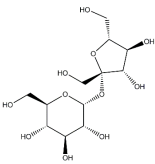
of the DASH-SP and the HGF-calculation algorithm, control runs were also performed for pure ammonium sulfate aerosols. For all chemical systems, aerosols were generated by atomizing aqueous solutions prepared by dissolving the organic and inorganic components with the mass ratios given in Table 1 in Milli-Q water (resistivity  $\geq 18.2\text{ M}\Omega\text{ cm}$ ). Ammonium sulfate (purity  $\geq 99\%$ ) and ACS reagent-grade sucrose were purchased from Macron Fine Chemicals; all other organic components were purchased from Sigma-Aldrich (purity  $\geq 98\%$ ).

## 2.2 Modeling hygroscopic growth

Hygroscopic growth curves were modeled for the nine aerosol systems with the Aerosol Inorganic–Organic Mixtures Functional groups Activity Coefficients (AIOMFAC) model (Zuend et al., 2008, 2010, 2011; Appendix A). AIOMFAC is a thermodynamic model that explicitly accounts for molecular interactions between all components in an aqueous solution through the calculation of activity coefficients. A group-contribution concept based on UNIFAC (UNiversal quasi-chemical Functional group Activity Coefficients), in which the thermodynamic properties of organic compounds are determined on the basis of their molecular structures, is employed to account for interactions among organic functional groups, inorganic ions, and water (Zuend et al., 2008, 2011). In these AIOMFAC-based equilibrium calculations, the potential existence of a LLPS is determined and corresponding liquid-phase compositions are computed by the method of Zuend and Seinfeld (2013). Diameter growth factors are calculated for RH values ranging from near 0 to 99 % for both dehydration (from high RH to low RH) and hydration (low RH to high RH) cycles for all systems. For dehydration-branch calculations, growth factors at RH values lower than the particle/inorganic salt deliquescence point are representative of metastable conditions, where a supersaturated solution is present with respect to the dissolved inorganic salt. Hydration calculations include the presence of a solid inorganic phase at RH values before the full deliquescence of ammonium sulfate and the partial dissolution of ammonium sulfate into the aqueous organic solution (solid–liquid equilibrium; SLE). The hydration calculations are the most relevant to the hygroscopic growth experiments, as the atomized aerosols were dried before being exposed to elevated humidities in the DASH-SP. AIOMFAC-calculated diameter growth factors are compared to measured values to provide a detailed evaluation of the interactions likely to be occurring between aerosol chemical components.

Following Zuend and Seinfeld (2012), in addition to the full AIOMFAC-based equilibrium calculations, several simplified calculations were performed to explore the influence of phase separation and the effects of other non-ideal interactions on hygroscopic growth. These comparisons also evaluate the need for accounting for such interactions in modeling the water-uptake behavior of atmospheric aerosols.

Table 1. Aerosol systems studied.

| Aerosol system   | Organic-component structures  | Organic-component density ( $\text{kg m}^{-3}$ ) | Organic : inorganic dry mass ratio | Previous experimentally determined phase behavior   | References                                |
|--|---|--|------------------------------------|---|---|
| Citric acid + ammonium sulfate   |    | 1.580  | 2 : 1                              | No LLPS observed  | Bertram et al. (2011), You et al. (2013)  |
| Diethylmalonic acid + ammonium sulfate   |    | 1.131  | 2 : 1                              | LLPS at $\text{RH} \leq 89\%$   | You et al. (2013)                         |
| 2-Methylglutaric acid + ammonium sulfate   |    | 1.169  | 2 : 1                              | LLPS at $\text{RH} \leq 75\%$   | You et al. (2013)                         |
| C <sub>5</sub> dicarboxylic acids mixture (glutaric, methylsuccinic, dimethylmalonic) + ammonium sulfate               |    | 1.219  | 1 : 1                              | No LLPS observed  | Song et al. (2012a)                       |
| C <sub>6</sub> dicarboxylic acid mixture (2-methylglutaric, 3-methylglutaric, 2,2-dimethylsuccinic) + ammonium sulfate |  | 1.169  | 1 : 1                              | Transition from LLPS with partially engulfed morphology to single liquid phase at $\text{RH} = 74\%$    | Song et al. (2012a)                       |
| C <sub>7</sub> dicarboxylic acid mixture (3-methyladipic, 3,3-dimethylglutaric, diethylmalonic) + ammonium sulfate     |  | 1.131  | 1 : 1                              | Transition from LLPS with core-shell morphology to single liquid phase at $\text{RH} = 89\text{--}90\%$ | Song et al. (2012a)                       |
| Sucrose  |  | 1.309  | not applicable                     | Glass transition at $\text{RH} = 24\text{--}53\%$ , depending on timescale of RH change                 | Tong et al. (2011), Zobrist et al. (2011) |
| Sucrose + ammonium sulfate   |   |  | 1 : 1                              | Unknown   | This study                                |
| Sucrose + ammonium sulfate   |   |  | 2 : 1                              | No LLPS observed  | You and Bertram (2015)                    |

Two hygroscopic growth calculations in which no LLPS was allowed to occur were performed: (1) one in which non-ideal interactions are taken into account through AIOMFAC-calculated activity coefficients and (2) one in which it is assumed that the condensed phase behaves as an ideal mixture. Water-uptake calculations were also performed in a mode in which complete separation between an aqueous inorganic electrolyte phase and an organic phase is assumed and, thus, no organic-ion interactions are accounted for. This latter case is similar to a Zdanovskii–Stokes–Robinson (ZSR) relation assumption, since the water uptake of individual components (here two separate phases) are added up to estimate the HGF. In our ZSR-like calculation case, the influence of non-ideality on water activity, and therefore water content, is accounted for within the individual phases with AIOMFAC-based activity coefficients. A calculation in which a solid organic phase is assumed at all RH values was also performed for comparison against the DASH-SP measurements in order to evaluate whether the presence of a solid organic phase was likely in any of the chemical systems studied. All growth-curve calculations were performed at 298 K.

Note that AIOMFAC predicts phase compositions, which can be used to derive mass growth factors but not the densities of the phases necessary to calculate diameter growth factors (assuming spherical particles). Solid and liquid-state densities of ammonium sulfate were taken from Clegg and Wexler (2011). The density of citric acid was calculated based on the data and parameterizations of Lienhard et al. (2012). The densities of all other organic compounds were estimated using the structure-based method of Girolami (1994) with the online density-calculation tools available on the E-AIM website (<http://www.aim.env.uea.ac.uk/aim/aim.php>). Densities of mixtures within particles and those of individual phases were calculated assuming additive molar volumes of each component (i.e., ideal mixing in terms of density). Organic component densities are given in Table 1.

### 3 Results and discussion

#### 3.1 Experimental hygroscopic growth curves and AIOMFAC modeling

##### 3.1.1 Two-component carboxylic acid–ammonium sulfate systems

Measured and AIOMFAC-predicted HGFs for the two-component carboxylic acid–ammonium sulfate systems (organic : inorganic dry mass ratios = 2 : 1) are shown in Fig. 1. Panels below the hygroscopic growth curves illustrate AIOMFAC predictions of the occurrence of phase separation and the composition of each phase. All of the two-component carboxylic acid–ammonium sulfate systems demonstrate suppressed water uptake at high RH values com-

pared to pure ammonium sulfate (Figs. 1a–c, B1). This is expected because, based on approximately linear additivity in water uptake by the different particle components, a lesser degree of water uptake by the organic fraction in comparison to inorganic salts (per unit mass) is typically the case. At RH = 80 %, ratios of the HGFs for the mixed organic–inorganic aerosols to those for pure ammonium sulfate were 0.88, 0.86, and 0.89 for the systems containing diethylmalonic acid, 2-methylglutaric acid, and citric acid, respectively. Similarly, these values were 0.90, 0.88, and 0.88 at RH = 90 %. At low to moderate RH values (40–70 %), however, the shapes and characteristics of the growth curves vary across the systems due, at least in part, to differences in phase behavior, as is discussed below.

Mixed diethylmalonic acid–ammonium sulfate particles demonstrated little to no water uptake ( $\text{HGF} \approx 1.0$ ) before the particle deliquesced at an RH of approximately 80 % (Fig. 1a). This suggests the presence of a viscous semi-solid, an amorphous solid, or a crystalline solid organic phase (with no water uptake on the timescale of the 4 s residence time in the humidifier). The presence of a solid organic at low to moderate RH is supported by a comparison between measured and AIOMFAC-calculated growth factors. For RH = 40–70 %, model–measurement agreement is closest for the case in which diethylmalonic acid is assumed to be solid. Measured values then approach the full equilibrium AIOMFAC calculation in which the organic is assumed to be in a liquid state. Note that all AIOMFAC-based calculations shown by the solid curves assume that the organic compounds are in a liquid-like state at all RH levels. For this system, AIOMFAC predicts a SLE state, with diethylmalonic acid dominating the liquid phase and with the solid phase fully comprised of ammonium sulfate. Following the deliquescence of ammonium sulfate at RH = 79.75 %, the particle is predicted to undergo LLPS. The organic-dominated and the ammonium sulfate-dominated phases are then predicted to merge to a single phase at RH = 94 %. The AIOMFAC-predicted RH at which merging of the two phases occurs is 5 % higher than that observed by You et al. (2013). It is likely that this small discrepancy can be attributed to uncertainty in modeled organic–ion interactions. However, it is also possible that optical methods cannot discern the presence of two phases at RH  $\geq$  89 % if one of the two predicted liquid phases is small in mass or volume compared to the other phase.

In addition, You et al. (2013) performed dehydration experiments to explore the onset of phase separation (from high to low RH), while the present study focused on hydration experiments (from low to high RH). AIOMFAC predictions are made under the assumption that there is no hysteresis between LLPS and the merging of two liquid phases to a single phase in terms of the onset RH. This is because experiments (e.g., Song et al., 2012a) show that there is little to no hysteresis in such a phase transition, at least for systems with liquid-like viscosities. In contrast to the typical hysteresis behavior



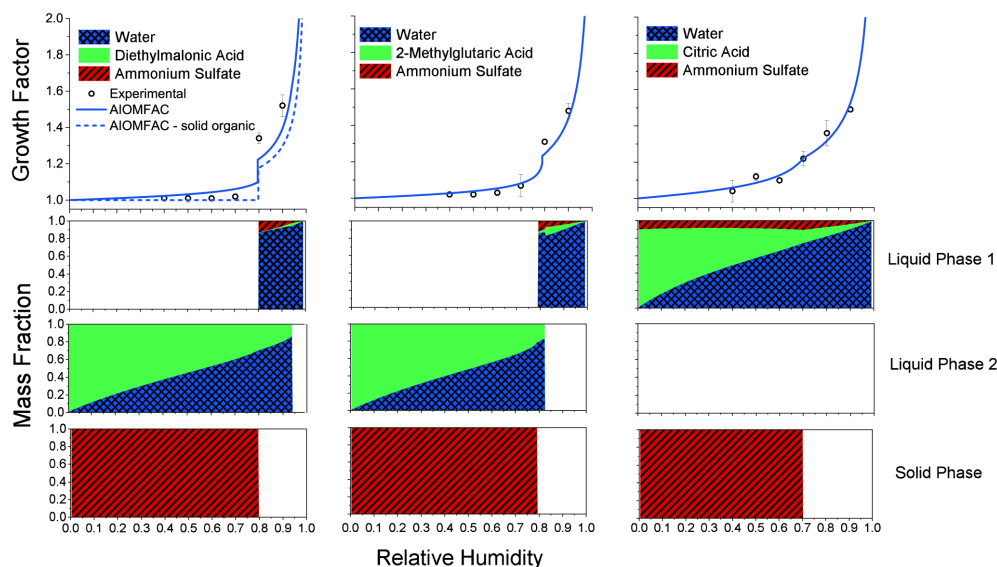


**Figure 1.** Top panels: Measured and AIOMFAC-predicted hygroscopic diameter growth factors for (a) diethylmalonic acid–ammonium sulfate particles, (b) 2-methylglutaric acid–ammonium sulfate particles, and (c) citric acid–ammonium sulfate particles, with dry organic : inorganic mass ratios of 2 : 1 for all systems. The black circles indicate the average growth factor measured across ten experiments and error bars indicate the standard deviation of the measured growth factors. Panels below the hygroscopic growth curves indicate the AIOMFAC-predicted composition of each of three possible phases present in the particles (liquid phase 1, liquid phase 2, and a solid phase) as a function of relative humidity. Empty boxes indicate that no second liquid phase is predicted.

of liquid–crystal/crystal–liquid phase transitions (i.e., deliquescence vs. crystallization), liquid–liquid to single-liquid phase transitions involve only disordered phase states (rather than crystalline solids with long-range order). Exceptions to this may exist for some systems in a particular composition range involving the metastable region of a liquid–liquid equilibrium phase diagram (e.g., Zuend et al., 2010). However, the energy barrier for the nucleation and growth of a new liquid phase is small in comparison to the larger energy barrier that needs to be overcome when a new crystalline phase is formed. Because the merging of the phases is predicted to occur at an RH at which aqueous diethylmalonic acid is expected to be of low viscosity (Fig. 1a), no hysteresis behavior is expected. Thus, we do not expect that a hysteresis behavior influenced the disagreement in the RH of phase merging discussed above.

Like the diethylmalonic acid–ammonium sulfate system, the 2-methylglutaric-containing aerosols demonstrate a marked increase in water uptake at RH = 80 %; however, more gradual and continuous water uptake was observed prior to particle deliquescence (Fig. 1b). Good agreement was achieved between measured and AIOMFAC-predicted growth curves at all RH values. AIOMFAC again predicts a SLE state prior to the deliquescence of ammonium sulfate at RH = 79.25 %. This is followed by the presence of two liquid phases before full merging of the phases into a single liquid phase at RH = 82.25 %. As was true for the

diethylmalonic acid–ammonium sulfate system, this LLPS phase transition value is higher than the RH of 75 % observed by You et al. (2013). As noted above, this could be related to uncertainty associated with the parameterization of the AIOMFAC group-contribution method. In addition, with the gradual merging of the phases, it is possible that a remaining LLPS was not visible in the experiments at RH > 75 %. Again, as is explained above, no hysteresis is expected for the phase separation and merging for hydration and dehydration conditions for this system.

For the citric acid–ammonium sulfate particles, measured growth factors suggest gradual, continuous water uptake at all experimental RH values (Fig. 1c). This is in agreement with measurements for this system at different dry organic : inorganic ratios reported by Zardini et al. (2008). The AIOMFAC-predicted growth curve indicates a small increase in slope with the deliquescence of ammonium sulfate at RH = 70.25 %, lower than that for pure ammonium sulfate. This is expected in the presence of a hygroscopic organic compound like citric acid (O : C = 1.17) due to the partial solubility of ammonium sulfate in the aqueous, citric-acid-rich phase. Measured and predicted growth factors are in very good agreement at all RH values. For this system, a single, well-mixed liquid phase is predicted following the complete deliquescence of ammonium sulfate. This is in agreement with the experimental results of You et al. (2013) and

Bertram et al. (2011), who observed no evidence of LLPS for citric acid–ammonium sulfate particles.

A comparison of hygroscopic growth curves across the three two-component systems suggests that growth curve shape reflects phase behavior in mixed organic–ammonium sulfate systems. Growth curves approach smoother, more continuous water uptake with decreasing prevalence of LLPS (i.e., looking from left to right for Fig. 1a–c). In addition to higher miscibility of the aerosol components for particles with no LLPS or those for which LLPS persists for only a small range of RH values, this can likely be attributed to the fact that both the prevalence of LLPS and aerosol hygroscopicity vary with the O : C ratios of the organic components of mixed organic–inorganic particles (Massoli et al., 2010; Bertram et al., 2011; Duplissy et al., 2011; Song et al., 2012a; You et al., 2013). Note that the O : C ratios of diethylmalonic, 2-methylglutaric, and citric acid are 0.57, 0.67, and 1.17, respectively. Thus, the smoothing of the growth curves with increasing O : C (and, incidentally, lower prevalence of LLPS) is consistent with the higher propensity of the more polar compounds to take up water and dissolve some ammonium sulfate (in an SLE) at lower RH.

### 3.1.2 Complex mixed dicarboxylic acid–ammonium sulfate systems

In general, water-uptake behavior was similar across the more complex dicarboxylic acid–ammonium sulfate mixtures, regardless of the carbon number of the acids included in the system and the differences in the phase morphologies of the particles observed previously in experiments by Song et al. (2012a). All systems demonstrated gradual water uptake with growth factors increasing from 1.0 to  $\sim 1.05$  prior to a rapid increase in particle diameter of  $\sim 30$ – $45$  % at  $\text{RH} \approx 80$  % (Fig. 2). This is in agreement with the results of Song et al. (2012a), who observed nearly complete or complete particle deliquescence at RH values of 79–80 % for all three systems. At  $\text{RH} \geq 80$  %, suppressed hygroscopic growth as compared to ammonium sulfate is evident, but to a lesser degree than for the two-component systems discussed above, with reductions in diameter growth factors ranging from 1 to 7 %. This is likely attributable to the smaller organic : inorganic ratios of these systems as compared to the two-component systems (dry mass ratios of 1 : 1 rather than 2 : 1). In addition, mixing effects due to the presence of multiple organics, which can inhibit crystallization (Cruz and Pandis, 2000; Marcolli et al., 2004), likely influenced the water-uptake behavior of these systems. One constituent of the  $\text{C}_7$  acid mixture, diethylmalonic acid, demonstrated behavior indicative of the presence of a crystalline solid or highly viscous organic phase in the two-component mixture discussed above. In the more complex  $\text{C}_7$  acid mixture, however, it is possible that there is limited, but more gradual, water uptake at low to moderate RH, suggesting a liquid (perhaps moderately viscous) phase. Owing to their complexity, the multi-

acid aerosol systems may provide a better analog for the majority of mixed organic–inorganic atmospheric aerosols than the two-component systems. As was true for the two-component carboxylic acid–ammonium sulfate systems, we observed a smoothing of the growth curves with increasing O : C ratio of the  $\text{C}_5$ ,  $\text{C}_6$ , and  $\text{C}_7$  dicarboxylic acid mixtures (O : C = 0.80, 0.67, 0.57, respectively).

As determined both through previous experimental work and with the AIOMFAC modeling, there is variability in phase behavior across the mixed dicarboxylic acid–ammonium sulfate aerosol systems. For the  $\text{C}_5$  dicarboxylic acid–ammonium sulfate system, AIOMFAC predicts an SLE state of ammonium sulfate prior to complete deliquescence at  $\text{RH} = 77$  % (Fig. 2a). At this point, ammonium sulfate fully dissolves into the organic-dominated liquid phase. For the  $\text{C}_6$  and  $\text{C}_7$  systems, however, AIOMFAC predicts LLPS following the complete deliquescence of ammonium sulfate at  $\text{RH} = 79.25$  and  $79.75$  %, respectively (Fig. 2b, c). For the  $\text{C}_6$  system, the inorganic- and organic-dominated phases are then predicted to merge to a single phase at  $\text{RH} = 83$  %, while LLPS persists up to  $\text{RH} = 92.75$  % for the  $\text{C}_7$  system. AIOMFAC predictions of phase behavior are in qualitative agreement with the observations of Song et al. (2012a). In agreement with AIOMFAC predictions of particle-phase state during the humidification process (i.e., starting from dry conditions), no evidence of LLPS was observed for the  $\text{C}_5$  system (Song et al., 2012a). Contrary to the experiments reported by Song et al. (2012a), AIOMFAC does predict LLPS at RH values below 80 % for the dehydration process of the  $\text{C}_5$  system (i.e., when no solid ammonium sulfate phase is allowed to form). For both the  $\text{C}_6$  and  $\text{C}_7$  systems, AIOMFAC overpredicts the RH at which separated phases merge to a single phase by 10 and 3 %, respectively, in comparison to the observations by Song et al. (2012a). Song et al. (2012a) also observed differences in the morphology of the LLPS states of the  $\text{C}_6$  and  $\text{C}_7$  systems. For the  $\text{C}_6$  system, an ammonium sulfate core was partially engulfed by an organic-dominated outer phase containing ammonium sulfate satellite inclusions. The  $\text{C}_7$  system displayed a distinct, fully engulfed core–shell morphology. Despite the small degree of model–experiment disagreement in the RHs at which merging of two liquid phases occur in the  $\text{C}_6$  and  $\text{C}_7$  systems, good agreement between measured and AIOMFAC-predicted growth curves is achieved for the  $\text{C}_5$ ,  $\text{C}_6$ , and  $\text{C}_7$  systems (Fig. 2a–c). This suggests that the presence or absence of LLPS, as well as the morphology of LLPS (which is not taken into account in AIOMFAC), might influence water uptake to a lesser degree than other thermodynamic properties. This is explored subsequently when we compare various modeling methods that vary in the degree to which they consider thermodynamic non-ideality and LLPS.

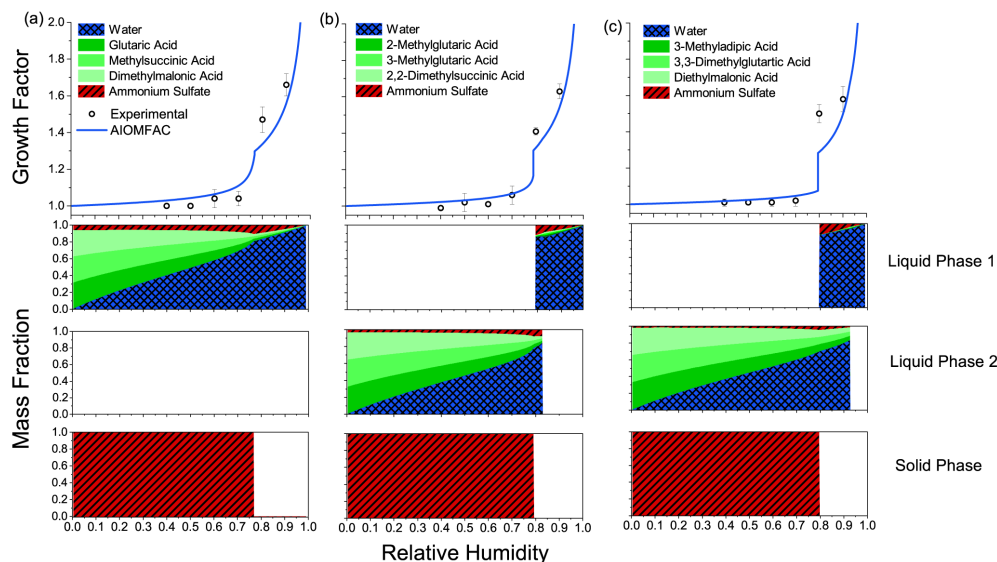


**Figure 2.** Top panels: measured and AIOMFAC-predicted hygroscopic diameter growth factors for (a) C<sub>5</sub> dicarboxylic acid mixture–ammonium sulfate particles, (b) C<sub>6</sub> dicarboxylic acid mixture–ammonium sulfate particles, and (c) C<sub>7</sub> dicarboxylic acid mixture–ammonium sulfate particles, with dry organic : inorganic mass ratios of 1 : 1 for all systems. The black circles indicate the average growth factor measured across 10 experiments and error bars indicate the standard deviation of the measured growth factors. Panels below the hygroscopic growth curves indicate the AIOMFAC-predicted composition of each of three possible phases present in the particles (liquid phase 1, liquid phase 2, and a solid phase) as a function of relative humidity. Empty boxes indicate that no second liquid phase is predicted.

### 3.1.3 Sucrose-containing aerosols

The pure sucrose aerosols demonstrate continuous, but limited, water uptake with growth factors reaching only 1.25 at RH = 90 % (Fig. 3a). Consequently, as RH approaches 100 %, the growth factor is expected to show a steep increase. Such a steep increase is predicted by the AIOMFAC-based equilibrium model at RH ≈ 95 %. For RH ≤ 50 %, average measured values of HGF fall below the equilibrium calculations of AIOMFAC; however, this deviation is within experimental uncertainty. Previous studies demonstrated that the glass transition RH of sucrose droplets at room temperature (~298 K) ranges between 25 and 53 %, depending on the rate of dehumidification (Zobrist et al., 2011; Tong et al., 2011). Thus, it is possible that a glass transition occurred with the rapid drying of the atomized sucrose droplets (total residence time in the silica gel diffusion and Nafion dryers ~ 5 s). However, no quantitative conclusions can be drawn about the extent to which this affected HGFs in our measurements. Nevertheless, such a glass transition may have influenced the growth factor measurement at RH < 53 % and could partially explain the observed discrepancy between the measured and modeled growth factors at those RH levels. Measured HGFs are in agreement with equilibrium-condition measurements and modeling of Tong et al. (2011) and Zobrist et al. (2011), as well as AIOMFAC-modeled HGFs, particularly at RH ≥ 60 %.

Like pure sucrose, the sucrose–ammonium sulfate systems demonstrate continuous water-uptake behavior, with smaller HGFs compared to pure ammonium sulfate at RH = 80 and 90 % (Fig. 3b, c). The magnitude of the deviations in HGF for the sucrose–ammonium sulfate particles from those for pure ammonium sulfate varies with the organic : inorganic ratio but is within the range observed for the other aerosol systems. At RH = 80 %, ratios of the HGFs for the sucrose–ammonium sulfate particles to those for pure ammonium sulfate were 0.86 and 0.91 for the 2 : 1 and 1 : 1 sucrose–ammonium sulfate systems, respectively. These values were 0.85 and 0.89 at RH = 90 %.

Evidence for the influence of a highly viscous phase state on hygroscopic behavior is stronger for the mixed sucrose–ammonium sulfate aerosols. While for stable thermodynamic equilibrium AIOMFAC predicts distinct deliquescence behavior at RH = 80 % for both organic : inorganic ratios, we observed smooth, continuous water uptake for RH = 40–90 % in the DASH-SP experiments (Fig. 3b, c). Note that before entering the DASH-SP, particles were dried after atomization from a solution, at which point ammonium sulfate crystallization may occur. Since the viscosity of the solution is expected to increase considerably toward lower RH, however, the high viscosity (potentially accompanied by a glass transition) may suppress the crystallization of ammonium sulfate in these systems. The corresponding AIOMFAC calculations for the humidification process are shown by the

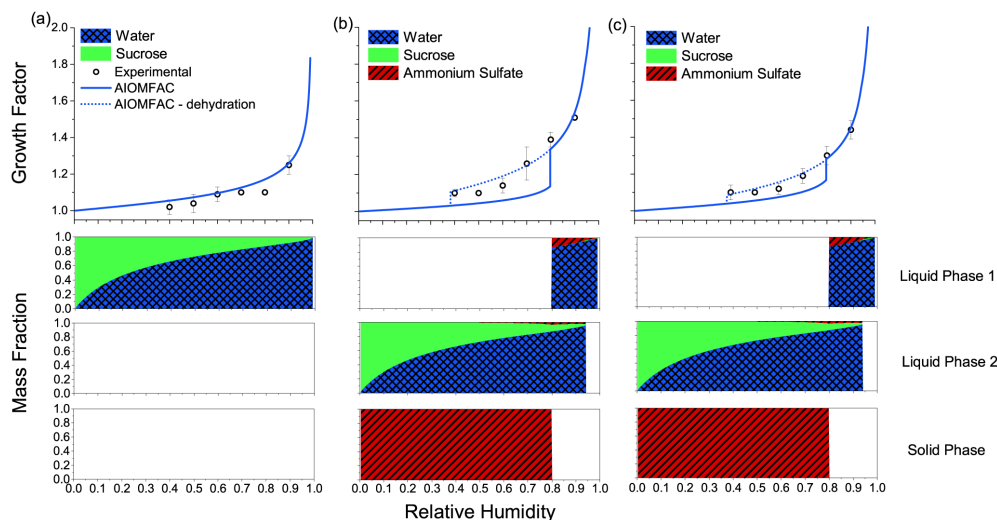


**Figure 3.** Top panels: Measured and AIOMFAC-predicted hygroscopic growth factors for (a) sucrose particles, (b) mixed sucrose–ammonium sulfate particles with an organic:inorganic ratio of 1:1, and (c) mixed sucrose–ammonium sulfate particles with an organic:inorganic ratio of 2:1. The black circles indicate the average growth factor measured across 10 experiments, and error bars indicate the standard deviation of the measured growth factors. Solid lines indicate the hydration curve calculated with the AIOMFAC-based equilibrium model, while dashed lines illustrate the dehydration branch in which a supersaturated solution is present with respect to the dissolved ammonium sulfate. The three panels below the hygroscopic growth curves indicate the AIOMFAC-predicted composition of each of three possible phases present in the particles during the hydration process (liquid phase 1, liquid phase 2, and a solid phase) as a function of relative humidity. Empty boxes indicate that either no second liquid phase or no solid phase is predicted.

solid curves in Fig. 3 (where ammonium sulfate is in a crystalline state at low RH), while the dashed curves show the model predictions of HGF for the case where both sucrose and ammonium sulfate are present in a liquid (potentially viscous) solution. This latter scenario is often observed experimentally during a dehydration process (starting at very high RH with a homogenous liquid solution). The measured HGFs are in good agreement with the metastable conditions of the AIOMFAC-modeled “dehydration branch.” This is in agreement with the results of Robinson et al. (2014), who also observed continuous water uptake and evidence for the inhibition of the crystallization of ammonium sulfate in the presence of viscous sucrose. Minor differences ( $\leq 10\%$ ) in the HGFs reported in their work ( $\text{RH} = 60\text{--}80\%$ ) and those described here can likely be attributed to differences in technique, as they derived growth factor based on light extinction using Mie theory, or to variances in particle drying and/or humidification times (humidification residence time = 1 s vs. 4 s in this work). Our results suggest that rapid particle drying within HGF instrumentation can induce a steep increase in particle viscosity, potentially even leading to a glass transition. As a result, such measurements may not accurately reflect the equilibrium water-uptake behavior of viscous particles. This has implications for the measurement of HGFs for ambient aerosol such as the highly oxygenated SOA for which sucrose serves as a surrogate in these experiments.

The formation of a highly viscous liquid or semi-solid phase may also lead to kinetic limitations, affecting the loss of water by evaporation during the drying process prior to humidification in the DASH-SP. There is increasing evidence from laboratory and field studies that viscous liquid or semi-solid SOA components may be present in atmospheric aerosol (e.g., Virtanen et al., 2010; Vaden et al., 2011; Saukko et al., 2012; Renbaum-Wolff et al., 2013). Thus, accounting for kinetic limitations to water uptake and release is crucial to accurately modeling the dynamic hygroscopic behavior of SOA. However, the good agreement between measured HGFs and the AIOMFAC-based dehydration-branch equilibrium calculations indicates that water loss was not substantially inhibited during particle drying. If a glassy sucrose shell had formed in these particles and this shell was of sufficient thickness to inhibit water evaporation during the  $\sim 5$  s residence time in the dryers, the measured effective “dry” reference diameter would have been affected by the higher water content. This oversized shell would, in turn, affect all the experimental HGFs obtained at higher RH due to the normalization by the “dry” particle diameter. If this were the case, HGFs from the experimental data would likely be lower and discrepancies from the AIOMFAC-based calculations of the dehydration growth curve would be larger. Another possible factor contributing to model–measurement disagreement for the sucrose–ammonium sulfate systems is the lower confidence in the treatment of ether groups by

AIOMFAC as compared to functional groups present in the other systems studied here. This is due to limited experimental data for the development of parameterizations of ether-group-ion interactions (Zuend et al., 2011). This might also contribute to uncertainty in the predicted phase behavior of the sucrose-ammonium sulfate aerosols, which indicates an SLE prior to the complete deliquescence of ammonium sulfate at  $\text{RH} = 80\%$ . It is predicted that LLPS then persists up to  $\text{RH} = 94.25\%$  for both organic:inorganic ratios explored here (Fig. 3b, c). The predicted occurrence of LLPS for sucrose ( $\text{O}:\text{C} = 0.92$ ) contrasts with previous studies that suggest that LLPS is unlikely for organic compounds with  $\text{O}:\text{C} > 0.7\text{--}0.8$  (Bertram et al., 2011; Song et al., 2012b; You et al., 2013) as well as the experimental results of You and Bertram (2015), in which no LLPS was observed for sucrose-ammonium sulfate particles with an organic to inorganic dry mass ratio of 2:1.

### 3.1.4 Measurement and modeling limitations and uncertainty

As noted above, data availability limitations and variability in experimental conditions for the data sets used in developing parameterizations of functional-group-ion interactions in AIOMFAC contribute to uncertainties in ether-ion interactions and other functional-group-ion interactions. In addition, other measurement and modeling limitations can contribute to uncertainty in measured and predicted HGFs. Because experimental data regarding the densities of organic compounds are limited, the densities of many of the organic compounds studied in this work were estimated with a group-contribution method (Girolami, 1994). Furthermore, for all aerosol systems and all phases present within the particles it was assumed that the molar volumes of the aerosol components are additive (i.e., ideal mixing in terms of volume and density contributions), regardless of the thermodynamic properties of the mixture under consideration.

Complex particle-phase morphologies can also present unique sources of error and uncertainty in HGF measurement methods that use optical methods, such as the DASH-SP. For example, the algorithm that calculates diameter growth factor assumes that the refractive index of the non-water aerosol components is constant at the value measured in the dry DASH-SP channel. For systems with non-uniform surfaces (e.g., the  $\text{C}_6$  dicarboxylic acid-ammonium sulfate system, which has been shown to have an organic outer shell with satellite ammonium sulfate inclusions or partially engulfed morphology; Song et al., 2012a), this assumption might not be accurate. In addition, the effective refractive index of the organic and inorganic particle components might evolve upon humidification as previously separated phases merge. This behavior has the potential to influence hygroscopicity measurements for systems that have core-shell morphologies at low to moderate RH that then transition to a single liquid-phase state with increasing water content

and might contribute to the greater model-measurement disagreement at  $\text{RH} = 80\%$  observed for the  $\text{C}_7$  dicarboxylic acid-ammonium sulfate system. However, the overall agreement achieved between measured HGFs and AIOMFAC-calculated values in this work suggests that these factors, and their corresponding uncertainties, are not a substantial issue for the measurement of HGFs for the aerosol compositions and particle size range studied here.

In addition, as noted above, the DASH-SP HGF experiments were performed with particles much smaller than those used in the microscopy or electrodynamic balance experiments that had previously been used to directly characterize LLPS and glass transitions in the particle systems studied. Thus, the phase behavior of the particles studied here was not characterized directly. There is some limited evidence that the prevalence of LLPS can vary with particle size. Veghte et al. (2013) observed that LLPS did occur in larger particles comprised of ammonium sulfate and succinic acid or pimelic acid (diameters  $\geq 170$  and  $270\text{ nm}$ , respectively); however, that LLPS was not evident in smaller particles with the same composition and organic:inorganic mass ratios. While the DASH-SP experiments do not directly reveal whether a phase separation is present in the particles, the observed hygroscopic growth in comparison to the model calculations is in agreement with such phase behavior in the corresponding LLPS RH ranges. Finally, the timescale of humidification in our experiments differs from that in the single-particle studies. For example, in the mixed dicarboxylic acid-ammonium sulfate single-particle experiments, RH was changed at a rate of  $0.14\text{--}0.34\% \text{ min}^{-1}$  (Song et al., 2012a). The extent to which the timescale of humidification influences the occurrence of phase separation is unknown; however, again, agreement between the measured hygroscopic growth and those calculated under equilibrium conditions suggests the humidification timescale did not have a substantial impact on phase behavior.

### 3.2 Evaluation of simplified thermodynamic assumptions

For the multicomponent systems for which we expect that observed water-uptake behavior is governed by thermodynamic equilibrium conditions (i.e., excluding the sucrose-containing systems, which display evidence of kinetic limitations to the crystallization of ammonium sulfate), we compared the rigorous thermodynamic modeling of the AIOMFAC-based equilibrium HGF predictions (“AIOMFAC, equilibrium” in Fig. 4) to that based on several simplified thermodynamic assumptions: (1) representing particles as ideal, well-mixed liquids (“ideal – well-mixed liquid”), (2) forcing a single liquid phase following the deliquescence of ammonium sulfate but accounting for non-ideal interactions through activity coefficient calculations and allowing for a SLE of ammonium sulfate (“no LLPS – non-ideal”), and (3) a ZSR-like calculation in which complete separa-

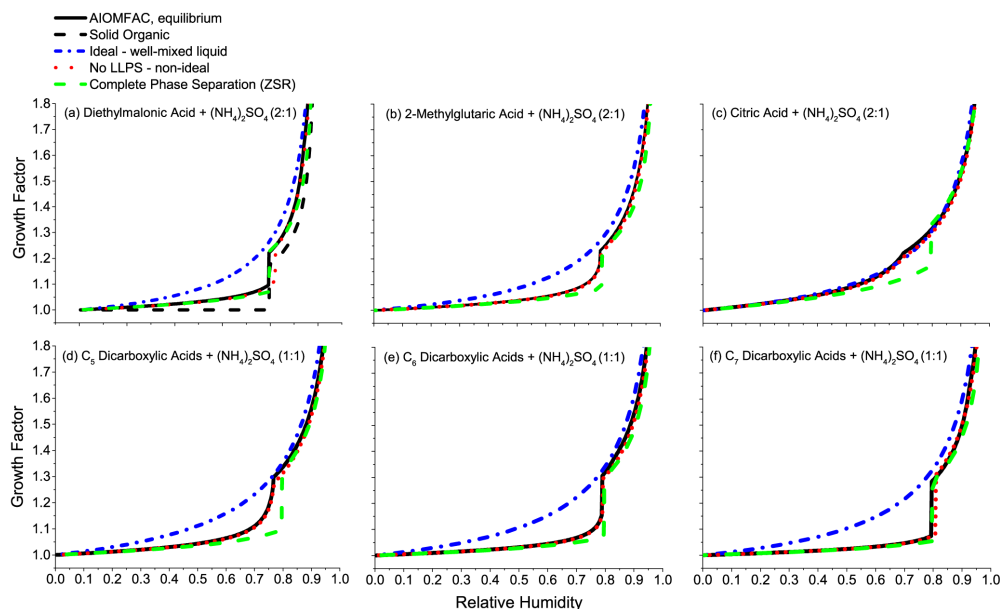


**Figure 4.** Comparison of simplified thermodynamic assumptions to the full AIOMFAC hygroscopic growth calculations for the multi-component systems for which we expect observed water-uptake behavior to be governed by thermodynamic equilibrium conditions. Organic : inorganic dry mass ratios, which can substantially influence the extent to which non-ideal interactions affect water uptake, are given in parentheses. The performance of the simplified modeling approaches varies across the systems with variations in phase behavior. Disagreement between the full AIOMFAC-based equilibrium calculations and the simplified models is greatest at low to moderate RH (RH = 20–80 %).

tion of the inorganic and organic components is assumed at all RH levels (“complete phase separation (ZSR)”). Water is the only component allowed to partition to both phases in this ZSR-like calculation case. In all of these simplified calculation cases, the formation of a solid ammonium sulfate phase is allowed to occur (below its deliquescence point at the given temperature), except for the single-phase, ideal mixture case. We evaluate the extent to which these simple, relatively computationally inexpensive modeling approaches capture the hygroscopic behavior of particles with varied and complex phase states. Note that for the diethylmalonic acid–ammonium sulfate system, we first focus on the calculation for which the presence of a solid organic is predicted prior to particle deliquescence (“solid organic” in Fig. 4). At  $\text{RH} \geq 80\%$ , we then consider the full AIOMFAC equilibrium calculation in our discussion of model error, as this offered the best agreement between measured and modeled values (Fig. 1a). For all other systems, we focus on the full AIOMFAC-based equilibrium calculations at all RH values.

Figure 4 shows a comparison of the AIOMFAC-predicted HGFs for the hydration branch of a humidity cycle and those calculated with the simplified modeling approaches. The performance of each of the simplified modeling approaches differs for particles depending on phase state. This suggests that a single simplified modeling approach cannot be used to cap-

ture the water-uptake behavior for the diversity of particle-phase behaviors expected in the atmosphere. For all systems except the citric acid–ammonium sulfate particles, the assumption that the particles could be represented as thermodynamically ideal liquid mixtures leads to the greatest deviation from AIOMFAC-predicted growth curves. We also note that such discrepancies depend on the organic : inorganic dry-state mass ratios. Generally, the smaller the ammonium sulfate mass fraction, the lower the degree of hysteresis behavior of hydration/dehydration processes. Overpredictions of diameter growth factors increase from those at low RH to a maximum just prior to the rapid increase in water uptake associated with deliquescence of ammonium sulfate, then drop to within  $\sim 5\%$  of AIOMFAC values (Fig. 4). Maximum errors for the assumption of ideality ranged from 10 to 26 % and increased with increased prevalence of LLPS (i.e., looking from right to left from Fig. 4a to c and from left to right from Fig. 4d to f). For the citric acid–ammonium sulfate system, which does not undergo LLPS, ideal and AIOMFAC calculated growth curves are in good agreement for  $\text{RH} \leq 80\%$ . Error then increases slightly to  $\sim 5\%$ .

Not surprisingly, the forced single-phase calculations, in which non-ideal interactions are taken into account but LLPS is not, perform well for the  $\text{C}_5$  dicarboxylic–ammonium sulfate and citric acid–ammonium sulfate systems, which



demonstrated no LLPS (Fig. 4c, d). For these systems, the ZSR-like calculation leads to the largest disagreement, with maximum errors of between 10 and 18 % occurring between RH values of 60 and 80 %. This can be attributed to delayed particle deliquescence in the ZSR-like calculations, since the partial dissolution of ammonium sulfate in the aqueous organic phase is not considered in this case. Similarly, for systems for which LLPS persists for only a small range of RH values, the single-phase assumption performs well, with errors never exceeding 5 % (e.g., the 2-methylglutaric–ammonium sulfate and C<sub>6</sub> dicarboxylic acid–ammonium sulfate systems; Fig. 4b, e). The single-phase assumption also performs well for the systems for which LLPS does occur over a wider RH range, but delayed prediction of particle deliquescence leads to a large spike in underprediction of particle diameter at RH  $\approx$  80 %. The good performance of the single-phase assumption at most RH values suggests that accounting for LLPS in calculations of hygroscopic growth might be less important than accounting for other non-ideal interactions between condensed-phase components. However, this result is likely not applicable to mixed organic–inorganic systems with less water-soluble (i.e., less hygroscopic) organic components, where LLPS is more prevalent and water uptake by the organic fraction is limited (Zuend and Seinfeld, 2012).

For systems that do undergo LLPS, the ZSR-like calculation also performs relatively well across the range of RH values studied but displays discrepancies to the AIOMFAC-based equilibrium prediction of 12–18 % at moderate RH values due to deviations in the predicted SLE and deliquescence transition of ammonium sulfate. For these systems, the ZSR-like calculation also underpredicts water uptake at RH values above the point at which separated liquid phases merged to a single phase, with relative deviations approaching 10 %. As expected, growth curves begin to converge towards the AIOMFAC equilibrium predictions as RH approaches 100 % for all systems, as the solutions become very dilute (Fig. 4). Our results suggest that a lack of accounting for non-ideal interactions and phase separations leads to errors in predicted sub-saturated hygroscopic growth. Note that while maximum deviations in HGFs for the simplified approaches (compared to the AIOMFAC-based equilibrium calculation) are generally on the order of 10–25 %, the corresponding errors in particle size and refractive index can substantially impact estimates of aerosol scattering and radiative forcing (Finlayson-Pitts and Pitts, 2000).

#### 4 Conclusions

Measurements and detailed thermodynamic modeling of the water uptake of model organic–inorganic atmospheric aerosol systems demonstrate variability in hygroscopic behavior across aerosol systems with differing RH-dependent phase behavior. Measured and modeled growth curves ap-

proach smoother, more continuous water uptake with decreasing prevalence of LLPS and increasing O : C ratios of the OA components. AIOMFAC-predicted growth curves reproduce the measured hygroscopic behavior reasonably well for all systems. A comparison of measured and modeled HGFs for the sucrose–ammonium sulfate particles indicates the presence of a viscous semi-solid phase that inhibits the crystallization of ammonium sulfate. We conclude that particle drying within HGF instrumentation may induce the formation of a highly viscous, amorphous phase (potentially accompanied by a moisture-loss-related glass transition). As a result, such measurements may not accurately reflect equilibrium water-uptake behavior. This is an important consideration when applying similar instruments to measure the hygroscopic behavior of ambient aerosols, particularly for the highly oxygenated SOA for which sucrose serves as a surrogate in our experiments. Our results add support to the growing body of literature suggesting that accounting for the influence of viscous liquid or semi-solid phases to water uptake and release can be important for accurately modeling the hygroscopic behavior of atmospheric aerosols. The performance of simplified approaches for modeling water uptake differs for particles with differing phase states/equilibria, suggesting that a single simplified modeling approach cannot be used to capture the water-uptake behavior for the diversity of particle-phase behavior expected in the atmosphere. Errors in HGFs calculated using the simplified models are of sufficient magnitude to contribute substantially to uncertainties in estimates of particle optical and radiative properties. Parameterizations of LLPS and other complex phase behavior based on commonly measured variables such as O : C (e.g., Bertram et al., 2011; Koop et al., 2011; Song et al., 2012a) may prove valuable in applying the simplified HGF calculation approaches explored here in large-scale models. Average carbon oxidation state ( $\overline{\text{OS}}_{\text{C}}$ ) has also been presented as an indicator of the degree of aerosol oxidation (Kroll et al., 2011) and may be a useful measure when the goal is to track changes in hygroscopicity with the progression of oxidation and fragmentation of organic molecules in an atmospheric chemistry model. Parameterizations of hygroscopicity based on  $\overline{\text{OS}}_{\text{C}}$  might also lead to advancements in the modeling of aerosol water uptake for complex organic and mixed organic–inorganic systems and should be a consideration in future work. Finally, while the majority of field-based hygroscopicity studies focus on relatively high RH values, future measurements could also focus on the growth factors of atmospheric aerosol at low to moderate RH values, as this is the region where water-uptake behavior demonstrates the greatest variability with particle-phase behavior.

### Appendix A: AIOMFAC model and phase equilibrium calculations

AIOMFAC is a group-contribution, thermodynamic model for the calculation of component activity coefficients in binary and multicomponent mixtures. It was developed to explicitly account for molecular interactions among organic functional groups and inorganic ions in aqueous solutions relevant to atmospheric aerosol chemistry. Descriptions of model details and parameterizations are available elsewhere (Zuend et al., 2008, 2010, 2011; Zuend and Seinfeld, 2012; <http://www.aiomfac.caltech.edu>). Herein, we provide a brief overview of the key aspects of the AIOMFAC model.

Within the model, organic molecules are represented as assemblies of functional groups. This treatment of organic molecules is based on the concept that the physiochemical properties of organic compounds can be related to their chemical structure and characteristic structural groups, which allows for treatment of the hundreds to thousands of organic compounds that characterize atmosphere organic aerosol. The organic functional groups included in AIOMFAC (alkyl (standard), alkyl (in alcohols), alkyl (in hydrophobic tails of alcohols), alkyl (bonded to hydroxyl group), alkenyl, aromatic hydrocarbons, hydroxyl, aromatic carbon-alcohol, ketone, aldehyde, ester, ether, carboxyl, hydroperoxide, peroxy acid, peroxide (organic), peroxyacyl nitrate, organonitrate) allow for the representation of a large variety of compounds observed in atmospheric aerosols. In addition, AIOMFAC includes seven atmospherically relevant cations ( $\text{H}^+$ ,  $\text{Li}^+$ ,  $\text{Na}^+$ ,  $\text{K}^+$ ,  $\text{NH}_4^+$ ,  $\text{Mg}^{2+}$ ,  $\text{Ca}^{2+}$ ), five anions ( $\text{Cl}^-$ ,  $\text{Br}^-$ ,  $\text{NO}_3^-$ ,  $\text{HSO}_4^-$ ,  $\text{SO}_4^{2-}$ ), and water.

Non-ideality (i.e., deviations from Raoult's law) in organic–inorganic aqueous solutions is accounted for through the calculation of activity coefficients for all components in a given mixture. When considering the partitioning of water vapor to a multicomponent liquid mixture, the vapor pressure of water ( $p_w$ ) over the mixture is related to water activity by

$$p_w = p_w^0 a_w^{(x)}, \quad (\text{A1})$$

where  $p_w^0 = p_w^0(T)$  is the saturation vapor pressure over pure liquid water at temperature  $T$  and  $a_w^{(x)}$  is the water activity defined on a mole fraction basis. Under thermodynamic equilibrium conditions, relative humidity and water activity are related by

$$\text{RH} = a_w^{(x)} = \gamma_w^{(x)} x_w, \quad (\text{A2})$$

where  $\gamma_w^{(x)}$  is the activity coefficient of water on a mole fraction basis and  $x_w$  is the mole fraction of water in the particle-phase liquid mixture (here, for the case of a single liquid phase). Similarly, activity coefficients are key to accurately describing the partitioning of semi-volatile organic compounds between the gas and particle phases under thermodynamic equilibrium.

In AIOMFAC, activity coefficients are derived from expressions for the long-range, middle-range, and short-range molecular interactions that contribute to total Gibbs excess energy, which is a descriptor of the overall non-ideality of a thermodynamic system. In addition to their application in calculations of the gas-particle partitioning of water and other semi-volatile species (i.e., vapor-liquid equilibria), activity coefficients of all components in a multi-component mixture are required for the calculation of solid-liquid (SLE) and liquid-liquid equilibria. The prevalence of liquid-liquid phase separation and the composition of each phase is calculated in this work by application of AIOMFAC to compute activity coefficients in distinct liquid phases based on a reliable and efficient algorithm for finding the phase compositions that correspond to an equilibrium state. A liquid-liquid equilibrium state of a closed thermodynamic system is a state of minimum Gibbs energy of that system. The same applies to SLE and, likewise, to coupled vapor-liquid-liquid-solid equilibrium calculations, such as those performed in this work at given temperature and relative humidity to determine the number and composition of the particle phases at equilibrium. Hence, while the AIOMFAC model is at the heart of such equilibrium calculations, the distinct phases and their compositions are determined using a more general thermodynamic equilibrium model, as described by Zuend et al. (2010) and Zuend and Seinfeld (2012). For the calculation of a potential liquid-liquid phase separation, the equilibrium model essentially solves a system of nonlinear equations numerically to determine the phase state (i.e., one liquid phase vs. two liquid phases) that achieves a minimum in Gibbs energy for a given overall particle-phase composition at constant temperature and pressure. Full details regarding the algorithm used to diagnose the prevalence of LLPS and to calculate the corresponding phase composition are available in Zuend and Seinfeld (2013).



### Appendix B: Control hygroscopic growth experiments

Following the same methods as described in the main text of the paper, control hygroscopic growth experiments were conducted for pure ammonium sulfate aerosols with dry mobility diameters of 250 nm. HGF experiments were conducted at room temperature ( $\sim 298$  K). The control experiments were conducted for comparison against the mixed organic–ammonium sulfate aerosol systems (i.e., to explore the influence of the organic species on the mixed organic–inorganic particle hygroscopicity when starting with the same dry size) and to evaluate the performance of the DASH-SP and the growth-factor-calculation algorithm using this well-characterized aerosol system. DASH-SP measurements reproduced previous experimental characterizations of ammonium sulfate aerosol hygroscopicity (e.g., Tang, 1980; Sorooshian et al., 2008) and are in agreement with AIOMFAC-predicted diameter growth factors (Fig. B1).

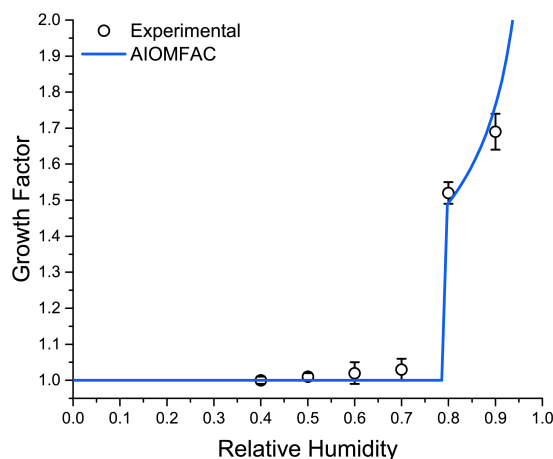


**Figure B1.** Measured and modeled hygroscopic growth factors for ammonium sulfate particles with dry mobility diameters of 250 nm. The black circles indicate the average growth factor measured across 10 experiments and error bars indicate the standard deviation of the measured growth factors.

**Author contributions.** N. Hodas, J. H. Seinfeld, and R. C. Flagan designed the experiments. N. Hodas carried out the experiments with assistance from W. Mui. A. Zuend developed the modeling tools and performed all simulations. N. Hodas prepared the manuscript with contributions from all co-authors.

**Acknowledgements.** This work was supported by the National Science Foundation under award no. 1433246 and the Office for Naval Research under award no. N00014-14-1-0097. W. Mui was supported by an NSF graduate research fellowship (grant no. DGE-1144469) and NSF grant no. CBET-1236909. A. Zuend was supported by a McGill University start-up grant.

Edited by: T. Koop

## References

- Abbatt, J. P. D., Lee, A. K. Y., and Thornton J. A.: Quantifying trace gas uptake to tropospheric aerosol: recent advances and remaining challenges, *Chem. Soc. Rev.*, 41, 6555–6581, 2012.
- Bertram, A. K., Martin, S. T., Hanna, S. J., Smith, M. L., Bodsworth, A., Chen, Q., Kuwata, M., Liu, A., You, Y., and Zorn, S. R.: Predicting the relative humidities of liquid-liquid phase separation, efflorescence, and deliquescence of mixed particles of ammonium sulfate, organic material, and water using the organic-to-sulfate mass ratio of the particle and the oxygen-to-carbon elemental ratio of the organic component, *Atmos. Chem. Phys.*, 11, 10995–11006, doi:10.5194/acp-11-10995-2011, 2011.
- Binkowski, F. S. and Roselle, S. J.: Models-3 Community Multiscale Air Quality (CMAQ) model aerosol component 1. Model description, *J. Geophys. Res.*, 108, 4183, doi:10.1029/2001JD001409, 2003.
- Bones, D. L., Reid, J. P., Lienhard, D. M., and Krieger, U. K.: Comparing the mechanism of water condensation and evaporation in glassy aerosol, *P. Natl. Acad. Sci.*, 109, 11613–11618, 2012.
- Brooks, S. D., DeMott, P. J., and Kreidenweis, S. M.: Water uptake by particles containing humic materials and mixtures of humic materials with ammonium sulfate, *Atmos. Environ.*, 38, 1859–1868, 2004.
- Cappa, C. D., Lovejoy, E. R., and Ravishankara, A. R.: Evidence for liquid-like and nonideal behavior of a mixture of organic aerosol components, *P. Natl. Acad. Sci.*, 105, 18687–18691, 2008.
- Chan, M. N., Choi, M. Y., Ng, N. L., and Chan, C. K.: Hygroscopicity of water-soluble organic compounds in atmospheric aerosols: amino acids and biomass burning derived organic species, *Environ. Sci. Technol.*, 39, 1555–1562, 2005.
- Chan, M. N., Lee, A. K. Y., and Chan, C. K.: Responses of ammonium sulfate particles coated with glutaric acid to cyclic changes in relative humidity: hygroscopicity and Raman characterization, *Environ. Sci. Technol.*, 40, 6983–6989, 2006.
- Choi, M. Y. and Chan, C. K.: Continuous measurements of the water activities of aqueous droplets of water-soluble organic compounds, *J. Phys. Chem. A.*, 106, 4566–4572, 2002a.
- Choi, M. Y. and Chan, C. K.: The effects of organic species on the hygroscopic behaviors of inorganic aerosols, *Environ. Sci. Technol.*, 36, 2422–2428, 2002b.
- Chung, S. H. and Seinfeld, J. J.: Global distribution and climate forcing of carbonaceous aerosols, *J. Geophys. Res.*, 107, 4407, doi:10.1029/2001JD001397, 2002.
- Ciobanu, V. G., Marcolli, C., Krieger, U. K., Weers, U., and Peter, T.: Liquid-liquid phase separation in mixed organic/inorganic aerosol particles, *J. Phys. Chem.*, 113, 10966–10978, 2009.
- Clegg, S. L. and Seinfeld, J. H.: Thermodynamic models of aqueous solutions containing inorganic electrolytes and dicarboxylic acids at 298.25 K, 1. The acids as nondissociating components, *J. Phys. Chem. A*, 110, 5692–5717, 2006.
- Clegg, S. L. and Wexler, A. S.: Densities and Apparent Molar Volumes of Atmospherically Important Electrolyte Solutions. 1. The Solutes  $\text{H}_2\text{SO}_4$ ,  $\text{HNO}_3$ ,  $\text{HCl}$ ,  $\text{Na}_2\text{SO}_4$ ,  $\text{NaNO}_3$ ,  $\text{NaCl}$ ,  $(\text{NH}_4)_2\text{SO}_4$ ,  $\text{NH}_4\text{NO}_3$ , and  $\text{NH}_4\text{Cl}$  from 0 to 50 °C, including extrapolations to very low temperature and to the pure liquid state, and  $\text{NaHSO}_4$ ,  $\text{NaOH}$ , and  $\text{NH}_3$  at 25 °C, *J. Phys. Chem. A*, 115, 3393–3460, 2011.
- Clegg, S. L., Seinfeld, J. H., and Brimblecombe, P.: Thermodynamic modeling of aqueous aerosols containing electrolytes and dissolved organic compounds, *J. Aerosol Sci.*, 32, 713–738, 2001.
- Cruz, C. and Pandis, S. N.: Deliquescence and hygroscopic growth of mixed inorganic-organic atmospheric aerosol, *Environ. Sci. Technol.*, 32, 4313–4319, 2000.
- Dette, H. P., Qi, M., Schröder, D. C., Godt, A., and Koop, T.: Glass-forming properties of 3-methylbutane-1,2,3-tricarboxylic acid and its mixtures with water and pinonic acid, *J. Phys. Chem. A*, 118, 7024–7033, 2014.
- Drury, E., Jacob, D. J., Wang, J., Spurr, R. J. D., and Chance, K.: Improved algorithm for MODIS satellite retrievals for aerosol optical depth over western North America, *J. Geophys. Res.*, 113, D16204, doi:10.1029/2007JD009573, 2008.
- Duplissy, J., DeCarlo, P. F., Dommen, J., Alfarra, M. R., Metzger, A., Barmapadimos, I., Prevot, A. S. H., Weingartner, E., Tritscher, T., Gysel, M., Aiken, A. C., Jimenez, J. L., Canagaratna, M. R., Worsnop, D. R., Collins, D. R., Tomlinson, J., and Baltensperger, U.: Relating hygroscopicity and composition of organic aerosol particulate matter, *Atmos. Chem. Phys.*, 11, 1155–1165, doi:10.5194/acp-11-1155-2011, 2011.
- Erdakos, G. B. and Pankow, J. F.: Gas/particle partitioning of neutral and ionizing compounds to single- and multi-phase aerosol particles. 2. Phase separation in liquid particulate matter containing both polar and low-polarity organic compounds, *Atmos. Environ.*, 38, 1005–1013, 2004.
- Ervens, B., Turpin, B. J., and Weber, R. J.: Secondary organic aerosol formation in cloud droplets and aqueous particles (aqSOA): a review of laboratory, field and model studies, *Atmos. Chem. Phys.*, 11, 11069–11102, doi:10.5194/acp-11-11069-2011, 2011.
- Ervens, B., Wang, Y., Eagar, J., Leaitch, W. R., Macdonald, A. M., Valsaraj, K. T., and Herckes, P.: Dissolved organic carbon (DOC) and select aldehydes in cloud and fog water: the role of the aqueous phase in impacting trace gas budgets, *Atmos. Chem. Phys.*, 13, 5117–5135, doi:10.5194/acp-13-5117-2013, 2013.
- Finlayson-Pitts, B. J. and Pitts Jr., J. N.: Chemistry of the Upper and Lower Atmosphere, Academic Press, San Diego, CA, 2000.
- Gao, Y., Yu, L. E., and Chen, S. B.: Effects of organics on the efflorescence relative humidity of ammonium sulfate or sodium chloride particles, *Atmos. Environ.*, 42, 4433–4445, 2008.

- Girolami, G. S.: A simple “back of the envelope” method for estimating the densities and molecular volumes of liquids and solids, *J. Chem. Educ.*, 71, 962–964, 1994.
- Goldstein, A. H. and Galbally, I. E.: Known and unexplored organic constituents in the Earth’s atmosphere, *Environ. Sci. Technol.*, 41, 1514–1521, 2007.
- Gysel, M., Weingartner, E., Nyeki, S., Paulsen, D., Baltensperger, U., Galambos, I., and Kiss, G.: Hygroscopic properties of water-soluble matter and humic-like organics in atmospheric fine aerosol, *Atmos. Chem. Phys.*, 4, 35–50, doi:10.5194/acp-4-35-2004, 2004.
- Hallquist, M., Wenger, J. C., Baltensperger, U., Rudich, Y., Simpson, D., Claeys, M., Dommen, J., Donahue, N. M., George, C., Goldstein, A. H., Hamilton, J. F., Herrmann, H., Hoffmann, T., Iinuma, Y., Jang, M., Jenkin, M. E., Jimenez, J. L., Kiendler-Scharr, A., Maenhaut, W., McFiggans, G., Mentel, Th. F., Monod, A., Prévôt, A. S. H., Seinfeld, J. H., Surratt, J. D., Szmigielski, R., and Wildt, J.: The formation, properties and impact of secondary organic aerosol: current and emerging issues, *Atmos. Chem. Phys.*, 9, 5155–5236, doi:10.5194/acp-9-5155-2009, 2009.
- Hatch, C. D., Gierlus, K. M., Zahardis, J., Schuttlefield, J., and Grassian, V. H.: Water uptake of humic and fulvic acid: measurements and modelling using single parameter Köhler theory, *Environ. Chem.*, 6, 380–388, 2009.
- Kanakidou, M., Seinfeld, J. H., Pandis, S. N., Barnes, I., Dentener, F. J., Facchini, M. C., Van Dingenen, R., Ervens, B., Nenes, A., Nielsen, C. J., Swietlicki, E., Putaud, J. P., Balkanski, Y., Fuzzi, S., Horth, J., Moortgat, G. K., Winterhalter, R., Myhre, C. E. L., Tsigaridis, K., Vignati, E., Stephanou, E. G., and Wilson, J.: Organic aerosol and global climate modelling: a review, *Atmos. Chem. Phys.*, 5, 1053–1123, doi:10.5194/acp-5-1053-2005, 2005.
- Koepke, P., Hess, M., Schult, I., and Shettle, E. P.: Global Aerosol Data Set, Rep. No. 243, Max-Planck-Institut für Meteorol., Hamburg, Germany, 1997.
- Koop, T., Bookhold, J., Shiraiwa, M., and Pöschl, U.: Glass transition and phase state of organic compounds: dependency on molecular properties and implications for secondary organic aerosols in the atmosphere, *Phys. Chem. Chem. Phys.*, 13, 1923–19255, 2011.
- Krieger, U., Marcolli, C., and Reid, J. P.: Exploring the complexity of aerosol particle properties and processes using single particle techniques, *Chem. Soc. Rev.*, 41, 6631–6662, 2012.
- Kroll, J. H., Donahue, N. M., Jimenez, J. L., Kessler, S. H., Canagaratna, M. R., Wilson, K. R., Altieri, K. E., Mazzoleni, L. R., Wozniak, A. S., Bluhm, H., Mysak, E. R., Smith, J. D., Kolb, C. E., and Worsnop, D. R.: Carbon oxidation state as a metric for describing the chemistry of atmospheric organic aerosol, *Nature Chemistry*, 3, 133–139, 2011.
- Lei, T., Zuend, A., Wang, W. G., Zhang, Y. H., and Ge, M. F.: Hygroscopicity of organic compounds from biomass burning and their influence on the water uptake of mixed organic ammonium sulfate aerosols, *Atmos. Chem. Phys.*, 14, 11165–11183, doi:10.5194/acp-14-11165-2014, 2014.
- Lienhard, D. M., Bones, D. L., Zuend, A., Krieger, U. K., Reid, J. P., and Peter, T.: Measurements of thermodynamic and optical properties of selected aqueous organic and organic-inorganic mixtures of atmospheric relevance, *J. Phys. Chem. A*, 116, 9954–9968, 2012.
- Lienhard, D. M., Huisman, A. J., Bones, D. L., Te, Y.-F., Luo, B. P., Krieger, U. K., and Reid, J. P.: Retrieving the translational diffusion coefficient of water from experiments on single levitated aerosol droplets, *Phys. Chem. Chem. Phys.*, 16, 16677–16683, 2014.
- Liu, X. and Wang, J.: How important is organic aerosol hygroscopicity to aerosol indirect forcing?, *Environ. Res. Lett.*, 5, 044010, doi:10.1088/1748-9326/5/4/044010, 2010.
- Marcolli, C. and Krieger, U. K.: Phase changes during hygroscopicity cycles of mixed organic/inorganic model systems of tropospheric aerosols, *J. Phys. Chem. A*, 110, 1881–1893, 2006.
- Marcolli, C., Luo, B. P., Peter, Th., and Wienhold, F. G.: Internal mixing of the organic aerosol by gas phase diffusion of semivolatile organic compounds, *Atmos. Chem. Phys.*, 4, 2593–2599, doi:10.5194/acp-4-2593-2004, 2004.
- Massoli, P., Lambe, A. T., Ahern, A. T., Williams, L. R., Ehn, M., Mikkilä, J., Canagaratna, M. R., Brune, W. H., Onasch, T. B., Jayne, J. T., Petäjä, T., Kulmala, M., Laaksonen, A., Kolb, C. E., Davidovits, P., and Worsnop, D. R.: Relationships between aerosol oxidation level and hygroscopic properties of laboratory generated secondary organic aerosol (SOA) particles, *Geophys. Res. Lett.*, 37, L24801, doi:10.1029/2010GL045258, 2010.
- Mikhailov, E., Vlasenko, S., Martin, S. T., Koop, T., and Pöschl, U.: Amorphous and crystalline aerosol particles interacting with water vapor: conceptual framework and experimental evidence for restructuring, phase transitions and kinetic limitations, *Atmos. Chem. Phys.*, 9, 9491–9522, doi:10.5194/acp-9-9491-2009, 2009.
- Mochida, M. and Kawamura, K.: Hygroscopic properties of levoglucosan and related organic compounds characteristic to biomass burning aerosol particles, *J. Geophys. Res.*, 109, D21202, doi:10.1029/2004JD004962, 2004.
- Moore, R. H. and Raymond, T. M.: HTDMA analysis of multicomponent dicarboxylic acid aerosols with comparison to UNIFAC and ZSR, *J. Geophys. Res.*, 113, D04206, doi:10.1029/2007JD008660, 2008.
- Murphy, D. M., Cziczo, D. J., Froyd, K. D., Hudson, P. K., Matthew, B. M., Middlebrook, A. M., Peltier, R. E., Sullivan, A., Thomson, D. S., and Weber, R. J.: Single-particle mass spectrometry of tropospheric aerosol particles, *J. Geophys. Res.*, 111, D23S32, doi:10.1029/2006JD007340, 2006.
- Peters, M. D. and Kreidenweis, S. M.: A single parameter representation of hygroscopic growth and cloud condensation nucleus activity, *Atmos. Chem. Phys.*, 7, 1961–1971, doi:10.5194/acp-7-1961-2007, 2007.
- Pope, F. D., Harper, L., Dennis-Smith, B. J., Griffiths, P. T., Clegg, S. L., and Cox, R. A.: Laboratory and modeling study of the hygroscopic properties of two model humic acid aerosol particles, *J. Aerosol Sci.*, 41, 457–467, 2010.
- Pöhlker, C., Wiedemann, K. T., Sinha, B., Shiraiwa, M., Gunthe, S. S., Smith, M., Su, H., Artaxo, P., Chen, Q., Cheng, Y. F., Elbert, W., Gilles, M. K., Kilcoyne, A. L. D., Moffet, R. C., Weigand, M., Martin, S. T., Pöschl, U., and Andreae, M. O.: Biogenic potassium salt particles as seeds for secondary organic aerosol in the Amazon, *Science* 337, 1075–1078, 2012.

- Pöschl, U.: Atmospheric aerosols: composition, transformation, climate and health effects, *Angew. Chem. Int. Edit.*, 44, 7520–7540, doi:10.1002/anie.200501122, 2005.
- Prenni, A. J., DeMott, P. J., Kreidenweis, S. M., Sherman, D. E., Russell, L. M., and Ming, Y.: The effects of low molecular weight dicarboxylic acids on cloud formation, *J. Phys. Chem.*, 105, 11240–11248, 2001.
- Prenni, A. J., DeMott, P. J., and Kreidenweis, S. M.: Water uptake of internally mixed particles containing ammonium sulfate and dicarboxylic acids, *Atmos. Environ.*, 37, 4243–4251, 2003.
- Raatikainen, T. and Laaksonen, A.: Application of several activity coefficient models to water-organic-electrolyte aerosols of atmospheric interest, *Atmos. Chem. Phys.*, 5, 2475–2495, doi:10.5194/acp-5-2475-2005, 2005.
- Renbaum-Wolff, L., Grayson, J. W., Bateman, A. P., Kuwata, M., Sellier, M., Murray, B. J., Shilling, J. E., Martin, S. T., and Bertram, A. K.: Viscosity of  $\alpha$ -pinene secondary organic material and implications for particle growth and reactivity, *P. Natl. Acad. Sci.*, 110, 8014–8019, 2013.
- Robinson, C. B., Schill, G. P., and Tolbert, M. A.: Optical growth of highly viscous organic/sulfate particles, *J. Atmos. Chem.*, 71, 145–156, 2014.
- Saukko, E., Lambe, A. T., Massoli, P., Koop, T., Wright, J. P., Croasdale, D. R., Pedernera, D. A., Onasch, T. B., Laaksonen, A., Davidovits, P., Worsnop, D. R., and Virtanen, A.: Humidity-dependent phase state of SOA particles from biogenic and anthropogenic precursors, *Atmos. Chem. Phys.*, 12, 7517–7529, doi:10.5194/acp-12-7517-2012, 2012.
- Seinfeld, J. H. and Pandis S. N.: *Atmospheric Chemistry and Physics*, 2nd Edition, John Wiley & Sons, New York, NY, 2006.
- Seinfeld, J. H. and Pankow, J. F.: Organic atmospheric particulate matter, *Rev. Phys. Chem.*, 54, 121–140, 2003.
- Shiraiwa, M., Ammann, M., Koop, T., and Pöschl, U.: Gas uptake and chemical aging of organic aerosol particles, *P. Natl. Acad. Sci.*, 108, 11003–11008, 2011.
- Shiraiwa, M., Zuend, A., Bertram, A. K., and Seinfeld, J. H.: Gas-particle partitioning of atmospheric aerosols: interplay of physical state, non-ideal mixing and morphology, *Phys. Chem. Chem. Phys.*, 15, 1141–11453, 2013.
- Sjogren, S., Gysel, M., Weingartner, E., Baltensperger, U., Cubison, M. J., Coe, H., Zardini, A. A., Marcolli, C., Krieger, U. K., and Peter T.: Hygroscopic growth and water uptake kinetics of two-phase aerosol particles consisting of ammonium sulfate, adipic and humic acid mixtures, *J. Aerosol Sci.*, 38, 157–171, 2007.
- Song, M., Marcolli, C., Krieger, U. K., Zuend, A., and Peter, T.: Liquid-liquid phase separation and morphology of internally mixed dicarboxylic acids/ammonium sulfate/water particles, *Atmos. Chem. Phys.*, 12, 2691–2712, doi:10.5194/acp-12-2691-2012, 2012a.
- Song, M., Marcolli, C., Krieger, U. K., Zuend, A., and Peter, T.: Liquid-liquid phase separation: Dependence on O:C, organic functionalities, and compositional complexity, *Geophys. Res. Lett.*, 39, L19801, doi:10.1029/2012GL052807, 2012b.
- Song, M., Marcolli, C., Krieger, U. K., Lienhard, D. M., and Peter, T.: Morphologies of mixed organic/inorganic/aqueous aerosol droplets, *Faraday Discuss.*, 165, 289–316, 2014.
- Sorooshian, A., Hersey, S., Brechtel, F. J., Corless, A., Flagan, R. C., and Seinfeld, J. H.: Rapid, size-resolved aerosol hygroscopic growth measurements: Differential Aerosol Sizing and Hygroscopicity Spectrometer Probe (DASH-SP), *Aerosol Sci. Technol.*, 42, 445–464, 2008.
- Svenningsson, B., Rissler, J., Swietlicki, E., Mircea, M., Bilde, M., Facchini, M. C., Decesari, S., Fuzzi, S., Zhou, J., Mønster, J., and Rosenørn, T.: Hygroscopic growth and critical supersaturations for mixed aerosol particles of inorganic and organic compounds of atmospheric relevance, *Atmos. Chem. Phys.*, 6, 1937–1952, doi:10.5194/acp-6-1937-2006, 2006.
- Tang, I. N.: Deliquescence properties and particle size change of hygroscopic aerosols, in: *Generation of Aerosols and Facilities for Exposure Experiments*, edited by: Willekie, K., Ann Arbor Science Publishers, Ann Arbor, MI, 153–167, 1980.
- Tong, H.-J., Reid, J. P., Bones, D. L., Luo, B. P., and Krieger, U. K.: Measurements of the timescales for the mass transfer of water in glassy aerosol at low relative humidity and ambient temperature, *Atmos. Chem. Phys.*, 11, 4739–4754, doi:10.5194/acp-11-4739-2011, 2011.
- Vaden, T. D., Imre, D., Beranek, J., Shrivastava, M., and Zelenyuk, A.: Evaporation kinetics and phase of laboratory and ambient secondary organic aerosol, *P. Natl. Acad. Sci.*, 108, 2190–2195, 2011.
- Veghte, D. P., Altaf, M. B., and Freedman, M. A.: Size dependence of the structure of organic aerosol, *J. Am. Chem. Soc.*, 135, 16046–16049, 2013.
- Virtanen, A., Joutsensaari, J., Koop, T., Kannosto, J., Yli-Pirila, P., Leskinen, J., Makela, J. M., Holopainen, J. K., Pöschl, U., Kulmala, M., Worsnop, D. R., and Laaksonen A.: An amorphous solid state of biogenic secondary organic particles, *Nature*, 467, 824–827, 2010.
- Wise, M. W., Surratt, J. D., Curtis, D. B., Shilling, J. E., and Tolbert, M. A.: Hygroscopic growth of ammonium sulfate/dicarboxylic acids, *J. Geophys. Res.*, 108, 4638, doi:10.1029/2003JD003775, 2003.
- Xu, W., Guo, S., Gomez-Hernandez, M., Zambora, M. L., Secret, J., Marrero-Ortiz, W., Zhang, A. L., Collins, D. R., and Zhang, R.: Cloud forming potential of oligomers relevant to secondary organic aerosols, *Geophys. Res. Lett.*, 41, 6538–6545, 2014.
- You, Y. and Bertram, A. K.: Effects of molecular weight and temperature on liquid-liquid phase separation in particles containing organic species and inorganic salts, *Atmos. Chem. Phys.*, 15, 1351–1365, doi:10.5194/acp-15-1351-2015, 2015.
- You, Y., Renbaum-Wolff, L., Carreras-Sospedra, M., Hanna, S. J., Hiranuma, N., Kamal, S., Smith, M. L., Zhang, X. L., Weber, R. J., Shilling, J. E., Dabdub, D., Martin, S. T., and Bertram, A. K.: Images reveal that atmospheric particles can undergo liquid-liquid phase separations, *P. Natl. Acad. Sci.* 109, 13188–13193, 2012.
- You, Y., Renbaum-Wolff, L., and Bertram, A. K.: Liquid-liquid phase separation in particles containing organics mixed with ammonium sulfate, ammonium bisulfate, ammonium nitrate or sodium chloride, *Atmos. Chem. Phys.*, 13, 11723–11734, doi:10.5194/acp-13-11723-2013, 2013.
- You, Y., Smith, M. L., Song, M., Martin, S. T., and Bertram, A. K.: Liquid-liquid phase separation in atmospherically relevant particles consisting of organic species and inorganic salts, *Int. Rev. Phys. Chem.*, 33, 43–77, 2014.
- Yu, F., Luo, G., and Ma, X.: Regional and global modeling of aerosol optical properties with a size, composition, and mixing

- state resolved particle microphysics model, *Atmos. Chem. Phys.*, 12, 5719–5736, doi:10.5194/acp-12-5719-2012, 2012.
- Zardini, A. A., Sjogren, S., Marcolli, C., Krieger, U. K., Gysel, M., Weingartner, E., Baltensperger, U., and Peter, T.: A combined particle trap/HTDMA hygroscopicity study of mixed inorganic/organic aerosol particles, *Atmos. Chem. Phys.*, 8, 5589–5601, doi:10.5194/acp-8-5589-2008, 2008.
- Zaveri, R. A., Easter, R. C., Fast, J. D., and Peters, L. K.: Model for Simulating Aerosol Interactions and Chemistry (MOSAIC), *J. Geophys. Res.*, 113, D13204, doi:10.1029/2007JD008782, 2008.
- Zaveri, R. A., Easter, R. C., Shilling, J. E., and Seinfeld, J. H.: Modeling kinetic partitioning of secondary organic aerosol and size distribution dynamics: representing effects of volatility, phase state, and particle-phase reaction, *Atmos. Chem. Phys.*, 14, 5153–5181, doi:10.5194/acp-14-5153-2014, 2014.
- Zhang, Q., Canagaratna, M. R., Jayne, J. T., Worsnop, D. R., and Jimenez, J. L.: Time- and size-resolved chemical composition of submicron particles in Pittsburgh: Implications for aerosol sources and processes, *J. Geophys. Res.*, 110, D07S09, doi:10.1029/2004JD004649, 2005.
- Zobrist, B., Marcolli, C., Pedernera, D. A., and Koop, T.: Do atmospheric aerosols form glasses?, *Atmos. Chem. Phys.*, 8, 5221–5244, doi:10.5194/acp-8-5221-2008, 2008.
- Zobrist, B., Soonsin, V., Luo, B. P., Krieger, U. K., Marcolli, C., Peter, T., and Koop, T.: Ultra-slow water diffusion in aqueous sucrose glasses, *Phys. Chem. Chem. Phys.*, 13, 3514–3526, 2011.
- Zuend, A. and Seinfeld, J. H.: Modeling the gas-particle partitioning of secondary organic aerosol: the importance of liquid-liquid phase separation, *Atmos. Chem. Phys.*, 12, 3857–3882, doi:10.5194/acp-12-3857-2012, 2012.
- Zuend, A. and Seinfeld, J. H.: A practical method for the calculation of liquid-liquid equilibria in multicomponent organic-water-electrolyte systems using physiochemical constraints, *Fluid Phase Equilib.*, 337, 201–213, 2013.
- Zuend, A., Marcolli, C., Luo, B. P., and Peter, T.: A thermodynamic model of mixed organic-inorganic aerosols to predict activity coefficients, *Atmos. Chem. Phys.*, 8, 4559–4593, doi:10.5194/acp-8-4559-2008, 2008.
- Zuend, A., Marcolli, C., Peter, T., and Seinfeld, J. H.: Computation of liquid-liquid equilibria and phase stabilities: implications for RH-dependent gas/particle partitioning of organic-inorganic aerosols, *Atmos. Chem. Phys.*, 10, 7795–7820, doi:10.5194/acp-10-7795-2010, 2010.
- Zuend, A., Marcolli, C., Booth, A. M., Lienhard, D. M., Soonsin, V., Krieger, U. K., Topping, D. O., McFiggans, G., Peter, T., and Seinfeld, J. H.: New and extended parameterization of the thermodynamic model AIOMFAC: calculation of activity coefficients for organic-inorganic mixtures containing carboxyl, hydroxyl, carbonyl, ether, ester, alkenyl, alkyl, and aromatic functional groups, *Atmos. Chem. Phys.*, 11, 9155–9206, doi:10.5194/acp-11-9155-2011, 2011.